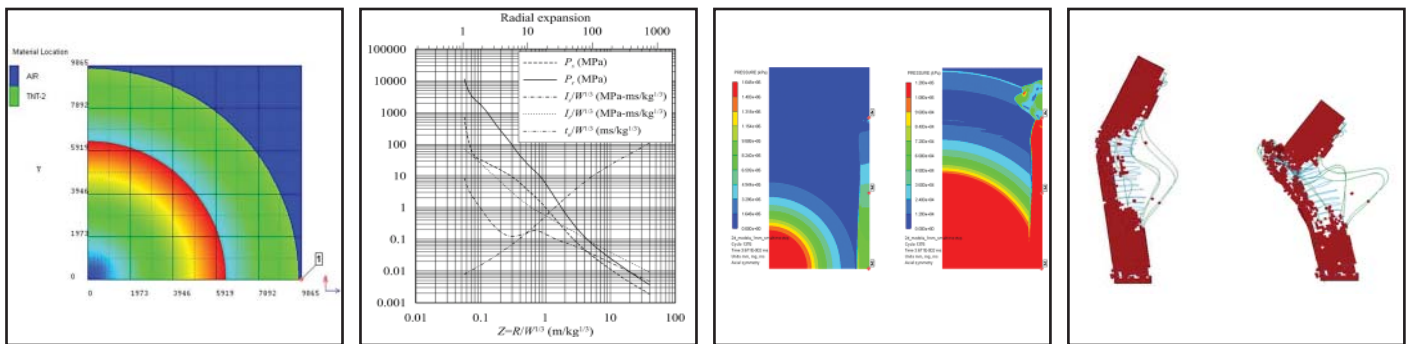


# Air-Blast Effects on Civil Structures

by  
 Jinwon Shin, Andrew S. Whittaker, Amjad J. Aref  
 and David Cormie



Technical Report MCEER-14-0006

October 30, 2014

## NOTICE

This report was prepared by the University at Buffalo, State University of New York, as a result of research sponsored by MCEER. Neither MCEER, associates of MCEER, its sponsors, the University at Buffalo, State University of New York, nor any person acting on their behalf:

- a. makes any warranty, express or implied, with respect to the use of any information, apparatus, method, or process disclosed in this report or that such use may not infringe upon privately owned rights; or
- b. assumes any liabilities of whatsoever kind with respect to the use of, or the damage resulting from the use of, any information, apparatus, method, or process disclosed in this report.

Any opinions, findings, and conclusions or recommendations expressed in this publication are those of the author(s) and do not necessarily reflect the views of MCEER or other sponsors.

## Air-Blast Effects on Civil Structures

by

Jinwon Shin,<sup>1</sup> Andrew S. Whittaker,<sup>2</sup> Amjad J. Aref<sup>3</sup> and David Cormie<sup>4</sup>

Publication Date: October 30, 2014

Submittal Date: July 24, 2014

Technical Report MCEER-14-0006

MCEER Thrust Area 3, Innovative Technologies

- 1 Research Fellow, Department of Civil, Structural and Environmental Engineering, University at Buffalo, State University of New York
- 2 Professor, Chair, and MCEER Director, Department of Civil, Structural and Environmental Engineering; University at Buffalo, State University of New York
- 3 Professor, Department of Civil, Structural and Environmental Engineering, University at Buffalo, State University of New York
- 4 Associate Director, Resilience, Security and Risk, Arup, London, United Kingdom

MCEER

University at Buffalo, State University of New York

212 Ketter Hall, Buffalo, NY 14260

E-mail: [mceer@buffalo.edu](mailto:mceer@buffalo.edu); Website: <http://mceer.buffalo.edu>

---



## Preface

MCEER is a national center of excellence dedicated to the discovery and development of new knowledge, tools and technologies that equip communities to become more disaster resilient in the face of earthquakes and other extreme events. MCEER accomplishes this through a system of multidisciplinary, multi-hazard research, in tandem with complimentary education and outreach initiatives.

Headquartered at the University at Buffalo, The State University of New York, MCEER was originally established by the National Science Foundation in 1986, as the first National Center for Earthquake Engineering Research (NCEER). In 1998, it became known as the Multidisciplinary Center for Earthquake Engineering Research (MCEER), from which the current name, MCEER, evolved.

Comprising a consortium of researchers and industry partners from numerous disciplines and institutions throughout the United States, MCEER's mission has expanded from its original focus on earthquake engineering to one which addresses the technical and socio-economic impacts of a variety of hazards, both natural and man-made, on critical infrastructure, facilities, and society.

The Center derives support from several Federal agencies, including the National Science Foundation, Federal Highway Administration, National Institute of Standards and Technology, Department of Homeland Security/Federal Emergency Management Agency, and the State of New York, other state governments, academic institutions, foreign governments and private industry.

The overarching goal of the research described in this report is to characterize the effects of detonations of high explosives, inside and in the immediate vicinity of the fireball. A computational fluid dynamics code is verified in 1D and validated in 2D for air blast calculations. The code is used to develop recommendations for modeling the effects of explosions in the near field, to generate new design charts appropriate for near-field air-blast calculations, and to update design charts for reflection coefficients for peak overpressure and for scaled impulse as a function of angle of incidence. Recommendations are provided for calculating values of erosion strain for finite element analysis of reinforced concrete components subjected to near-field air-blast loadings.



## ABSTRACT

The effects of detonations of high explosives are the focus of this report. Analyses are performed using computational fluid dynamics (CFD) and finite element codes, theoretical formulations and empirical data.

The effects of detonations of high explosives are characterized in terms of incident and reflected overpressures and impulses. Calculations are performed to verify and validate a CFD code in 1D and 2D; estimate blast effects using 1D models; predict incident overpressures and impulses; provide guidance on the use of reflecting and transmitting boundaries in 2D and 3D models, and provide recommendations on cell size for CFD analysis. The complex wave field in the Mach stem region is studied.

Air-blast parameters, including incident and reflected peak overpressures and impulses, and shock-front arrival times, are typically estimated for protective design using charts developed by Kingery and Bulmash. The charts underpredict incident and normally reflected peak overpressures and incident impulse near the face of the charge. Numerical analyses of detonations of spherical charges of TNT in free air are performed to understand the shortcomings of current approaches and to provide data for the development of new equations and design charts for incident and normally reflected overpressures and impulses and for shock-front arrival time.

Reflection coefficients are often used to transform incident to reflected peak overpressures for varying angles of incidence. Values for the reflection coefficient are available in textbooks and technical manuals but these values vary by document, especially in the region of Mach reflection. Numerical studies are presented to resolve differences between the documents. The corresponding reflected scaled impulses are also evaluated. Recommendations for design practice are provided.

Material erosion is often used for simulations of extreme damage to structural components, and elements are eroded from a finite element mesh based on user-specified criteria. Single element simulations of concrete are performed to establish reliable values of concrete erosion strain as a

function of strain rate, compressive strength, element size and loading condition. Numerical simulations of a sample reinforced concrete column subjected to blast loadings are undertaken to demonstrate the utility of the proposed erosion criteria and to characterize, for a single case, the importance of concrete compressive strength, transverse reinforcement, and axial load on estimations of damage.

## **ACKNOWLEDGMENTS**

Financial support for this work was provided by MCEER and the State of New York under Thrust Area 3, Innovative Technologies. This support is gratefully acknowledged. Any opinions, findings, conclusions or recommendations expressed in this report are those of the authors and do not necessarily reflect the views of MCEER, the State of New York, or other sponsors.

The authors would like to express their most sincere gratitude to Professor Gray Dargush of the University at Buffalo for his careful review of this report.



# TABLE OF CONTENTS

SECTION	TITLE	PAGE
<b>SECTION 1</b>	<b>BLAST ANALYSIS OF STRUCTURES .....</b>	<b>1</b>
1.1	Introduction .....	1
1.2	State of Practice .....	2
1.3	Goals of the Report.....	4
1.4	Notation and Definitions .....	5
1.5	Report Organization .....	8
<b>SECTION 2</b>	<b>MODELING NEAR-FIELD DETONATIONS OF HIGH EXPLOSIVES .</b>	<b>11</b>
2.1	Introduction .....	11
2.2	Modeling Detonations in AUTODYN .....	12
2.3	Verification and Validation of AUTODYN .....	16
2.3.1	Introduction .....	16
2.3.2	Verification of AUTODYN in 1D for Near-Field Detonations .....	17
2.3.3	Verification of AUTODYN in 1D and 2D for Far-Field Detonations .....	54
2.3.4	Validation of AUTODYN in 2D for Near-Field Detonations .....	62
2.3.5	Validation of AUTODYN in 2D for Far-Field Detonations .....	69
2.4	One-Dimensional Blast Wave Propagation.....	72
2.4.1	Introduction .....	72
2.4.2	Mesh Sensitivity Study.....	72
2.4.3	Temperature in the Vicinity of the Charge Face .....	80
2.4.4	Afterburning .....	88
2.4.5	Blast Wave Propagation in AUTODYN and Air3D .....	97
2.4.6	Equations of State.....	108
2.5	Two-Dimensional Blast Wave Propagation .....	111
2.6	Three-Dimensional Wave Propagation .....	130
2.7	Air-Blast Loadings on Sample Reinforced Concrete Columns.....	144
2.7.1	Introduction .....	144
2.7.2	Square Column, Model VI .....	145
2.7.3	Circular Column, Model VII.....	156
2.7.4	Influence of Target Shape on Air-Blast Loadings.....	164
<b>SECTION 3</b>	<b>INCIDENT AND NORMALLY REFLECTED OVERPRESSURE AND IMPULSE FOR DETONATIONS IN FREE AIR .....</b>	<b>173</b>
3.1	Blast-Resistant Design.....	173
3.2	Air-Blast Parameter Studies .....	173
3.2.1	Kingery and Pannill, 1964: Hemispherical TNT Surface Bursts .....	173

## TABLE OF CONTENTS (CONT'D)

SECTION	TITLE	PAGE
3.2.2	Kingery, 1966: Hemispherical TNT Surface Bursts .....	174
3.2.3	Kingery and Bulmash, 1984: Spherical Free Air and Hemispherical Surface Bursts of TNT .....	175
3.2.4	Implementation in UFC 3-340-02 using Design Charts.....	177
3.3	Studies by Swisdak and Bogosian et al. ....	177
3.4	Evaluation of the KB Charts.....	178
3.5	Numerical Studies .....	179
3.5.1	Spherical Charges used for Numerical Analysis .....	179
3.5.2	Overpressures, Particle Velocities and Accelerations Near the Charge Face ...	180
3.5.3	Mesh Sensitivity Analysis .....	188
3.6	Incident Overpressure and Impulse .....	199
3.6.1	Results and Observations .....	199
3.6.2	Cell Size for CFD Analysis .....	211
3.7	Reflected Overpressure and Impulse.....	212
3.7.1	Results and Observations .....	212
3.7.2	Cell Size for CFD Analysis .....	221
3.8	Shock Front Arrival Time .....	222
<b>SECTION 4</b>	<b>DESIGN CHARTS AND POLYNOMIALS FOR AIR-BLAST PARAMETERS .....</b>	<b>225</b>
4.1	Introduction .....	225
4.2	Accuracy of KB and Numerical Predictions of Blast Parameters.....	225
4.2.1	Incident Peak Overpressure and Impulse .....	225
4.2.2	Normally Reflected Peak Overpressure and Impulse.....	226
4.2.3	Shock Front Arrival Time .....	226
4.3	Updated Polynomials and Charts for Overpressure, Impulse and Arrival Time.....	226
4.3.1	Charts for Design.....	226
4.3.2	Polynomials .....	228
4.3.3	Sample Results .....	237
4.3.4	Use of Design Charts and Considerations of Non-Ideal Explosives.....	237
<b>SECTION 5</b>	<b>REFLECTED OVERPRESSURE AND IMPULSE AS A FUNCTION OF ANGLE OF INCIDENCE .....</b>	<b>243</b>
5.1	Introduction .....	243
5.2	Regular and Mach Reflections .....	250
5.3	A Numerical Model for Calculating Reflection Coefficients.....	253

## TABLE OF CONTENTS (CONT'D)

SECTION	TITLE	PAGE
5.3.1	Modeling and Domains .....	253
5.3.2	Cell Size.....	255
5.4	Numerical Models for Calculating Reflected Impulses .....	255
5.4.1	Modeling and Domains .....	255
5.4.2	Cell Size.....	258
5.4.3	Effect of Transmitting Boundary.....	260
5.5	Incident and Normally Reflected Overpressures.....	267
5.6	Reflected Overpressure as a Function of Angle of Incidence .....	267
5.7	Incident and Normally Reflected Impulses .....	280
5.8	Reflected Impulse as a Function of Angle of Incidence.....	284
<b>SECTION 6</b>	<b>MODELING CONCRETE EROSION STRAIN FOR BLAST ANALYSIS OF STRUCTURAL COMPONENTS .....</b>	<b>295</b>
6.1	Introduction .....	295
6.2	Criteria for Eroding Elements .....	297
6.3	Wave Passage Effects in Reinforced Concrete Columns .....	301
6.4	Material Models.....	309
6.4.1	Concrete.....	309
6.4.2	Steel Reinforcement .....	315
6.5	Single Element Simulations .....	319
6.6	Blast Analysis of a Sample Reinforced Concrete Column.....	329
6.6.1	Introduction .....	329
6.6.2	Blast Loading.....	330
6.6.3	Mesh Convergence Study.....	331
6.6.4	Values of Concrete Erosion Strain .....	333
6.6.5	Simulation Results.....	335
6.6.6	Alternate Concrete Material Models, Influence of Concrete Compressive Strength, Confinement, and Axial Pressure Loading .....	346
6.7	Values of Erosion Strain for Near-Field Blast Analysis .....	366
<b>SECTION 7</b>	<b>SUMMARY AND CONCLUSIONS.....</b>	<b>367</b>
7.1	Summary.....	367
7.2	Conclusions .....	369
<b>SECTION 8</b>	<b>REFERENCES .....</b>	<b>373</b>
<b>APPENDIX A</b>	<b>SPEED OF SOUND.....</b>	<b>385</b>

## TABLE OF CONTENTS (CONT'D)

SECTION	TITLE	PAGE
A.1	Introduction .....	385
A.2	Determination of Speed of Sound in Solids and Fluids .....	385
<b>APPENDIX B DETONATION WAVE AND PRESSURE.....</b>		<b>387</b>
B.1	Introduction .....	387
B.2	Hugoniot Curves and Rayleigh Line for the Detonation Front .....	388
<b>APPENDIX C INCIDENT AND REFLECTED OVERPRESSURES VERY CLOSE TO THE CHARGE FACE .....</b>		<b>393</b>
C.1	Introduction .....	393
C.2	AUTODYN Results.....	393
<b>APPENDIX D KINGERY AND BULMASH CHARTS .....</b>		<b>397</b>
<b>APPENDIX E CSCM MODEL PARAMETERS IN LS-DYNA .....</b>		<b>401</b>
<b>APPENDIX F SINGLE-DEGREE-OF-FREEDOM (SDOF) CALCULATIONS FOR STRAIN RATE.....</b>		<b>403</b>
F.1	Introduction .....	403
F.2	SDOF Calculations.....	404

## LIST OF FIGURES

FIGURE	TITLE	PAGE
2-1	JWL and ideal gas EOS for TNT.....	15
2-2	Hydrodynamic parameters at $\bar{r} = 1.1$ for a 20 mm mesh.....	19
2-3	Hydrodynamic parameters at $\bar{r} = 2.4$ for a 20 mm mesh.....	20
2-4	Hydrodynamic parameters at $\bar{r} = 2.6$ for a 20 mm mesh.....	21
2-5	Hydrodynamic parameters at $\bar{r} = 4.5$ for a 20 mm mesh.....	22
2-6	Hydrodynamic parameters at $\bar{r} = 8$ for a 20 mm mesh.....	23
2-7	Hydrodynamic parameters at $\bar{r} = 11.7$ for a 20 mm mesh.....	24
2-8	Hydrodynamic parameters at $\bar{r} = 18$ for a 20 mm mesh.....	25
2-9	Hydrodynamic parameters at $\bar{r} = 26$ for a 20 mm mesh.....	26
2-10	Hydrodynamic parameters at $\bar{r} = 34$ for a 20 mm mesh.....	27
2-11	Hydrodynamic parameters for a 20 mm mesh in AUTODYN (cont.).....	30
2-12	Acceleration histories at discrete points along the 1D expansion.....	31
2-13	Histories of hydrodynamic parameters at $\bar{r} = 1.1$ for a 20 mm mesh.....	33
2-14	Histories of hydrodynamic parameters at $\bar{r} = 2.4$ for a 20 mm mesh.....	34
2-15	Histories of hydrodynamic parameters at $\bar{r} = 2.6$ for a 20 mm mesh.....	35
2-16	Histories for hydrodynamic parameters at $\bar{r} = 4.5$ for a 20 mm mesh.....	36
2-17	Histories of hydrodynamic parameters at $\bar{r} = 8$ for a 20 mm mesh.....	37
2-18	Histories of hydrodynamic parameters at $\bar{r} = 11.7$ for a 20 mm mesh.....	38
2-19	Histories of hydrodynamic parameters at $\bar{r} = 18$ for a 20 mm mesh.....	39
2-20	Histories of hydrodynamic parameters at $\bar{r} = 26$ for a 20 mm mesh.....	40
2-21	Histories of hydrodynamic parameters at $\bar{r} = 34$ for a 20 mm mesh.....	41
2-22	Mesh convergence study at $\bar{r} = 0.5$ .....	44
2-23	Mesh convergence study at $\bar{r} = 0.9$ .....	45
2-24	Mesh convergence study for $\bar{r} = 1.1$ .....	46
2-25	Mesh convergence study for $\bar{r} = 2.4$ .....	47
2-26	Mesh convergence study for $\bar{r} = 2.6$ .....	48
2-27	Overpressure histories at distance, $r$ , from the center of a spherical charge of 18735 kg of TNT; JWL EOS.....	49
2-28	Impulse histories at distance, $r$ , from the center of a spherical charge of 18735 kg of TNT; JWL EOS.....	52
2-29	Incident overpressure and impulse histories from AUTODYN; $Z = 3, 4$ and $5 \text{ ft/lb}^{1/3}$ ; cell sizes = 1, 2 and 3 in.....	58
2-30	Incident peak overpressure and impulse from AUTODYN; $Z = 3, 4$ and $5 \text{ ft/lb}^{1/3}$ ; cell sizes = 1, 2 and 3 in.....	59

## LIST OF FIGURES (CONT'D)

FIGURE	TITLE	PAGE
2-31	Summary of AUTODYN (this study) and LS-DYNA and CTH (Browning et al.) results for incident peak overpressure .....	60
2-32	Summary of AUTODYN (this study) and LS-DYNA and CTH (Browning et al.) results for incident impulse.....	61
2-33	Incident and normally reflected overpressure and impulse histories calculated using AUTODYN for 50/50 Pentolite of 1 kg; $Z = 0.08 \text{ m/kg}^{1/3}$ ; ( $Z = 0.20 \text{ ft/lb}^{1/3}$ ); $\bar{r} = 1.52$ .....	65
2-34	Incident and reflected normally overpressure and impulse histories calculated using AUTODYN for 50/50 Pentolite of 1 kg; $Z = 0.12 \text{ m/kg}^{1/3}$ ; ( $Z = 0.30 \text{ ft/lb}^{1/3}$ ); $\bar{r} = 2.28$ .....	66
2-35	Incident and normally reflected overpressure and impulse histories calculated using AUTODYN for 50/50 Pentolite of 1 kg; $Z = 0.16 \text{ m/kg}^{1/3}$ ; ( $Z = 0.40 \text{ ft/lb}^{1/3}$ ); $\bar{r} = 3.04$ . .....	67
2-36	Incident and normally reflected overpressure and impulse histories calculated using AUTODYN for 50/50 Pentolite of 1 kg; $Z = 0.20 \text{ m/kg}^{1/3}$ ; ( $Z = 0.50 \text{ ft/lb}^{1/3}$ ); $\bar{r} = 3.80$ .....	68
2-37	Comparison between AUTODYN calculations and measurements of Goodman (1960) and Huffington and Ewing (1985) for normally reflected scaled impulses... ..	68
2-38	Incident and normally reflected overpressure and impulse histories calculated using AUTODYN for C4 of 1 kg; $Z = 1.2 \text{ m/kg}^{1/3}$ ( $r = 1.2 \text{ m}$ ).....	70
2-39	Incident and normally reflected overpressure and impulse histories calculated using AUTODYN for C4 of 0.5 kg; $Z = 1.51 \text{ m/kg}^{1/3}$ ( $r = 1.2 \text{ m}$ ).....	71
2-40	Comparison between AUTODYN calculations and Frost et al. measurements (2008) for normally reflected peak overpressure, $P_r$ , and scaled impulse, $I_r/W^{1/3}$ ; $Z = 1.2$ and $1.51 \text{ m/kg}^{1/3}$ .....	71
2-41	Overpressure histories at distance, $r$ , from the center of a spherical charge of 22.68 kg of TNT; JWL EOS; no afterburning.....	74
2-42	Overpressure histories at distance, $r$ , from the center of a spherical charge of 22.68 kg of TNT; JWL EOS; no afterburning.....	77
2-43	Overpressure histories at distance, $r$ , from the center of a spherical charge of 22.68 kg of TNT; JWL EOS; no afterburning (cont.) .....	80
2-44	Overpressure, density and temperature histories at $Z = 0.054 \text{ m/kg}^{1/3}$ ; spherical charge of 22.68 kg of TNT; JWL EOS; 0.5 mm mesh.....	82
2-45	Overpressure, density and temperature histories at $Z = 0.058 \text{ m/kg}^{1/3}$ ; spherical charge of 22.68 kg of TNT; JWL EOS; 0.5 mm mesh.....	83
2-46	Overpressure, density and temperature histories at $Z = 0.071 \text{ m/kg}^{1/3}$ ; spherical charge of 22.68 kg of TNT; JWL EOS; 0.5 mm mesh.....	84

## LIST OF FIGURES (CONT'D)

FIGURE	TITLE	PAGE
2-47	Overpressure, density and temperature histories at $Z = 0.088 \text{ m/kg}^{1/3}$ ; spherical charge of 22.68 kg of TNT; JWL EOS; 0.5 mm mesh .....	85
2-48	Overpressure, density and temperature histories at $Z = 0.177 \text{ m/kg}^{1/3}$ ; spherical charge of 22.68 kg of TNT; JWL EOS; 0.5 mm mesh .....	86
2-49	Overpressure, density and temperature histories at $Z = 0.353 \text{ m/kg}^{1/3}$ ; spherical charge of 22.68 kg of TNT; JWL EOS; 0.5 mm mesh .....	87
2-50	Variation of temperature with radial expansion of detonation product .....	88
2-51	Input of afterburning energy with time for 22.68 kg of TNT .....	90
2-52	Weight of TNT for volumes of air to release maximum afterburning energy .....	92
2-53	Available volumes of air for radial expansion of detonation products .....	92
2-54	Overpressure histories at distance, $r$ , from the center of a spherical charge of 22.68 kg of TNT for a 0.5 mm mesh; JWL EOS; 129 MJ afterburning .....	93
2-55	Impulse histories at distance, $r$ , from the center of a spherical charge of 22.68 kg of TNT for a 0.5 mm mesh; JWL EOS; 129 MJ afterburning .....	95
2-56	Overpressure histories as a function of time after detonation at distance $x (= r)$ from the center of a spherical charge of 22.68 kg of TNT for a 0.5 mm mesh; JWL EOS; no afterburning .....	99
2-57	Air3D overpressure histories as a function of distance and time after detonation for a spherical charge of 22.68 kg of TNT for a 0.5 mm mesh; ideal gas EOS .....	104
2-58	Influence of EOS on overpressure histories as a function of distance and time after detonation for a spherical charge of 22.68 kg of TNT for a 0.5 mm mesh .....	109
2-59	Effect of boundary condition; spherical charge of TNT of 22.68 kg; 0.5 mm cells; Model I-I .....	112
2-60	AUTODYN analysis results for 1D and 2D (I-I with the left transmitting boundary) models; spherical charge of 22.68 kg of TNT; 0.5 mm mesh; monitoring location 1; 114	
2-61	Effect of boundary condition; spherical charge of TNT of 22.68 kg; 0.5 mm cells; Model I-II .....	115
2-62	Effect of boundary condition; spherical charge of TNT of 22.68 kg; 0.5 mm cells; Model I-III and Model I-IV .....	117
2-63	Reflected overpressure histories on a vertical reflecting surface; Model II; spherical charge of 22.68 kg of TNT; JWL EOS; varying mesh size .....	123
2-64	Pressure fringes as a function of time; Model I; spherical charge of 22.68 kg of TNT; JWL EOS; TNT density = $1636.8 \text{ kg/m}^3$ ; 1.0 mm mesh .....	125
2-65	Reflected overpressure histories on a vertical reflecting surface; Model III; spherical charge of 22.68 kg of TNT; JWL EOS; varying mesh size .....	128

## LIST OF FIGURES (CONT'D)

FIGURE	TITLE	PAGE
2-66	Reflected overpressure histories on a vertical reflecting surface; Model IV; spherical charge of 22.68 kg of TNT; JWL EOS; 4 mm mesh (4.027 mm for $y = 149$ mm); varying perpendicular dimension, $y$ .....	132
2-67	Reflected overpressure histories on a vertical reflecting surface; Model II and Model IV; spherical charge of 22.68 kg of TNT; JWL EOS; $y = 100$ mm for 3D analysis	135
2-68	Reflected overpressure histories on a vertical reflecting surface; Model II and Model IV; spherical charge of 22.68 kg of TNT; JWL EOS; $y = 200$ mm for 3D analysis	137
2-69	Reflected overpressure histories on a vertical reflecting surface; Model II and Model IV; spherical charge of 22.68 kg of TNT; JWL EOS; 2 mm mesh .....	139
2-70	Reflected overpressure histories on a vertical reflecting surface; Model V; spherical charge of 22.68 kg of TNT; JWL EOS; $y = 200$ mm .....	141
2-71	Reflected overpressure histories on a vertical reflecting surface; Model V; spherical charge of 22.68 kg of TNT; JWL EOS; 2 mm and 4 mm meshes.....	142
2-72	Model VI; spherical charge of 22.68 kg of TNT; square column 1000×1000 mm	146
2-73	Monitoring locations for Model VI; spherical charge of 22.68 kg of TNT; square column 1000×1000 mm .....	147
2-74	Reflected overpressure histories; Model VI; spherical charge of 22.68 kg of TNT; JWL EOS .....	148
2-75	Net loading and impulse histories; Model VI.....	153
2-76	Comparison of reflected overpressure histories from Models V and VI.....	154
2-77	Model VII; spherical charge of 22.68 kg of TNT; 1000 mm diameter column .....	157
2-78	Monitoring locations for Model VII; spherical charge of 22.68 kg of TNT; 1000 mm diameter column .....	158
2-79	Reflected overpressure histories; Model VII; spherical charge of 22.68 kg of TNT; JWL EOS .....	159
2-80	Net load and impulse histories; Model VII; spherical charge of 22.68 kg of TNT; JWL EOS .....	163
2-81	Reflected overpressure histories at 0 mm above the ground surface; Models VI and VII; spherical charge of 22.68 kg of TNT; JWL EOS.....	164
2-82	Reflected overpressure histories at 149 mm above the ground surface; Models VI and VII; spherical charge of 22.68 kg of TNT; JWL EOS .....	167
2-83	Reflected overpressure histories at 298 mm above the ground surface; Models VI and VII; spherical charge of 22.68 kg of TNT; JWL EOS .....	169
2-84	Reflected overpressure histories at 447 mm above the ground surface; Models VI and VII; spherical charge of 22.68 kg of TNT; JWL EOS .....	171

## LIST OF FIGURES (CONT'D)

FIGURE	TITLE	PAGE
3-1	Incident overpressures and particle velocities and accelerations near the face of the charge ; TNT weight of 23 kg; 0.1 mm cells.....	182
3-2	Incident overpressures and particle velocities and accelerations near the face of the charge ; TNT weight of 23 kg; 0.05 mm cells.....	183
3-3	Incident overpressures and particle velocities and accelerations near the face of the charge ; TNT weight of 23 kg; 0.1 and 0.05 mm cells .....	184
3-4	Incident overpressures and particle velocities and accelerations near the face of the charge; TNT weight of 960 kg; 0.1 mm cells.....	185
3-5	Incident overpressures and particle velocities and accelerations near the face of the charge; TNT weight of 960 kg; 0.05 mm cells.....	186
3-6	Incident overpressures and particle velocities and accelerations near the face of the charge; TNT weight of 960 kg; 0.1 and 0.05 mm cells .....	187
3-7	AUTODYN 2D simulation using 1D remapped data for $Z = 1.0 \text{ m/kg}^{1/3}$ .....	194
3-8	Ratios of incident peak overpressure for different cell sizes; $0.0553 \leq Z < 40.0 \text{ m/kg}^{1/3}$ .....	200
3-9	Ratios of incident impulse for different cell sizes; $0.0553 \leq Z < 40.0 \text{ m/kg}^{1/3}$ .....	201
3-10	Ratios of incident peak overpressure and impulse for the fine meshes; charge weights of 18735, 960 and 23 kg; $0.0553 \leq Z < 40.0 \text{ m/kg}^{1/3}$ .....	202
3-11	Incident peak overpressure versus scaled distance.....	203
3-12	Incident impulse versus scaled distance .....	207
3-13	Ratios of reflected peak overpressure for different cell sizes; $0.0553 \leq Z < 40.0 \text{ m/kg}^{1/3}$ .....	213
3-14	Ratios of reflected impulse for different cell sizes; $0.0553 \leq Z < 40.0 \text{ m/kg}^{1/3}$ .....	214
3-15	Ratios of reflected peak overpressure and impulse for the smallest cell sizes; charge weights of 18735, 960 and 23 kg; $0.0553 \leq Z < 40.0 \text{ m/kg}^{1/3}$ .....	215
3-16	Normally reflected peak overpressure versus scaled distance.....	216
3-17	Normally reflected impulse versus scaled distance.....	219
3-18	AUTODYN calculations and KB predictions for specific arrival time.....	222
3-19	Ratios of AUTODYN calculations and KB predictions of specific arrival time ....	223
3-20	Effect of charge weight on specific arrival times calculations: 18735, 960 and 23 kg charges .....	223
4-1	Spherical charge and radial expansions, $\bar{r}$ , of 1.025, 1.050 and 1.100.....	227
4-2	Incident peak overpressure impulse and arrival time, spherical free-air bursts .....	233
4-3	Reflected peak overpressure and impulse, spherical free-air bursts.....	234
4-4	Proposed polynomial charts in SI units, spherical free-air bursts .....	235

## LIST OF FIGURES (CONT'D)

FIGURE	TITLE	PAGE
4-5	Proposed polynomial charts in US units, spherical free-air bursts .....	236
4-6	Use of the proposed polynomials and charts .....	240
5-1	Shock wave reflection phenomena from explosion in free air (adapted from Norris et al. 1959) .....	244
5-2	Reflection coefficient versus angle of incidence .....	246
5-3	Reflected scaled impulse versus angle of incidence (UFC 3-340-02 (DoD 2008)) .....	247
5-4	Incident, $P_s$ , and normally reflected, $P_r$ , peak overpressures developed by Kingery and Bulmash (1984) and in Chapter 4 .....	248
5-5	Incident, $I_s/W^{1/3}$ , and normally reflected, $I_r/W^{1/3}$ , scaled impulses developed by Kingery and Bulmash (1984) and in Chapter 4 .....	249
5-6	Regular and Mach reflections (e.g., Smith and Hetherington 1994) .....	250
5-7	Dual solution domain (Ivanov et al. 2001) .....	251
5-8	Angle of incidence for Mach reflection as a function of Mach number for an ideal gas (Kinney and Graham 1985) .....	252
5-9	Incident overpressure as a function of Mach number for an ideal gas (Kinney and Graham 1985) .....	252
5-10	2D numerical model of air for calculating reflection coefficients .....	255
5-11	2D numerical models of air for calculating reflected impulses .....	257
5-12	Models 1, 2 and 3 in AUTODYN for angle of incidence of 80° .....	258
5-13	Mesh sensitivity study for simulating reflected impulse; Model 1 .....	259
5-14	Effect of transmitting boundary on calculation of reflected impulse for $Z = 0.16$ m/kg <sup>1/3</sup> .....	261
5-15	Effect of transmitting boundary on calculation of reflected impulse for $Z = 0.40$ m/kg <sup>1/3</sup> .....	263
5-16	Effect of transmitting boundary on calculation of reflected impulse for $Z = 1.2$ m/kg <sup>1/3</sup> .....	265
5-17	Incident and normally reflected peak overpressures .....	268
5-18	Overpressure reflection coefficients as a function of angle of incidence .....	272
5-19	Reflected overpressure histories; $Z = 0.16, 0.40, 0.80$ and $1.2$ m/kg <sup>1/3</sup> ( $1$ m/kg <sup>1/3</sup> = $2.52$ ft/lb <sup>1/3</sup> ; $1$ MPa = $145$ psi) .....	276
5-20	Overpressure reflection coefficients with angle of incidence from TM 5-858-3 (DoA 1984), UFC 3-340-02 (DoD 2008), numerical analyses by AUTODYN; $P_s$ in units of MPa .....	278
5-21	Incident and normally reflected scaled impulses .....	281

## LIST OF FIGURES (CONT'D)

FIGURE	TITLE	PAGE
5-22	Reflected scaled impulse as a function of angle of incidence ( $Z$ in units of $\text{m/kg}^{1/3}$ ).... .....	285
5-23	Reflected overpressure and scaled impulse histories for cell sizes of $R/400$ and $R/800$ ; $\alpha = 30^\circ, 40^\circ, 45^\circ, 50^\circ$ and $55^\circ$ ; $Z = 0.16 \text{ m/kg}^{1/3}$ .....	287
5-24	Reflected overpressure and scaled impulse histories for cell sizes of $R/400$ and $R/800$ ; $\alpha = 30^\circ, 40^\circ, 45^\circ, 50^\circ$ and $55^\circ$ ; $Z = 0.40 \text{ m/kg}^{1/3}$ .....	288
5-25	Reflected overpressure and scaled impulse histories for cell sizes of $R/400$ and $R/800$ ; $\alpha = 30^\circ, 40^\circ, 45^\circ, 50^\circ$ and $55^\circ$ ; $Z = 1.2 \text{ m/kg}^{1/3}$ .....	289
5-26	Pressure fringes at $t = 1.0 \text{ ms}$ for $Z = 0.4 \text{ m/kg}^{1/3}$ ; $R/800$ cells .....	291
5-27	Reflected scaled impulse as a function of angle of incidence; $P_s$ in units of MPa. ....	292
6-1	Reinforced concrete column (units in meters).....	302
6-2	Rectangular pulse used for the elastic simulation of the sample RC column.....	303
6-3	Cross section at the mid-height of the sample RC column.....	304
6-4	Stress histories in the $x$ -direction for elements No. 1, 3 and 7 .....	304
6-5	Stress histories in the $x$ -direction for elements No. 4, 5, 6 and 7 .....	304
6-6	Cross section at the mid-height of the 1.2-m-deep column .....	306
6-7	Comparison of stress histories of elements No. 1 through 7 in the $x$ -direction between 0.6-m- and 1.2-m-deep columns (cont.) .....	308
6-8	Differences in the stress histories of elements No. 4, 5, 6 and 7 in the $x$ -direction between the 0.6-m- and 1.2-m-deep columns.....	308
6-9	Dynamic Increase Factor for compressive and tensile strength of concrete .....	310
6-10	General shape of the CSCM yield surface (Murray 2007).....	310
6-11	Stress-strain relationship for Grade 60 rebar at a strain rate of $5 \times 10^{-4} \text{ s}^{-1}$ .....	317
6-12	Compressive stress–strain curves for concrete models of the CSCM and by Popovics (1970) for the compressive strength of 35.5 MPa .....	319
6-13	Loading conditions used in single element simulations when the peak tensile load = 10 MPa.....	320
6-14	Time step convergence analysis for an element size of $40 \times 40 \times 40 \text{ mm}$ .....	322
6-15	Erosion strain versus traction rate in single element simulations for different peak tensile tractions, $f'_c = 35.5 \text{ MPa}$ .....	323
6-16	Erosion strain versus traction rate in single element simulations for different peak tensile tractions, $f'_c = 50 \text{ MPa}$ .....	325
6-17	Erosion strain versus traction rate in single element simulations for different element sizes, $f'_c = 35.5 \text{ MPa}$ .....	327

## LIST OF FIGURES (CONT'D)

FIGURE	TITLE	PAGE
6-18	Erosion strain versus traction rate in single element simulations for different element sizes, $f'_c = 50$ MPa .....	328
6-19	Blast loading calculations (units: m) .....	329
6-20	Reflected pressure histories on the sample reinforced concrete column .....	332
6-21	Mesh convergence study of the sample RC column.....	333
6-22	FE models of the sample RC column to estimate traction rates and peak tensile stresses (tractions) for 30 elements near or on the rear face of the column at its mid-height .....	334
6-23	Maximum principal tensile stress history of an elastic element in models 1 and 2, 40 mm mesh.....	334
6-24	Maximum principal tensile stress histories for 30 elements near or on the rear face of the column at its mid-height; model 2 .....	335
6-25	Displacement histories at the mid-height of the column for the 20×20×20 mm mesh .....	336
6-26	Displacement histories at the mid-height of the column for the 30×30×30 mm mesh .	336
6-27	Displacement histories at the mid-height of the column for the 40×40×40 mm mesh .	337
6-28	Displacement histories at the mid-height of the column for the 60×60×60 mm mesh .	337
6-29	Reaction histories at the bottom of the column for the 20×20×20 mm mesh .....	337
6-30	Reaction histories at the bottom of the column for the 30×30×30 mm mesh .....	338
6-31	Reaction histories at the bottom of the column for the 40×40×40 mm mesh .....	338
6-32	Reaction histories at the bottom of the column for the 60×60×60 mm mesh .....	338
6-33	Internal energy histories for the 20×20×20 mm mesh .....	339
6-34	Internal energy histories for the 30×30×30 mm mesh .....	339
6-35	Internal energy histories for the 40×40×40 mm mesh .....	340
6-36	Internal energy histories for the 60×60×60 mm mesh .....	340
6-37	Simulation results for the 20×20×20 mm mesh at time = 25 msec .....	342
6-38	Simulation results for the 30×30×30 mm mesh at time = 25 msec .....	343
6-39	Simulation results for the 40×40×40 mm mesh at time = 25 msec .....	344
6-40	Simulation results for the 60×60×60 mm mesh at time = 25 msec .....	345
6-41	Maximum principal stress histories for 30 elements near or on the rear face of the column, near its mid-height, CONCRETE_DAMAGE_REL3 .....	347

## LIST OF FIGURES (CONT'D)

FIGURE	TITLE	PAGE
6-42	Internal energy histories for the concrete material models of the CSCM using calculated erosion strains and an erosion algorithm of damage function, and the CONCRETE_DAMAGE_REL3 model using calculated erosion strains .....	348
6-43	Simulation results for the CONCRETE_DAMAGE_REL3 model.....	349
6-44	Internal energy histories for $f'_c = 50$ MPa .....	351
6-45	Simulation results for the 20 mm mesh at time = 25 msec, $f'_c = 50$ MPa .....	352
6-46	Simulation results for the 30 mm mesh at time = 25 msec, $f'_c = 50$ MPa .....	352
6-47	Simulation results for the 40 mm mesh at time = 25 msec, $f'_c = 50$ MPa .....	353
6-48	Loading and boundary conditions of the single element for studying the effects of confinement .....	355
6-49	Displacement-controlled loading at the top of the single element .....	355
6-50	Confinement effects on stress-strain relationships, 20×20×20 mm element.....	356
6-51	3D symmetry model of concrete cylinder (units: mm).....	356
6-52	Compressive stress versus strain relationships .....	357
6-53	Simulation results for the 20 mm mesh with the spacing of transverse reinforcement of 20 cm at time = 25 msec, $f'_c = 35.5$ MPa .....	358
6-54	Simulation results for the 30 mm mesh with the spacing of transverse reinforcement of 20 cm at time = 25 msec, $f'_c = 35.5$ MPa .....	358
6-55	Simulation results for the 40 mm mesh with the spacing of transverse reinforcement of 20 cm at time = 25 msec, $f'_c = 35.5$ MPa .....	359
6-56	Simulation results for the 20 mm mesh with axial pressure loading, $f'_c = 35.5$ MPa .. .....	360
6-57	Simulation results for the 30 mm mesh with axial pressure loading, $f'_c = 35.5$ MPa .. .....	362
6-58	Simulation results for the 40 mm mesh with axial pressure loading, $f'_c = 35.5$ MPa .. .....	364
B-1	States across a detonation (shock) wave in unsteady flow (adapted from Fickett and Davis 1979).....	388
B-2	States across a detonation (shock) wave in steady flow flow (adapted from Fickett and Davis 1979).....	391
B-3	Hugoniot curves and Rayleigh line (adapted from Smith and Hetherington 1994)	392
C-1	Incident and reflected peak overpressures near the charge face for cell sizes of 0.1 mm and 0.05 mm .....	394
C-2	Incident peak overpressures inside and reflected peak overpressures at the charge face as a function of cell size.....	394
C-3	Reflection coefficients for distances between 151 and 155 mm .....	396

## LIST OF FIGURES (CONT'D)

<b>FIGURE</b>	<b>TITLE</b>	<b>PAGE</b>
C-4	Peak particle velocities for distances between 151 and 155 mm.....	396
D-1	Air-blast parameters as a function of scaled distance in SI units; spherical free-air burst of TNT .....	397
D-2	Air-blast parameters as a function of scaled distance in US units; spherical free-air burst of TNT .....	398
D-3	Air-blast parameters as a function of scaled distance in SI units; hemispherical surface burst of TNT.....	399
D-4	Air-blast parameters as a function of scaled distance in US units; hemispherical surface burst of TNT.....	400
F-1	Strain-rate histories for three single element simulations.....	405

## LIST OF TABLES

TABLE	TITLE	PAGE
2-1	JWL EOS parameters for TNT (Dobratz and Crawford 1985) .....	13
2-2	Monitoring locations used by Browning et al. (2013).....	55
2-3	JWL EOS parameters for modeling TNT used by Browning et al. (2013).....	55
2-4	Values of input parameters for modeling air for far-field verification.....	55
2-5	Results for incident peak overpressure; cell size of 1 in; units of psi.....	56
2-6	Results for incident peak overpressure; cell size of 2 in; units of psi.....	56
2-7	Results for incident peak overpressure; cell size of 3 in; units of psi.....	57
2-8	Results for incident impulse; cell size of 1 in; units of psi-ms.....	57
2-9	Results for incident impulse; cell size of 2 in; units of psi-ms.....	57
2-10	Results for incident impulse; cell size of 3 in; units of psi-ms.....	57
2-11	Properties for 50/50 Pentolite and C4.....	63
2-12	JWL EOS parameters for 50/50 Pentolite and C4 (Dobratz and Crawford 1985) ....	63
2-13	Normally reflected scaled impulse from AUTODYN calculations and measurements of Goodman (1960) and Huffington and Ewing (1985); units of MPa-ms/kg <sup>1/3</sup> .....	64
2-14	Calculations for the afterburning energy at each interval between radial expansions of detonation products for a spherical charge of 22.68 kg of TNT. ....	90
3-1	AUTODYN dataset for incident calculations.....	189
3-2	Cell sizes for incident peak overpressure and impulse; 960 kg charge with a radius of 520 mm .....	191
3-3	Cell sizes for incident peak overpressure and impulse; 18735 kg charge with a radius of 1400 mm.....	192
3-4	Cell sizes for incident peak overpressure and impulse; 23 kg charge with a radius of 150 mm .....	193
3-5	AUTODYN dataset for reflected calculations.....	196
3-6	Cell sizes for reflected peak overpressure and impulse; 960 kg charge with a radius of 520 mm.....	197
3-7	Cell sizes for reflected peak overpressure and impulse; 18735 kg charge with a radius of 1400 mm.....	198
3-8	Cell sizes for reflected peak overpressure and impulse; 23 kg charge with a radius of 150 mm .....	198
4-1	Constants of polynomials for incident and normally reflected peak overpressure, impulse and arrival time for $0.0553 \leq Z \leq 40$ m/kg <sup>1/3</sup> .....	230
4-2	Constants of polynomials for incident and normally reflected peak overpressure, impulse and arrival time for ranges of scaled distance $0.0553 \leq Z < 0.5$ m/kg <sup>1/3</sup> and $0.5 \leq Z \leq 40$ m/kg <sup>1/3</sup> .....	231

## LIST OF TABLES (CONT'D)

TABLE	TITLE	PAGE
4-3	Values and slopes at $Z = 0.5 \text{ m/kg}^{1/3}$ on the polynomials curves plotted using the two ranges of scaled distance .....	232
4-4	Sample calculations for spherical 25 kg and 1000 kg charges and scaled distances of $0.25 \text{ m/kg}^{1/3}$ and $1.00 \text{ m/kg}^{1/3}$ .....	239
5-1	Incident and reflected overpressures for normal incidence .....	269
5-2	Ratios of AUTODYN calculations to proposed polynomial values and UFC 3-340-02 (DoD 2008) predictions .....	270
5-3	Reflection coefficients as a function of angle of incidence, $\alpha$ , and scaled distance, $Z$ , calculated using AUTODYN.....	271
5-4	Incident and normally reflected scaled impulses in SI units of $\text{MPa}\cdot\text{ms}/\text{kg}^{1/3}$ and US units of $\text{psi}\cdot\text{ms}/\text{lb}^{1/3}$ .....	282
5-5	Ratios of AUTODYN calculations to polynomial and UFC 3-340-02 predictions for reflected scaled impulse.....	283
5-6	Reflected scaled impulses as a function of angle of incidence, $\alpha$ , and scaled distance, $Z$ , calculated using AUTODYN (units: $\text{MPa}\cdot\text{ms}/\text{kg}^{1/3}$ ; $1 \text{ MPa}\cdot\text{ms}/\text{kg}^{1/3} = 111 \text{ psi}\cdot\text{ms}/\text{lb}^{1/3}$ ).....	286
6-1	Assumed model parameters for Grade 6d0 reinforcement (adopted from Børvik et al. 2001) .....	316
6-2	Gruneisen EOS parameters for steel (Tan et al. 2009) .....	318
6-3	Johnson and Cook damage model parameters for Weldox 460 E steel (Børvik et al. 2001) .....	318
6-4	Influence of boundary conditions in the single element simulations for a compressive strength of 35.5 MPa at 200 MPa/msec .....	321
6-5	Percentage erosion of the cross section at the mid-height of the column.....	341
E-1	CSCM model parameters in LS-DYNA .....	401
F-1	Properties of single elements .....	403

# SECTION 1

## BLAST ANALYSIS OF STRUCTURES

### 1.1 Introduction

The effects of air-blast loadings are routinely considered for the design of mission-critical buildings, bridges and infrastructure. Textbooks and technical manuals for blast-resistant design are available (e.g., Smith and Hetherington 1994, FEMA 2003, DOD 2008, Krauthammer 2008, Cormie et al. 2009, Dusenberry 2010), but most of the guidance was written around large far-field loadings. Empirical charts are provided in some of these documents to compute air-blast loadings (incident and reflected overpressures and impulses) but these charts have not been validated in the near field because either the target is within the fireball or the overpressures are too high to be measured by commercially available transducers. Some of the mid-field data used to generate the charts were inferred and not measured directly.

The empirical charts return values of incident and reflected peak overpressure, incident and reflected (specific) impulse, arrival time, positive phase duration and shock front velocity. Overpressure histories are calculated using the Friedlander equation (e.g., Smith and Hetherington 1994):

$$p_s(t) = P_s \left[ 1 - \frac{t}{t_o} \right] e^{-bt/t_o} \quad \text{and} \quad p_r(t) = P_r \left[ 1 - \frac{t}{t_o} \right] e^{-bt/t_o} \quad (1-1)$$

where  $p_s$  and  $p_r$  are incident and reflected overpressures, respectively;  $P_s$  and  $P_r$  are incident and reflected peak overpressures, respectively;  $t$  is time;  $t_o$  is positive phase duration, and  $b$  is a waveform parameter. The parameter  $b$  in Equation 1-1 can be back-calculated using the peak overpressure, positive phase duration, and the impulse calculated using the charts for a given scaled distance and charge weight.

Over the past decade, the rapid development of computational fluid dynamics (CFD) codes has enabled the simulation of complex blast phenomena. CFD codes are deployed in LS-DYNA (LSTC 2013) and AUTODYN (ANSYS 2009). Air3D (Rose 2006) is a CFD code written

specifically for the calculation of air-blast loadings. These codes, once verified and validated, enable a critical review of empirical design charts and approaches, with a focus here on the most common threat, namely, small-to-medium weight weapons and a small stand-off distance: near-field detonations.

## **1.2 State of Practice**

The practice of blast-resistant design is bimodal; namely, 1) CFD simulations and finite element analysis, and 2) empirical charts, simplified loading functions, and single degree of freedom analysis. The former should inform the latter. The latter were developed in the 1950s, with a focus on design of above-ground military infrastructure against the threat posed by far-field thermonuclear detonations. The seminal texts of Biggs (1964) and Norris et al. (1959) enabled design against these threats. Loadings were calculated using first principles calculations of idealized detonations (e.g., Brode 1955, Henrych 1979, Kinney and Graham 1985) and charts presented in government manuals (e.g., TM-5-1300 (Department of the Army, Navy and Air Force 1990) and text books (e.g., Smith and Hetherington 1994, Cormie et al. 2009, Dusenberry 2010).

The blast-resistant design of a structure or a component thereof first involves modeling the effects of the detonation. Traditional practice in the United States, United Kingdom, Australia and elsewhere involves the use of empirical charts developed by Kingery and Bulmash (1984), as presented in US government documents such as UFC 3-340-02 (DOD 2008). Computer codes, such as CONWEP (Hyde 1992), implement the Kingery and Bulmash (KB) polynomials. The charts provide estimates of incident and normally reflected overpressures for spherical TNT explosions in free air and hemispherical TNT explosions on a rigid reflecting surface. Other charts are available in textbooks and government manuals to estimate reflected overpressures and impulses for angles of incidence other than 0 degrees (the so-called normal reflection).

For large far-field detonations of high explosives, one pressure history can represent the load effect over the height and width of a component or structure. The typical history is characterized by an instantaneous rise in pressure to a peak value and a linear decay to ambient pressure. This loading history is a simplification of the true loading history that shows an exponential decay in

overpressure to ambient (the positive phase) and a period of underpressure, which may be interrupted by the arrival of a secondary shock front. The Friedlander curve describes the exponential decay to ambient pressure, noting that values for the parameters that define the curve must be determined by curve fitting to a dataset.

For near-field detonations, the expansion of the detonation products and afterburning affect the amplitude and shape of the overpressure histories. Charge shapes different from a sphere or hemisphere are not addressed in sufficient detail, and the point of detonation within the charge is assumed to be the middle of the sphere. Alternate trigger points for the detonation, which can significantly influence the overpressure histories in the near-field (Sherkar 2010), cannot be considered.

Detonations can be modeled numerically using the finite difference method, which is well suited for fluid dynamics and can solve the Euler equations (e.g., Rose 2006), but the chemistry of a detonation is rarely modeled. Many equations of states (EOS) have been developed to model expanding explosives (e.g., Becker-Kistiakowsky-Wilson (BKW) EOS, Jones-Wilkins-Lee (JWL) EOS, Kihara-Hikita-Tanaka (KHT) EOS, Lennard-Jones-Devonshire (LJD) EOS). The EOS defines the relationships between state variables of thermodynamics such as pressure, volume, density and internal energy. The JWL EOS is the most widely used EOS for explosives due to its ease of implementation in hydrodynamic calculations. For air, the ideal gas EOS is typically adopted in the modeling scheme.

Components of structures, and indeed structural systems, can be modeled in great detail (e.g., a micro-level finite element model) or simplistically using single-degree-of-freedom systems, wherein the mechanical properties of continuous systems are transformed using shape and resistance functions for idealized boundary conditions. For detailed analysis, the finite element (FE) method can be used. Constitutive models, which define the relationships between stress, strain, strain rate, and temperature have been developed for different materials (e.g., Johnson and Cook 1983, Malvar and Simons 1996, Murray 2007a) and are deployed at the element (brick) level for FE analysis. For single-degree-of-freedom analysis, strain-rate effects are addressed using dynamic increase factors, which have been developed for concrete (e.g., Malvar and Ross

1998, Hao and Zhou 2007) and metals (e.g., Johnson and Cook 1983, DOD 2008), for compressive, tensile, and shearing forces.

When concrete structures are subjected to close-in detonations of high explosives, material failure may occur with the associated fragmentation (damage) of concrete. The effect of damage can be simulated in FE models using erosion algorithms, which eliminate material from a model to avoid the numerical errors associated with highly distorted FE meshes. Erosion has been implemented in FE codes (e.g., ABAQUS, AUTODYN, and LS-DYNA) using erosion parameters or damage algorithms. Erosion cannot be addressed with single-degree-of-freedom analysis.

### **1.3 Goals of the Report**

The primary goals of this report are to characterize the effects of detonations of high explosives and their influence on structures, for the purpose of informing blast-resistant design. The specific objectives are,

1. to verify and validate a CFD code for calculating air blast effects in the near and far fields,
2. to develop validated methodologies and guidance for modeling detonations,
3. to update the Kingery and Bulmash charts and polynomials for incident and normally reflected overpressures and impulses, and shock front arrival times, with an emphasis on the near field,
4. to reconcile differences between the US government technical manuals for reflection coefficients as a function of angle of incidence and to evaluate the corresponding reflected scaled impulses, and
5. to provide a technical basis for selecting values of erosion strain suitable for the blast analysis of reinforced concrete components.

## 1.4 Notation and Definitions

A number of terms are used throughout this report and are defined here:

<b>Notation</b>	<b>Definition</b>
$b$	Wave form parameter of the Friedlander equation
$b_w$	Width of the stem (web) of a concrete
$C_r$	Reflection coefficient
$c$	Speed of sound
$c_{fluid}$	Speed of sound in fluids
$c_p$	Specific heats at constant pressure
$c_{solid}$	Speed of sound in solids
$c_v$	Specific heats at constant volume
$D$	Detonation velocity
$d_e$	Effective depth from the top of a reinforced concrete beam to the centroid of the compressive steel
$d(\tau_c)$	Damage parameter for compression; CSCM model
$d(\tau_t)$	Damage parameter for tension; CSCM model
$E$	Young's modulus
$e$	Specific internal energy
$F_c$	Hardening cap function; CSCM model
$F_f$	Shear failure surface function; CSCM model
$f'_c$	Compressive strength of concrete
$f'_l$	Effective confining pressure
$f_n$	Natural cyclic frequency
$G$	Shear modulus
$G_f$	Fracture energy
$G_f^{vp}$	Viscoplastic fracture energy
$h$	Enthalpy
$I_r$	Reflected impulse
$I_s$	Incident impulse
$J_1$	First invariant of the stress tensor
$J_2$	Second invariant of the deviatoric stress tensor
$J_3$	Third invariant of the deviatoric stress tensor
$K$	Bulk modulus

<b>Notation</b>	<b>Definition</b>
$K_f$	Material constant for the Tuler-Butcher failure criterion
$K$	Stiffness
$M$	Mach number
$m$	Mass
$P_r$	Reflected peak overpressure
$P_s$	Incident peak overpressure
$p_r$	Reflected overpressure
$p_s$	Incident overpressure
$p$	Pressure
$p_0$	Ambient pressure
$p_{CJ}$	CJ detonation pressure
$p_t$	Hydrostatic tensile pressure
$q_s$	Dynamic pressure
$R$	Standoff distance
$r$	Radial distance from the center of detonation
$\bar{r}$	Radial expansion of a shock front normalized by charge radius
$\bar{r}_d$	Radial expansion of a front of detonation products normalized by charge radius
$r_0$	Damage threshold; CSCM model
$r_s$	Initial damage threshold; CSCM model
$S_{ij}$	Deviatoric stress tensor
$s$	Entropy
$T_m$	Melting temperature
$T_n$	Period
$T_r$	Room temperature
$t$	Time
$t_a$	Arrival time
$t_o$	Positive phase duration
$U$	Shock front velocity
$u$	Velocity
$u_p$	Particle velocity
$V$	Relative volume
$V_n$	Nominal shear strength of concrete
$v$	Particle velocity
$v_s$	Particle velocity for incident shock

<b>Notation</b>	<b>Definition</b>
$W$	Weight of an explosive
$w$	Adiabatic constant; JWL EOS
$w_n$	Natural circular frequency
$X_0$	Initial location of a cap; CSCM model
$Y$	Common (base 10) logarithm of a blast parameter
$Z$	Scaled distance; $R/W^{1/3}$
$\alpha$	Angle of incidence
$\alpha_D$	Angle of incidence for the detachment criteria
$\alpha_N$	Angle of incidence for the von Neumann criteria
$\beta$	Angle of reflection
$\varepsilon$	Strain
$\dot{\varepsilon}$	Strain rate
$\dot{\varepsilon}_0$	Reference strain rate
$\varepsilon_1$	First principal strain
$\varepsilon_3$	Third principal strain
$\varepsilon_{eff}$	Effective strain
$\varepsilon_{eff}^{dev}$	Effective deviatoric strain
$\varepsilon_{eff}^p$	Effective plastic strain
$\varepsilon_f$	Accumulated plastic strain to failure
$\varepsilon_{ij}$	Components of the strain tensor
$\varepsilon_{ij}^{ft}$	Components of the failure strain tensor
$\dot{\varepsilon}_{ij}$	Components of the strain-rate tensor
$\dot{\varepsilon}_{ij}^p$	Components of the plastic strain-rate tensor
$\varepsilon_p$	Equivalent plastic strain
$\varepsilon_{incr}$	Incremental geometric strain
$\varepsilon_{inst}$	Instantaneous geometric strain
$\varepsilon_{jj}$	Volumetric strain
$\varepsilon_p$	Equivalent plastic strain
$\dot{\varepsilon}_p$	Equivalent plastic strain rate
$\Delta\varepsilon_p$	Increment of accumulated effective plastic strain
$\varepsilon_v^p$	Plastic volume strain
$\gamma$	Specific heat ratio
$\gamma_0$	Gruneisen coefficient
$\eta$	Strain-rate effect parameter; CSCM model

<b>Notation</b>	<b>Definition</b>
$\kappa$	Cap hardening parameter; CSCM model
$\lambda$	Wave length
$\mu$	Compression ratio
$\nu$	Poisson's ratio
$\rho$	Density
$\rho_0$	Initial density
$\rho_s$	Density for incident shock
$\sigma$	Stress
$\sigma_0$	Specified threshold stress for the Tuler-Butcher failure criterion
$\sigma_1$	First principal stress
$\sigma_3$	Third principal stress
$\sigma_{eff}$	Effective stress
$\sigma_{eff}^{dev}$	Effective deviatoric stress
$\sigma_{ij}^{fi}$	Components of the failure stress tensor
$\sigma_{ij}^{vp}$	Components of the viscoplastic stress tensor
$\sigma_m$	Hydrostatic stress
$\sigma_y$	Yield stress
$\tau_c$	Ductile damage; CSCM model
$\tau_t$	Brittle damage; CSCM model
$\mathfrak{R}$	Rubin three-invariant reduction factor; CSCM model

## 1.5 Report Organization

This report consists of eight chapters and six appendices. Chapter 2 verifies and validates a CFD code for analysis of air blast effects, discusses the modeling of close-in (near field) detonations, and develops an understanding of the characteristics of incident and reflected overpressures in the near field.

Chapter 3 summarizes past studies on air-blast parameters, including those that underpin US government documents, presents results of CFD analysis for air-blast parameters across a very wide range of scaled distance, and compares CFD results to the predictions of Kingery and Bulmash (1984).

Chapter 4 mines the CFD data of Chapter 3 and presents recommendations for a family of polynomials to be used for air-blast calculations across the range of scaled distance  $0.0553 \leq Z \leq 40 \text{ m/kg}^{1/3}$  ( $0.139 \leq Z \leq 100 \text{ ft/lb}^{1/3}$ ).

Chapter 5 examines incident and reflected overpressures and impulses from the detonation of a high explosive as a function of angle of incidence. A chart and a table to enable the calculation of reflection coefficients and reflected scaled impulses as a function of the angle of incidence are presented.

Chapter 6 discusses erosion strain for blast analysis of concrete components for the purpose of providing a technical basis for the choice of a value of erosion strain. Single element simulations are performed to develop recommendations. Blast analysis of a sample reinforced concrete column is performed to identify the importance of correctly assigning a value of erosion strain for analysis. A step-by-step procedure is provided to compute a value of concrete erosion strain for blast analysis of concrete components.

Chapter 7 summarizes the technical contributions of this report and presents key conclusions. A list of references is presented in Chapter 8.

Six appendices supplement this report. Appendix A introduces the speed of sound and its calculation in solids and fluids. Appendix B describes the relationships between the Chapman-Jouguet (CJ) condition, Hugoniot equations, Rayleigh line and the von Neumann spike. Appendix C assesses incident and reflected overpressures very close to the face of a charge. Appendix D presents the Kingery and Bulmash charts used in Chapters 3 and 4. Appendix E presents values of parameters for the constitutive model of concrete used in Chapter 5. Appendix F describes the single-degree-of-freedom (SDOF) calculations for strain rate to validate the LS-DYNA single element simulations in Chapter 6.



## SECTION 2

### MODELING NEAR-FIELD DETONATIONS OF HIGH EXPLOSIVES

#### 2.1 Introduction

The need to accurately quantify blast pressure loadings in the near field is important because near-field detonations represent a common threat for the security design of buildings, bridges and critical infrastructure. Incident and reflected overpressures in the near-field region are too high to be measured directly by available pressure transducers, or indirectly using air density, because of the presence of the fireball, requiring a verified (and validated if possible) computational fluid dynamics (CFD) code to be used to predict the near-field overpressures.

This chapter examines numerical modeling techniques for detonations of spherical high explosives and characterizes their effects in the near field. The near-field region is defined here as the region within which the shock wave is affected by local phenomena (e.g., expansion of detonation products, afterburning) that are insignificant in the far field. These studies are intended to provide a) confidence in the numerical modeling tools, and b) estimates of incident and reflected overpressure histories.

Studies are performed using the CFD codes AUTODYN (ANSYS 2009) and Air3D (Rose 2006). The early expansion of the detonation products is simulated using radial symmetry in one dimension (1D) before the model is re-mapped into two (2D) and three dimensions (3D) immediately prior to a boundary being encountered. The Jones-Wilkins-Lee (JWL) Equation of State (e.g., Fickett and Davis 1979, Needham 2010) is used to model the expanding explosive; air is modeled as an ideal gas. The JWL Equation of State (EOS) is described in Section 2.2.

AUTODYN is *verified* for 1D near-field calculations, and 1D and 2D far-field calculations, in Sections 2.3.2 and 2.3.3, respectively. AUTODYN is *validated* for 2D near-field calculations and 2D far-field calculations in Sections 2.3.4 and 2.3.5, respectively. Results of one-dimensional (1D) propagations of blast waves are presented in Section 2.4 to characterize incident overpressures in the near field. The influences of mesh size, expansion of detonation products

and afterburning on pressures and impulses are investigated. AUTODYN and Air3D predictions are also contrasted.

Two- and three-dimensional simulations are performed in Sections 2.5 and 2.6, respectively, to study the influence of alternate boundary conditions (or modeling assumptions), to characterize incident and reflected overpressures, and to confirm the efficacy of reflecting and transmitting boundaries in AUTODYN. Results of 1D, 2D and 3D simulations are compared to ensure consistency. The complexity of the wave field in the Mach stem region is identified. The applicability of the traditional Friedlander waveform (e.g., Baker 1973, Smith and Hetherington 1994, Cormie et al. 2009), namely, an instantaneous rise to peak overpressure followed by an exponential decay to the ambient condition, to describe near-field pressure loadings is discussed.

Three-dimensional air blast analysis of sample square and circular rigid columns is performed in Section 2.7 to evaluate reflected overpressures on the surfaces of the columns and the effects of column shape on the reflected overpressures.

## **2.2 Modeling Detonations in AUTODYN**

AUTODYN is a general-purpose hydrocode used for a wide variety of applications. It uses finite volume and finite element methods to solve the governing conservation equations. Outputs are remapped from 1D to 2D/3D and 2D to 3D. The remapping feature allows use of higher resolution grid in the analysis of the initial stages of the shock wave expansion (ANSYS 2005). Remapping in AUTODYN is manual and requires user intervention.

Detonation modeling in AUTODYN is two-step process. The first step involves the early time expansion of the explosive products in 1D using radial symmetry, which continues until a reflecting surface is reached. The output of the 1D analysis is then transmitted to the 2D/3D domain that is generated separately. The analysis is the run until a termination time. Although modeling detonations in AUTODYN is similar to Air3D, the AUTODYN and Air3D solution methodologies and capabilities differ. Air3D addresses air-blast only.

Analysis of detonations requires the choice of equations of state. For the analyses described in this report, TNT is modeled using the JWL EOS and air is modeled as an ideal gas. Although

AUTODYN has its own material library with default values for the various EOS parameters, the values of the JWL EOS parameters listed in column 2 of Table 2-1 are used. These values are identical to those presented by Dobratz and Crawford (1985). The multi-material Euler-Godunov solver (Godunov 1959) is used for the 1D calculations. (The Euler-FCT solver cannot be used for radial (1D) calculations.)

**Table 2-1 JWL EOS parameters for TNT (Dobratz and Crawford 1985)**

Parameter	Value
Density (kg/m <sup>3</sup> )	1630
$A$ (GPa)	371.2
$B$ (GPa)	3.231
$R_1$	4.15
$R_2$	0.95
Adiabatic constant, $w$	0.30
Detonation velocity, $D$ (m/s)	6930
Energy per unit volume, $E_0$ (GPa)	7
CJ pressure, $P_{CJ}$ (GPa)	21

The JWL EOS is a pressure-volume relationship:

$$p = A \left( 1 - \frac{w}{R_1 V} \right) e^{-R_1 V} + B \left( 1 - \frac{w}{R_2 V} \right) e^{-R_2 V} + \frac{w}{V} e \quad (2-1)$$

where  $p$  is the pressure,  $V$  is the relative volume,  $e$  is the specific internal energy and  $A$ ,  $B$ ,  $R_1$ ,  $R_2$ , and  $w$  are constants obtained by calibration of test data.

Air is modeled as an ideal gas with an initial pressure of 101.3 kPa by specifying an initial energy of  $0.204 \times 10^6$  J/kg. The initial temperature, density and adiabatic constant (specific heat ratio)  $\gamma$  were set to 288 K (15°C), 1.225 kg/m<sup>3</sup>, and 1.4, respectively. The multi-material Eulerian solver is used for both the explosive and air.

One-dimensional analysis is performed until the blast wave reaches the end of the 1D domain. The analysis is typically interrupted when the explosive has expanded to approximately 10 times its original volume. At this point in the expansion, the value of the compression ratio,  $\mu$ , presented in Equation 2-2 is approximately -0.99. AUTODYN uses the compression ratio to calculate the density of the detonation products; see Equation 2-3. The density of the detonation products becomes very small if  $\mu$  falls below -0.99 and this can lead to numerical difficulties.

$$\mu = \frac{\rho}{\rho_0} - 1 \quad (2-2)$$

$$\rho = \rho_0(1 + \mu) \quad (2-3)$$

where  $\rho$  and  $\rho_0$  are the current density and initial density, respectively. At large volumetric ratios, the first two terms on the right side of the JWL EOS (Equation 2-1) become negligible and the EOS collapses to that of an ideal gas EOS, namely:

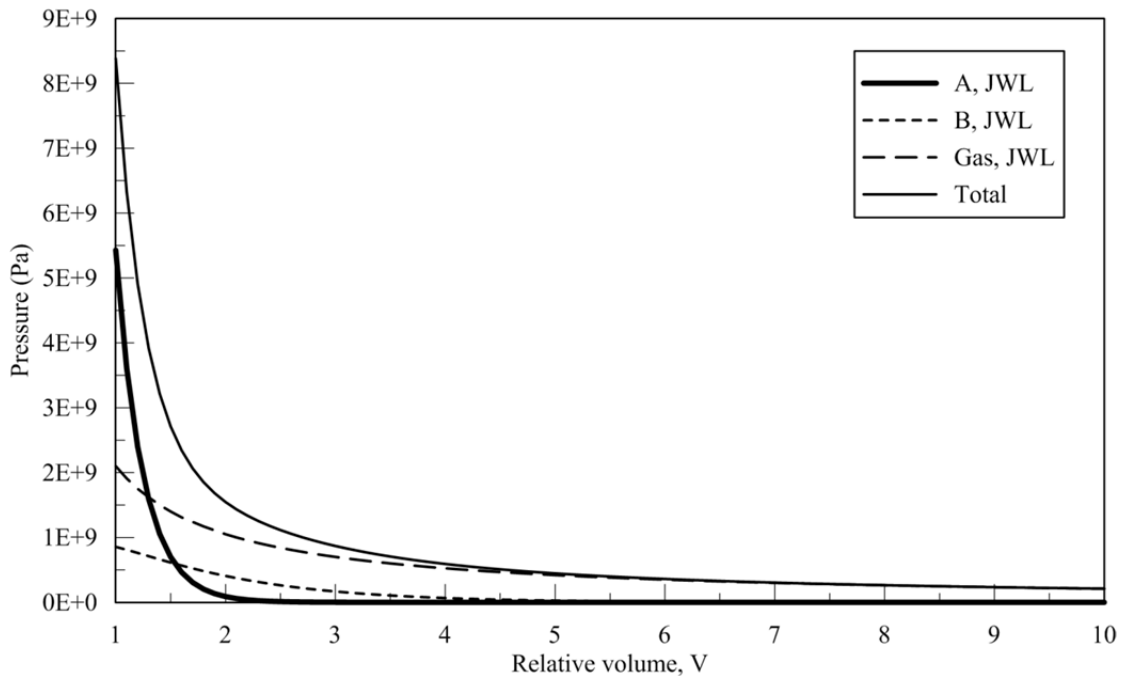
$$p = (\gamma - 1) \frac{\rho}{\rho_0} e \quad (2-4)$$

where all terms have been previously defined. Equating Equation 2-4 with Equation 2-1,  $\gamma = 1+w = 1+0.3 = 1.3$  for large volumetric ratios. When the compression ratio reaches a value of -0.99, the EOS for the expanding detonation products is replaced by the EOS for an ideal gas with  $\gamma = 1.30$  and  $\rho_0 = 1 \times 10^{-4} \text{ gm/cm}^3$  (ANSYS 2009) and the compression ratio is correspondingly increased to avoid possible numerical instabilities. No change is made to the EOS for the gas (air) beyond the detonation products. Defining the reference density of a material associated with the EOS transition is described below based on a personal communication (ANSYS 2013).

1. When users fill a material to a part in AUTODYN, they will be always asked about the initial conditions: density, specific internal energy and initial velocity. The initial material density defaults to the reference density. The specific internal energy is calculated automatically from the internal energy per volume. The reference density is equal to the material density in most cases.

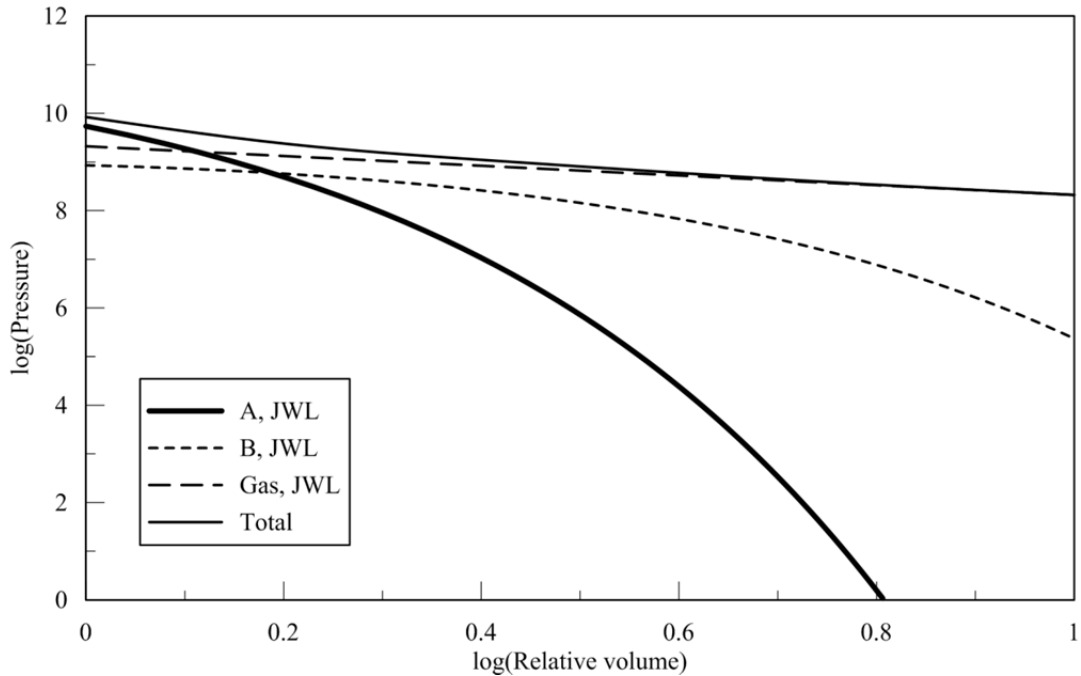
2. When TNT detonates, its specific internal energy decreases and the element pressure increases. Internal energy per volume is not used in the EOS calculations and thus the reference density does not play a key role in the EOS calculations.
3. When the reference density is changed by converting the JWL EOS to the ideal gas EOS, AUTODYN will not change the material density, specific internal energy, pressure, and other physical variables. The program only changes the compression ratio,  $\mu$ .

Figure 2-1 presents the JWL EOS for TNT using linear and log scales. The legend in each panel of the figure identifies the terms on the right hand side of Equation 2-1: “A, JWL” is the first term, “B, JWL” is the second term and “Gas, JWL” is the third term. The line “Total” is the sum of these three terms. The contributions of the first two terms, A and B, are significant for relative volume of 3 and smaller, and insignificant for relative volumes of 5 and greater, where the relative volume is the ratio of the volume of the expanding explosive to its original volume.



a. Pressure versus relative volume, linear scale

**Figure 2-1 JWL and ideal gas EOS for TNT**



b. Pressure versus relative volume, log (base 10) scale

**Figure 2-1 JWL and ideal gas EOS for TNT (cont.)**

## 2.3 Verification and Validation of AUTODYN

### 2.3.1 Introduction

Verification and validation of numerical codes is standard practice in computational solid mechanics. Verification is the process of determining that a computational model accurately represents the underlying mathematical model and its solution. Validation is the process of determining the degree to which a model is an accurate representation of the real world, as determined by physical experiments, from the perspective of the intended uses of the model. Numerical codes, such as the computational fluid dynamics code AUTODYN, should not be used unless they have been verified and validated. ASME (2006) presents guidance on verification and validation for computational solid mechanics and that guidance is applied to AUTODYN.

In this section, AUTODYN is 1) verified using independent numerical predictions and analytical calculations reported by Needham (2010) for 1D analysis in the near and intermediate fields

(Section 2.3.2), 2) verified by cross-code comparisons for 1D and 2D analysis in the far field (Section 2.3.3), 3) validated in 2D using measurements of normally reflected scaled impulse reported by Goodman (1960) and Huffington and Ewing (1985) in the near field (Section 2.3.4), and 4) validated in 2D using measurements of reflected peak overpressures and impulses reported by Frost et al. (2008) in the far field (Section 2.3.5). Data are not available in the open literature for either verification in 2D or validation in the near field in 1D. Calculations of overpressure history cannot be validated in the near field at this time<sup>1</sup> and the 2D near-field validation uses measurements from impulse plugs (e.g., Huffington and Ewing 1985).

The 1D verification study for near-field detonations and the 1D and 2D verification study for far-field detonations are performed using a spherical charge of TNT. The 2D validation study for near-field detonations is performed using a spherical charge of Pentolite because the only near-field test data that could be found are measurements of normally reflected scaled impulse reported by Goodman and Huffington and Ewing for detonations of this explosive. There are no (reliable) test data (in the open literature) on reflected peak overpressure in the near field. There are no near field data for detonations of TNT. The 2D validation study for far-field detonations is performed using measurements of reflected peak overpressure and impulse reported by Frost et al. for detonations of spherical charges of C4.

### ***2.3.2 Verification of AUTODYN in 1D for Near-Field Detonations***

Needham (2010) reports the results of an analysis of a charge of 18000 kg of TNT, with a radius of 140 cm. The density of the packed TNT was 1570 kg/m<sup>3</sup>. The analysis was performed using a Lagrangian finite difference code, detonation products were modeled using the LSZK Equation of State (EOS) and air was modeled using the Doan Nickel EOS (Doan and Nickel 1963). The

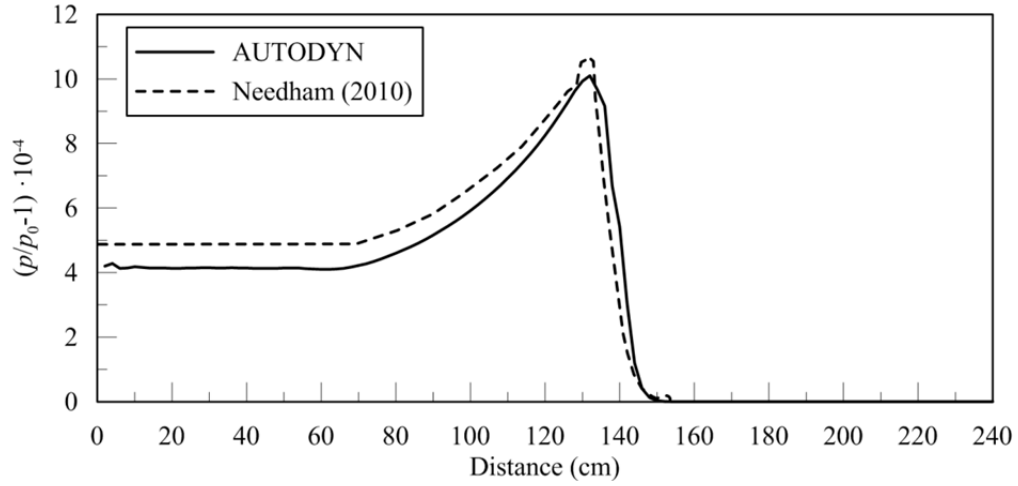
---

<sup>1</sup> Incident and reflected overpressures cannot be measured in the near field (including inside the fireball) using commercially available pressure transducers because the temperatures are too high. Transducers capable of measuring very high pressures operate at temperatures less than approximately 600 K: a) the OMEGA PX1009 sensor can measure pressure up to 34 MPa but at a maximum temperature of 616 K (www.omega.com), b) the PCB PIEZOTRONICS 112A05 sensor can measure pressure up to 34 MPa but at a maximum temperature of 589 K (www.pcb.com), and c) the PAINE 211-55-010 sensor can measure pressure up to 206 MPa but at a maximum temperature of 589 K (www.paineelectronics.com). CFD analysis of an explosion in free air predicts that the fireball expands to a scaled distance of approximately 0.8 m/kg<sup>1/3</sup> (2 ft/lb<sup>1/3</sup>), or a shock front radial expansion of approximately 15, or an incident overpressure of approximately 2 MPa. The predicted temperature at a scaled distance of 0.8 m/kg<sup>1/3</sup> is greater than 1000 K, with much higher temperatures predicted at smaller values of scaled distance.

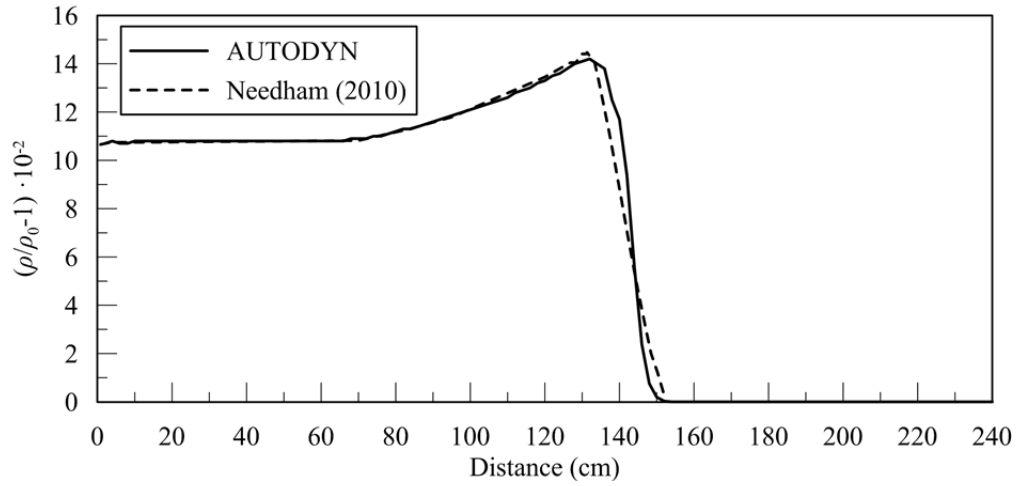
results presented in Needham were digitized to enable a direct comparison with results computed using AUTODYN. Needham reported results using centimeters for distance. This unit is adopted in this chapter where comparisons of Needham and CFD data are made.

A 1D AUTODYN model of the charge described above is prepared using the JWL EOS for the detonation products and the ideal gas EOS for air. The values of the parameters used for the JWL EOS, presented in Table 2-1, are those reported in the LLNL Explosives Handbook (Dobratz and Crawford 1985). (Needham did not report the values he used for the EOS.) The LLNL density for packed TNT is  $1630 \text{ kg/m}^3$ , and that is 4% greater than that assumed by Needham. To use a consistent set of properties for the JWL EOS, and a charge shape identical to that of Needham to enable reporting at the same values of radial expansion provided in Needham, the TNT weight for the AUTODYN analysis is 18735 kg. The 4% increase in weight will have a minor effect on the overpressure histories but small differences between AUTODYN predictions and results reported by Needham are inevitable.

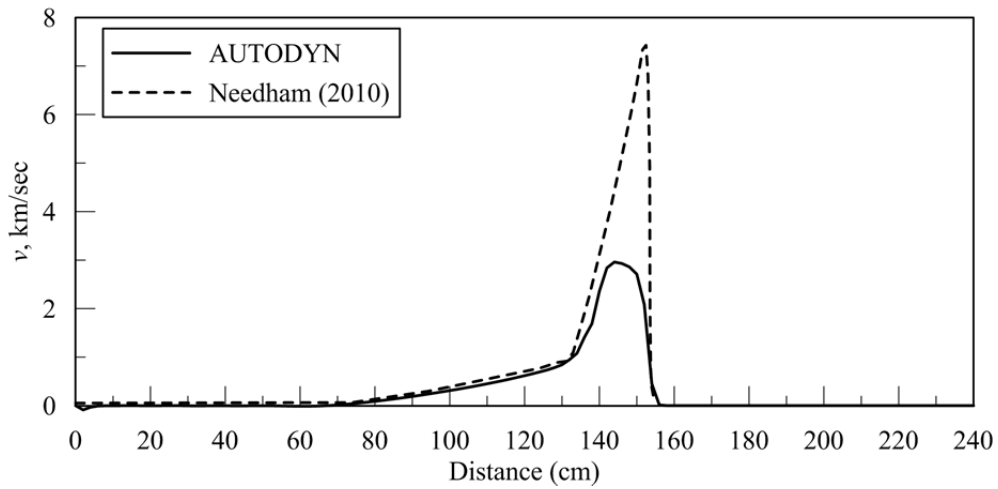
Needham (2010) reported hydrodynamic parameters at different values of shock front radial expansion,  $\bar{r}$ : 1.1, 2.4, 2.6, 4.5, 11.7, 26 and 34. Needham and AUTODYN results are presented in Figures 2-2, 2-3, 2-4, 2-5, 2-7, 2-9 and 2-10. Additional data are presented in Figures 2-6 and 2-8 for shock front radial expansions of 8 and 18 because the hydrodynamic parameters vary greatly between shock front radial expansions of 4.5 and 11.7, and 11.7 and 26, respectively. The hydrodynamic parameters reported in each figure are relative overpressure ( $p/p_0 - 1$ ), relative over density ( $\rho/\rho_0 - 1$ ), and particle velocity,  $v$ , in units of km/second. Relative overpressure is presented as the total pressure,  $p$ , normalized by the ambient air pressure ( $p_0 = 101.3 \text{ kPa}$ ) minus 1, and relative over density is presented as the total density normalized by the ambient atmospheric density ( $\rho_0 = 1.225 \text{ kg/m}^3$ ) minus 1. The AUTODYN calculations were performed using an Eulerian solver and a mesh with a cell dimension of 20 mm.



a. Pressure ( $p_0 = 0.1$  MPa)

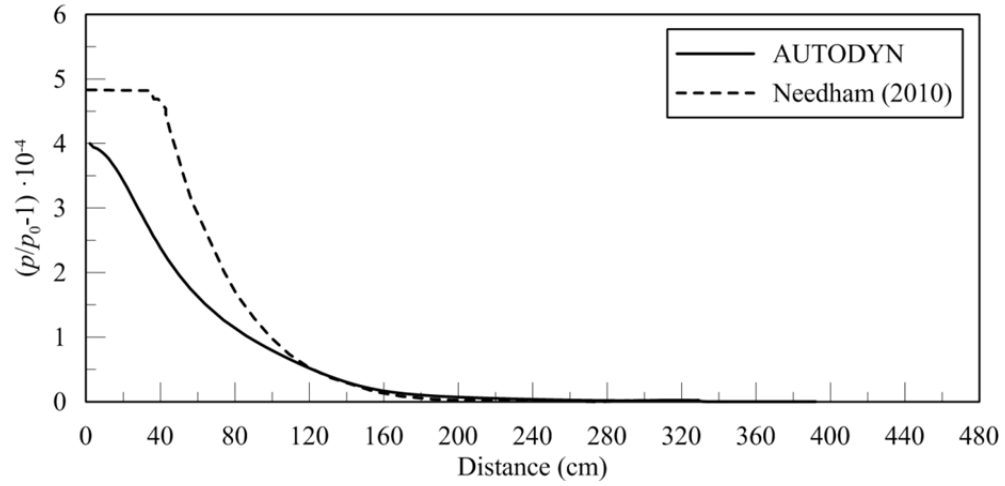


b. Density ( $\rho_0 = 0.001225$  g/cm<sup>3</sup>)

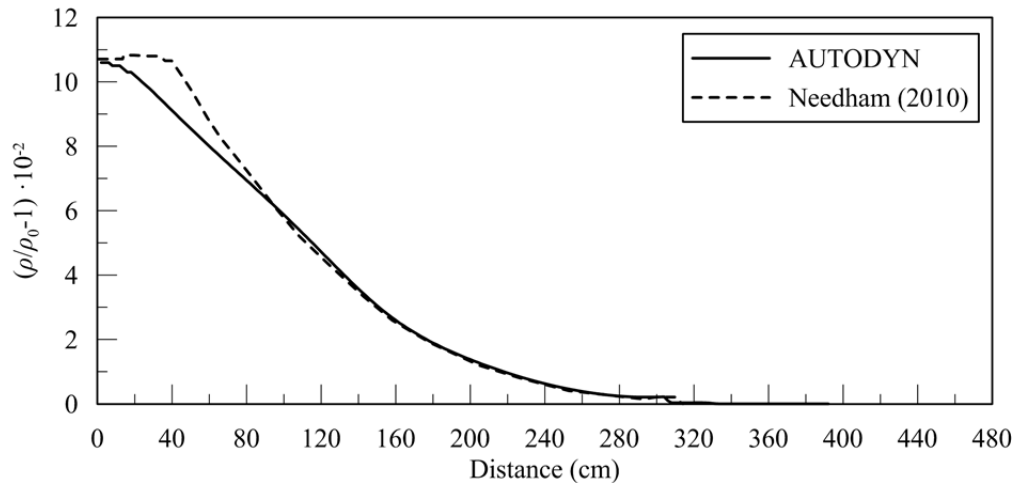


c. Particle velocity,  $v$

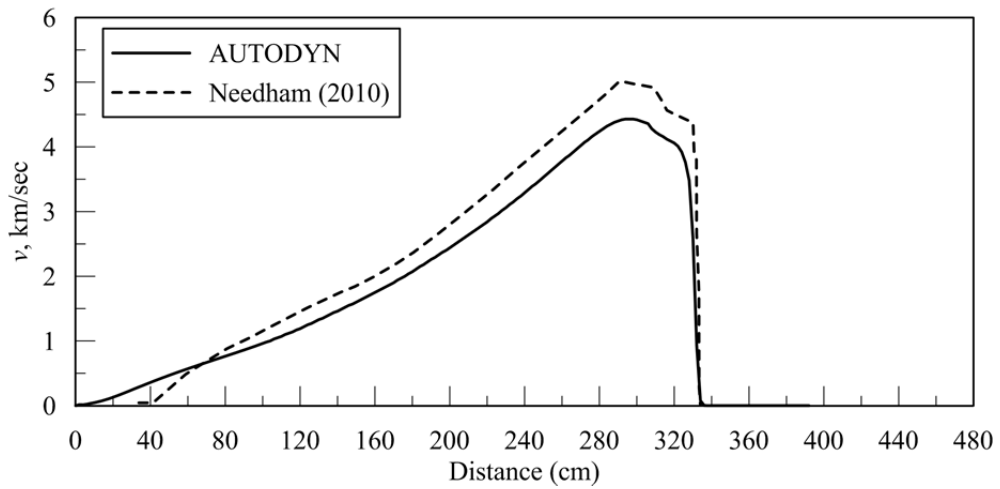
**Figure 2-2 Hydrodynamic parameters at  $\bar{r} = 1.1$  for a 20 mm mesh**



a. Pressure ( $p_0 = 0.1$  MPa)

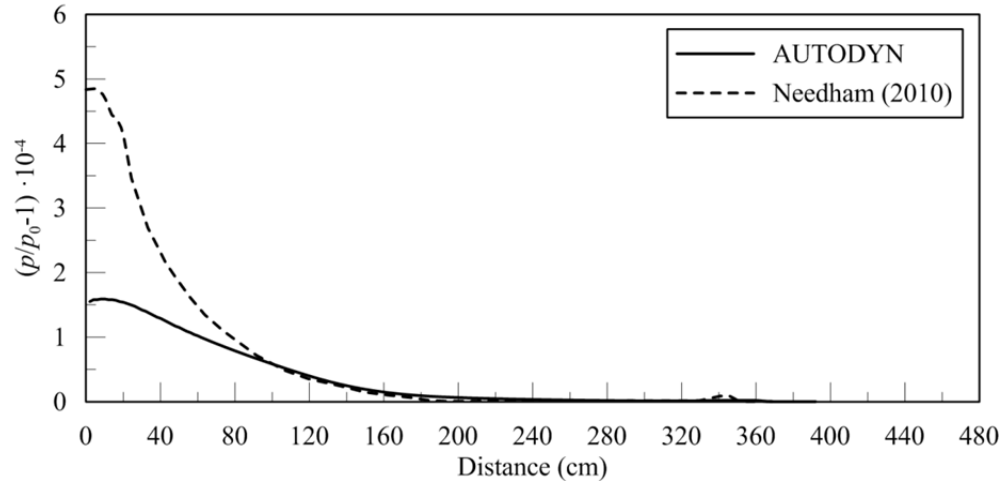


b. Density ( $\rho_0 = 0.001225$  g/cm<sup>3</sup>)

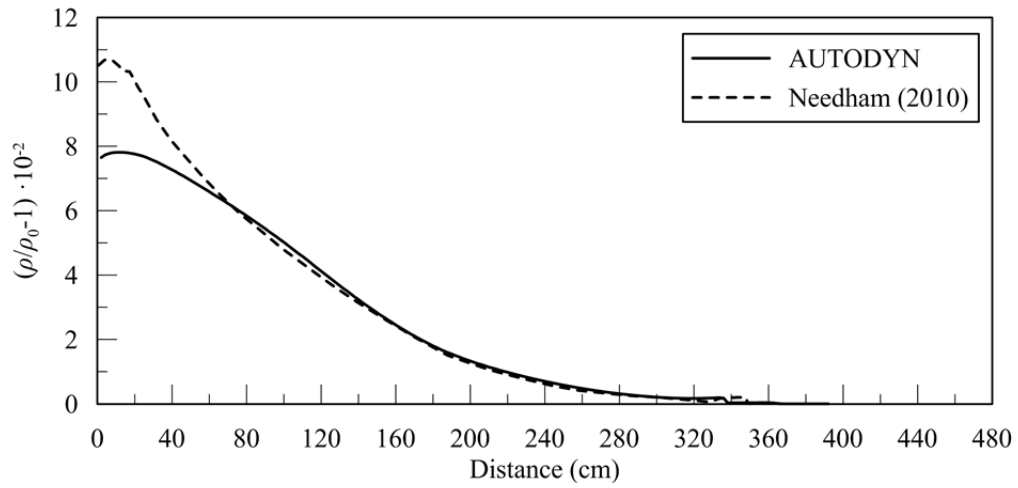


c. Particle velocity,  $v$

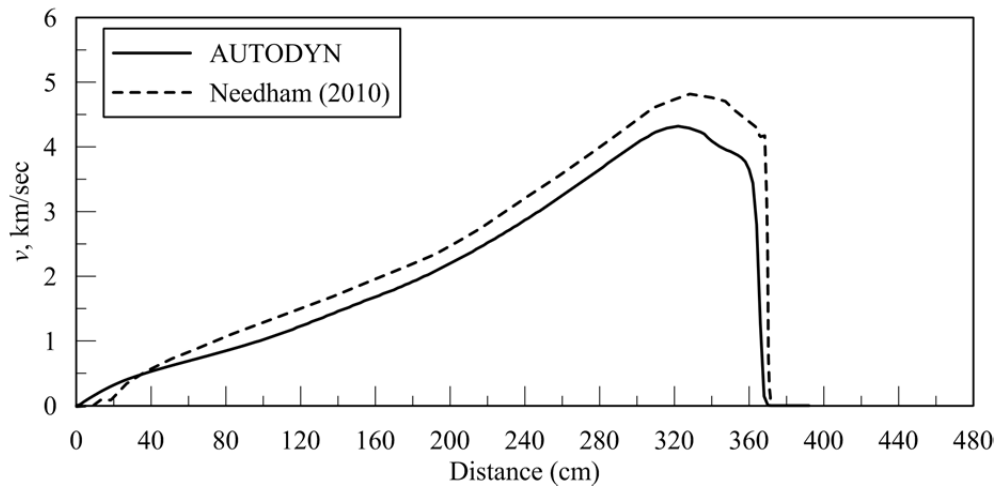
**Figure 2-3 Hydrodynamic parameters at  $\bar{r} = 2.4$  for a 20 mm mesh**



a. Pressure ( $p_0 = 0.1$  MPa)

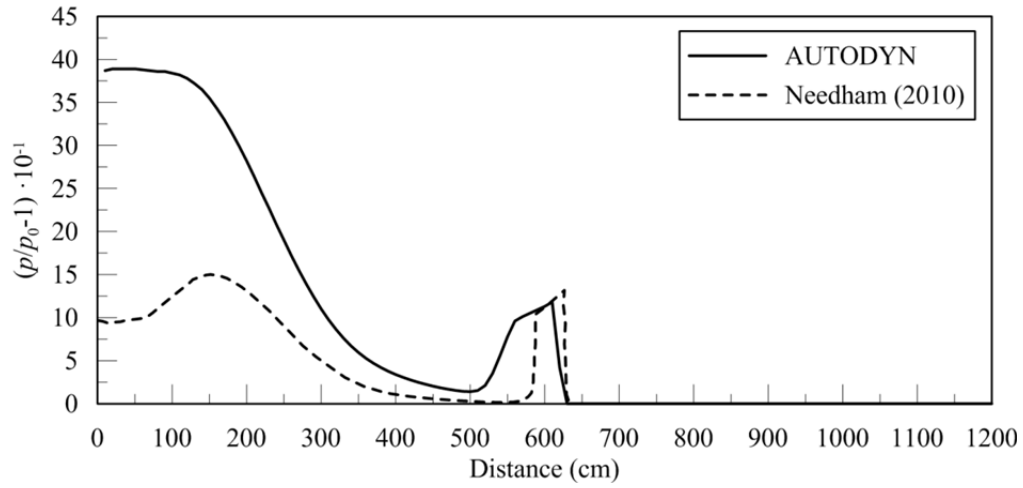


b. Density ( $\rho_0 = 0.001225$  g/cm<sup>3</sup>)

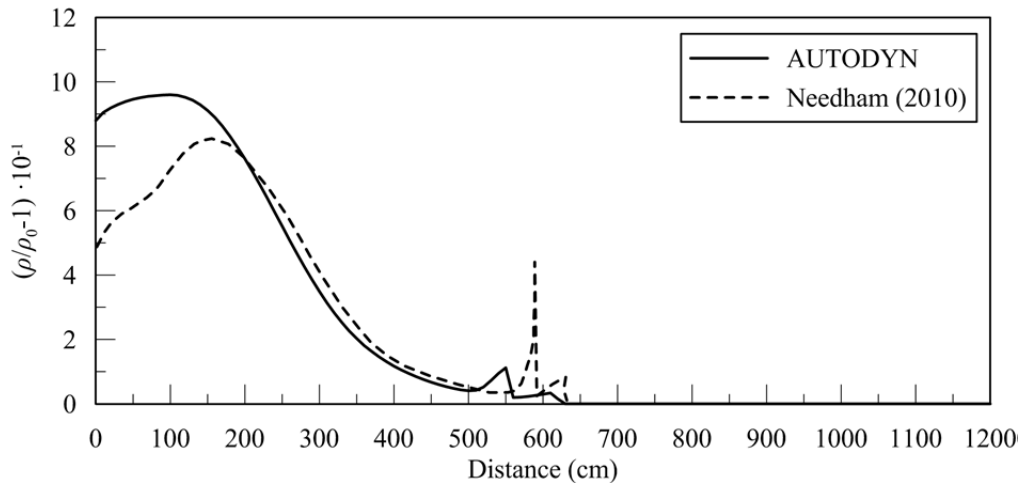


c. Particle velocity,  $v$

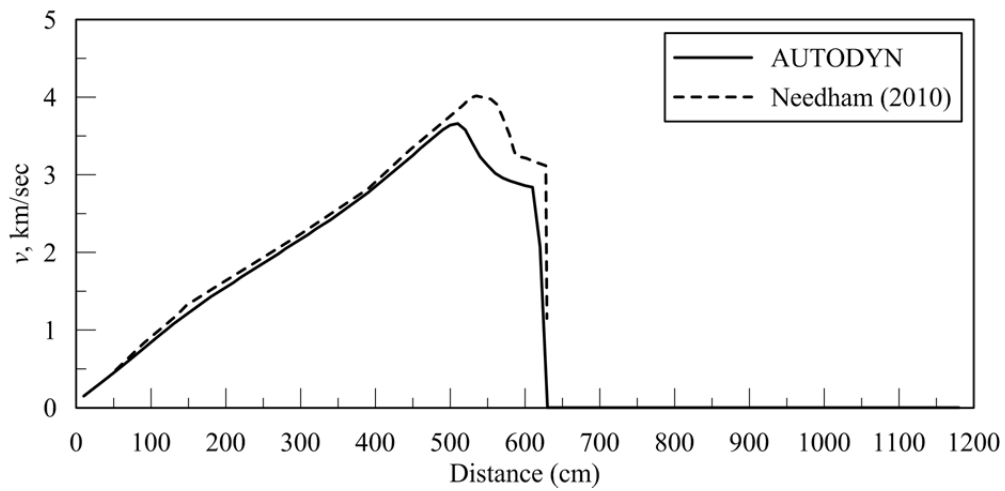
**Figure 2-4 Hydrodynamic parameters at  $\bar{r} = 2.6$  for a 20 mm mesh**



a. Pressure ( $p_0 = 0.1$  MPa)

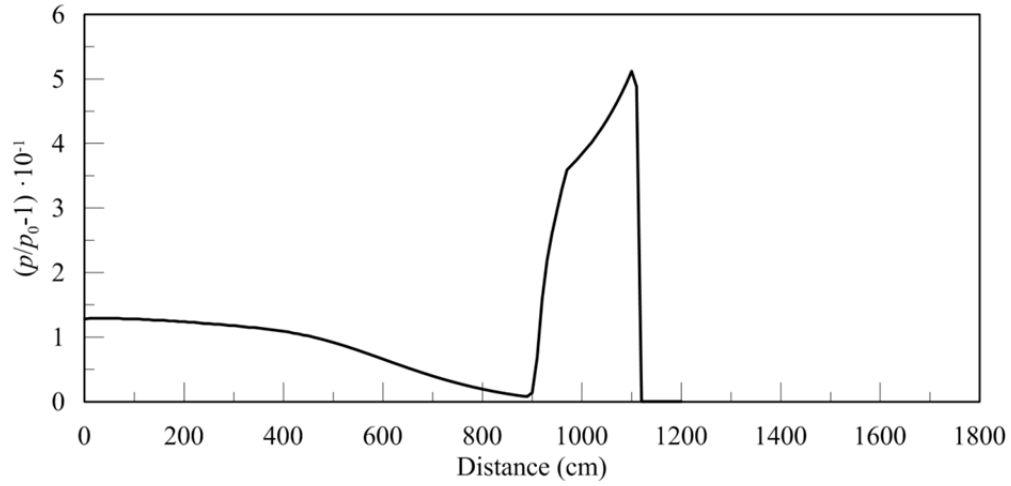


b. Density ( $\rho_0 = 0.001225$  g/cm<sup>3</sup>)

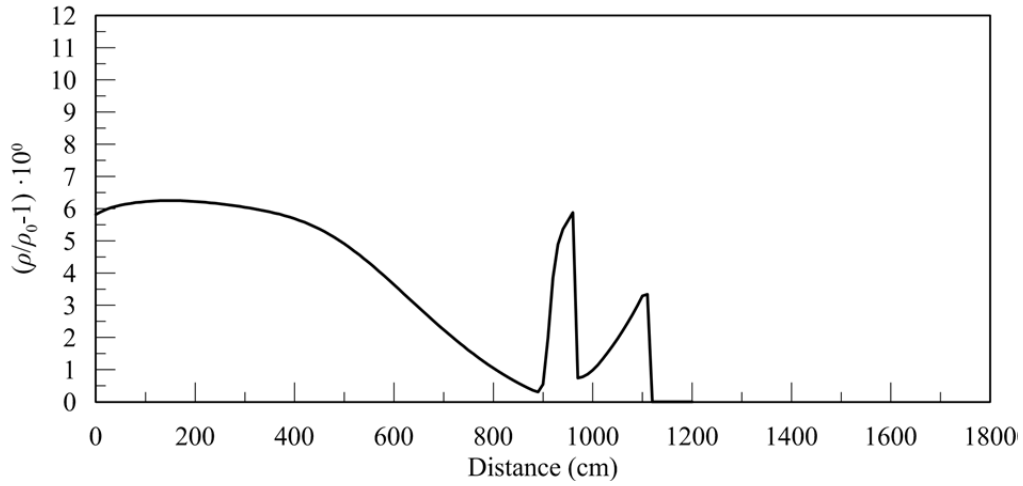


c. Particle velocity,  $v$

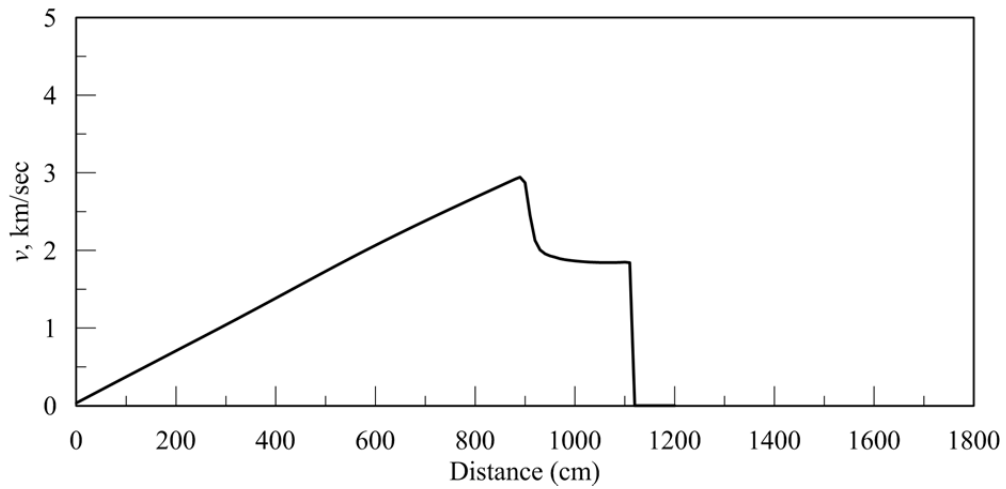
**Figure 2-5 Hydrodynamic parameters at  $\bar{r} = 4.5$  for a 20 mm mesh**



a. Pressure ( $p_0 = 0.1$  MPa)

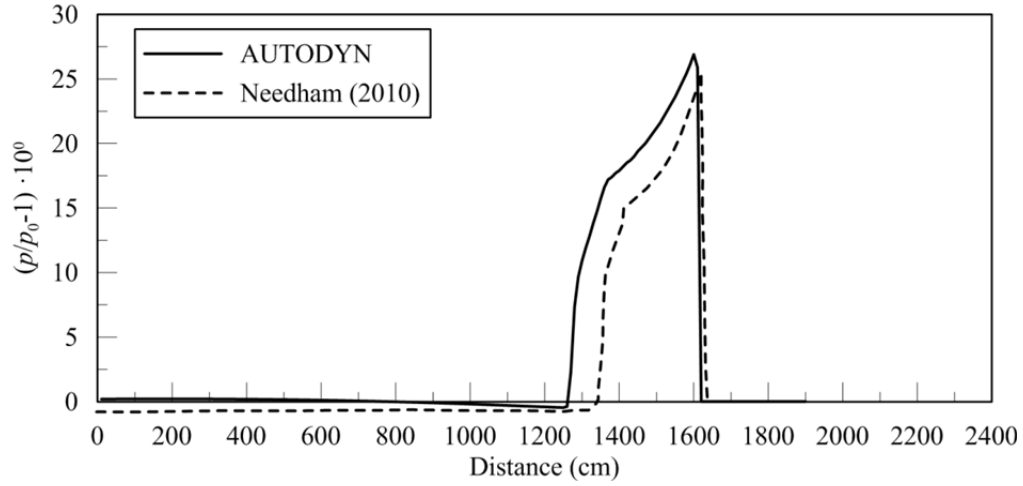


b. Density ( $\rho_0 = 0.001225$  g/cm<sup>3</sup>)

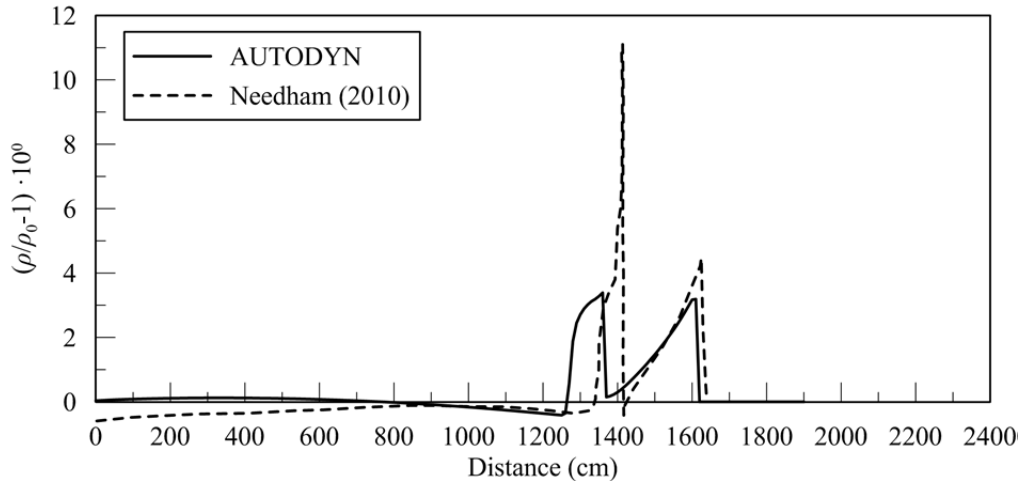


c. Particle velocity,  $v$

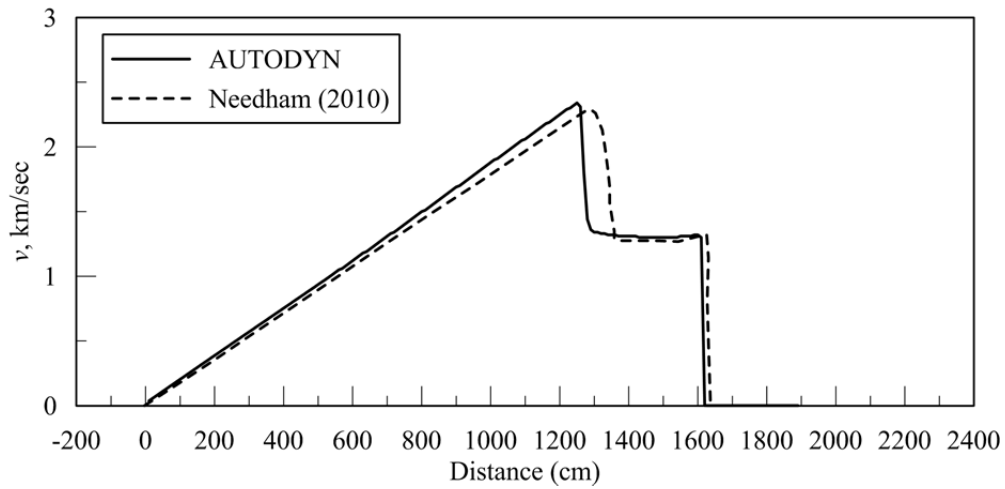
**Figure 2-6 Hydrodynamic parameters at  $\bar{r} = 8$  for a 20 mm mesh**



a. Pressure ( $p_0 = 0.1$  MPa)

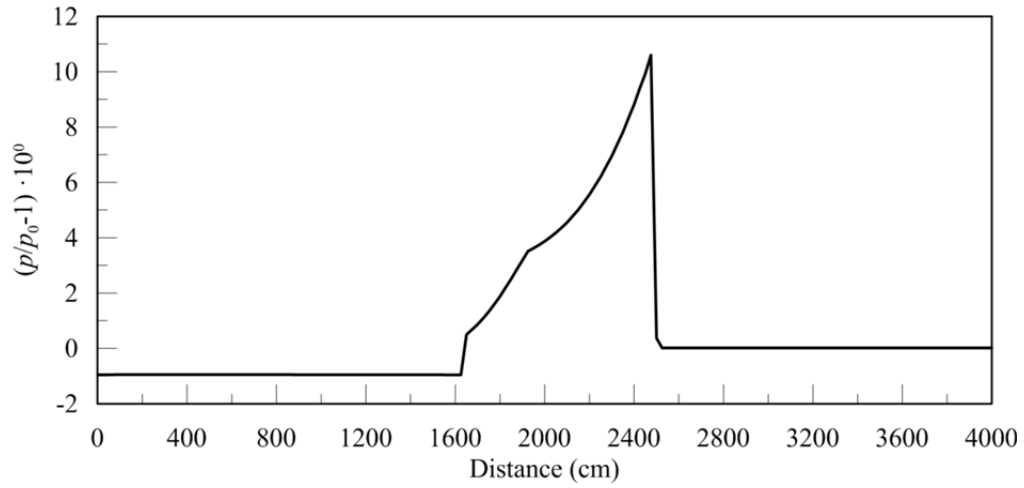


b. Density ( $\rho_0 = 0.001225$  g/cm<sup>3</sup>)

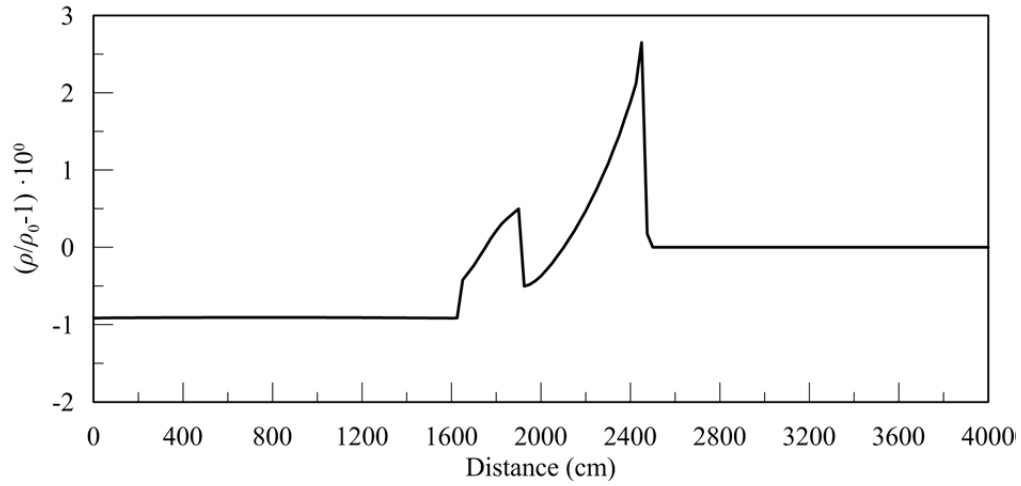


c. Particle velocity,  $v$

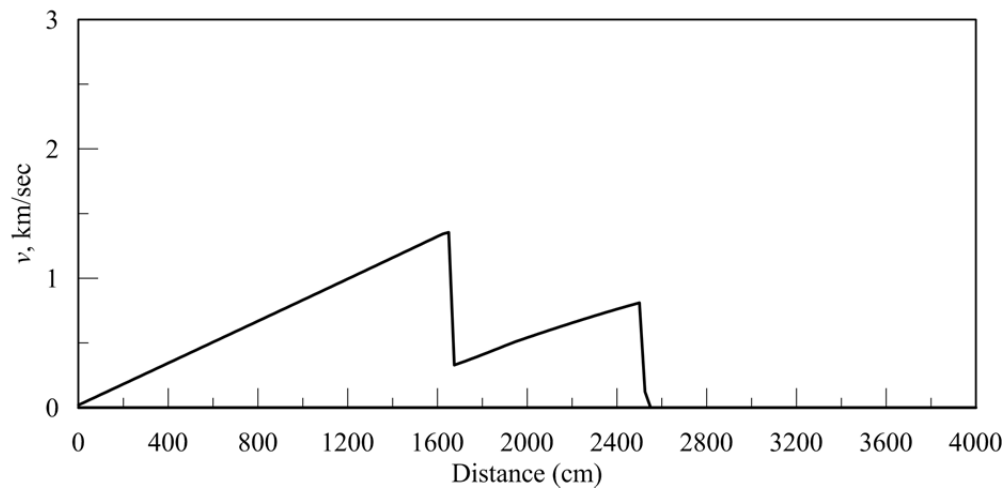
**Figure 2-7 Hydrodynamic parameters at  $\bar{r} = 11.7$  for a 20 mm mesh**



a. Pressure ( $p_0 = 0.1$  MPa)

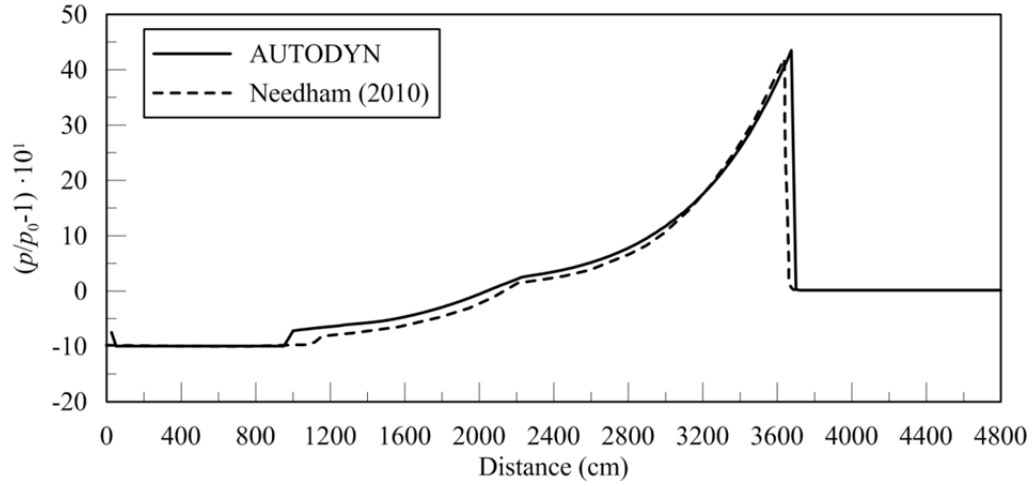


b. Density ( $\rho_0 = 0.001225$  g/cm<sup>3</sup>)

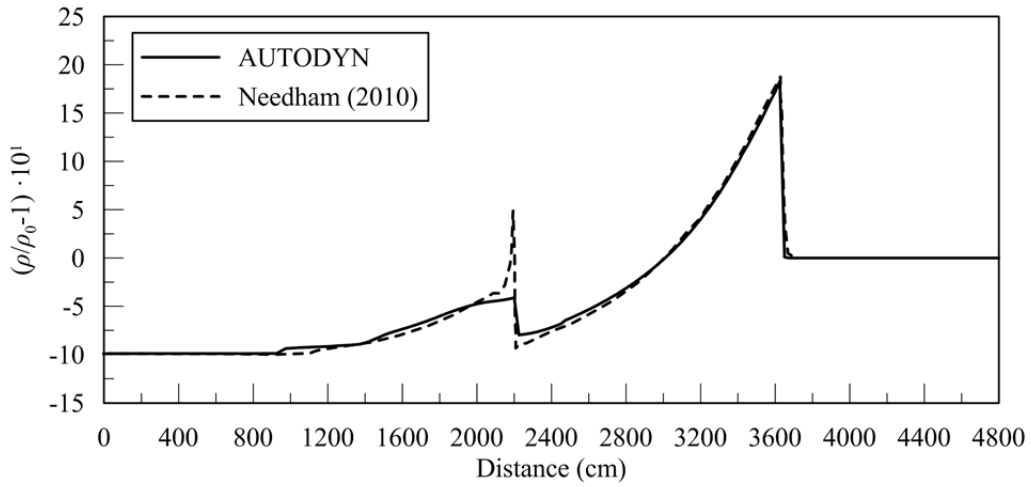


c. Particle velocity,  $v$

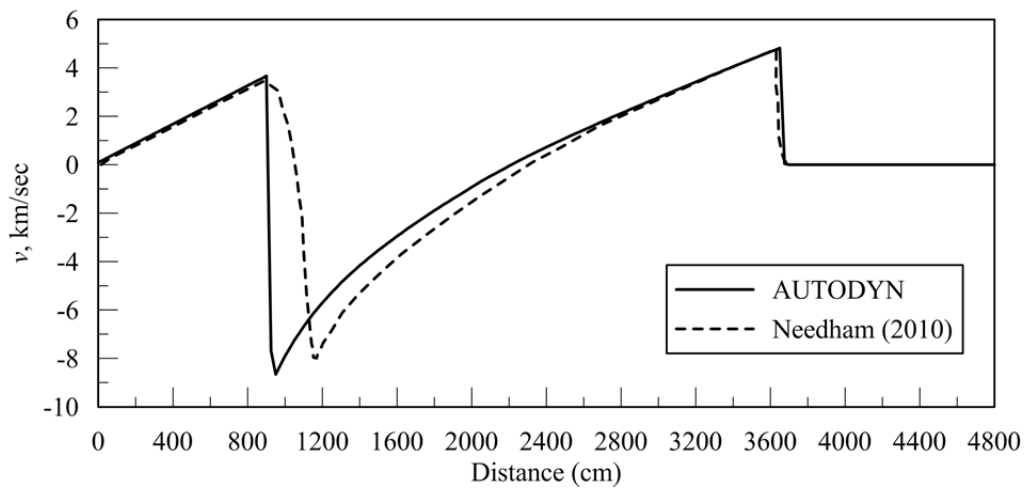
**Figure 2-8 Hydrodynamic parameters at  $\bar{r} = 18$  for a 20 mm mesh**



a. Pressure ( $p_0 = 0.1$  MPa)

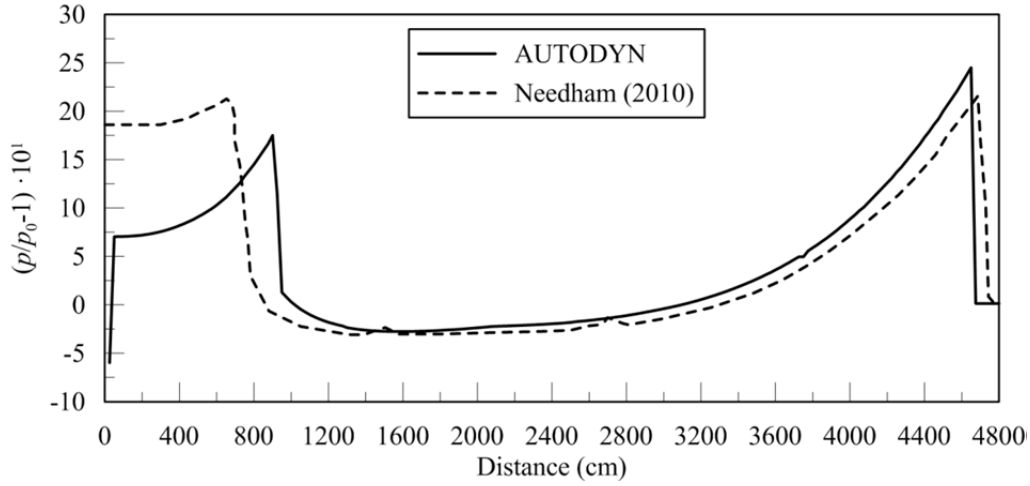


b. Density ( $\rho_0 = 0.001225$  g/cm<sup>3</sup>)

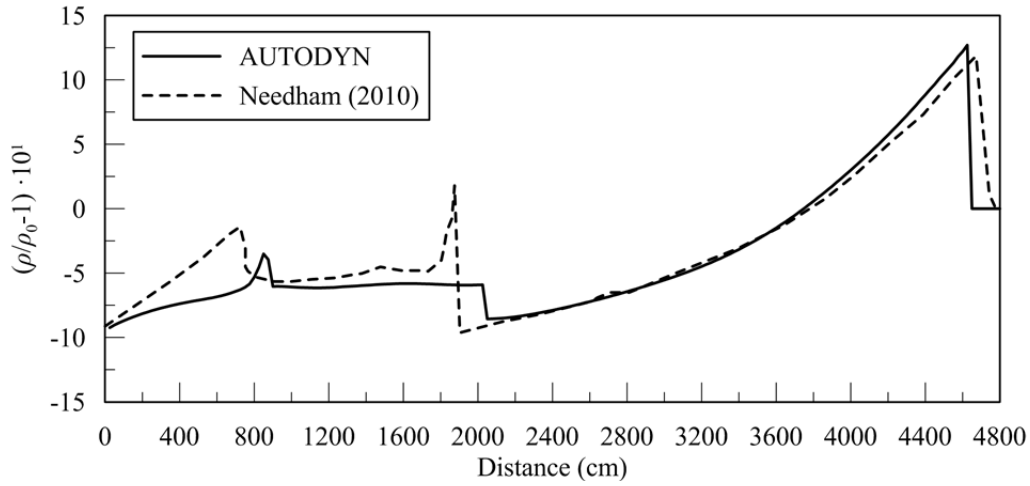


c. Particle velocity,  $v$

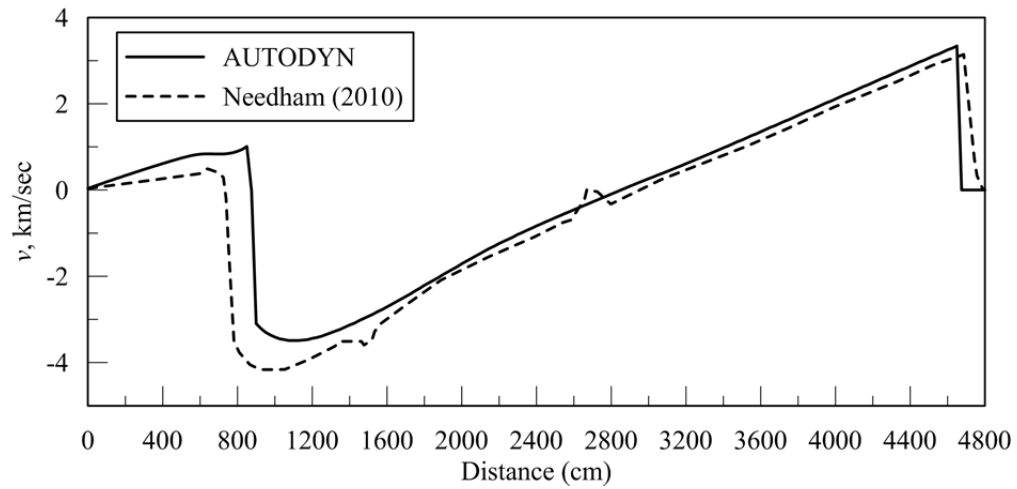
**Figure 2-9 Hydrodynamic parameters at  $\bar{r} = 26$  for a 20 mm mesh**



a. Pressure ( $p_0 = 0.1$  MPa)



b. Density ( $\rho_0 = 0.001225$  g/cm<sup>3</sup>)



c. Particle velocity,  $v$

**Figure 2-10 Hydrodynamic parameters at  $\bar{r} = 34$  for a 20 mm mesh**

Needham reported that the detonation velocity, composed of a sound speed (see Appendix A) at the detonation front of 5.2 km/sec and a peak material velocity of 1.8 km/sec, was 7 km/sec, immediately prior to completion of the detonation (i.e., shock front radial expansion,  $\bar{r}$ , of 1.0). Figure 5.1 of Needham shows that the material velocity at this time instant decays from 1.8 km/sec at the shock front to zero at a radius of 65 cm and that the density (1300 kg/m<sup>3</sup>) and pressure (4.7 MPa) are constant for a radial distance of less than 65 cm where the particles are stationary.

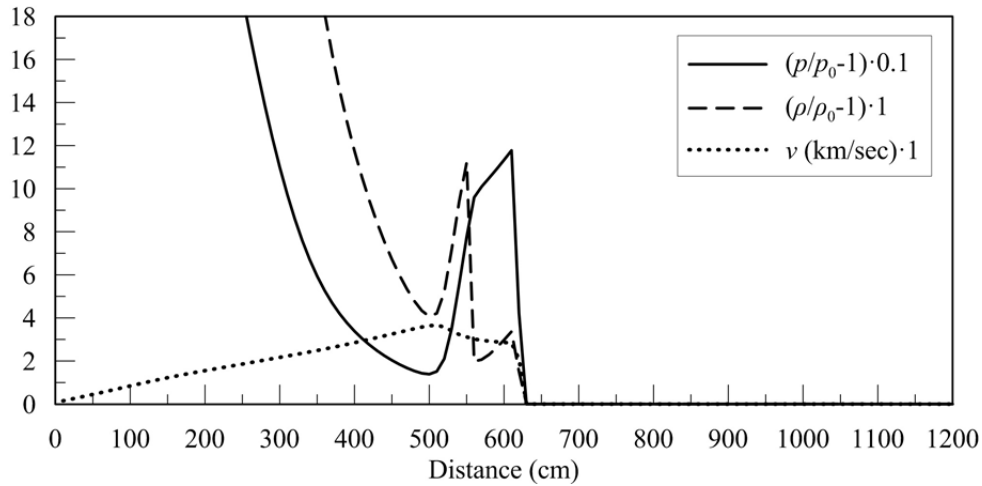
At a shock front radial expansion of 1.1, the normalized pressures and densities are most similar but the AUTODYN peak velocity is substantially smaller than that of Needham of 7.4 km/sec, which is attributed to the coarseness of the chosen mesh (see mesh convergence study later in this section). The peak material velocity of 7.4 km/sec, which is recovered with a much finer mesh (see mesh convergence study later in this section), has increased from 1.8 km/sec at a shock front radial expansion of 1.0. The shock front velocity, which is the sum of the sound speed (0.34 km/s) in air and the peak material velocity, is 7.7 km/s and greater than the detonation velocity. In panel a) of Figure 2-2, it can be seen that the head of the rarefaction wave is at approximately  $r = 130$  cm and 10 cm inside the radius of the charge prior to detonation.

At a shock front radial expansion of 2.4, the AUTODYN and Needham results are similar, with the greatest differences observed for relative overpressure in which it is seen that the rarefaction wave propagates fastest in AUTODYN. In panel a) of Figure 2-3, it is evident that the head of the rarefaction wave has reached the point of detonation ( $r = 0$  cm) in the AUTODYN analysis but only  $r = 35$  cm in the Needham analysis.

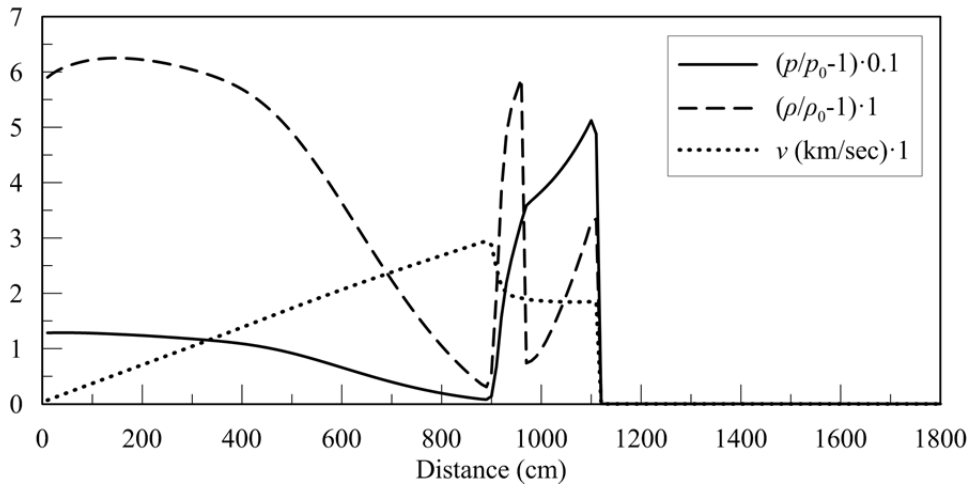
At a shock front radial expansion of 2.6, the hydrodynamic parameters for pressure and density are similar for distances of  $r \geq 80$  cm and at all distances for particle velocity.

At shock front radial expansions of 11.7, 26 and 34, the differences between the AUTODYN and Needham results are by-and-large small. A difference is observed in the relative overdensity at a distance of 1400 cm at a shock front radial expansion of 11.7 (i.e., shock front at 1638 cm from the center of the charge), where a 20 mm mesh cannot resolve the sharp density spike.

Figure 2-11 is provided to observe the relationship between the pressure, density and velocity for shock front radial expansions of 4.5, 8, 11.7, 18 and 26. For a shock front radial expansion of 4.5, the local increase at approximately  $r = 550$  cm is due to the front of the detonation product, at which the pressure history is discontinuous. The peak particle velocity is at  $r \approx 500$  cm, immediately behind the front of the detonation products. The tail of the rarefaction wave is at the point of the peak particle velocity. Similar observations are made for all other shock front radial expansions. For a shock front radial expansion of 26, the velocity at the front of the detonation products (located by an open circle) is nearly zero, which is associated with the discontinuities at  $r \approx 2200$  cm in the pressure and density profiles, respectively, also shown with open circles.

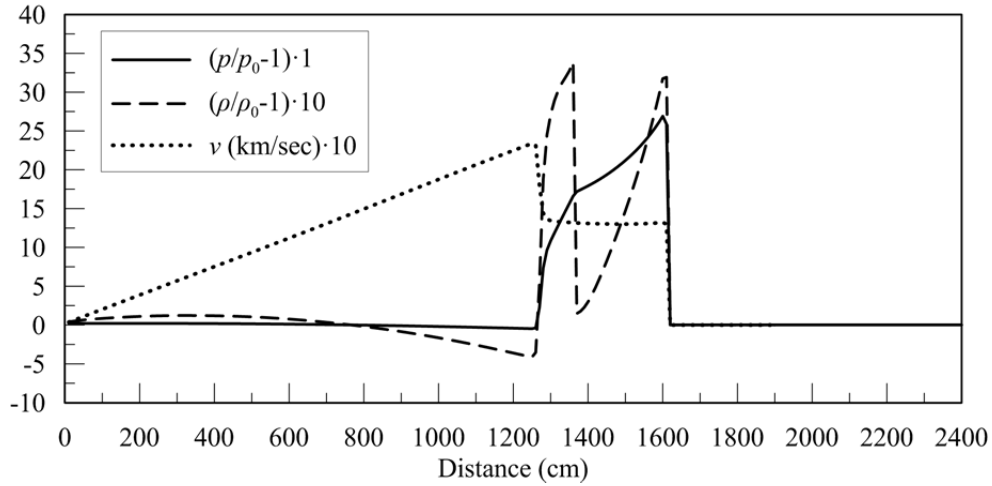


a.  $\bar{r} = 4.5$

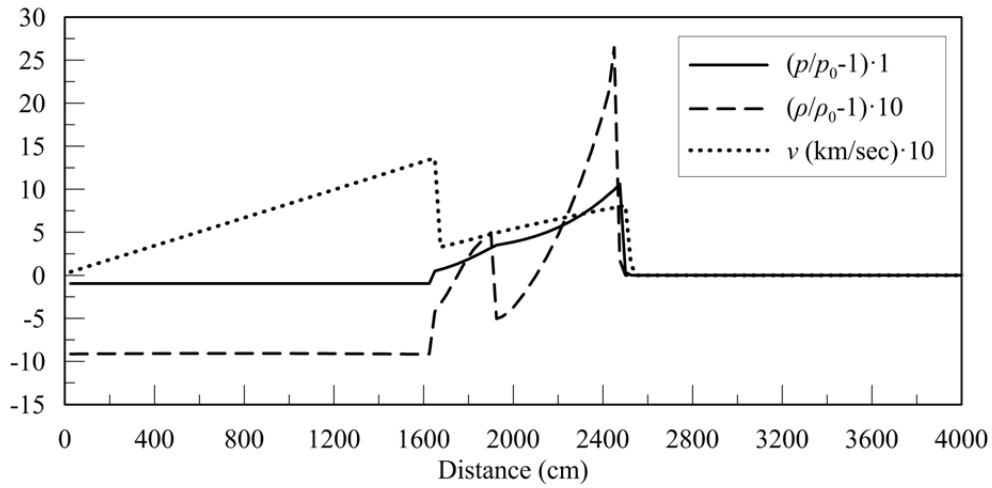


b.  $\bar{r} = 8$

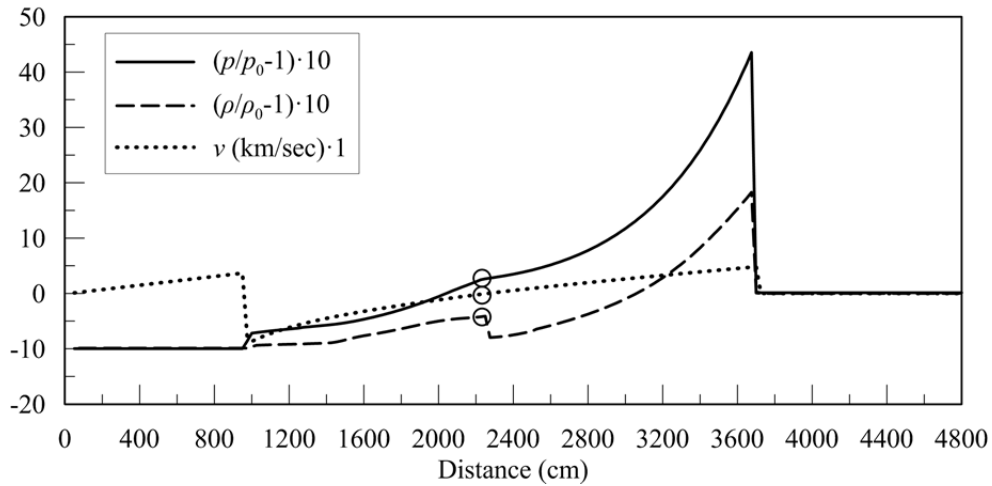
**Figure 2-11 Hydrodynamic parameters for a 20 mm mesh in AUTODYN**



c.  $\bar{r} = 11.7$



d.  $\bar{r} = 18$



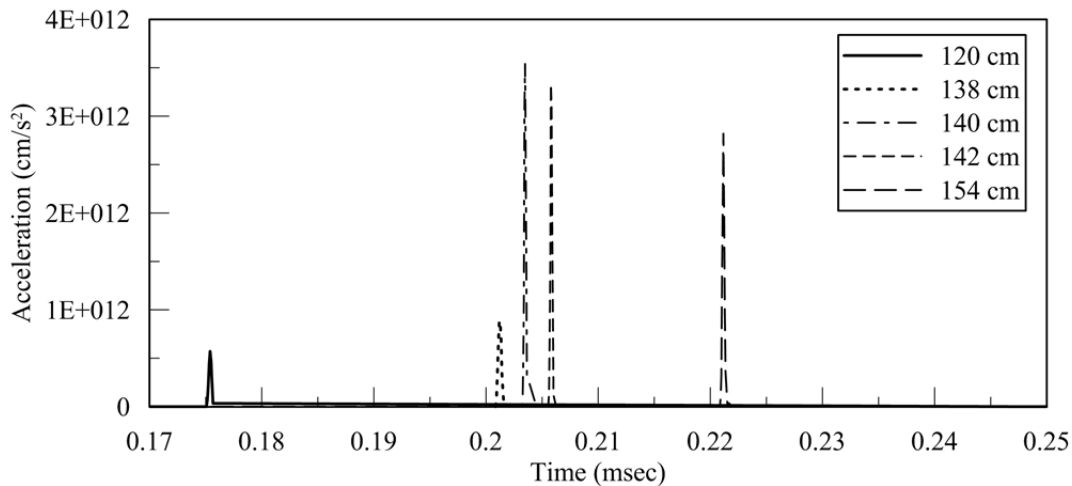
e.  $\bar{r} = 26$

Figure 2-11 Hydrodynamic parameters for a 20 mm mesh in AUTODYN (cont.)

Needham estimated the acceleration of the air immediately beyond the face of the charge at the time the detonation is complete using

$$\frac{dv}{dt} = -\frac{1}{\rho_0} \frac{dp}{dr} \quad (2-5)$$

where  $v$  is the particle velocity,  $\rho_0$  is the ambient density of air,  $p$  is pressure and  $r$  is radius. For  $p$  equal to the average of the detonation pressure<sup>2</sup> (approximately 21000 MPa) and ambient air pressure, an ambient air density of 1.225 kg/m<sup>3</sup>, and a value of  $dr$  equal to 0.01 m (1 cm), the particle acceleration is approximately  $8.6 \times 10^{11}$  m/sec<sup>2</sup>, or  $8.6 \times 10^{10}$  g. Figure 2-12 plots acceleration histories calculated using a cell size of 1 mm at five distances from the center of the explosive; a radius of 140 cm represents the face of the charge. The calculated peak accelerations are smaller than those computed using Equation 2-5, in part due to cell size, as noted above.



**Figure 2-12 Acceleration histories at discrete points along the 1D expansion**

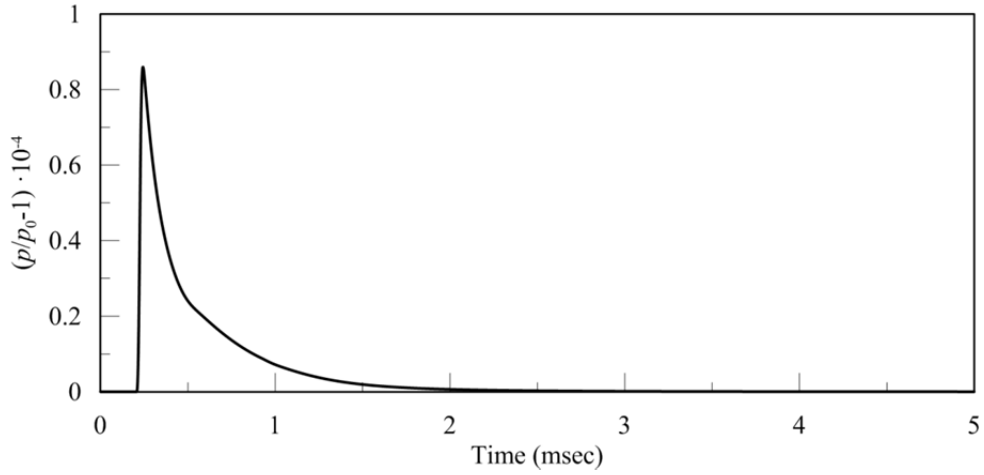
Needham also showed the process of the formation of a secondary shock wave. The (expanding) rarefaction waves moving toward the center of the charge reduce the pressures and densities behind the front of the expanding detonation products. The particle velocity behind the front of the expanding detonation products also decreases and becomes negative. At this time, particles moving at negative velocities lead to shock waves propagating toward the center of the charge. These shock waves are shown in Figure 2-9, where the front of the shock waves is at about  $r \approx$

<sup>2</sup> The calculation of the detonation pressure is discussed in Appendix B.

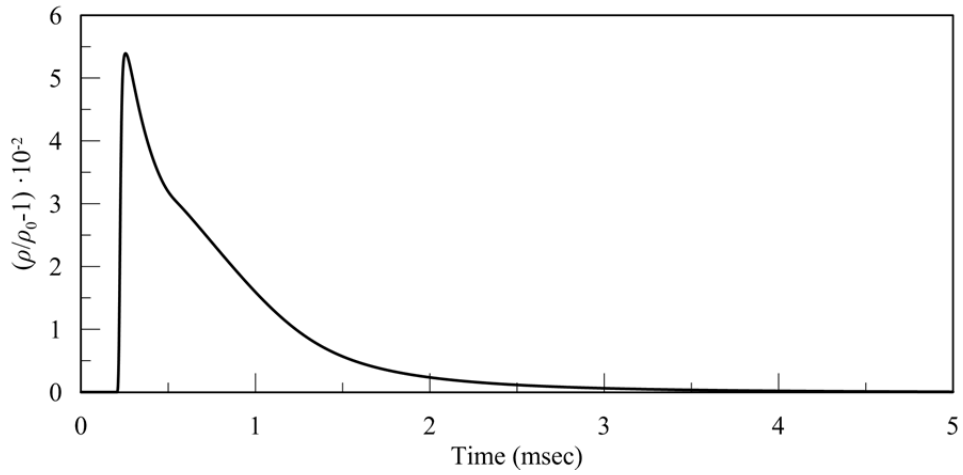
1000 cm and 1200 cm in the AUTODYN and Needham analyses, respectively. The shock wave moving inward is then reflected outward from the center of the charge, which is typically described as the secondary shock wave. The formation of this secondary shock wave is seen in Figure 2-10 for the shock front radial expansion of 34. The secondary shock front is at  $r \approx 650$  cm and 900 cm in the AUTODYN and Needham analyses, respectively.

In summary, the Needham and AUTODYN results are close but not identical. This is attributed to differences in meshing, the choice of solvers and equations of state, and initial choice of TNT density. The fact that the relative overpressures, overdensities, and particle velocities are similar provides confidence in the use of AUTODYN. The importance of choice of cell size, especially for small values of shock front radial expansion, is discussed below in this section and Sections 2.3.3, 2.4, 2.5 and 2.6.

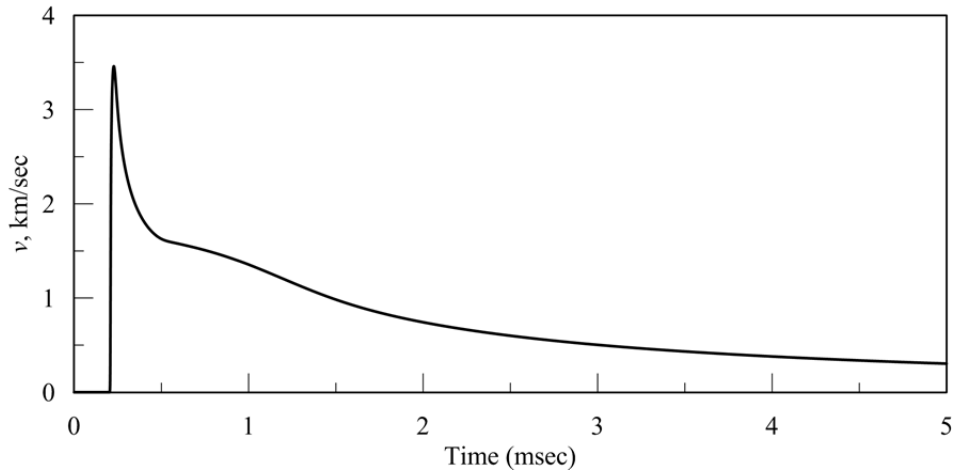
Figures 2-13 through 2-21 present histories of the hydrodynamic parameters at different values of shock front radial expansion. The normalized density history in Figure 2-14 shows three peaks at 0.59 msec, 0.65 msec, and 1.5 msec, which are associated with the arrival of the shock front, arrival of the front of the detonation products, and the peak outflow of detonation products (affected by rarefaction waves moving toward the center of the charge), respectively. The peak in the normalized pressure history in Figure 2-14 (and Figures 2-13, 2-15, 2-16, 2-17, 2-18, 2-19, 2-20, 2-21) is associated with the arrival of the shock front and not the expanding detonation products.



a. Pressure ( $p_0 = 0.1$  MPa)

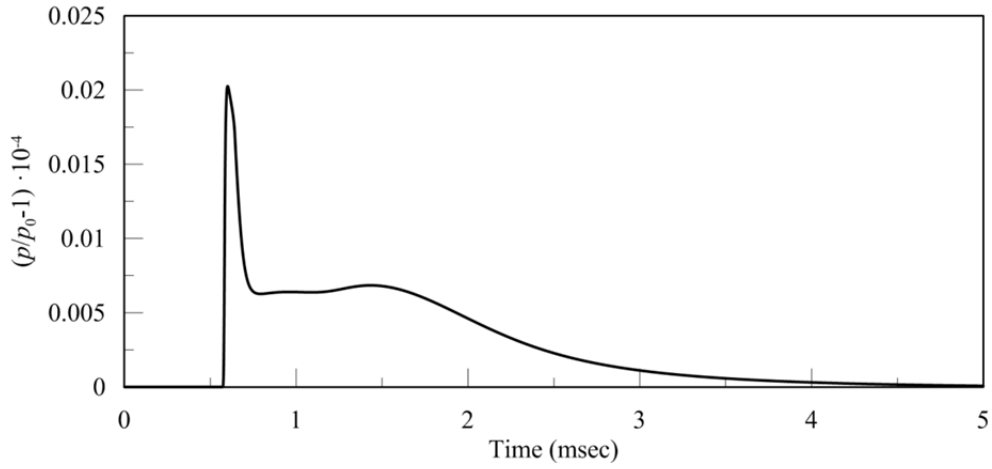


b. Density ( $\rho_0 = 0.001225$  g/cm<sup>3</sup>)

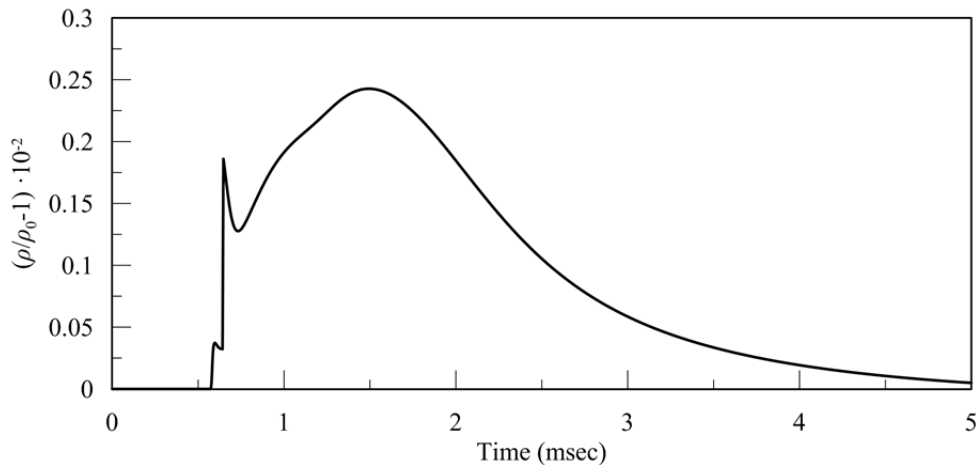


c. Particle velocity,  $v$

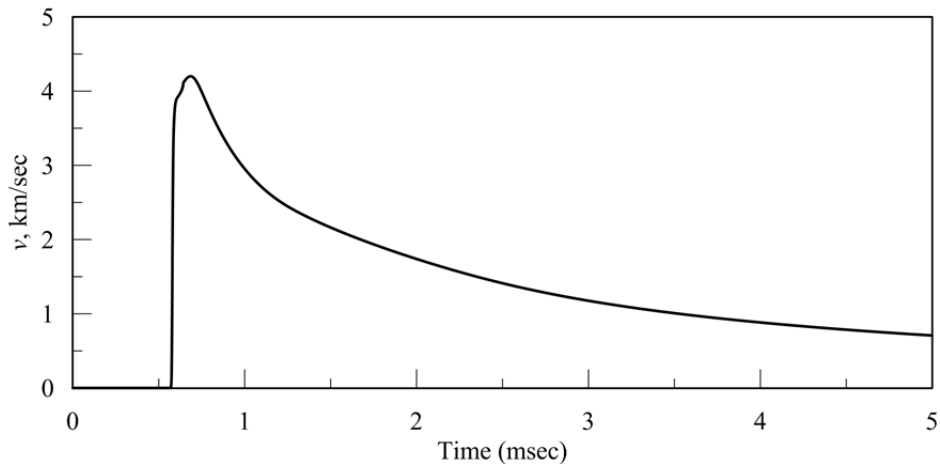
**Figure 2-13 Histories of hydrodynamic parameters at  $\bar{r} = 1.1$  for a 20 mm mesh**



a. Pressure ( $p_0 = 0.1$  MPa)

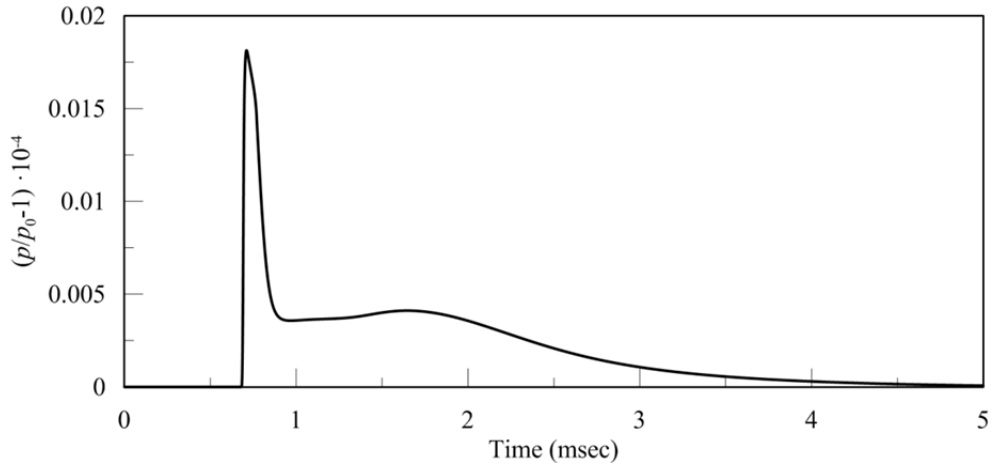


b. Density ( $\rho_0 = 0.001225$  g/cm<sup>3</sup>)

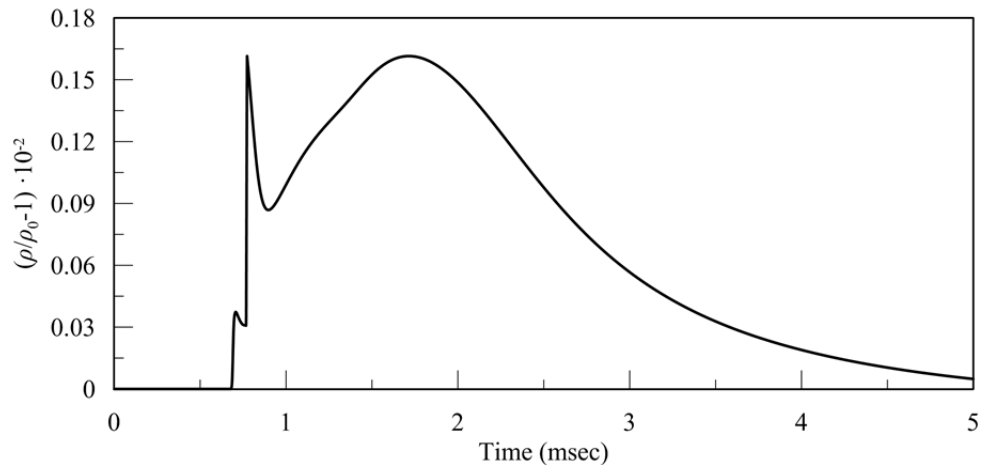


c. Particle velocity,  $v$

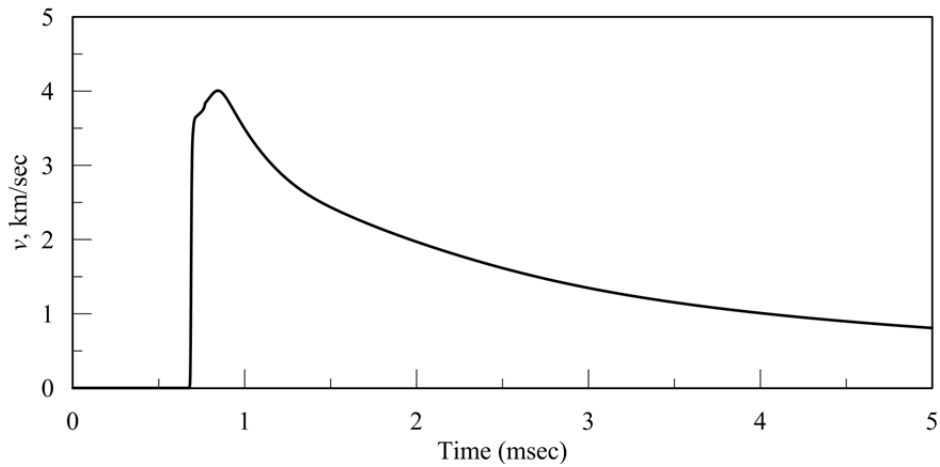
**Figure 2-14 Histories of hydrodynamic parameters at  $\bar{r} = 2.4$  for a 20 mm mesh**



a. Pressure ( $p_0 = 0.1$  MPa)

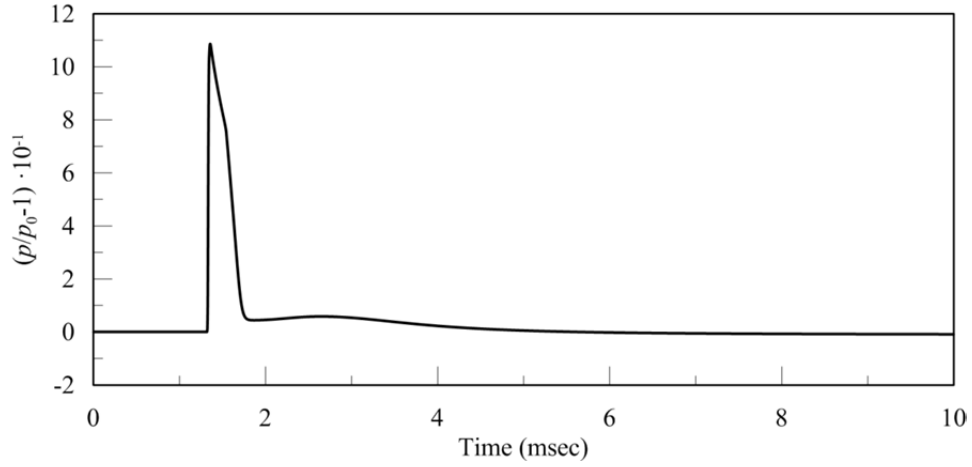


b. Density ( $\rho_0 = 0.001225$  g/cm<sup>3</sup>)

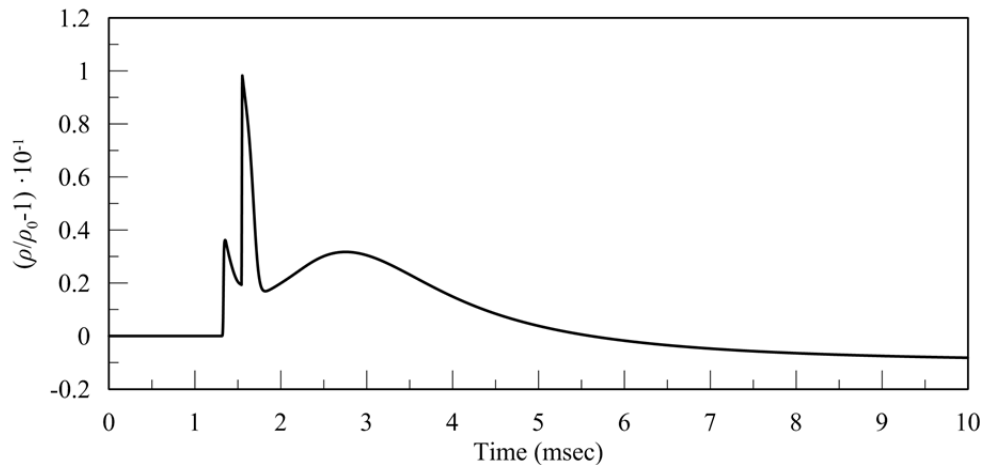


c. Particle velocity,  $v$

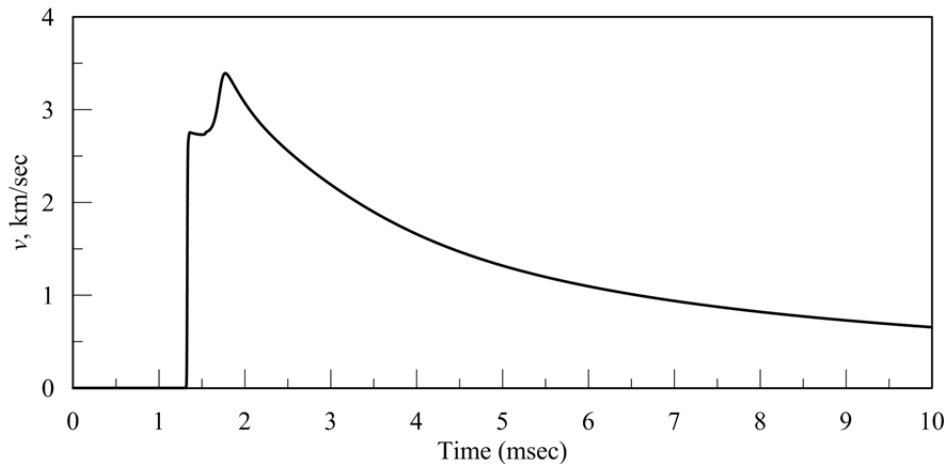
**Figure 2-15 Histories of hydrodynamic parameters at  $\bar{r} = 2.6$  for a 20 mm mesh**



a. Pressure ( $p_0 = 0.1$  MPa)

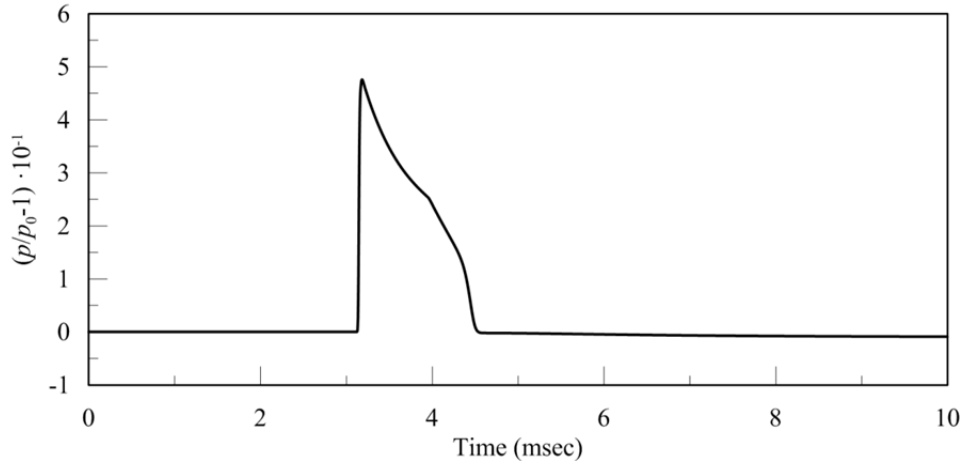


b. Density ( $\rho_0 = 0.001225$  g/cm<sup>3</sup>)

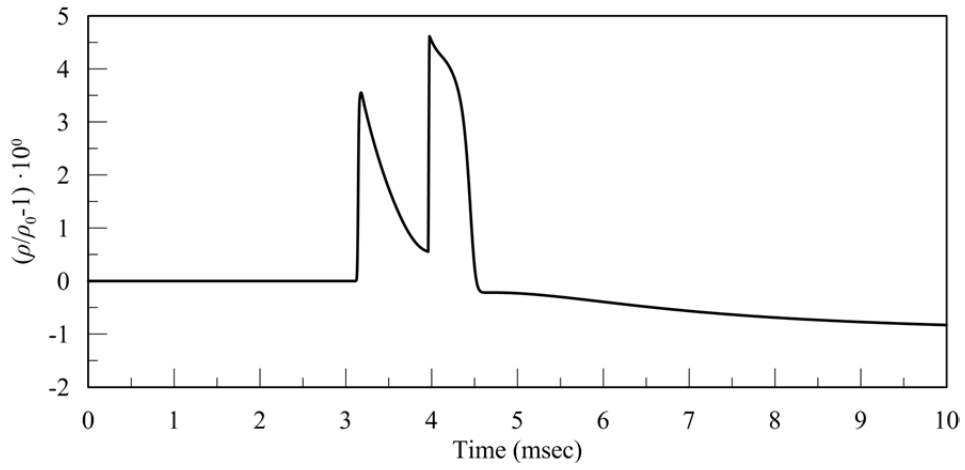


c. Particle velocity,  $v$

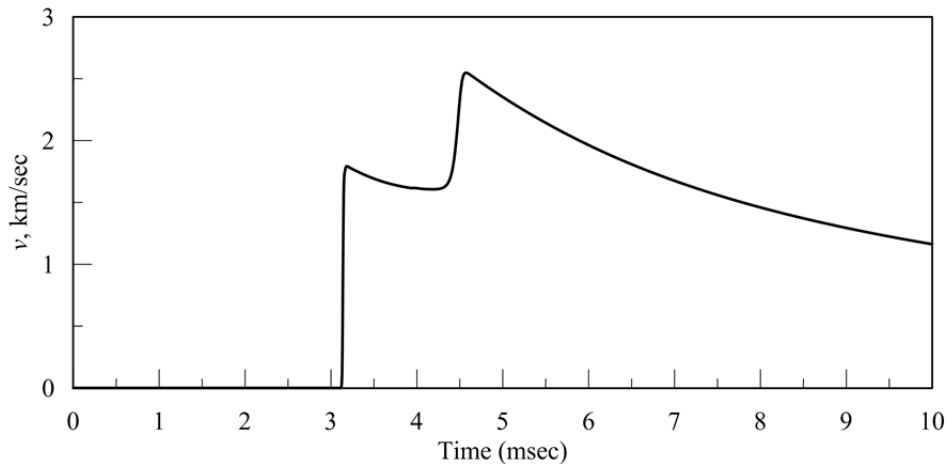
**Figure 2-16 Histories for hydrodynamic parameters at  $\bar{r} = 4.5$  for a 20 mm mesh**



a. Pressure ( $p_0 = 0.1$  MPa)

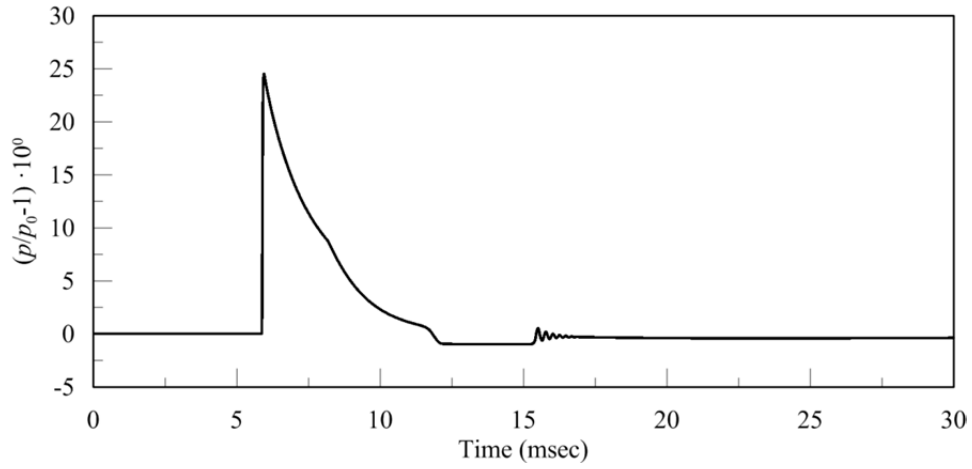


b. Density ( $\rho_0 = 0.001225$  g/cm<sup>3</sup>)

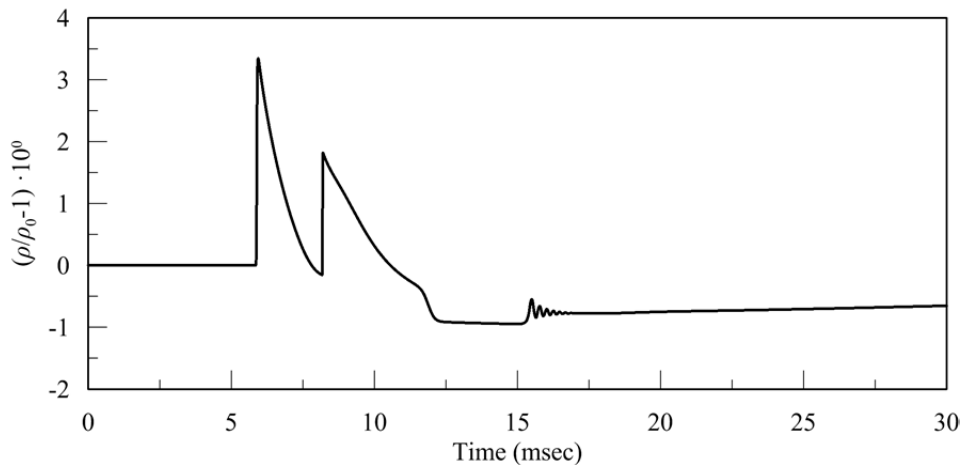


c. Particle velocity,  $v$

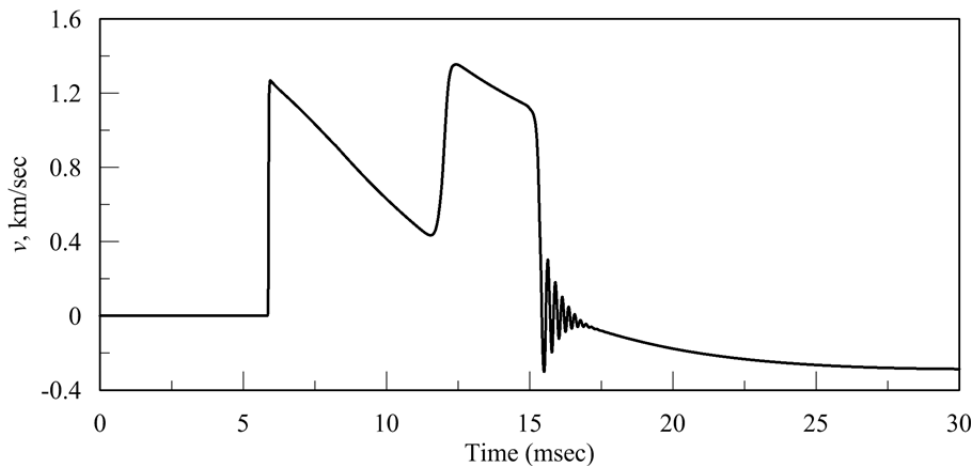
**Figure 2-17 Histories of hydrodynamic parameters at  $\bar{r} = 8$  for a 20 mm mesh**



a. Pressure ( $p_0 = 0.1$  MPa)

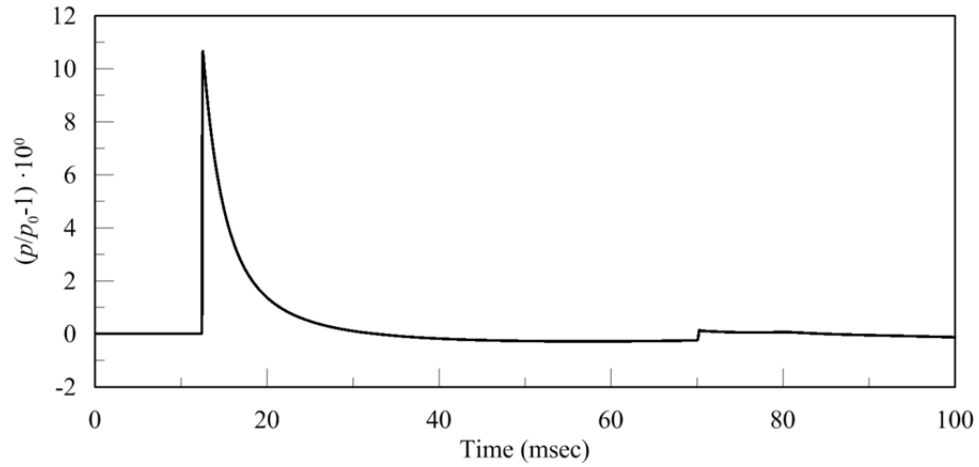


b. Density ( $\rho_0 = 0.001225$  g/cm<sup>3</sup>)

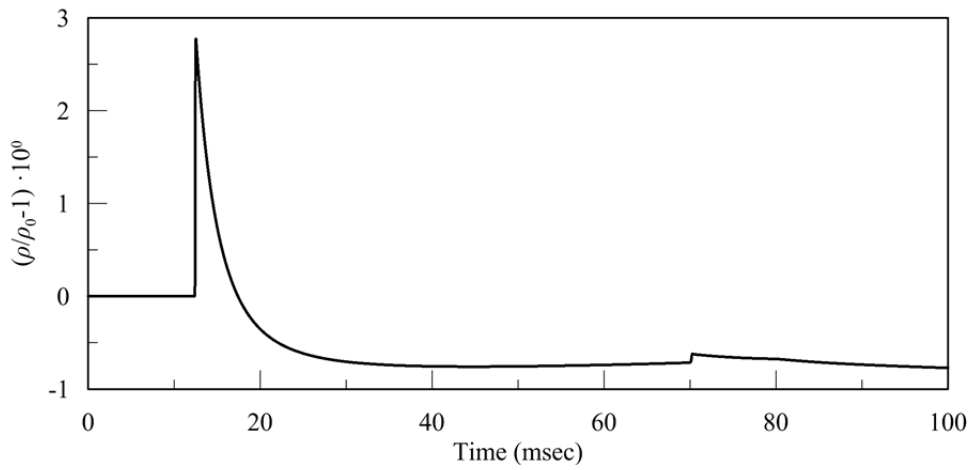


c. Particle velocity,  $v$

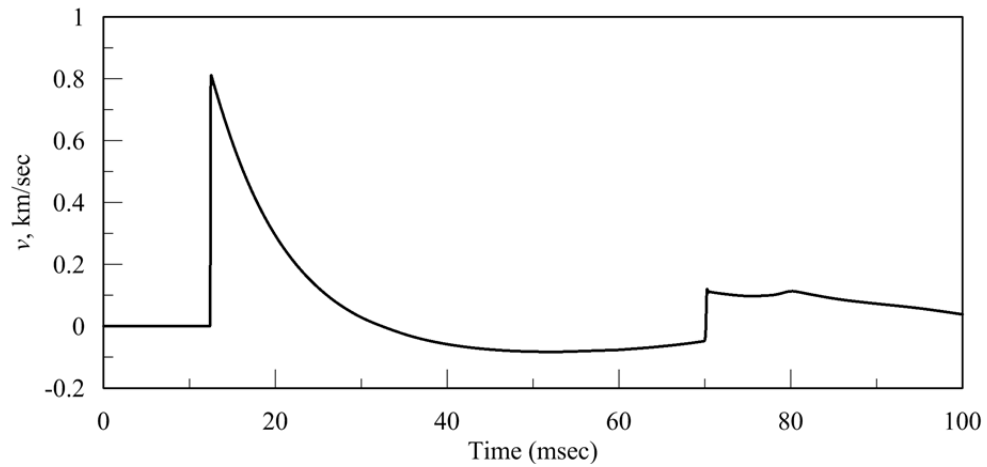
**Figure 2-18 Histories of hydrodynamic parameters at  $\bar{r} = 11.7$  for a 20 mm mesh**



a. Pressure ( $p_0 = 0.1$  MPa)

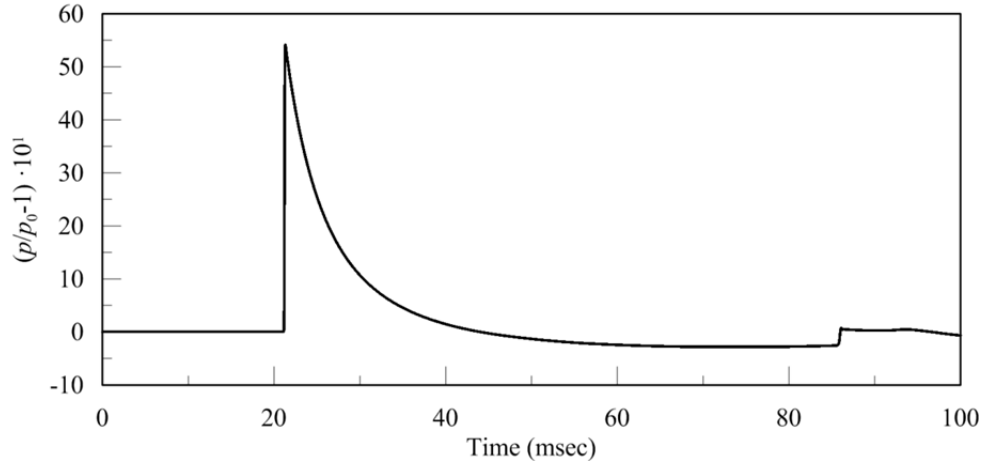


b. Density ( $\rho_0 = 0.001225$  g/cm<sup>3</sup>)

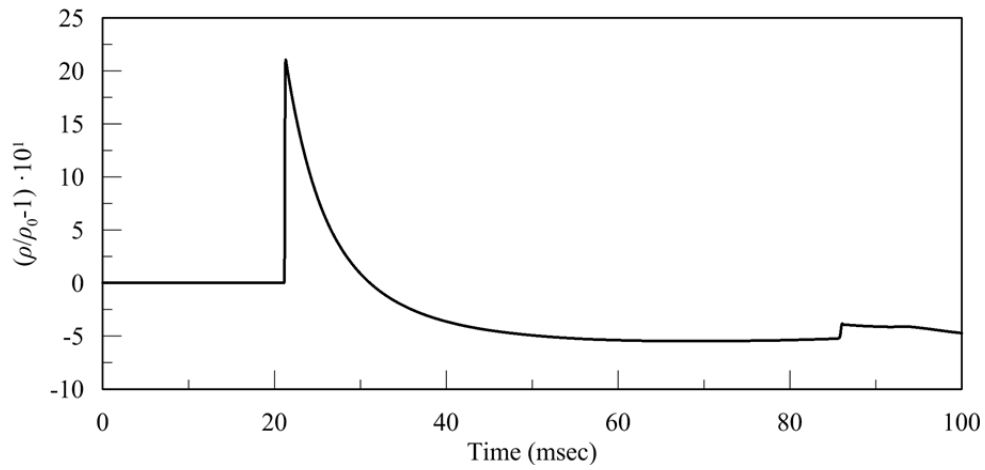


c. Particle velocity,  $v$

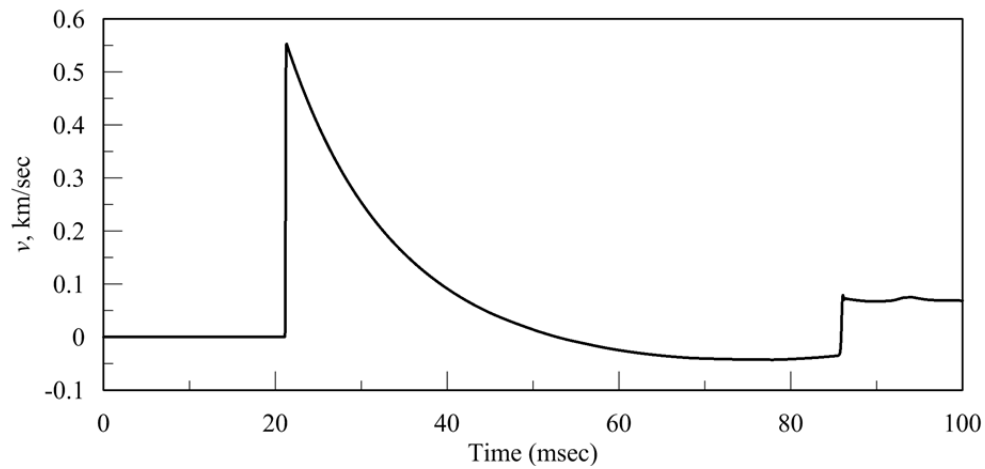
**Figure 2-19 Histories of hydrodynamic parameters at  $\bar{r} = 18$  for a 20 mm mesh**



a. Pressure ( $p_0 = 0.1$  MPa)

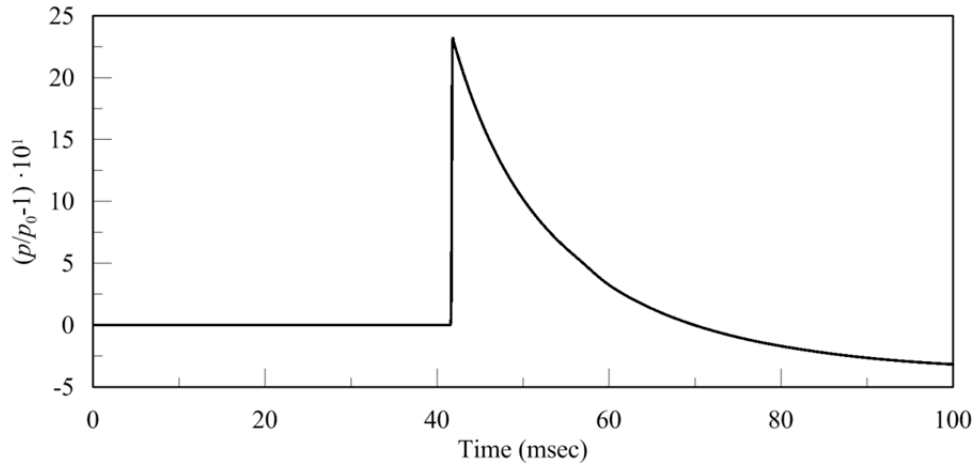


b. Density ( $\rho_0 = 0.001225$  g/cm<sup>3</sup>)

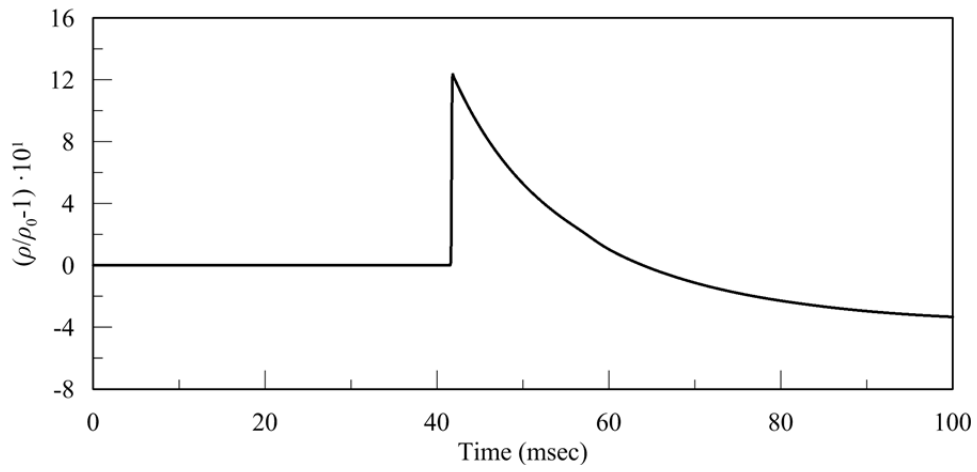


c. Particle velocity,  $v$

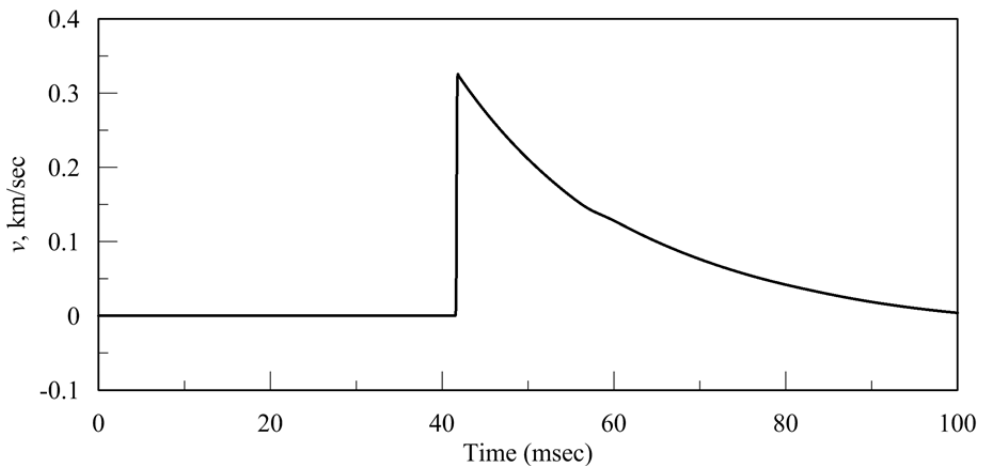
**Figure 2-20 Histories of hydrodynamic parameters at  $\bar{r} = 26$  for a 20 mm mesh**



a. Pressure ( $p_0 = 0.1$  MPa)



b. Density ( $\rho_0 = 0.001225$  g/cm<sup>3</sup>)



c. Particle velocity,  $v$

**Figure 2-21 Histories of hydrodynamic parameters at  $\bar{r} = 34$  for a 20 mm mesh**

A mesh (cell size) convergence study is performed for small values of shock front radial expansion: 0.5, 0.9, 1.1, 2.4 and 2.6. Results are presented in Figures 2-22 through 2-26, respectively. For values less than 1, the shock front lies within the explosive. Data from Needham (2010) are presented here for shock front radial expansions of 1.1, 2.4 and 2.6<sup>3</sup>. The cell (mesh) sizes chosen for AUTODYN analysis were 20 mm (see Figures 2-2 through 2-10), 10 mm, 5 mm and 1 mm. A comparison of results for the radial expansions greater than 1 shows that the finer the AUTODYN mesh, the closer the results are to those reported by Needham. The influence of cell size is pronounced for particle velocity at a shock front radial expansion of 1.1. The speed of propagation of the rarefaction wave is better resolved with the finer meshes as seen in Figure 2-25a. For the mesh with 20 mm cells, AUTODYN predicts the rarefaction wave has reached the point of detonation at a shock front radial expansion of 2.4. For the 1 mm cell size, AUTODYN predicts that the rarefaction wave has reached a distance,  $r$ , equal to 25 cm from the point of detonation at a shock front radial expansion of 2.4, which correlates better with the Needham prediction of  $r = 35$  cm.

The importance of cell size for the correct modeling of the propagation of the shock front through the explosive is seen clearly in Figures 2-22 and 2-23. The rapid changes in pressure, density and particle velocity across the shock front are not captured with the meshes constructed with 10 mm and 20 mm cells.

In Figures 2-22 and 2-23, the detonation fronts are identified at  $r \approx 68$  cm and 125 cm, respectively. The peak relative overpressure at the detonation front is approximately 180000 for the 1 mm mesh. The relative overdensity of the charge near its center after detonation is 1090, which is 18% less than that of a cold (unreacted) TNT ( $\approx 1330$  ( $= 1630 \text{ kg/m}^3 / 1.225 \text{ kg/m}^3 - 1$ , where 1630 and 1.225 are the TNT packing density and ambient air density, respectively). At the detonation front, the relative overdensity is approximately 1650, which is 24% greater than that of cold TNT, which shows that the detonation products are not very compressible because the

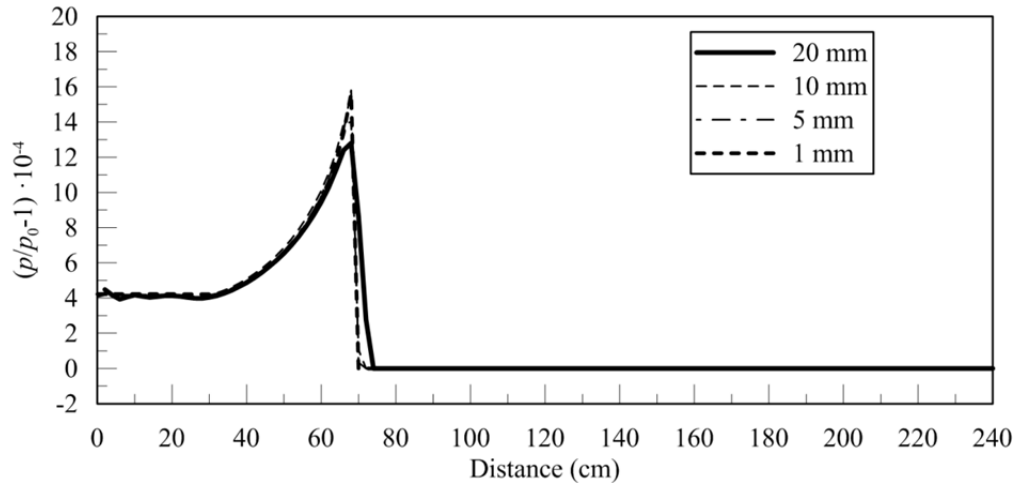
---

<sup>3</sup> Numerical studies to investigate incident peak overpressure and reflected peak overpressure in very close proximity to the face of a charge,  $0.981 \leq \bar{r} \leq 1.034$ , are presented in Appendix C. Those studies are not integrated into this presentation because Needham did not report results in this region. A charge with a radius of 150 mm is used in Appendix C and results are reported at distances of  $147 \leq r \leq 155$  mm, namely,  $0.981 \leq \bar{r} \leq 1.034$  and  $0.517 \leq Z \leq 0.545 \text{ m/kg}^{1/3}$ .

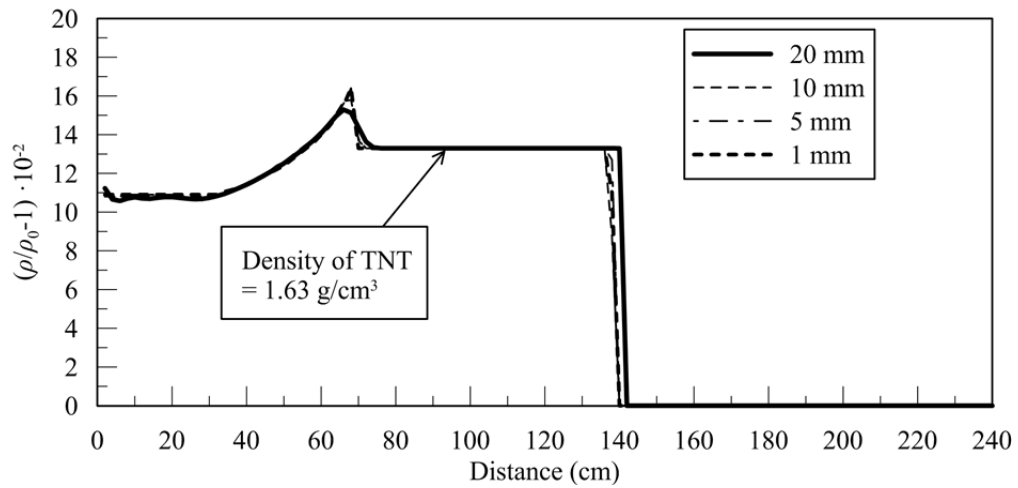
pressure at the detonation front ( $\approx 180$  kbars) is extremely high. The peak velocity is approximately 1.6 km/sec for the finest mesh of 1 mm in panel c) of Figure 2-23, which is similar to that in the Needham analysis (=1.8 km/sec).

A mesh convergence study for overpressure and impulse is also performed for the 18735 kg charge used in this section at shock front radial expansions of 1.025, 1.1, 2.4, 4.5 and 11.7;  $Z = 0.054, 0.058, 0.13, 0.24$  and  $0.62 \text{ m/kg}^{1/3}$ , respectively, where  $Z$  is the scaled distance, defined in Section 1.4. The radial expansion of  $\bar{r} = 1.025$  is chosen in preference to  $\bar{r} = 1.0$  because the particle acceleration and velocity very close to the face of the charge change rapidly but both stabilize at a radial expansion  $\bar{r} = 1.025$  (see Section 3.5). Cell sizes of 400, 200, 100, 40, 20, 10, 5 and 2 mm are considered. Results are presented in Figures 2-27 and 2-28. For the five shock front radial expansions of 1.025, 1.1, 2.4, 4.5 and 11.7, the overpressure histories converge for cell sizes of 5, 5, 10, 20 and 200 mm, respectively, ( $r/287, r/308, r/336, r/315$  and  $r/82$ ), where convergence is defined as a result within 20% of the “true” result calculated with the smallest cell size (2 mm here). For impulse, the results converge for cell sizes of 10, 10, 10, 40 and 400 mm, respectively ( $r/144, r/154, r/336, r/158$  and  $r/41$ ). The overpressure histories, especially for Figures 2-27c and 2-27d are quite different from the Friedlander curve (described in Section 2.1) due to the influence of expanding detonation products, which are discussed in more detail in Sections 2.4 and 2.5.

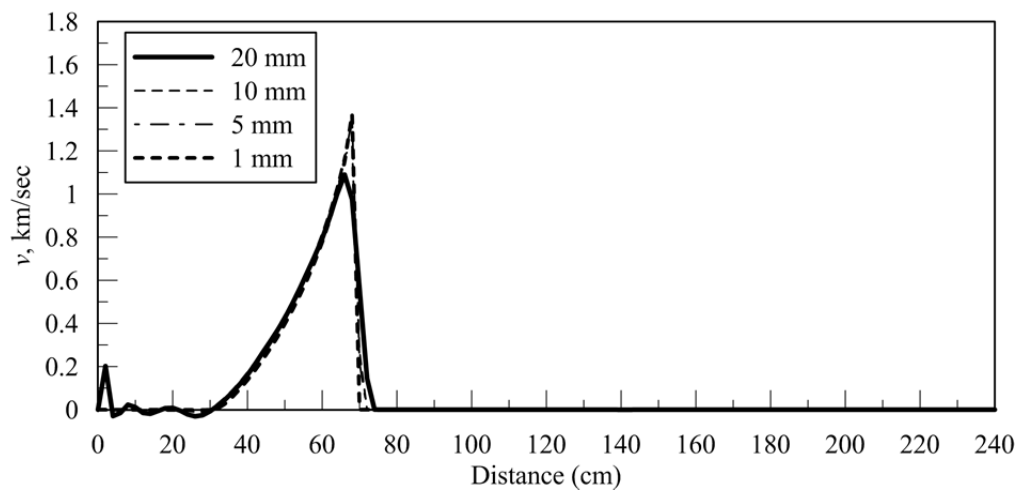
We thus consider AUTODYN to be *verified* for 1D calculations of overpressure and impulse for near-field detonations.



a. Pressure ( $p_0 = 0.1$  MPa)

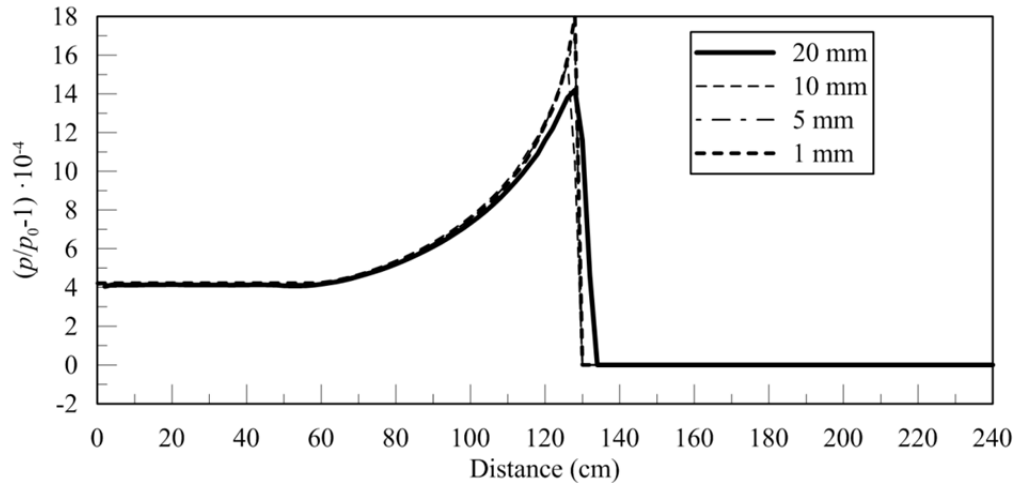


b. Density ( $\rho_0 = 0.001225 \text{ g/cm}^3$ )

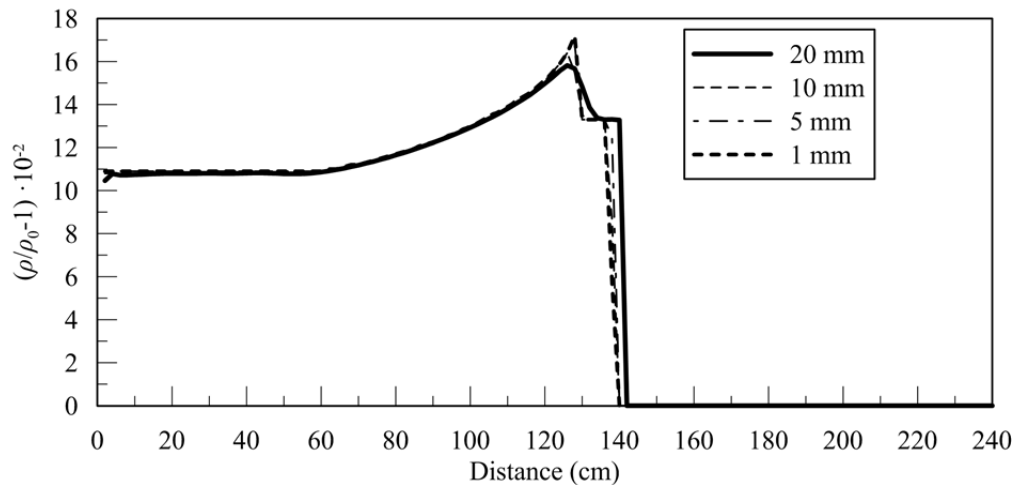


c. Particle velocity,  $v$

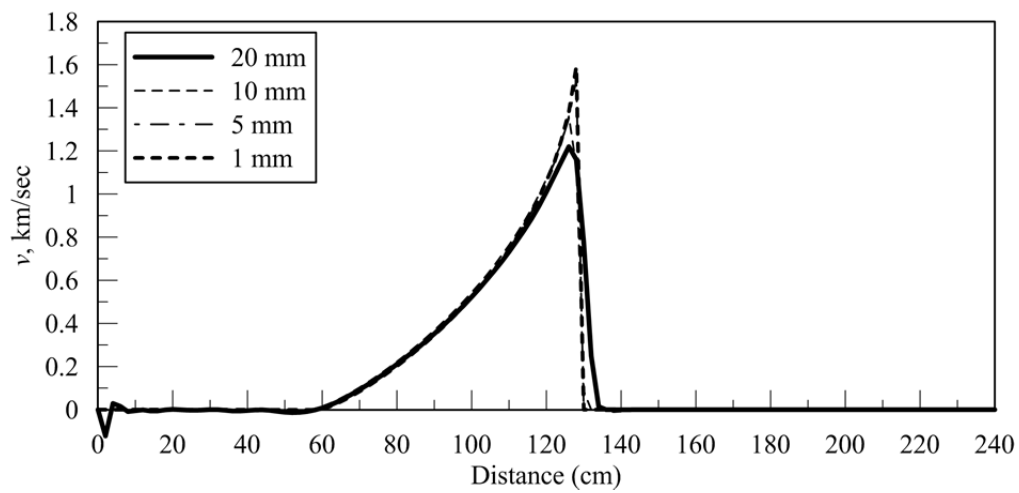
**Figure 2-22 Mesh convergence study at  $\bar{r} = 0.5$**



a. Pressure ( $p_0 = 0.1$  MPa)

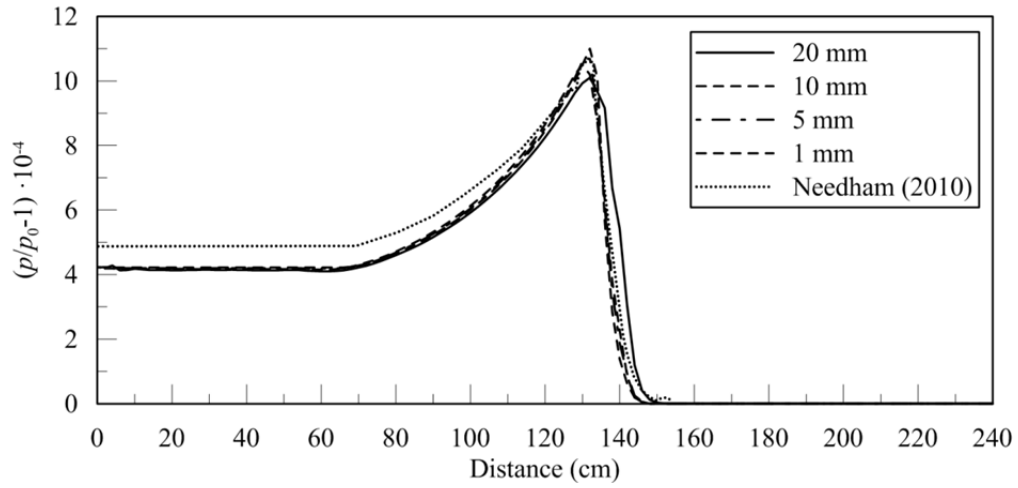


b. Density ( $\rho_0 = 0.001225$  g/cm<sup>3</sup>)

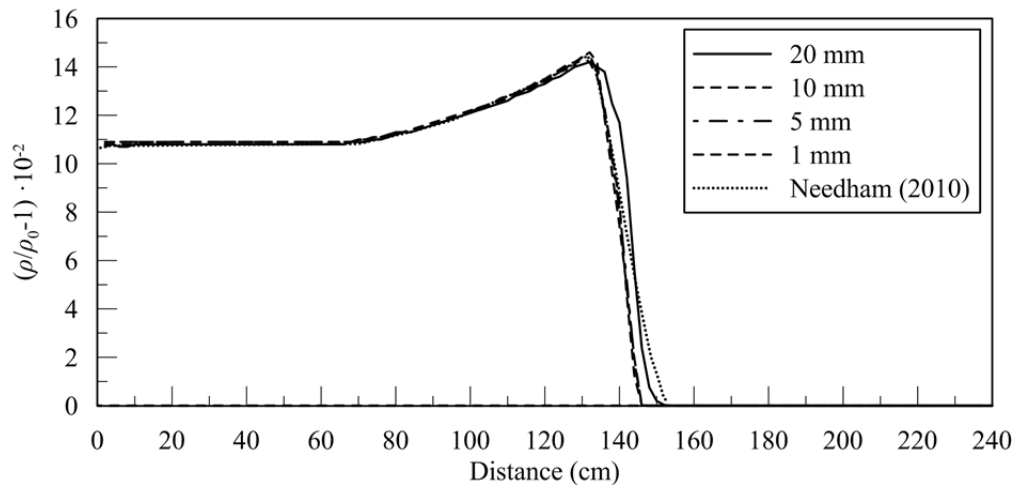


c. Particle velocity,  $v$

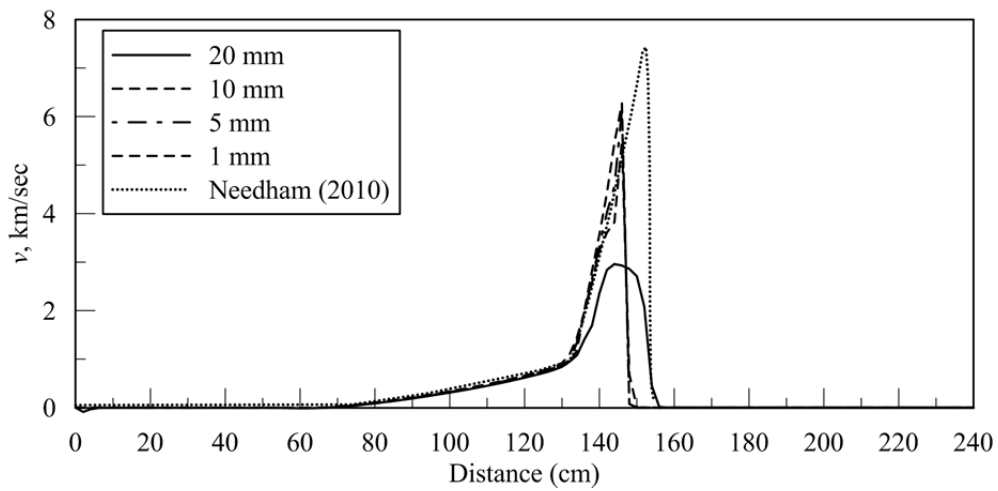
**Figure 2-23 Mesh convergence study at  $\bar{r} = 0.9$**



a. Pressure ( $p_0 = 0.1$  MPa)

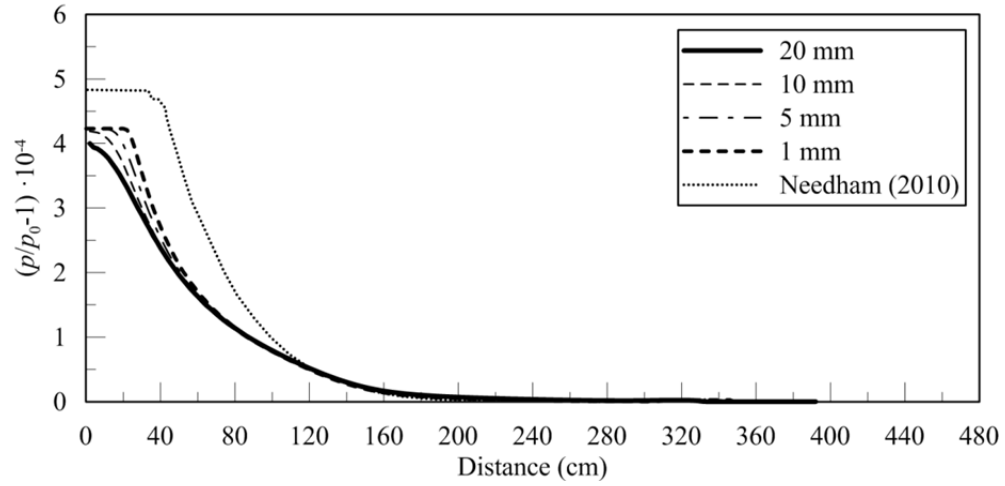


b. Density ( $\rho_0 = 0.001225$  g/cm<sup>3</sup>)

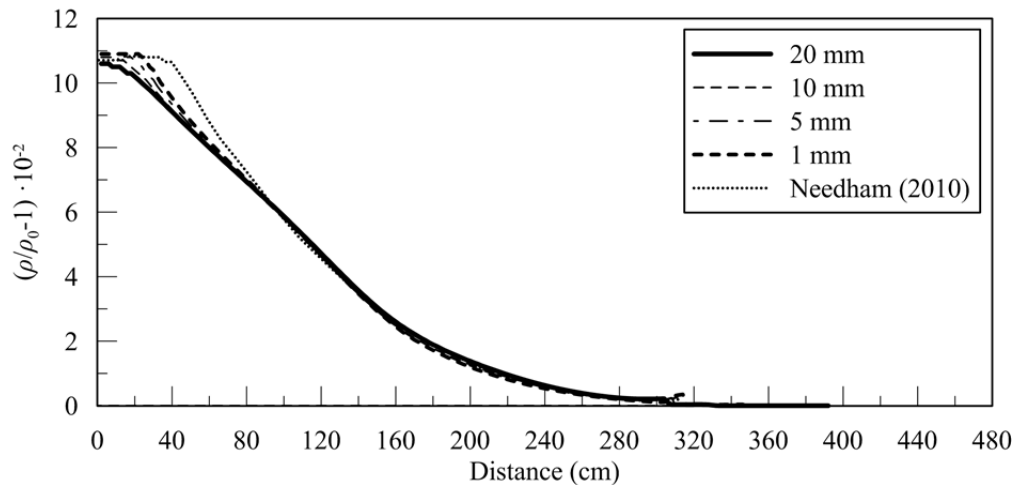


c. Particle velocity,  $v$

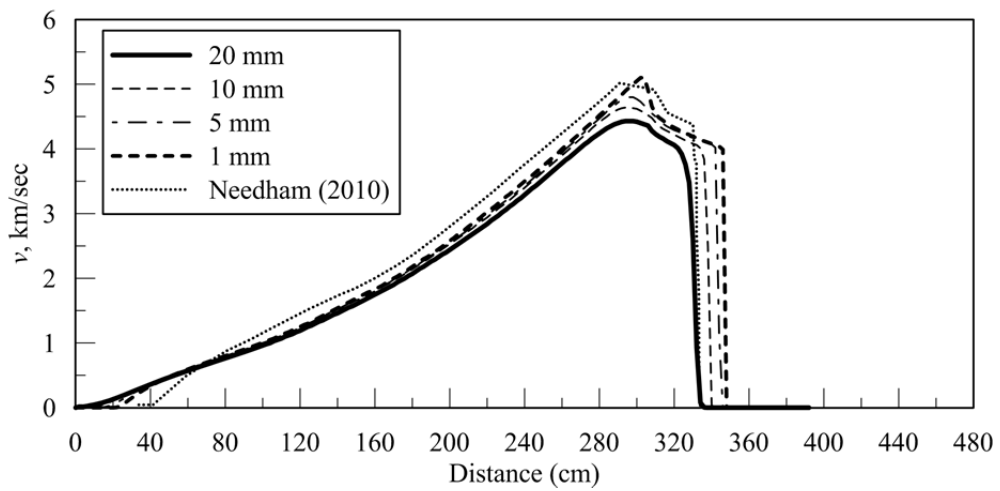
**Figure 2-24 Mesh convergence study for  $\bar{r} = 1.1$**



a. Pressure ( $p_0 = 0.1$  MPa)

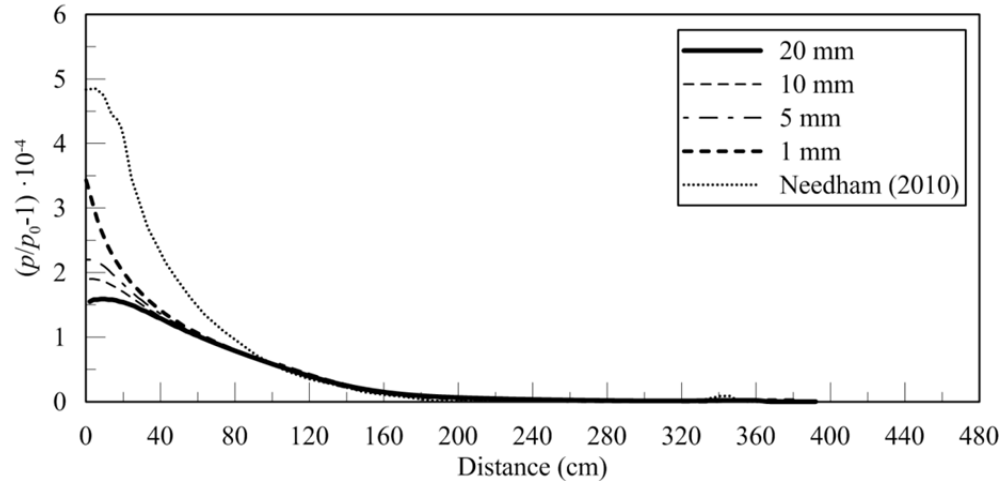


b. Density ( $\rho_0 = 0.001225$  g/cm<sup>3</sup>)

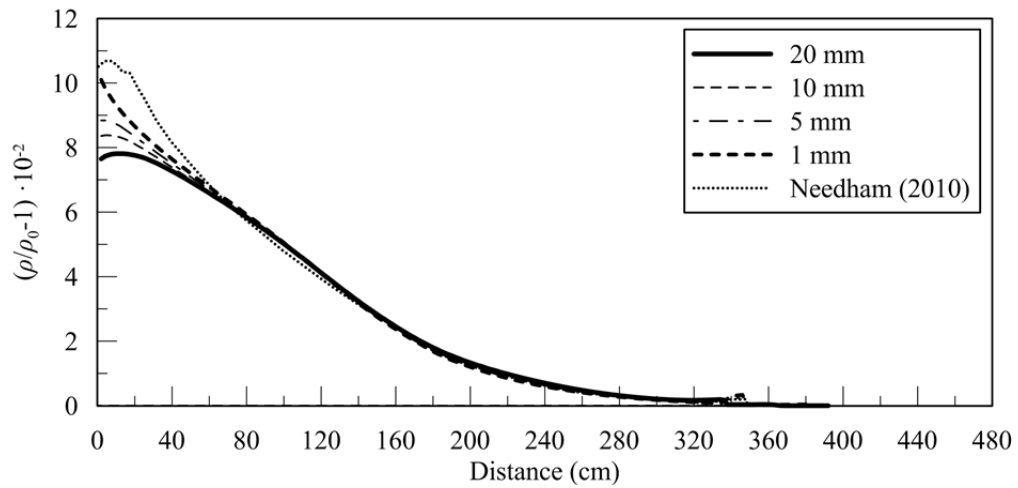


c. Particle velocity,  $v$

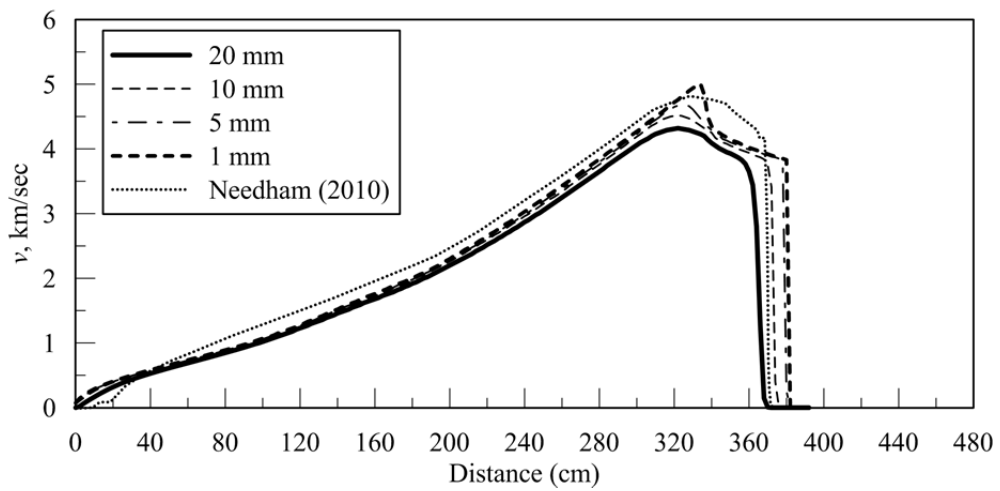
**Figure 2-25 Mesh convergence study for  $\bar{r} = 2.4$**



a. Pressure ( $p_0 = 0.1$  MPa)

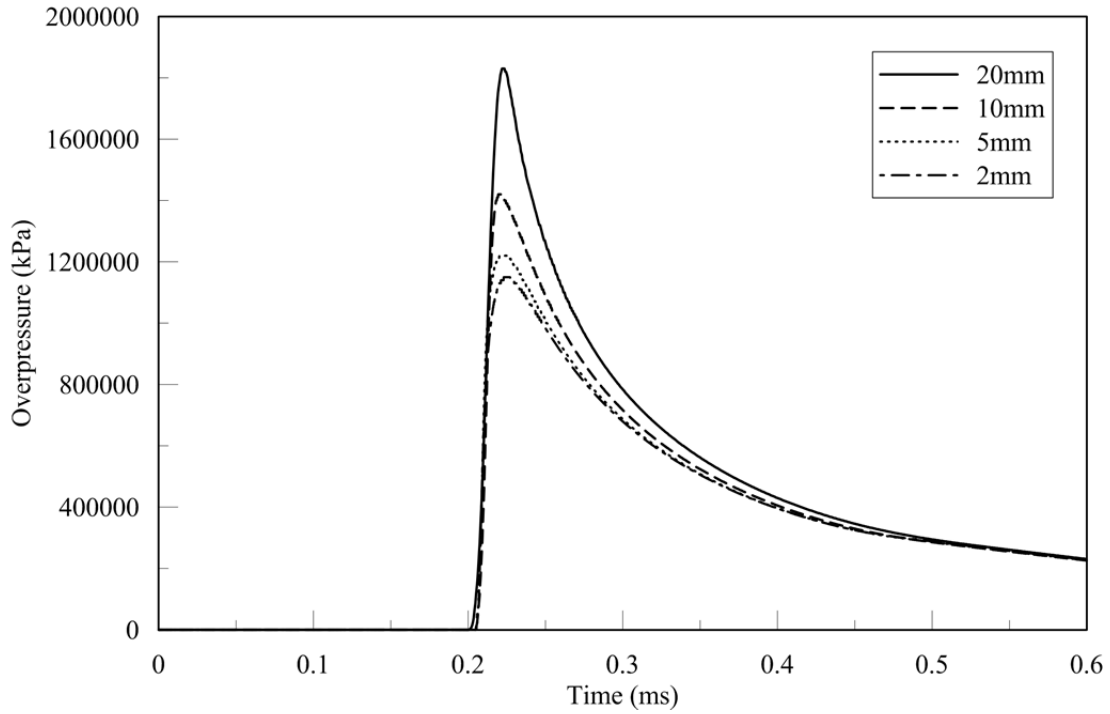


b. Density ( $\rho_0 = 0.001225$  g/cm<sup>3</sup>)

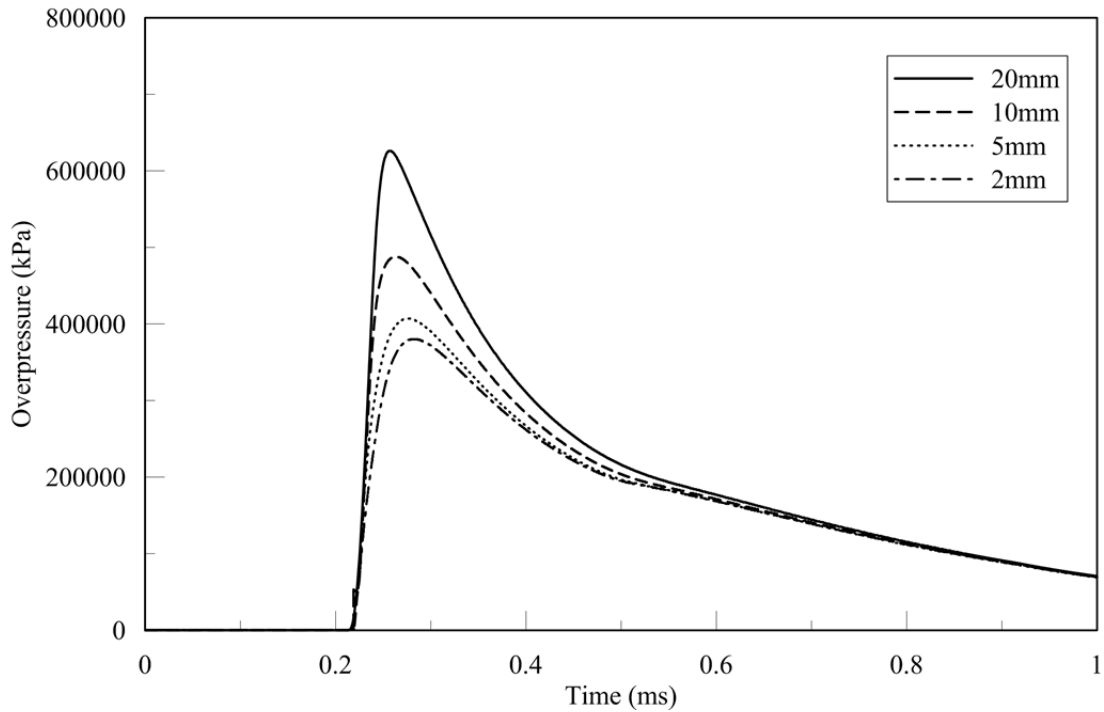


c. Particle velocity,  $v$

**Figure 2-26 Mesh convergence study for  $\bar{r} = 2.6$**

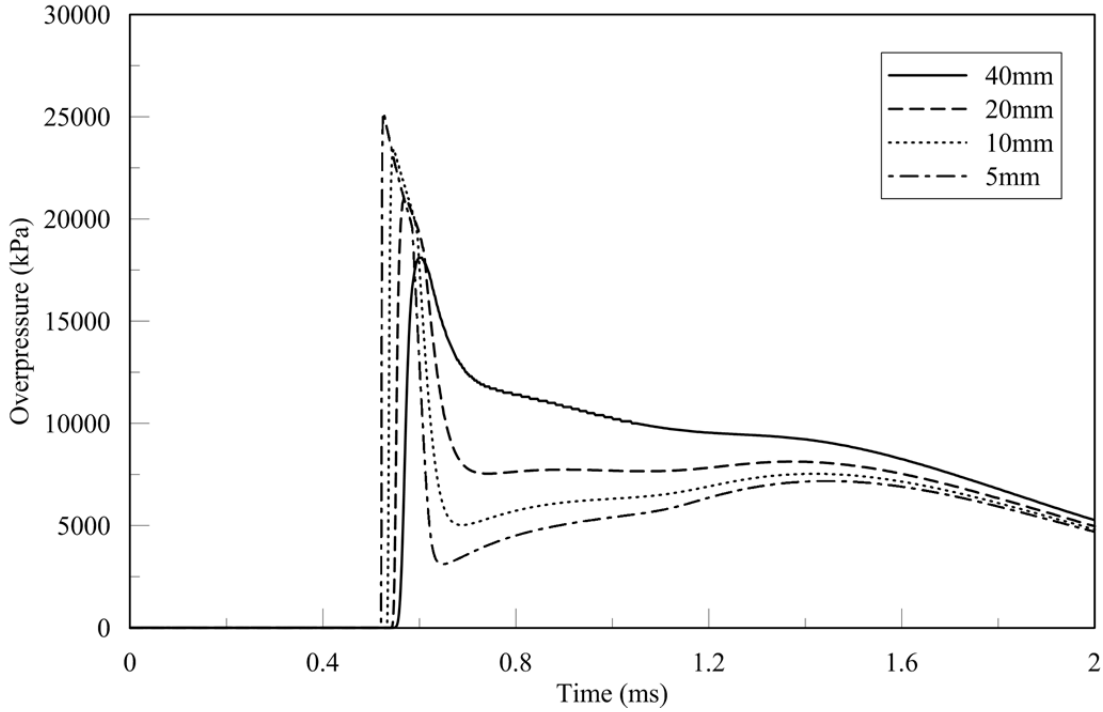


a.  $r = 1435$  m (35 mm from face of charge);  $Z = 0.054$  m/kg<sup>1/3</sup>;  $\bar{r} = 1.025$

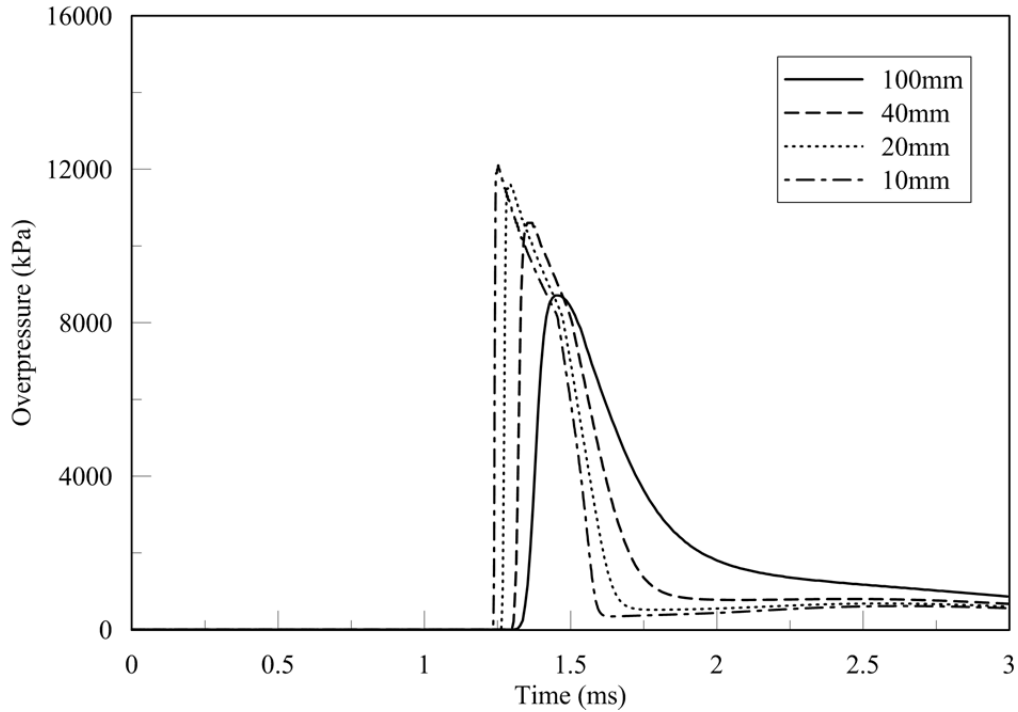


b.  $r = 1540$  mm (140 mm from face of charge);  $Z = 0.058$  m/kg<sup>1/3</sup>;  $\bar{r} = 1.10$

**Figure 2-27 Overpressure histories at distance,  $r$ , from the center of a spherical charge of 18735 kg of TNT; JWL EOS**

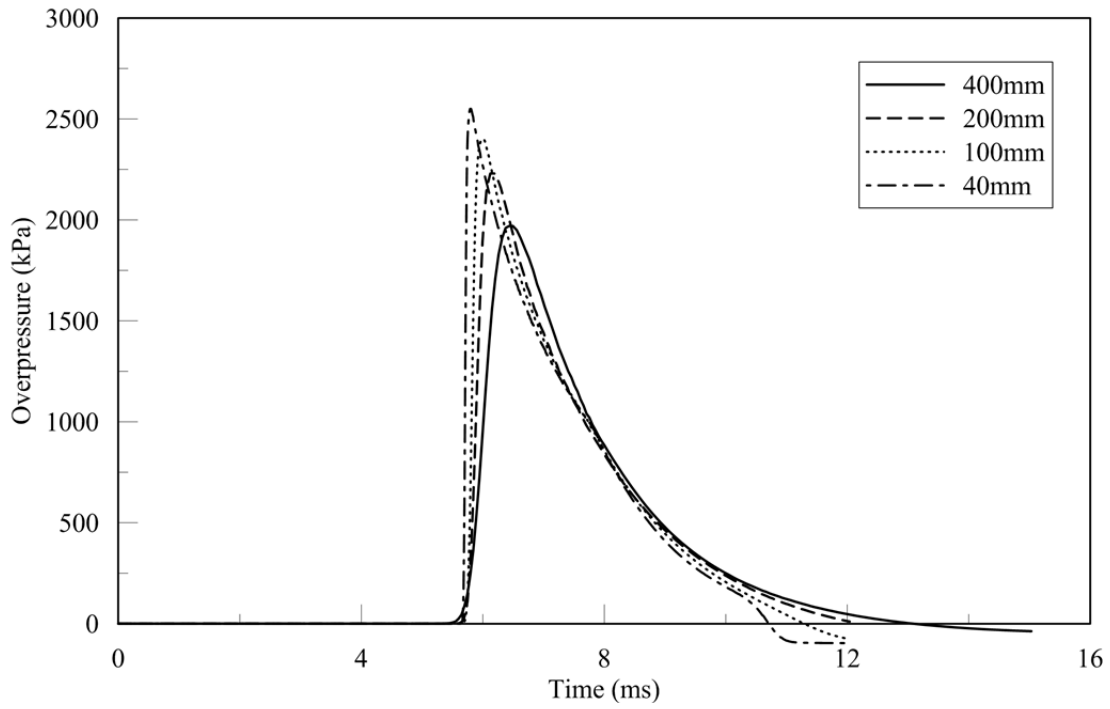


c.  $r = 3360$  mm (1960 mm from face of charge);  $Z = 0.013$  m/kg<sup>1/3</sup>;  $\bar{r} = 2.4$



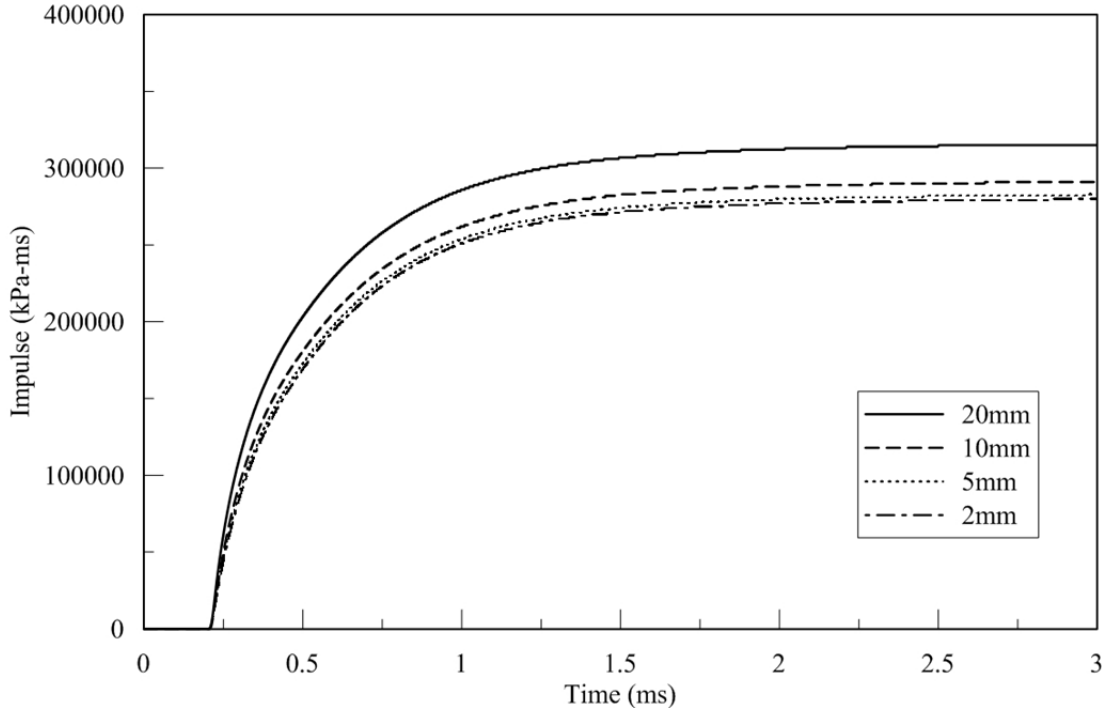
d.  $r = 6300$  mm (4900 mm from face of charge);  $Z = 0.24$  m/kg<sup>1/3</sup>;  $\bar{r} = 4.5$

**Figure 2-27 Overpressure histories at distance,  $r$ , from the center of a spherical charge of 18735 kg of TNT; JWL EOS (cont.)**

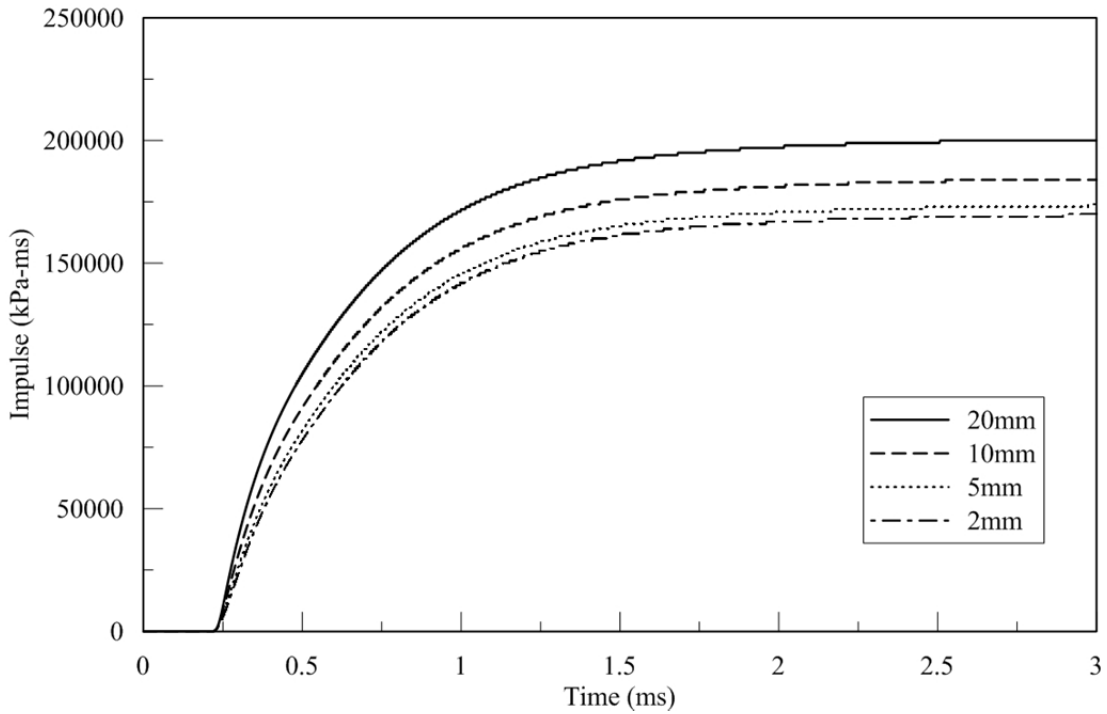


e.  $r = 16380$  mm (14980 mm from face of charge);  $Z = 0.62$  m/kg<sup>1/3</sup>;  $\bar{r} = 11.7$

**Figure 2-27 Overpressure histories at distance,  $r$ , from the center of a spherical charge of 18735 kg of TNT; JWL EOS (cont.)**

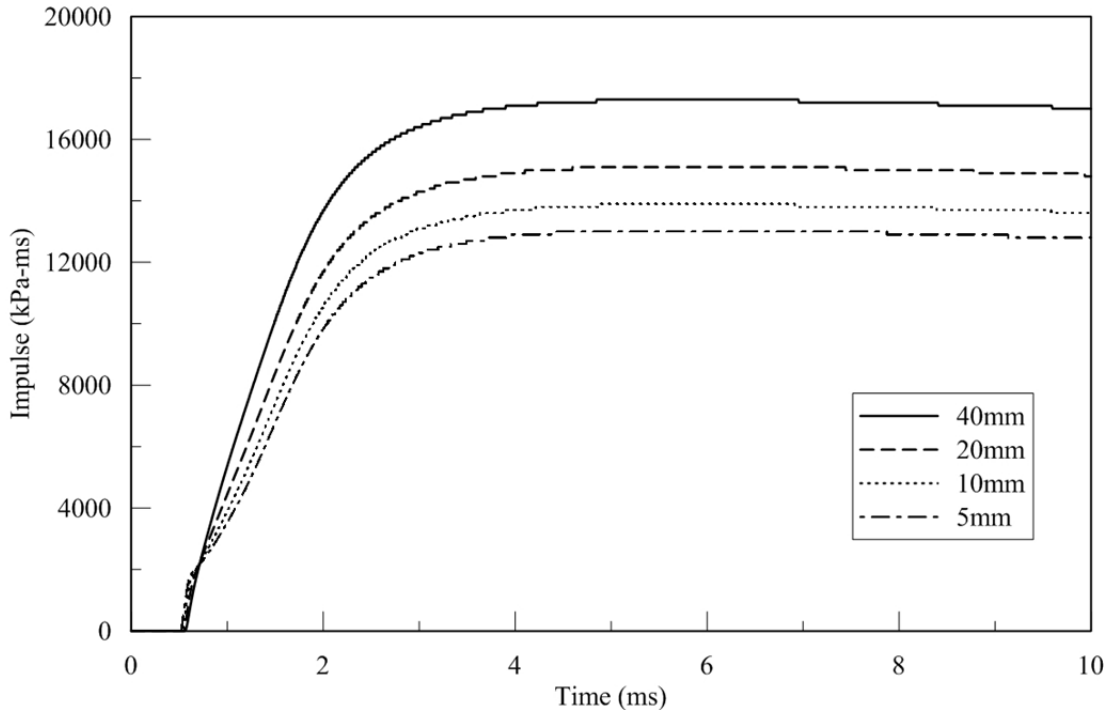


a.  $r = 1435$  m (35 mm from face of charge);  $Z = 0.054$  m/kg<sup>1/3</sup>;  $\bar{r} = 1.025$

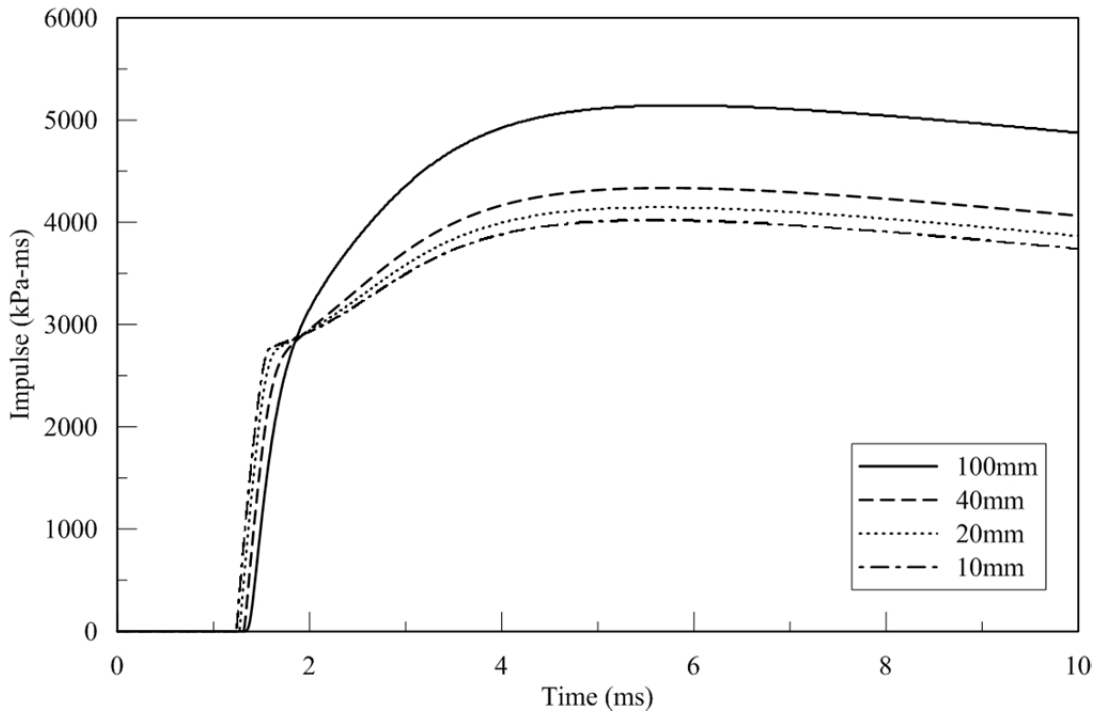


b.  $r = 1540$  mm (140 mm from face of charge);  $Z = 0.058$  m/kg<sup>1/3</sup>;  $\bar{r} = 1.10$

**Figure 2-28 Impulse histories at distance,  $r$ , from the center of a spherical charge of 18735 kg of TNT; JWL EOS**

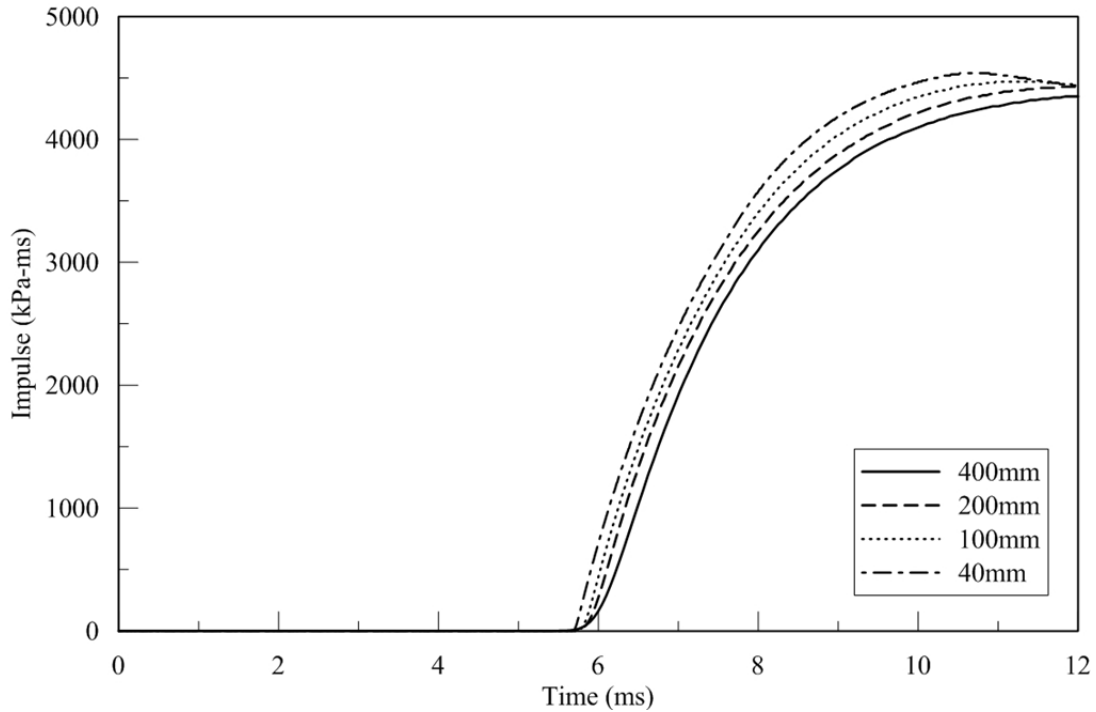


c.  $r = 3360$  mm (1960 mm from face of charge);  $Z = 0.013$  m/kg<sup>1/3</sup>;  $\bar{r} = 2.4$



d.  $r = 6300$  mm (4900 mm from face of charge);  $Z = 0.24$  m/kg<sup>1/3</sup>;  $\bar{r} = 4.5$

**Figure 2-28 Impulse histories at distance,  $r$ , from the center of a spherical charge of 18735 kg of TNT; JWL EOS (cont.)**



e.  $r = 16380$  mm (14980 mm from face of charge);  $Z = 0.62$  m/kg<sup>1/3</sup>;  $\bar{r} = 11.7$

**Figure 2-28 Impulse histories at distance,  $r$ , from the center of a spherical charge of 18735 kg of TNT; JWL EOS (cont.)**

### 2.3.3 Verification of AUTODYN in 1D and 2D for Far-Field Detonations

Browning et al. (2013) simulated an 8000 lb (3629 kg) detonation of TNT in 2D using LS-DYNA (LSTC 2013) and CTH (McGlaun et al. 1990). Three cell sizes were used for the simulations: 1, 2 and 3 in. (25.4, 50.8 and 76.2 mm, respectively). They reported results at scaled distances of 3, 4 and 5 ft/lb<sup>1/3</sup> (1.190, 1.587 and 1.987 m/kg<sup>1/3</sup>, respectively) as noted in Table 2-2. The Browning et al. calculations of incident peak overpressure, incident impulse, and arrival time were repeated using AUTODYN. Table 2-3 presents the values of the JWL parameters for modeling TNT used by Browning et al. and in this verification study. (The values are essentially identical to those provided in Table 2-1.) Values for modeling air are presented in Table 2-4.

**Table 2-2 Monitoring locations used by Browning et al. (2013)**

Range, ft [m]	Scaled distance, ft/lb <sup>1/3</sup> [m/kg <sup>1/3</sup> ]
60 [18.3]	3.00 [1.190]
80 [24.4]	4.00 [1.587]
100 [30.5]	5.00 [1.984]

**Table 2-3 JWL EOS parameters for modeling TNT used by Browning et al. (2013)**

Parameter	Value
Charge radius (in) [mm]	31.89 [810]
Density (lb/in <sup>3</sup> ) [kg/m <sup>1/3</sup> ]	0.058887 [1630]
<i>A</i> (psi) [GPa]	5.384×10 <sup>7</sup> [371.2]
<i>B</i> (psi) [GPa]	4.685×10 <sup>5</sup> [3.230]
<i>R</i> <sub>1</sub>	4.15
<i>R</i> <sub>2</sub>	0.95
Adiabatic constant, <i>w</i>	0.3
Detonation velocity, <i>D</i> (in/s) [m/s]	2.728×10 <sup>5</sup> [6929]
Energy per unit volume, <i>E</i> <sub>0</sub> (psi) [GPa]	1.015×10 <sup>6</sup> [6.998]
CJ pressure, <i>P</i> <sub>CJ</sub> (psi) [GPa]	3.046×10 <sup>6</sup> [21]

**Table 2-4 Values of input parameters for modeling air for far-field verification**

Parameter	This study	Browning et al. (2013)
EOS	Ideal gas	Linear polynomial (ideal gas)
Density (lb/in <sup>3</sup> ) [kg/m <sup>1/3</sup> ]	4.426×10 <sup>-5</sup> [1.225]	4.420×10 <sup>-5</sup> [1.223]
Specific heat ratio, <i>γ</i>	1.4	1.4
Energy per unit volume, <i>E</i> <sub>0</sub> (psi) [kPa]	36.738 [253.3]	36.740 [253.3]

Figure 2-29 presents AUTODYN histories of incident overpressure and impulse in 1D at scaled distances of 3, 4 and 5 ft/lb<sup>1/3</sup> and cell sizes of 1, 2 and 3 in. The incident overpressure and impulse histories are effectively independent of cell size. Figure 2-30 enables a comparison of

the AUTODYN predictions of incident peak overpressures, incident impulses and arrival times for the three cell sizes. The influence of cell size on these results is not significant.

Figures 2-31 and 2-32 summarize numerical results from the 1D AUTODYN, 2D LS-DYNA (Browning et al.) and 2D CTH (Browning et al.) simulations for cell sizes of 1, 2 and 3 in. Incident peak overpressures are provided in Tables 2-5, 2-6 and 2-7 for cell sizes of 1, 2 and 3 in, respectively. Maximum values of incident impulse are provided in Tables 2-8, 2-9 and 2-10. The LS-DYNA and CTH calculations presented in Tables 2-5 through 2-10 are from Browning et al.

AUTODYN, LS-DYNA and CTH provide comparable values of incident peak overpressure and impulse in the far field. Small differences are expected, even in the far field and for the same cell size, because different algorithms and solvers are employed in these codes.

We thus consider AUTODYN to be *verified* for 1D and 2D calculations of overpressure and impulse for far-field detonations.

**Table 2-5 Results for incident peak overpressure; cell size of 1 in; units of psi**

Z (ft/lb <sup>1/3</sup> )	AUTODYN	LS-DYNA	CTH
3	94.1	86.2	79.9
4	46.6	42.8	39.0
5	27.8	25.8	23.2

**Table 2-6 Results for incident peak overpressure; cell size of 2 in; units of psi**

Z (ft/lb <sup>1/3</sup> )	AUTODYN	LS-DYNA	CTH
3	88.3	82.7	79.3
4	44.3	41.7	38.0
5	26.7	25.3	22.6

**Table 2-7 Results for incident peak overpressure; cell size of 3 in; units of psi**

Z (ft/lb <sup>1/3</sup> )	AUTODYN	LS-DYNA	CTH
3	83.8	80.0	76.2
4	42.5	40.7	37.5
5	25.8	24.9	22.4

**Table 2-8 Results for incident impulse; cell size of 1 in; units of psi-ms**

Z (ft/lb <sup>1/3</sup> )	AUTODYN	LS-DYNA	CTH
3	264	236	215
4	206	191	175
5	176	164	151

**Table 2-9 Results for incident impulse; cell size of 2 in; units of psi-ms**

Z (ft/lb <sup>1/3</sup> )	AUTODYN	LS-DYNA	CTH
3	259	236	214
4	203	191	175
5	174	164	151

**Table 2-10 Results for incident impulse; cell size of 3 in; units of psi-ms**

Z (ft/lb <sup>1/3</sup> )	AUTODYN	LS-DYNA	CTH
3	255	237	214
4	201	191	174
5	172	164	151

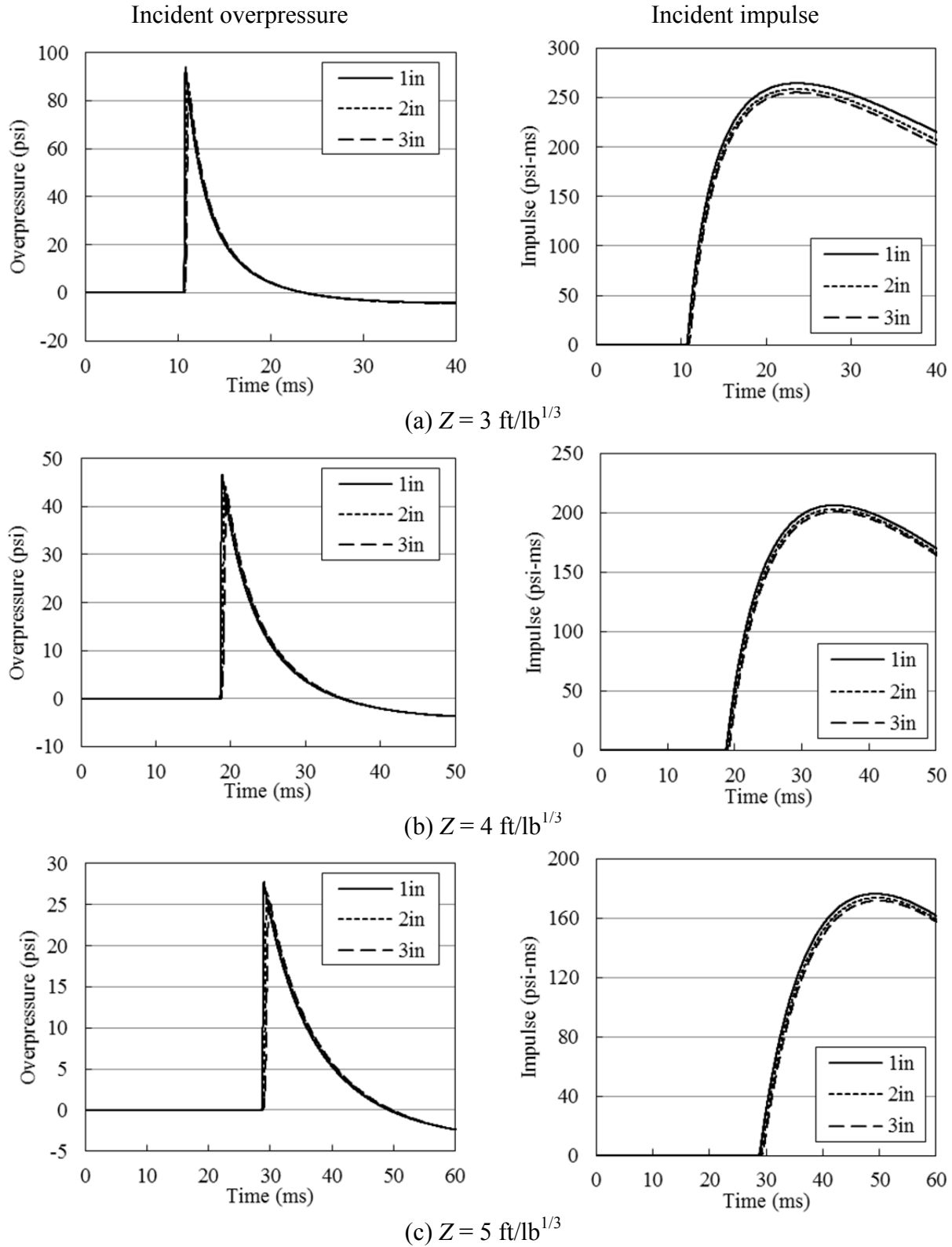
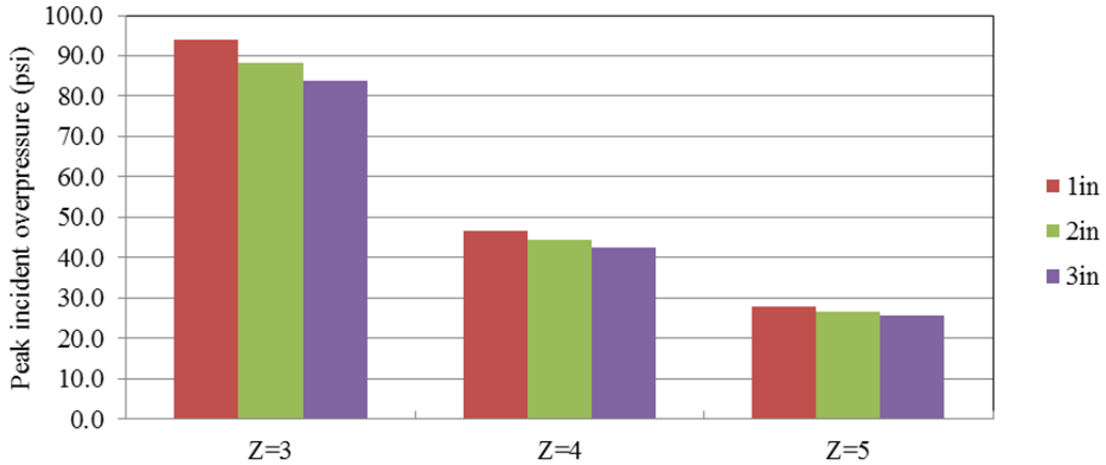
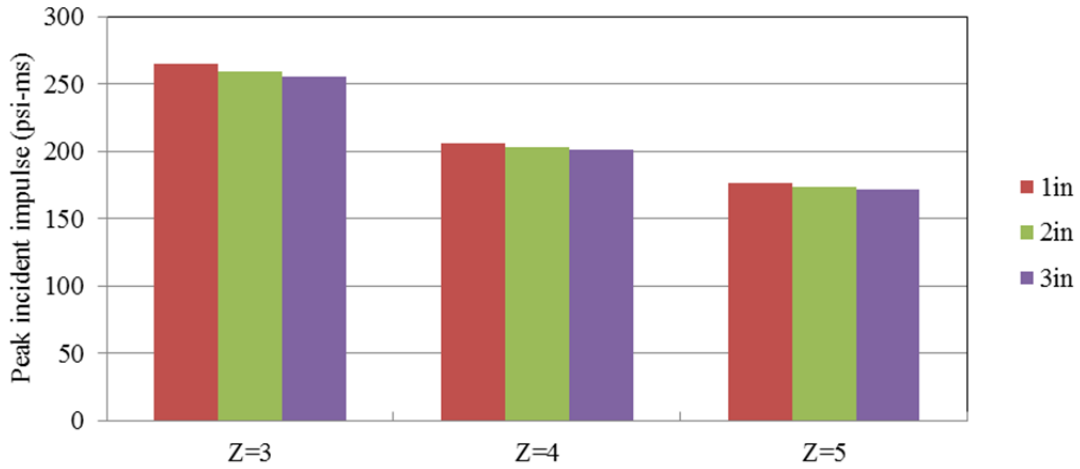


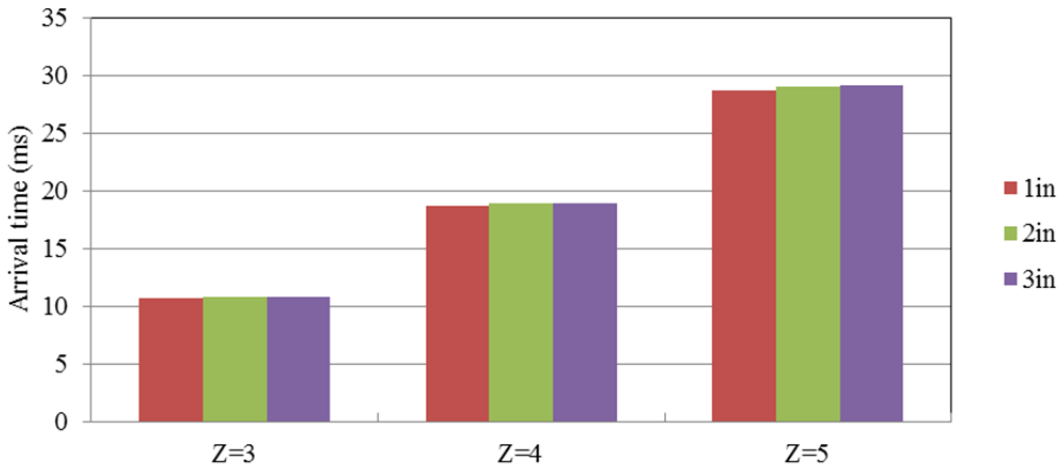
**Figure 2-29 Incident overpressure and impulse histories from AUTODYN;  $Z = 3, 4$  and  $5 \text{ ft/lb}^{1/3}$ ; cell sizes = 1, 2 and 3 in**



(a) Incident peak overpressure

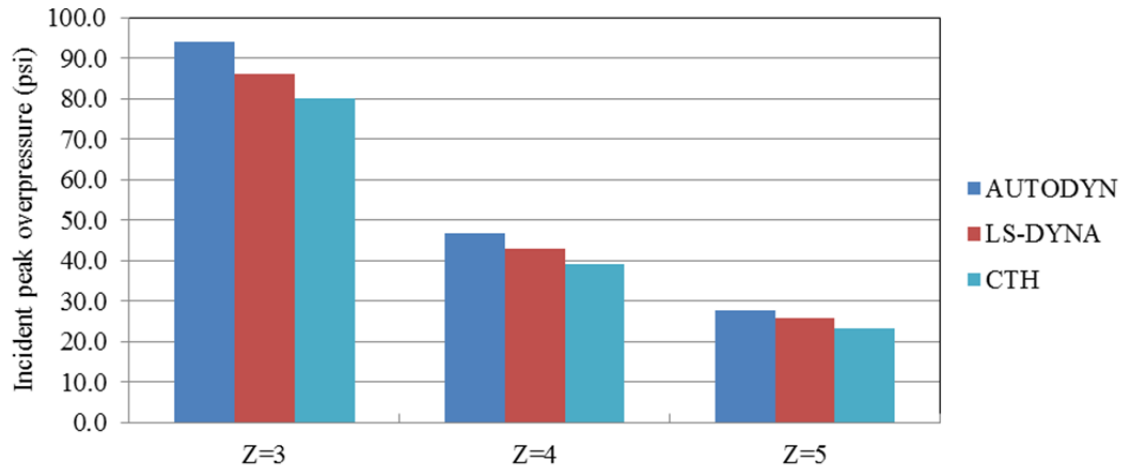


(b) Incident impulse

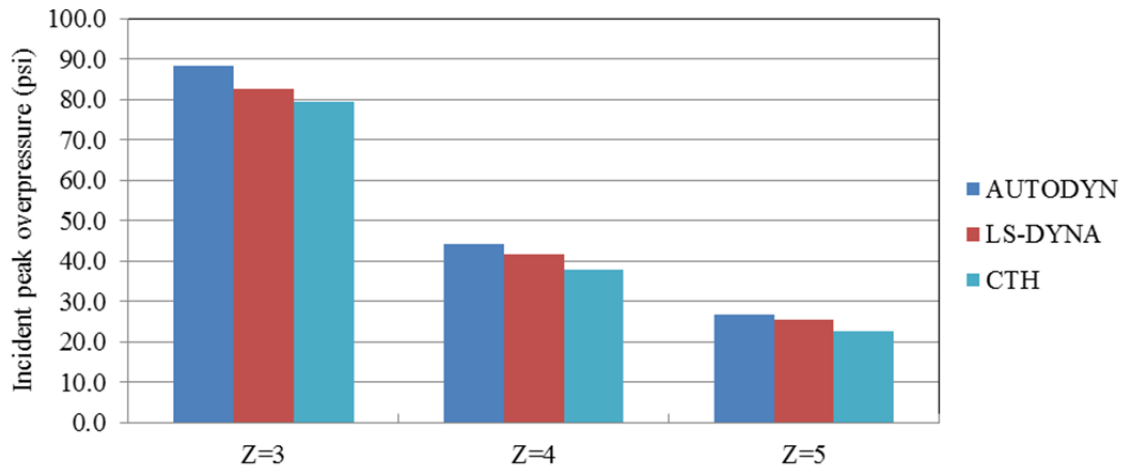


(c) Arrival time

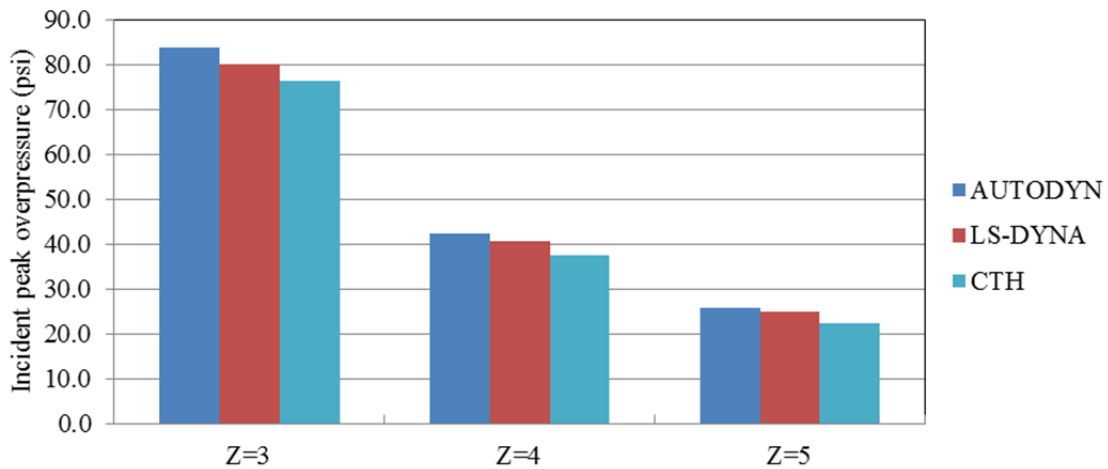
**Figure 2-30 Incident peak overpressure and impulse from AUTODYN; Z = 3, 4 and 5 ft/lb<sup>1/3</sup>; cell sizes = 1, 2 and 3 in**



(a) 1 in cell size

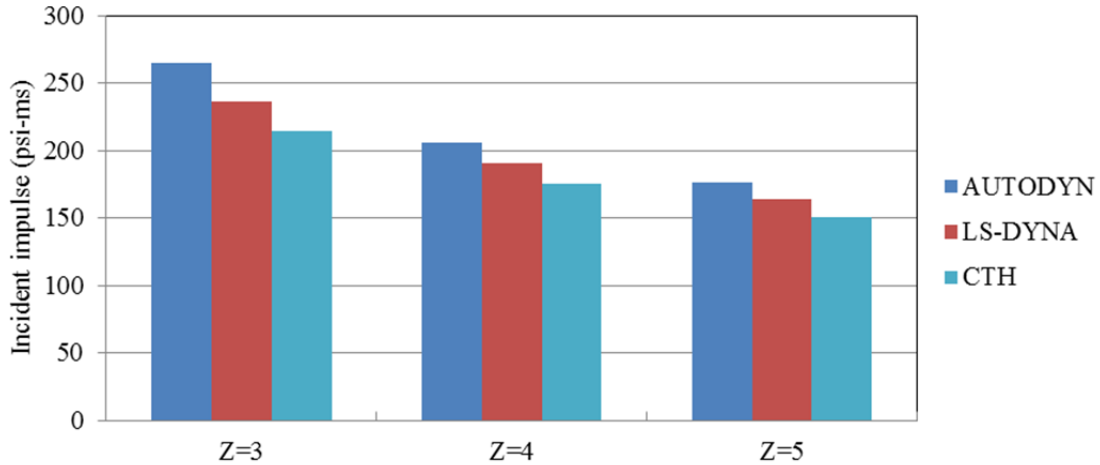


(b) 2 in cell size

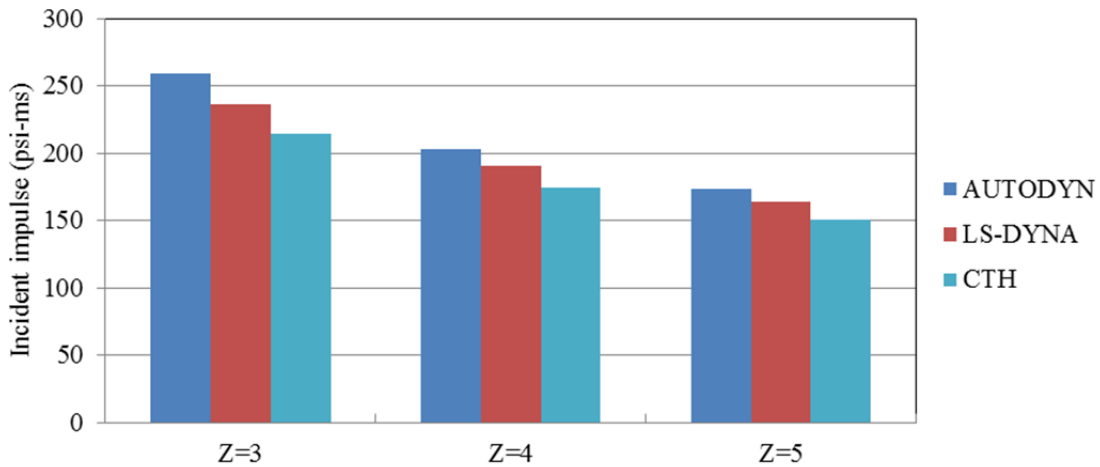


(c) 3 in cell size

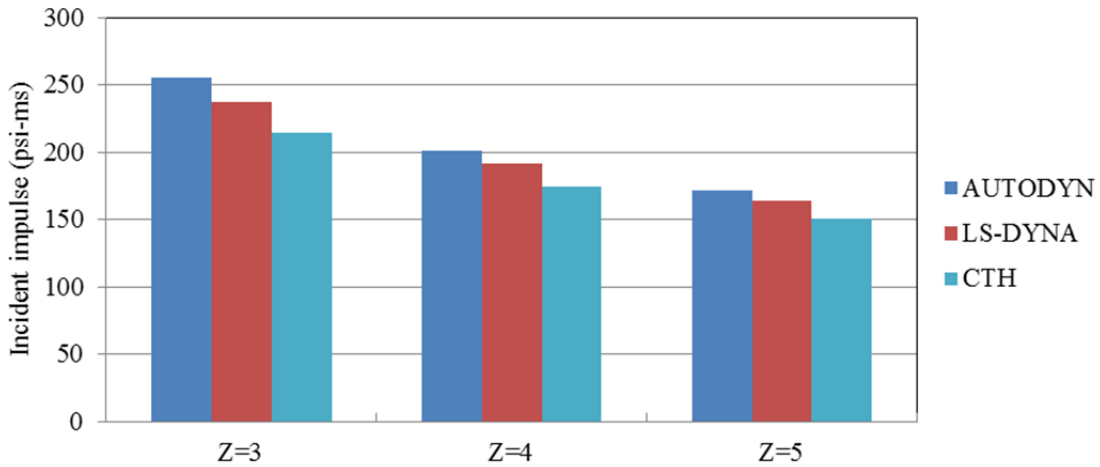
**Figure 2-31 Summary of AUTODYN (this study) and LS-DYNA and CTH (Browning et al.) results for incident peak overpressure**



(a) 1 in cell size



(b) 2 in cell size



(c) 3 in cell size

**Figure 2-32 Summary of AUTODYN (this study) and LS-DYNA and CTH (Browning et al.) results for incident impulse**

### ***2.3.4 Validation of AUTODYN in 2D for Near-Field Detonations***

Two-dimensional (2D) numerical analysis is performed to validate AUTODYN for calculations of reflected overpressure and impulse in the near field. There is a limited body of well-documented test data with which to validate computational fluid dynamics codes.

This validation exercise uses measured values of normally reflected scaled impulse reported by Goodman (1960) and Huffington and Ewing (1985) for detonations of spherical charges of 50/50 Pentolite. No peer reviewed data were found in the open literature for TNT. Goodman compiled and presented experimental data for incident (side-on) and normally reflected overpressure and impulse for detonations of spherical 50/50 Pentolite in free air. No data were reported for incident impulse and normally reflected overpressure for  $Z < 0.4 \text{ m/kg}^{1/3}$ . Data for incident peak overpressure were reported for small values of scaled distance but these were inferred from optical measurements of shock front velocity and not measured directly. The values of normally reflected scaled impulse were measured using an impulse plug (e.g., Johnson et al. 1957, Huffington and Ewing 1985) and are used here to validate AUTODYN. Goodman presented normally reflected scaled impulse data for  $Z = 0.0742, 0.0869, 0.127, 0.150, 0.174$  and  $0.198 \text{ m/kg}^{1/3}$  ( $0.187, 0.219, 0.320, 0.378, 0.438$  and  $0.500 \text{ ft/lb}^{1/3}$ , respectively), based on 9, 9, 7, 26, 8 and 37 tests, respectively (see Table II of the appendix in Goodman). The values of normally reflected scaled impulse for  $Z = 0.08, 0.12, 0.16$  and  $0.20 \text{ m/kg}^{1/3}$  were interpolated from these data for comparison with AUTODYN predictions.

Huffington and Ewing report measured normally reflected impulses for spherical charges of 50/50 Pentolite from 57 experiments at scaled distances between  $0.06$  and  $0.20 \text{ m/kg}^{1/3}$  ( $0.15$  and  $0.50 \text{ ft/lb}^{1/3}$ , respectively). The masses of the charges used for these experiments were 0.5, 1 and 2 lbs ( $0.227, 0.454$  and  $0.907 \text{ kg}$ , respectively). Huffington and Ewing presented 13, 16, 15 and 10 test results for  $Z = 0.08, 0.12, 0.16$  and  $0.20 \text{ m/kg}^{1/3}$ , respectively (see Table 1 in Huffington and Ewing), and the mean results at each value of scaled distance are used to validate AUTODYN.

Pentolite is modeled using the JWL EOS and air is modeled as an ideal gas. Four charge weights of 0.5, 1, 22.68 and 18735 kg, with a packing density of  $1700 \text{ m/kg}^{1/3}$ , are analyzed to observe

the effect of charge weight; see Table 2-11. The JWL parameters for 50/50 Pentolite used in the AUTODYN simulations are those reported in Dobratz and Crawford (1985); see Table 2-12.

**Table 2-11 Properties for 50/50 Pentolite and C4**

Parameter	Pentolite				C4	
Weight (kg)	0.5	1.0	22.68	18735	1	0.5
Radius (mm)	41.25	52.00	147.13	1380.5	53	42
Density (kg/m <sup>3</sup> )	1700	1700	1700	1700	1601	1601

**Table 2-12 JWL EOS parameters for 50/50 Pentolite and C4 (Dobratz and Crawford 1985)**

Parameter	Pentolite	C4
Density (kg/m <sup>3</sup> )	1700	1601
$A$ (GPa)	540.94	609.77
$B$ (GPa)	9.3726	12.95
$R_1$	4.5	4.5
$R_2$	1.1	1.4
Adiabatic constant, $w$	0.35	0.25
Detonation velocity, $D$ (m/s)	7530	8193
Energy per unit volume, $E_0$ (GPa)	8.1	9.0
CJ pressure, $P_{CJ}$ (GPa)	25.5	28

One-dimensional (1D) radial analysis for the 1kg Pentolite is performed using AUTODYN until the shock wave reaches a reflecting boundary. Five cell sizes of  $r/125$ ,  $r/250$ ,  $r/500$ ,  $r/1000$  and  $r/2000$  are used for all four scaled distances, where  $r$  is the distance of a monitoring location from the center of the charge. Note that these five cell sizes produce differences of 4.8%, 1.0%, 1.0%, 0.13% and 0.13%, respectively, from the exact charge weight (= 1 kg), but these will have a minor effect on the overpressure histories. The 1D analysis results calculated using the  $r/2000$  cell size are mapped into a 2D air domain at  $(x, y) = (0, 0)$  for analysis using three cell sizes:  $r/125$ ,  $r/250$  and  $r/500$ . The dimension of the 2D domain is  $r \times r$ , where the lower horizontal boundary is axially symmetric, the left vertical and the top horizontal boundaries are transmitting

planes, and the right vertical boundary is perfectly reflecting plane. Energy will seldom escape across the left transmitting (upstream) boundary because the pressure waves initially propagate radially from the source and away from this boundary. The monitoring location is on the right perfect-reflecting boundary, at  $(x, y) = (r, 0)$ .

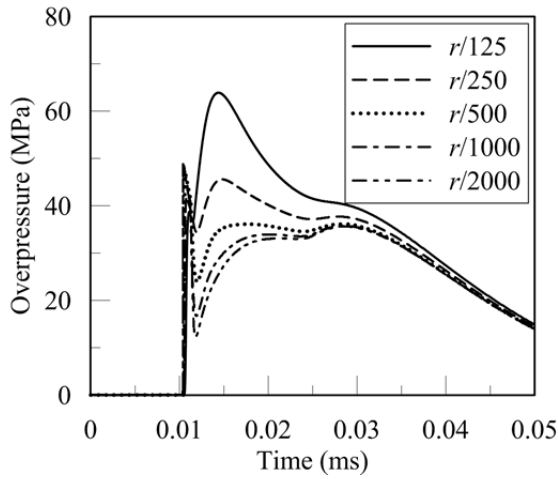
Figure 2-33 presents simulation results for 1kg of Pentolite at  $Z = 0.08 \text{ m/kg}^{1/3}$ . Figures 2-33a and 33b show the converged 1D results using a cell size of  $r/2000$ . The reflected overpressure and impulse histories in Figures 2-33c and 2-33d, respectively, are similar for all three (2D) cell sizes. Identical observations are made for  $Z = 0.12, 0.16$  and  $0.20 \text{ m/kg}^{1/3}$ , as shown in Figures 2-34, 2-35, and 2-36, respectively. Analyses for Pentolite masses of 0.5, 22.68 and 18735 kg are also performed using 1D and 2D cell sizes of  $r/2000$  and  $r/500$ , respectively.

Figure 2-37 enables a comparison of the AUTODYN-calculated normally reflected scaled impulses, with the smallest cell sizes for four scaled distances and four charge weights, and the measurements of Goodman and of Huffington and Ewing. See Table 2-13. For all four scaled distances, the AUTODYN calculations are in good agreement with the measured data. The effect of charge weight on scaled impulse is insignificant.

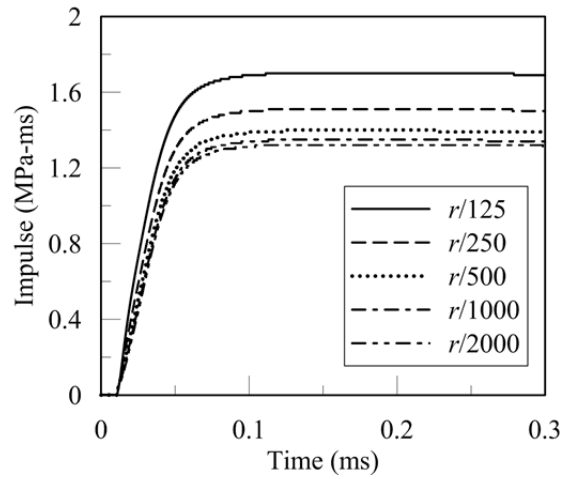
We thus consider AUTODYN to be *validated* for 2D calculations of reflected overpressure and impulse for near-field detonations.

**Table 2-13 Normally reflected scaled impulse from AUTODYN calculations and measurements of Goodman (1960) and Huffington and Ewing (1985); units of MPa-ms/kg<sup>1/3</sup>**

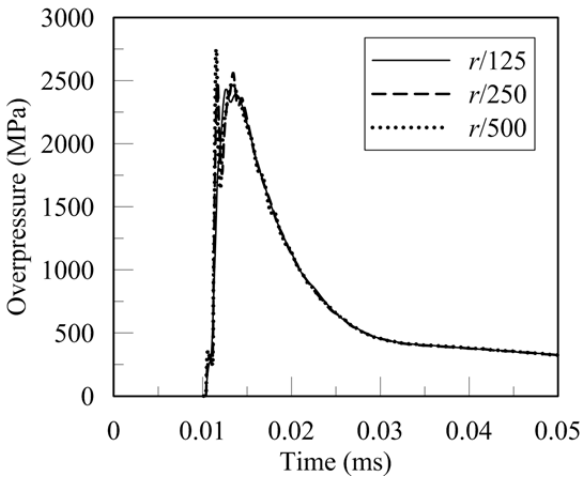
$Z \text{ (m/kg}^{1/3}\text{)}$	AUTODYN				Goodman	Huffington and Ewing
	0.5 kg	1 kg	22.68 kg	18735 kg		
0.08	38.95	38.95	38.93	38.94	41.76	42.25
0.12	18.16	18.15	18.11	18.13	19.49	18.92
0.16	10.53	10.54	10.52	10.54	11.47	10.81
0.2	6.880	6.882	6.873	6.84	7.14	7.21



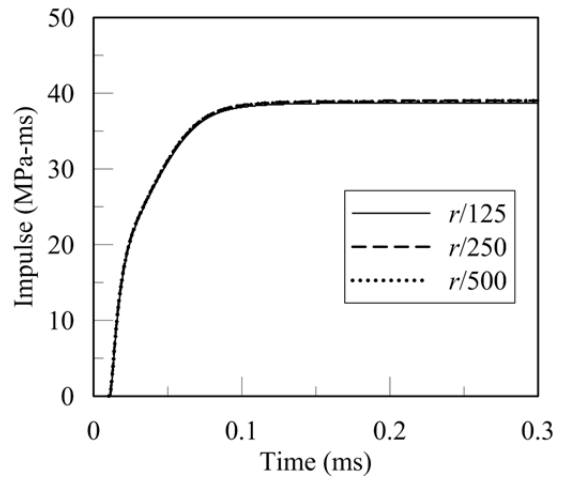
(a) Incident overpressure



(b) Incident impulse

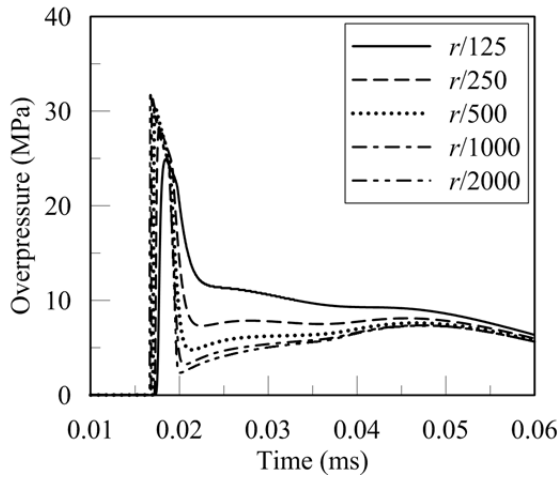


(c) Reflected overpressure

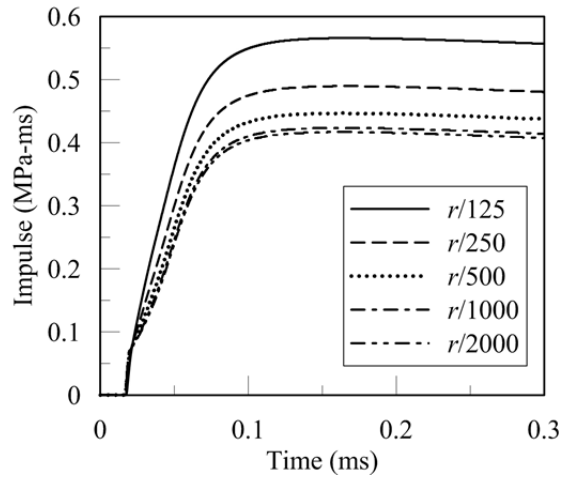


(d) Reflected impulse

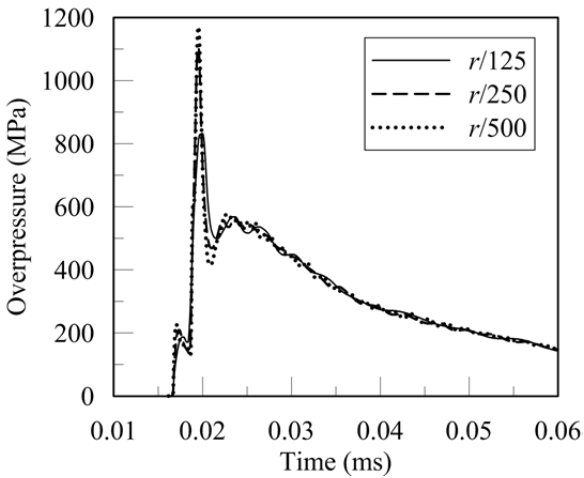
**Figure 2-33 Incident and normally reflected overpressure and impulse histories calculated using AUTODYN for 50/50 Pentolite of 1 kg;  $Z = 0.08 \text{ m/kg}^{1/3}$ ; ( $Z = 0.20 \text{ ft/lb}^{1/3}$ );  $\bar{r} = 1.52$**



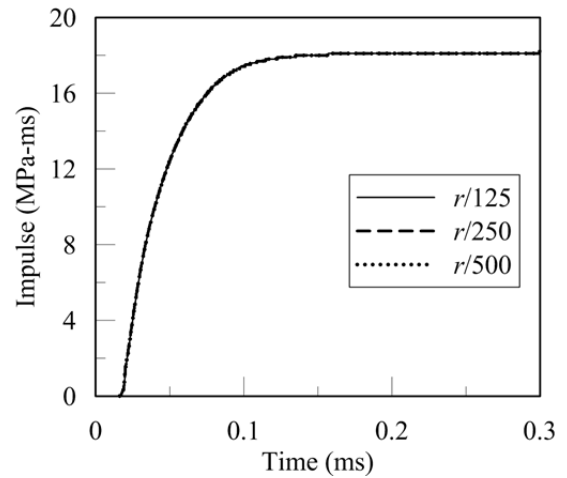
(a) Incident overpressure



(b) Incident impulse

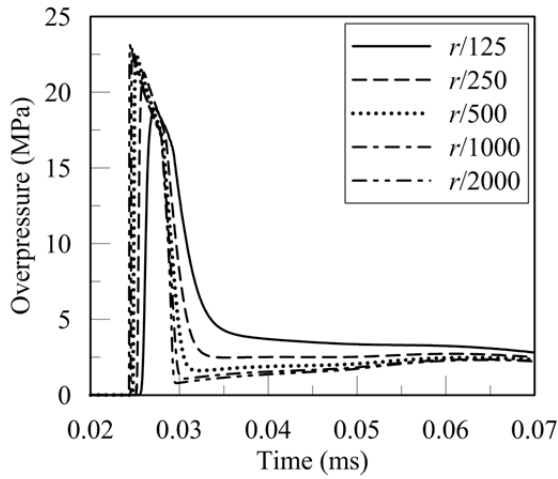


(c) Reflected overpressure

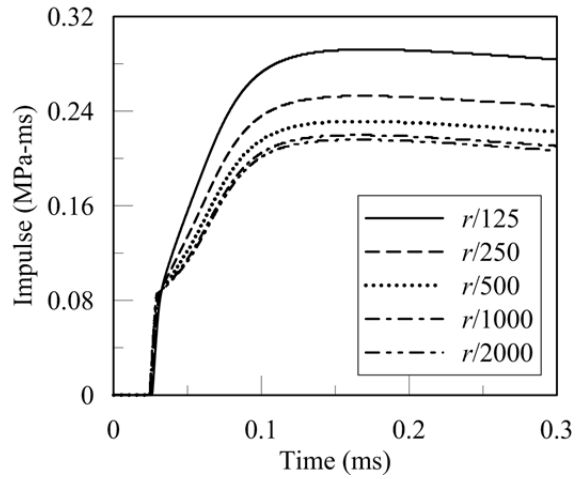


(d) Reflected impulse

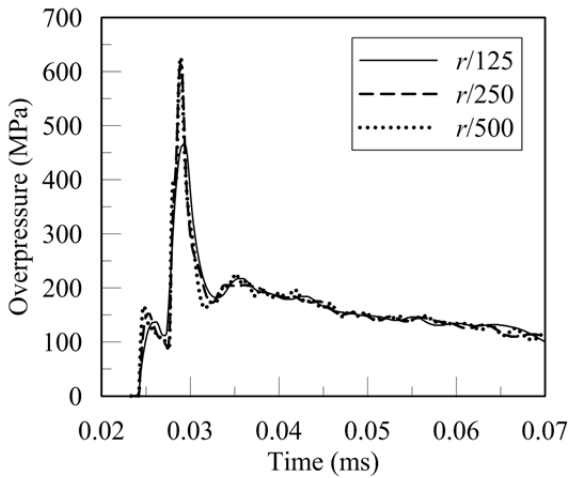
**Figure 2-34 Incident and reflected normally overpressure and impulse histories calculated using AUTODYN for 50/50 Pentolite of 1 kg;  $Z = 0.12 \text{ m/kg}^{1/3}$ ; ( $Z = 0.30 \text{ ft/lb}^{1/3}$ );  $\bar{r} = 2.28$**



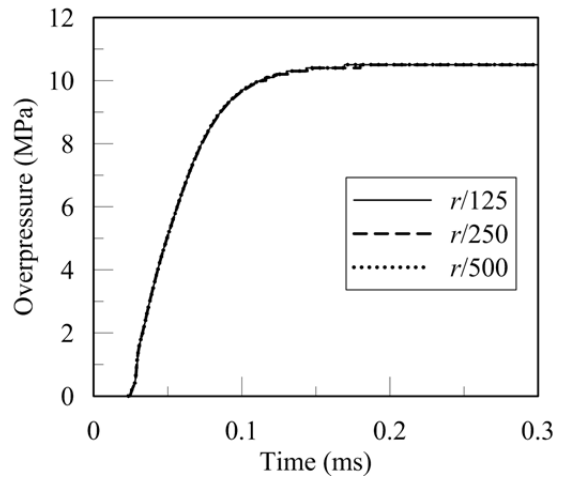
(a) Incident overpressure



(b) Incident impulse

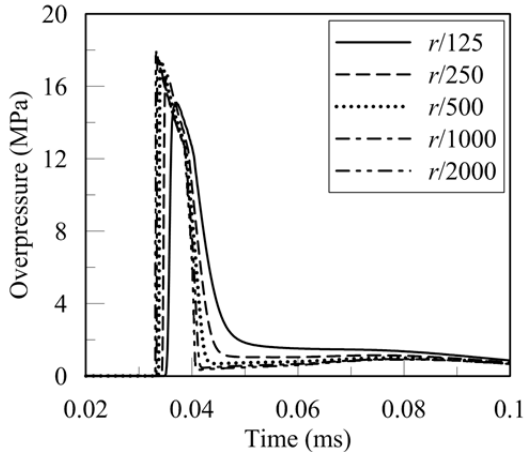


(c) Reflected overpressure

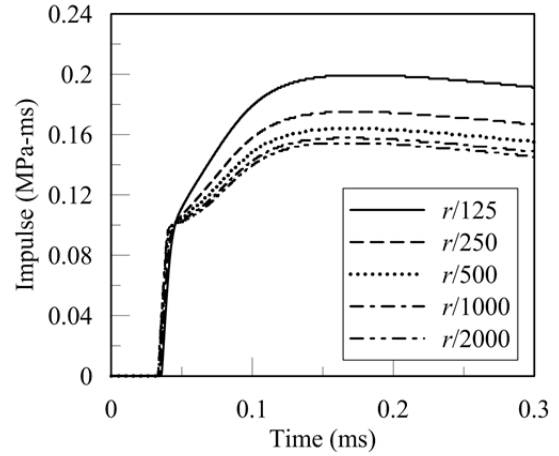


(d) Reflected impulse

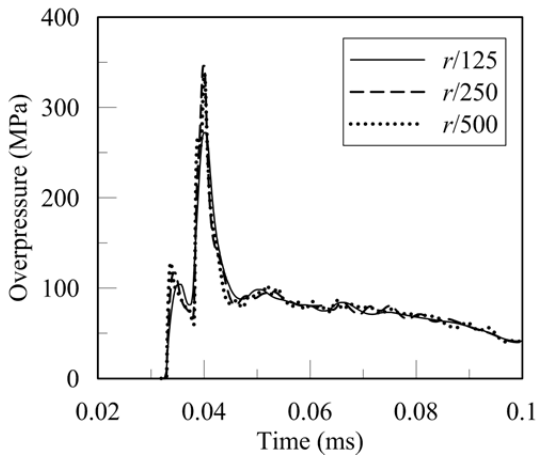
**Figure 2-35 Incident and normally reflected overpressure and impulse histories calculated using AUTODYN for 50/50 Pentolite of 1 kg;  $Z = 0.16 \text{ m/kg}^{1/3}$ ; ( $Z = 0.40 \text{ ft/lb}^{1/3}$ );  $\bar{r} = 3.04$**



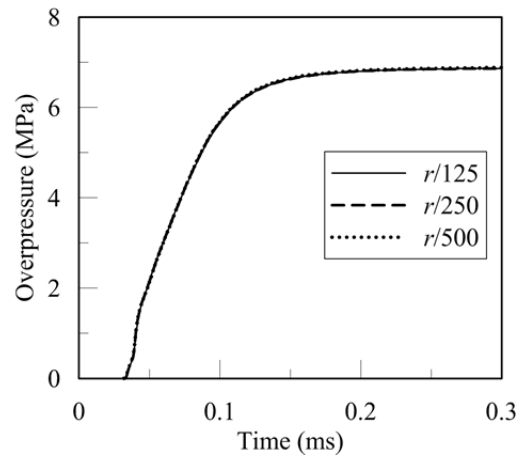
(a) Incident overpressure



(b) Incident impulse



(c) Reflected overpressure



(d) Reflected impulse

**Figure 2-36 Incident and normally reflected overpressure and impulse histories calculated using AUTODYN for 50/50 Pentolite of 1 kg;  $Z = 0.20 \text{ m/kg}^{1/3}$ ; ( $Z = 0.50 \text{ ft/lb}^{1/3}$ );  $\bar{r} = 3.80$**

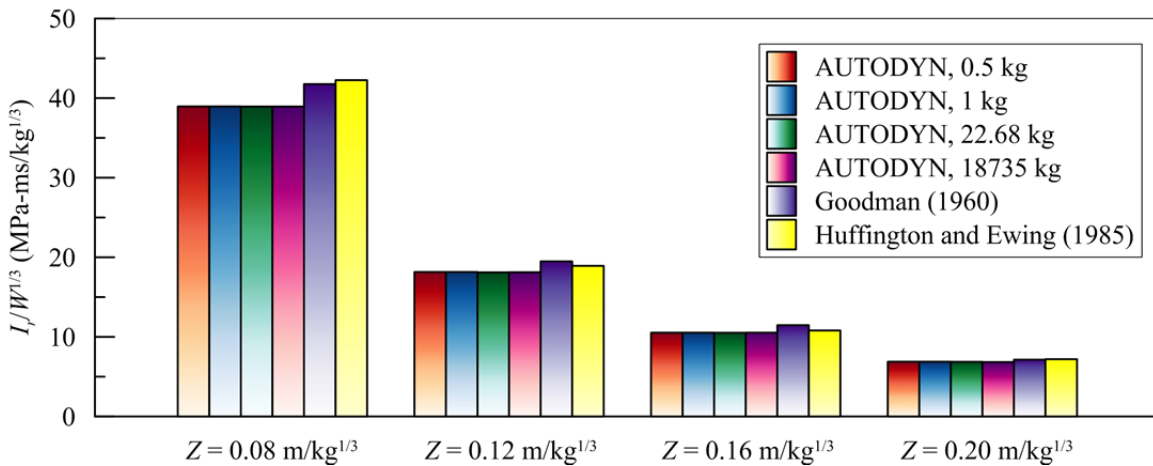


**Figure 2-37 Comparison between AUTODYN calculations and measurements of Goodman (1960) and Huffington and Ewing (1985) for normally reflected scaled impulses**

### ***2.3.5 Validation of AUTODYN in 2D for Far-Field Detonations***

Two-dimensional (2D) numerical analysis for far-field detonations is performed to validate the code for the calculations of reflected overpressures and impulses in the far field. This validation study uses measurements of normally reflected peak overpressures and impulses reported by Frost et al. (2008) for spherical charges of C4. AUTODYN Analysis is performed and values of normally reflected peak overpressures and scaled impulses at scaled distances,  $Z$ , of 1.2 and 1.51  $\text{m/kg}^{1/3}$  are reported and compared.

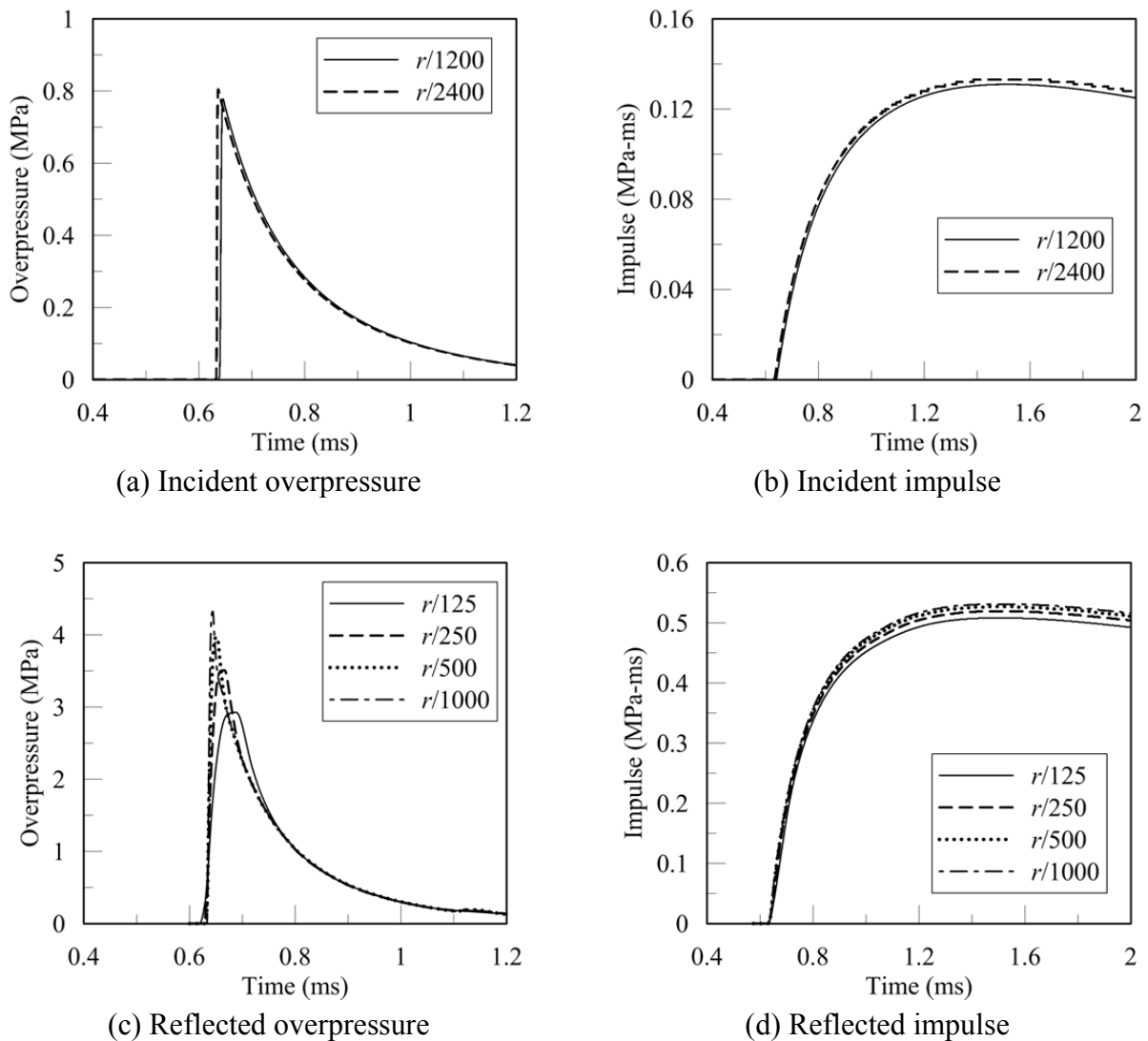
Frost et al. presented measured data of reflected peak overpressures and impulses for normal incidences and angles of incidence for detonations of spherical charges of 1 kg and 0.5 kg of C4, 1.2 m from the center of the charge ( $Z = 1.2$  and  $1.51 \text{ m/kg}^{1/3}$ , respectively). The weight, radius and packing density of both C4 charges are presented in Table 2-11. The results presented by Frost et al. for normal incidence were digitized to enable a direct comparison with results computed using AUTODYN.

The JWL parameters for C4, from Dobratz and Crawford (1985), are used for the AUTODYN simulations, and are presented in Table 2-12. Cell sizes of  $r/1200$  and  $r/2400$  (1 mm and 0.5 mm, respectively) are used for 1D radial analysis because these enable exact modeling of the charge radii of 53 mm and 42 mm, for the C4 weights of 1.0 kg and 0.5 kg, respectively, and the packing density of  $1601 \text{ kg/m}^3$ . The 1D analysis results calculated using the  $r/2400$  cell size are used for 2D analysis, where four cell sizes of  $r/125$ ,  $r/250$ ,  $r/500$  and  $r/1000$  are considered. Modeling of the 2D domain is similar to that described in the previous section.

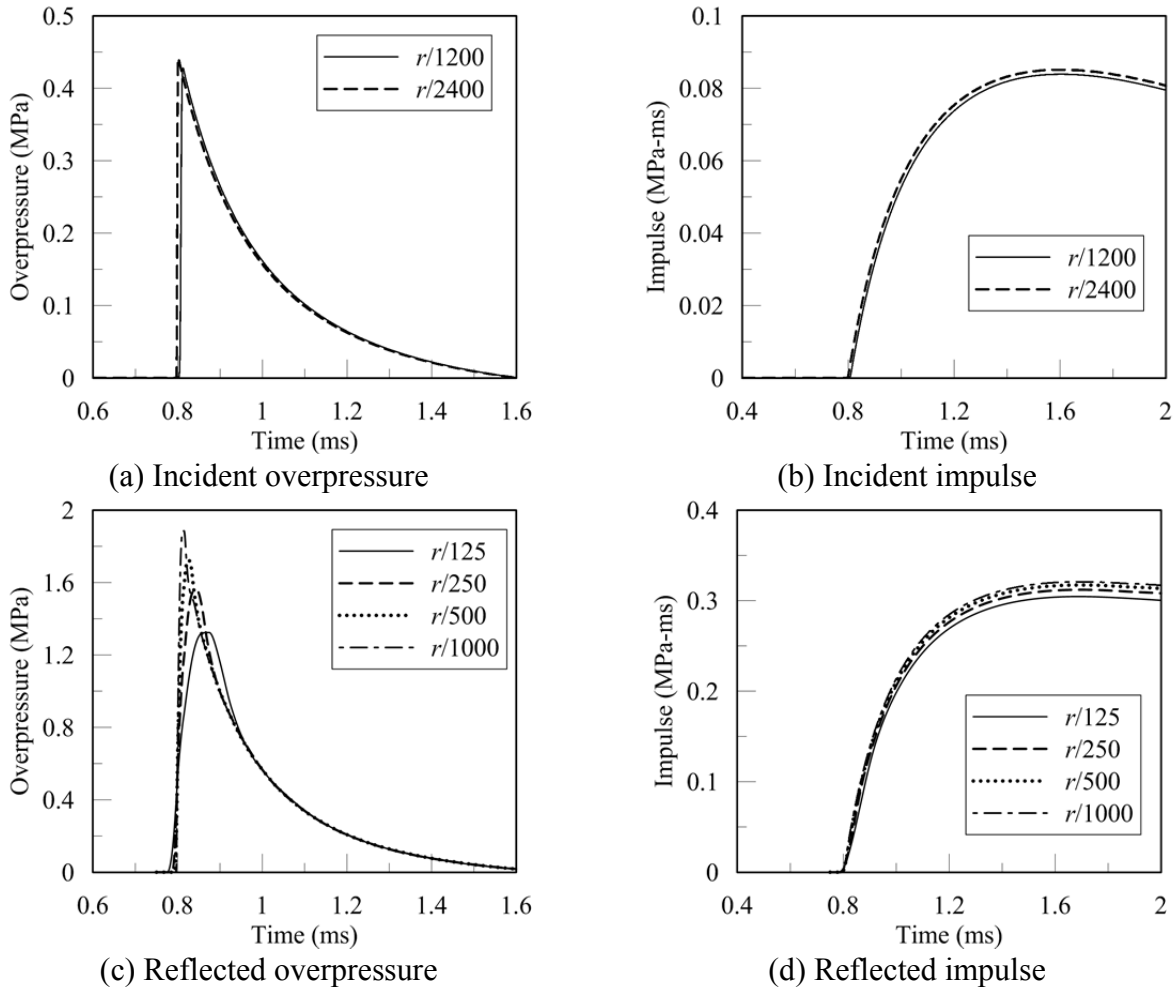
Figure 2-38 presents simulation results for  $Z = 1.2 \text{ m/kg}^{1/3}$  (1 kg C4). The incident overpressure and impulse histories are virtually identical for the two cell sizes, as shown in Figures 2-38a and 2-38b, respectively. For normally reflected peak overpressure, the use of cell sizes of  $r/500$  and  $r/1000$  lead to similar results, as shown in Figure 2-38c, where the difference is less than 10%. Figure 2-38d shows the normally reflected impulse histories, which are essentially identical for all four cell sizes. Identical observations are made for  $Z = 1.51 \text{ m/kg}^{1/3}$  (0.5 kg C4), as shown in Figure 2-39.

Figure 2-40 enables a comparison between AUTODYN results calculated using the  $r/1000$  cell size and Frost et al. predictions. The calculated reflected peak overpressure for  $1.51 \text{ m/kg}^{1/3}$  is somewhat (32%) smaller than that predicted by Frost et al., but the value for  $1.2 \text{ m/kg}^{1/3}$  is close to that predicted by Frost et al. Further, the calculated reflected scaled impulses for both scaled distances and the Frost et al. predictions are in good agreement.

We thus consider AUTODYN to have been *validated* for 2D calculations of reflected overpressure and impulse for far-field detonations.



**Figure 2-38 Incident and normally reflected overpressure and impulse histories calculated using AUTODYN for C4 of 1 kg;  $Z = 1.2 \text{ m/kg}^{1/3}$  ( $r = 1.2 \text{ m}$ )**



**Figure 2-39 Incident and normally reflected overpressure and impulse histories calculated using AUTODYN for C4 of 0.5 kg;  $Z = 1.51 \text{ m/kg}^{1/3}$  ( $r = 1.2 \text{ m}$ )**

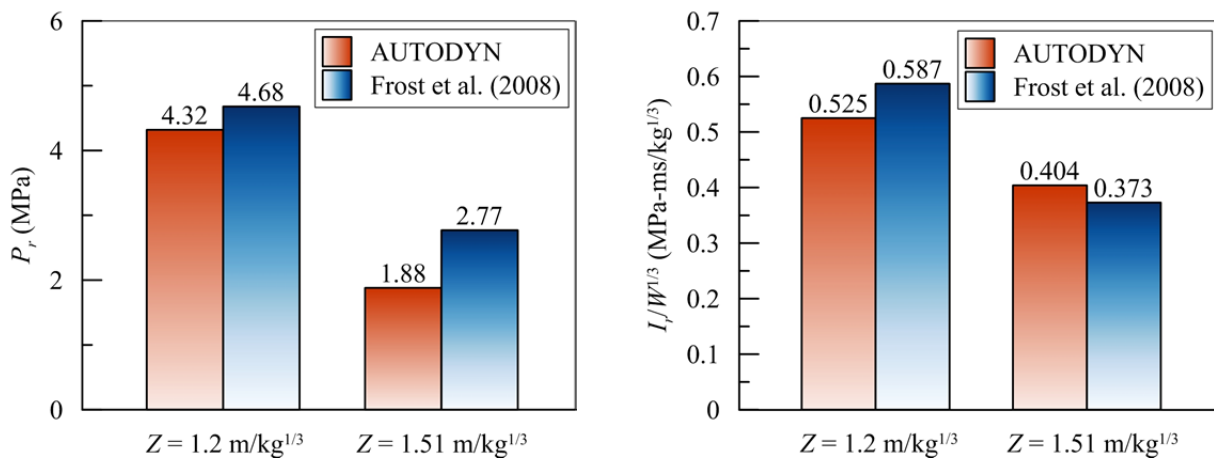


**Figure 2-40 Comparison between AUTODYN calculations and Frost et al. measurements (2008) for normally reflected peak overpressure,  $P_r$ , and scaled impulse,  $I_r/W^{1/3}$ ;  $Z = 1.2$  and  $1.51 \text{ m/kg}^{1/3}$**

## 2.4 One-Dimensional Blast Wave Propagation

### 2.4.1 Introduction

A series of 1D studies is performed using AUTODYN and Air3D (Rose 2006). The purpose of the 1D studies is to characterize the incident overpressure histories in close proximity to the face of a spherical weapon of 22.68 (50 lb) of TNT. A 22.68 kg weapon is a typical hand-delivered threat for security design of buildings and infrastructure. The influences of mesh size, afterburning, and equations of state (EOS) on overpressure history, and temperature in the vicinity of the face of the charge are studied.

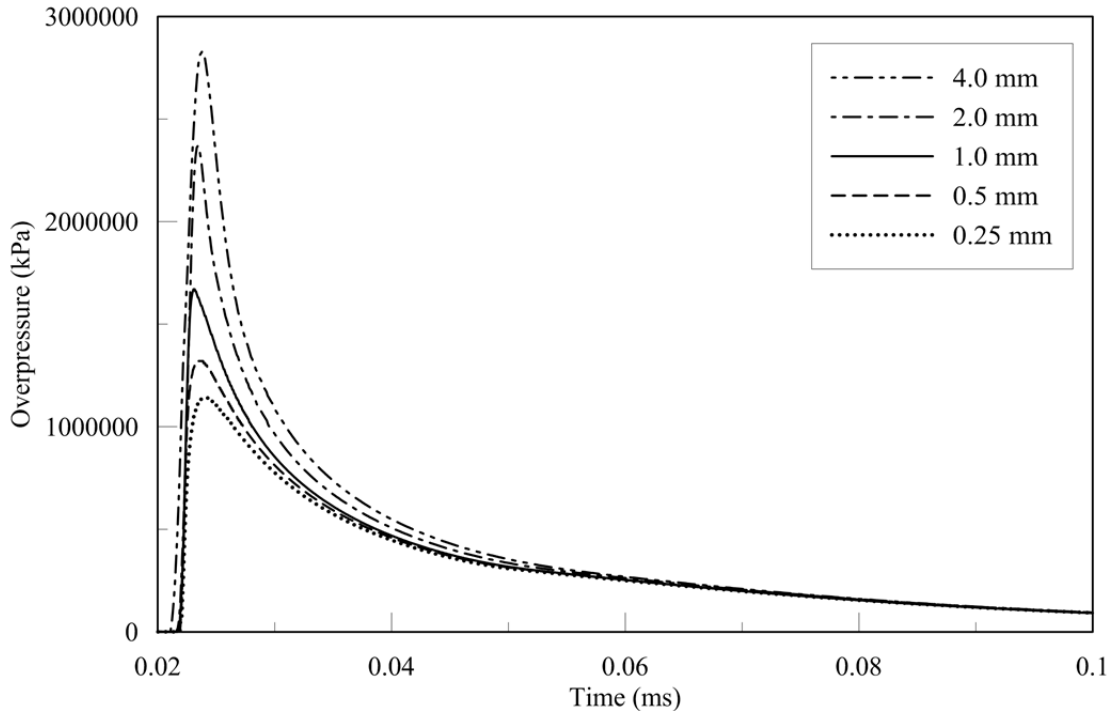
A charge radius of 149 mm corresponding to the 22.68 kg TNT is modeled in 1D and is meshed with 4, 2, 1, 0.5 and 0.25 mm cells. A TNT packing density of  $1636.8 \text{ kg/m}^3$  is used to recover the weight of 22.68 kg with a charge radius of 149 mm. The JWL EOS is used to model the TNT products and air is modeled as an ideal gas. The multi-material Euler-Godunov solver is used for the 1D calculations.

### 2.4.2 Mesh Sensitivity Study

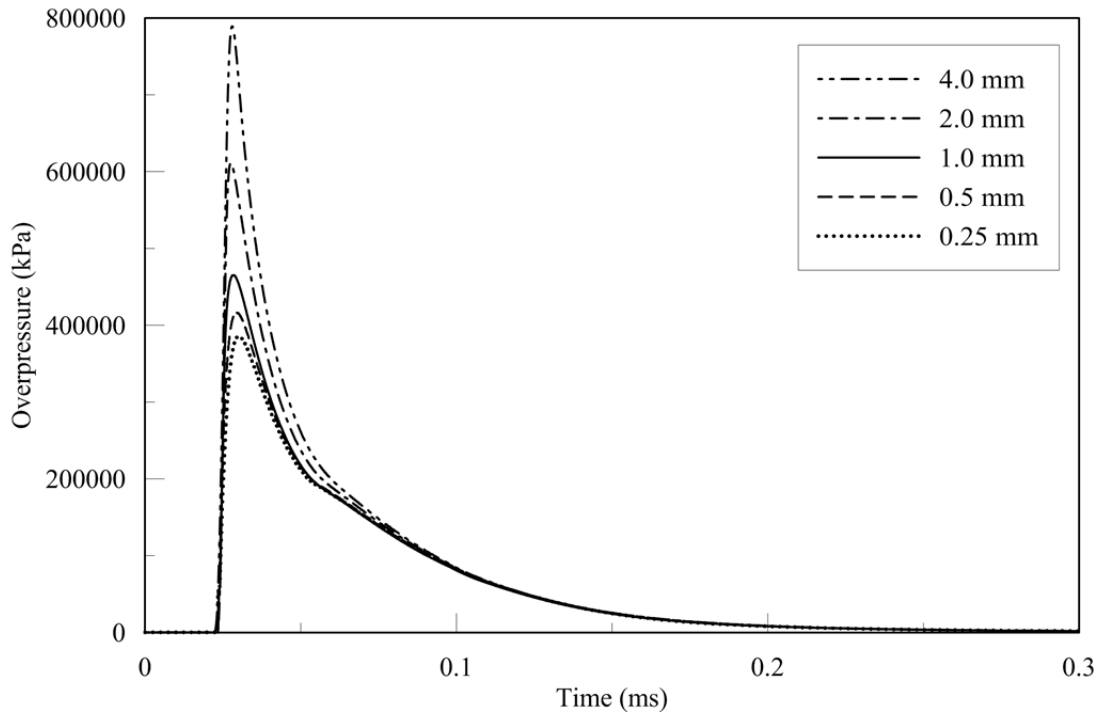
A mesh sensitivity study is performed for simulating 1D wave propagation using the 22.68 kg charge of TNT. Afterburning is not considered. An  $h$ -refinement of the mesh is performed using five cell sizes: 4 mm, 2 mm, 1 mm, 0.5 mm and 0.25 mm. The choice of cell size influences the results, over the range considered, for a distance  $r$  of less than seven times the charge radius (= 1043 mm), or a radial expansion of 7. Results are presented in Figures 2-41 and 2-42 as a function of distance,  $r$ , from the center of the charge. For distances greater than 416 mm ( $Z = 0.147 \text{ m/kg}^{1/3}$ ), results are also compared with data from CONWEP (Hyde 1992) as implemented in LS-DYNA (LSTC 2013). CONWEP data are available only for  $Z > 0.147 \text{ m/kg}^{1/3}$ . The rate of decay in overpressure is described by the Friedlander curve (see Equation 1.1) and the waveform parameter ( $b$  in that equation) is back-calculated from the CONWEP values for peak overpressure, impulse, and positive phase duration. At distances of 152.7 mm, 164 mm, 200 mm and 250 mm ( $Z = 0.054, 0.058, 0.071$  and  $0.088 \text{ m/kg}^{1/3}$ , respectively;  $\bar{r} = 1.025, 1.1, 1.34$  and  $1.68$ , respectively), the overpressures are resolved sufficiently well, as measured by the small

differences of generally less than 10% in results for cell sizes of 0.5 mm and 0.25 mm. Consider Figure 2-41c. The 0.5 mm and 0.25 mm cells capture the spike associated with the arrival of the shock front (peak overpressure of approximately 40 MPa; see open circle) and the expanding detonation products (peak overpressure of approximately 77 MPa for the 0.5 mm cell size), immediately behind the initial peak. Similar observations are made for Figure 2-41d although the relative amplitudes of the peaks in the overpressure histories have changed because the meshes are better able to resolve the initial shock front. At a distance of 500 mm ( $Z = 0.177 \text{ m/kg}^{1/3}$ ;  $\bar{r} = 3.36$ ; Figure 2-41e), the calculated overpressure histories are quite different from CONWEP due to the effect of the expanding detonation products. At a distance of 1000 mm ( $Z = 0.353 \text{ m/kg}^{1/3}$ ;  $\bar{r} = 6.71$ ; Figure 2-41f), the five meshes generated similar results. The distance of 1000 mm (Figure 2-41f) represents a volume expansion of 302. The shock front dominates the overpressure history at this radial expansion. The differences between the calculated results and CONWEP predictions at  $t = 0.3$  to  $0.4$  ms are also due to the effect of the expanding detonation products. At distances of 152.7, 164, 200, 250, 500 and 1000 mm ( $\bar{r} = 1.025, 1.1, 1.34, 1.68, 3.36$  and  $6.71$ , respectively), the overpressure histories converge for cell sizes of 0.5, 0.5, 0.5, 0.5, 1.0 and 2.0 mm, respectively (or  $r/306, r/328, r/400, r/500, r/500$  and  $r/500$ ). For the total impulse, the results converge at larger cell sizes, namely,  $r/153, r/164, r/100, r/125, r/250$  and  $r/250$ , respectively. None of the pressure time series presented in Figures 2-41c through 2-41f are similar in shape to the widely adopted Friedlander equation. The time series in Figures 2-41a and 2-41b are different because at these small radial expansions (1.025 and 1.10, respectively), the effect of the expanding detonation products on the shape of pressure history is not significant because the distance between the shock front and the front of the expanding detonation products is small.

Figure 2-43 plots the arrival time of the shock front at distances of  $r$  equal to 148 mm (1 mm inside the face of the charge) and 250 mm (101 mm from the face of the charge) as a function of cell size. The arrival times are insensitive to the choice of cell size, of the four considered.

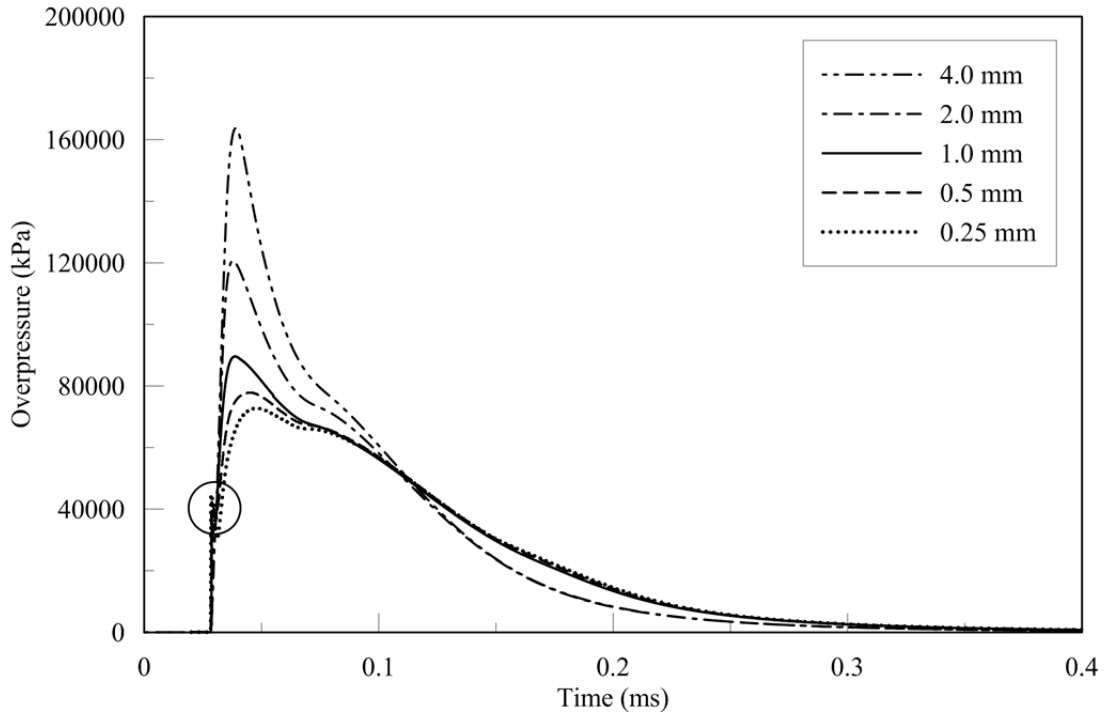


a.  $r = 152.7$  m (3.7 mm from face of charge);  $Z = 0.054$  m/kg<sup>1/3</sup>;  $\bar{r} = 1.025$

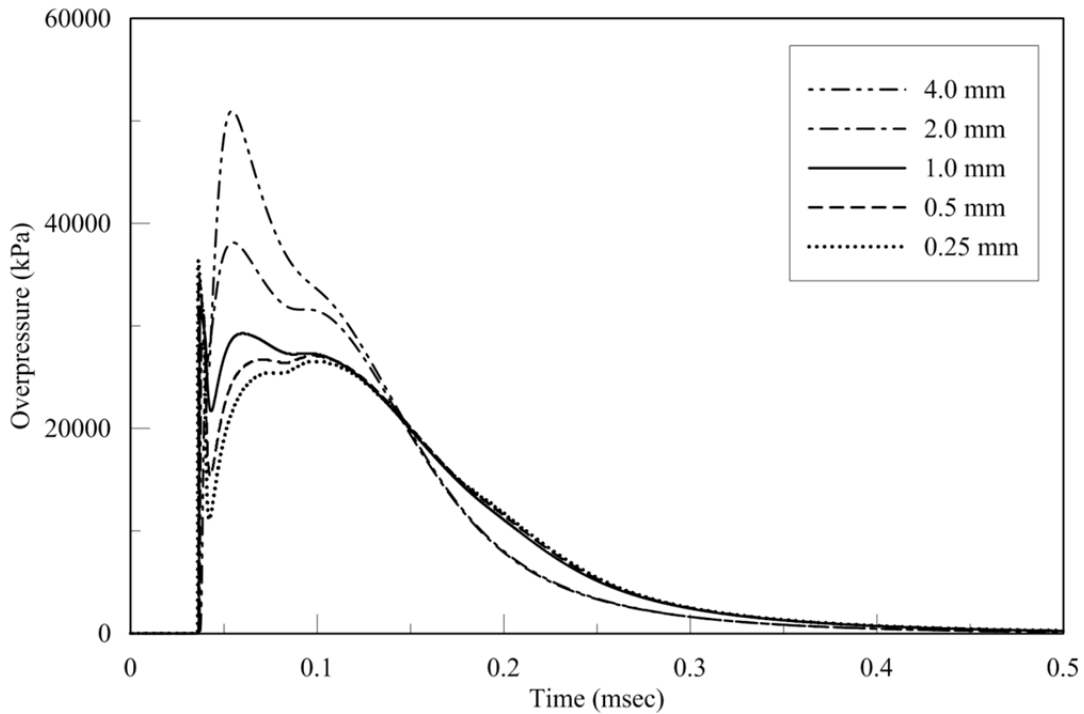


b.  $r = 164$  mm (15 mm from face of charge);  $Z = 0.058$  m/kg<sup>1/3</sup>;  $\bar{r} = 1.10$

**Figure 2-41 Overpressure histories at distance,  $r$ , from the center of a spherical charge of 22.68 kg of TNT; JWL EOS; no afterburning**

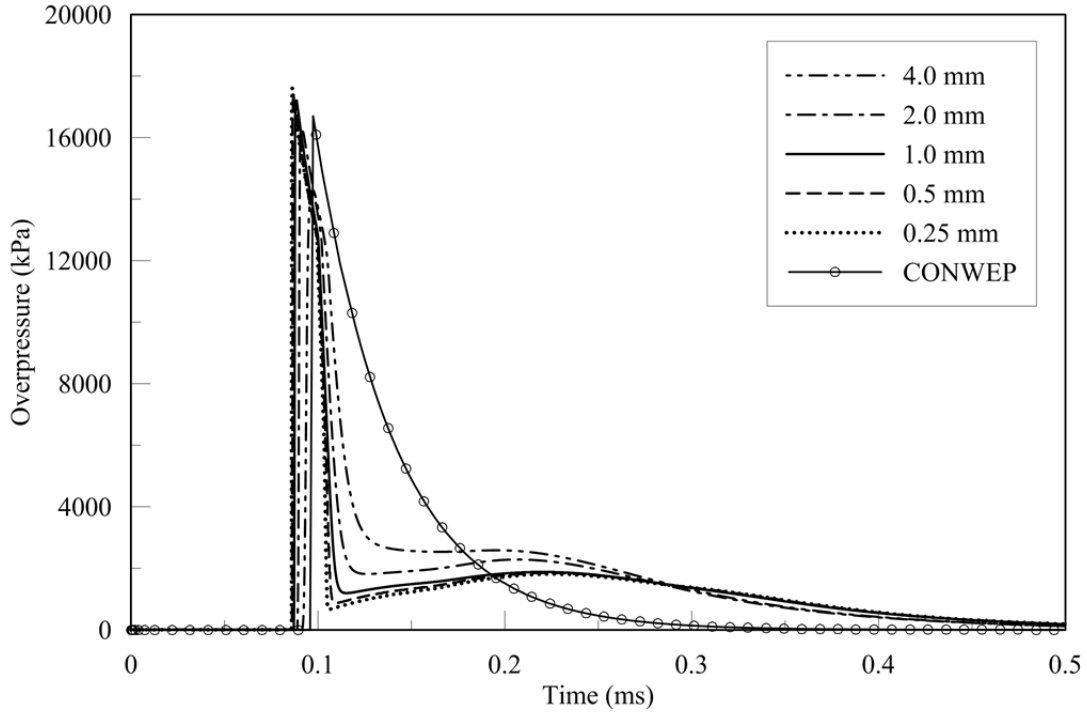


c.  $r = 200$  mm (51 mm from face of charge);  $Z = 0.071$  m/kg<sup>1/3</sup>;  $\bar{r} = 1.34$

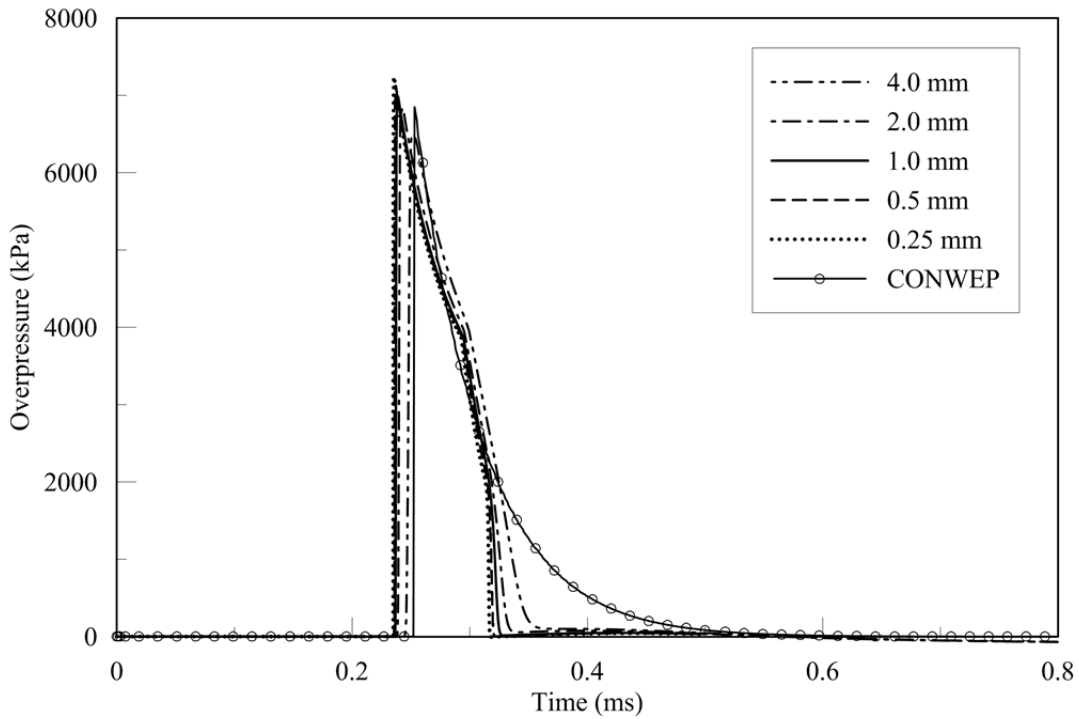


d.  $r = 250$  mm (101 mm from face of charge);  $Z = 0.088$  m/kg<sup>1/3</sup>;  $\bar{r} = 1.68$

**Figure 2-41 Overpressure histories at distance,  $r$ , from the center of a spherical charge of 22.68 kg of TNT; JWL EOS; no afterburning (cont.)**

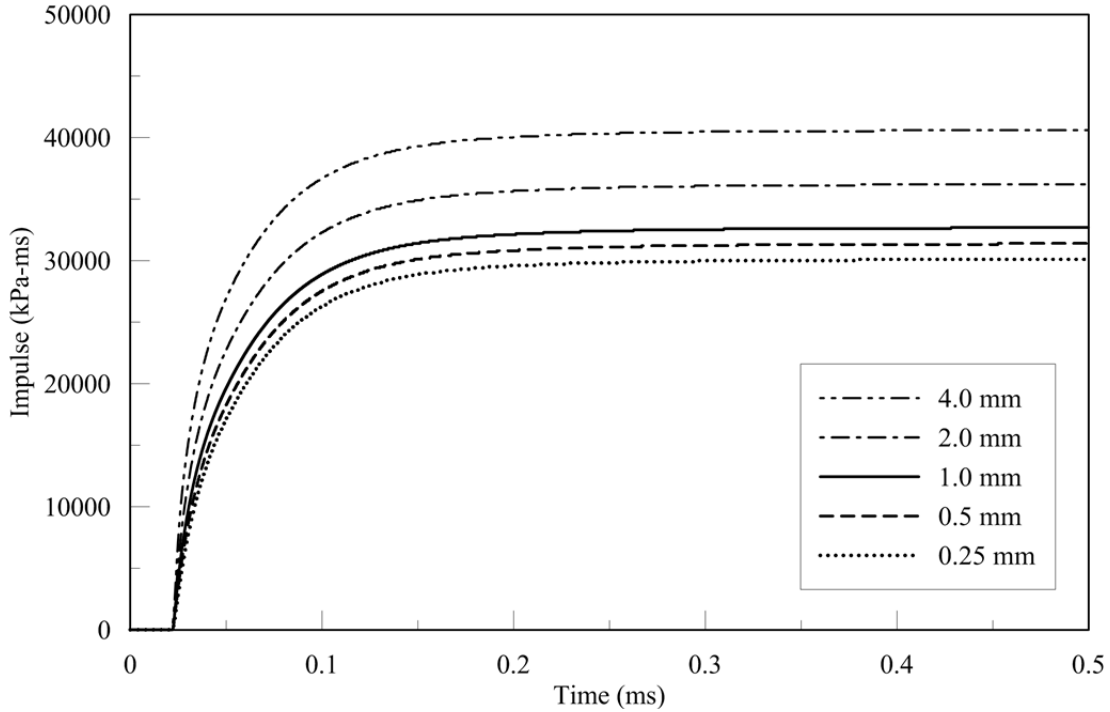


e.  $r = 500$  mm (351 mm from face of charge);  $Z = 0.177$  m/kg<sup>1/3</sup>;  $\bar{r} = 3.36$

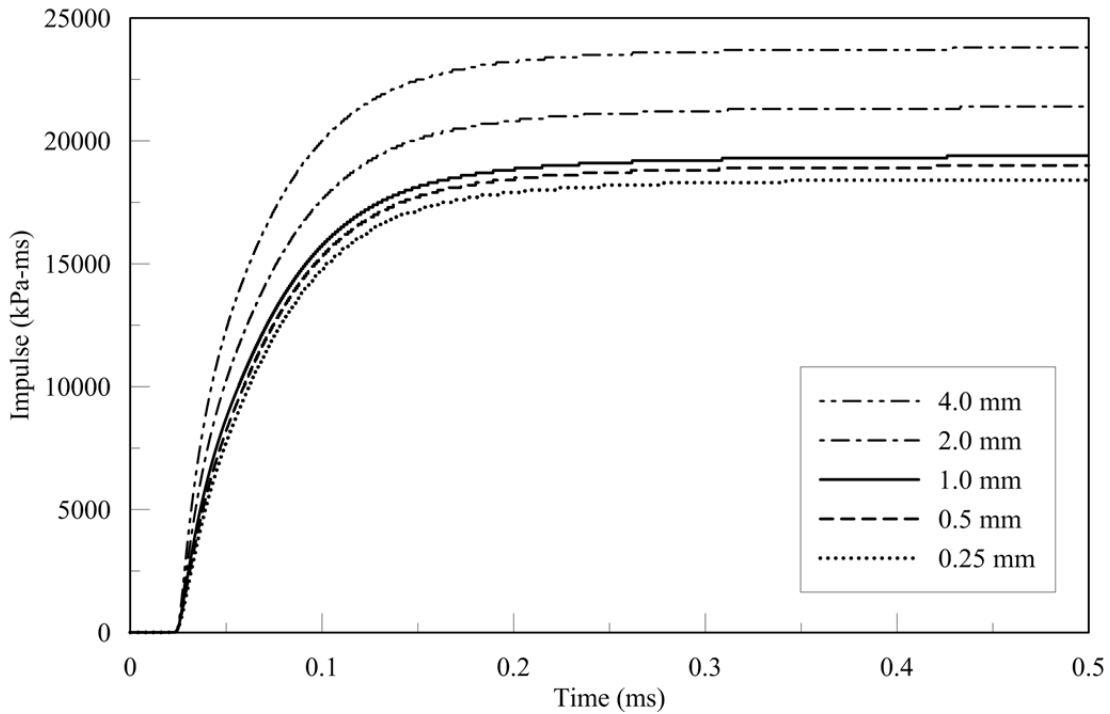


f.  $r = 1000$  mm (851 mm from face of charge);  $Z = 0.353$  m/kg<sup>1/3</sup>;  $\bar{r} = 6.71$

**Figure 2-41 Overpressure histories at distance,  $r$ , from the center of a spherical charge of 22.68 kg of TNT; JWL EOS; no afterburning (cont.)**

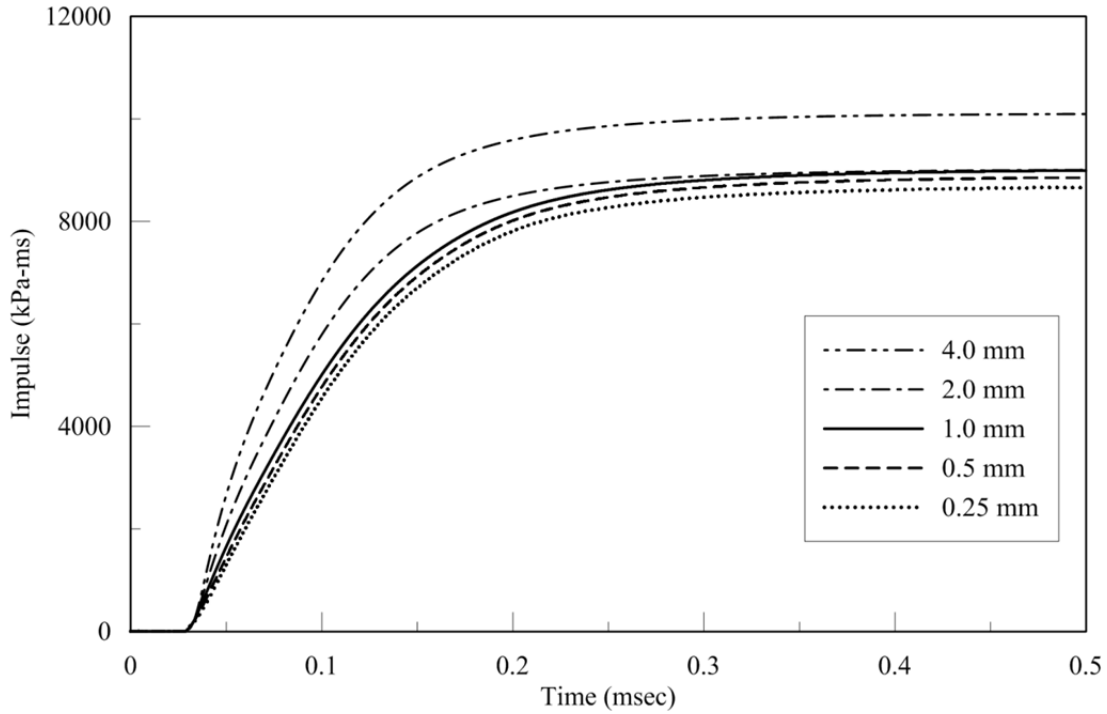


a.  $r = 152.7$  mm (3.7 mm from face of charge);  $Z = 0.054$  m/kg<sup>1/3</sup>;  $\bar{r} = 1.025$

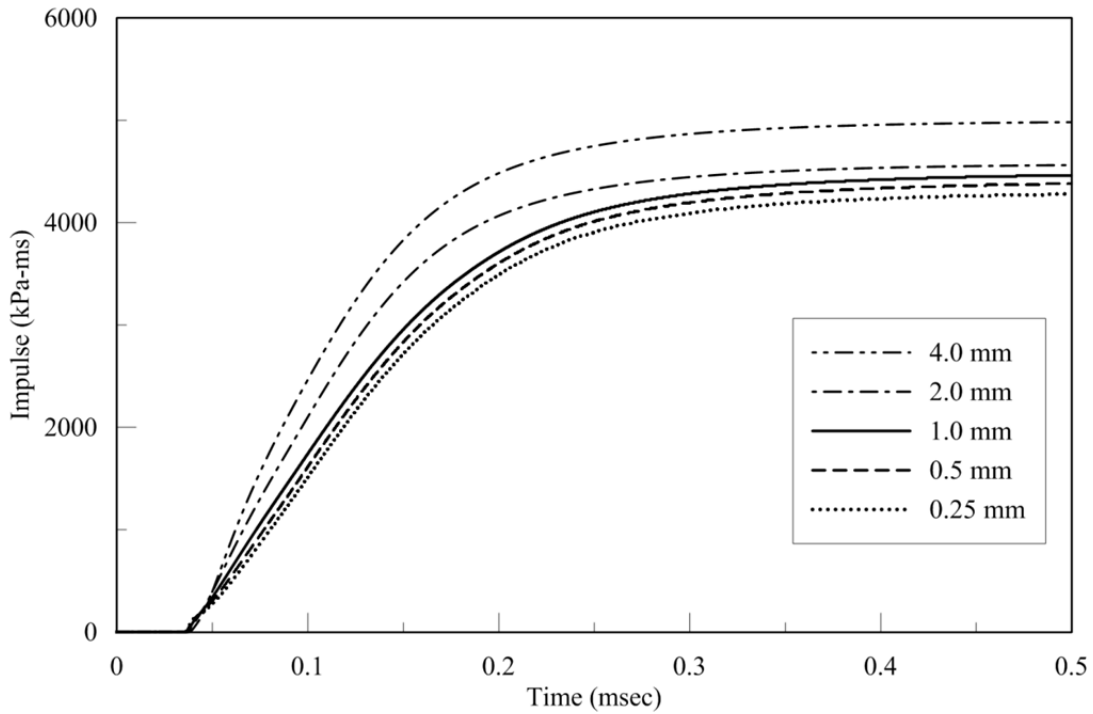


b.  $r = 164$  mm (15 mm from face of charge);  $Z = 0.058$  m/kg<sup>1/3</sup>;  $\bar{r} = 1.10$

**Figure 2-42 Overpressure histories at distance,  $r$ , from the center of a spherical charge of 22.68 kg of TNT; JWL EOS; no afterburning**

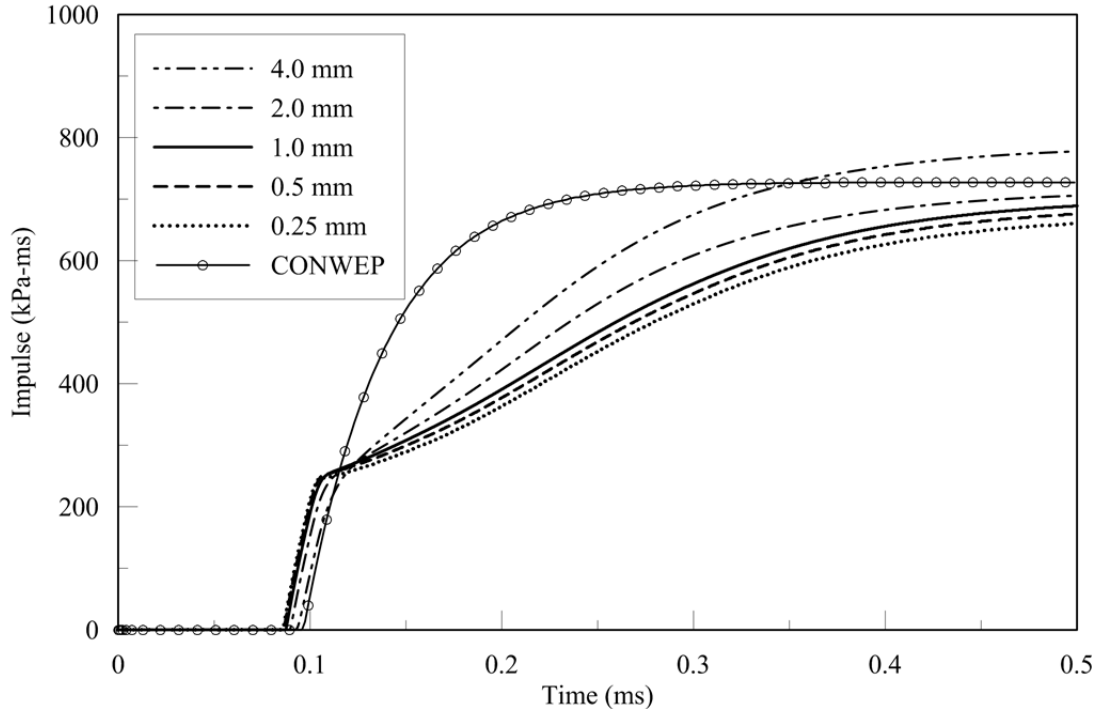


c.  $r = 200$  mm (51 mm from face of charge);  $Z = 0.071$  m/kg<sup>1/3</sup>;  $\bar{r} = 1.34$

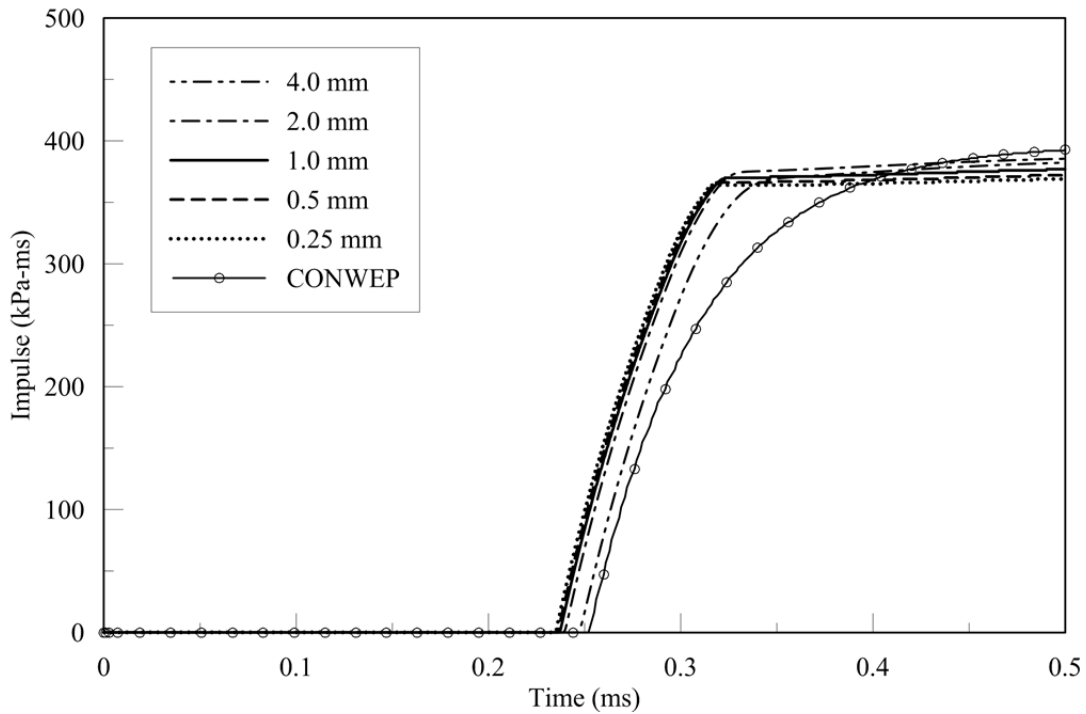


d.  $r = 250$  mm (101 mm from face of charge);  $Z = 0.088$  m/kg<sup>1/3</sup>;  $\bar{r} = 1.68$

**Figure 2-42 Overpressure histories at distance,  $r$ , from the center of a spherical charge of 22.68 kg of TNT; JWL EOS; no afterburning (cont.)**



e.  $r = 500$  mm (351 mm from face of charge);  $Z = 0.177$  m/kg<sup>1/3</sup>;  $\bar{r} = 3.36$



f.  $r = 1000$  mm (851 mm from face of charge);  $Z = 0.353$  m/kg<sup>1/3</sup>;  $\bar{r} = 6.71$

**Figure 2-42 Overpressure histories at distance,  $r$ , from the center of a spherical charge of 22.68 kg of TNT; JWL EOS; no afterburning (cont.)**

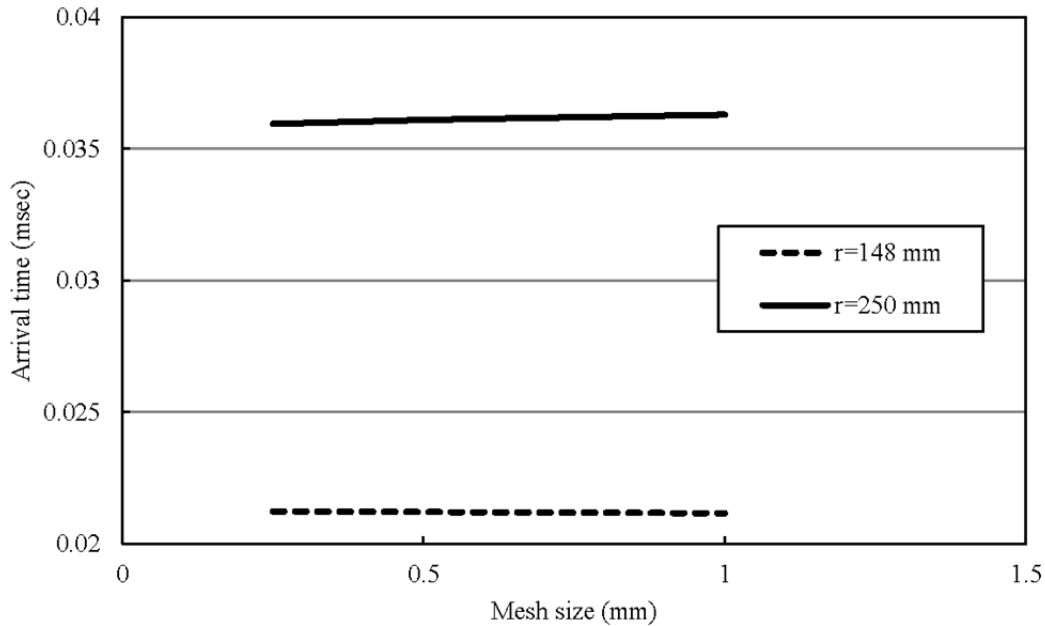


**Figure 2-43 Overpressure histories at distance,  $r$ , from the center of a spherical charge of 22.68 kg of TNT; JWL EOS; no afterburning (cont.)**

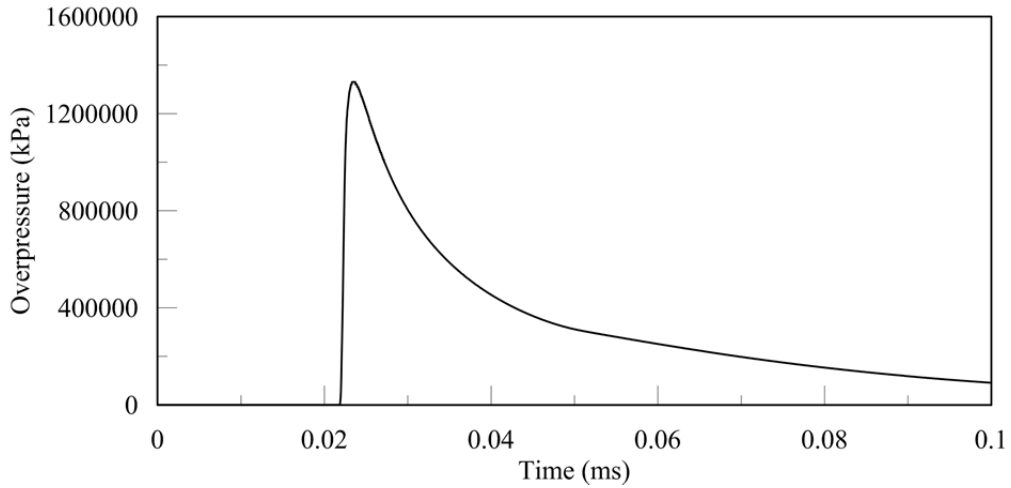
### 2.4.3 Temperature in the Vicinity of the Charge Face

In the vicinity of the face of the charge, the temperature is extremely high, and these high temperatures can enable afterburning as discussed in Section 2.4.4. Temperatures for the 22.68 kg charge of TNT are monitored using a cell size of 0.5 mm at  $Z = 0.054, 0.058, 0.071, 0.088, 0.177$  and  $0.353 \text{ m/kg}^{1/3}$ , used in the mesh convergence study of Section 2.4.2. Afterburning is not considered.

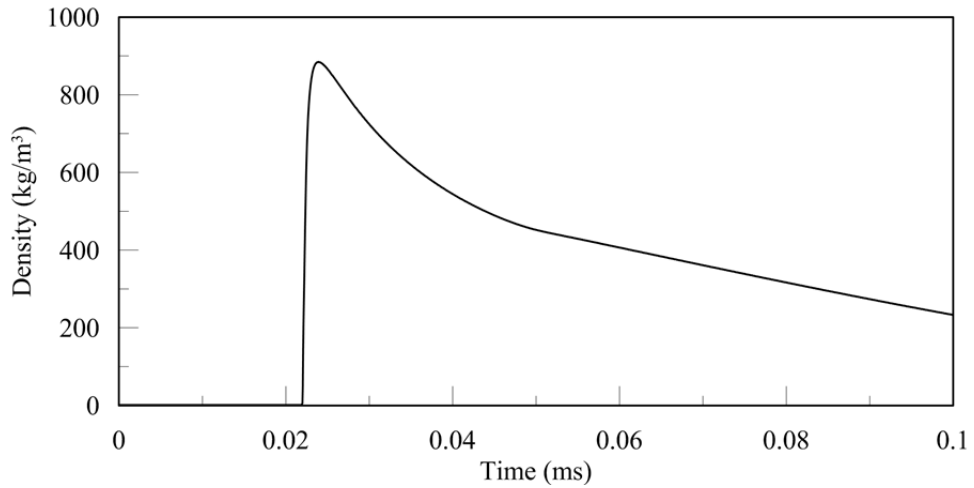
Histories of temperature for the range considered are presented in Figures 2-44 through 2-49, together with those of overpressure and density. Very close to the face of the charge (i.e.,  $Z = 0.054 \text{ m/kg}^{1/3}$ ; Figure 2-44), the peak temperature is approximately 200000 K. The temperature rises nearly instantaneously with the arrival of the shock front but the peak temperature occurs at the front of the expanding detonation products. Consider Figure 2-47 ( $Z = 0.088 \text{ m/kg}^{1/3}$ ). In the density history, the first (shown with open circle) and the second peaks near  $t = 0.04 \text{ ms}$  indicate the arrival of the shock front and the front of the expanding detonation products, respectively. The peak temperature shown in Figure 2-47c is associated with the second peak in the density history, which is also observed in Figures 2-48 and 2-49 ( $Z = 0.177$  and  $0.353 \text{ m/kg}^{1/3}$ ,

respectively). The relationship between the peak temperature and the expanding detonation products cannot be seen for  $Z = 0.054, 0.058$  and  $0.71 \text{ m/kg}^{1/3}$ , as shown in Figures 2-44, 2-45 and 2-46, respectively, because the distances between the shock front and the front of the expanding detonation products cannot be resolved at this scale.

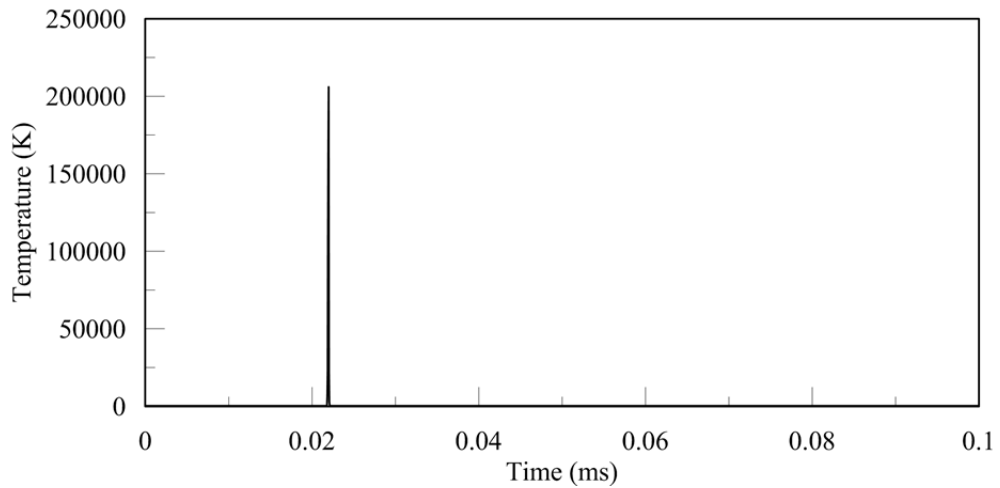
Figure 2-50 shows peak temperature as a function of radial expansion of the detonation products for three charges of TNT of 22.68, 960 and 18735 kg. The influence of the charge weight on the results is insignificant. These data inform the afterburning study that is presented next.



a. Overpressure

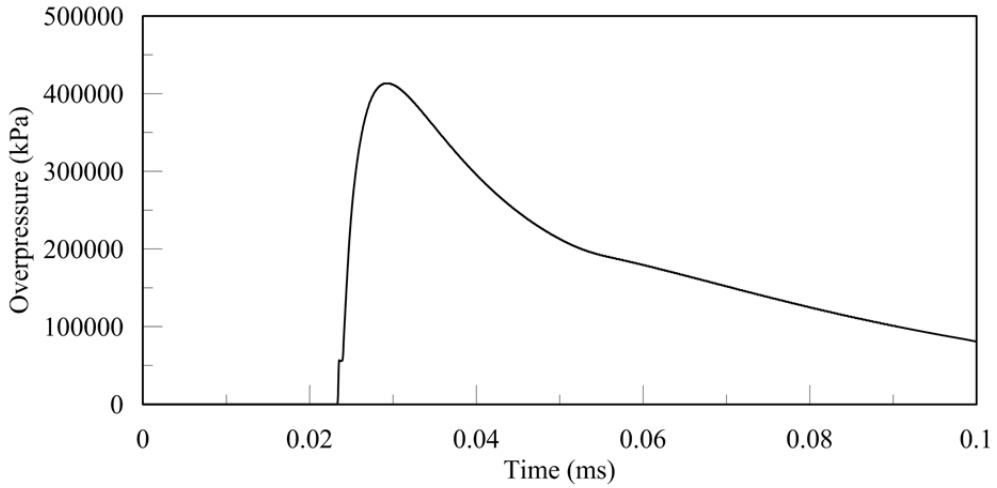


b. Density

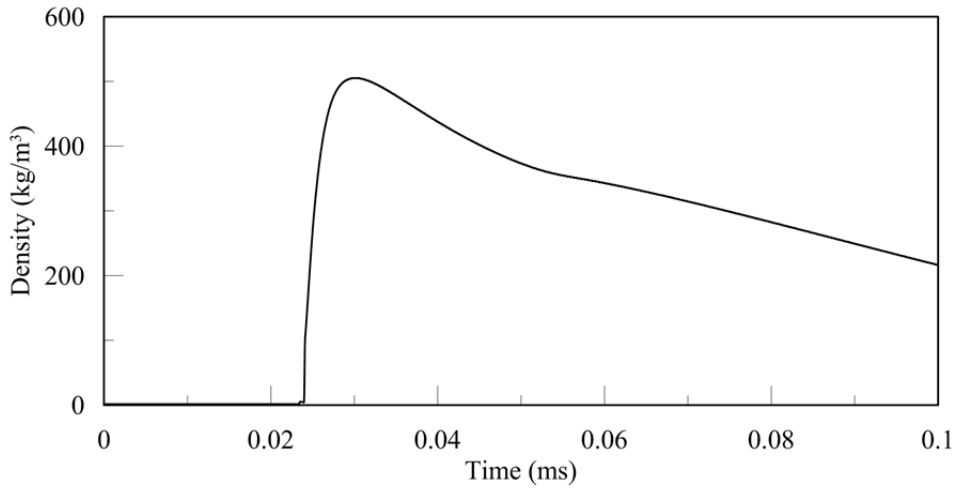


c. Temperature

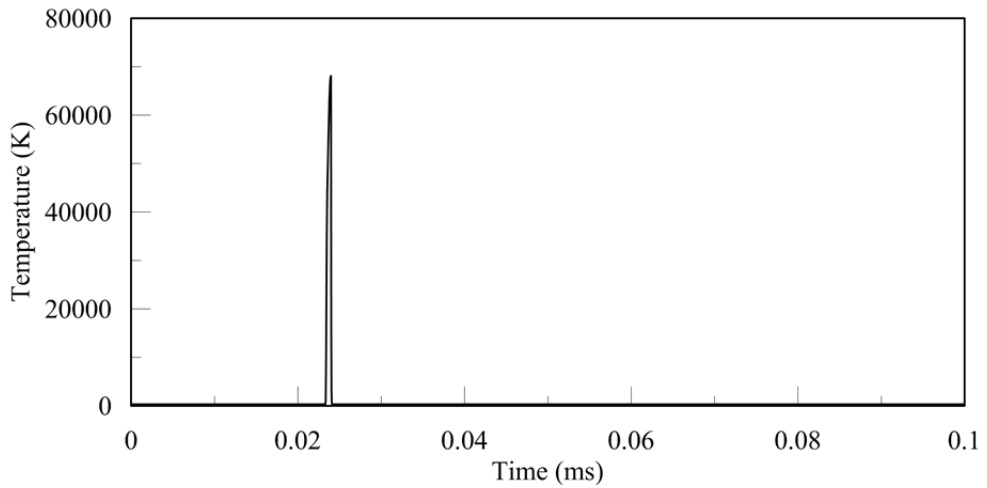
**Figure 2-44 Overpressure, density and temperature histories at  $Z = 0.054 \text{ m/kg}^{1/3}$ ; spherical charge of 22.68 kg of TNT; JWL EOS; 0.5 mm mesh**



a. Overpressure

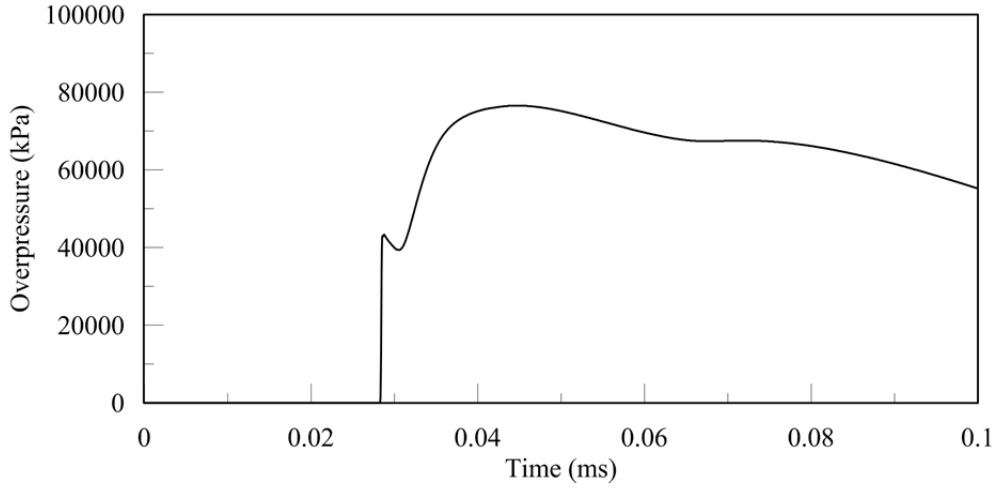


b. Density

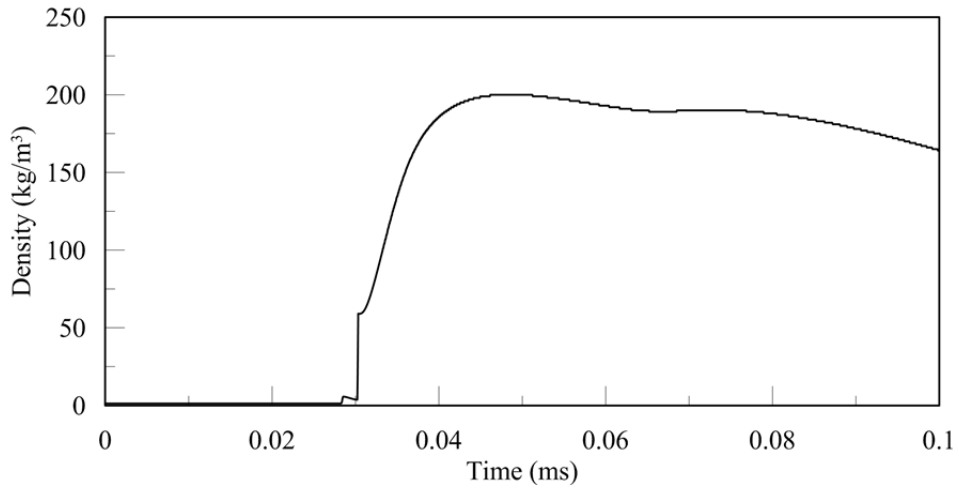


c. Temperature

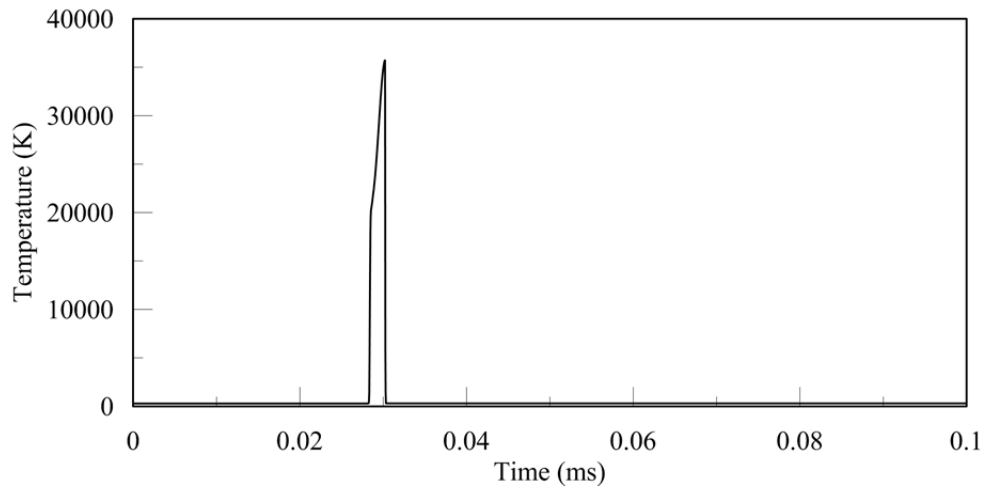
**Figure 2-45 Overpressure, density and temperature histories at  $Z = 0.058 \text{ m/kg}^{1/3}$ ; spherical charge of 22.68 kg of TNT; JWL EOS; 0.5 mm mesh**



a. Overpressure

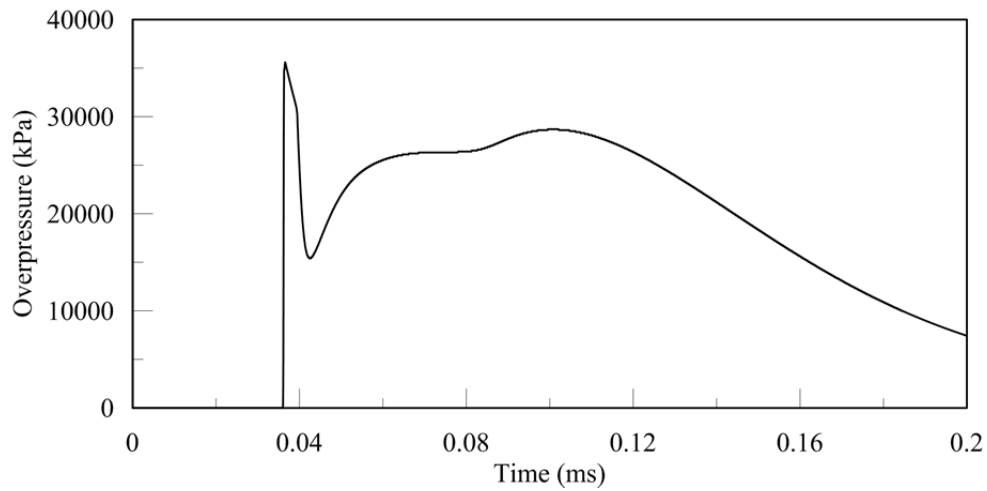


b. Density

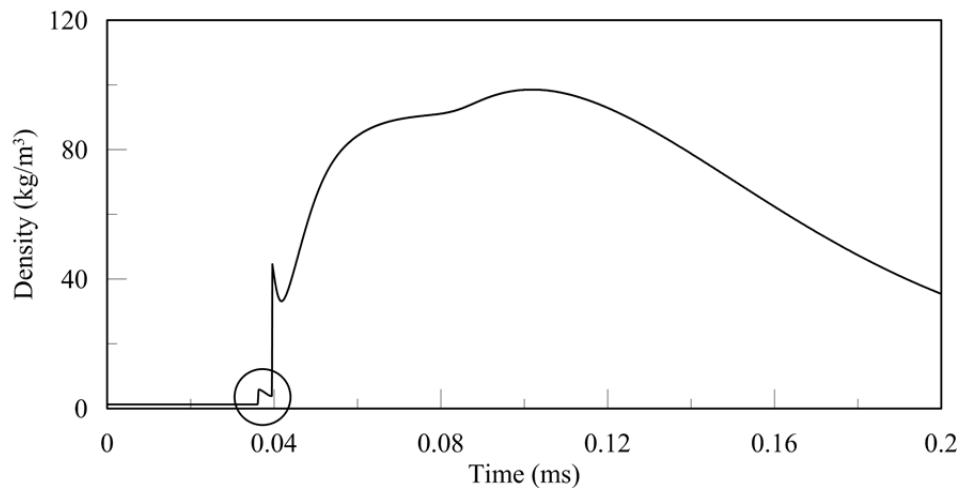


c. Temperature

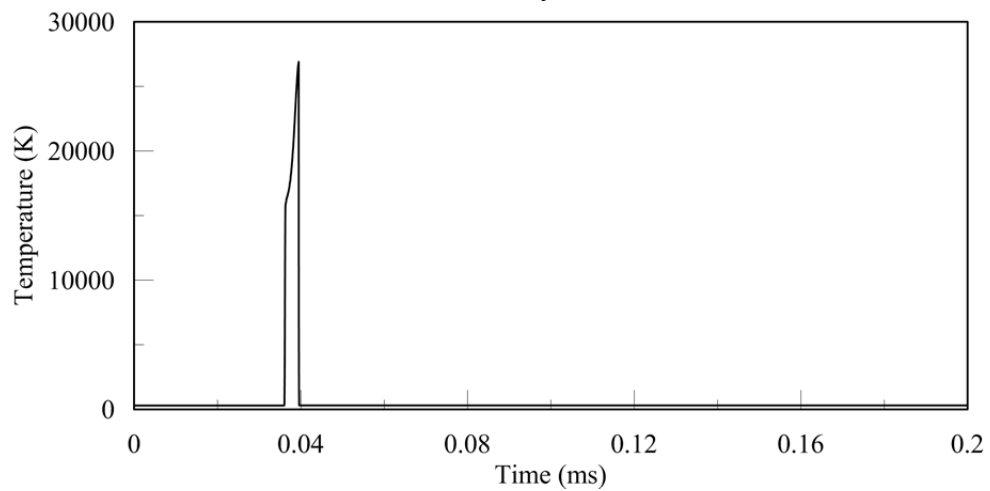
**Figure 2-46 Overpressure, density and temperature histories at  $Z = 0.071 \text{ m/kg}^{1/3}$ ; spherical charge of 22.68 kg of TNT; JWL EOS; 0.5 mm mesh**



a. Overpressure

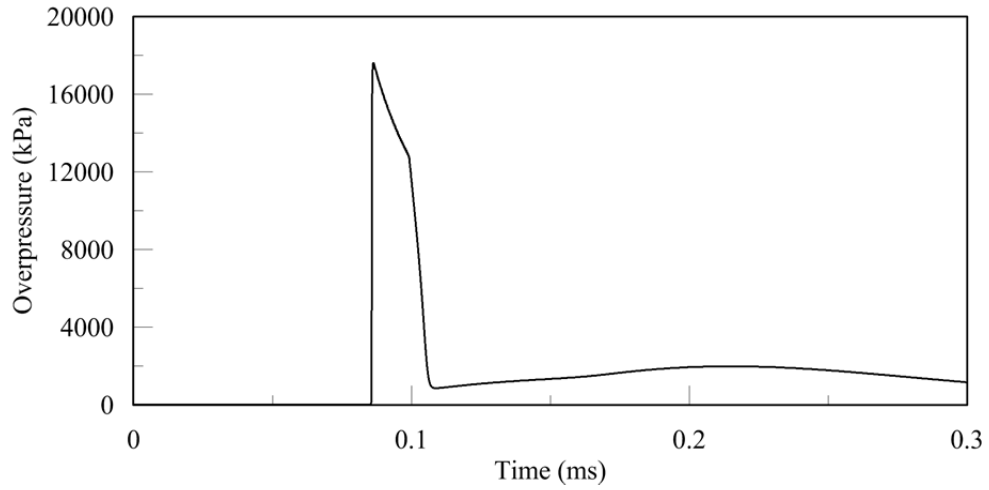


b. Density

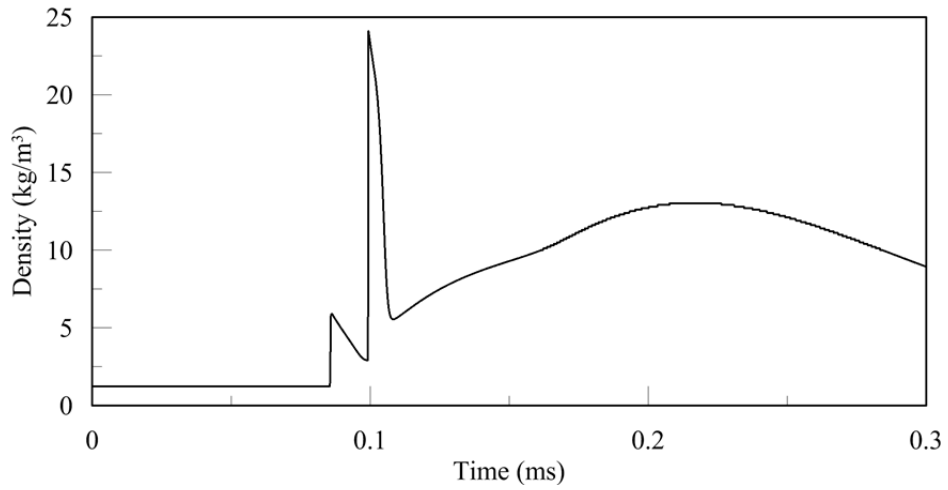


c. Temperature

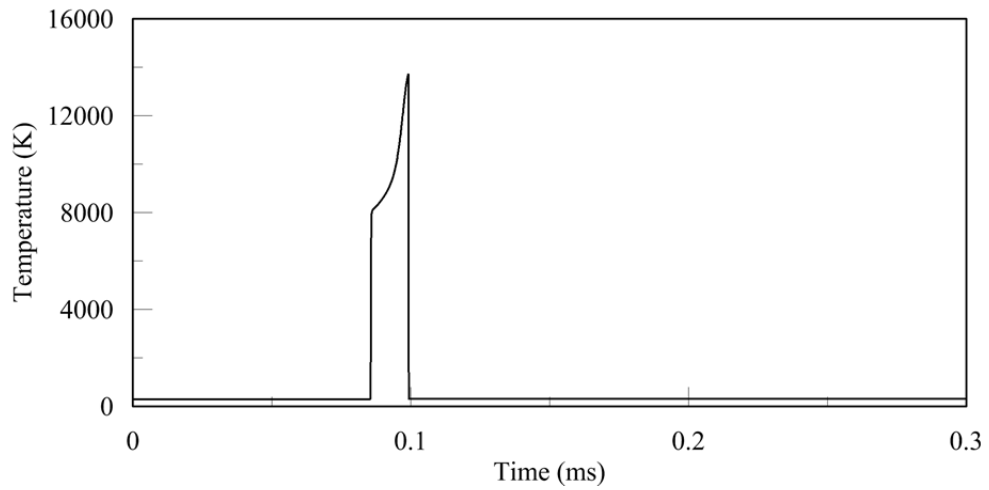
**Figure 2-47 Overpressure, density and temperature histories at  $Z = 0.088 \text{ m/kg}^{1/3}$ ; spherical charge of 22.68 kg of TNT; JWL EOS; 0.5 mm mesh**



a. Overpressure

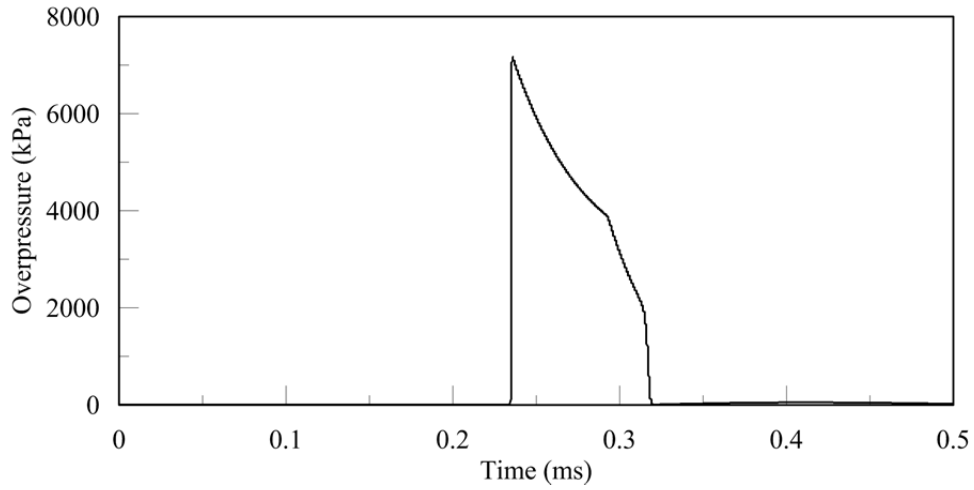


b. Density

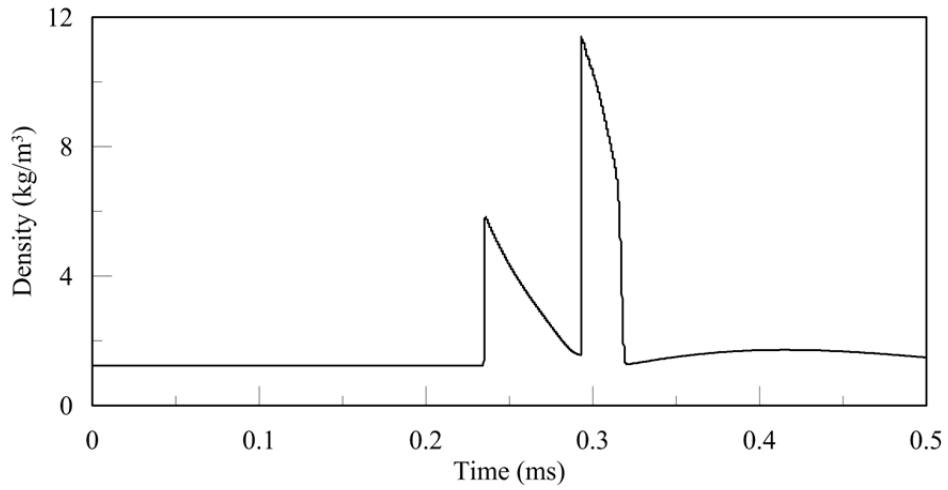


c. Temperature

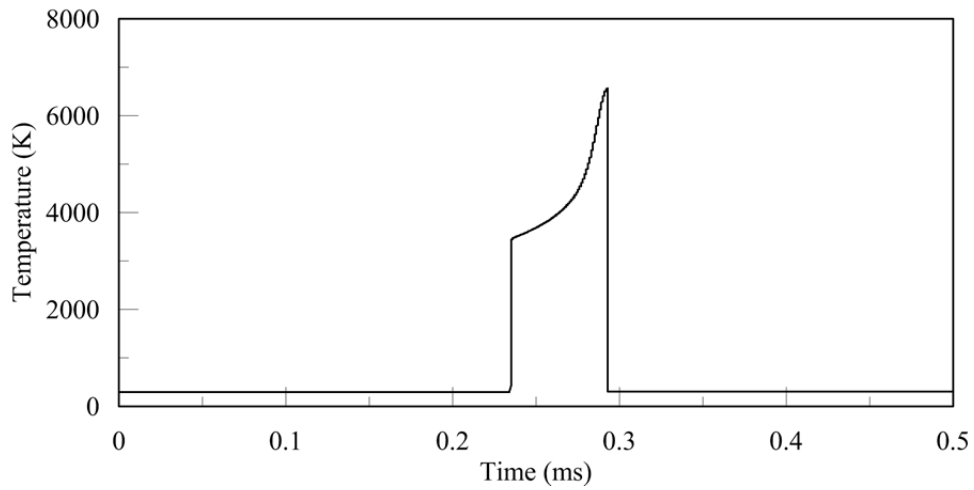
**Figure 2-48 Overpressure, density and temperature histories at  $Z = 0.177 \text{ m/kg}^{1/3}$ ; spherical charge of 22.68 kg of TNT; JWL EOS; 0.5 mm mesh**



a. Overpressure



b. Density



c. Temperature

**Figure 2-49 Overpressure, density and temperature histories at  $Z = 0.353 \text{ m/kg}^{1/3}$ ; spherical charge of 22.68 kg of TNT; JWL EOS; 0.5 mm mesh**

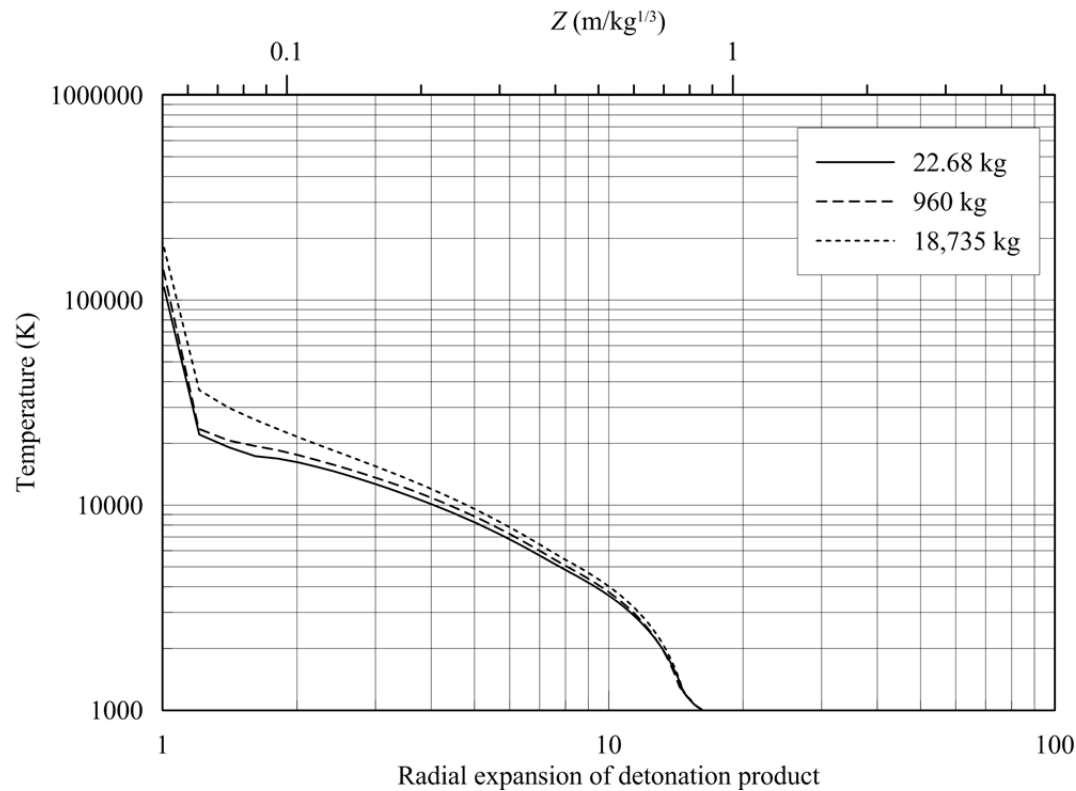


**Figure 2-50 Variation of temperature with radial expansion of detonation product**

#### **2.4.4 Afterburning**

To date, the analysis has assumed that all the energy of the explosive is released upon detonation and used to drive the shock front forward. However, for under-oxidized explosives, this assumption is not necessarily correct. For such explosives, there exists an additional energy-release mechanism. TNT is an under-oxidized explosive that does not have sufficient oxygen to completely oxidize. As the shock wave expands into the atmosphere, the detonation products consume oxygen from the surrounding air and oxidize; the process is called *afterburning* (Donahue 2008). Afterburning involves combustion reactions that release energy and increase the temperature of the affected region, enhancing the effects of detonation. Unlike detonation, where the release of energy takes place in microseconds, afterburning is a process that can last milliseconds to seconds. There are two requirements essential for afterburning to occur: 1) the temperature in the region should be high enough for combustion reactions to take place, and 2) there must be enough oxygen in the ambient air. TNT is a fuel-rich explosive, with the main

fuels being Carbon, Carbon Monoxide, Hydrogen, and Methane. These fuels undergo combustion reactions at their respective ignition temperatures. If the temperature is 1800+ K, sufficient oxygen is present, and the oxygen is well mixed with the fuels, then all the combustion reactions can occur (e.g., Souers et al. 2001, McNesby et al. 2010). The temperatures computed by analysis exceed 10000 K during the initial stages of the expansion beyond the original surface of the charge. Given that afterburning should occur, AUTODYN is used to model it. The additional energy to be released due to afterburning and the duration of the release can be specified in AUTODYN in the definition of the JWL EOS.

In Figure 2-50, the temperature decreases to 1800 K at a radial expansion of the detonation products,  $\bar{r}_d$ , of 13.4 ( $Z = 0.71 \text{ m/kg}^{1/3}$ ), where the radial expansion of the shock front,  $\bar{r}$ , is 17.2 ( $Z = 0.91 \text{ m/kg}^{1/3}$ ). For a charge weight of 22.68 kg, the volume of air between the original surface of the charge and at a radial expansion,  $\bar{r}_d$ , of 13.4 is  $33.3 \text{ m}^3$ . Donahue (2008) reported that 3.18 kg of air is required per 1 kg of TNT to release the maximum afterburning energy. For a volume of air of  $33.3 \text{ m}^3$ , the maximum afterburning energy is 129 MJ ( $5.67 \text{ MJ/kg} \times 22.68 \text{ kg}$ ) (132% of the detonation energy, 96 MJ ( $4.23 \text{ MJ/kg} \times 22.68 \text{ kg}$ )). In the very early stages of the expansion, afterburning does not significantly affect the blast wave (e.g., Cullis and Huntington-Thresher 2007, McNesby et al. 2010), which is due to a lack of available oxygen (air) and incomplete mixing with air. Assuming that the fuels are completely mixed with the available oxygen, the afterburning energy of 129 MJ is divided into six intervals, as noted in Table 2-14 and Figure 2-51. The front of the detonation products reaches the radial expansions,  $\bar{r}_d$ , of 1, 4, 6, 8, 10, 12 and 13.4 at  $t = 0.0215, 0.123, 0.245, 0.406, 0.610, 0.897$  and 1.15 msec, respectively. The density of air at room temperature is assumed to be  $1.225 \text{ kg/m}^3$ . The maximum afterburning energy is 10.01 MJ per 1 kg of TNT (Donahue 2008). The weight of TNT for an amount of air to produce the maximum afterburning energy is the weight of air divided by 3.18 kg-air/kg-TNT. The total afterburning energy is the weight of TNT multiplied by 10.01 MJ/kg-TNT. The specific afterburning energy is thus calculated by dividing the total afterburning energy by the weight of TNT (= 22.68 kg) and is then added to the AUTODYN analysis.

**Table 2-14 Calculations for the afterburning energy at each interval between radial expansions of detonation products for a spherical charge of 22.68 kg of TNT.**

Range of radial expansion, $\bar{r}_d$	1 to 4	4 to 6	6 to 8	8 to 10	10 to 12	12 to 13	Total
Volume of air (m <sup>3</sup> )	0.87	2.1	4.1	6.8	10.1	9.4	33.3
Weight of air (kg)	1.07	2.58	5.02	8.28	12.4	11.5	40.8
Weight of TNT for an available air to produce the maximum afterburning energy (kg)	0.336	0.811	1.58	2.60	3.89	3.62	12.8
Total afterburning energy (MJ)	3.37	8.12	15.8	26.1	38.9	36.2	129
Specific afterburning energy (MJ/kg)	0.148	0.358	0.697	1.15	1.71	1.60	5.67
Percentage of the detonation energy	3.5	8.4	16.3	26.9	40.1	37.3	132

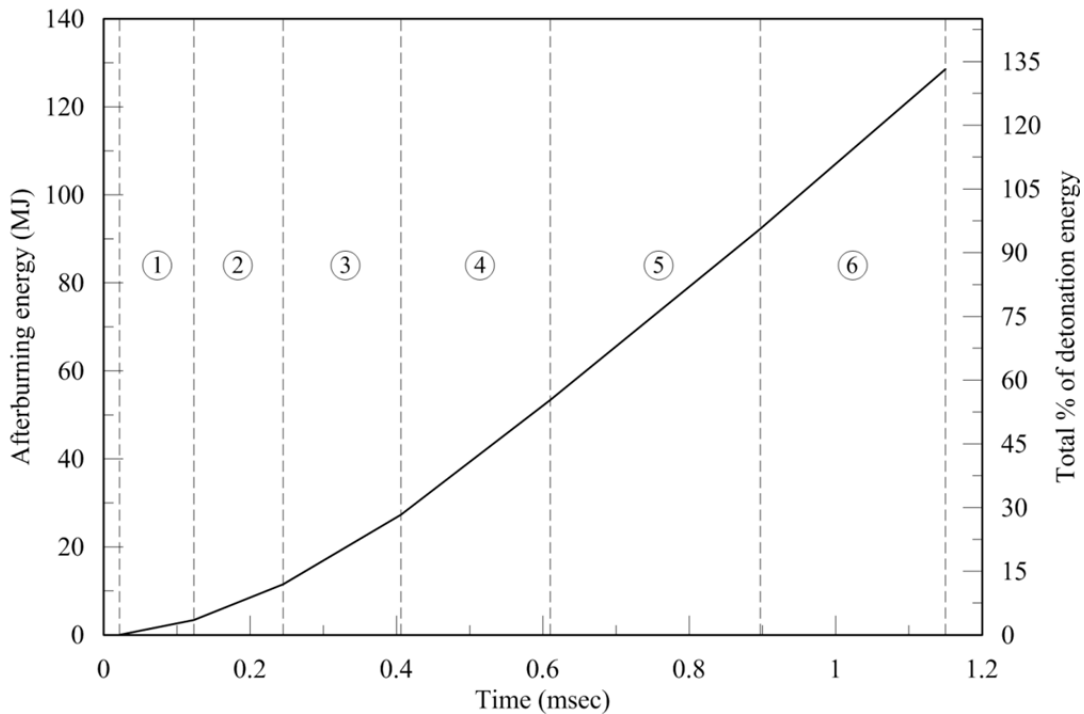


**Figure 2-51 Input of afterburning energy with time for 22.68 kg of TNT**

The afterburning energy is released from a problem time of 0.0215 msec (radial expansion of detonation products,  $\bar{r}_d = 1.0$ ) to 1.15 msec ( $\bar{r}_d = 13.4$ ). Figure 2-51 presents the afterburning energy with time, which is released at a constant rate (uniformly) in each interval of the simulation, as noted in the third last row of Table 2-14. Figure 2-52 describes the relationship between the weight of TNT and the available volume of air to release the maximum afterburning energy. Figure 2-53 describes the available volume of air as a function of the radial expansion of detonation products,  $\bar{r}_d$ , where the available volume of air is computed as the volume between the face of the charge and the spherical surface corresponding to  $\bar{r}_d$ .

Figures 2-54 and 2-55 present the results of an analysis for a mesh of 0.5 mm cells, assuming a total afterburning energy of 129 MJ (132% of the detonation energy; see Figure 2-51). For this explosive, the effect of afterburning (as modeled) is insignificant at a distance of 200 mm (corresponding to  $\bar{r}_d = 1.34$ ) due to a lack of available oxygen, but an increase in impulse is evident at the greater distance of 250 mm ( $\bar{r}_d = 1.68$ ). This increase is an upper bound on the effect of afterburning because perfect mixing of the available fuel and oxygen is assumed.

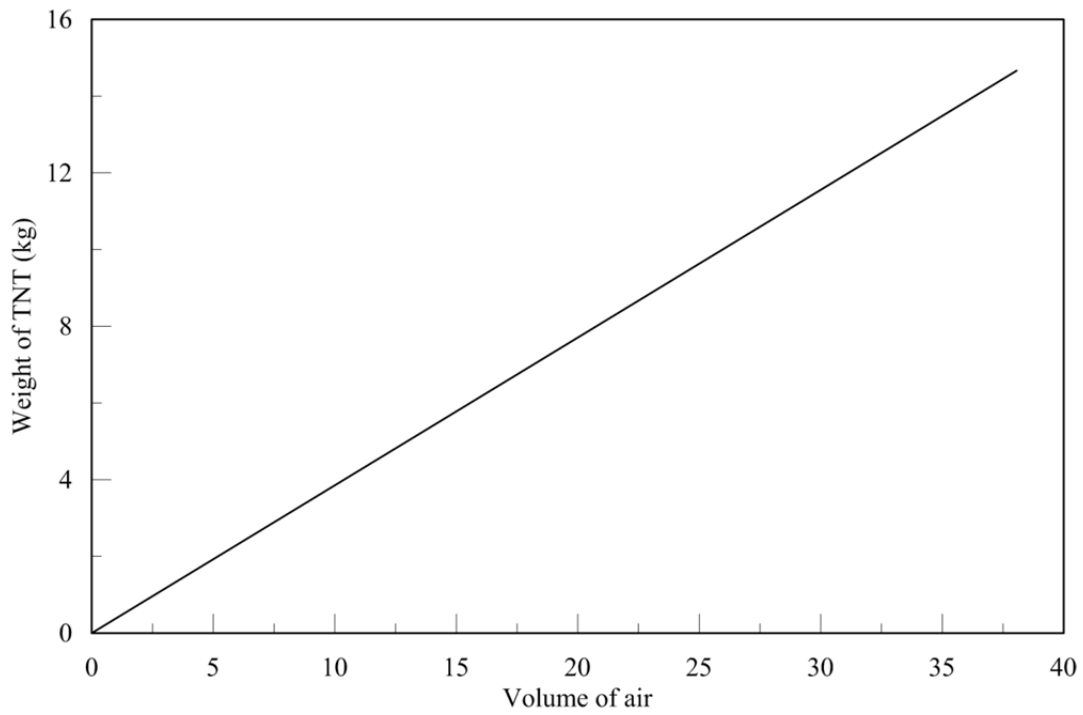


**Figure 2-52 Weight of TNT for volumes of air to release maximum afterburning energy**

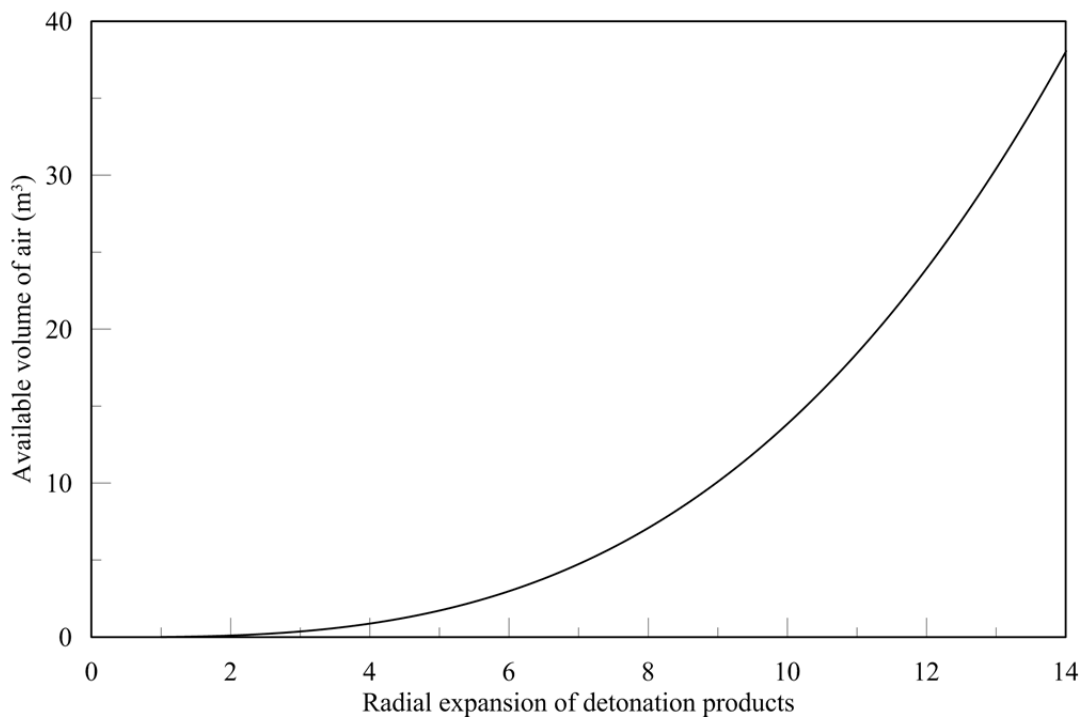
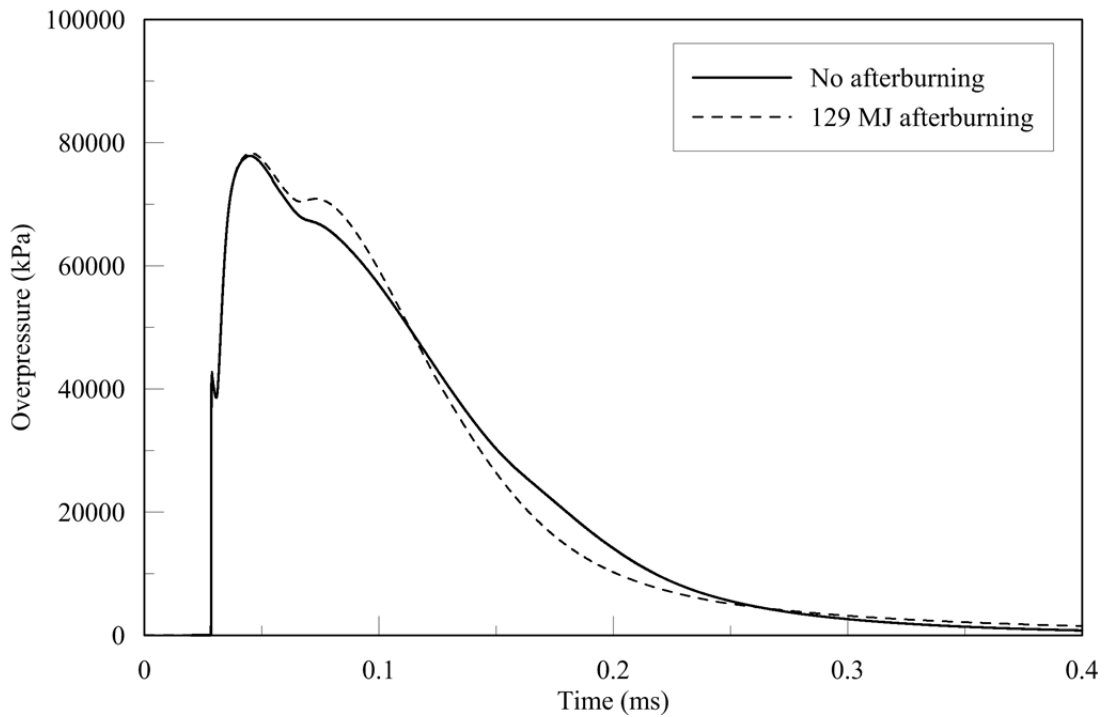
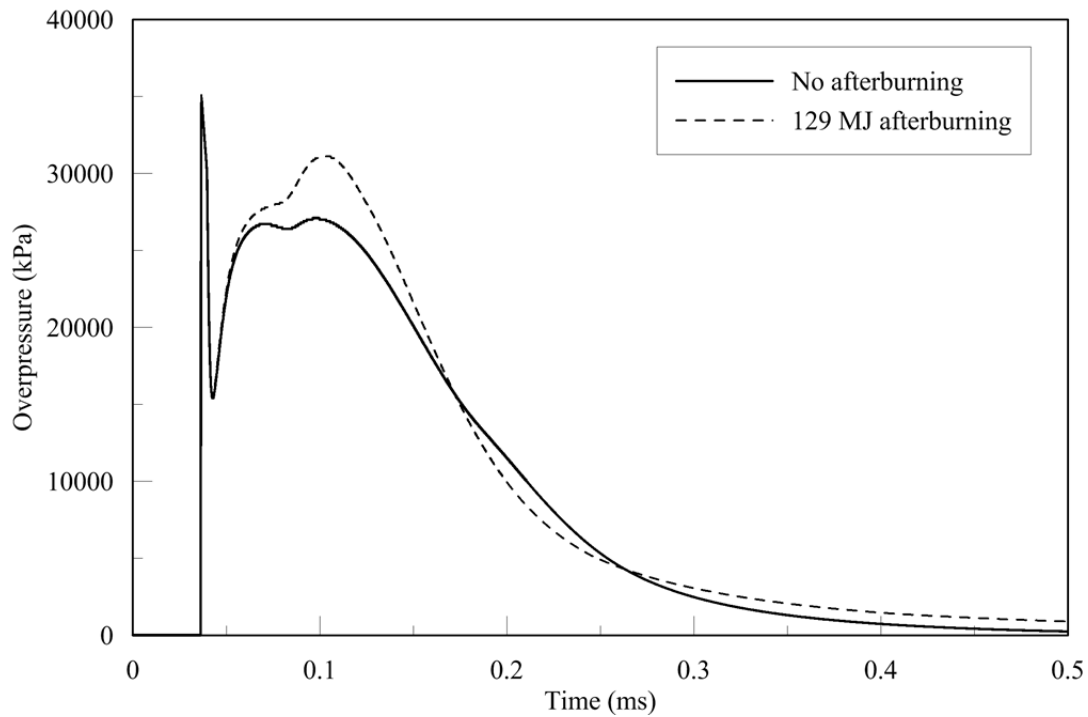


**Figure 2-53 Available volumes of air for radial expansion of detonation products**

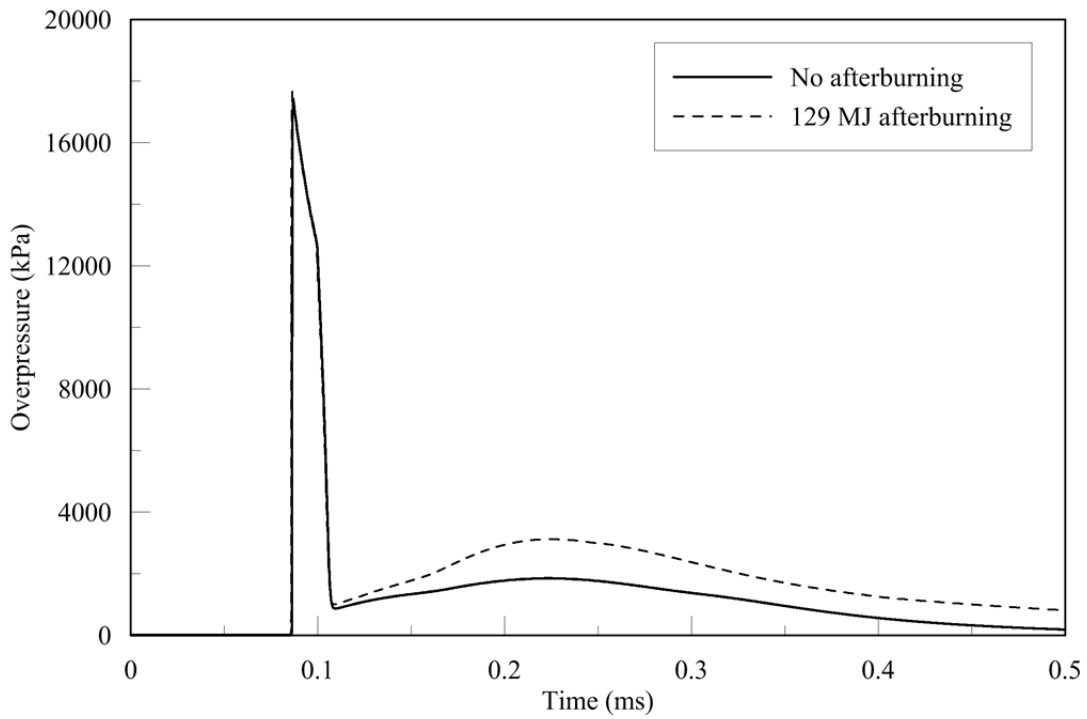


a.  $r = 200$  mm (51 mm from face of charge)

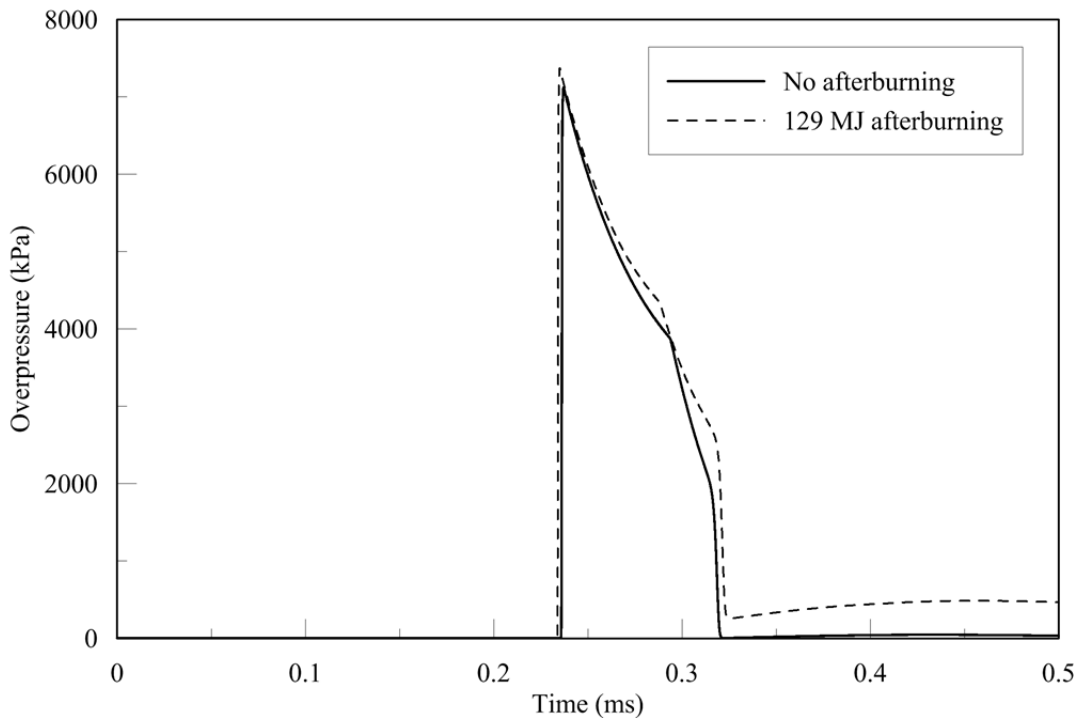


b.  $r = 250$  mm (101 mm from face of charge)

**Figure 2-54 Overpressure histories at distance,  $r$ , from the center of a spherical charge of 22.68 kg of TNT for a 0.5 mm mesh; JWL EOS; 129 MJ afterburning**

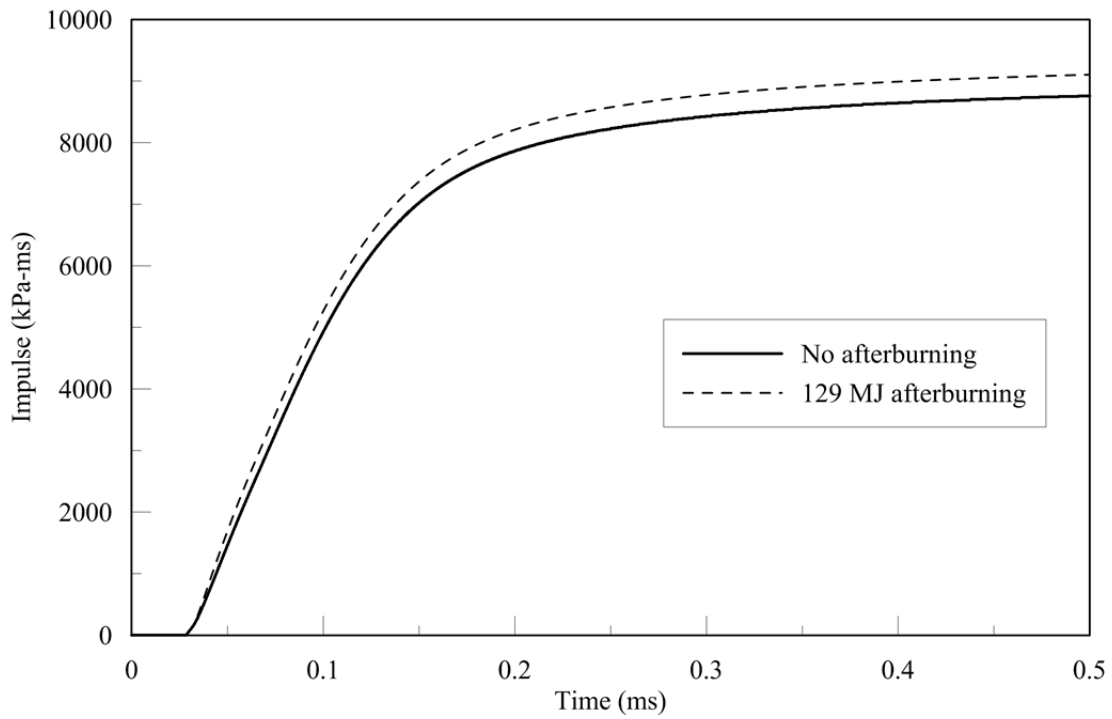


c.  $r = 500$  mm (351 mm from face of charge)

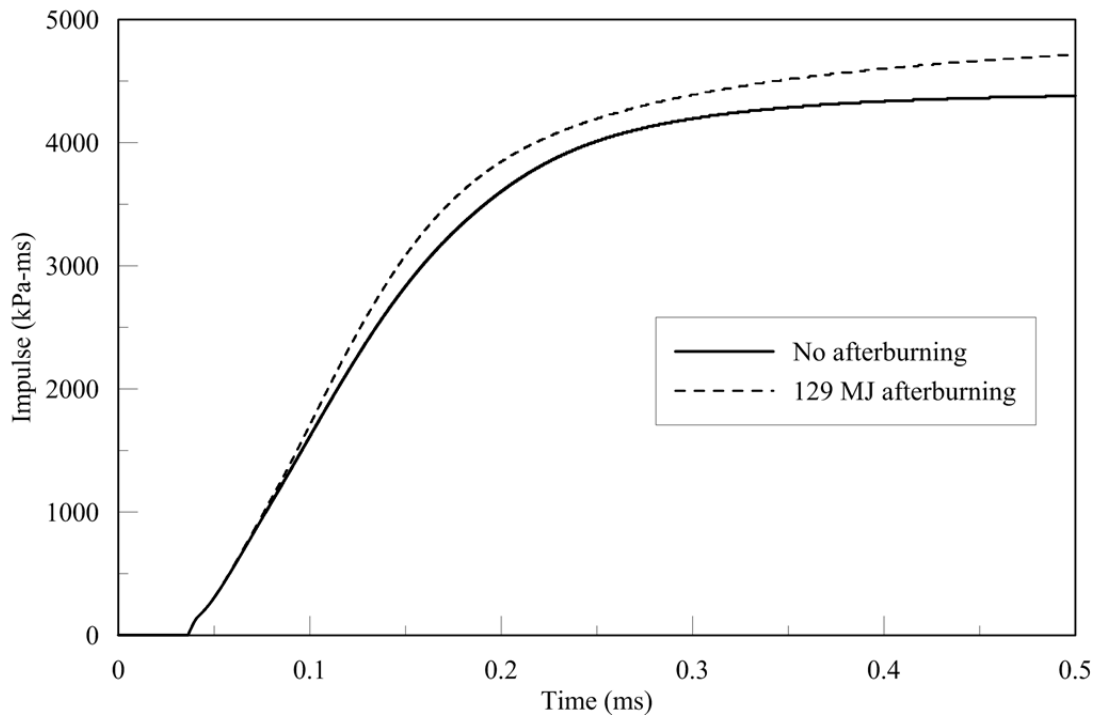


d.  $r = 1000$  mm (851 mm from face of charge)

**Figure 2-54 Overpressure histories at distance,  $r$ , from the center of a spherical charge of 22.68 kg of TNT for a 0.5 mm mesh; JWL EOS; 129 MJ afterburning (cont.)**

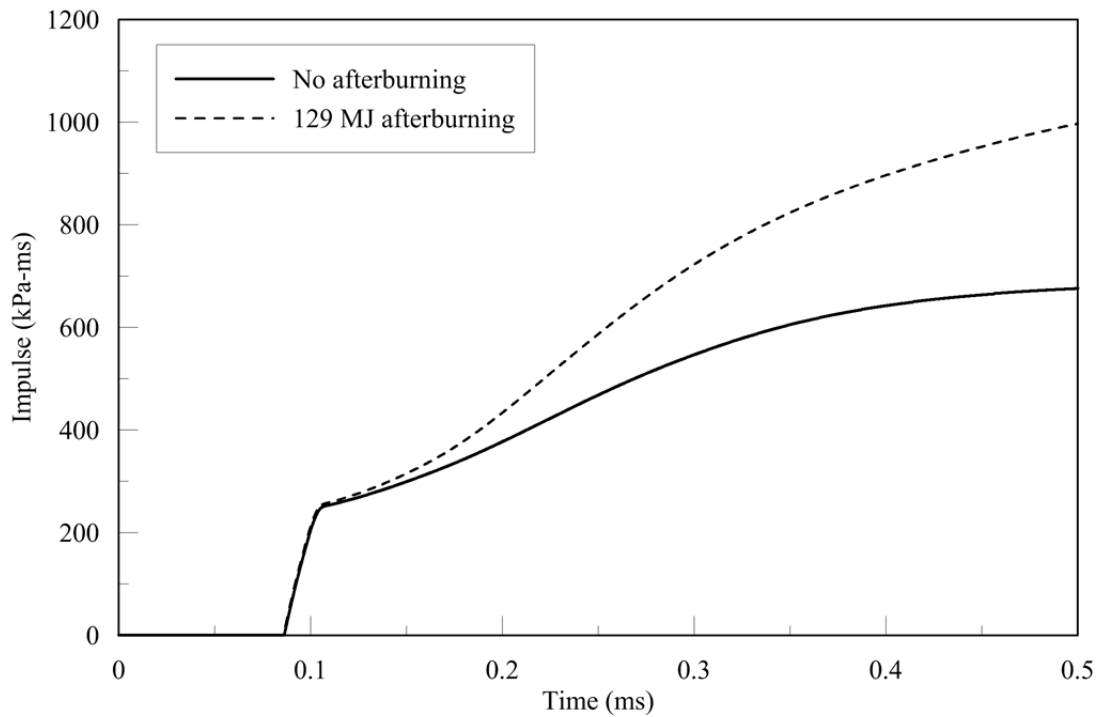


a.  $r = 200$  mm (51 mm from face of charge)

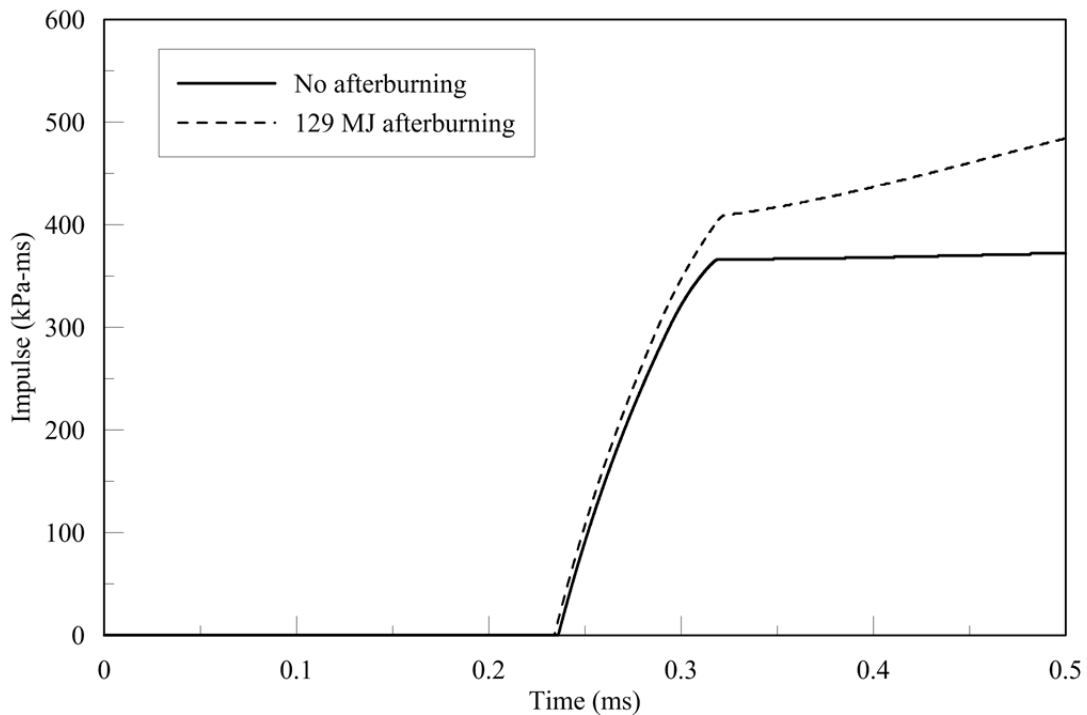


b.  $r = 250$  mm (101 mm from face of charge)

**Figure 2-55 Impulse histories at distance,  $r$ , from the center of a spherical charge of 22.68 kg of TNT for a 0.5 mm mesh; JWL EOS; 129 MJ afterburning**



c.  $r = 500$  mm (351 mm from face of charge)



d.  $r = 1000$  mm (851 mm from face of charge)

**Figure 2-55 Impulse histories at distance,  $r$ , from the center of a spherical charge of 22.68 kg of TNT for a 0.5 mm mesh; JWL EOS; 129 MJ afterburning (cont.)**

#### **2.4.5 Blast Wave Propagation in AUTODYN and Air3D**

One-dimensional blast wave propagation is studied using Air3D to contrast the predictions of Air3D and AUTODYN. Air3D (Rose 2006) is a computational fluid dynamics (CFD) code developed specifically for blast applications. The input data is specified via a text file, which is then run in batch mode. In a 3D analysis, there are three sections of the input file that are executed sequentially: spherical (1D), radial (2D) and main (3D). When the spherical input section is executed, the calculations proceed with spherical symmetry until the blast wave reaches a reflecting surface. The output of the 1D analysis is then remapped into 2D (the  $x, y$  domain) and then to a 3D domain.

Air3D uses the balloon analog of Ritzel and Matthews (1997) and assumes a constant  $\gamma$  for air. There are two versions of Air3D: ideal gas EOS and JWL EOS. The ideal gas version is used here. The input needed for the 1D section of the input file is initial weight (= 22.68 kg), density (= 1637 kg/m<sup>3</sup>) and energy (=  $4.3 \times 10^6$  J/kg) of the explosive, the cell size for the 1D calculations (= 0.5 mm) and the radius for the 1D calculations (= 2 m). In the 2D input section, the radial and axial boundaries for the 2D domain are specified by 'rmax' (= 3 m) and 'hmax' (= 3 m). The boundary conditions are specified by 'bru' (-1) and 'hru' (+1) in the input file; '-1' represents a 'stop' boundary and '+1' represents a 'transmit' boundary. The Air3D User Guide (Rose 2006) recommends a maximum cell size based on scaled distance; i.e., the cell size should represent roughly a scaled radial distance of 1 mm/kg<sup>1/3</sup>. If the mass of the explosive is 22.68 kg, the cell size should be less than  $1 \times 22.68^{1/3}$  or 2.82 mm. For a packing density of 1637 kg/m<sup>3</sup> and a charge radius of 149 mm, the initial pressure in the balloon is 2816 MPa.

Figure 2-56 presents fringe plots of pressure from the 1D AUTODYN analysis of the detonation of a 22.68 kg charge of TNT at time instants after detonation. The location of the shock front is identified by a fine line that is initially at a distance  $r = 149$  mm at  $t = 0.015$  and 0.020 msec, and  $r = 480$  mm at  $t = 0.1$  msec. The detonation front reached the face of the charge at a time between 0.020 msec and 0.025 msec. The shock wave then propagates continuously outward from the face of the charge and a rarefaction wave begins to propagate toward the center of the charge. Before the head of the rarefaction wave reaches the center of the charge, the peak

pressure at the center is approximately 4.2 GPa. The head of the rarefaction wave arrives at the center of the charge near  $t = 0.060$  msec and the pressure at the center decreases rapidly.

Figure 2-57 presents results of the 1D Air3D analysis for the same problem used in the AUTODYN analysis. The assumed detonation wave speed for the TNT is 6730 m/second (Rose 2006) and so the starting time for analysis is 0.02214 msec ( $= 0.149/6730$ ) and shortly following the time associated with the first panel in the figure ( $= 0.022$  msec). The initial pressure of the gas in the balloon is 2816 MPa, as noted previously. At  $t = 0.095$  msec, the head of the rarefaction wave has just reached the point of detonation. The shock front is clearly observed at  $t = 0.146$  msec, at which the tail of the rarefaction wave is near the front of the detonation products. The region between the shock front and the tail of the rarefaction wave is compressing, whereas the region behind the tail of the rarefaction wave is expanding. The pressures behind the tail of the rarefaction wave continuously decrease and become small enough to ignore at  $t = 0.500$  msec.

Time  
(msec)

### Pressure fringes

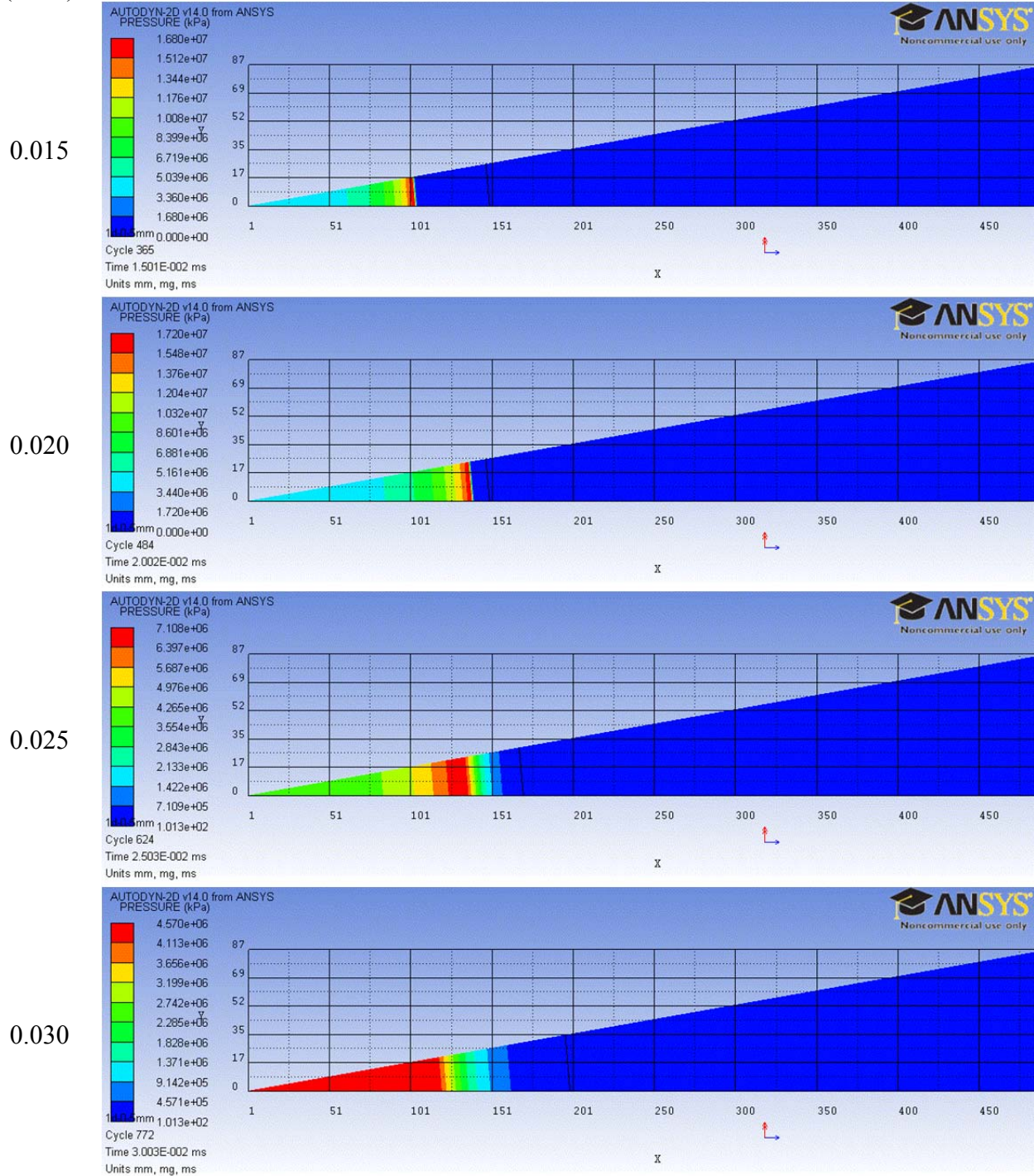


**Figure 2-56** Overpressure histories as a function of time after detonation at distance  $x (= r)$  from the center of a spherical charge of 22.68 kg of TNT for a 0.5 mm mesh; JWL EOS; no afterburning

Time  
(msec)

### Pressure fringes

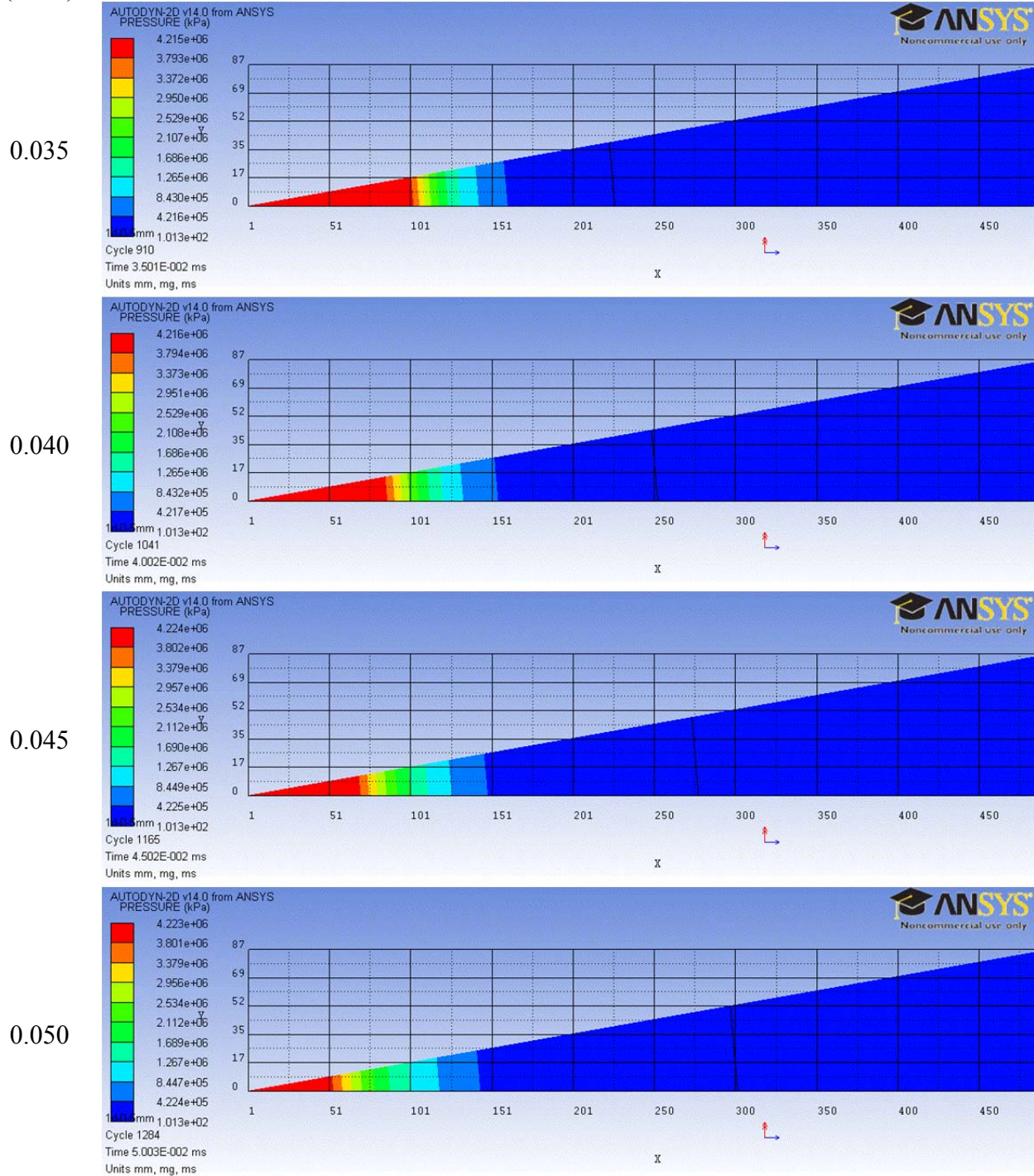


**Figure 2-56 Overpressure histories as a function of time after detonation at distance  $x (= r)$  from the center of a spherical charge of 22.68 kg of TNT for a 0.5 mm mesh; JWL EOS; no afterburning (cont.)**

Time  
(msec)

### Pressure fringes

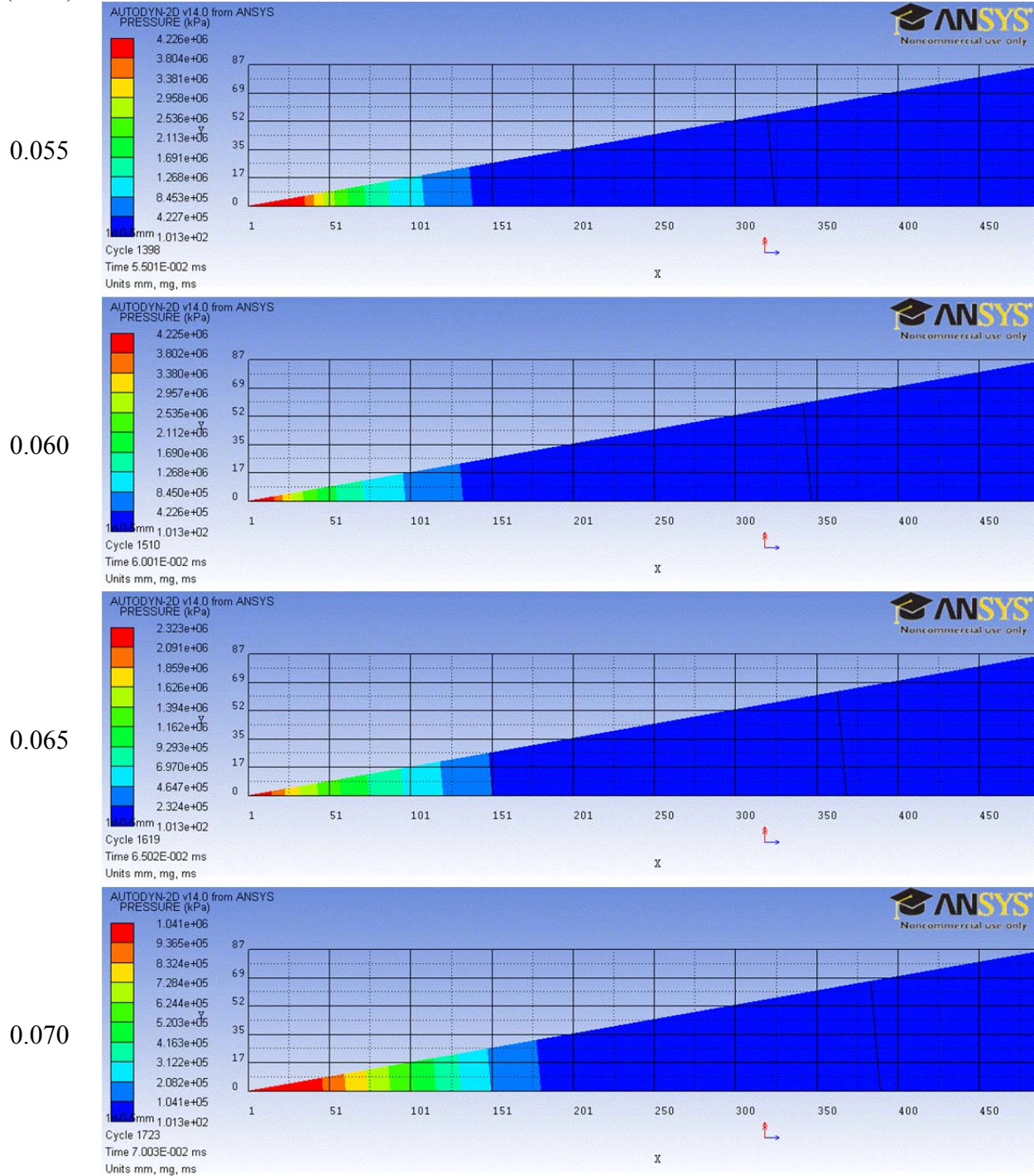


**Figure 2-56 Overpressure histories as a function of time after detonation at distance  $x (= r)$  from the center of a spherical charge of 22.68 kg of TNT for a 0.5 mm mesh; JWL EOS; no afterburning (cont.)**

Time  
(msec)

### Pressure fringes

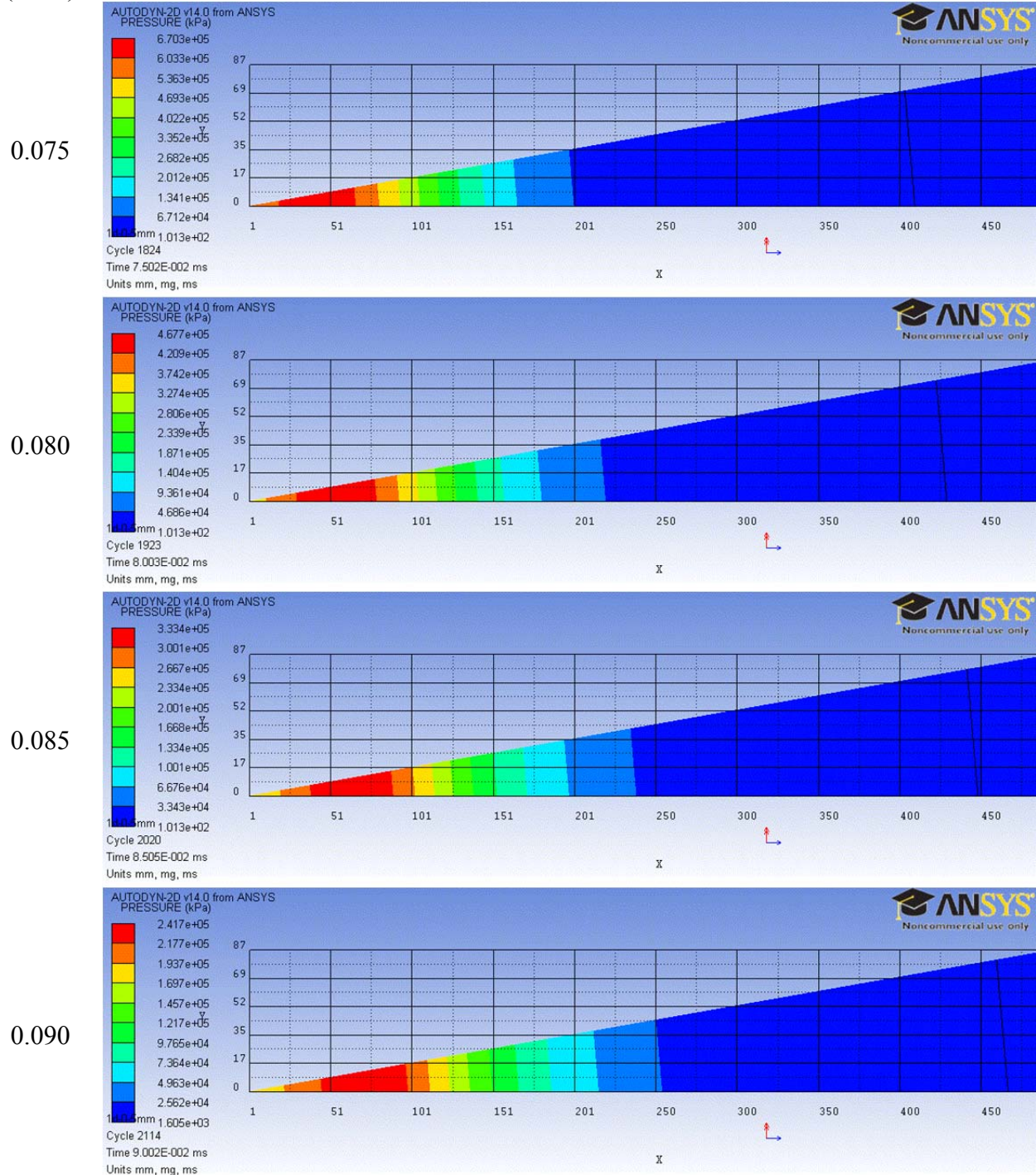


**Figure 2-56 Overpressure histories as a function of time after detonation at distance  $x (= r)$  from the center of a spherical charge of 22.68 kg of TNT for a 0.5 mm mesh; JWL EOS; no afterburning (cont.)**

Time  
(msec)

### Pressure fringes

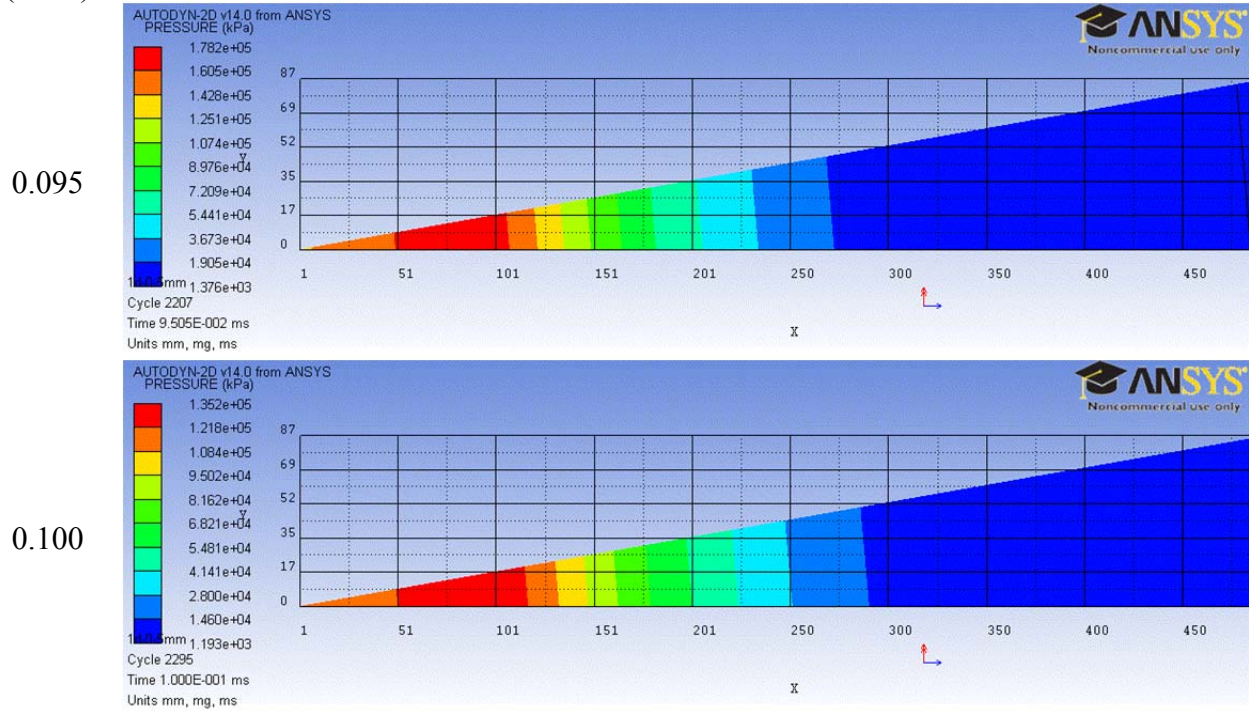
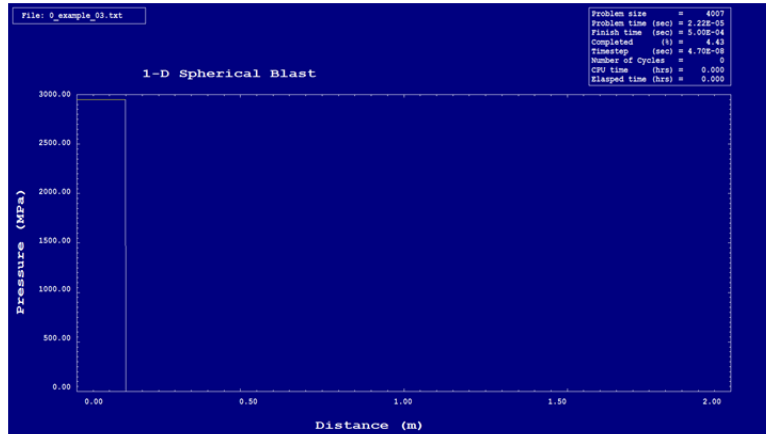


**Figure 2-56 Overpressure histories as a function of time after detonation at distance  $x (= r)$  from the center of a spherical charge of 22.68 kg of TNT for a 0.5 mm mesh; JWL EOS; no afterburning (cont.)**

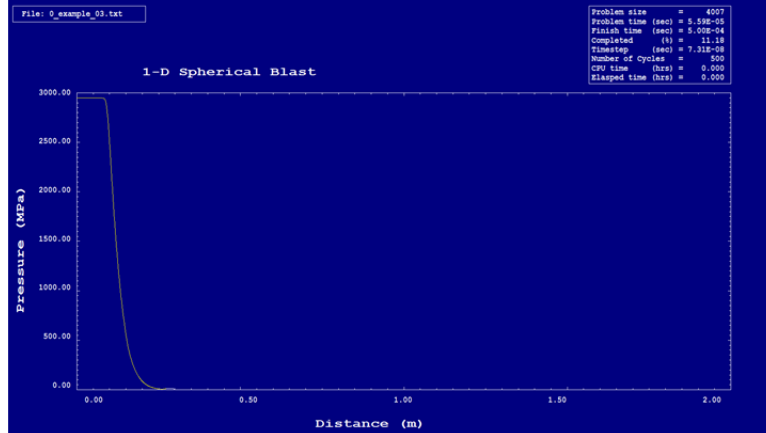
Time (msec)

Overpressure with distance

0.022



0.059



0.095

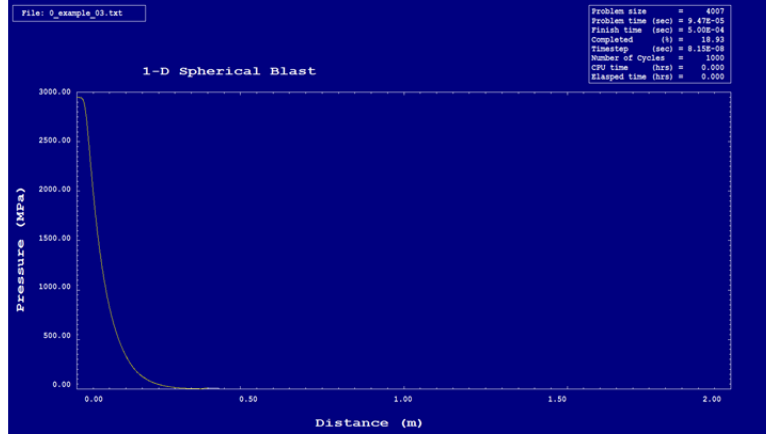
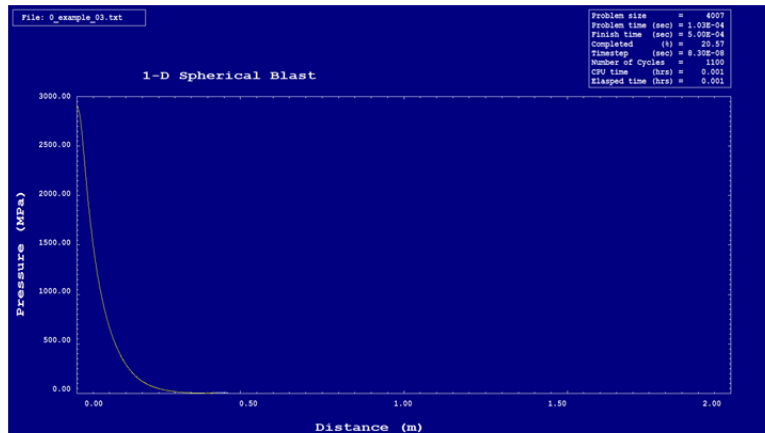


**Figure 2-57 Air3D overpressure histories as a function of distance and time after detonation for a spherical charge of 22.68 kg of TNT for a 0.5 mm mesh; ideal gas EOS**

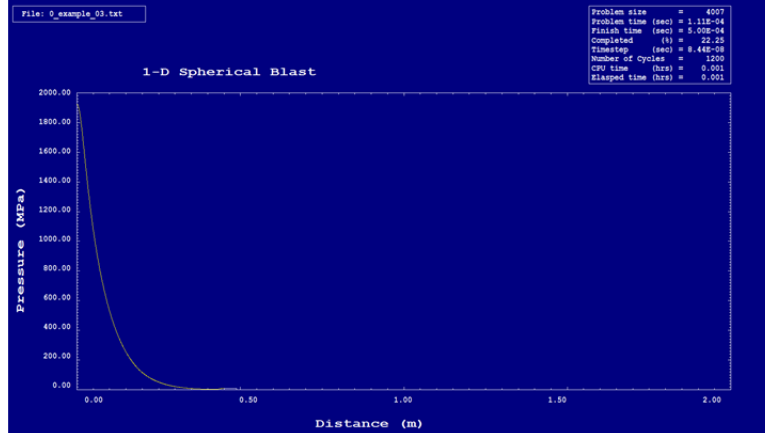
Time (msec)

Overpressure with distance

0.103



0.111



0.128

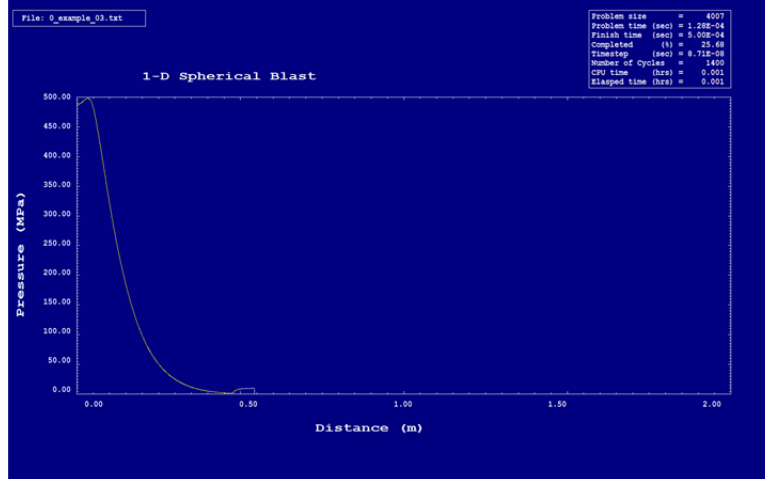
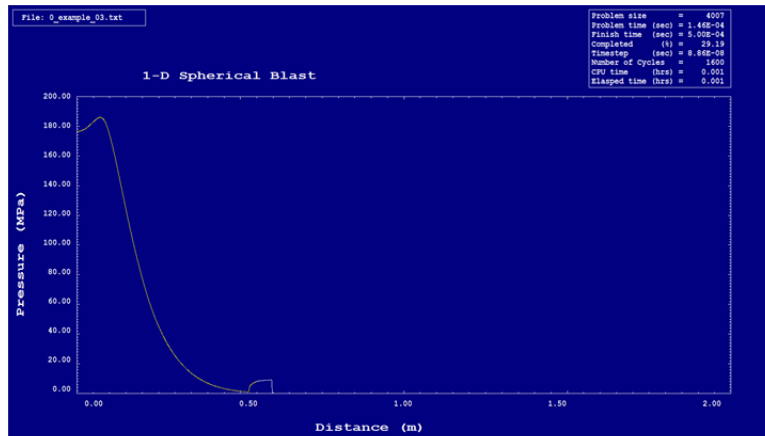


Figure 2-57 Air3D overpressure histories as a function of distance and time after detonation for a spherical charge of 22.68 kg of TNT for a 0.5 mm mesh; ideal gas EOS (cont.)

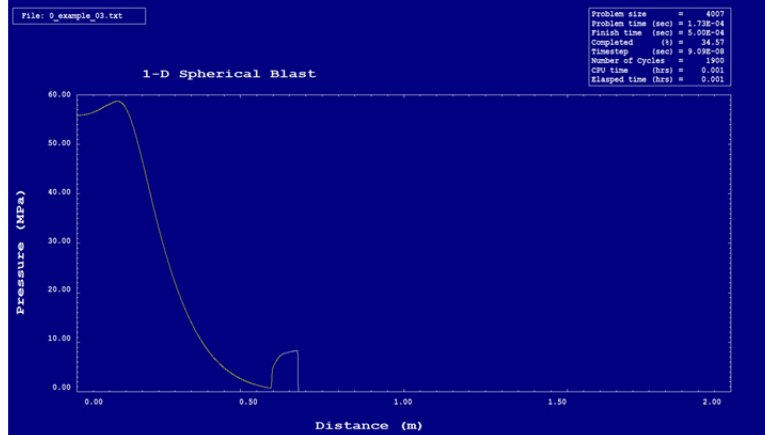
Time (msec)

Overpressure with distance

0.146



0.173



0.229

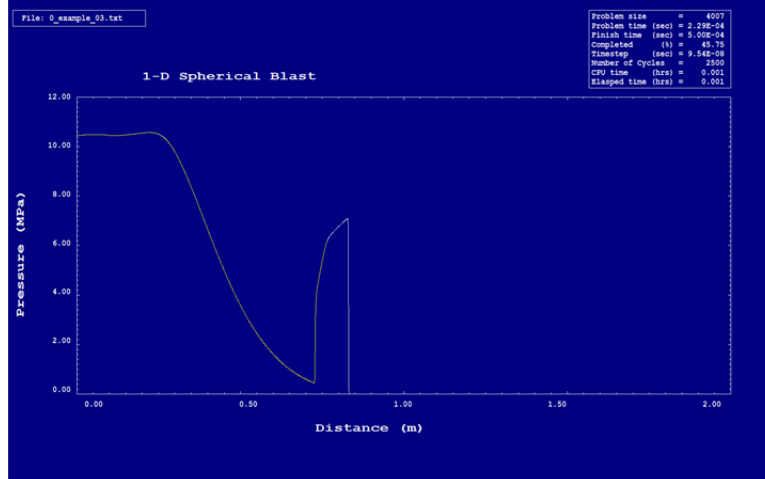
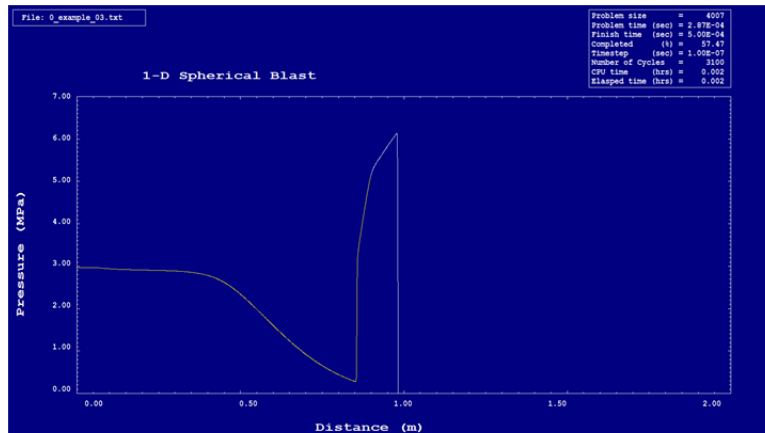


Figure 2-57 Air3D overpressure histories as a function of distance and time after detonation for a spherical charge of 22.68 kg of TNT for a 0.5 mm mesh; ideal gas EOS (cont.)

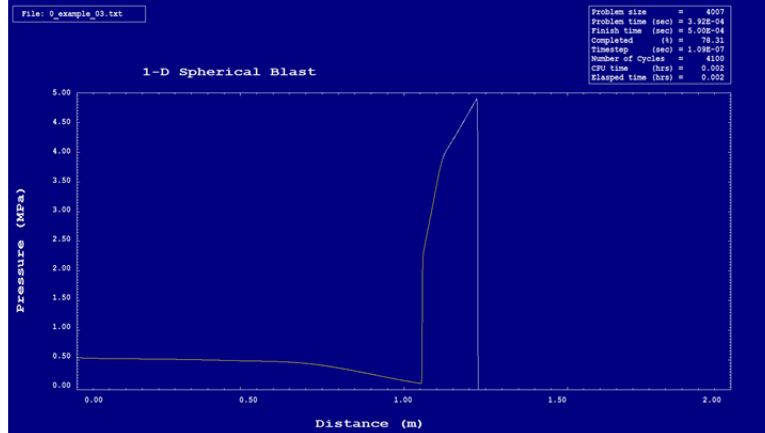
Time (msec)

Overpressure with distance

0.287



0.392



0.493

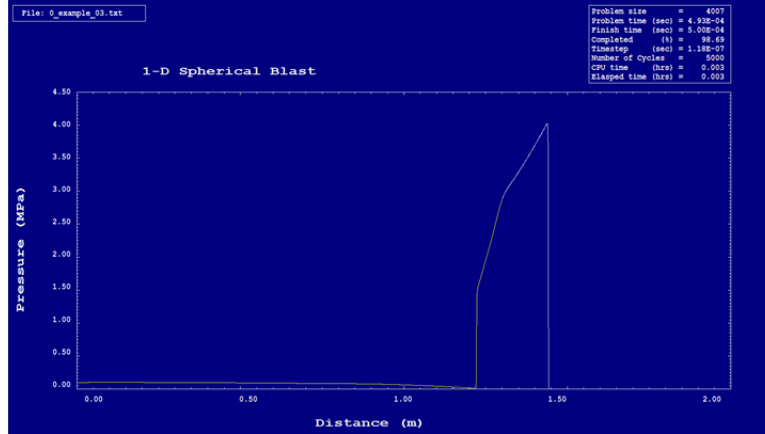
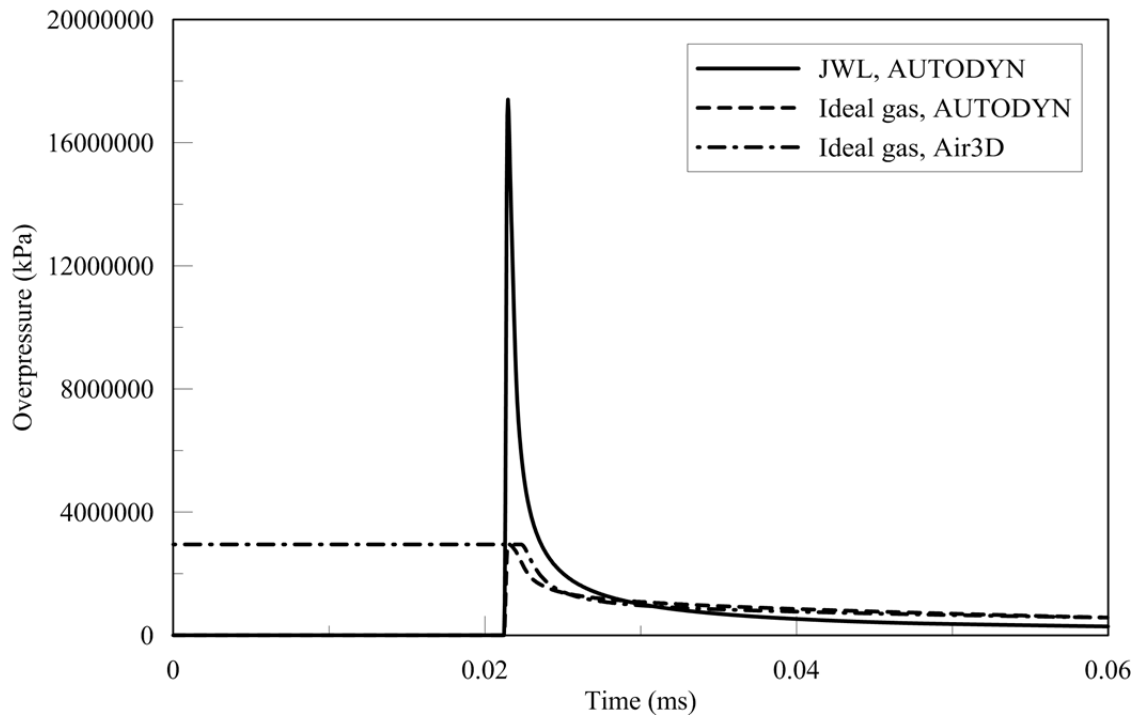


Figure 2-57 Air3D overpressure histories as a function of distance and time after detonation for a spherical charge of 22.68 kg of TNT for a 0.5 mm mesh; ideal gas EOS (cont.)

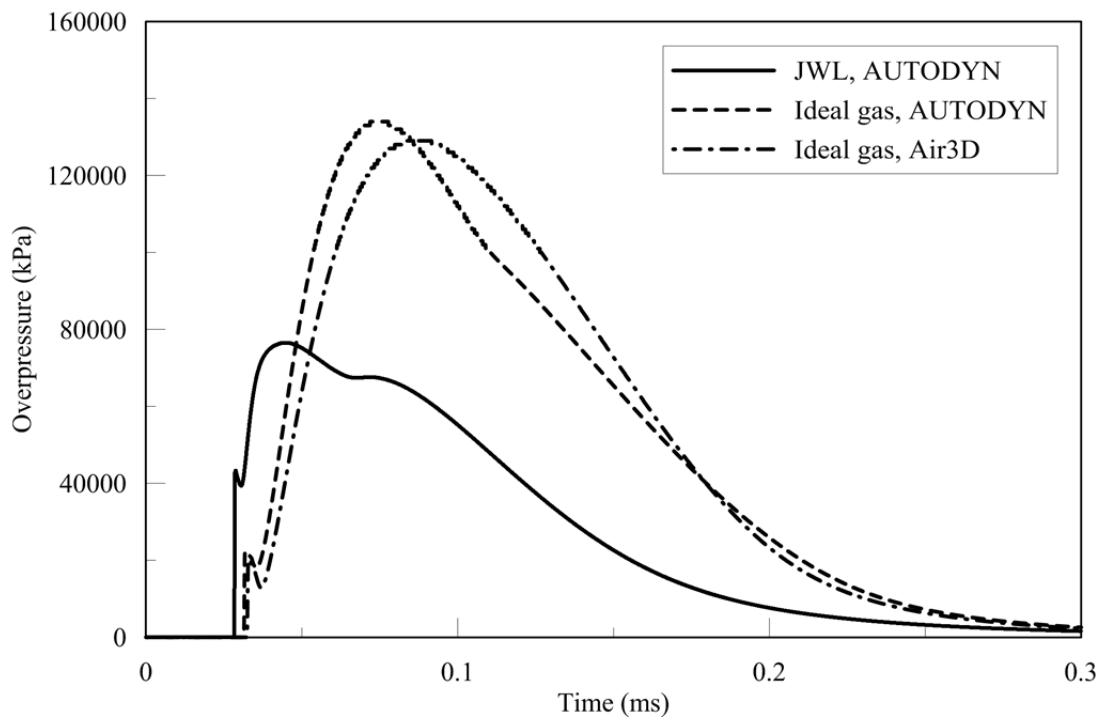
#### 2.4.6 Equations of State

To evaluate the ideal gas EOS in Air3D for modeling near-field detonations, the simulation results are compared with those using both the ideal gas EOS and the JWL EOS implemented in AUTODYN. Figure 2-58 presents the results of 1D analysis using a) AUTODYN, JWL EOS for the explosive and the ideal gas EOS for air, b) AUTODYN and the ideal gas EOS ( $\gamma = 1.4$ ) for both explosive and air, and c) Air3D and the ideal gas EOS ( $\gamma = 1.4$ ) for explosive and air. Results are presented for  $r = 148$  mm, 1 mm inside the face of the charge (panel a),  $r = 200$  mm (panel b),  $r = 250$  mm (panel c),  $r = 500$  mm (panel d), and  $r = 1000$  mm (panel e). Significant differences are observed for each value of  $r$  between the JWL EOS and the ideal gas EOS. At 1 mm inside the face of the charge, there are differences between all three models: the AUTODYN ideal gas EOS incident peak overpressure is dramatically smaller than that predicted using the JWL EOS, and the use of the Air3D balloon analog results in a higher incident overpressure at the face of the charge than AUTODYN using the ideal gas EOS. At  $r = 200$  mm (radial expansion of 1.34, volume expansion of 2.42), the AUTODYN and Air3D calculations using the ideal gas EOS provide similar predictions of peak pressure associated with the shock front (20 MPa) and the expanding detonation products (120 MPa). Both ideal gas computations underpredict the incident peak overpressure of the JWL EOS (40 MPa) and predict a greater value of peak overpressure associated with the expanding detonation products and a greater incident impulse. Note that the scale of overpressure in panel a is approximately two orders of magnitude higher than in panel b. An analysis of panel c ( $r = 250$  mm, radial expansion = 1.68, volume expansion = 4.72) leads to similar observations. At a distance of  $r = 500$  mm (351 mm from the face of the charge, radial expansion = 3.36, volume expansion = 37.8), the AUTODYN JWL computations predict a greater value of incident peak overpressure than the ideal gas computations. (The AUTODYN implementation of the JWL EOS collapses to an ideal gas EOS, default  $\gamma = 1.3$ , at a volume expansion = 10, radial expansion = 2.15.) The differences between the three overpressure histories and incident impulses at  $r = 1000$  mm (radial expansion = 6.71, scaled range =  $0.353 \text{ m/kg}^{1/3}$ ) are relatively small.

The ideal gas EOS should not be used for air-blast calculations at small values of scaled distance, say  $\bar{r} \leq 7$  based on the simulation results presented here.

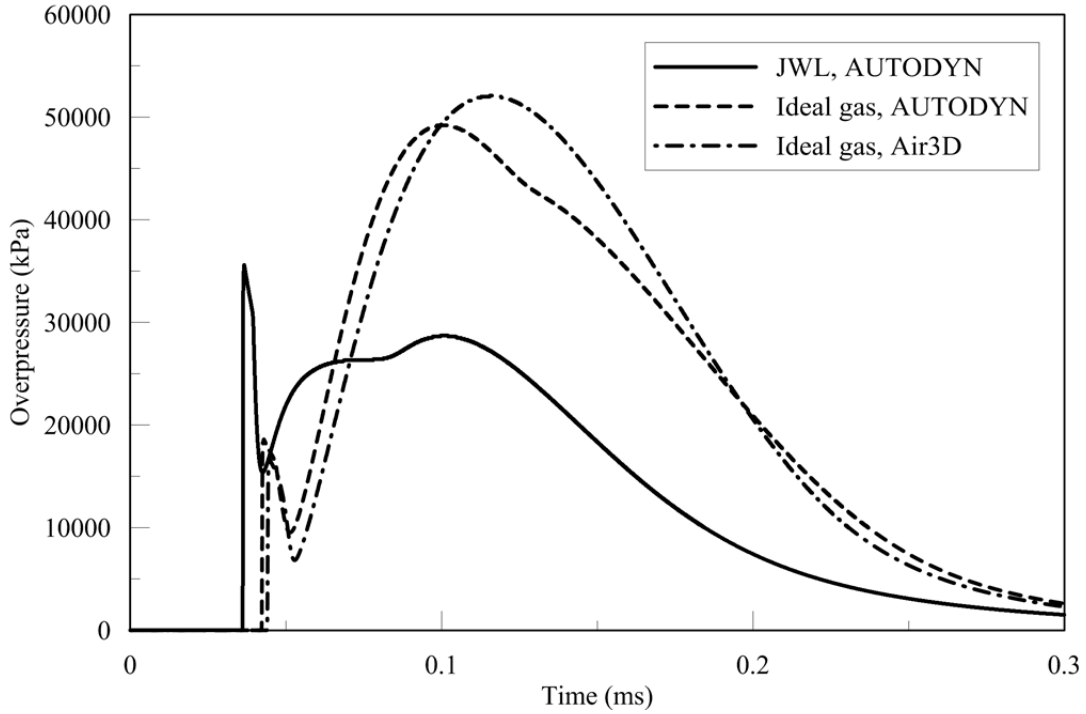


a.  $r = 0.148$  m (1 mm inside face of charge)

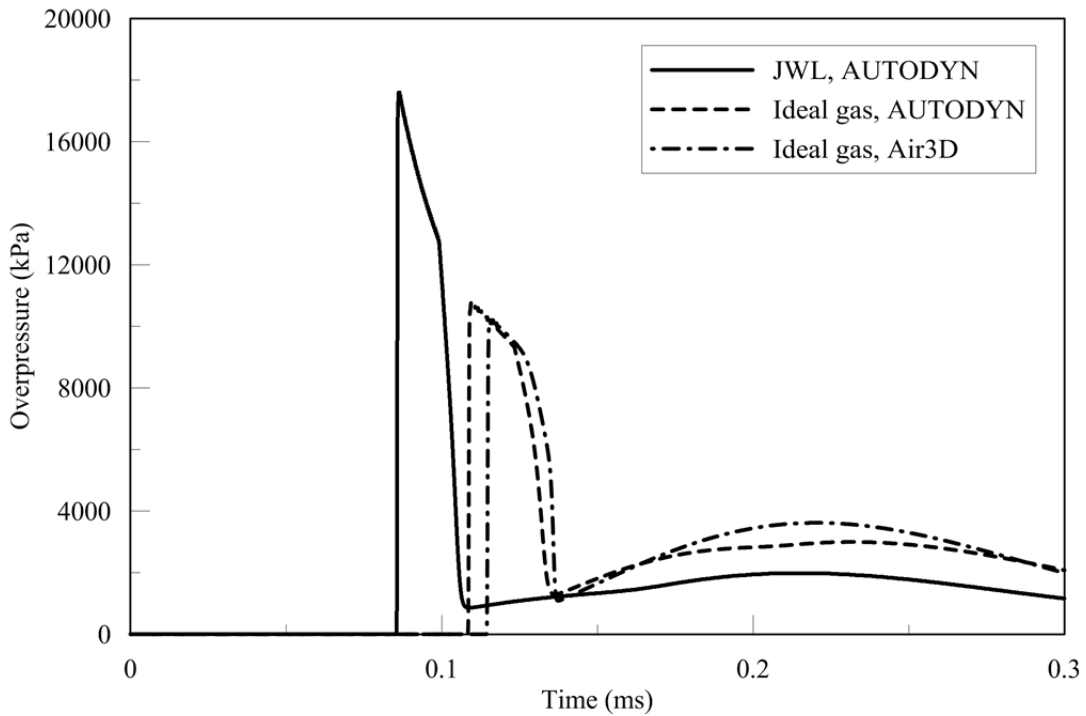


b.  $r = 0.200$  m (51 mm from face of charge)

**Figure 2-58 Influence of EOS on overpressure histories as a function of distance and time after detonation for a spherical charge of 22.68 kg of TNT for a 0.5 mm mesh**

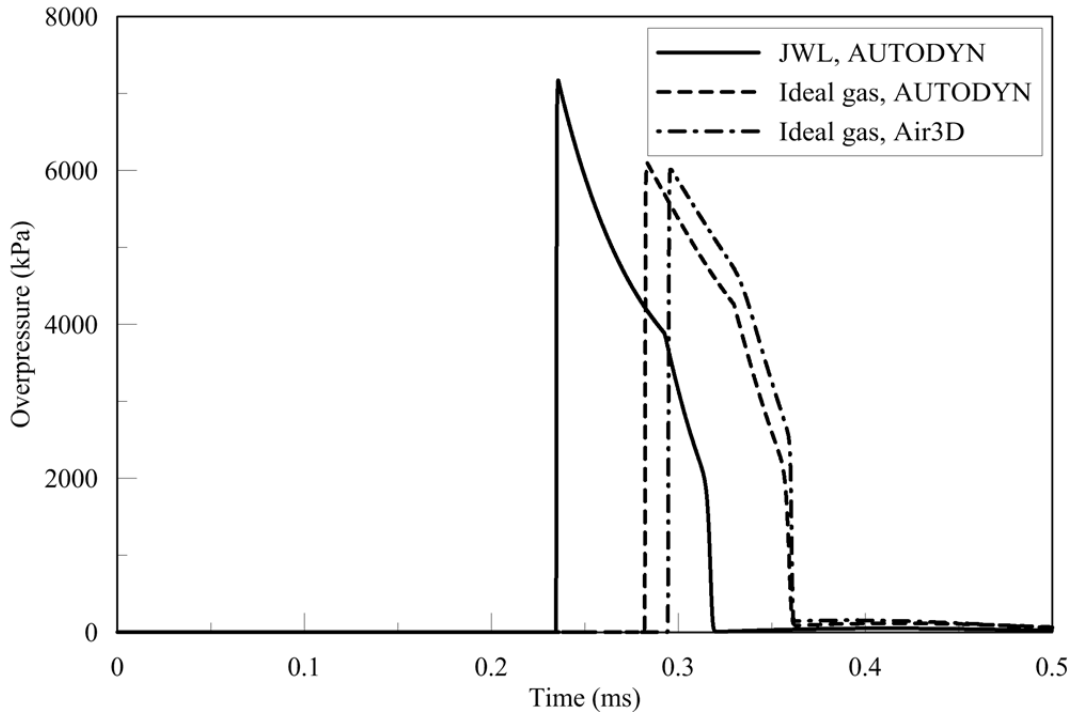


c.  $r = 0.250$  m (101 mm from face of charge)



d.  $r = 0.500$  m (351 mm from face of charge)

**Figure 2-58 Influence of EOS on overpressure histories as a function of distance and time after detonation for a spherical charge of 22.68 kg of TNT for a 0.5 mm mesh (cont.)**



e.  $r = 1.000$  m (851 mm from face of charge)

**Figure 2-58 Influence of EOS on overpressure histories as a function of distance and time after detonation for a spherical charge of 22.68 kg of TNT for a 0.5 mm mesh (cont.)**

## 2.5 Two-Dimensional Blast Wave Propagation

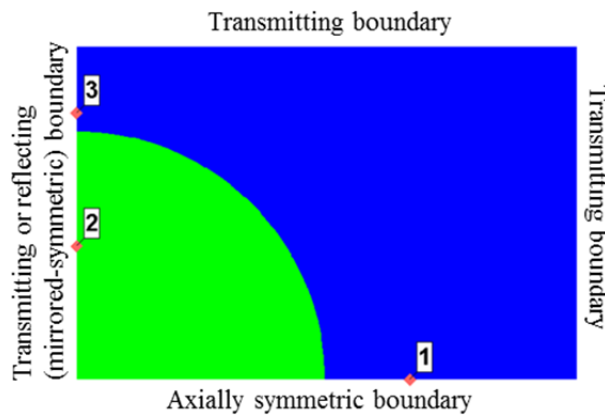
Two-dimensional blast wave propagation is simulated to predict reflected overpressures in the near field. The effects of boundary conditions, optimal cell sizes in 2D, consistency between 1D and 2D, and near-field effects on reflected overpressure histories are investigated.

Three 2D models are evaluated to examine the effect of boundary conditions on overpressure and impulse histories. The first two models include one quarter of the charge and a varied vertical boundary condition at the centerline of the (spherical) charge. The third model includes one half of the charge and places a transmitting (TR) vertical boundary away from the charge. Each model is described below.

Consider first the 2D Model I-I shown in Figure 2-59a. A quarter of the charge is modeled in a 2D domain with dimensions of 300×200 mm (horizontal × vertical). The spherical charge is 22.68 kg of TNT with a packing density of 1630 kg/m<sup>3</sup> and a charge radius of 149 mm. The left

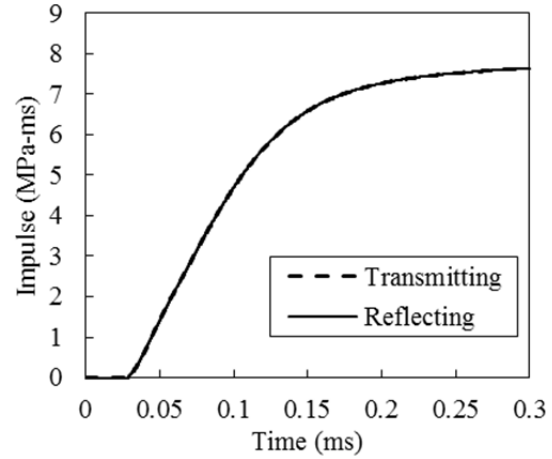
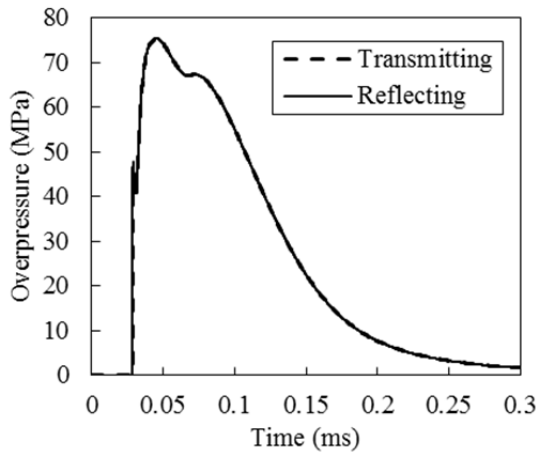
vertical boundary condition in this model is set as transmitting. The other two models investigate the use of alternate left vertical boundary conditions.

Figure 2-59 examines the effect of the left vertical boundary in Model I-I on incident overpressure and impulse histories. Energy should not escape across a left transmitting boundary because the pressure wave initially propagates radially from the source and away from this boundary. The left vertical TR boundary is replaced by a (mirrored-symmetric) reflecting (RE) boundary. Incident overpressure histories are calculated at monitoring points 1, 2 and 3 (see Figure 2-59a) using both left TR and RE boundaries. The coordinates of monitoring points 1, 2 and 3 are at  $(x, y) = (200, 0)$ ,  $(0, 80)$  and  $(0, 160)$ , respectively. A cell size of 0.5 mm is used for the analysis because the 1D analysis results converged at a distance of 200 mm for the 0.5 mm cell size (see Figure 2-41c). Overpressure and impulse histories are presented in Figures 2-59b, 2-59c and 2-59d at the three monitoring points. The histories are identical at each monitoring point. The differences are less than 1%.

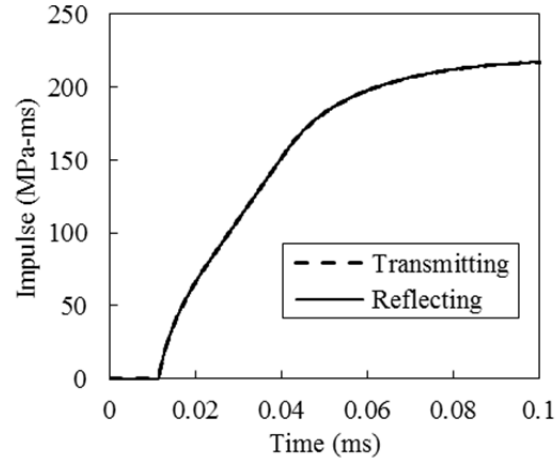
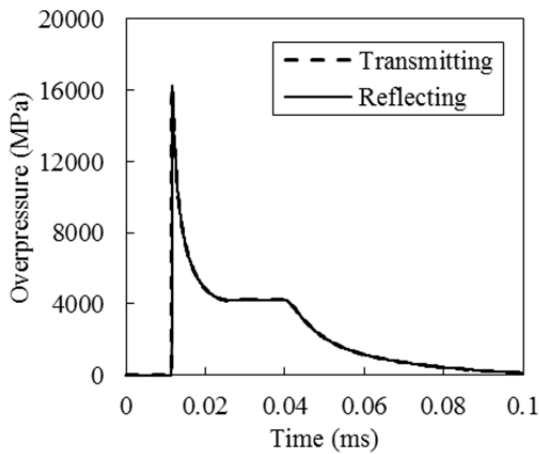


a. Model I-I

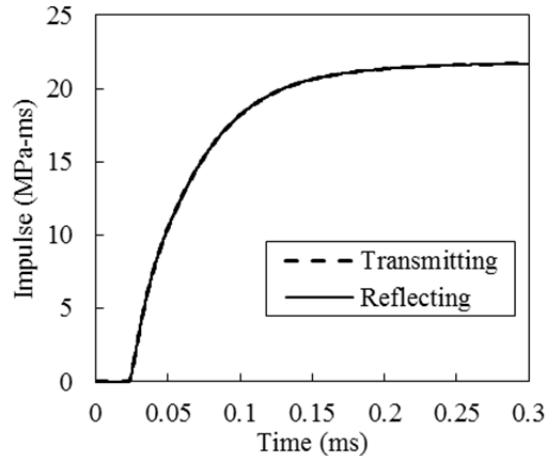
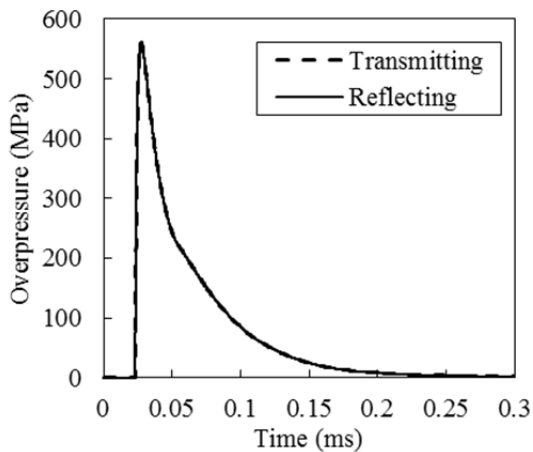
**Figure 2-59 Effect of boundary condition; spherical charge of TNT of 22.68 kg; 0.5 mm cells; Model I-I**



b. Overpressure and impulse histories at monitoring location 1



c. Overpressure and impulse histories at monitoring location 2



d. Overpressure and impulse histories at monitoring location 3

**Figure 2-59 Effect of boundary condition; spherical charge of TNT of 22.68 kg; 0.5 mm cells; Model I-I (cont.)**

Figure 2-60 enables a comparison of results of 1D (radial) and 2D analysis for the 2D Model I-I with the left transmitting boundary. Results of the two analyses are presented for a 0.5 mm mesh at monitoring location 1. The overpressure histories are identical, which is not surprising given the use of radial (axial) symmetry in both cases.

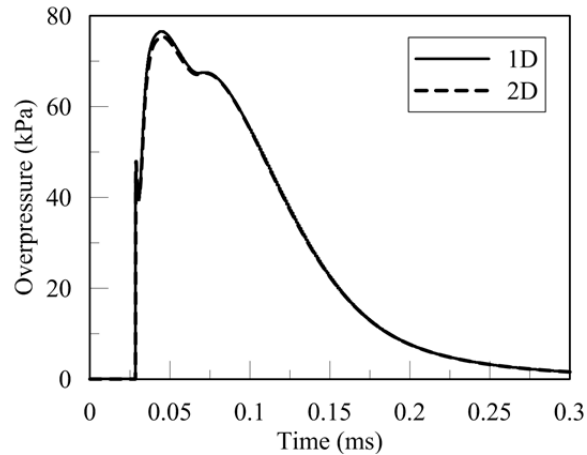


**Figure 2-60 AUTODYN analysis results for 1D and 2D (I-I with the left transmitting boundary) models; spherical charge of 22.68 kg of TNT; 0.5 mm mesh; monitoring location 1;**

Another 2D model, I-II, is presented in Figure 2-61a. One half of the spherical charge is modeled using a lower axially symmetric boundary. The left transmitting boundary of Model I-I is moved to the left at distance of two charge radii. The monitoring locations are same as those used in Model I-I. One might argue that this model is better than Model I-I with a left vertical transmitting boundary but it is computationally more expensive. Figures 2-61b, 2-61c and 2-61d enable a comparison of overpressure and impulse histories calculated using 1) Model I-I with a left vertical transmitting boundary, and 2) Model I-II, at monitoring locations, 1, 2 and 3, respectively. The histories are identical for all three monitoring locations.

Models I-III and I-IV, as shown in Figures 2-62a and 2-62b, respectively, are constructed from Models I-I and I-II, respectively, to study the effect of choice of boundary condition on reflected overpressure histories. The right vertical transmitting boundaries of Figures 2-59a and 2-61a are replaced by reflecting boundaries. Overpressure and impulse histories are calculated at five monitoring locations, where monitoring locations 1, 2 and 3 were identified previously and

monitoring locations 4, 5 and 6 are on the right reflecting boundary, 0, 80 and 160 mm, respectively, from the lower horizontal boundary.

Figures 2-62c through 2-62n enable a comparison of the overpressure and impulse histories calculated using models I-III and I-IV. In the legends, TR and RE identify the left transmitting and reflecting boundaries, respectively, for model I-III. The overpressure histories are plotted at two ranges on the y (overpressure) axis, full and part, where the part-range plots enable analysis of small differences in the histories. Analysis using Model I-III TR and Model I-IV produce identical results. The effects of multiple reflections from the model with two vertical reflecting boundaries (Model I-III RE) are clearly seen in the impulse histories at monitoring locations 1, 3, 4, 5 and 6.

In summary, analysis of a model that incorporates a left vertical transmitting boundary at the centerline of the charge produces identical overpressures and impulses to analysis of a model of one-half of the charge with a left transmitting boundary placed two charge radii from the center of the weapon. Hereafter, computationally more efficient models involving a vertical transmitting boundary at the center of the charges are analyzed.

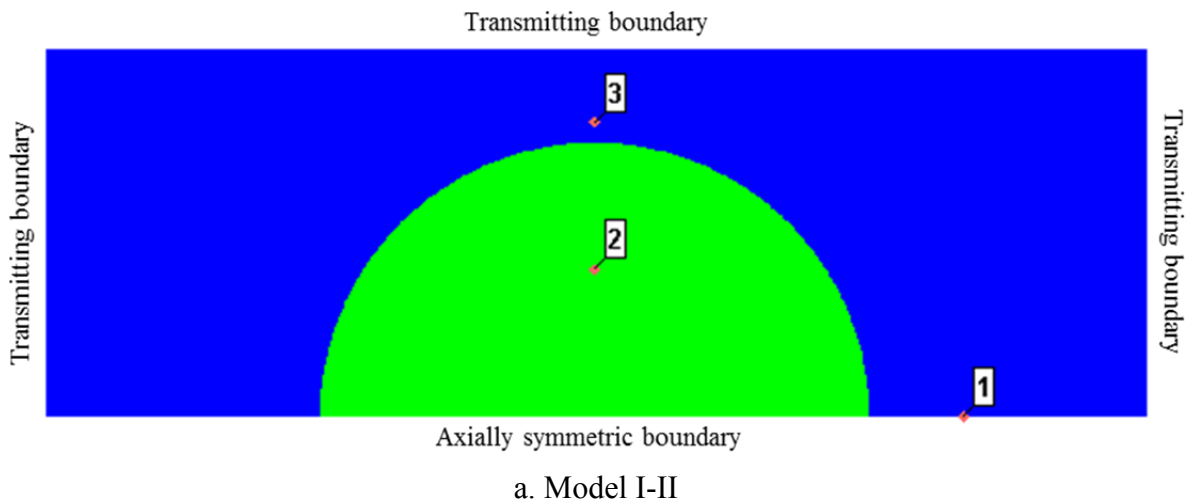
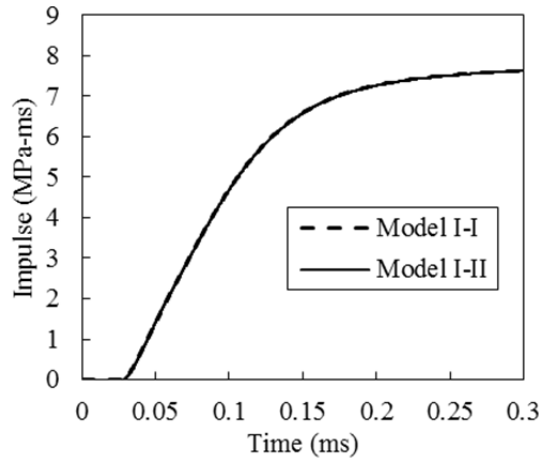
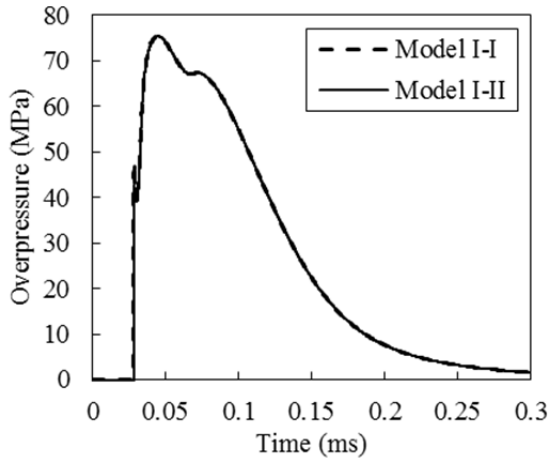
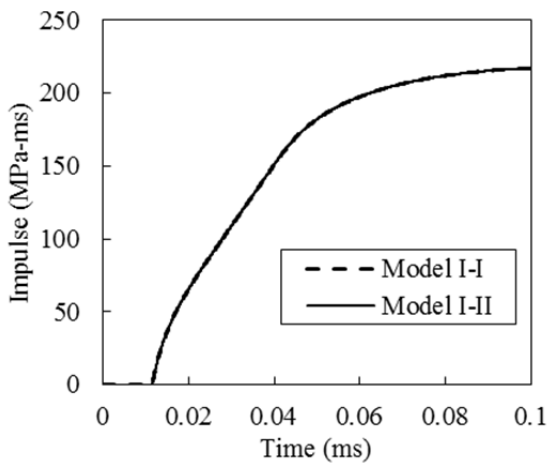
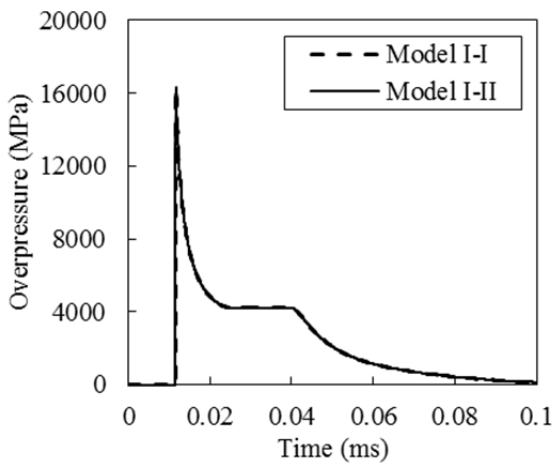


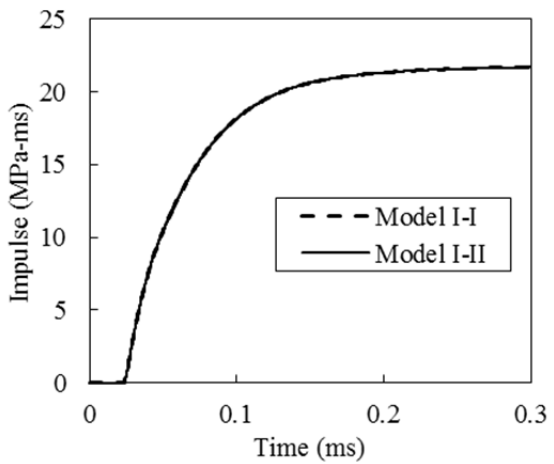
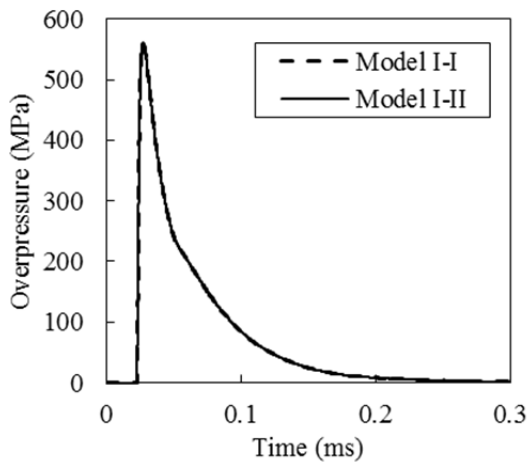
**Figure 2-61 Effect of boundary condition; spherical charge of TNT of 22.68 kg; 0.5 mm cells; Model I-II**



b. Overpressure and impulse histories at monitoring location 1

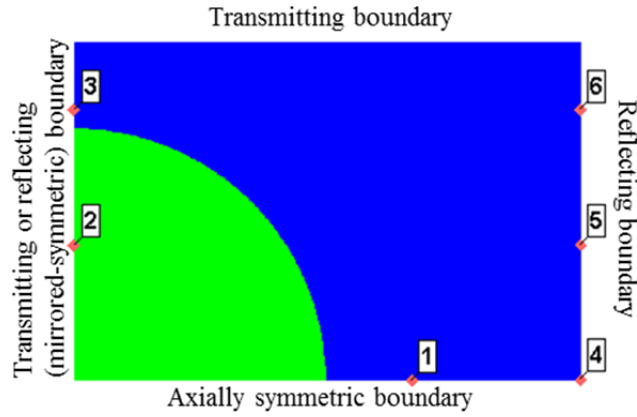


c. Overpressure and impulse histories at monitoring location 2

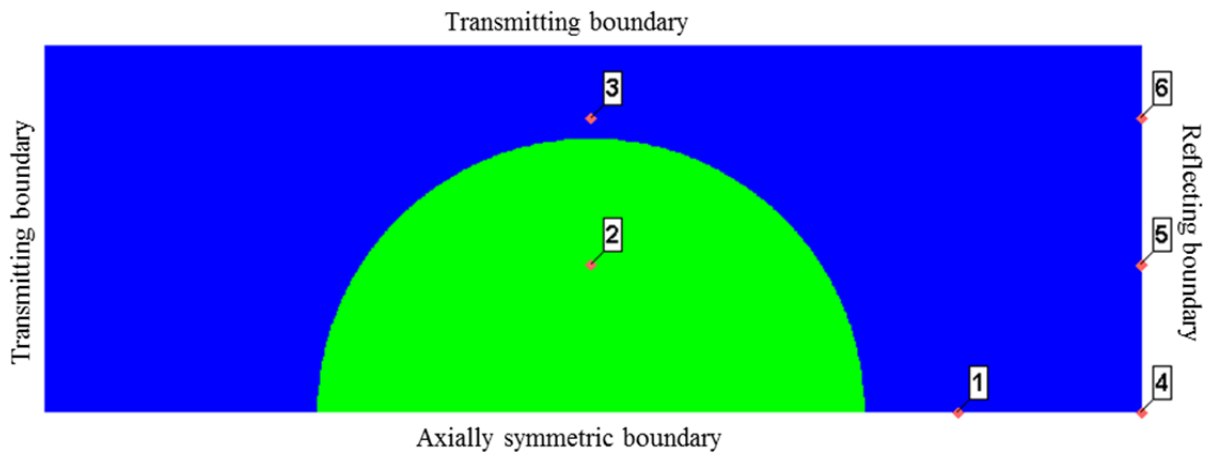


d. Overpressure and impulse histories at monitoring location 3

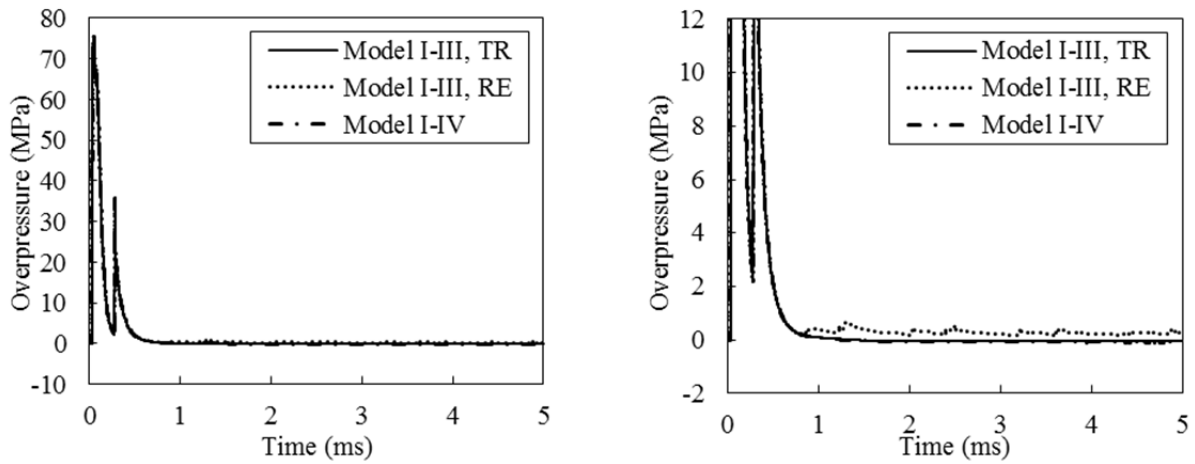
**Figure 2-61 Effect of boundary condition; spherical charge of TNT of 22.68 kg; 0.5 mm cells; Model I-II (cont.)**



a. Model I-III

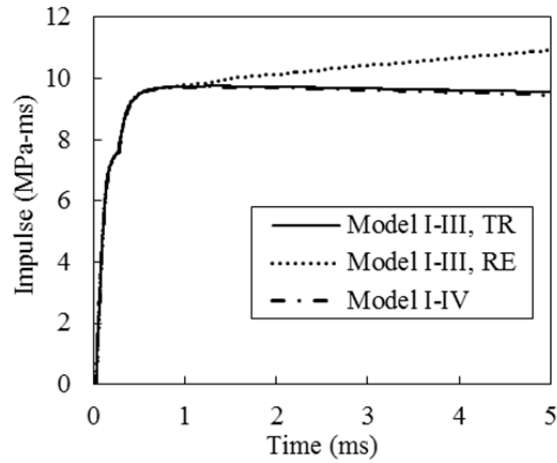


b. Model I-IV

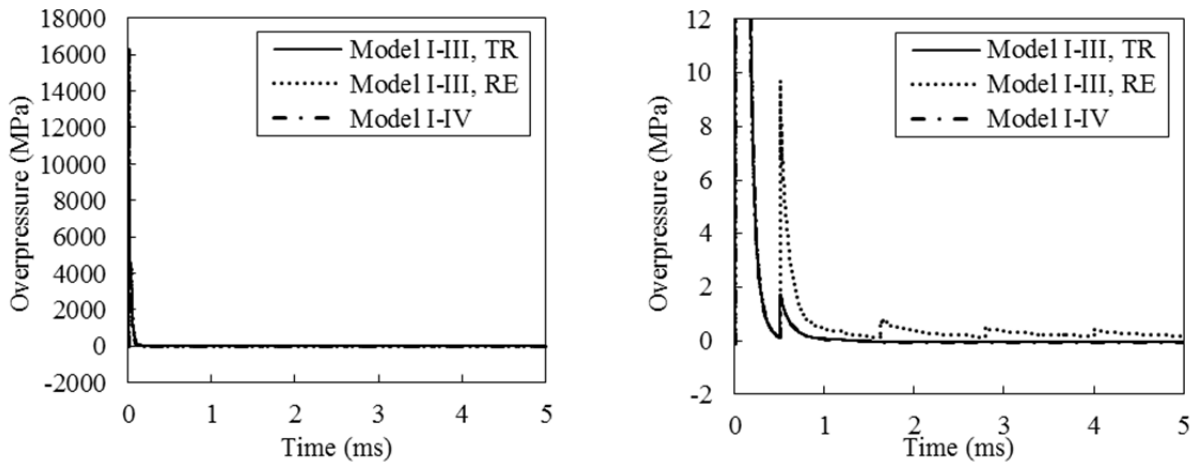


c. Overpressure histories in full (left) and part (right) ranges at monitoring location 1

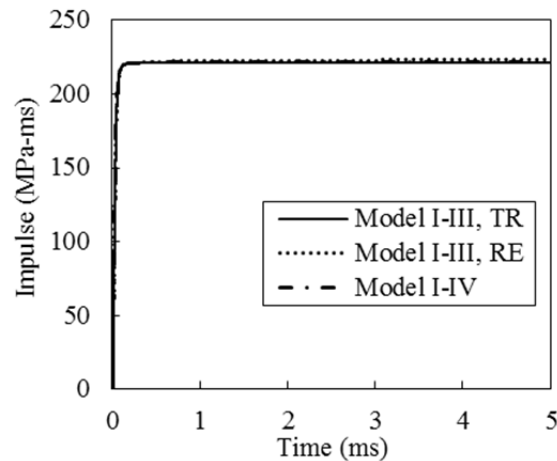
**Figure 2-62 Effect of boundary condition; spherical charge of TNT of 22.68 kg; 0.5 mm cells; Model I-III and Model I-IV**



d. Impulse history at monitoring location 1

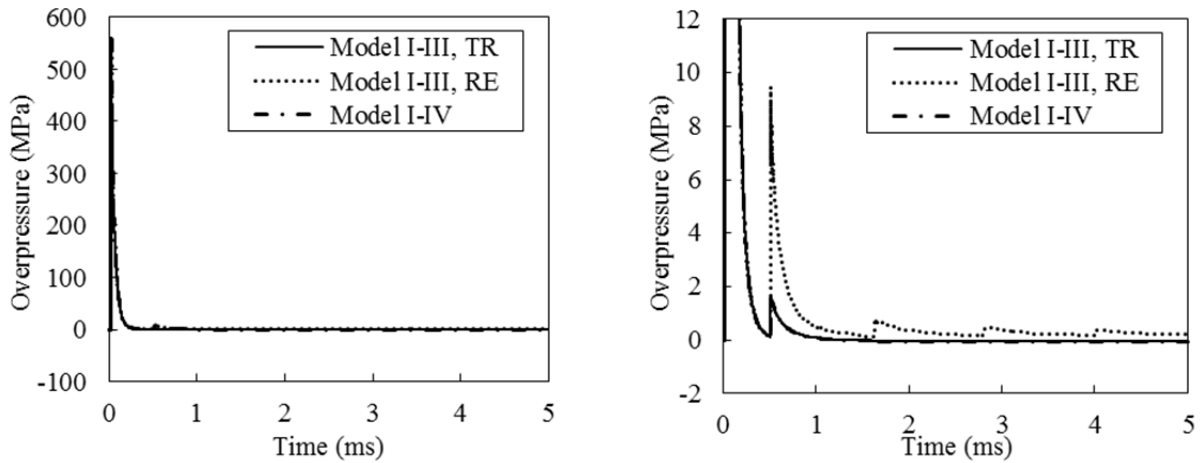


e. Overpressure histories in full (left) and part (right) ranges at monitoring location 2

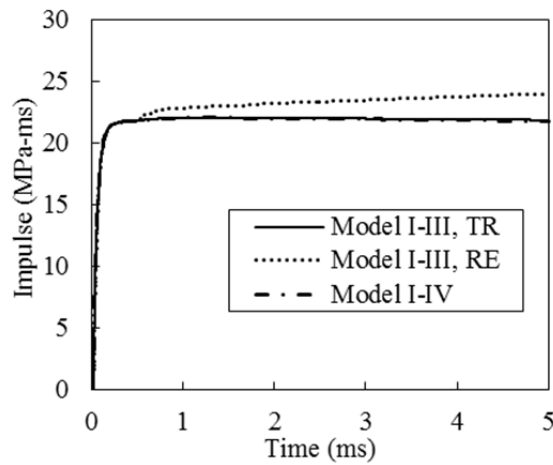


f. Impulse history at monitoring location 2

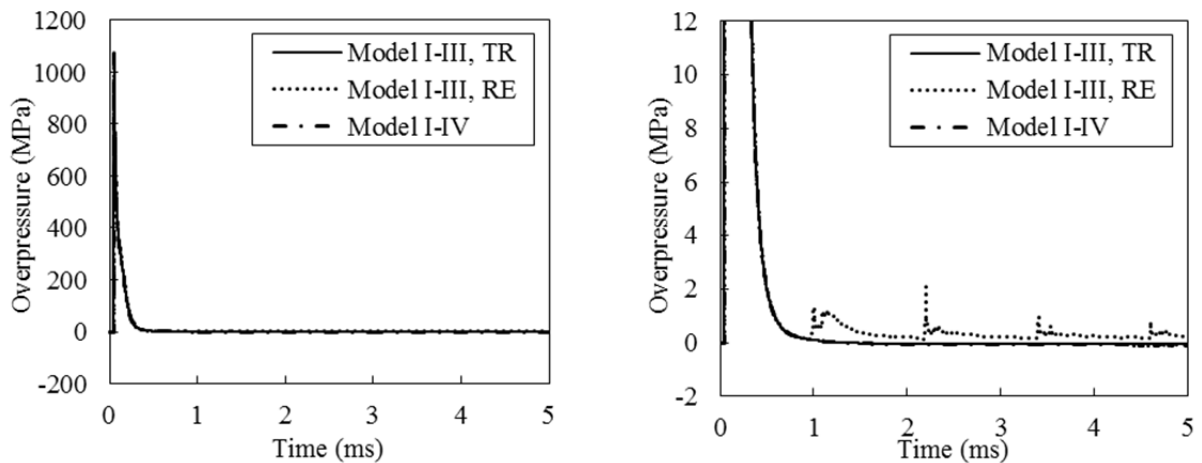
**Figure 2-62 Effect of boundary condition; spherical charge of TNT of 22.68 kg; 0.5 mm cells; Model I-III and Model I-IV (cont.)**



g. Overpressure histories in full (left) and part (right) ranges at monitoring location 3

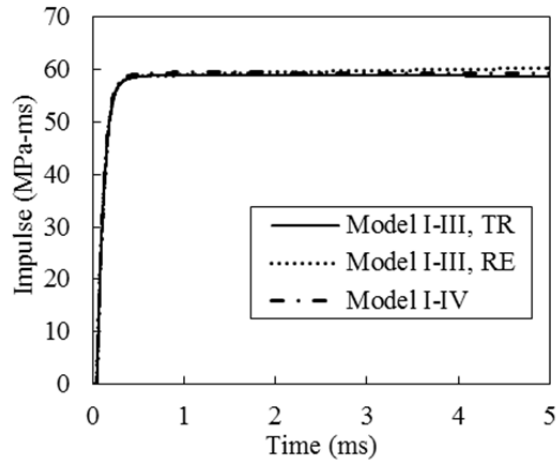


h. Impulse history at monitoring location 3

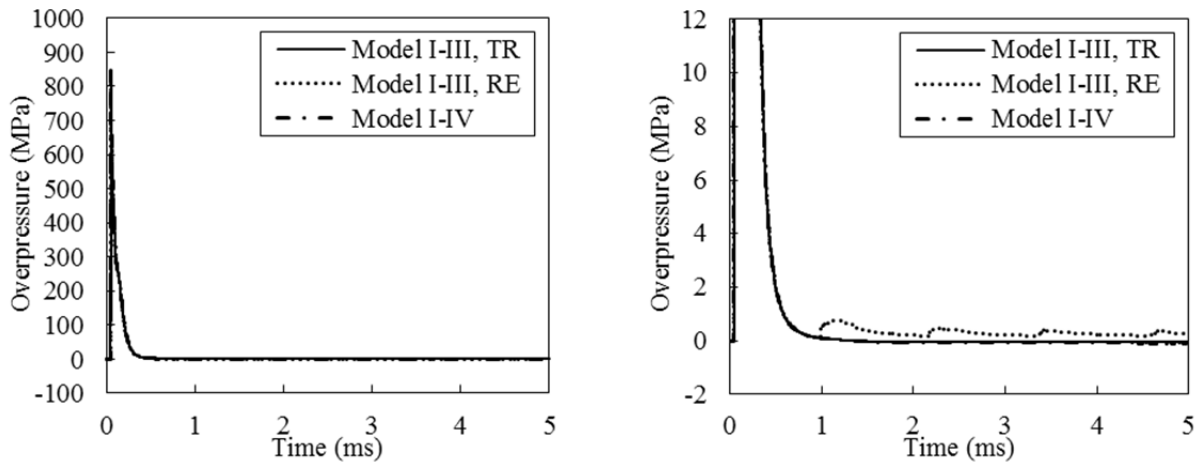


i. Overpressure histories in full (left) and part (right) ranges at monitoring location 4

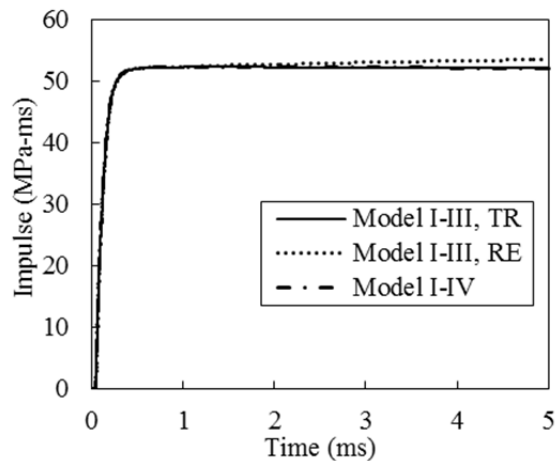
**Figure 2-62 Effect of boundary condition; spherical charge of TNT of 22.68 kg; 0.5 mm cells; Model I-III and Model I-IV (cont.)**



j. Impulse history at monitoring location 4

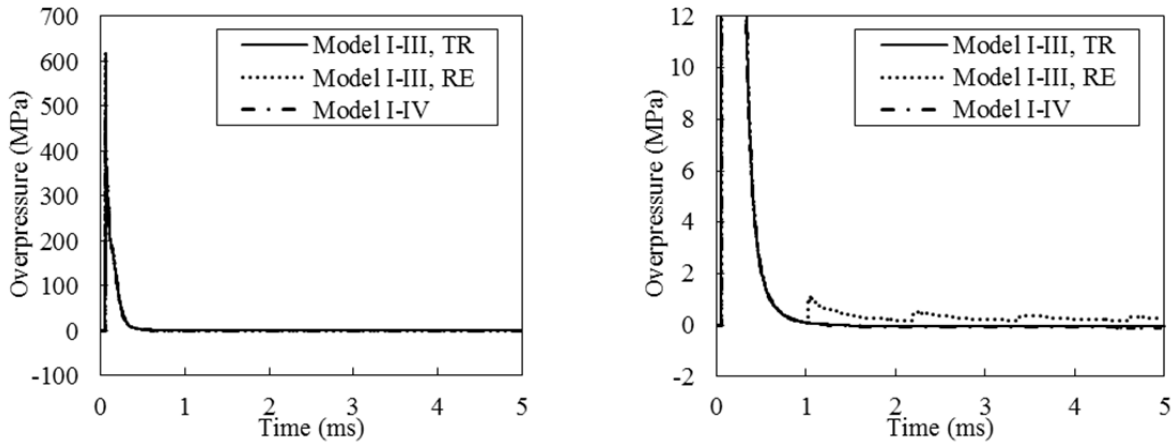


k. Overpressure histories in full (left) and part (right) ranges at monitoring location 5

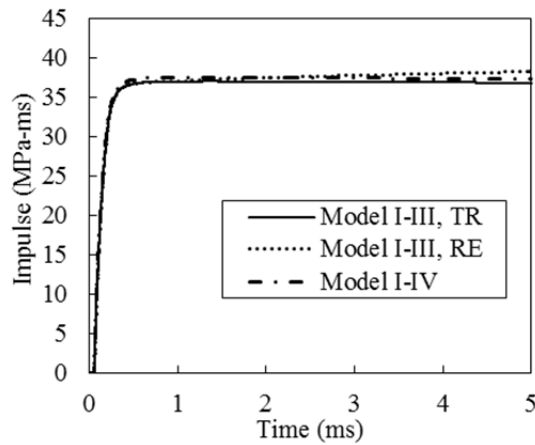


l. Impulse history at monitoring location 5

**Figure 2-62 Effect of boundary condition; spherical charge of TNT of 22.68 kg; 0.5 mm cells; Model I-III and Model I-IV (cont.)**



m. Overpressure histories in full (left) and part (right) ranges at monitoring location 6

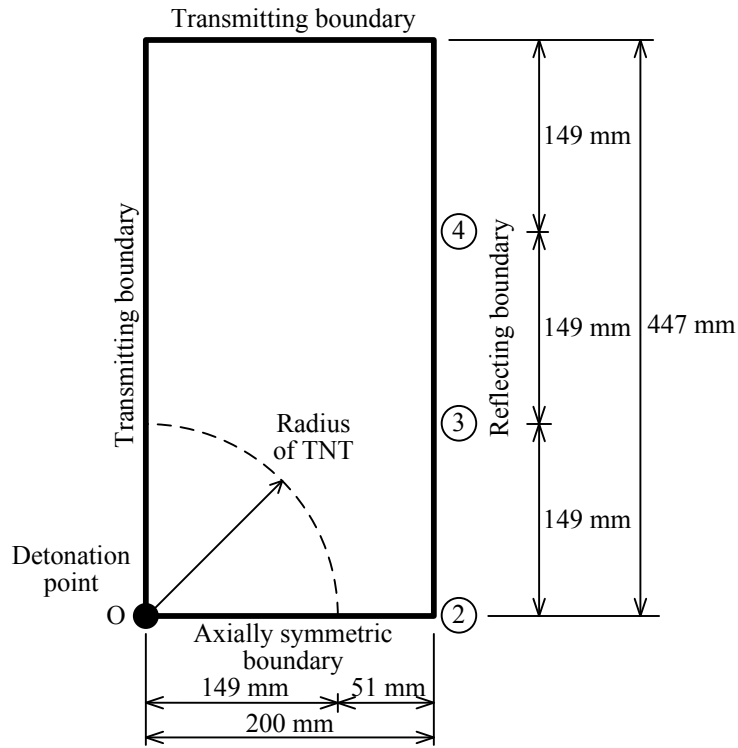


n. Impulse history at monitoring location 6

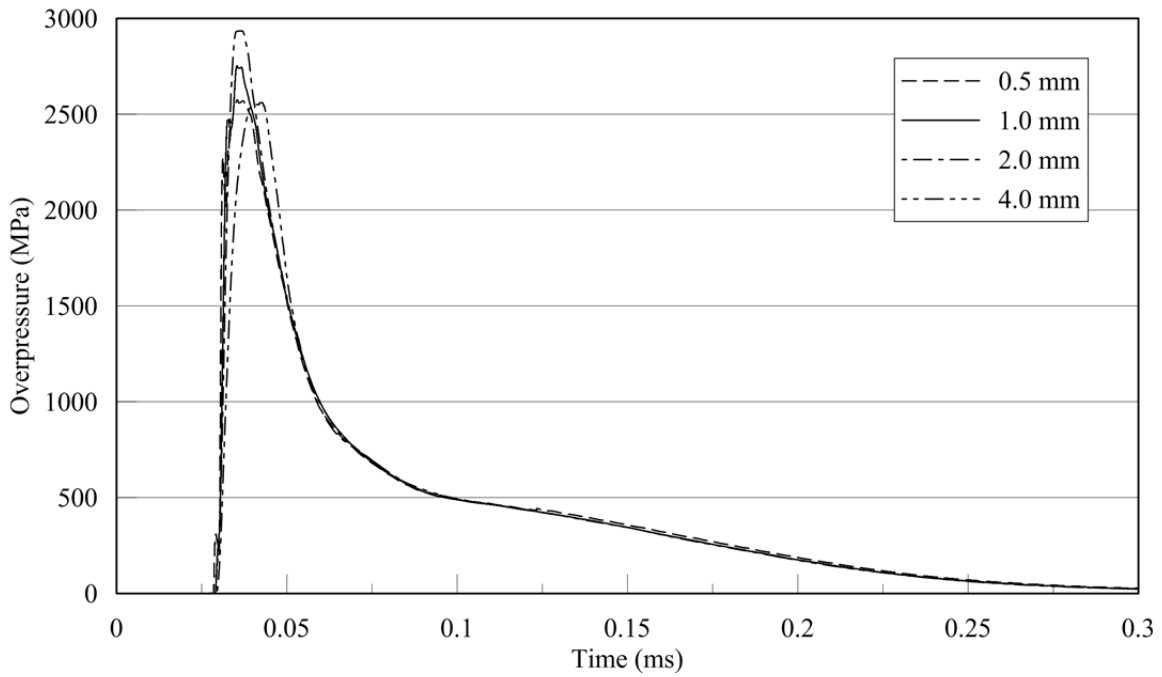
**Figure 2-62 Effect of boundary condition; spherical charge of TNT of 22.68 kg; 0.5 mm cells; Model I-III and Model I-IV (cont.)**

Figure 2-63 presents the results of 2D AUTODYN analysis with Model II, as shown in panel a. The radius of the charge is 149 mm. For this 2D analysis, 1D results using a cell size of 0.5 mm, chosen for the same reason described previously, are remapped into 2D. Cell sizes of 4, 2, 1 and 0.5 mm are used in the 2D analyses. The TNT packing density is  $1636.8 \text{ kg/m}^3$ , resulting in a charge weight of 22.68 kg (50.00 lb). The JWL EOS is used for analysis. Afterburning is ignored because the afterburning energy is less than 5% of the detonation energy due to the availability of oxygen. Figure 2-63a presents the AUTODYN model, the remaining boundary conditions and the locations of monitoring locations 2, 3 and 4 on the right hand boundary. The other panels in the figure present reflected overpressure histories at monitoring locations 2, 3 and 4. Monitoring locations 2, 3 and 4 are associated with angles of incidence of  $0^\circ$ ,  $36.7^\circ$  and  $56.1^\circ$ , respectively,

and  $Z = 0.071, 0.088$  and  $0.13 \text{ m/kg}^{1/3}$ . The results presented at monitoring locations 2, 3 and 4 are essentially identical for all four cell sizes; the effect of cell size on the results is insignificant. The jagged nature of the overpressure history at monitoring location 4, which may be counterintuitive, is studied using the pressure fringes presented in Figure 2-64. Two ranges of pressure are provided: full range (capturing the entire range of pressure) and fixed range (intended to capture the propagation of the shock front and the expanding detonation products). It is evident that the pressure histories at the monitoring locations are complex, which is due primarily to the expanding detonation products. At 0.029 msec, the shock front impinges on the vertical reflecting surface; the initial reflection of the shock front is captured in the panels at 0.030 msec, noting that the reflected pressure at monitoring location 2 increases to a maximum value of 2500 MPa at a later time. The presence of the expanding detonation products is observed immediately behind the shock front, as shown in the fixed range (second column) of Figure 2-64, but the distance between the front of the expanding detonation products and the shock front is so small that the arrival of the expanding detonation products cannot be identified in the overpressure histories at monitoring location 2 (see Figure 2-63b) at the scale presented. At 0.037 msec, the shock front impinges on the reflecting surface at monitoring location 3. The arrival of the expanding detonation products is not seen in the overpressure histories at monitoring location 3 (see Figure 2-63c) but it is observed behind the shock front in the fixed range of Figure 2-64. At 0.054 msec (fourth row of Figure 2-64), the incident shock wave has reached monitoring location 4 and the Mach stem has formed (between monitoring locations 2 and 3). At monitoring location 4, the arrivals of the shock front and of the front of the expanding detonation products can be distinguished in the overpressure histories of Figure 2-63d at approximately  $t = 0.5 \text{ ms}$  and  $0.7 \text{ ms}$ , respectively. The pressure fringes immediately behind the Mach stem are complex and irregular and provide an explanation for the jagged nature of the pressure history seen in Figure 2-63d.

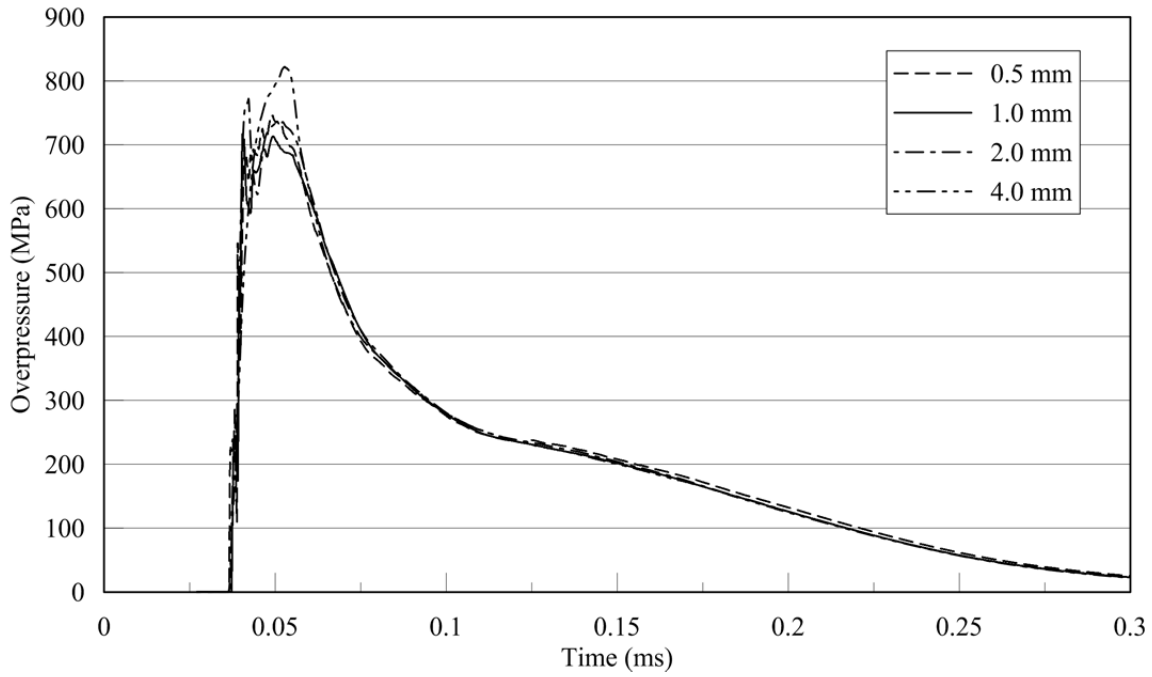


a. Model II

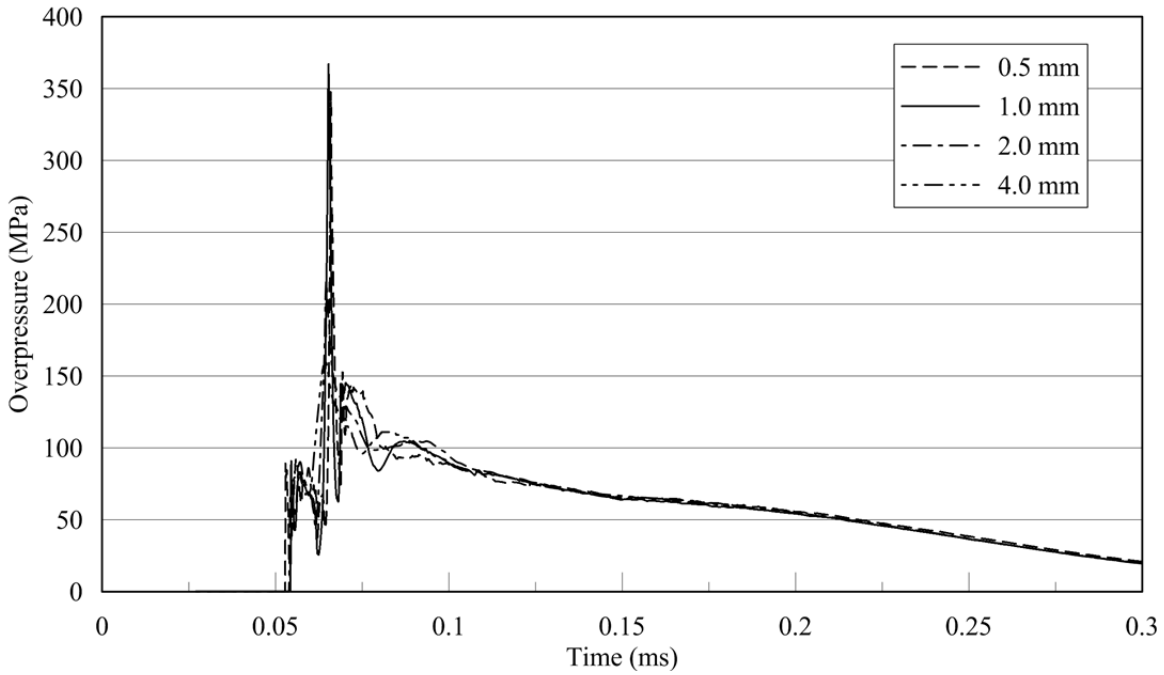


b. Monitoring location 2

**Figure 2-63 Reflected overpressure histories on a vertical reflecting surface; Model II; spherical charge of 22.68 kg of TNT; JWL EOS; varying mesh size**



c. Monitoring location 3



d. Monitoring location 4

**Figure 2-63 Reflected overpressure histories on a vertical reflecting surface; Model II; spherical charge of 22.68 kg of TNT; JWL EOS; varying mesh size (cont.)**

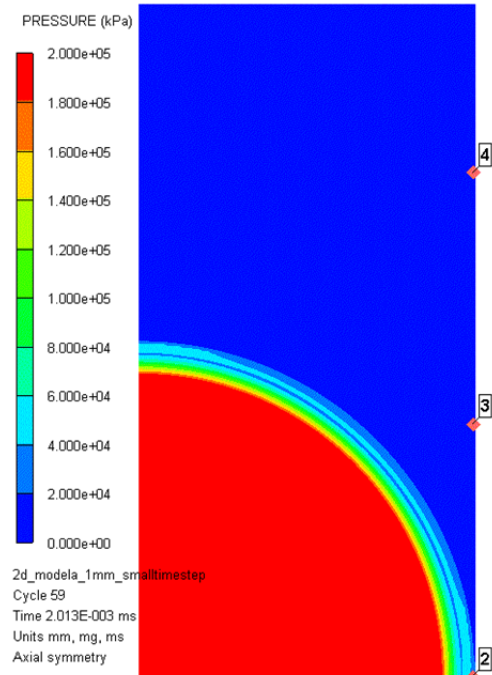
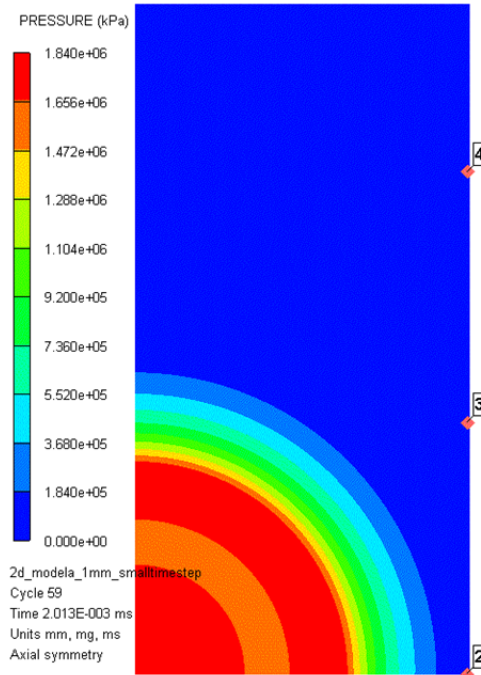
Time  
(msec)

Pressure fringes

Full range

Fixed range

0.029



0.030

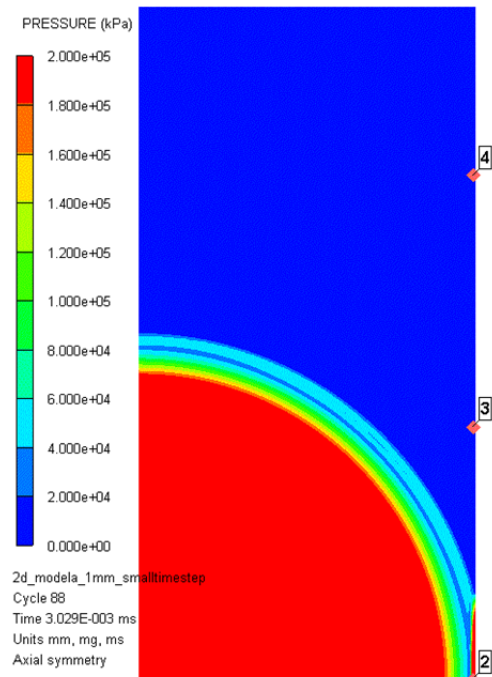
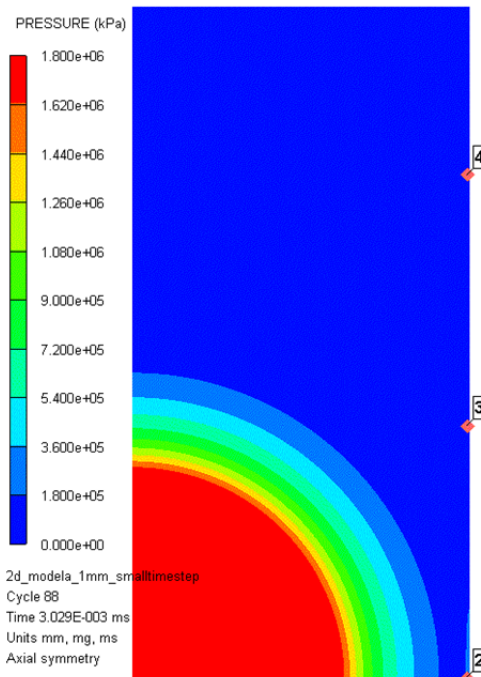


**Figure 2-64 Pressure fringes as a function of time; Model I; spherical charge of 22.68 kg of TNT; JWL EOS; TNT density = 1636.8 kg/m<sup>3</sup>; 1.0 mm mesh**

Time  
(msec)

Pressure fringes

Full range

Fixed range

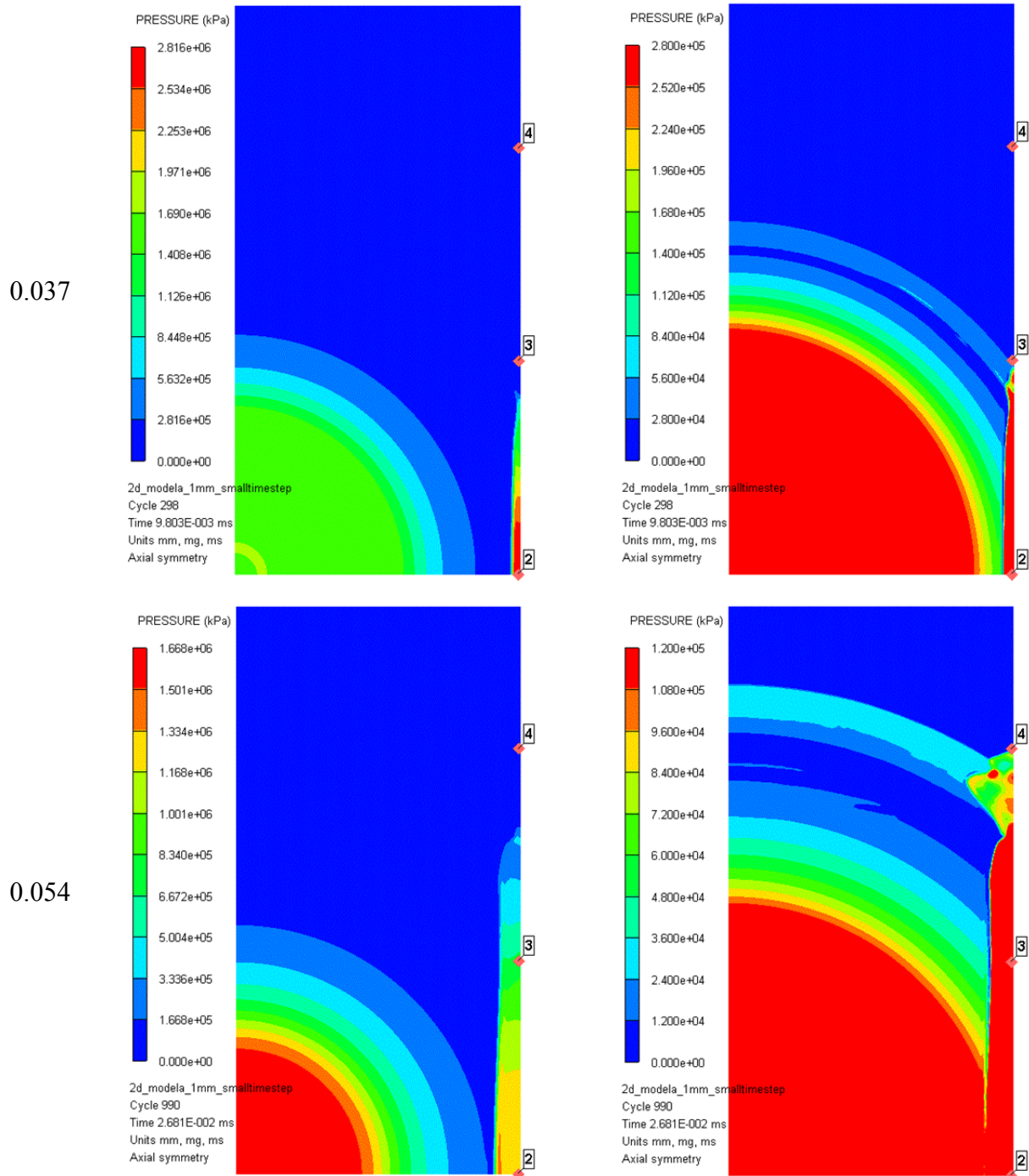


**Figure 2-64 Pressure fringes as a function of time; Model I; spherical charge of 22.68 kg of TNT; JWL EOS; TNT density = 1636.8 kg/m<sup>3</sup>; 1.0 mm mesh (cont.)**

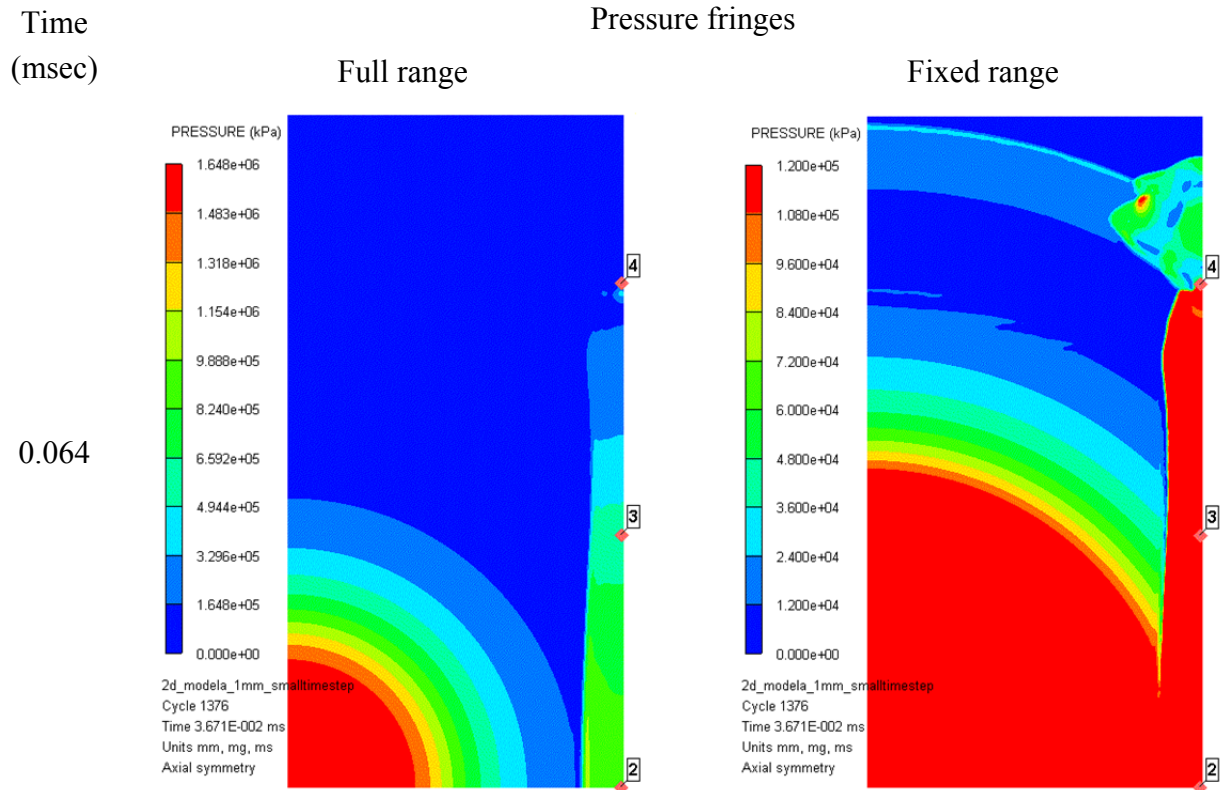
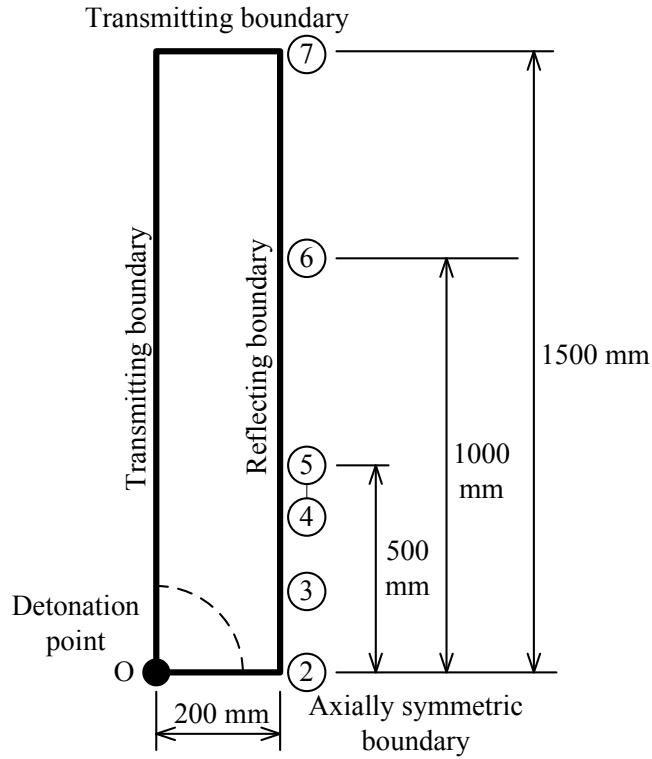
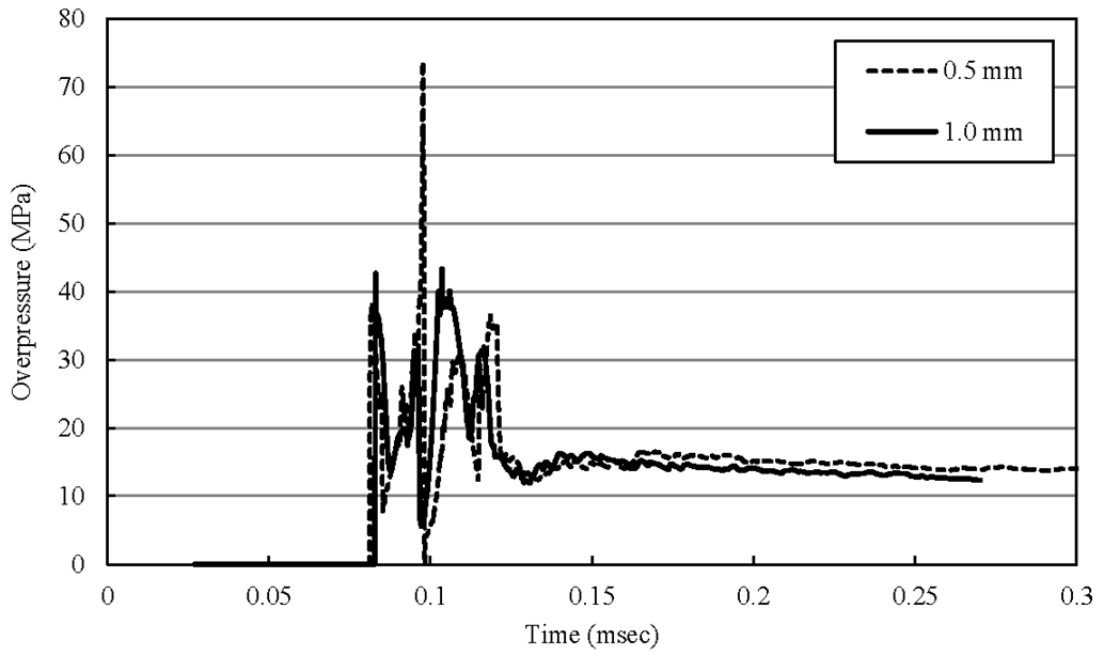


**Figure 2-64 Pressure fringes as a function of time; Model I; spherical charge of 22.68 kg of TNT; JWL EOS; TNT density = 1636.8 kg/m<sup>3</sup>; 1.0 mm mesh (cont.)**

Figure 2-65a presents Model III that is similar to Model II (Figure 2-63) except that the upper boundary is extended to a height of 1500 mm above the detonation point. Results are presented at three additional monitoring locations on the vertical reflecting surface: 5 (500 mm above the detonation point, panel b, angle of incidence = 68.2°), 6 (1000 mm above the detonation point, panel c, angle of incidence = 78.7°), and 7 (1500 mm above the detonation point, panel d, angle of incidence = 82.4°). Two cell sizes are used to generate results at monitoring locations 5 and 6; namely, 1 mm and 0.5 mm. The reflected pressure history at monitoring location 7 is computed using 1 mm cells. The jagged pressure histories are a result of wave reflection and Mach stem formation, as noted previously.

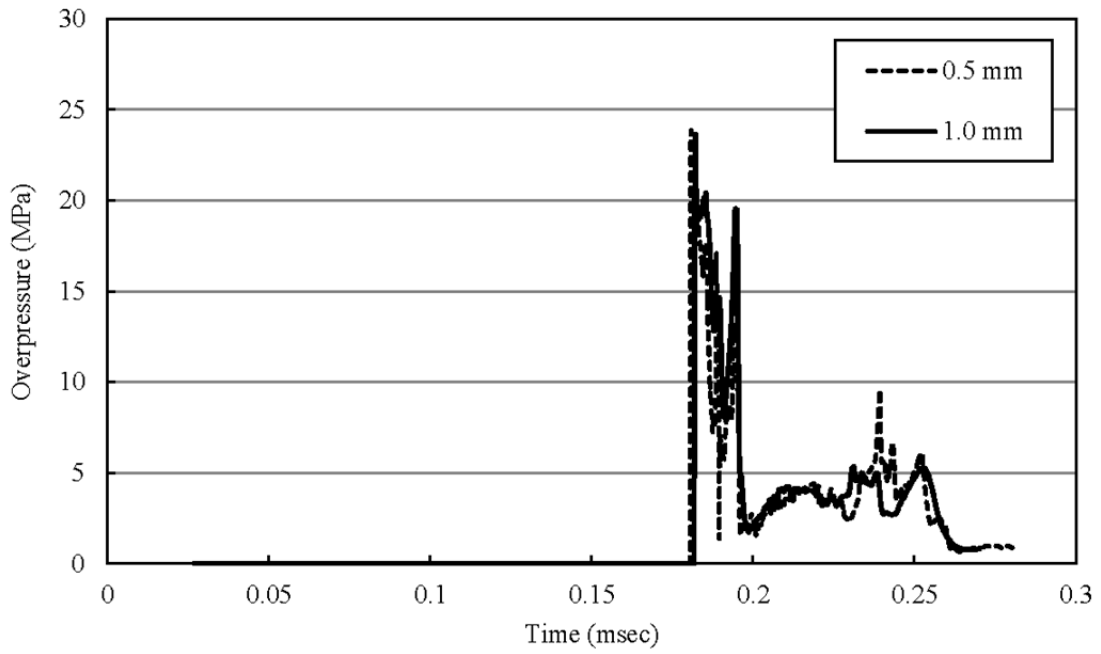


a. Model III

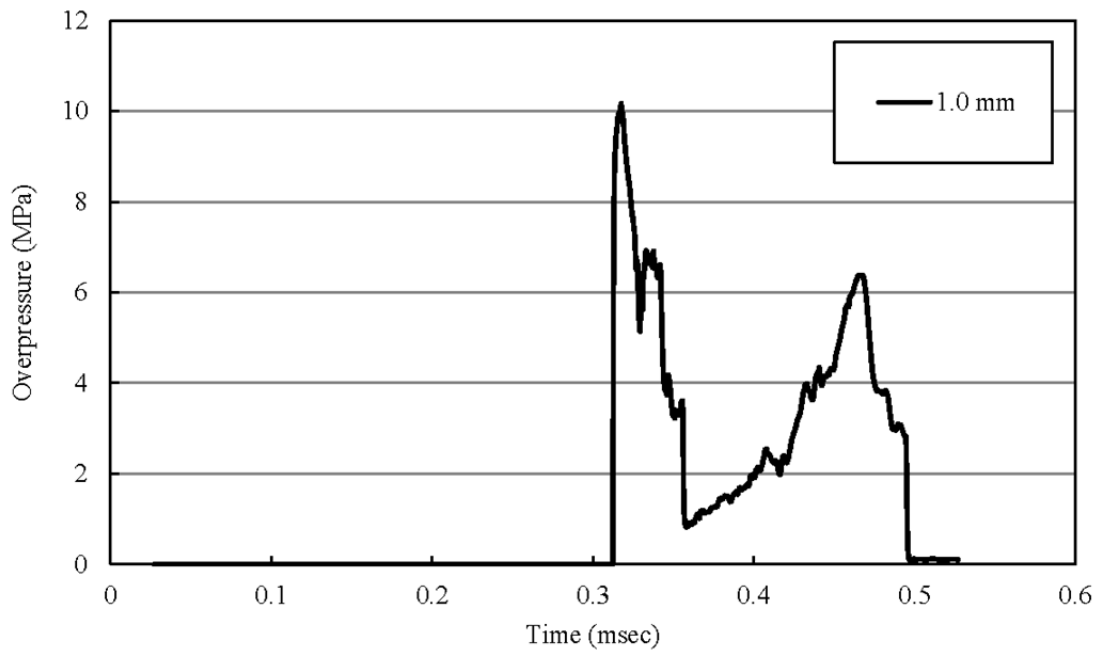


b. Monitoring location 5

**Figure 2-65 Reflected overpressure histories on a vertical reflecting surface; Model III; spherical charge of 22.68 kg of TNT; JWL EOS; varying mesh size**



c. Monitoring location 6



d. Monitoring location 7

**Figure 2-65 Reflected overpressure histories on a vertical reflecting surface; Model III; spherical charge of 22.68 kg of TNT; JWL EOS; varying mesh size (cont.)**

## 2.6 Three-Dimensional Wave Propagation

Three-dimensional blast wave simulations enable evaluation of reflected overpressure histories in complex environments with multiple reflecting boundaries (e.g., explosion in free air with buildings and ground).

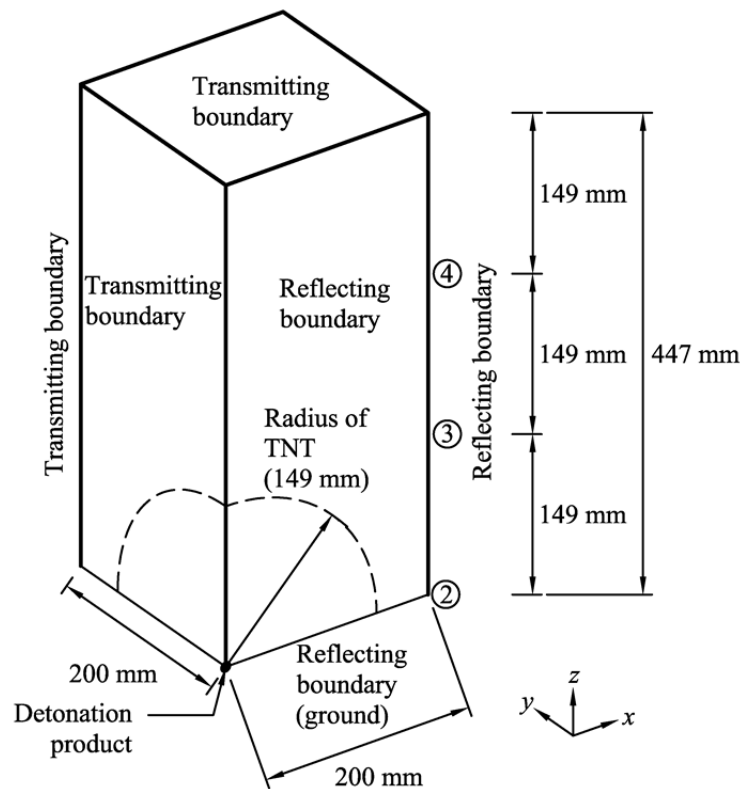
Three-dimensional meshes of Model II are constructed with different mesh sizes and different values of the perpendicular ( $y$ ) dimension, noting that the plane of Model II (and IV) shown in Figure 2-63a is  $x$  (horizontal) and  $z$  (vertical). Model II data are used because 2D axial symmetry results are available to verify the 3D models. The 3D variant of Model II denoted as Model IV with  $y = 200$  mm is shown in Figure 2-66a. The vertical planes through the center of the explosive are modeled as transmitting and reflecting boundaries in the  $yz$  and  $xz$  planes, respectively. Similar to the 2D analyses of Section 2.5, results of 1D analyses performed using the 0.5 mm cell size are remapped into the 3D meshes. Afterburning is not modeled for the reason given in Section 2.5. Figure 2-66 presents reflected overpressure histories at monitoring locations 2, 3 and 4, located 200 mm from the centerline of the charge at  $x = 200$ , 200 and 200 mm;  $z = 0$ , 149 and 298 mm; and varying  $y$ . Because of concerns regarding the transmissibility of the boundary in the perpendicular ( $y$ ) direction if the dimension was small, six values of the  $y$  dimension in Model IV are studied: 8, 12, 48, 100, 149 and 200 mm. Computational cells of 4 mm (4.027 mm for  $y = 149$  mm) are used to construct each mesh. Analysis of the three panels b, c and d in Figure 2-66 makes the influence of the choice of perpendicular dimension clear, with results stabilizing for a value of 48 mm ( $R/4$ ) and greater for peak overpressure and a value for 149 mm ( $3R/4$ ) and greater for impulse, where  $R$  is the shortest distance from the point of detonation (center of the charge) to the vertical reflecting surface (= 200 mm in this case), namely, the standoff distance. The increase in overpressure at 0.2 msec at each monitoring location for the 100 mm perpendicular dimension ( $y$ ) is due to reflections from the *transmitting* perpendicular boundary. Figure 2-67 (2-68) presents the results of an analysis of mesh size for  $y = 100$  mm (200 mm). Results of 2D analysis invoking radial (axial) symmetry are presented to inform the choice of cells size. For a given perpendicular dimension, 100 mm or 200 mm, the overpressure histories are identical for the 2 mm and 4 mm cells at monitoring location 3 and 4; the reflected peak overpressure is underestimated by approximately 10% at monitoring location 2

with the 4 mm cells. Both 3D meshes overestimate the reflected overpressure at 0.2 msec for  $y = 100$  mm. Figure 2-69 enables conclusions to be drawn regarding cell size and the minimum required perpendicular dimension for 3D analysis. Each panel in Figure 2-69 presents overpressure histories at a given monitoring location for 2D radial analysis (2 mm mesh) and 3D analysis (2 mm mesh) for perpendicular ( $y$ ) dimensions of 100 mm and 200 mm. The histories for 2D analysis (2 mm mesh) and 3D analysis (2 mm mesh,  $y = 200$  mm) are essentially identical. Transmitting boundaries do not function perfectly and a fraction of the pressure is reflected, causing both the overpressures and impulses to be over-predicted if the transverse ( $y$ ) dimension is too small. On the basis of this study, the transverse dimension should be always specified to be greater than the charge radius to avoid significant boundary effects.

Figure 2-70 presents Model V that is similar to Models II and IV except that the lower boundary is extended down to the ground and one-fourth of the explosive is modeled. The lower boundary is modeled as a reflecting surface. The vertical planes through the center of the explosive are modeled as transmitting and reflecting boundaries in the  $yz$  and  $xz$  planes, respectively. Two-dimensional radial (axial) symmetry cannot be used to solve this problem and three-dimensional models must be used. Alternate three-dimensional models are considered for the purpose of monitoring overpressure histories on the centerline of the charge at monitoring locations 1, 2, 3 and 4 per Figure 2-66.

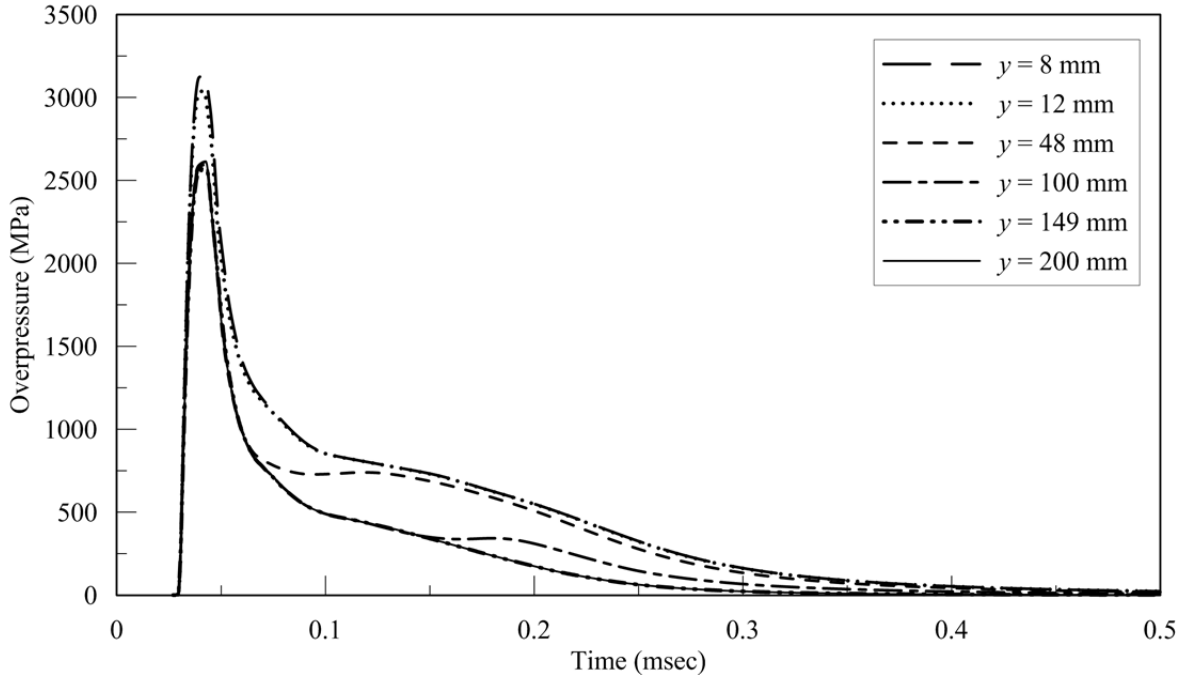
On the basis of the data presented in Figures 2-66 through 2-69, Model V is meshed with 1, 2 and 4 mm cells and a perpendicular ( $y$ ) dimension of 200 mm and uses 1D results for a cell size of 0.5 mm and a distance of 149 mm, which is adopted because 1D simulations should be performed before reflection occurs and the shock front is first reflected at the distance of 149 mm, on the lower reflecting boundary. Figure 2-71 presents reflected overpressure histories at monitoring locations 1, 2, 3 and 4, with all data presented in panel a (4 mm mesh) and histories for individual monitoring locations presented in panels b, c, d and e. The results are effectively identical for the cell sizes of 1, 2 and 4 mm. Results for the 1 mm cell size are not included at monitoring location 4 because the runtimes were excessive. The reflected overpressure at the vertical reflecting surface at the ground is 3.8 GPa (2 mm mesh) and approximately twice that at monitoring location 2 (2.1 GPa, 2 mm), 149 mm above monitoring location 1. The reflected peak

overpressure at monitoring location 2 calculated using Model V and a 2 mm mesh is approximately 10 percent less than that calculated using Model II, axial symmetry and a 1 mm mesh. The reflected peak overpressure at monitoring location 3 is similar for Model II (1 mm mesh) and Model V (2 mm mesh). The local increase in the overpressure history at monitoring location 2 at  $t = 0.15$  msec is due to the formation of a Mach stem. None of the Model V pressure histories resembles the shape of the Friedlander equation.

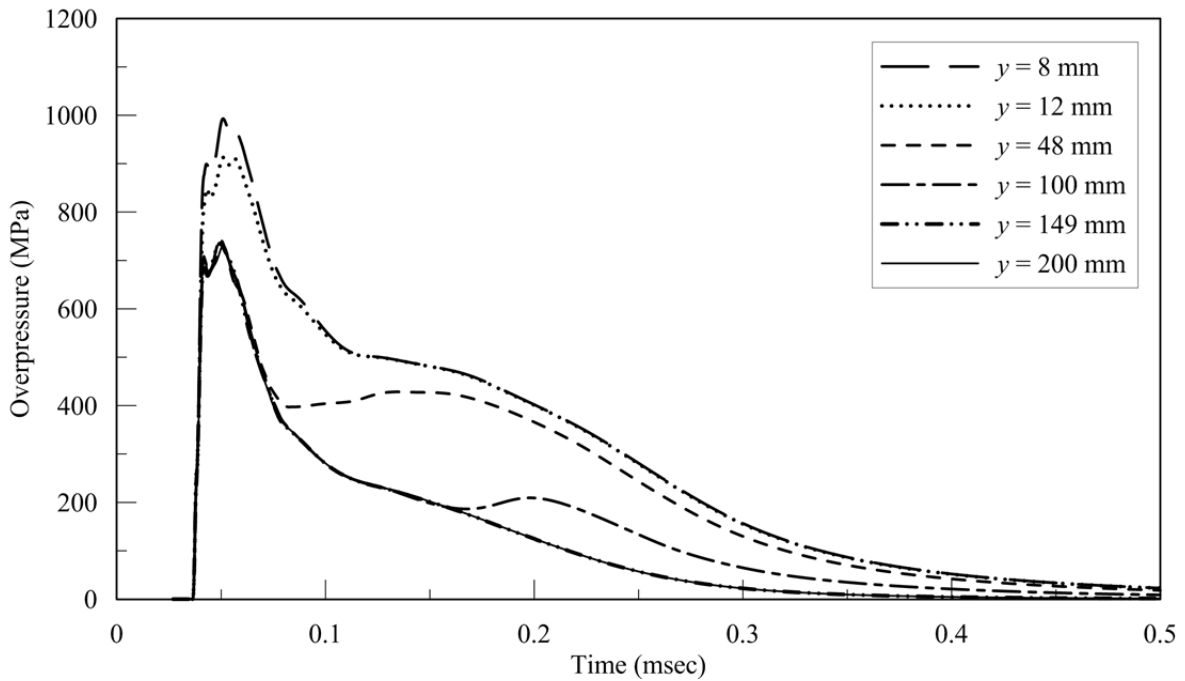


a. Model IV; 3D variant of Model II; perpendicular ( $y$ ) dimension = 200 mm

**Figure 2-66 Reflected overpressure histories on a vertical reflecting surface; Model IV; spherical charge of 22.68 kg of TNT; JWL EOS; 4 mm mesh (4.027 mm for  $y = 149$  mm); varying perpendicular dimension,  $y$**

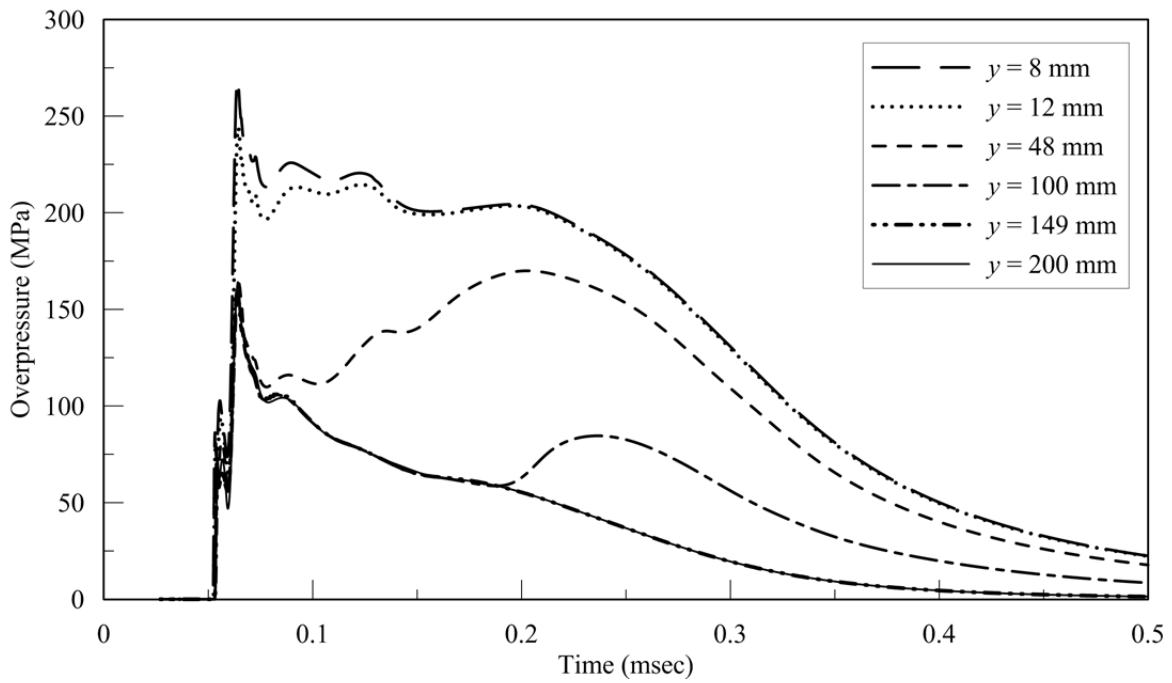


b. Monitoring location 2



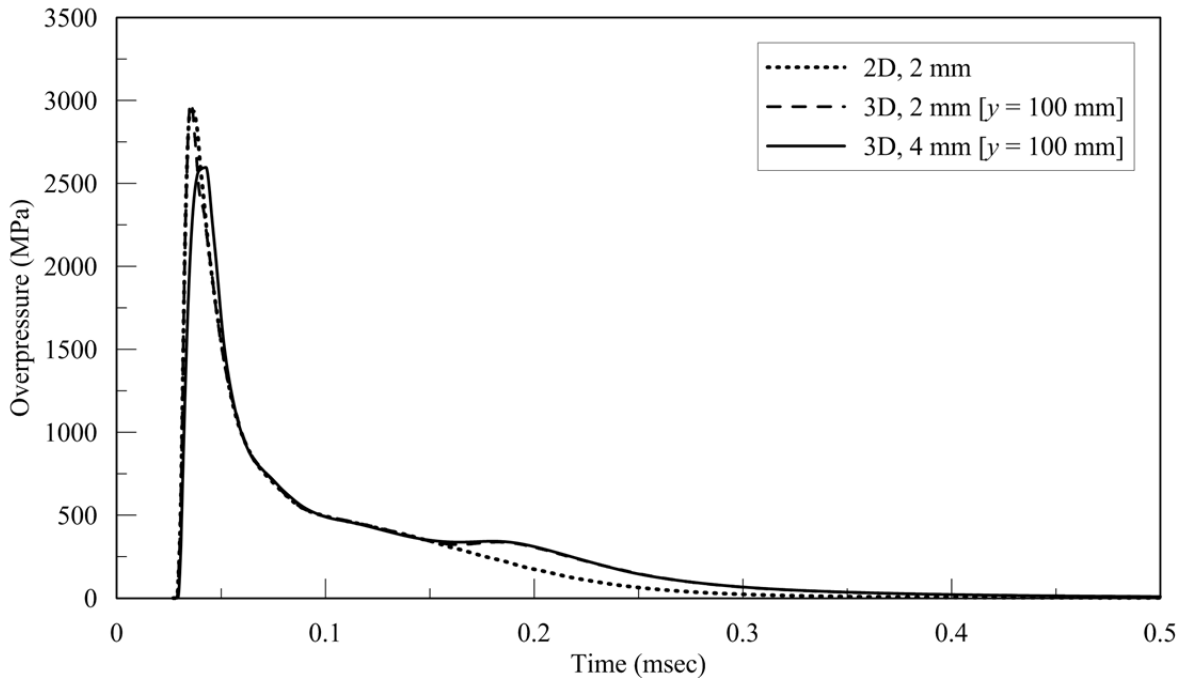
c. Monitoring location 3

**Figure 2-66 Reflected overpressure histories on a vertical reflecting surface; Model IV; spherical charge of 22.68 kg of TNT; JWL EOS; 4 mm mesh (4.027 mm for  $y = 149$  mm); varying perpendicular dimension,  $y$  (cont.)**

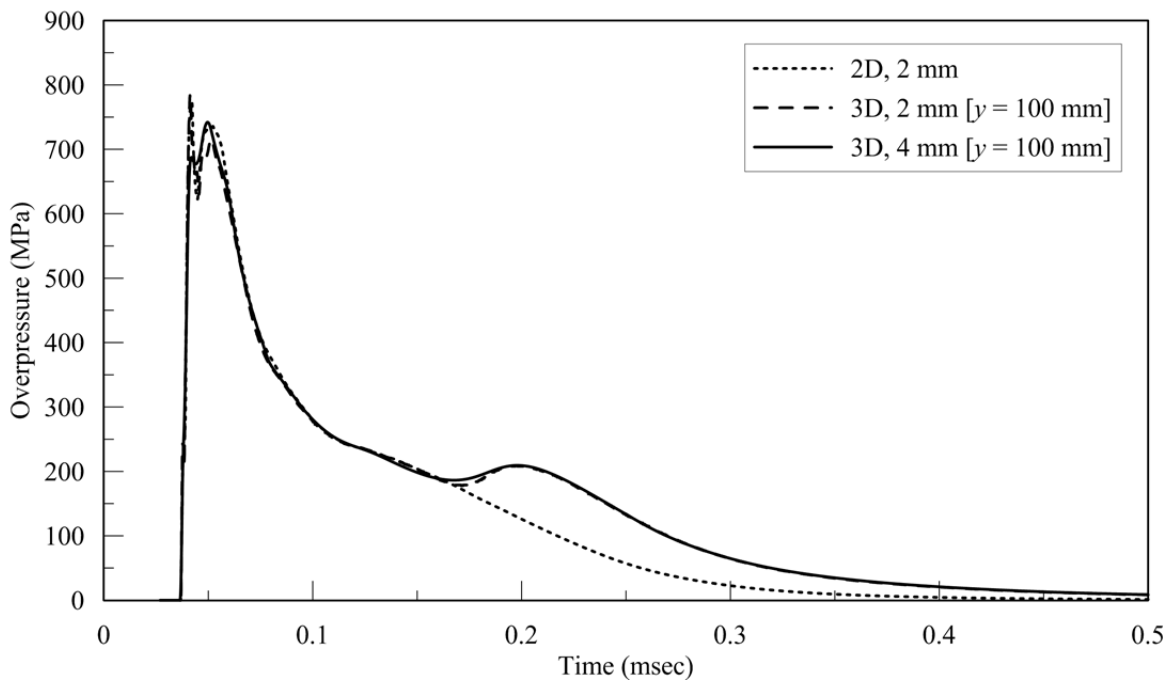


d. Monitoring location 4

**Figure 2-66 Reflected overpressure histories on a vertical reflecting surface; Model IV; spherical charge of 22.68 kg of TNT; JWL EOS; 4 mm mesh (4.027 mm for y = 149 mm); varying perpendicular dimension, y (cont.)**

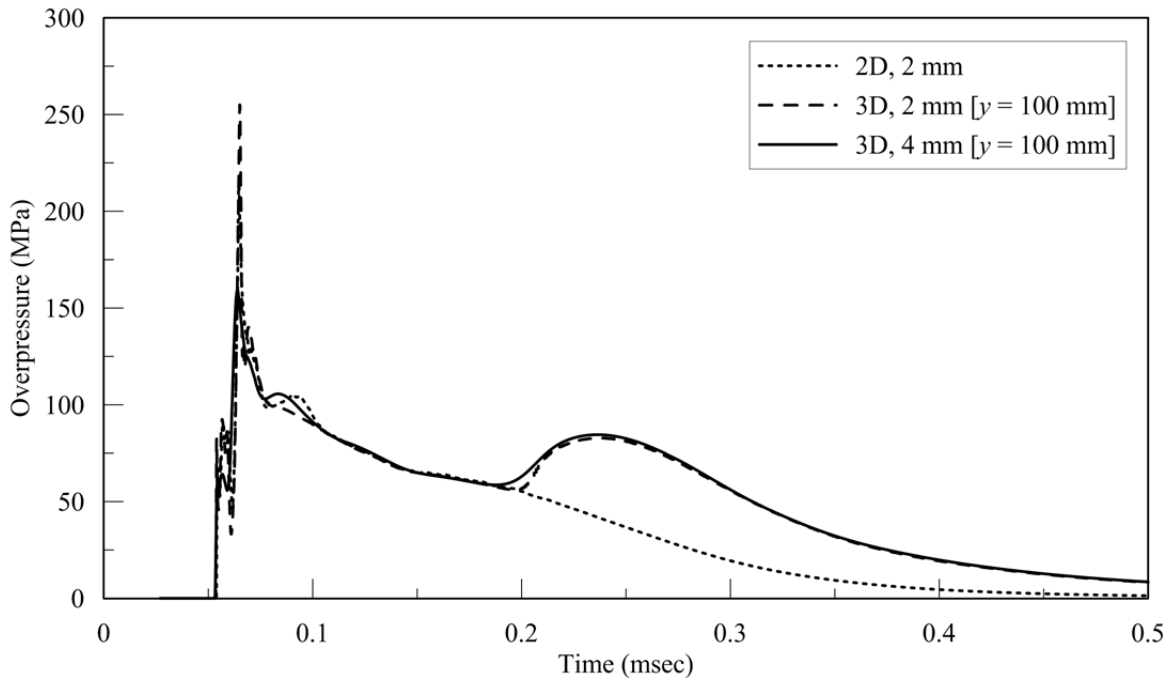


a. Monitoring location 2



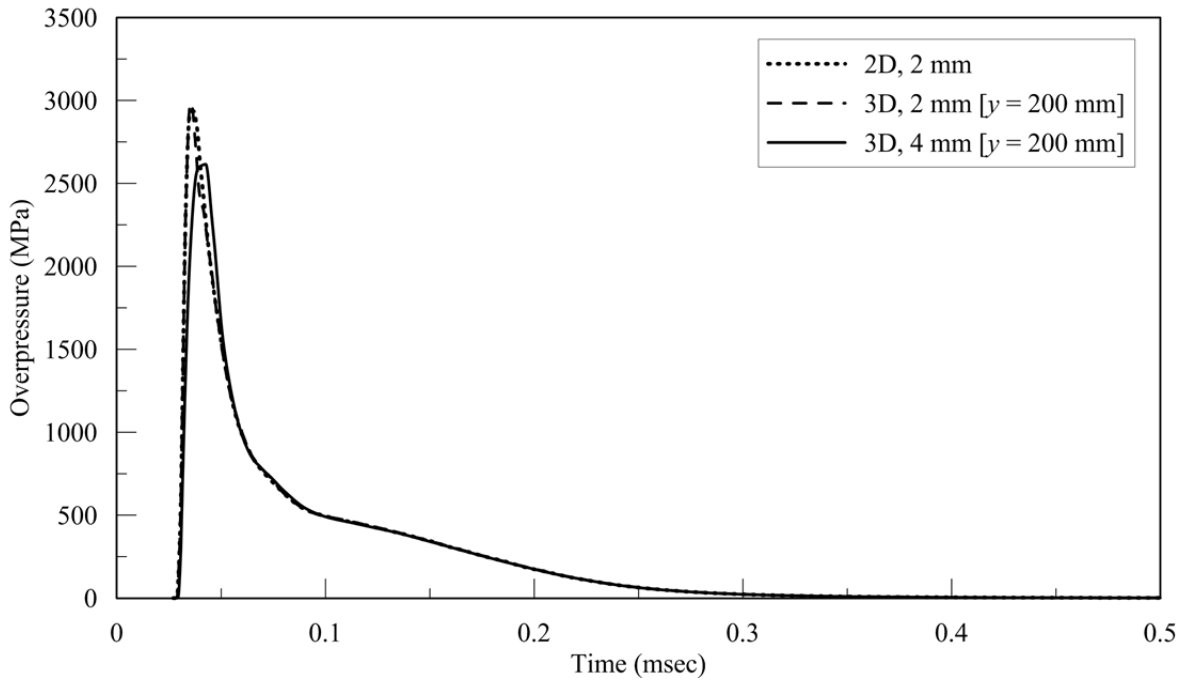
b. Monitoring location 3

**Figure 2-67 Reflected overpressure histories on a vertical reflecting surface; Model II and Model IV; spherical charge of 22.68 kg of TNT; JWL EOS;  $y = 100$  mm for 3D analysis**

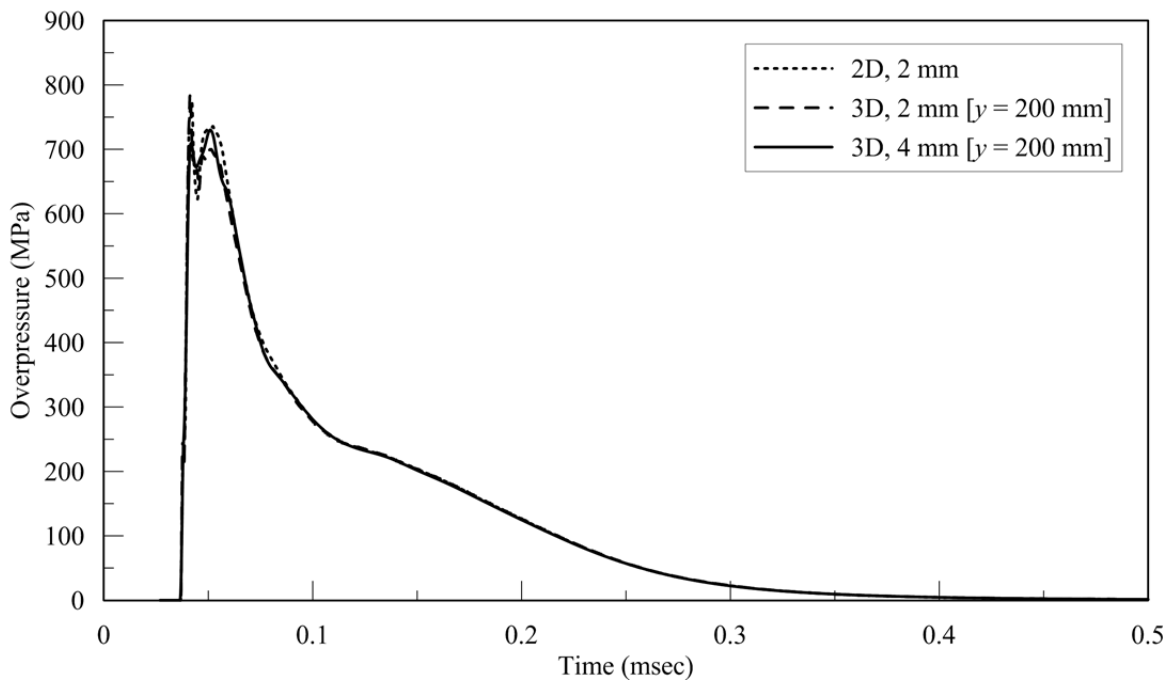


c. Monitoring location 4

**Figure 2-67 Reflected overpressure histories on a vertical reflecting surface; Model II and Model IV; spherical charge of 22.68 kg of TNT; JWL EOS;  $y = 100$  mm for 3D analysis (cont.)**

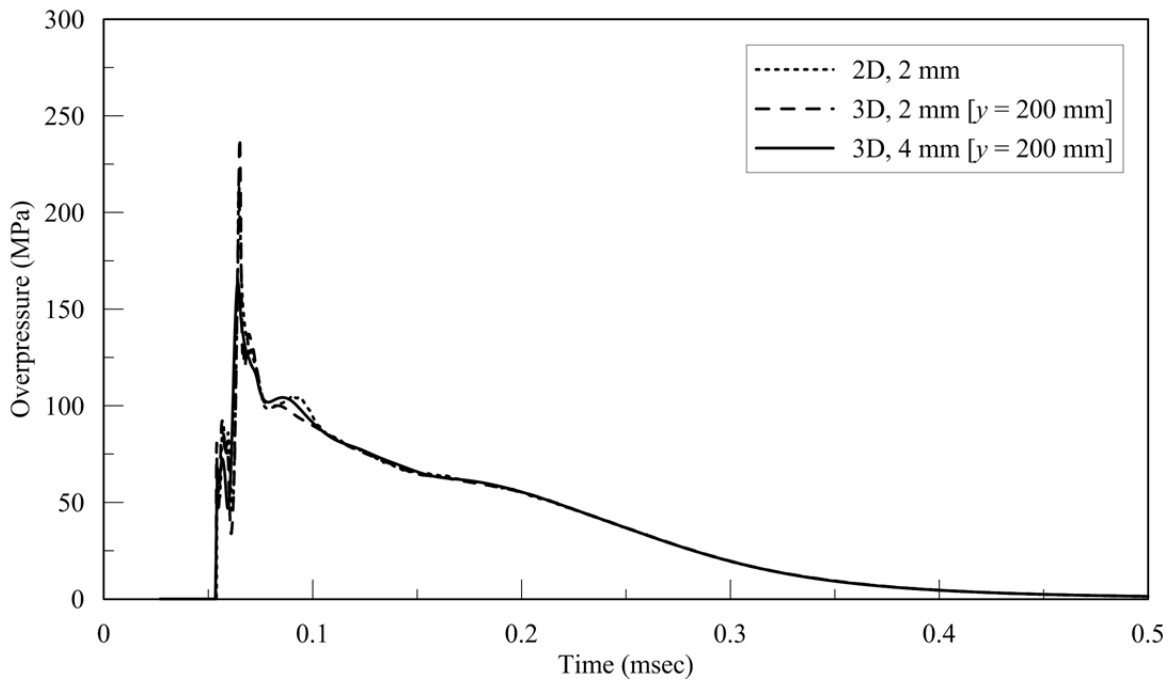


a. Monitoring location 2



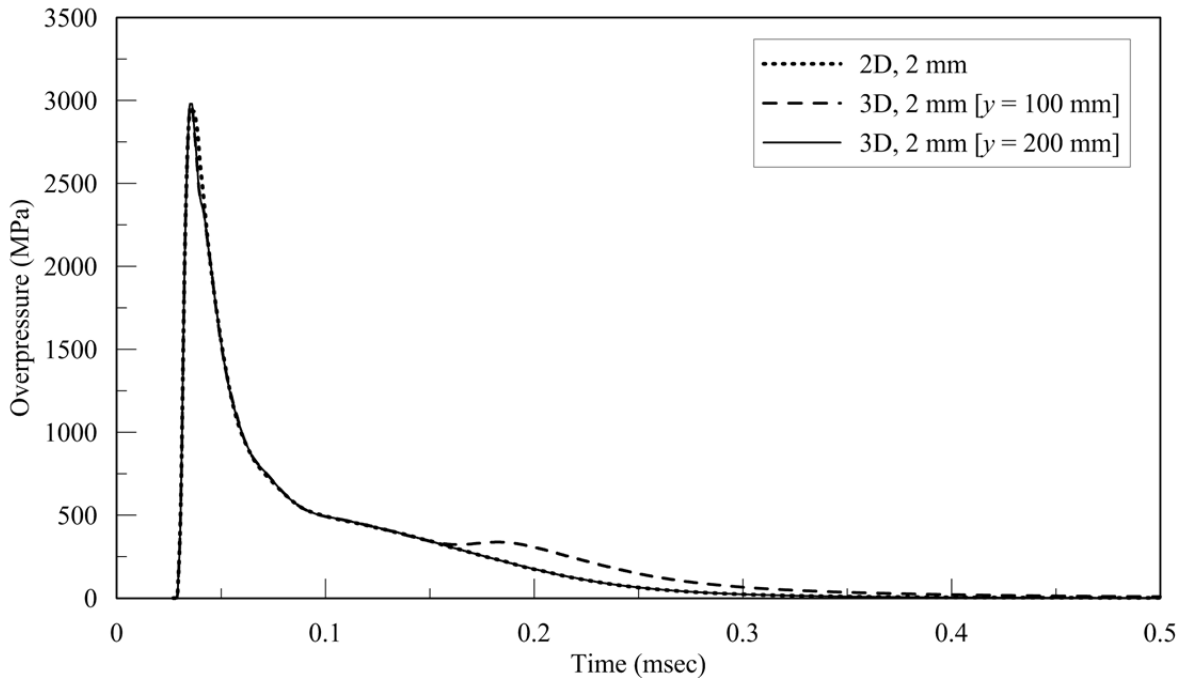
b. Monitoring location 3

**Figure 2-68 Reflected overpressure histories on a vertical reflecting surface; Model II and Model IV; spherical charge of 22.68 kg of TNT; JWL EOS;  $y = 200$  mm for 3D analysis**

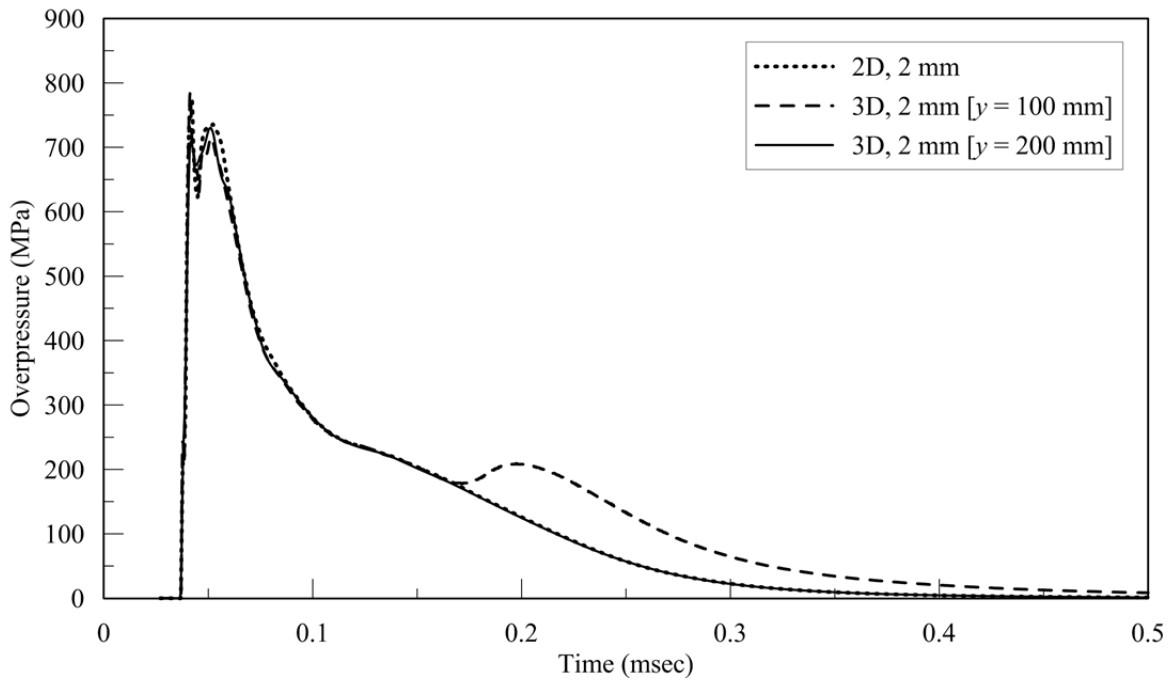


c. Monitoring location 4

**Figure 2-68 Reflected overpressure histories on a vertical reflecting surface; Model II and Model IV; spherical charge of 22.68 kg of TNT; JWL EOS; y = 200 mm for 3D analysis (cont.)**

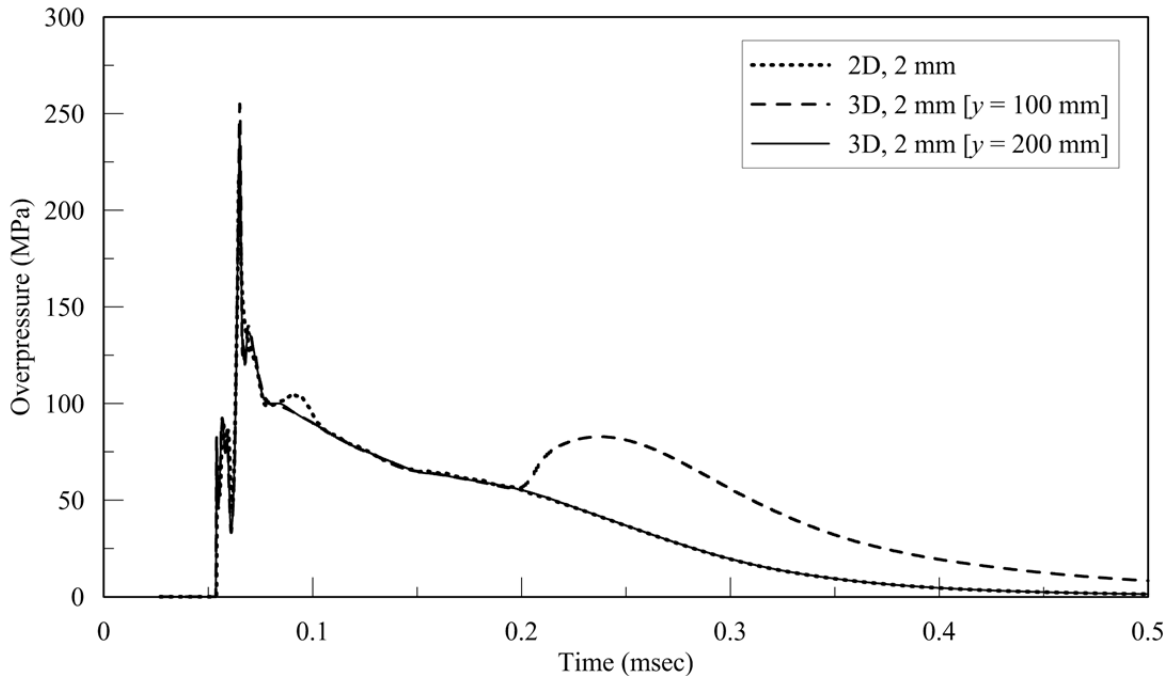


a. Monitoring location 2



b. Monitoring location 3

**Figure 2-69 Reflected overpressure histories on a vertical reflecting surface; Model II and Model IV; spherical charge of 22.68 kg of TNT; JWL EOS; 2 mm mesh**



c. Monitoring location 4

**Figure 2-69 Reflected overpressure histories on a vertical reflecting surface; Model II and Model IV; spherical charge of 22.68 kg of TNT; JWL EOS; 2 mm mesh (cont.)**

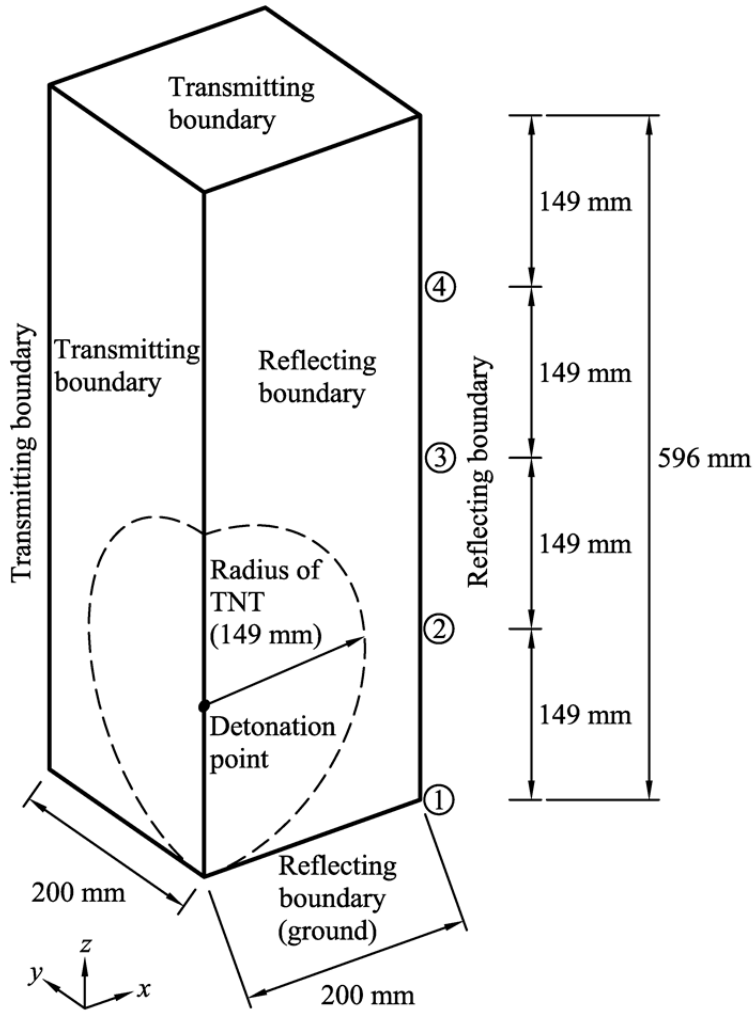
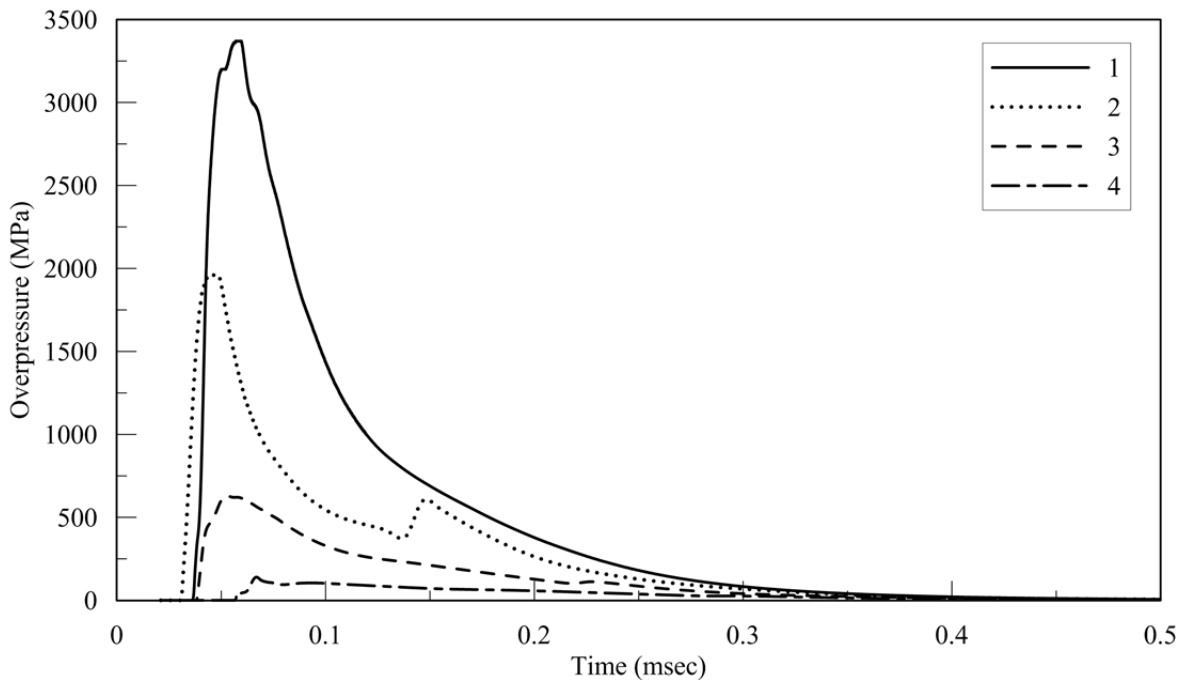
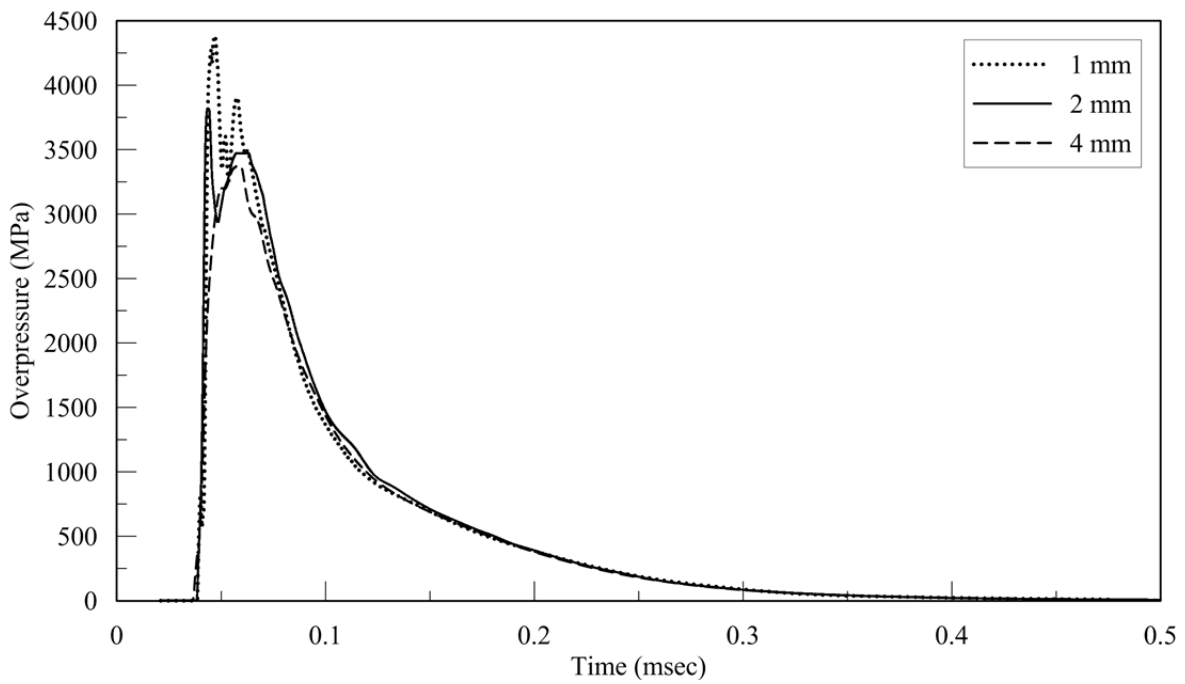


**Figure 2-70 Reflected overpressure histories on a vertical reflecting surface; Model V; spherical charge of 22.68 kg of TNT; JWL EOS;  $y = 200$  mm**

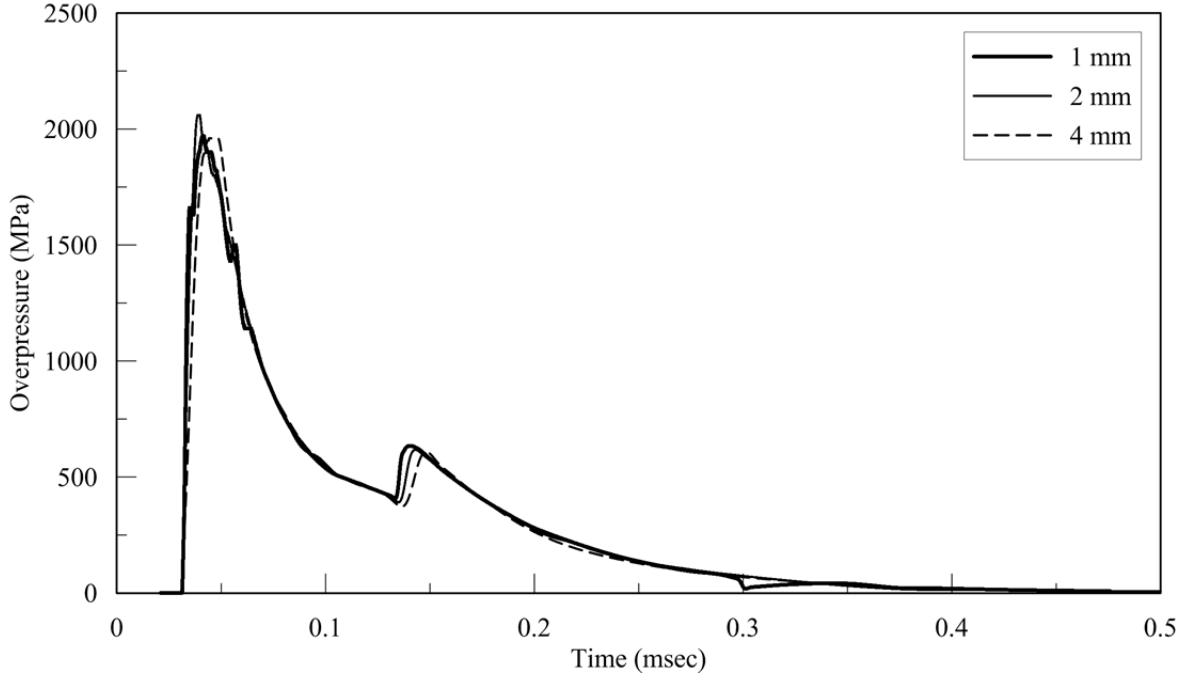


a. All monitoring locations (4 mm mesh)

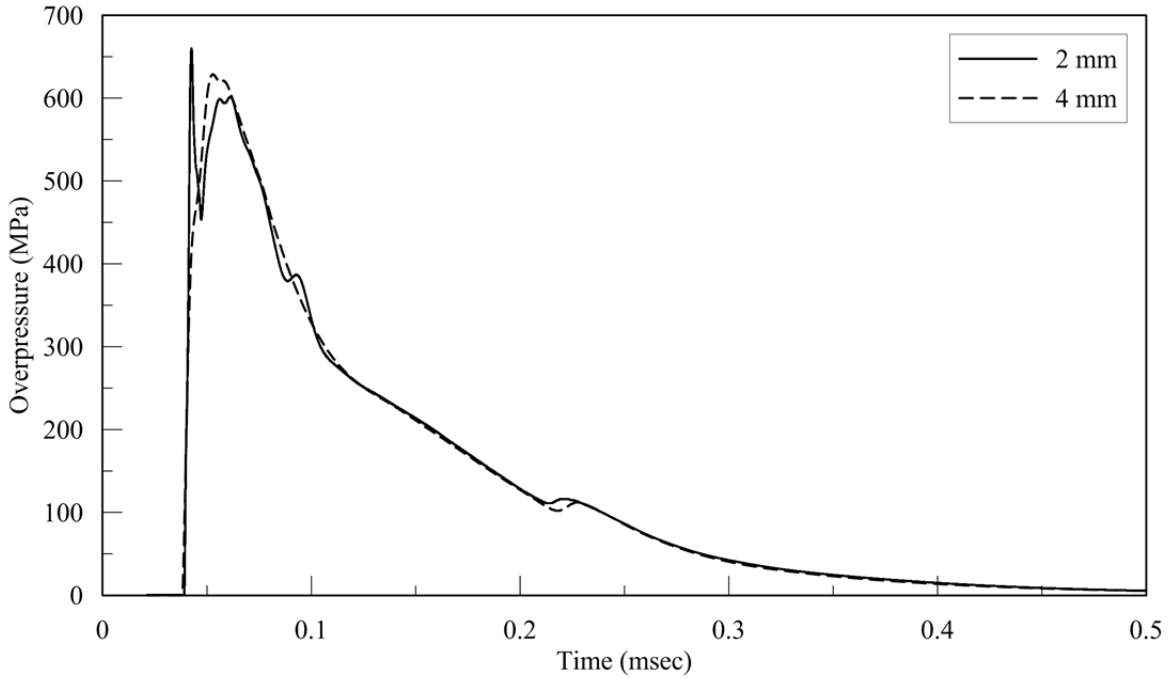


b. Monitoring location 1

**Figure 2-71 Reflected overpressure histories on a vertical reflecting surface; Model V; spherical charge of 22.68 kg of TNT; JWL EOS; 2 mm and 4 mm meshes**

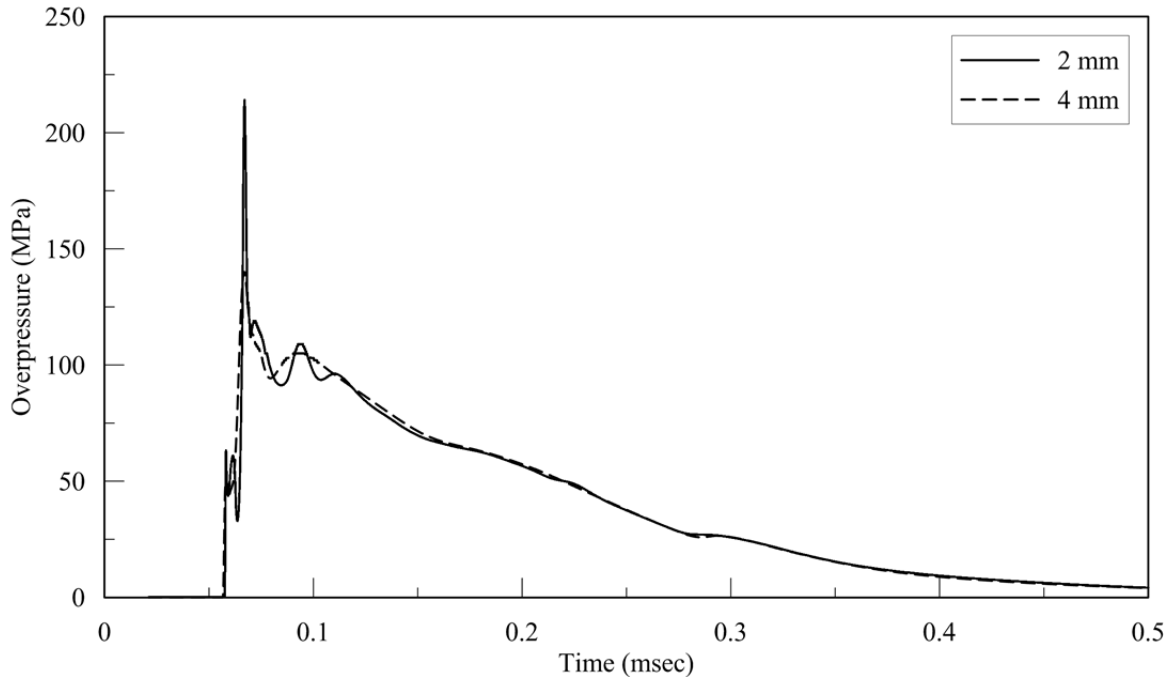


c. Monitoring location 2



d. Monitoring location 3

**Figure 2-71 Reflected overpressure histories on a vertical reflecting surface; Model V; spherical charge of 22.68 kg of TNT; JWL EOS; 2 mm and 4 mm meshes (cont.)**



e. Monitoring location 4

**Figure 2-71 Reflected overpressure histories on a vertical reflecting surface; Model V; spherical charge of 22.68 kg of TNT; JWL EOS; 2 mm and 4 mm mesh meshes (cont.)**

## 2.7 Air-Blast Loadings on Sample Reinforced Concrete Columns

### 2.7.1 Introduction

The studies of the prior sections are extended here to the calculation of near-field air-blast loadings on the perimeters of a square column and a circular column similar in size to those used in buildings and mission-critical infrastructure. The goals are to compare and contrast the reflected overpressures as a function of monitoring location on each column, and to establish the importance of column shape on net air-blast loadings.

The dimensions of the square column are 1000 mm × 1000 mm. The diameter of the circular column is 1000 mm. Both columns are assumed rigid for the purpose of the analysis. The weight of the TNT charge is 22.68 kg; the packing density of the TNT is 1636.8 m/kg<sup>1/3</sup>, and the radius of the charge is 149 mm. The shortest clear distance between the face of the charge and each column is 51 mm per Models II, III, IV and V. The centerline of each column aligns with the

centerline of the charge. The spherical charge is placed on a rigid reflecting surface. Symmetry is invoked on the centerline of the charge and column. Air is modeled using an Eulerian grid and the columns are modeled using a Lagrangian grid. The Lagrangian grid serves as a flow constraint for the Eulerian grid.

### ***2.7.2 Square Column, Model VI***

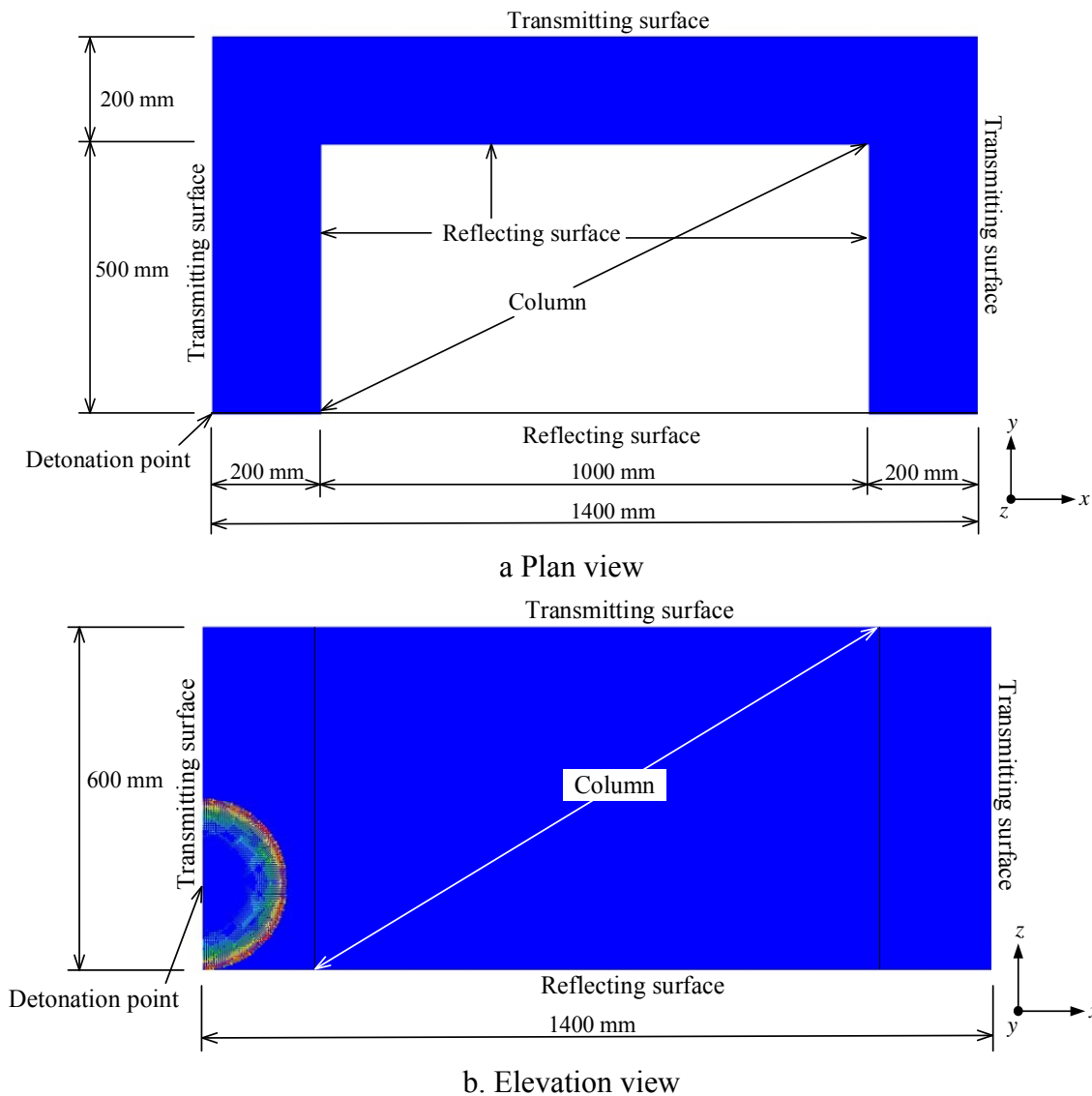
Figure 2-72 presents a plan view and an elevation of Model VI. The  $x$ - $y$ - $z$  coordinate system is shown. The transmitting  $y$ -boundary is set at  $y = 700$  mm: 200 mm beyond the face of the column. The transmitting  $z$ -boundary is set at  $z = 600$  mm because reflected overpressures were expected to be a factor of 25+ smaller at  $z = 600$  than  $z = 0$  on the centerline of the column. Figure 2-73 presents the monitoring locations. Monitoring locations 1, 2, 3 and 4 are evenly spaced at 160 mm across the front face of the column. Monitoring locations 5, 6, 7 and 8 are evenly spaced at 250 mm along the perpendicular face of the column. Monitoring location 10 aligns with Monitoring location 1 and Monitoring location 9 is midway (250 mm) between monitoring locations 8 and 10. Monitoring locations 11 through 20, 21 through 30, and 31 through 40 align vertically with Monitoring locations 1 through 10, respectively, but are 149 mm, 298 mm and 447 mm above the ground surface, respectively. A cell size of 4 mm is used based on the 3D analysis of Model V presented in Section 2.6.

Figure 2-74 presents reflected overpressure histories at all 40 monitoring locations. As expected, the reflected overpressures are greatest on the front face and (relatively) insignificant elsewhere. A comparison of the reflected peak overpressure histories at monitoring locations 11 (opposite to the center of the charge) and 34 [31], on the front face of the column, shows a difference of a factor greater than 50 [15], which is due to differences in scaled distance and angle of incidence.

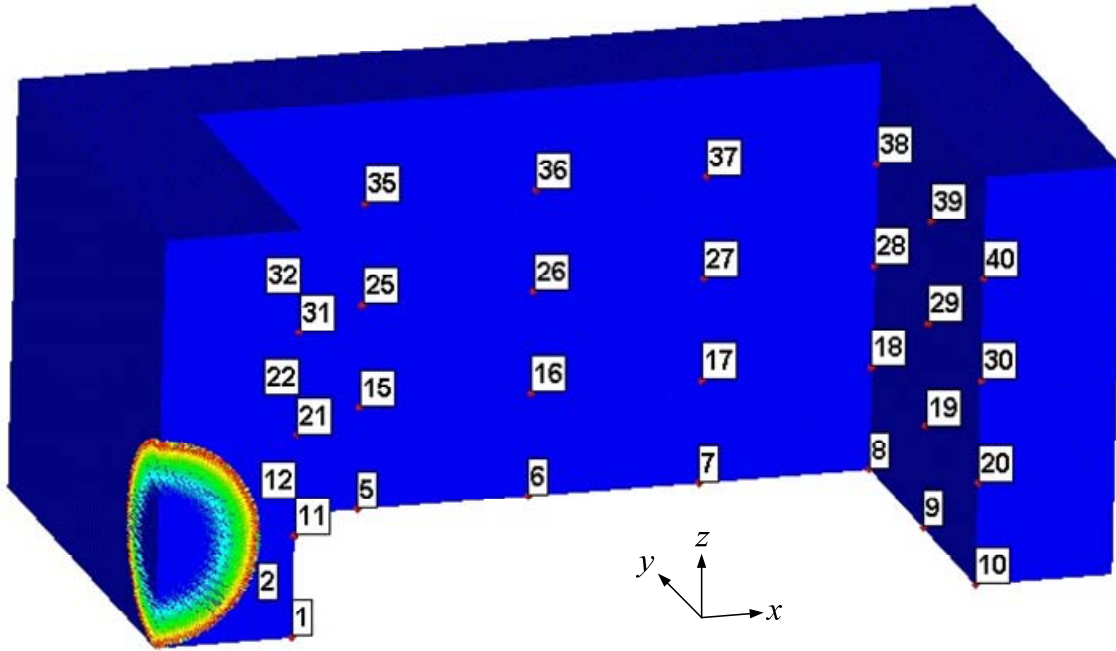
Figure 2-75 presents net loading and impulse histories on the lower 600 mm of the front face of the column calculated using a) overpressure history at locations 1, 11, 21 and 31, applied across the width of the column using tributary heights, and b) overpressure history at all monitoring locations on the front face, applied using tributary areas. The peak load (impulse) calculated considering all locations is 3.7 (2.3) times smaller than that calculated based on pressure histories at locations 1, 11, 21 and 31 only. At a distance of 200 mm ( $Z = 0.071 \text{ m/kg}^{1/3}$ ), discretization of

the front face of a square column will result in significantly smaller net loads (73% reduction here) and impulses (57% reduction here).

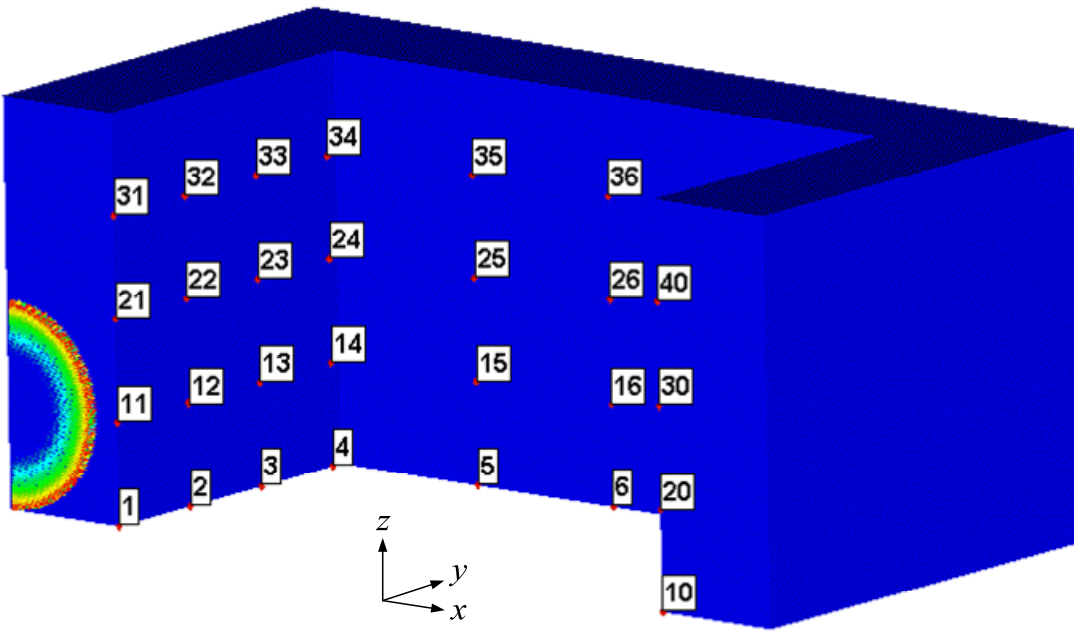
Panels a through d of Figure 2-76 enable a comparison of the overpressure histories from Model V (Figure 2-71a, locations 1, 2, 3 and 4) and Model VI (Figure 2-74i, locations 1, 11, 21 and 31), noting that locations 1, 2, 3 and 4 in Model V are identical to 1, 11, 21 and 31 in Model VI. The two models yield identical results.



**Figure 2-72 Model VI; spherical charge of 22.68 kg of TNT; square column 1000×1000 mm**

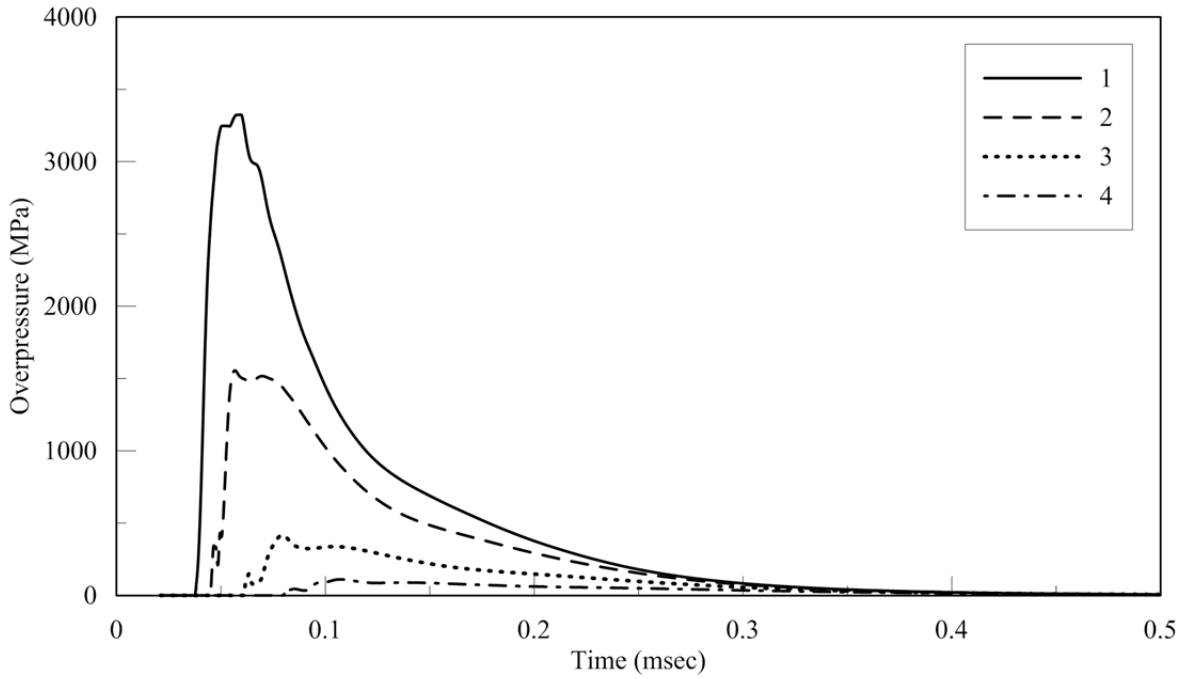


a. View 1

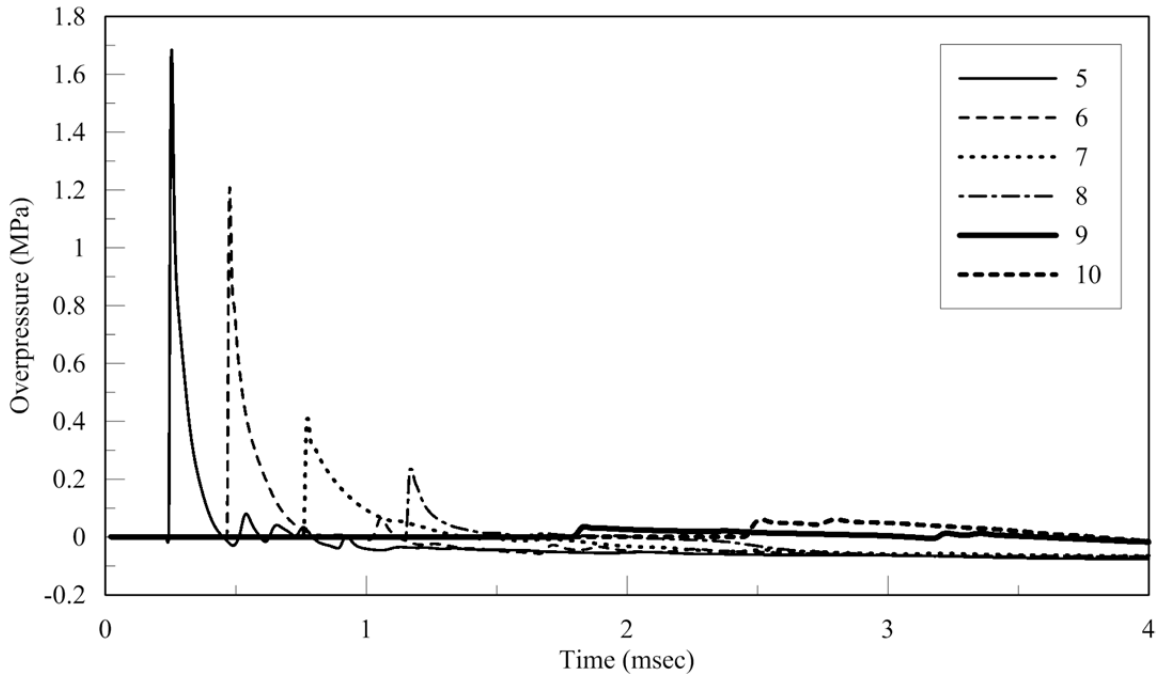


b. View 2

**Figure 2-73 Monitoring locations for Model VI; spherical charge of 22.68 kg of TNT; square column 1000×1000 mm**

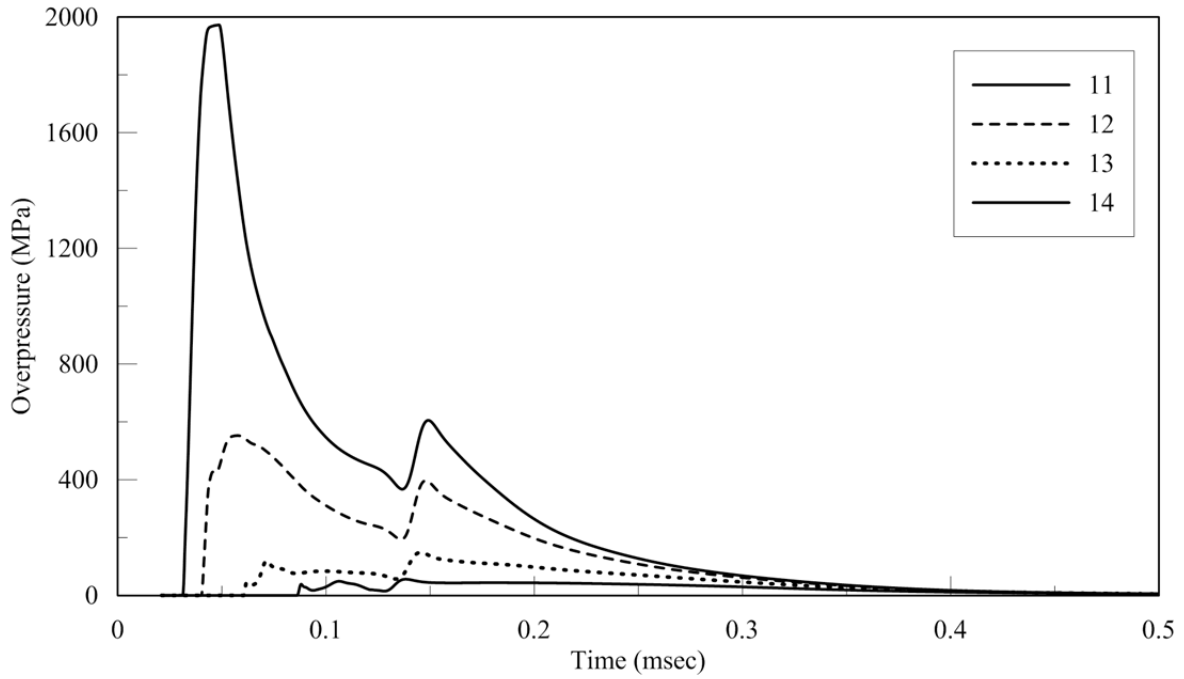


a. Monitoring locations 1, 2, 3 and 4

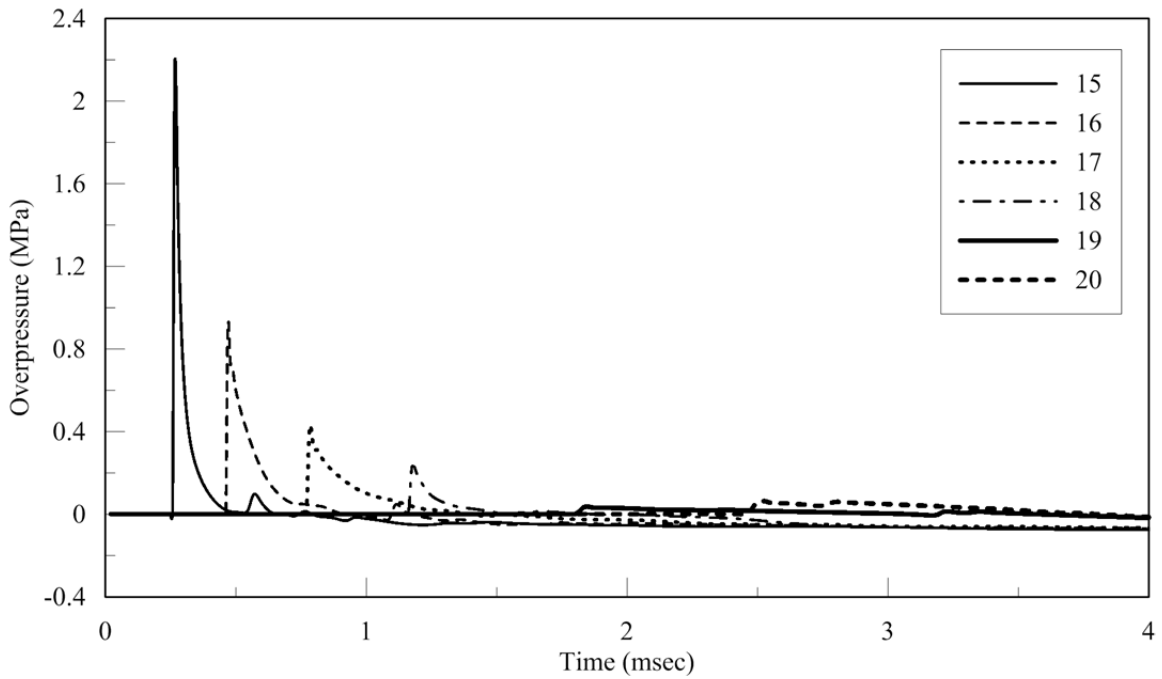


b. Monitoring locations 5, 6, 7, 8, 9 and 10

**Figure 2-74 Reflected overpressure histories; Model VI; spherical charge of 22.68 kg of TNT; JWL EOS**

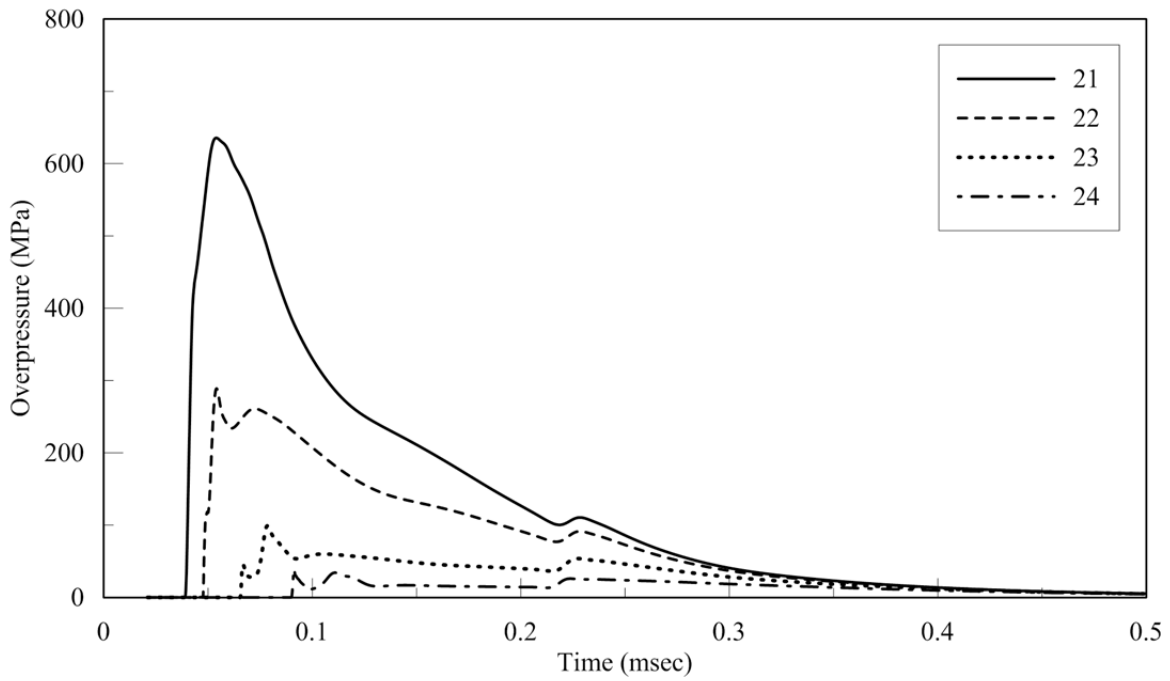


c. Monitoring locations 11, 12, 13 and 14

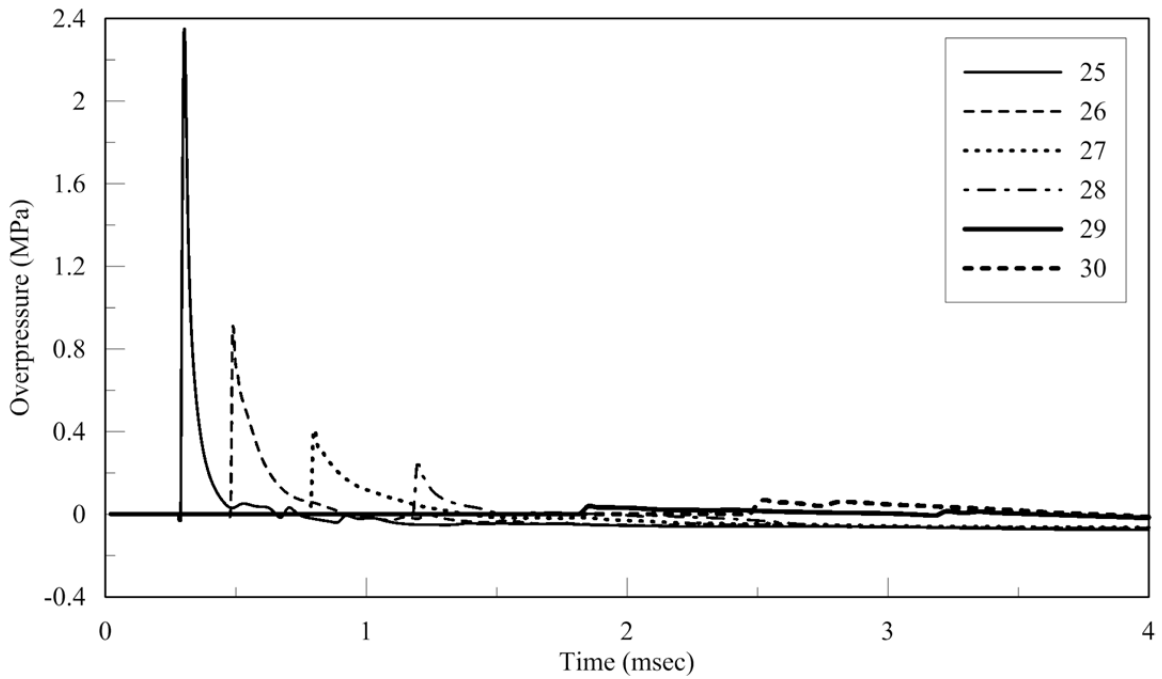


d. Monitoring locations 15, 16, 17, 18, 19 and 20

**Figure 2-74 Reflected overpressure histories; Model VI; spherical charge of 22.68 kg of TNT; JWL EOS (cont.)**

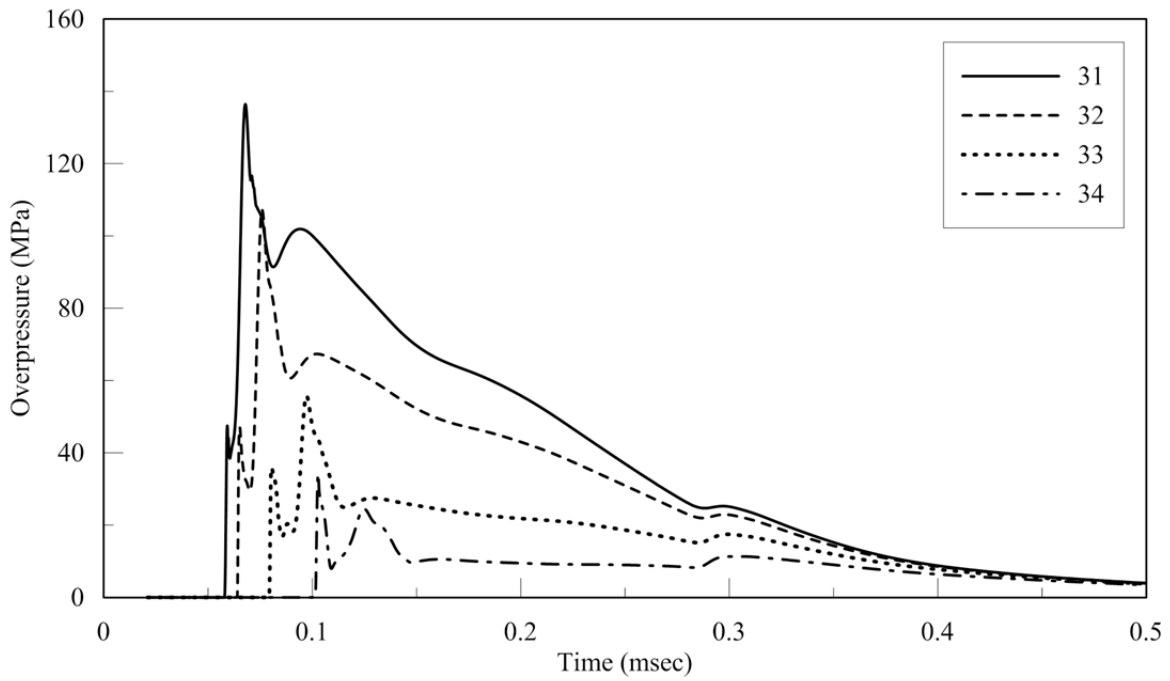


e. Monitoring locations 21, 22, 23 and 24

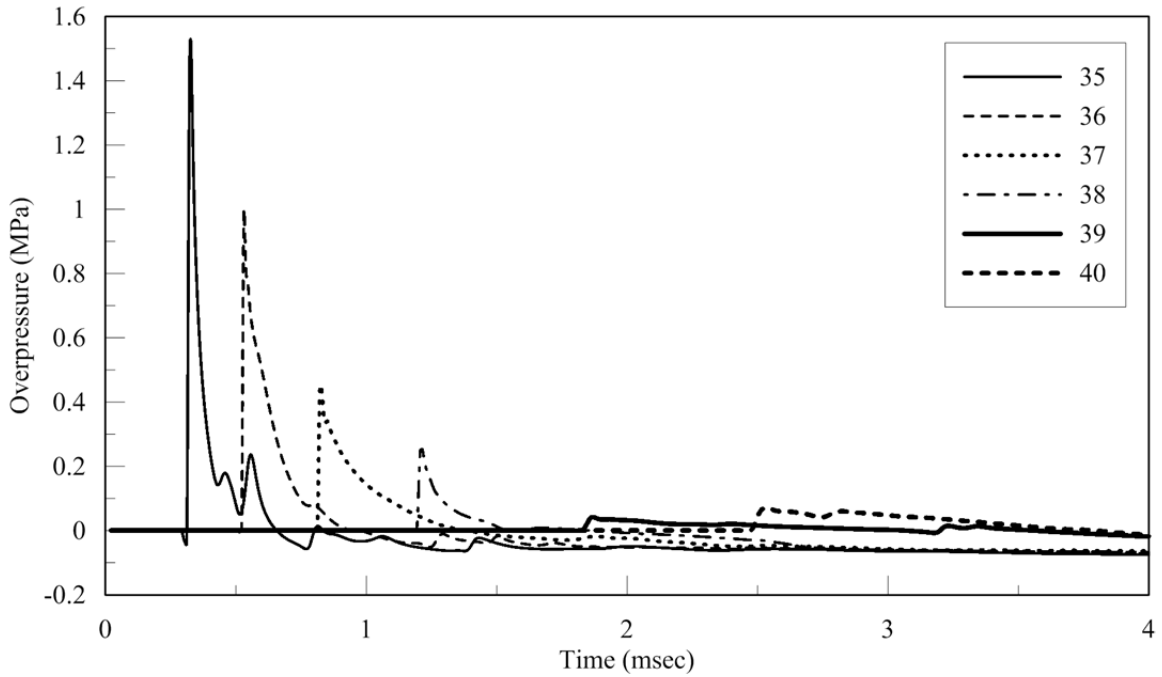


f. Monitoring locations 25, 26, 27, 28, 29 and 30

**Figure 2-74 Reflected overpressure histories; Model VI; spherical charge of 22.68 kg of TNT; JWL EOS (cont.)**

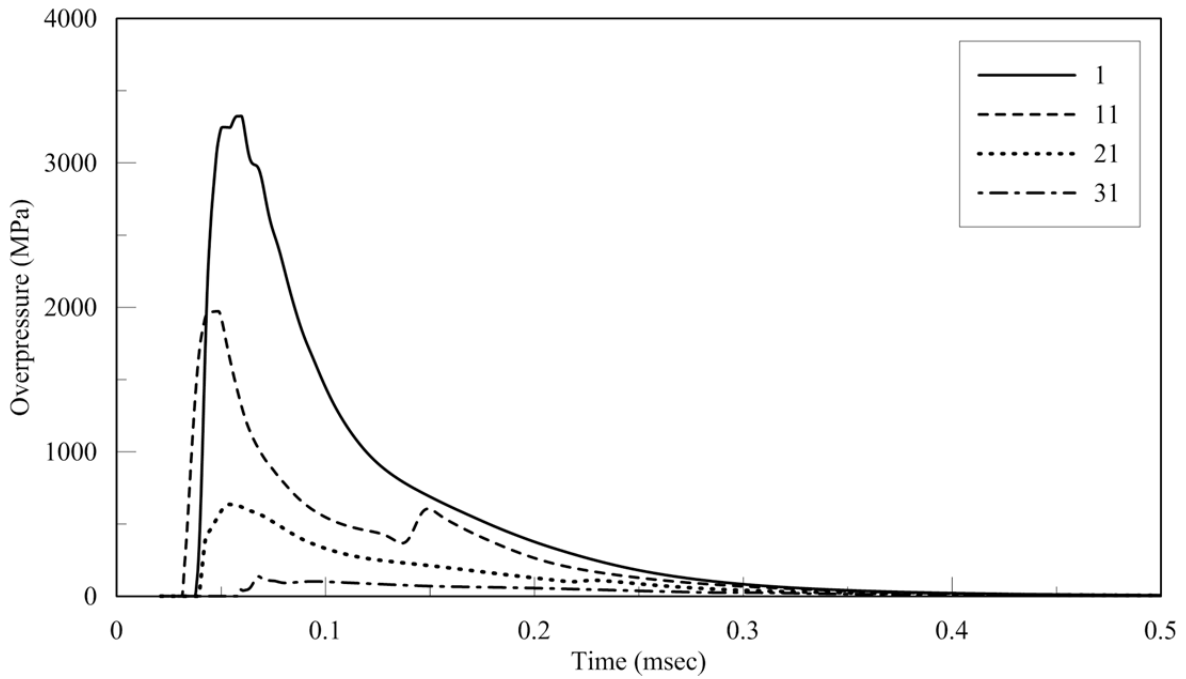


g. Monitoring locations 31, 32, 33 and 34



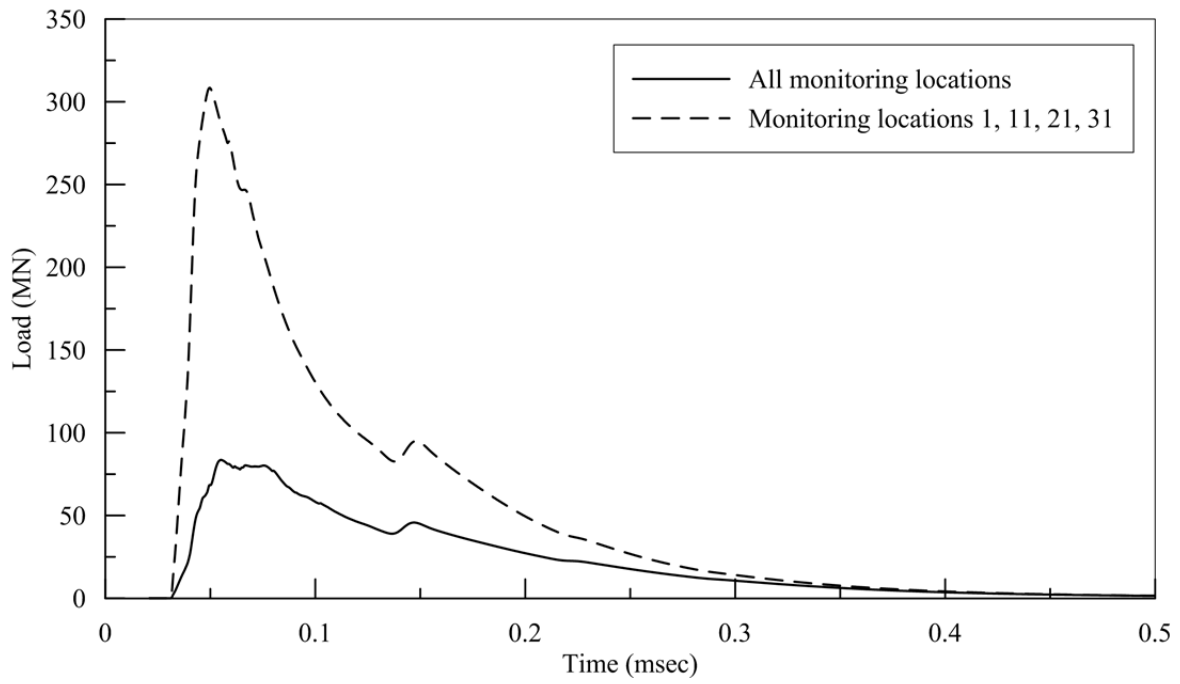
h. Monitoring locations 35, 36, 37, 38, 39 and 40

**Figure 2-74 Reflected overpressure histories; Model VI; spherical charge of 22.68 kg of TNT; JWL EOS (cont.)**

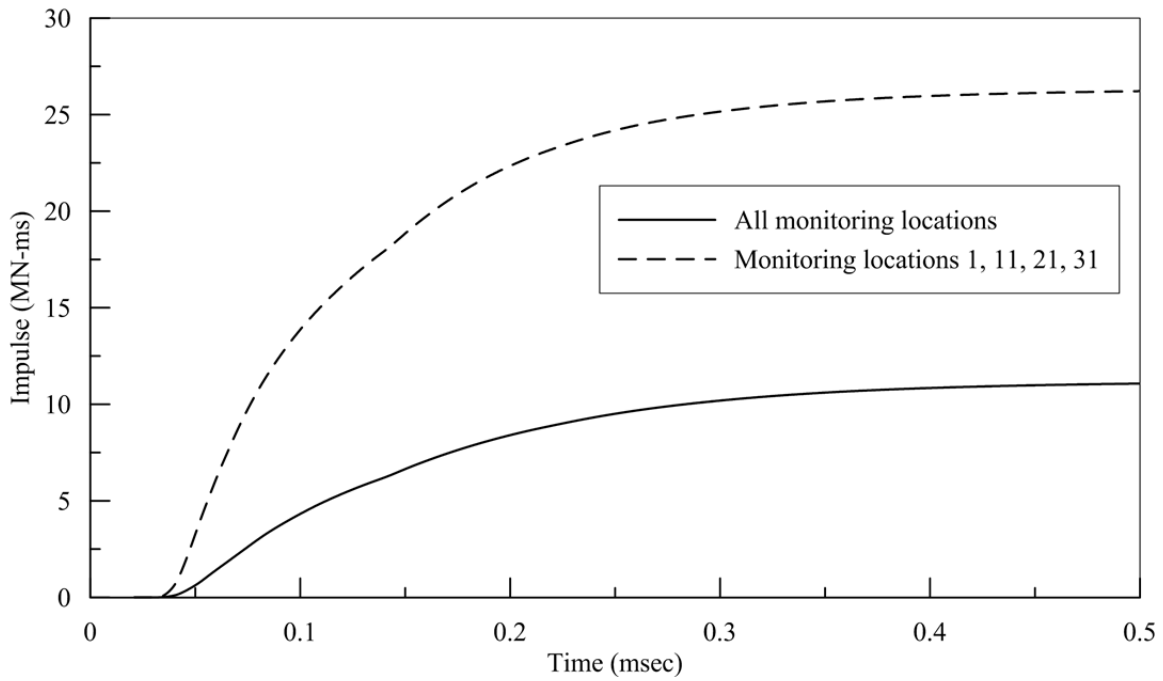


i. Monitoring locations 1, 11, 21 and 31

**Figure 2-74 Reflected overpressure histories; Model VI; spherical charge of 22.68 kg of TNT; JWL EOS (cont.)**

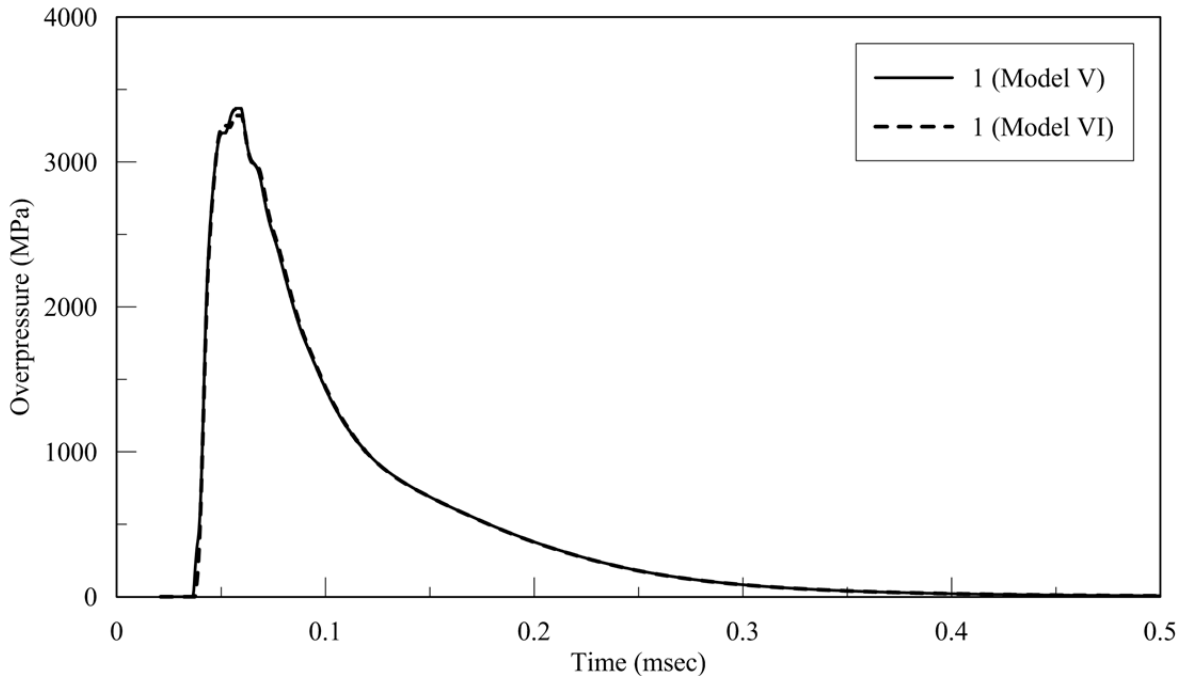


a. Net loading

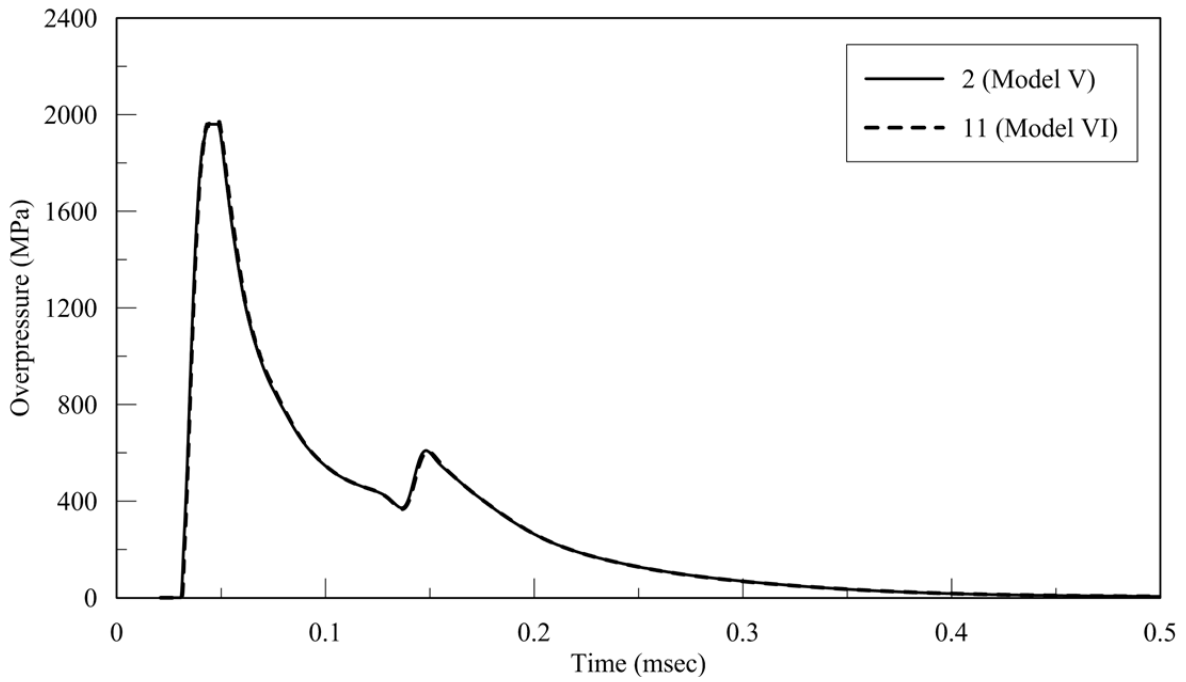


b. Impulse history

**Figure 2-75 Net loading and impulse histories; Model VI**

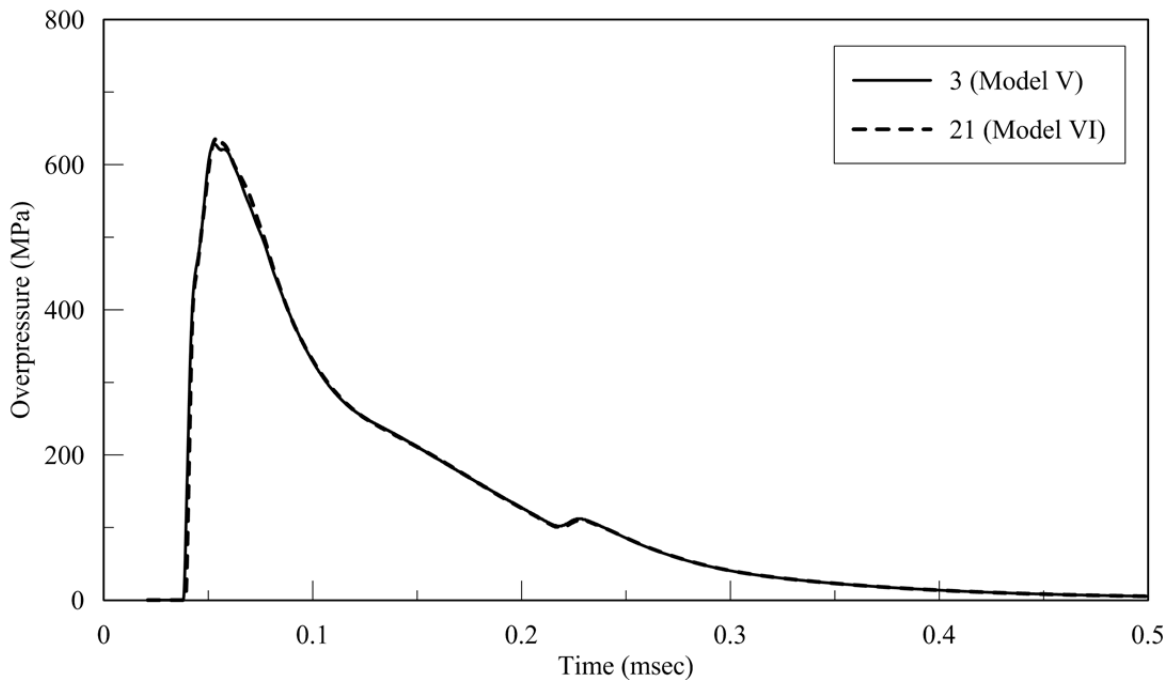


a. Monitoring locations 1 (Model V) and 1 (Model VI)

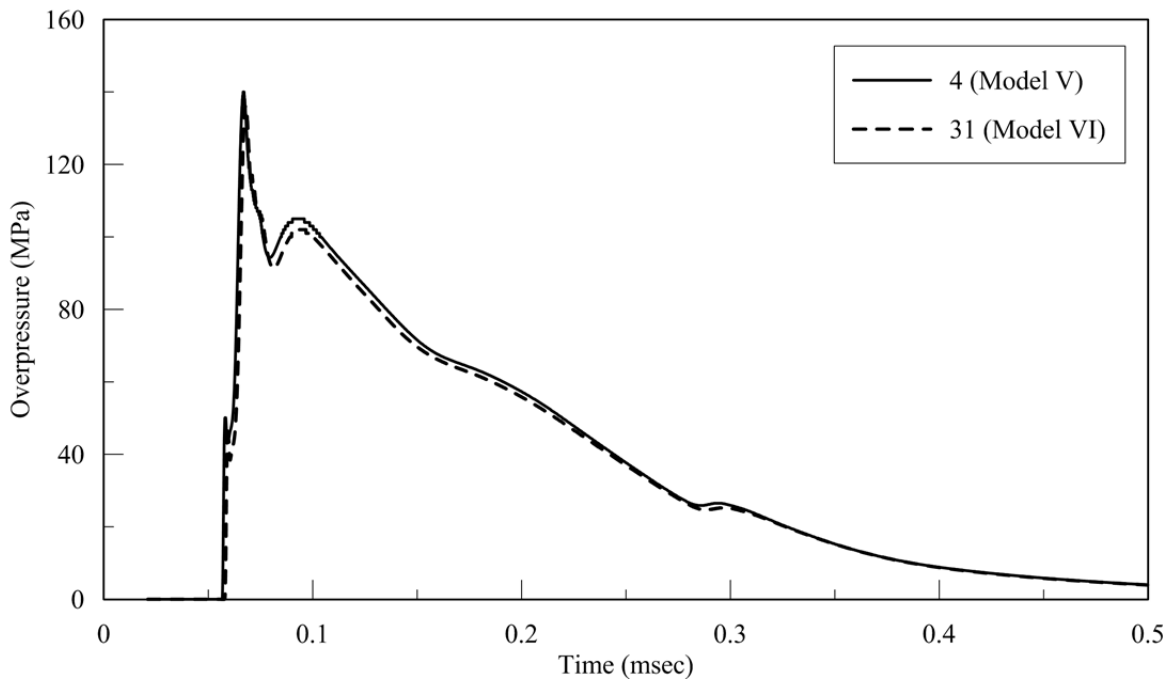


b. Monitoring locations 2 (Model V) and 11 (Model VI)

**Figure 2-76 Comparison of reflected overpressure histories from Models V and VI**



c. Monitoring locations 3 (Model V) and 21 (Model VI)



d. Monitoring locations 4 (Model V) and 31 (Model VI)

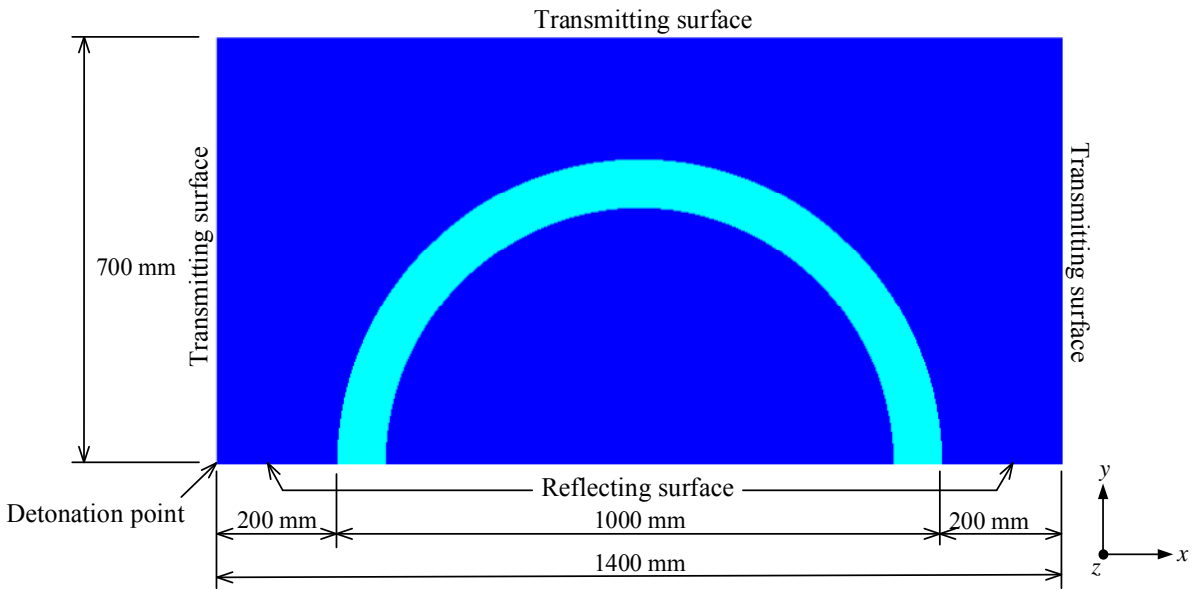
**Figure 2-76 Comparison of reflected overpressure histories from Models V and VI (cont.)**

### **2.7.3 Circular Column, Model VII**

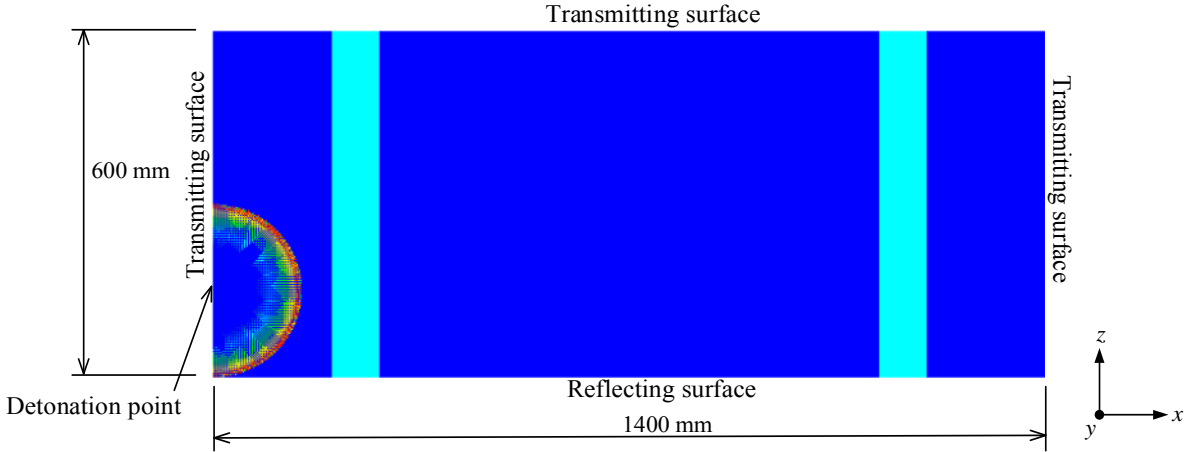
Figure 2-77 presents a plan view and an elevation of Model VII. The  $x$ - $y$ - $z$  coordinate system is shown. The transmitting  $y$ -boundary is set at  $y = 700$  mm: 200 mm beyond the face of the column. The transmitting  $z$ -boundary is set at  $z = 600$  mm. Figure 2-78 presents the monitoring locations. There are eight monitoring locations around the half-perimeter of the column. The  $y$  coordinates of monitoring locations 1 through 8 are 0, 160, 320, 480, 480, 320, 160 and 0 mm. Monitoring locations 9 through 16, 17 through 24, and 25 through 32 align vertically with monitoring locations 1 through 8, respectively, but are 149 mm, 298 mm and 447 mm above the ground surface, respectively. A cell size of 4 mm is used for the analysis per Section 2.7.2.

Figure 2-79 presents reflected pressure histories at all 32 monitoring locations. The pressures are greatest on the lines 1 through 25 and 2 through 26 (see Figure 2-78a), and (relatively) insignificant elsewhere, as expected. A comparison of the reflected peak overpressure histories at monitoring locations 9 (opposite to the center of the charge) and 28 [25], on the front face of the column, shows a difference of a factor greater than 245 [13], which is due to differences in scaled distance and angle of incidence.

Figure 2-80 presents net loading and impulse histories on the front face of the column calculated using a) overpressure history at locations 1, 9, 17 and 25, applied across the width of the column using tributary heights, and b) overpressure history at all monitoring locations on the front face, applied using tributary areas. For the calculations of the net loading and impulse histories for the circular column, Model VII, only translational ( $x$ ) loads in the direction of blast waves are considered. The peak load (impulse) calculated considering all locations is 4.7 (3.5) times smaller than that calculated based on pressure histories at locations 1, 9, 17 and 25 only. Similar to the analysis of the square column, Model VI, and at the scaled distance of  $0.071 \text{ m/kg}^{1/3}$ , discretization of the front face of a circular column will result in significantly smaller net loads (79% reduction here) and impulses (72% reduction here). These differences in the reflected overpressures and impulses are more substantial for the circular shape of column than that of the square shape.

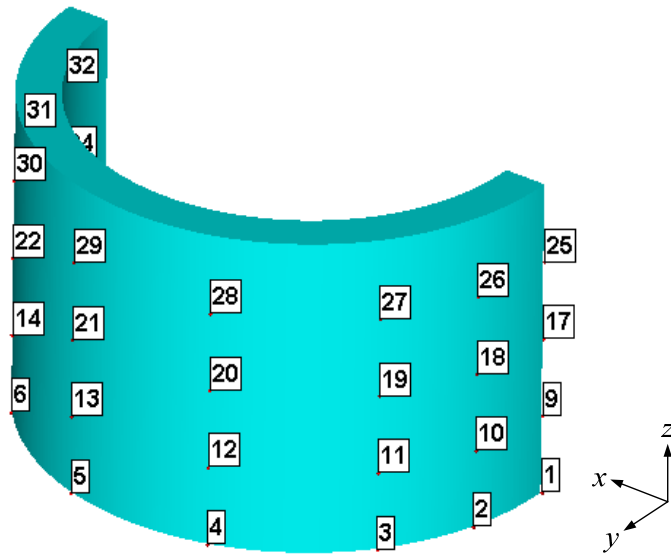


a. Plan view

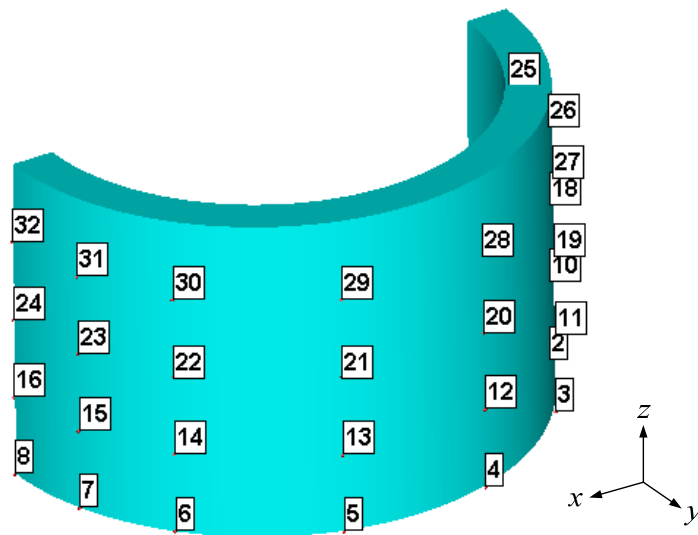


b. Elevation view

**Figure 2-77 Model VII; spherical charge of 22.68 kg of TNT; 1000 mm diameter column**

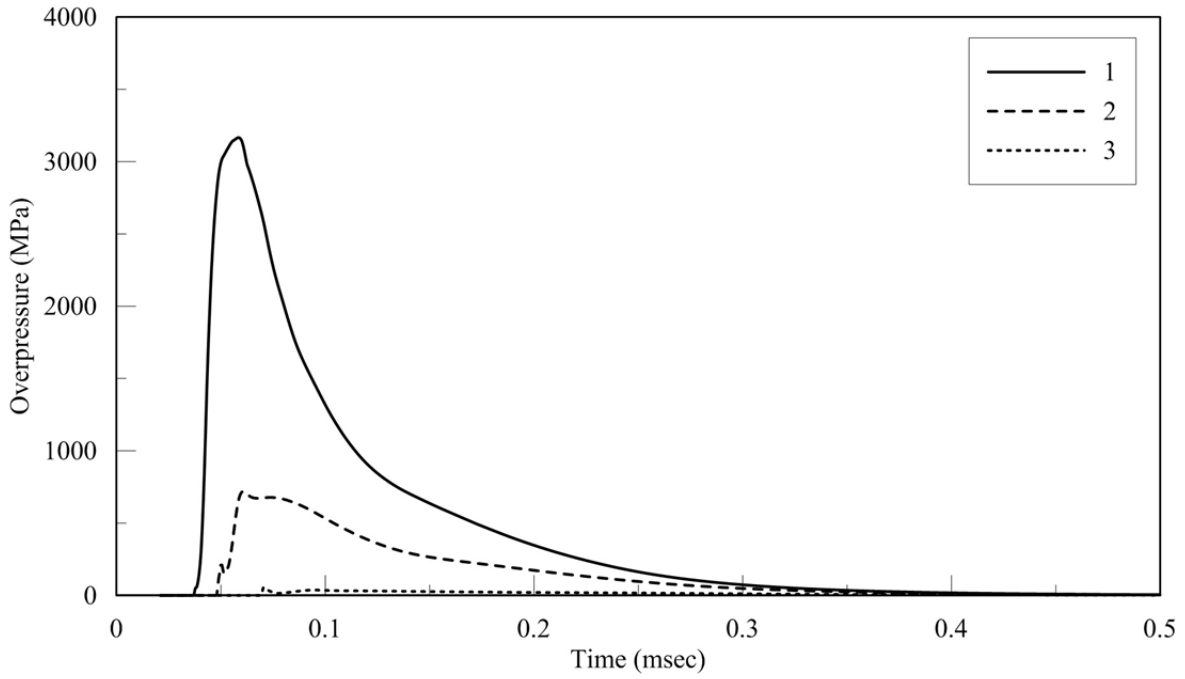


a. View 1

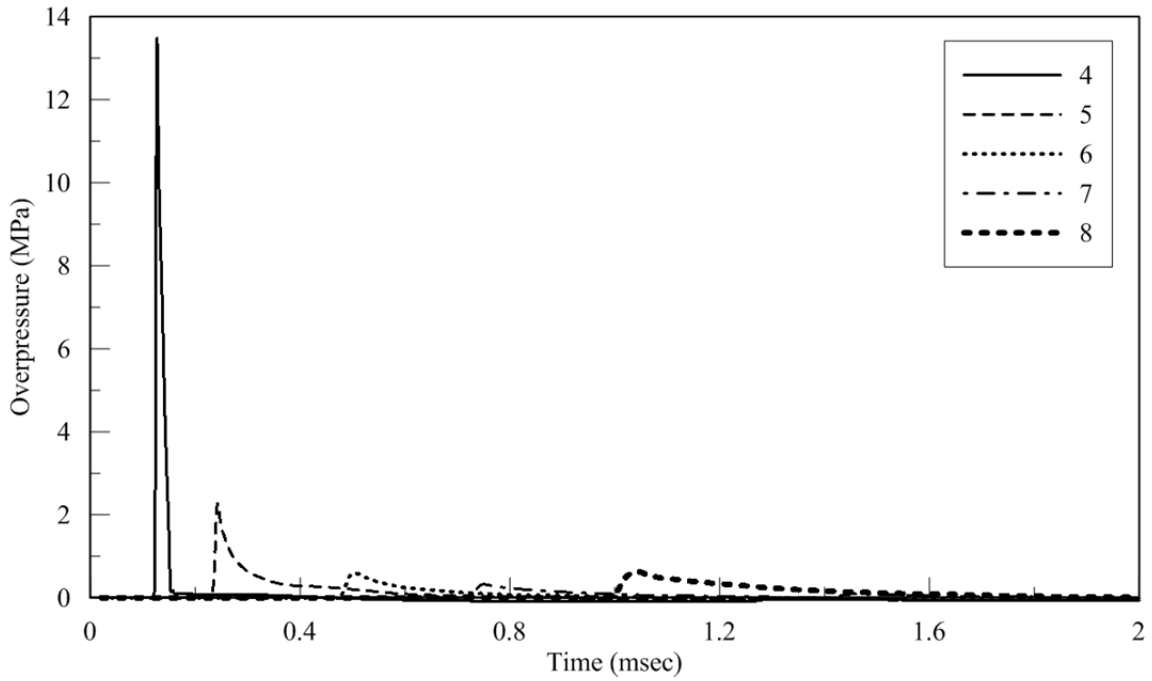


b. View 2

**Figure 2-78 Monitoring locations for Model VII; spherical charge of 22.68 kg of TNT; 1000 mm diameter column**

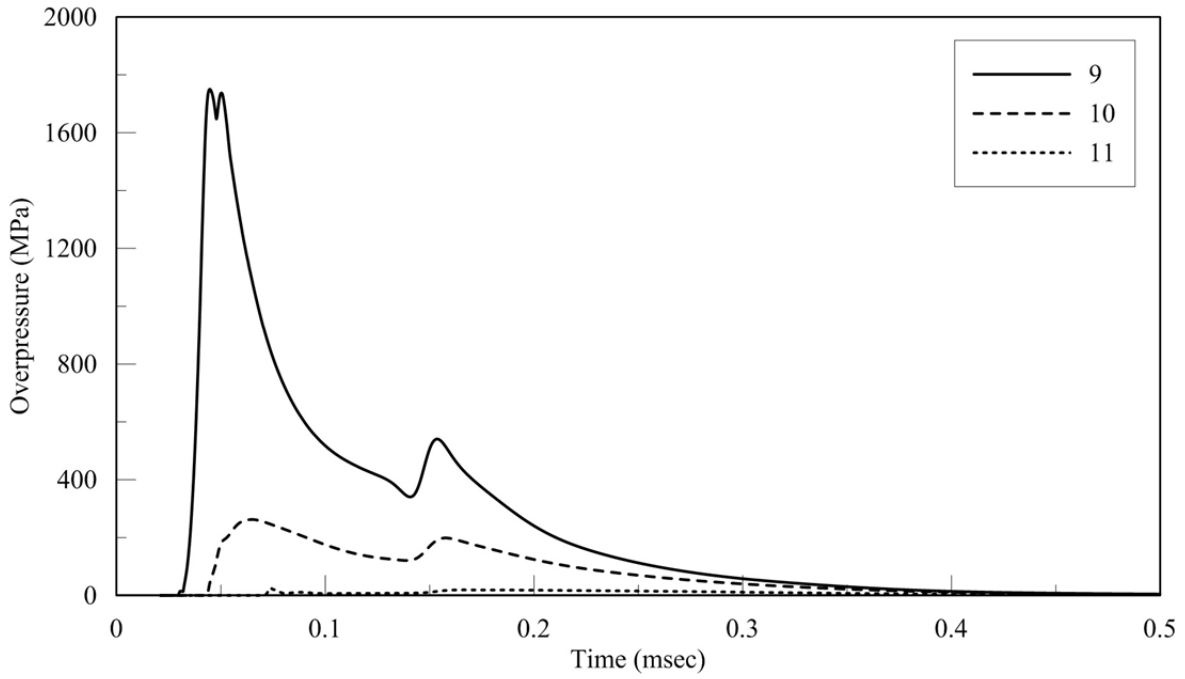


a. Monitoring locations 1, 2, and 3

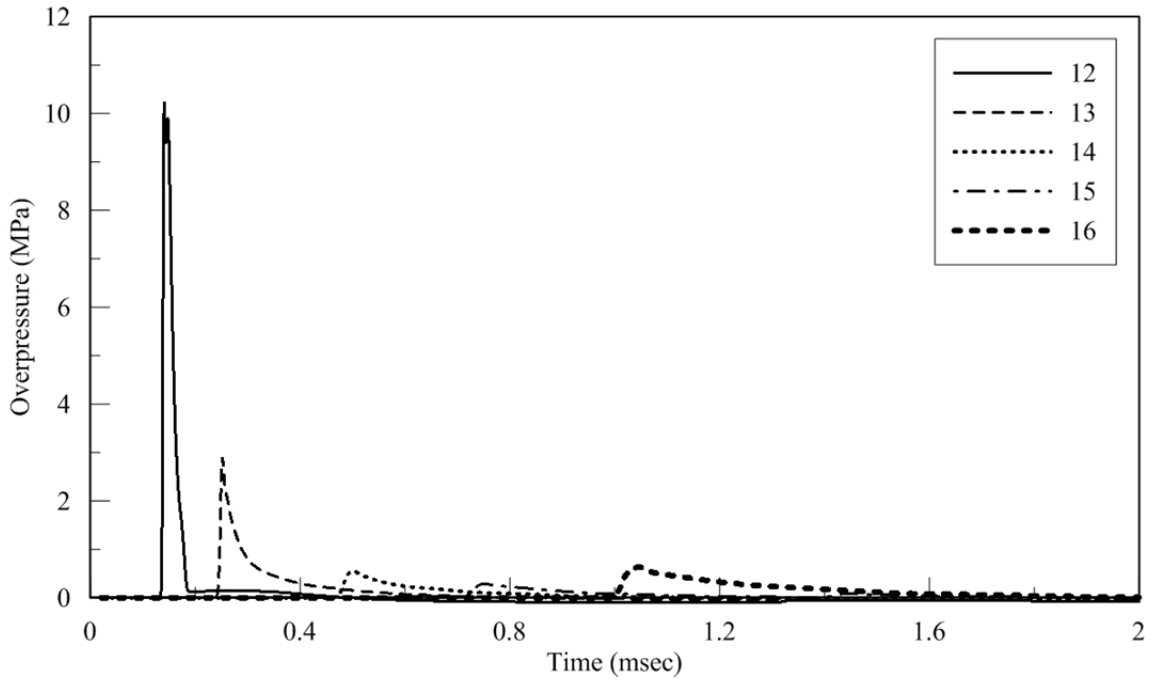


b. Monitoring locations 4, 5, 6, 7, and 8

**Figure 2-79 Reflected overpressure histories; Model VII; spherical charge of 22.68 kg of TNT; JWL EOS**

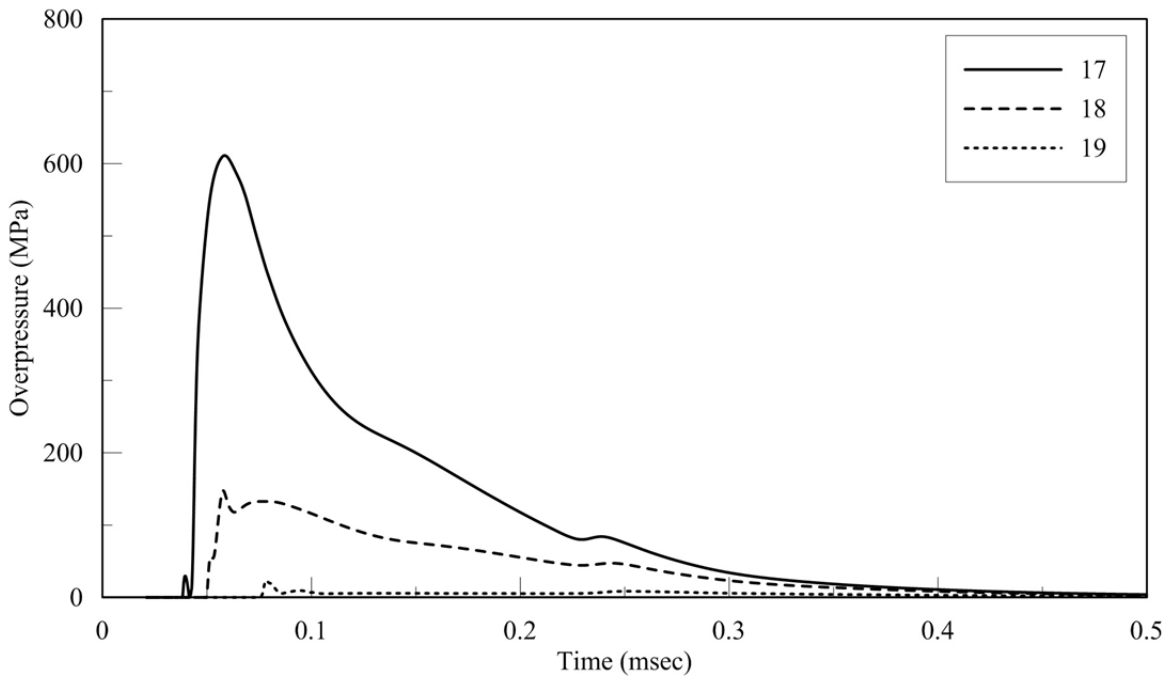


c. Monitoring locations 9, 10 and 11

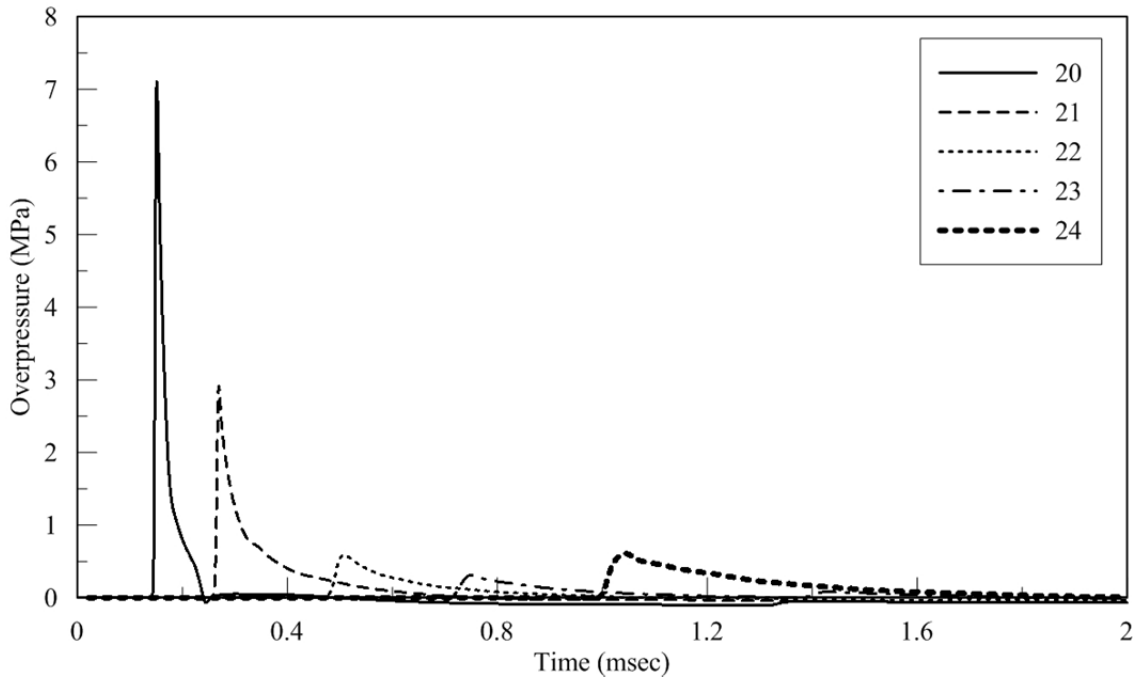


d. Monitoring locations 12, 13, 14, 15 and 16

**Figure 2-79 Reflected overpressure histories; Model VII; spherical charge of 22.68 kg of TNT; JWL EOS (cont.)**

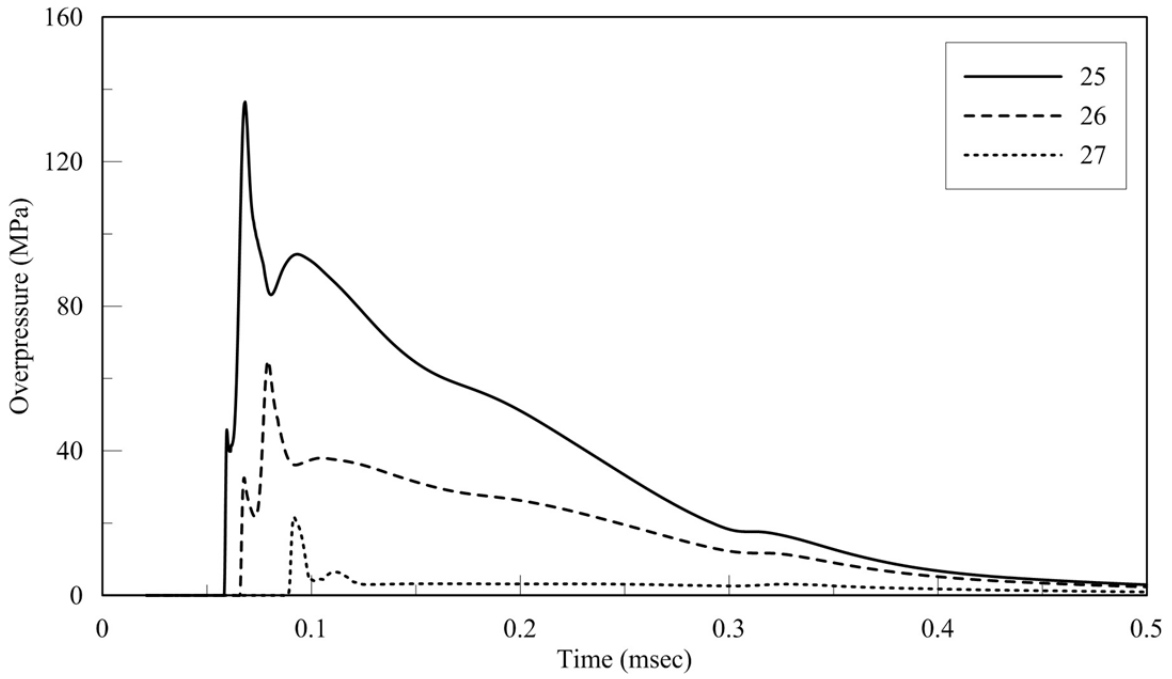


e. Monitoring locations 17, 18 and 19

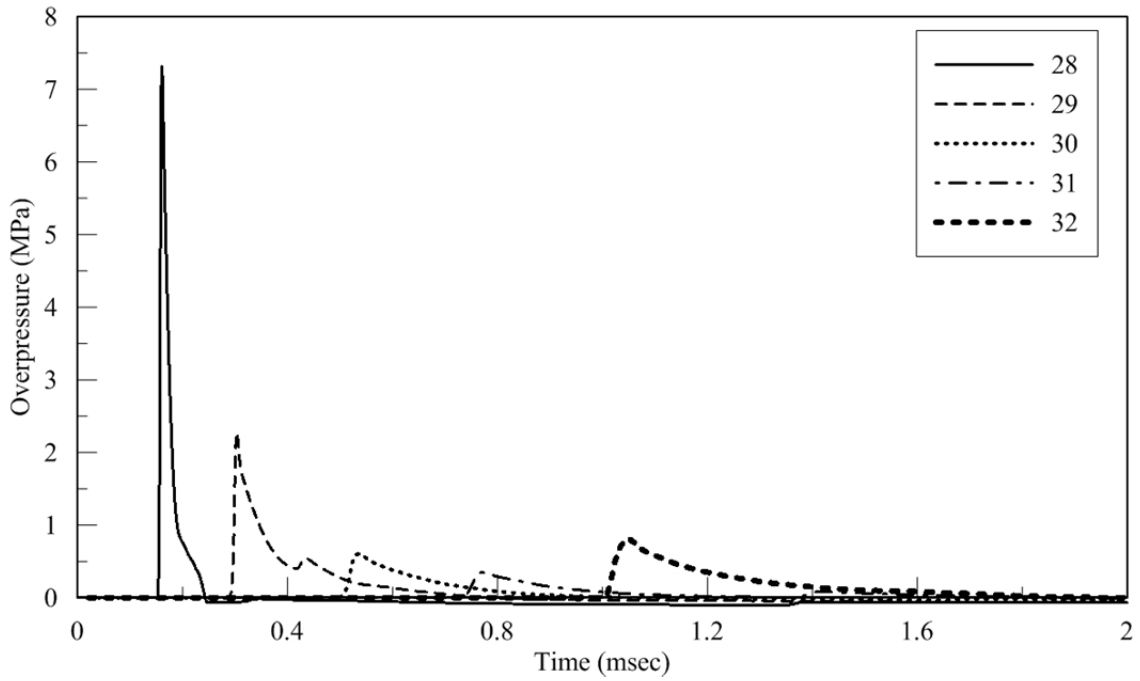


f. Monitoring locations 20, 21, 22, 23 and 24

**Figure 2-79 Reflected overpressure histories; Model VII; spherical charge of 22.68 kg of TNT; JWL EOS (cont.)**

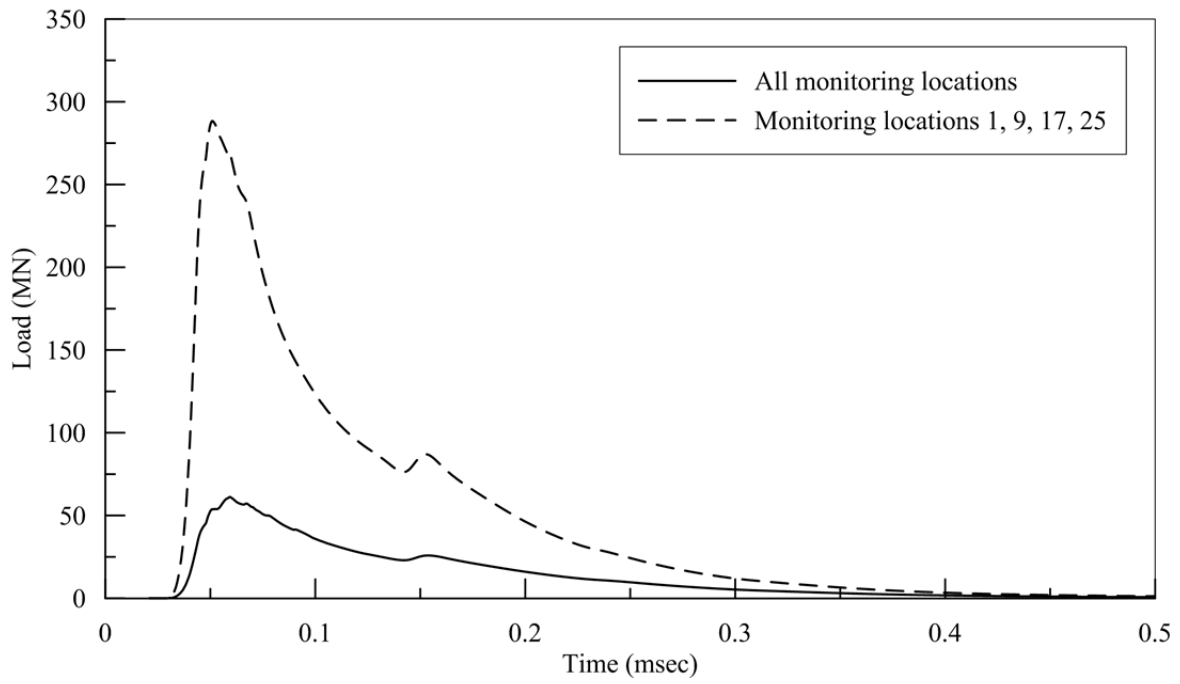


g. Monitoring locations 25, 26 and 27

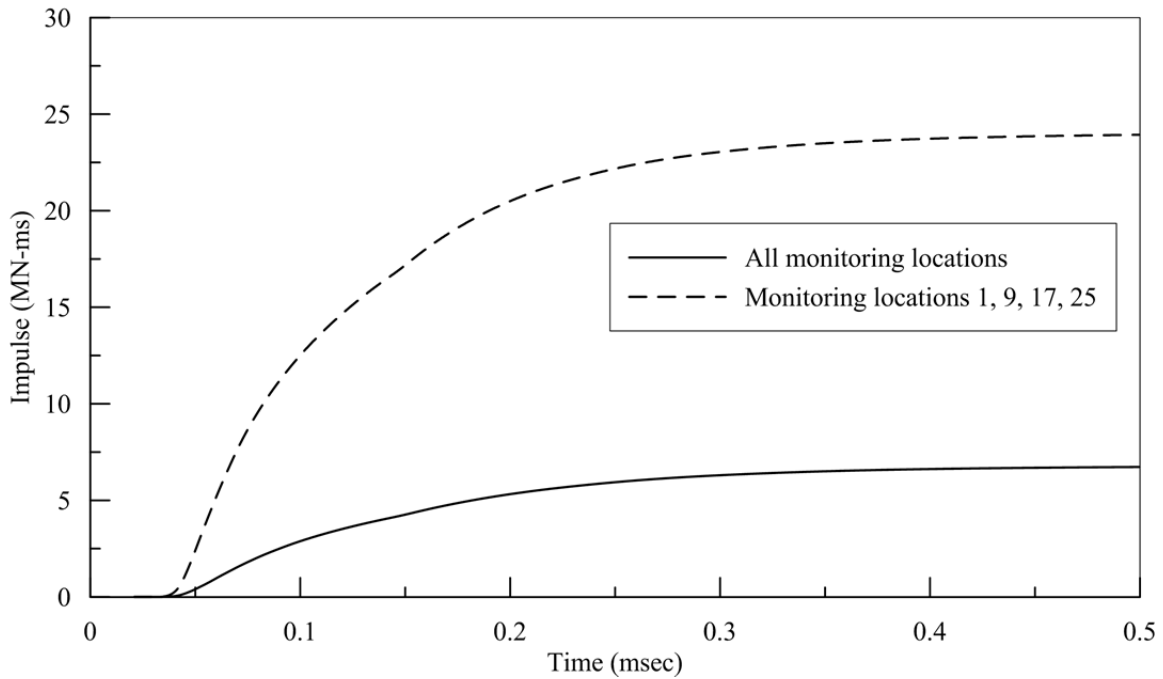


h. Monitoring locations 28, 29, 30, 31, and 32

**Figure 2-79 Reflected overpressure histories; Model VII; spherical charge of 22.68 kg of TNT; JWL EOS (cont.)**



a. Net loading

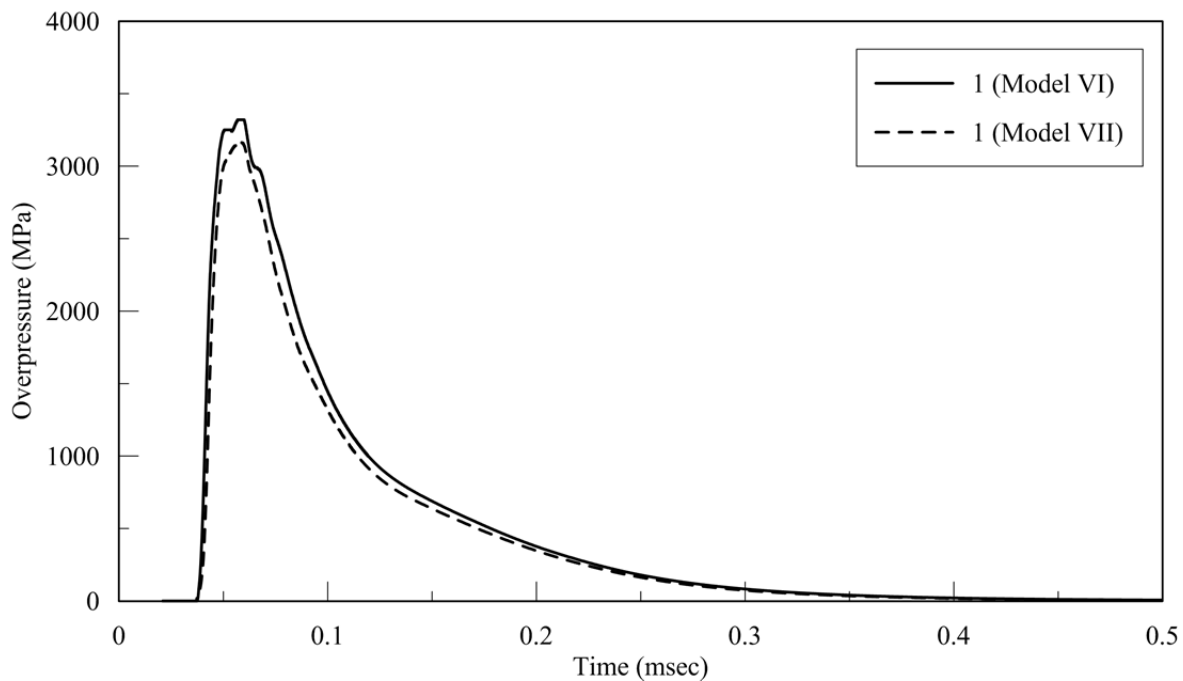


b. Impulse history

**Figure 2-80 Net load and impulse histories; Model VII; spherical charge of 22.68 kg of TNT; JWL EOS**

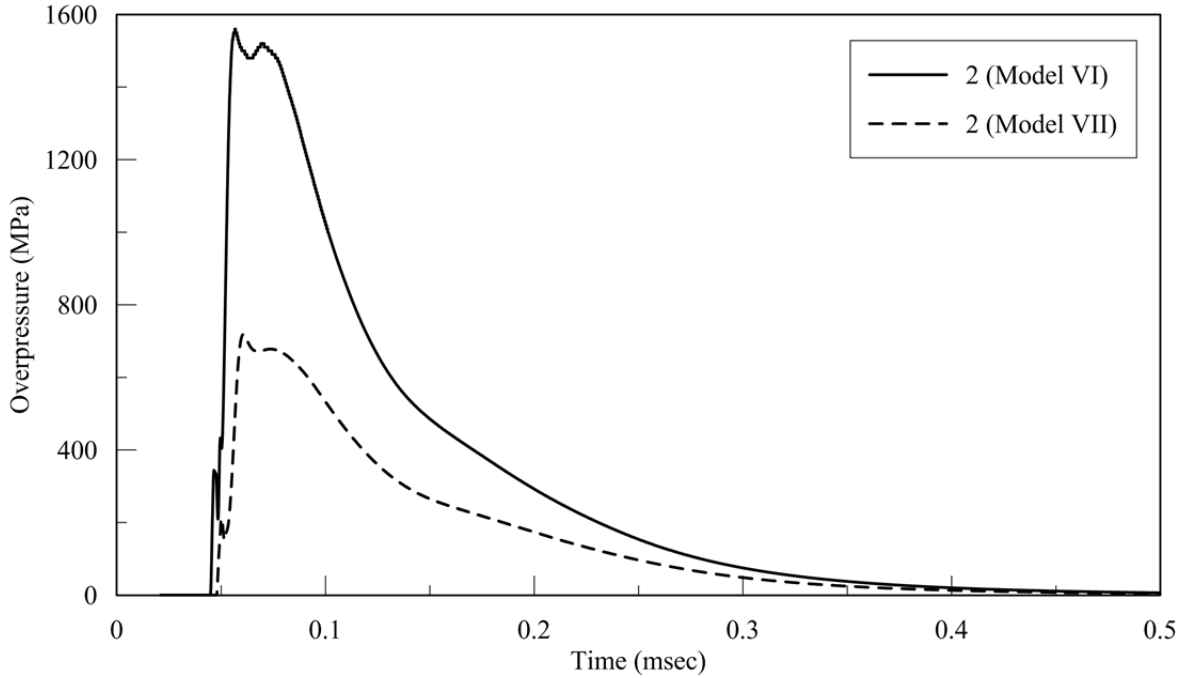
### 2.7.4 Influence of Target Shape on Air-Blast Loadings

Figures 2-81, 2-82, 2-83 and 2-84 enable a comparison of pressures on the front faces of the two columns at 0, 149, 298 and 447 mm, respectively, above the ground surface, and at  $y = 0$ , 160, 320 and 480 mm, respectively. As expected, the overpressure histories at identical locations on the centerline of the two columns are very similar, as shown in Figures 2-81a, 2-82a, 2-83a and 2-84a. Panels c through d of Figures 2-81 through 2-84 show that the column shape has a significant effect on the reflected peak overpressure, with large reductions of the circular shape for a given height and  $y$  dimension, due in part to the increased scaled range and increased angle of incidence.

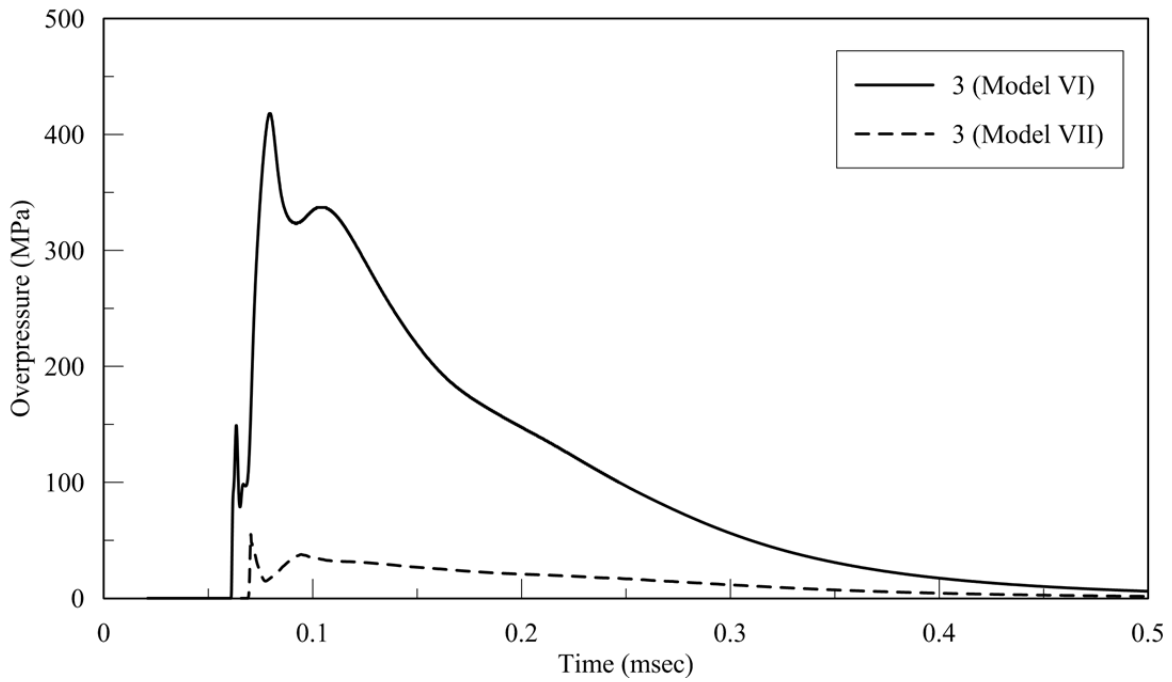


a. Monitoring locations 1 (Model VI) and 1 (Model VII)

**Figure 2-81 Reflected overpressure histories at 0 mm above the ground surface; Models VI and VII; spherical charge of 22.68 kg of TNT; JWL EOS**

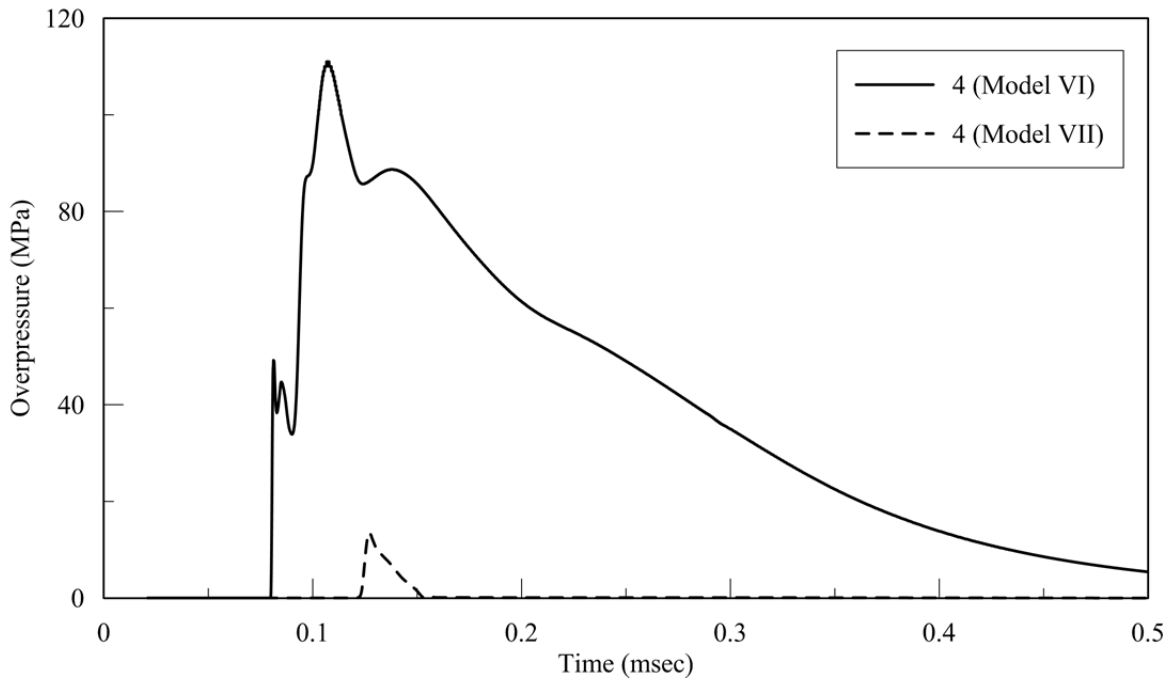


b. Monitoring locations 2 (Model VI) and 2 (Model VII)



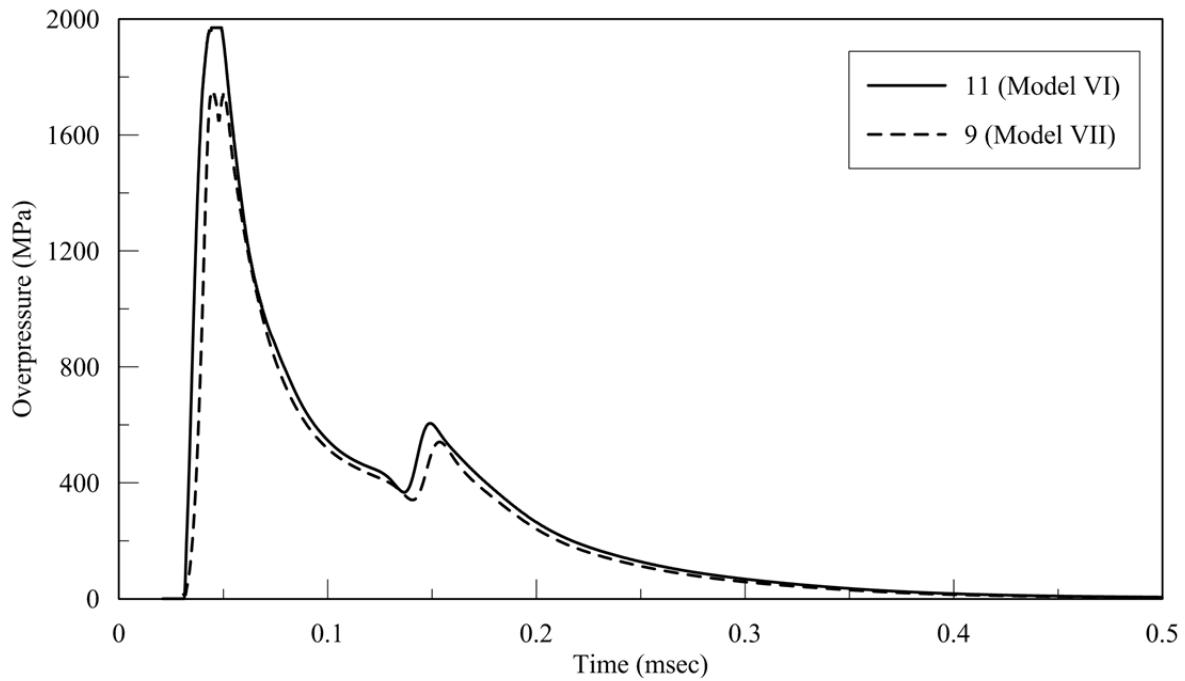
c. Monitoring locations 3 (Model VI) and 3 (Model VII)

**Figure 2-81 Reflected overpressure histories at 0 mm above the ground surface; Models VI and VII; spherical charge of 22.68 kg of TNT; JWL EOS (cont.)**

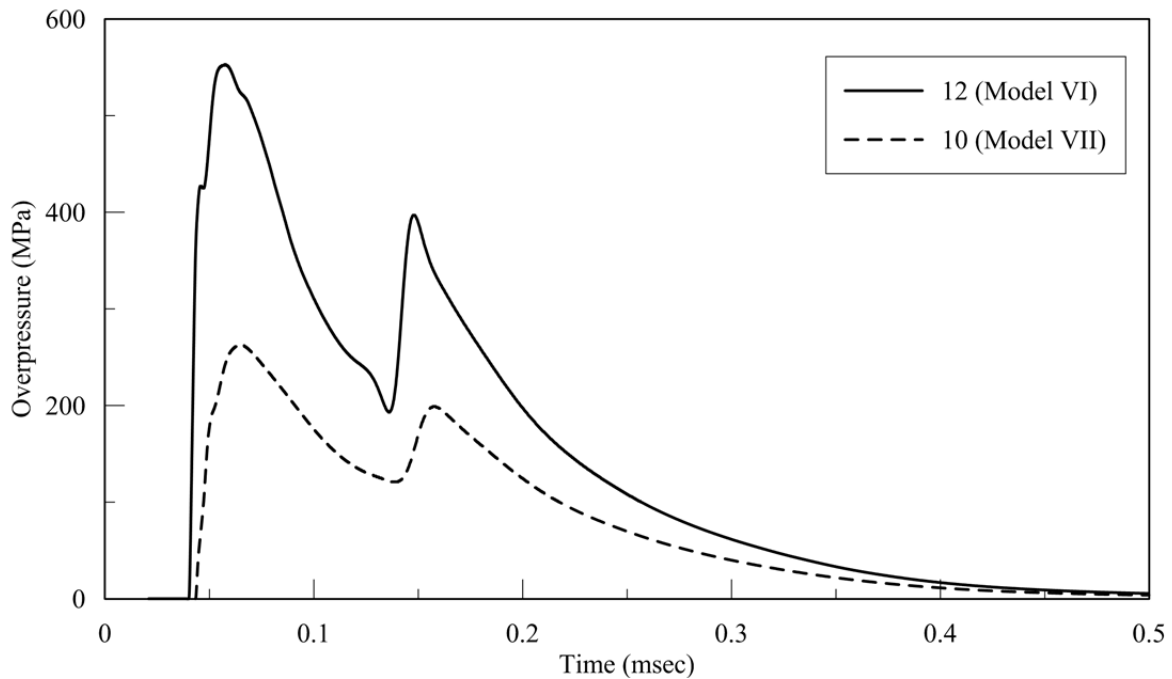


d. Monitoring locations 4 (Model VI) and 4 (Model VII)

**Figure 2-81 Reflected overpressure histories at 0 mm above the ground surface; Models VI and VII; spherical charge of 22.68 kg of TNT; JWL EOS (cont.)**

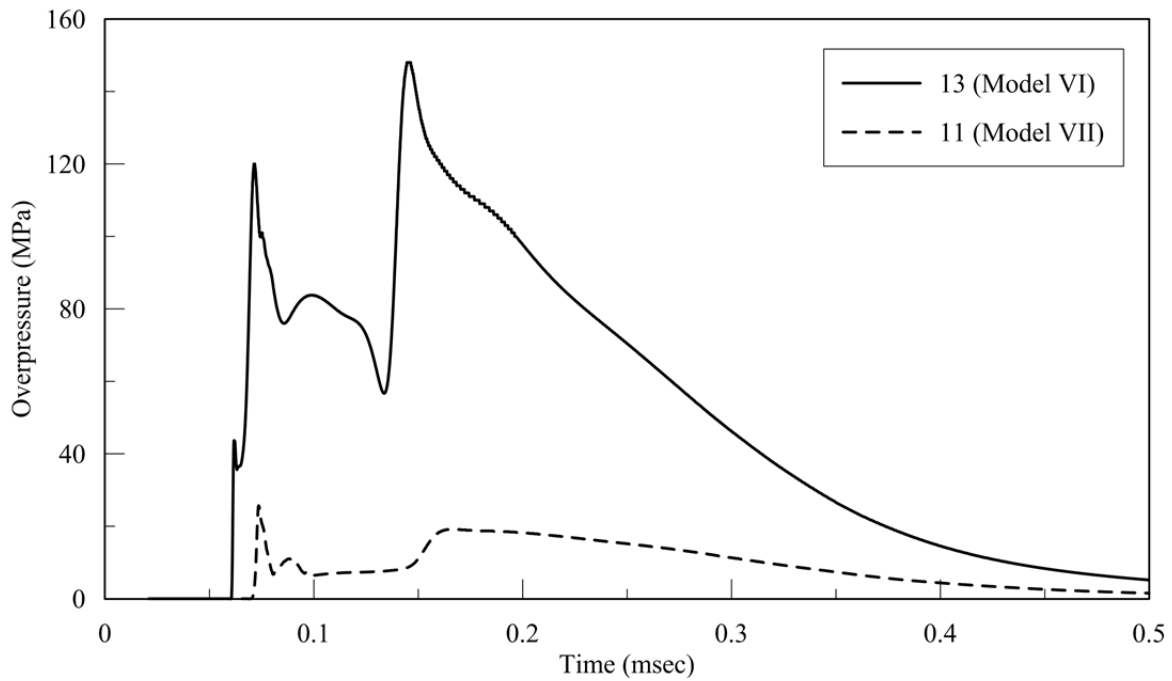


a. Monitoring locations 11 (Model VI) and 9 (Model VII)

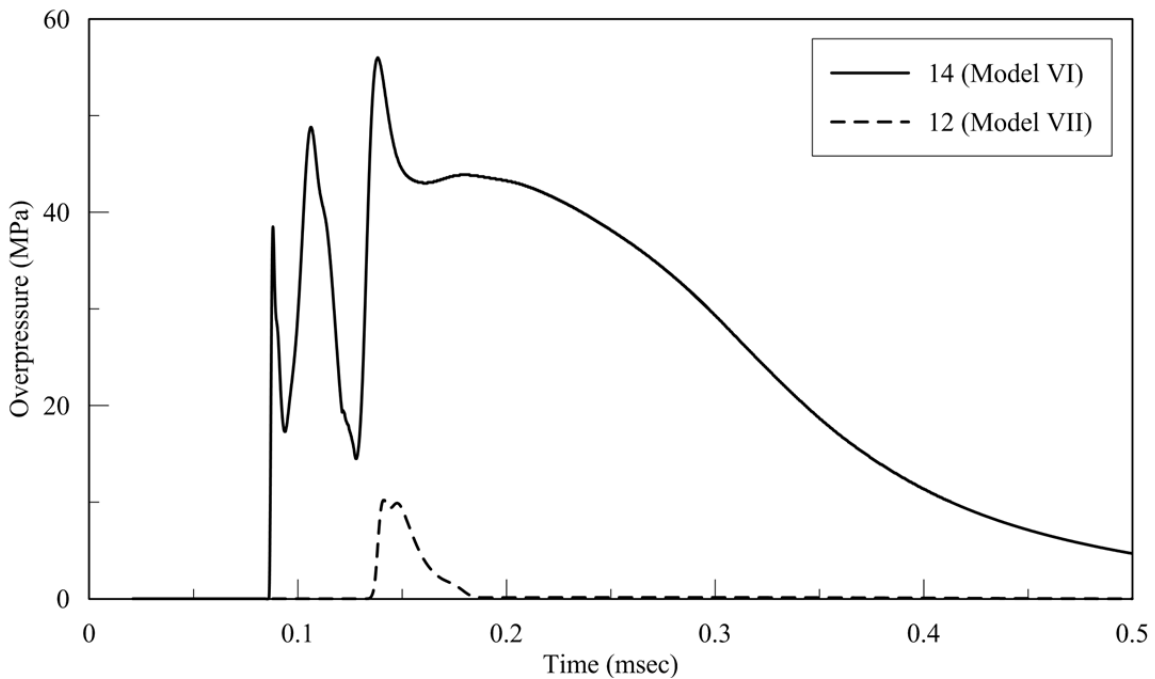


b. Monitoring locations 12 (Model VI) and 10 (Model VII)

**Figure 2-82 Reflected overpressure histories at 149 mm above the ground surface; Models VI and VII; spherical charge of 22.68 kg of TNT; JWL EOS**

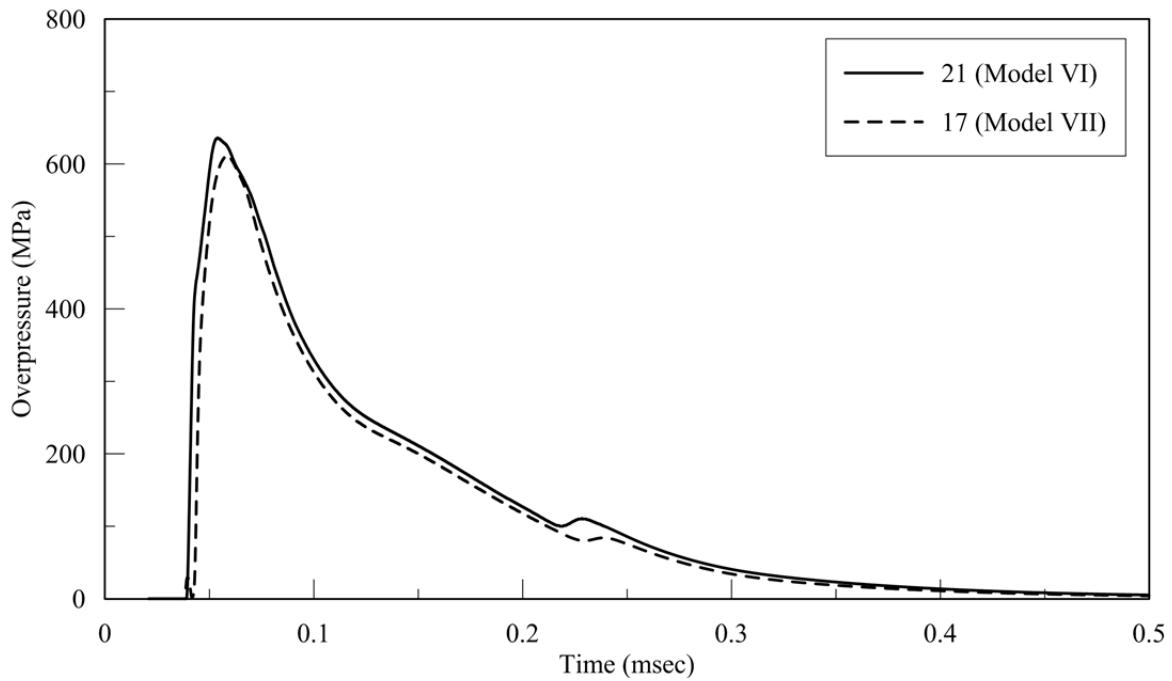


c. Monitoring locations 13 (Model VI) and 11 (Model VII)

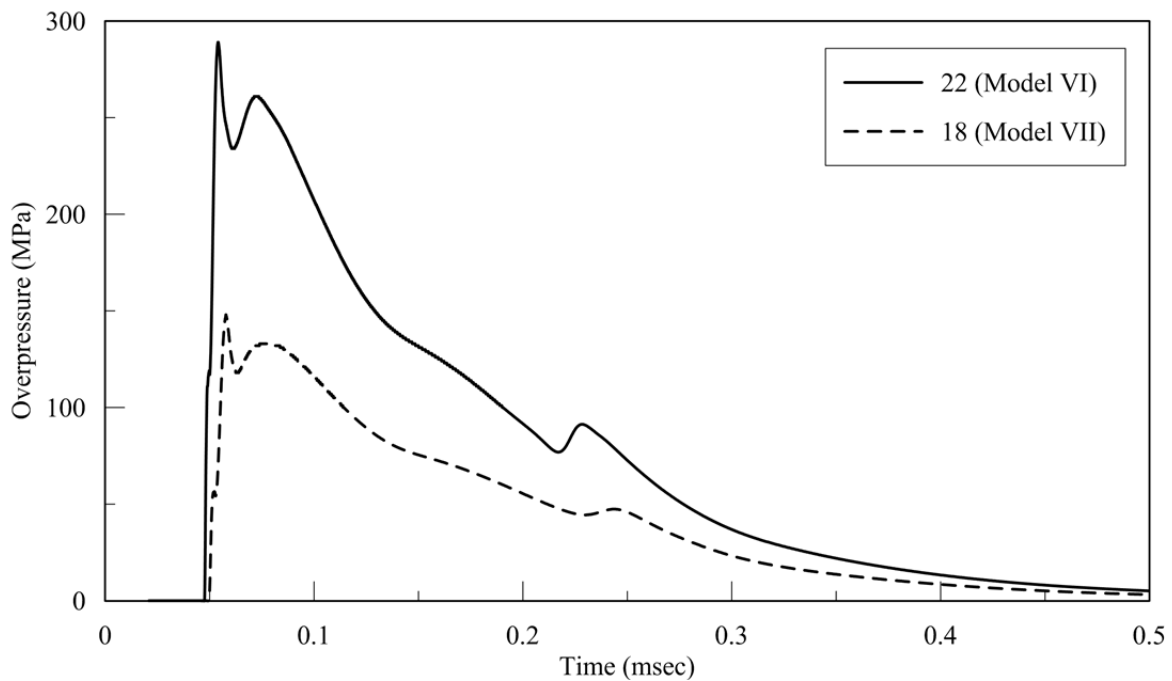


d. Monitoring locations 14 (Model VI) and 12 (Model VII)

**Figure 2-82 Reflected overpressure histories at 149 mm above the ground surface; Models VI and VII; spherical charge of 22.68 kg of TNT; JWL EOS (cont.)**

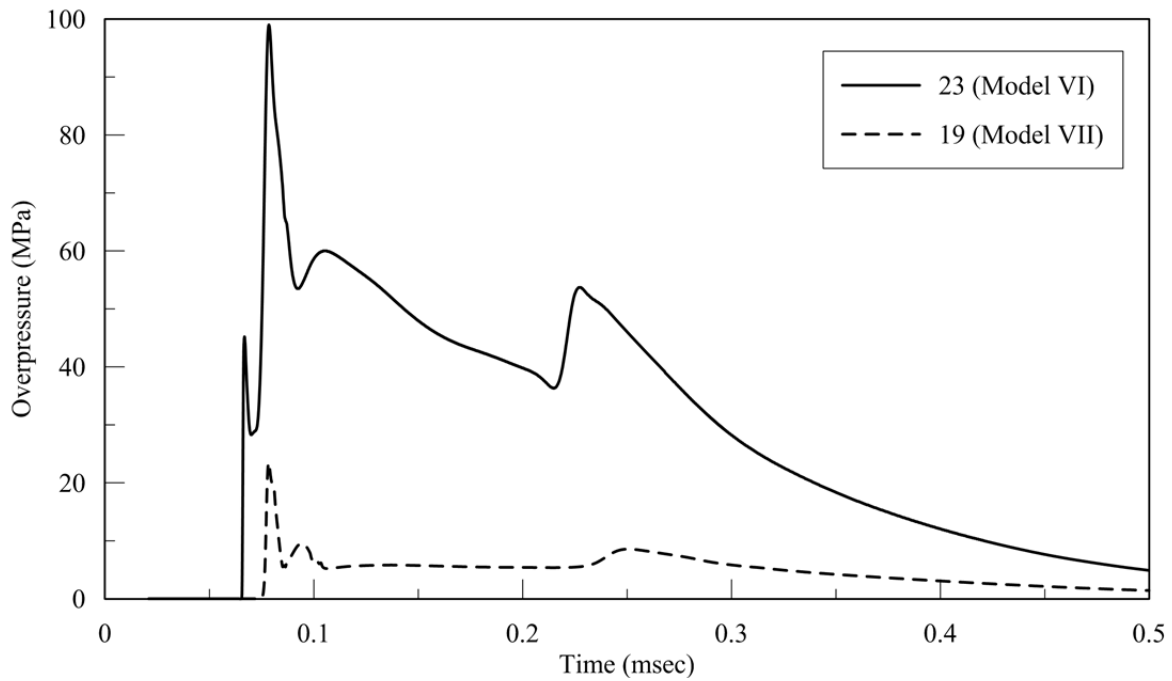


a. Monitoring locations 21 (Model VI) and 17 (Model VII)

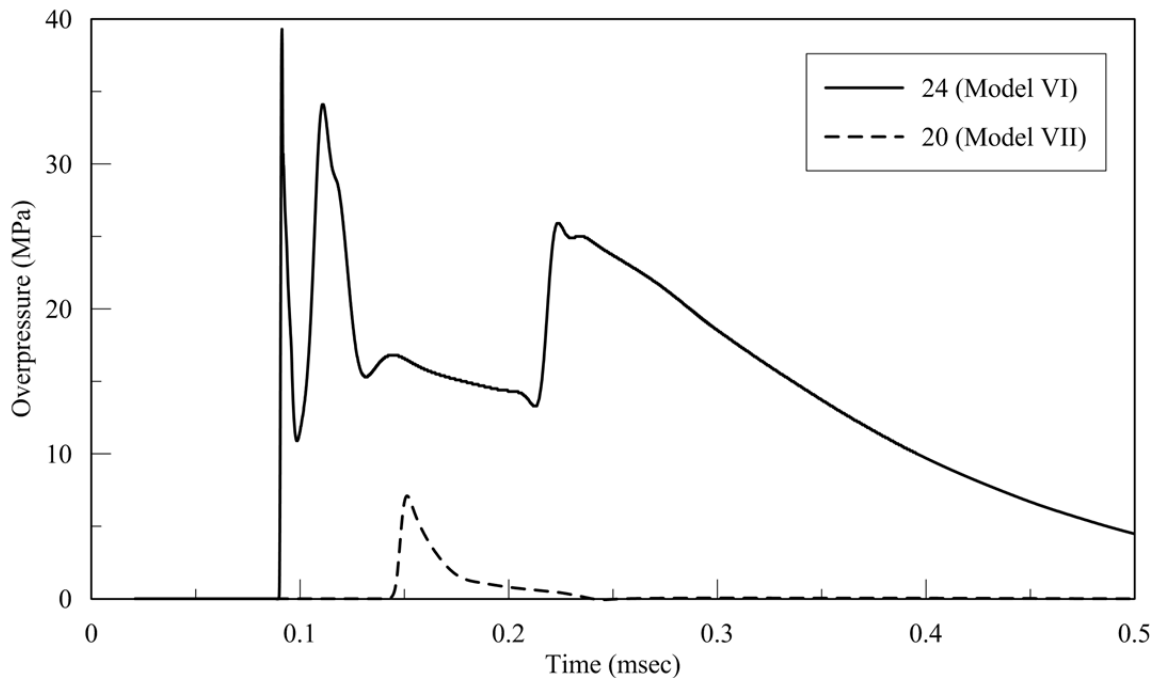


b. Monitoring locations 22 (Model VI) and 18 (Model VII)

**Figure 2-83 Reflected overpressure histories at 298 mm above the ground surface; Models VI and VII; spherical charge of 22.68 kg of TNT; JWL EOS**

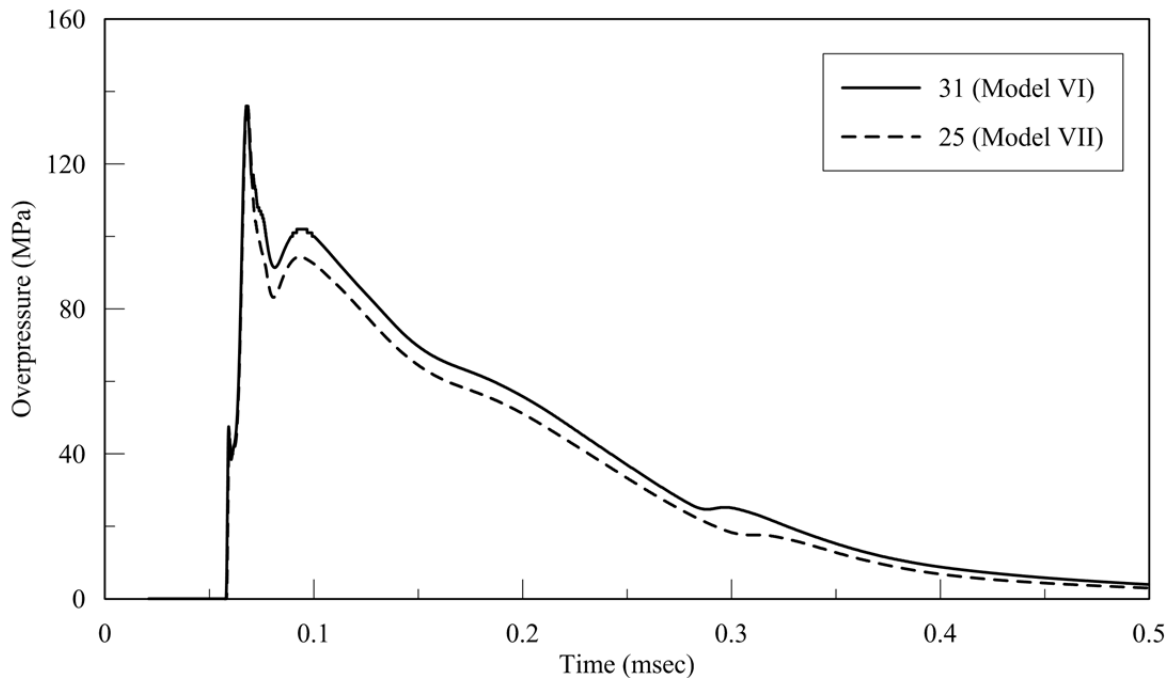


c. Monitoring locations 23 (Model VI) and 19 (Model VII)

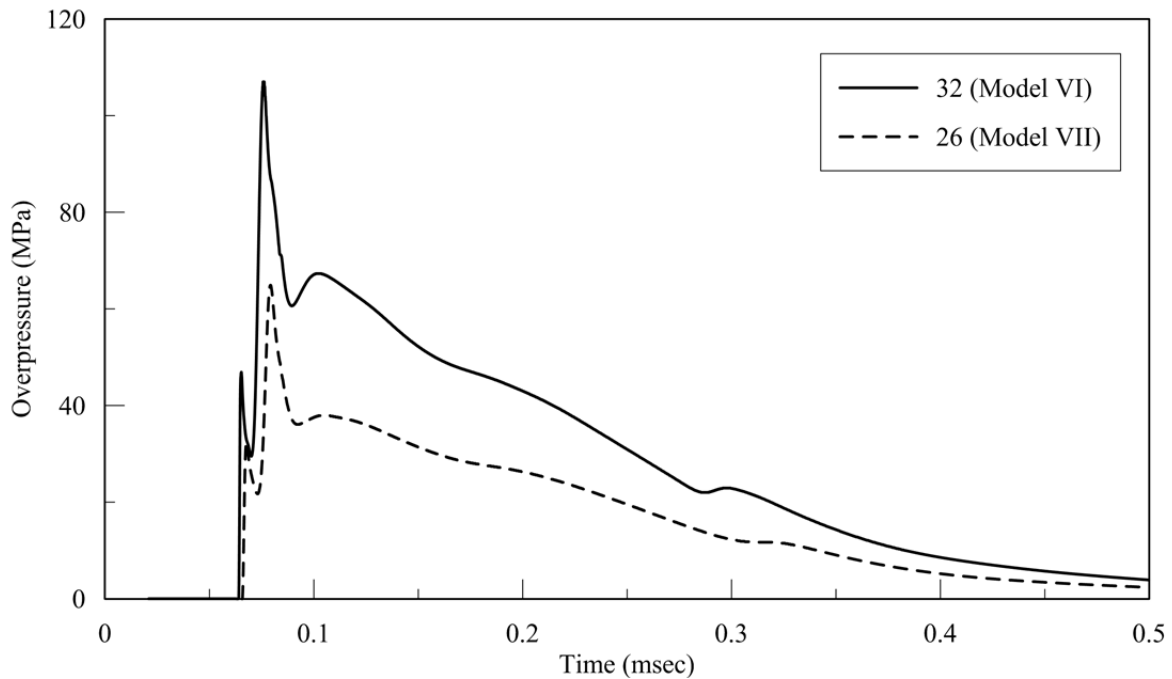


d. Monitoring locations 24 (Model VI) and 20 (Model VII)

**Figure 2-83 Reflected overpressure histories at 298 mm above the ground surface; Models VI and VII; spherical charge of 22.68 kg of TNT; JWL EOS (cont.)**

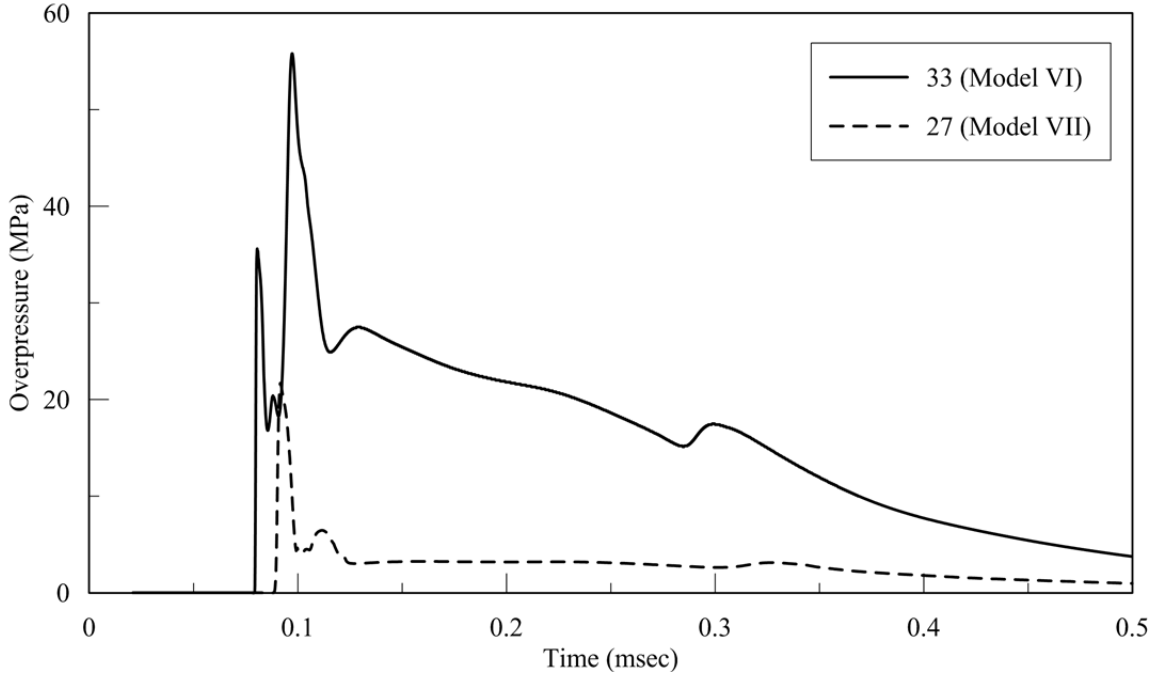


a. Monitoring locations 31 (Model VI) and 25 (Model VII)

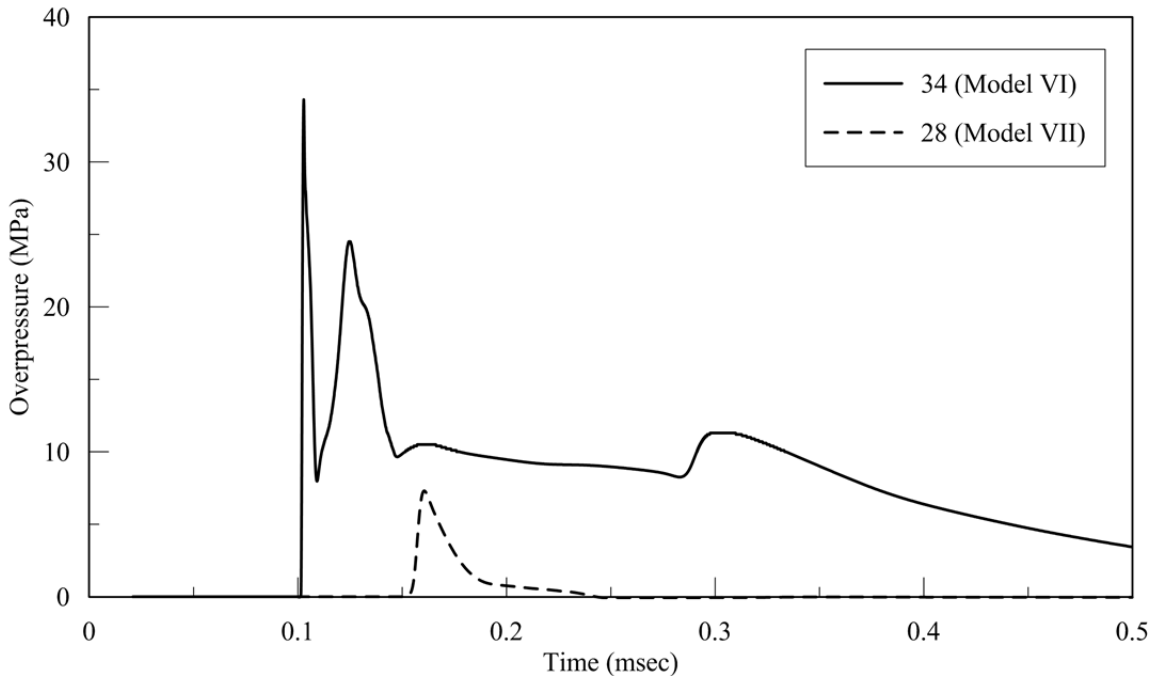


b. Monitoring locations 32 (Model VI) and 26 (Model VII)

**Figure 2-84 Reflected overpressure histories at 447 mm above the ground surface; Models VI and VII; spherical charge of 22.68 kg of TNT; JWL EOS**



c. Monitoring locations 33 (Model VI) and 27 (Model VII)



d. Monitoring locations 34 (Model VI) and 28 (Model VII)

**Figure 2-84 Reflected overpressure histories at 447 mm above the ground surface; Models VI and VII; spherical charge of 22.68 kg of TNT; JWL EOS (cont.)**

## SECTION 3

### INCIDENT AND NORMALLY REFLECTED OVERPRESSURE AND IMPULSE FOR DETONATIONS IN FREE AIR

#### 3.1 Blast-Resistant Design

Typical blast-resistant design practice, in the United States, United Kingdom, Australia, Canada, and elsewhere involves the use of empirical air-blast relationships developed by Kingery and his co-workers (Kingery and Pannill 1964, Kingery 1966, Kingery and Bulmash 1984). These relationships are presented as charts for spherical free-air and hemispherical surface bursts of TNT. The Kingery and Bulmash (KB) charts<sup>4</sup> are based on high order polynomials (Kingery and Bulmash 1984) that express incident and normally reflected overpressures, incident and normally reflected impulses, arrival time and other blast wave parameters as a function of scaled distance,  $Z$ .

#### 3.2 Air-Blast Parameter Studies

##### *3.2.1 Kingery and Pannill, 1964: Hemispherical TNT Surface Bursts*

Kingery and Pannill (1964) compiled and processed incident overpressure measurements from surface detonations of hemispheres of TNT with weights of 5, 20 and 100 tons. The tests were performed at the Suffield Experimental Station (SES), Alberta Canada. The 5, 20 and 100 ton shots were executed in 1959, 1960, and 1961, respectively.

Kingery and Pannill noted that the raw data (which is not readily available) was reported in Groves (1961), a 1961 SES internal report, Kingery et al. (1962), James (1962) and internal correspondence between Kingery and his SES colleagues. Information on the instrumentation used is not described by these authors beyond "...overpressure versus time gages and [a] photo-optical shock front velocity technique..." The gages and the photo-optical technique enable a calculation of the shock front arrival time and the shock front velocity. The calculated velocity

---

<sup>4</sup> The Kingery and Bulmash charts are reproduced in Appendix D in SI and US units. The air-blast parameters identified in the legend are defined in Section 1.4.

was input to the Rankine-Hugoniot equations to estimate incident peak overpressure. It is not clear if any direct measurements were made of incident peak overpressure. The authors do not report the range of scaled distance over which shock front velocities were measured.

Kingery and Pannill developed an equation for the relationship between incident peak overpressure and scaled distance. Two hundred and seventy three data (likely indirect measurements of peak overpressure) were used to develop an eighth order polynomial: forty five data from the 5-ton shot, one hundred and forty data from the 20-ton shot, and eighty eight data from the 100-ton shot. The authors performed a rudimentary statistical analysis of the proposed polynomial to characterize its ability to recover the inferred values of incident peak overpressure. The polynomial is provided for  $Z \geq 0.5 \text{ ft/lb}^{1/3}$  ( $0.198 \text{ m/kg}^{1/3}$ ) but no information is available on the accuracy of calculation at the low end of the range where the shock front velocity changes rapidly.

### ***3.2.2 Kingery, 1966: Hemispherical TNT Surface Bursts***

In 1966, Kingery extended the presentation of Kingery and Pannill (1964) to more completely describe blast wave parameters, including shock front arrival time, incident peak overpressure and impulse, and positive phase duration. Data from the three TNT hemispherical surface bursts discussed in Kingery and Pannill (1964) and from a 500-ton hemispherical surface-burst shot at SES in 1964 were evaluated.

Kingery reported the size of the blocks of TNT used to build the hemispherical 500-ton weapon ( $305 \times 305 \times 102 \text{ mm}$ ); the packing density of the TNT ( $1560 \text{ kg/m}^3$ ), the soil at the site (glacial silt with gravel, sand and clay at depth) and the methods used to calculate values of the blast wave parameters. These methods are summarized below to a) support the presentation of Section 3.2.1, and b) provide insight into the possible uncertainty and variability in the inferred values of the blast wave parameters.

Shock front arrival times were measured in the 500 ton shot by photo-optical techniques, blast switches, overpressure gages and slifer (coaxial) cables. The photo-optical technique, which involves high-speed cameras and angled black-and-white striped (zebra) boards, takes advantage

of the differences in density, overpressure and temperature across a shock front. Tracking the arrival of the shock front at points along the zebra boards enabled a calculation of shock front velocity and incident peak overpressure. Blast switches produce an electric signal when struck by a shock front and enable the direct measurement of shock front arrival. Information on the overpressure gages is not provided and so their operating range and accuracy is unknown. Seventy-eight data are reported for arrival time in the range  $0.208 \leq Z \leq 316 \text{ ft/lb}^{1/3}$  ( $0.083 \leq Z \leq 126 \text{ m/kg}^{1/3}$ ).

Kingery noted that incident peak overpressure was recorded directly by pressure transducers and inferred from measurements of shock front arrival. The data from the 500 ton shot was generally supportive of the polynomial described in Kingery and Pannill (1964) except for  $Z < 1.8 \text{ ft/lb}^{1/3}$  ( $Z < 0.71 \text{ m/kg}^{1/3}$ ). Positive phase duration was described as difficult to measure because the pressure transducers were prone to malfunction after the arrival of the shock front. The decay in some of the pressure histories was extrapolated to ambient. One hundred and thirty-four values of positive phase duration were reported in the range  $0.49 \leq Z \leq 428 \text{ ft/lb}^{1/3}$  ( $0.194 \leq Z \leq 170 \text{ m/kg}^{1/3}$ ); only two points were provided for  $Z < 1.0 \text{ ft/lb}^{1/3}$  ( $Z < 0.397 \text{ m/kg}^{1/3}$ ).

Ninety-four values of incident impulse were computed using pressure histories and information on incident peak overpressure, positive phase duration and rate of decay behind the shock front, over the range  $0.49 \leq Z \leq 428 \text{ ft/lb}^{1/3}$  ( $0.194 \leq Z \leq 170 \text{ m/kg}^{1/3}$ ). Only four data points were provided for  $Z < 3.0 \text{ ft/lb}^{1/3}$  ( $Z < 1.19 \text{ m/kg}^{1/3}$ ).

Hand drawn curves were generated as a function of scaled distance to best fit the available data for arrival time, incident peak overpressure and impulse, and positive phase duration. A rudimentary statistical analysis was performed to characterize the relative errors associated with the use of the curves, noting that the accuracy of the underlying data is unknown.

### ***3.2.3 Kingery and Bulmash, 1984: Spherical Free Air and Hemispherical Surface Bursts of TNT***

Kingery and Bulmash (1984) compiled, analyzed and documented airblast parameters for spherical free-air bursts and hemispherical surface bursts of TNT in support of a revision to the

tri-service manual TM 5-1300 (Department of the Army, the Navy, and the Air Force 1969). They developed polynomials to express the airblast parameters of arrival time, shock front velocity, incident peak overpressure and impulse, positive phase duration, and normally reflected peak overpressure and impulse as a function of scaled distance. The derived polynomials were reproduced in the form of design charts, which have been published in many government documents, design standards, and textbooks. The design charts are widely labeled as the Kingery-Bulmash (KB) charts.

Kingery and Bulmash compiled airblast data from many sources, which although identified in their Ballistics Research Laboratory report, are generally unavailable and so are not listed here. The raw data were corrected for charge weight and atmospheric conditions to enable calculations for a kilogram mass of TNT at atmospheric pressure at sea level (= 101.3 kPa, 14.7 psi).

Kingery and Bulmash described the methods used to measure airblast parameters and this provides insight into the likely uncertainties in the raw data used to generate the KB polynomials and charts. Arrival time and incident peak overpressure were measured using the methods described in Section 3.2.2. Impulse was determined by integrating overpressure over the duration of the positive phase. The duration of the positive phase was determined from overpressure histories (and described as “...one of the more difficult blast parameters to measure with consistency and repeatability”). Reflected overpressure was calculated a) indirectly using theory, measurements of incident overpressure, and the specific heat ratio, which is affected by overpressure and temperature, or b) directly from ground measurements of the effects of free-air bursts. Little information is provided on methods used to calculate reflected impulse although the authors note “...there is a lack of specific measurements of this blast parameter.”

#### *3.2.3.1 Polynomial Data for TNT Spherical Free-Air Bursts*

The figures presented in Kingery and Bulmash, together with an understanding of how data were collected and processed, enable an assessment of the likely accuracy of the KB polynomials over the scaled range considered here. Considerable data are provided for incident peak overpressure but the scatter at small values of scaled distance is significant, which is not surprising given that the data were inferred and not measured directly. Data for incident peak overpressure are

reported in the range  $0.134 \text{ ft/lb}^{1/3} \leq Z \leq 100 \text{ ft/lb}^{1/3}$  ( $0.0531 \text{ m/kg}^{1/3} \leq Z \leq 40 \text{ m/kg}^{1/3}$ ). Much less data were available for incident impulse, with only 3 data points below  $Z = 0.3 \text{ ft/lb}^{1/3}$  ( $0.119 \text{ m/kg}^{1/3}$ ). Kingery and Bulmash noted “At scaled distances less than 1 [ft/lb<sup>1/3</sup>] the measured values of incident impulse are very few and sometimes of suspect quality.” Values of normally reflected peak overpressure were typically calculated using theory and values of incident peak overpressure, as noted previously. There were no reflected overpressure data below  $Z = 0.25 \text{ ft/lb}^{1/3}$  ( $0.1 \text{ m/kg}^{1/3}$ ). There were little data for reflected impulse.

#### *3.2.3.2 Polynomial Data for TNT Hemispherical Surface Bursts*

Kingery and Bulmash used the incident airblast data of Kingery (1966) to generate polynomials and a design chart for hemispherical surface bursts of TNT. Values of reflected peak overpressure were calculated using theory and values of incident peak overpressure. Reflected impulse was calculated using the spherical free-air burst data and a factor on charge weight of 1.8.

#### *3.2.4 Implementation in UFC 3-340-02 using Design Charts*

The KB charts are presented in UFC 3-340-02 (DoD 2008) and are widely used for the protective design of structures. The incident and normally peak reflected overpressures and impulses obtained from the KB charts are combined with reflection coefficients that vary as a function of the angle of incidence to describe the pressure loading history on a surface. Reflection coefficients are discussed in Chapter 5. Swisdak (1994) and Bogosian et al. (2002) evaluated the utility of the KB charts, and those studies are described next.

### **3.3 Studies by Swisdak and Bogosian et al.**

Swisdak (1994) reviewed Kingery (1966) and Kingery and Bulmash (1984) for hemispherical surface bursts of TNT for the purpose of developing alternate equations that would 1) be simpler to apply than those presented in Kingery and Bulmash (1984), and 2) recover the values of the KB airblast parameters within 1%. The scope of the Swisdak study did not include a re-evaluation of the data used by Kingery and Bulmash to establish their polynomials. Swisdak provided polynomials for arrival time, incident peak overpressure, normally reflected peak

overpressure, positive phase duration, incident impulse, reflected impulse, and shock front velocity.

Bogosian et al. (2002) sought to 1) compare results from widely used airblast codes (CONWEP, SHOCK and BlastX) with KB predictions, 2) compare KB predictions with experimental data, and 3) quantify the uncertainty in test data and make recommendations regarding the use of the KB charts/predictions. The CONWEP predictions recovered the KB curves for incident and reflected peak overpressure and impulse exactly, which is expected because CONWEP implements the KB polynomials. The experimental data assembled by Bogosian et al., across eleven test series, represented a significant expansion of the dataset available to prior researchers. The data set comprised a wide range of charge weights, charge geometries, types of explosives, and heights of burst. Three hundred and three gage records were assembled and analyzed. Values of scaled distance ranged from approximately 2.5 ft/lb<sup>1/3</sup> to 60 ft/lb<sup>1/3</sup> (1.0 m/kg<sup>1/3</sup> to 24 m/kg<sup>1/3</sup>) for incident peak overpressure and impulse and from 3.5 ft/lb<sup>1/3</sup> to 40 ft/lb<sup>1/3</sup> (1.4 m/kg<sup>1/3</sup> to 16 m/kg<sup>1/3</sup>) for reflected peak overpressure and impulse. For incident peak overpressure, the KB curve recovered the experimental observations well for  $Z > 10$  ft/lb<sup>1/3</sup> (4.0 m/kg<sup>1/3</sup>) but substantially underpredicted the recorded data for  $Z < 6$  ft/lb<sup>1/3</sup> (2.4 m/kg<sup>1/3</sup>). For incident impulse, the KB curve overpredicted the recorded data by 15% to 20% across the range  $3.0 \leq Z \leq 60$  ft/lb<sup>1/3</sup> ( $1.2 \leq Z \leq 24$  m/kg<sup>1/3</sup>). For reflected peak overpressure, the KB curve recovered the mean of the experimental data reasonably well. For reflected impulse, the KB curve recovered the measured results well for  $Z < 7$  ft/lb<sup>1/3</sup> (2.8 m/kg<sup>1/3</sup>) but overpredicted the measured results by a wide margin for  $Z > 10$  ft/lb<sup>1/3</sup> (4 m/kg<sup>1/3</sup>). Bogosian attributed the overprediction of reflected impulse by the KB curves for  $Z > 7$  ft/lb<sup>1/3</sup> (2.8 m/kg<sup>1/3</sup>) to clearing.

### **3.4 Evaluation of the KB Charts**

The pressure inside an ideal high explosive after detonation is defined by the Chapman-Jouguet (CJ) point, which describes the minimum propagation velocity of the detonation front for the reacting gases to reach sonic velocity within the material. The CJ detonation pressure is associated with this condition, which is 21 GPa for the detonation of TNT of normal packing density (1630 kg/m<sup>3</sup>) in air at ambient pressure (Baker et al. 1983).

At the face of a spherical TNT charge ( $Z = 0.0527 \text{ m/kg}^{1/3}$ ) in free air, the KB chart predicts an incident peak overpressure of 50 MPa for a spherical free-air burst. This overpressure is a very small fraction ( $= 1/420$ ) of the CJ pressure of 21 GPa, suggesting a discontinuity in the flow field, which is physically impossible. The lack of direct measurements of overpressure, impulse, arrival time and positive phase duration in the near field, as described in prior sections of this chapter, and the significant discrepancy at the face of the charge noted above, calls into question the accuracy of the KB charts, especially in the near field.

The remaining sections of this chapter examine incident and normally reflected overpressures and impulses and shock-front arrival time for spherical free-air bursts of TNT. The near field is emphasized because many of the threats considered nowadays for security design are associated with small standoff distances. The near field is (loosely) defined here as the zone within approximately 7 charge radii ( $\bar{r} \leq 7, Z < 0.4 \text{ m/kg}^{1/3}$ ) of the point of detonation, where the blast wave has not yet fully formed and the expansion of the products of combustion has a significant effect on the blast wave parameters. In this region, direct measurement of pressure and impulse using commercially available transducers is not possible for the reasons given in Section 2.2.

Analysis is performed using the verified and validated computational fluid dynamics (CFD) code AUTODYN<sup>5</sup> (ANSYS 2013a) to 1) determine incident and normally reflected peak overpressures and impulses, and arrival time of the shock front, and to 2) judge the accuracy of the KB charts.

## **3.5 Numerical Studies**

### ***3.5.1 Spherical Charges used for Numerical Analysis***

A two-phase fluid is modeled numerically, comprising the explosive (combustion products) and the surrounding air. The ideal high explosive TNT is used for the CFD computations. Air is modeled as an ideal gas. Radial symmetry is used for analysis of the early expansion of the combustion products. The Jones-Wilkins-Lee (JWL) Equation of State (EOS) is employed for this purpose using the properties described in Dobratz and Crawford (1985); see Table 2-1. The

---

<sup>5</sup> AUTODYN was verified and validated in Section 2.3.

chemistry of the explosion is not modeled. Afterburning is not modeled because afterburning energy may not be realized for explosions of unconfined TNT due to incomplete mixing of fuel with available oxygen, and temperature less than the ignition temperature of the TNT fuels ( $\leq 1800$  K) (McNesby et al. 2010).

Three TNT charge weights (18735 kg, 960 kg and 23 kg) are used for the simulations. The TNT charge weight of 18735 kg is based on the charge radius of 1.4 m used for the Needham analysis, presented in Chapter 2, and a TNT packing density of  $1630 \text{ kg/m}^3$ . Twenty-three kilograms is equally to approximately 50 pounds, which is a typical satchel-type weapon considered in security design. The 960 kg (2116 pounds) charge could be representative of a vehicle-borne weapon. The packing density for the 960 and 23 kg charges is  $1630 \text{ kg/m}^3$ , and the corresponding charge radii are 0.520 m and 0.150 m, respectively. Simulations are performed with three charge weights to determine the effect, if any, of charge weight on the normalized blast wave parameters.

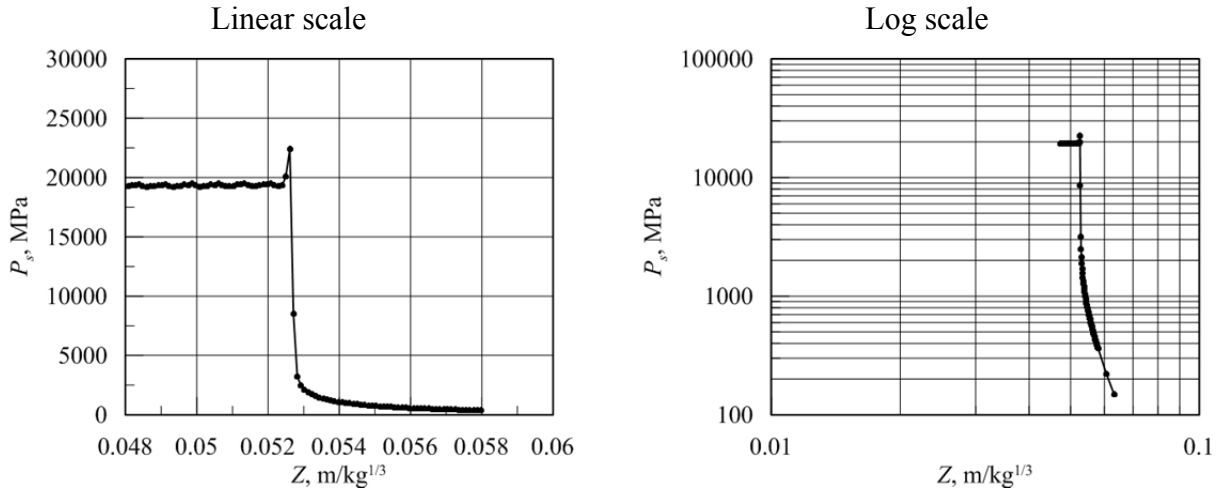
Preliminary analysis and a review of the literature (e.g., Needham 2010) showed that overpressure, particle velocity and particle acceleration change very rapidly close to the face of a charge. The following section provides an assessment of overpressures and hydrodynamic parameters close to the face of a charge and establishes a minimum value of scaled distance for the subsequent CFD analyses.

### ***3.5.2 Overpressures, Particle Velocities and Accelerations Near the Charge Face***

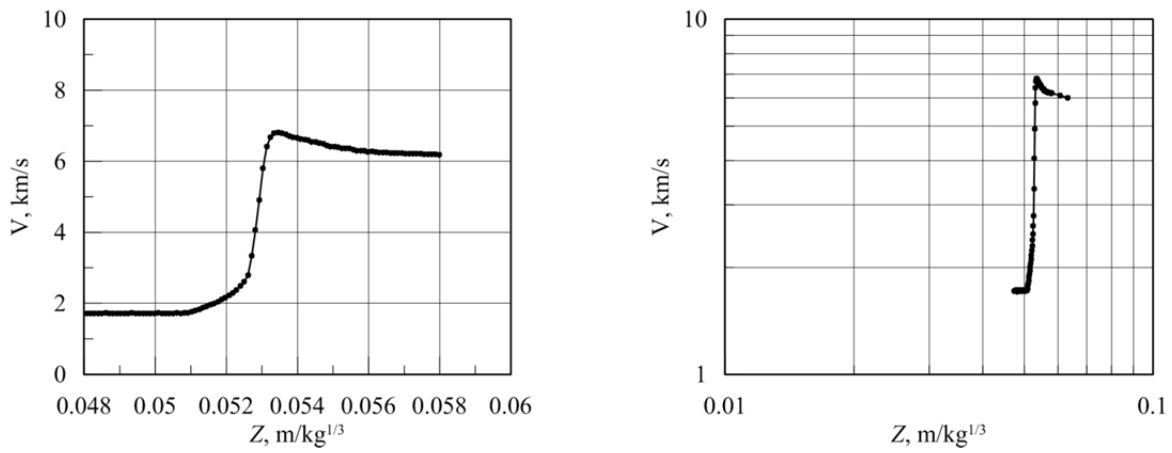
Incident peak overpressure changes rapidly in close proximity to the face of a charge, as seen in Chapter 2 and Appendix C. To explore these changes, and to help frame the presentations later in this chapter and in Chapter 4, incident overpressures, particle velocities and particle accelerations are calculated for two cell sizes (0.05 mm and 0.1 mm) and two charge weights (23 kg and 960 kg). Results are plotted as a function of scaled distance in Figures 3-1, 3-2, 3-3, 3-4, 3-5 and 3-6 to examine changes in the immediate vicinity of the face of the charge, namely,  $0.9 \leq \bar{r} \leq 1.1$  ( $0.0474 \leq Z \leq 0.0580 \text{ m/kg}^{1/3}$ ), where  $\bar{r} = 1$  at  $Z = 0.0527 \text{ m/kg}^{1/3}$ . Finer meshes are needed to resolve particle velocity and acceleration than for overpressure. Particle velocity is a function of differential pressure. Particle acceleration is derived from particle velocity. The calculated

particle acceleration and particle velocity very close to the face of the charge are dependent on cell size and change rapidly. Values stabilize at  $Z = 0.0553 \text{ m/kg}^{1/3}$  ( $\bar{r} = 1.05$ ) and are similar for the two charge weights. Peak particle accelerations at the face of the charge, where the pressure differential is greatest, are on the order of  $10^{11} \text{ g}$  ( $\approx 10^{12} \text{ m/s}^2$ ), which was noted in Section 2.2 and is consistent with the range reported by Needham (2010).

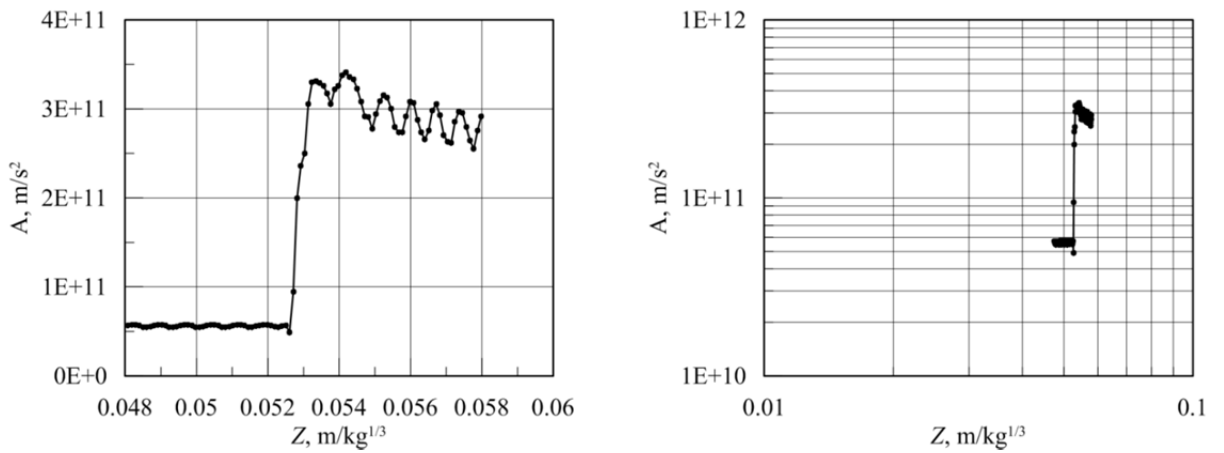
A minimum value of  $Z = 0.0553 \text{ m/kg}^{1/3}$  ( $\bar{r} = 1.05$ ) is used for the CFD calculations presented in the remaining sections of this chapter and in Chapter 4. The effect on design practice of not reporting pressures and impulses closer to the face of the charge than a radial expansion of 1.05 is insignificant, as discussed in Section 4.5.



(a) Overpressure



(b) Particle velocity



(c) Particle acceleration

**Figure 3-1 Incident overpressures and particle velocities and accelerations near the face of the charge ; TNT weight of 23 kg; 0.1 mm cells**

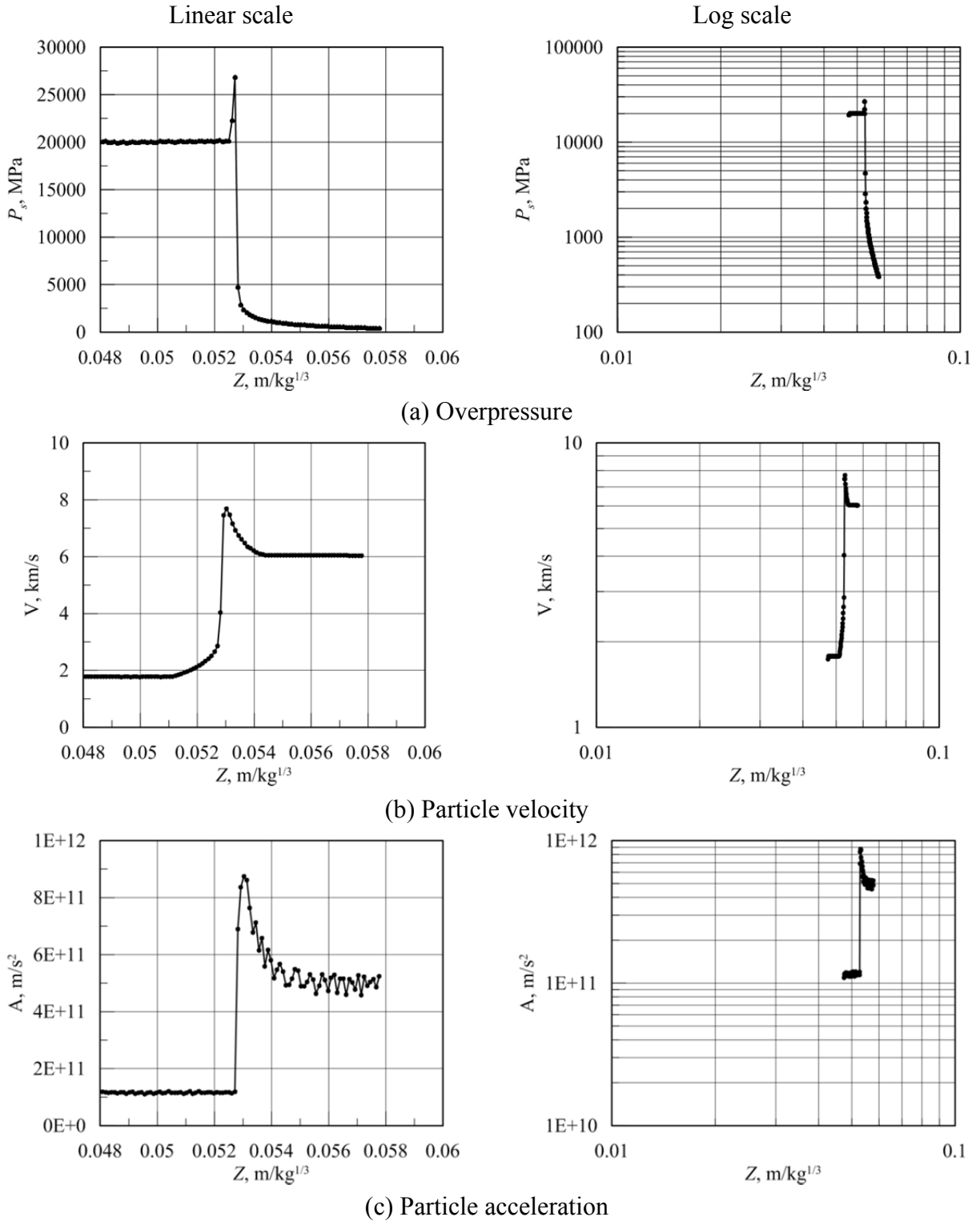
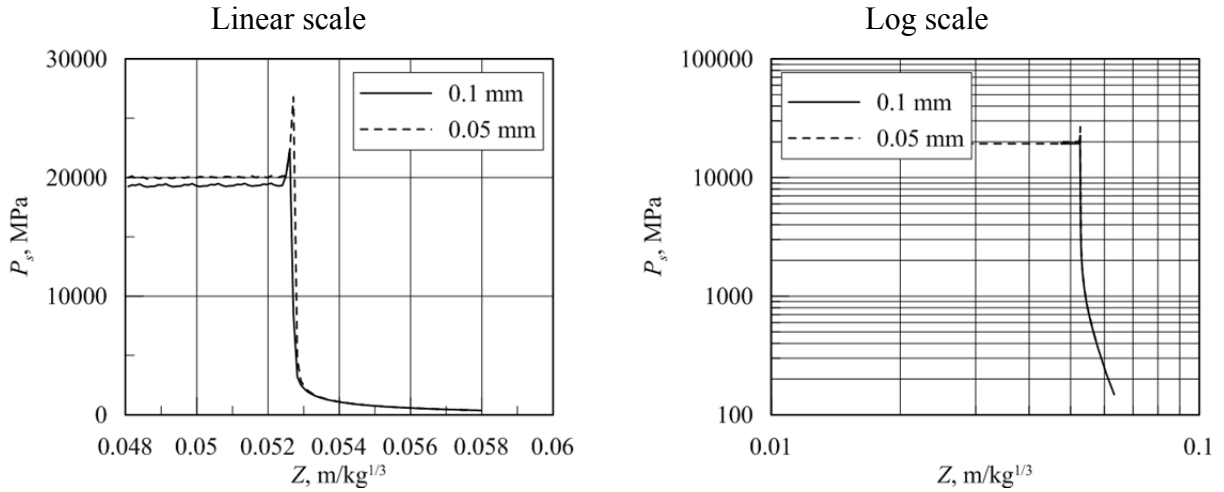
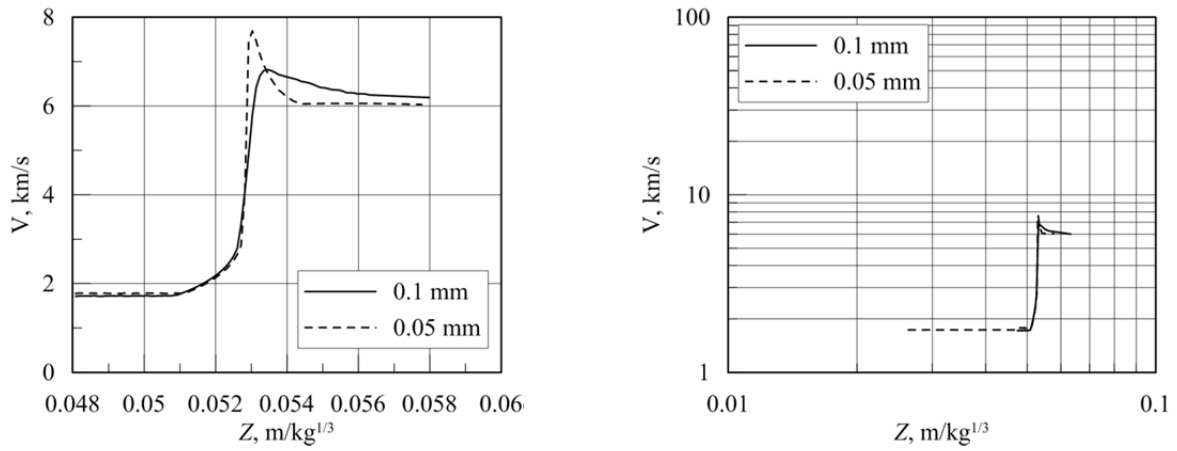


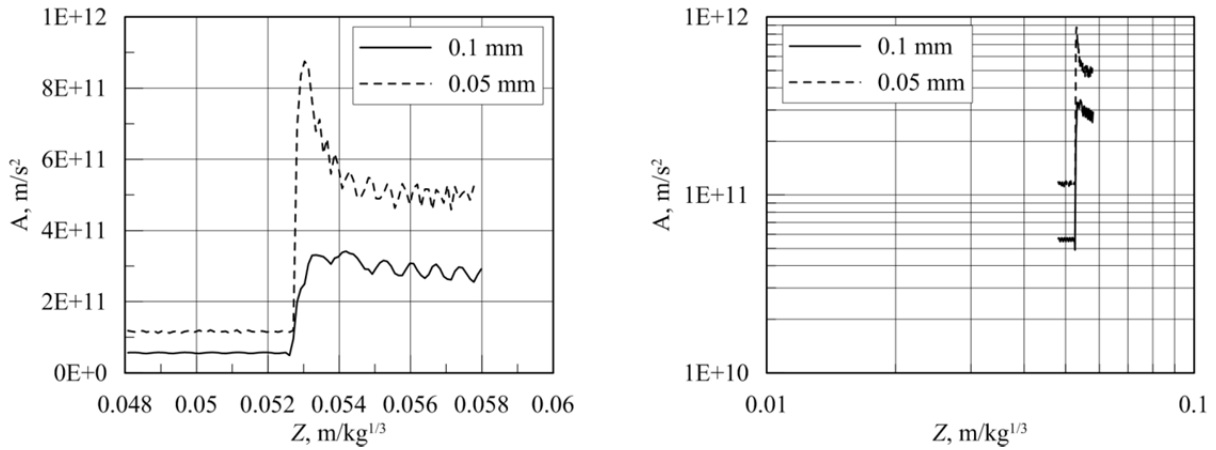
**Figure 3-2 Incident overpressures and particle velocities and accelerations near the face of the charge ; TNT weight of 23 kg; 0.05 mm cells**



(a) Overpressure

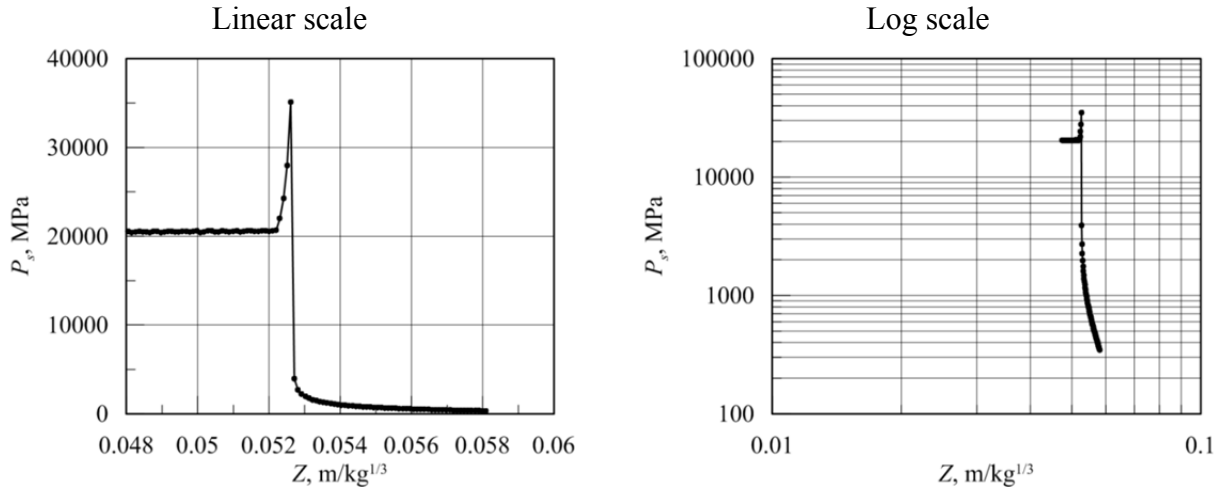


(b) Particle velocity

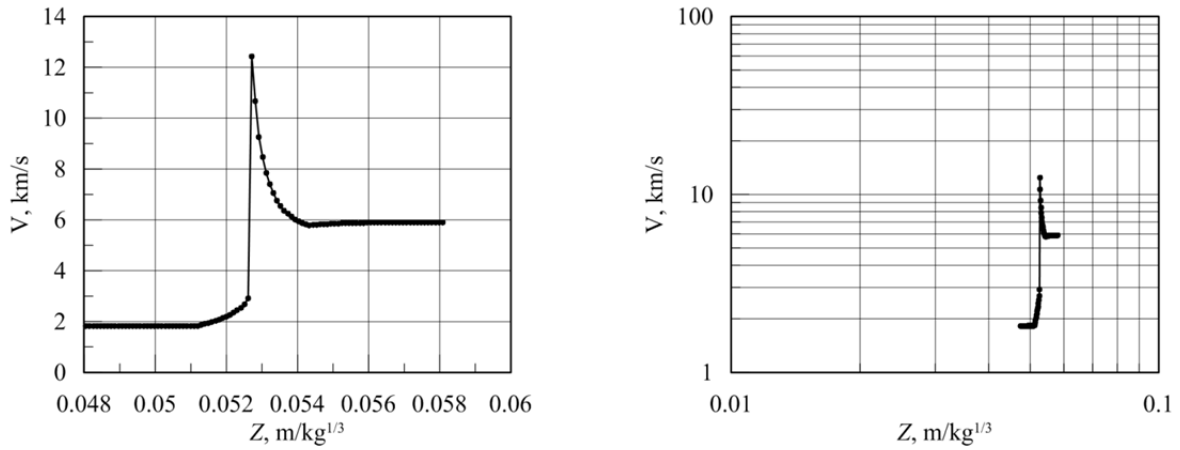


(c) Particle acceleration

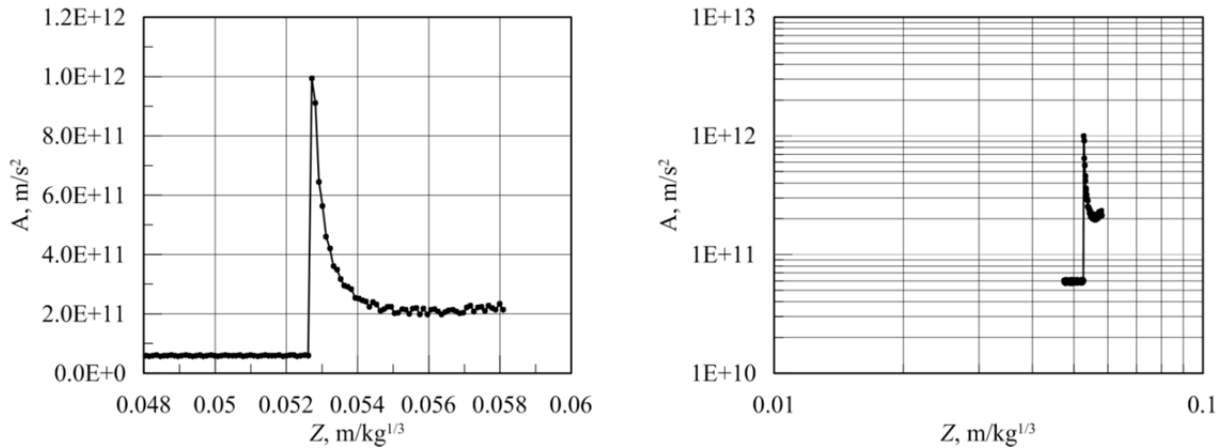
**Figure 3-3 Incident overpressures and particle velocities and accelerations near the face of the charge ; TNT weight of 23 kg; 0.1 and 0.05 mm cells**



(a) Overpressure

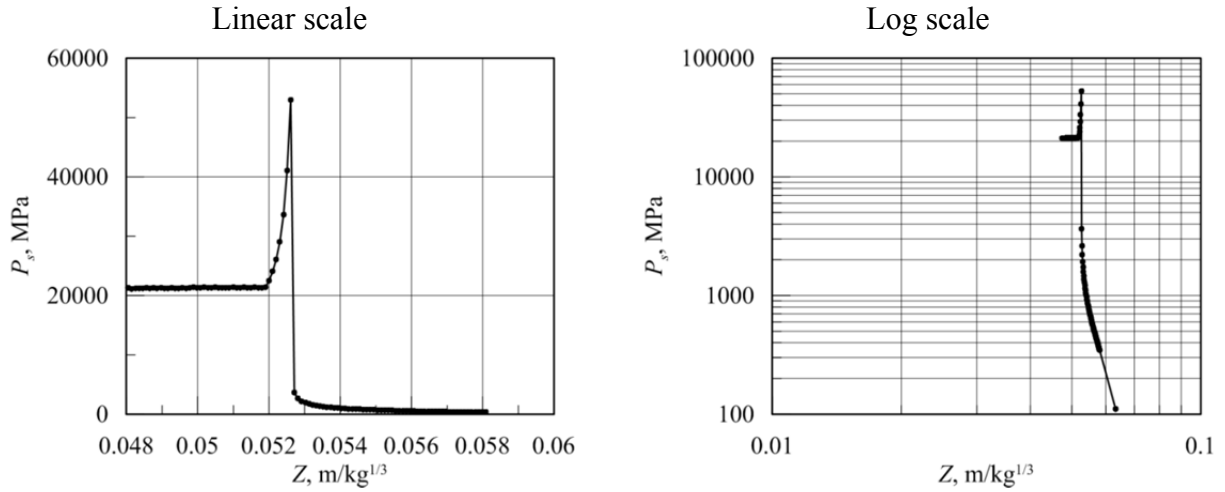


(b) Particle velocity

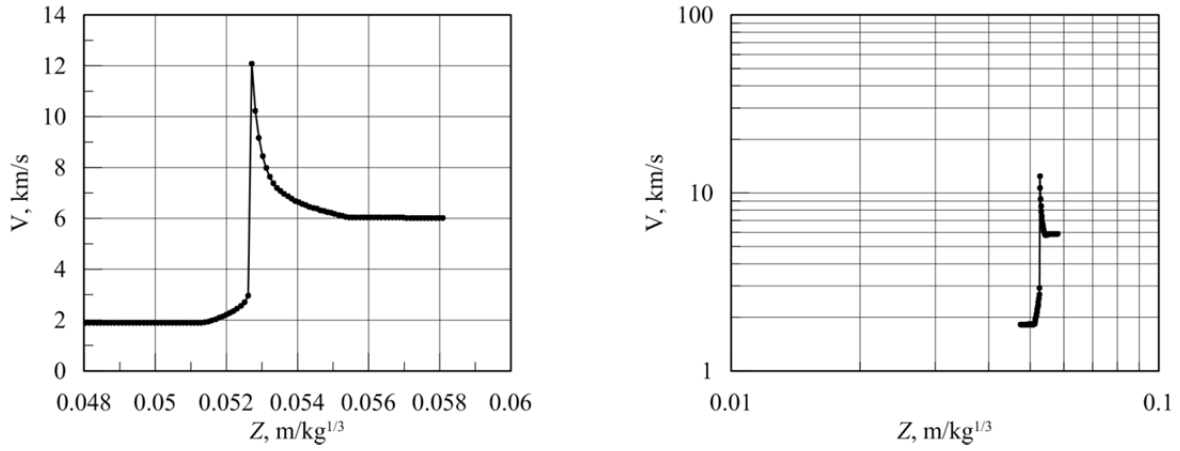


(c) Particle acceleration

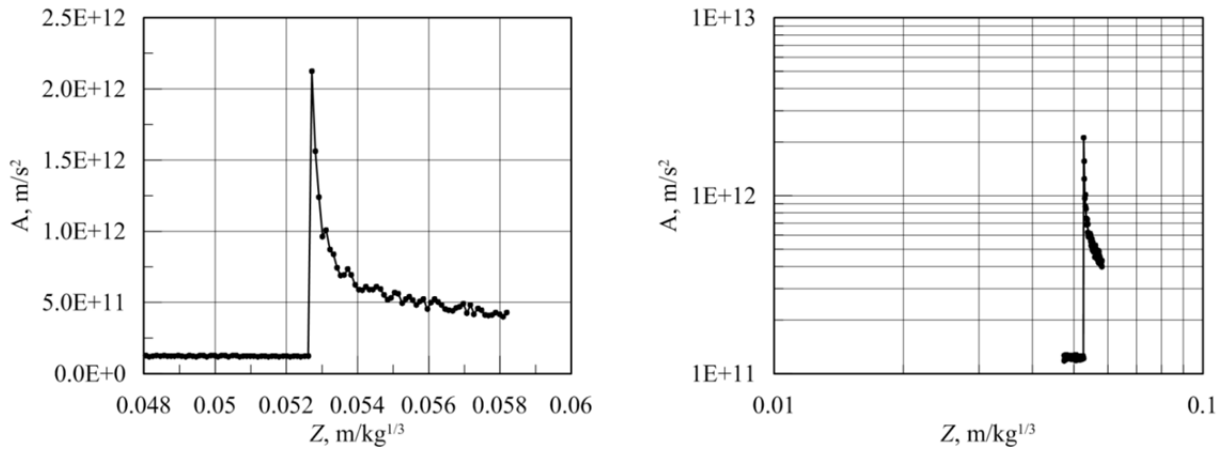
**Figure 3-4 Incident overpressures and particle velocities and accelerations near the face of the charge; TNT weight of 960 kg; 0.1 mm cells**



(a) Overpressure

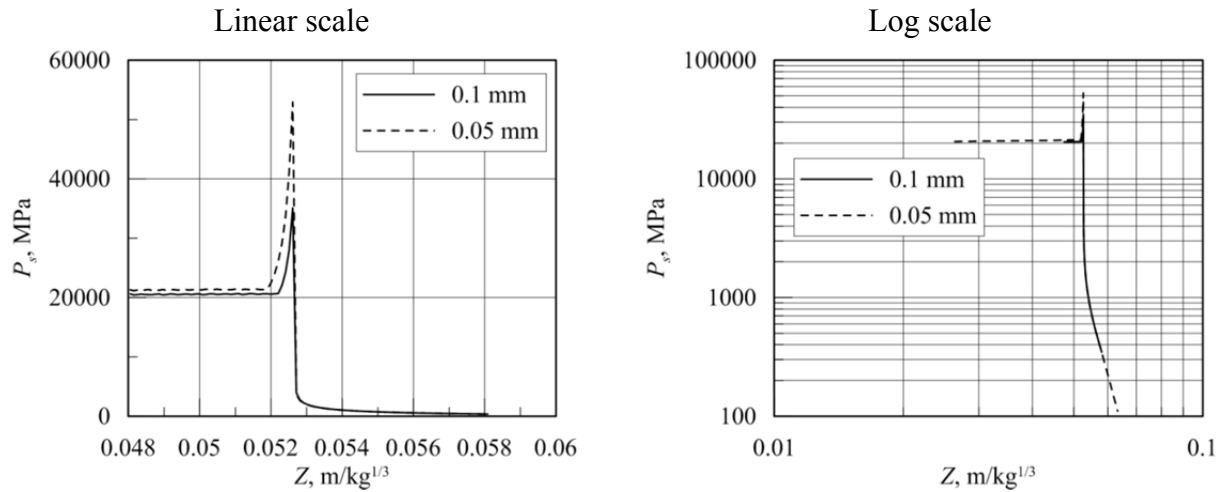


(b) Particle velocity

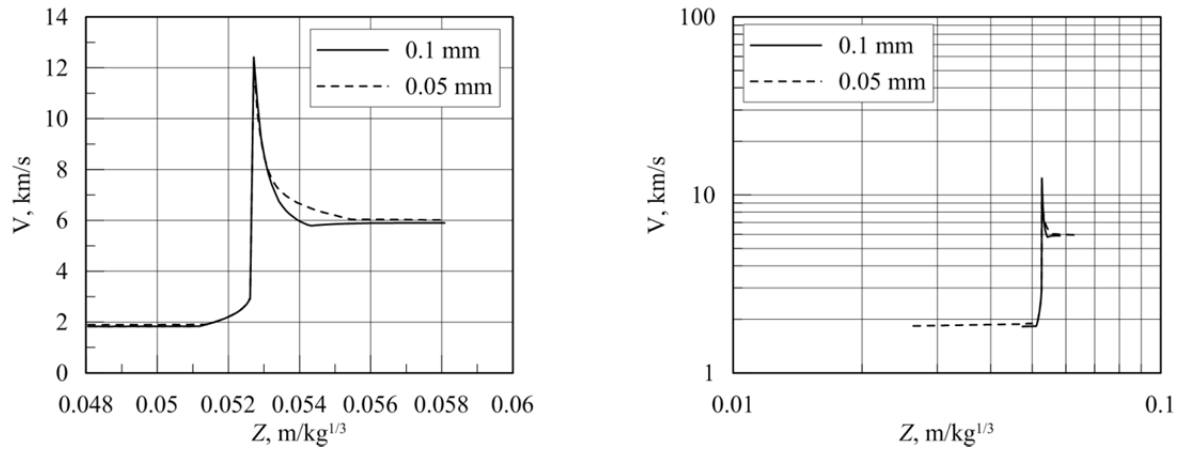


(c) Particle acceleration

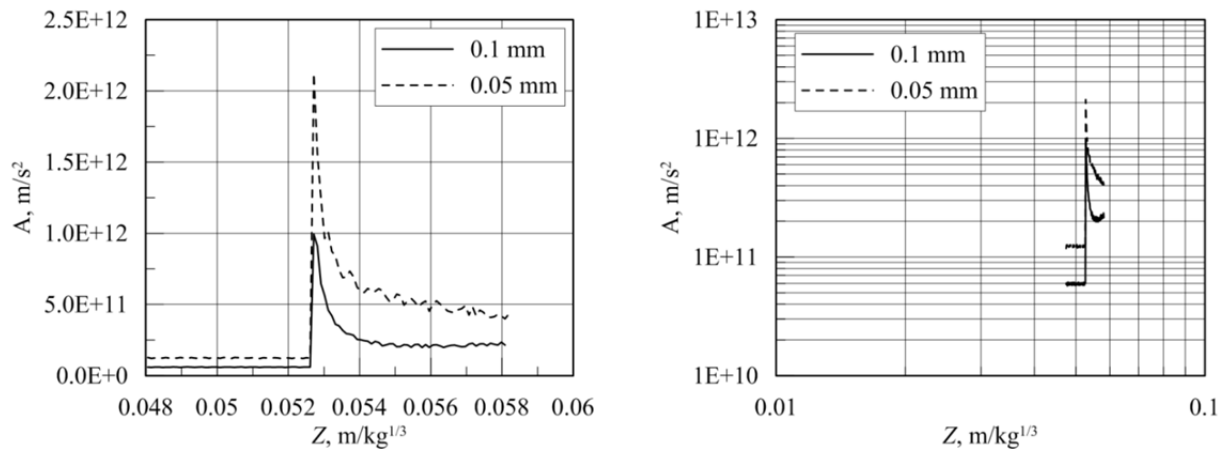
**Figure 3-5 Incident overpressures and particle velocities and accelerations near the face of the charge; TNT weight of 960 kg; 0.05 mm cells**



(a) Overpressure



(b) Particle velocity



(c) Particle acceleration

**Figure 3-6 Incident overpressures and particle velocities and accelerations near the face of the charge; TNT weight of 960 kg; 0.1 and 0.05 mm cells**

### 3.5.3 Mesh Sensitivity Analysis

Mesh sensitivity analysis for the simulations of incident and normally reflected overpressures and impulses is performed using  $h$ -refinement (Cook 2002) to a) determine a reasonable balance between solution accuracy and computational effort, and b) provide guidance to an analyst on the required cell size for CFD analysis of detonations. Mesh convergence is assumed when the results obtained using a cell size reduced by a factor of two change by less than 10%.

Simulations of incident overpressure and impulse are performed in a 1D domain using axial symmetry and the multi-material Euler-Godunov solver (Godunov 1959). The Euler-FCT solver (e.g., Boris and Book 1971) is not available in AUTODYN for 1D calculations. The fluid is modeled as described in Section 3.5.1. When the products of combustion have expanded to approximately 10 times their original volume, the JWL EOS is replaced by the ideal gas EOS to prevent possible numerical errors, as discussed in Section 2.2.1.

Table 3-1 summarizes the analyses that comprise the AUTODYN dataset for incident peak overpressure, impulse, and arrival time, subdivided into twenty-six intervals of scaled distance between  $0.0553 \leq Z \leq 40.0 \text{ m/kg}^{1/3}$ , where the basis for lower limit on  $Z$  of  $0.0553 \text{ m/kg}^{1/3}$  is provided in Section 3.5.2. The intervals correspond to the log-scaled distances seen in the KB charts that are reproduced in UFC 3-340-02. Each interval listed in Table 3-1 has data at no less than ten monitoring locations (different values of scaled distance) to enable accurate interpretation of the numerical data over the full range of scaled distance considered here.

**Table 3-1 AUTODYN dataset for incident calculations**

$Z_i \leq Z < Z_j$ (m/kg <sup>1/3</sup> )	Number of monitoring locations
$0.0553 \leq Z < 0.060$	10
$0.060 \leq Z < 0.070$	20
$0.070 \leq Z < 0.080$	20
$0.080 \leq Z < 0.090$	20
$0.090 \leq Z < 0.10$	20
$0.10 \leq Z < 0.20$	20
$0.20 \leq Z < 0.30$	20
$0.30 \leq Z < 0.40$	20
$0.40 \leq Z < 0.50$	10
$0.50 \leq Z < 0.60$	10
$0.60 \leq Z < 0.70$	10
$0.70 \leq Z < 0.80$	10
$0.80 \leq Z < 0.90$	10
$0.90 \leq Z < 1.0$	10
$1.0 \leq Z < 2.0$	10
$2.0 \leq Z < 3.0$	10
$3.0 \leq Z < 4.0$	10
$4.0 \leq Z < 5.0$	10
$5.0 \leq Z < 6.0$	10
$6.0 \leq Z < 7.0$	10
$7.0 \leq Z < 8.0$	10
$8.0 \leq Z < 9.0$	10
$9.0 \leq Z < 10.0$	10
$10.0 \leq Z < 20.0$	10
$20.0 \leq Z < 30.0$	10
$30.0 \leq Z < 40.0$	10

The 960 kg charge is used for the mesh sensitivity study of incident peak overpressure and impulse. The influence of charge size on the results is investigated at selected scaled distances using 18735 and 23 kg charges. Tables 3-2, 3-3 and 3-4 present the cell sizes in each interval used for analysis of incident peak overpressures and impulses, for charge weights of 960, 18735 and 23 kg, respectively. Each interval is defined by bounds on the scaled distance,  $Z$ . The upper bound on  $Z$  in a given interval is transformed to a distance in mm,  $R_j$ . Four cell sizes are selected for each interval. Three meshes with cell sizes smaller than  $R_j/500$  are analyzed because a cell size of  $R_j/500$  is expected to provide converged solutions based on the studies presented in Section 2.2. One mesh with a cell size equal to or greater than  $R_j/500$  is analyzed for the first twenty-four intervals because  $R_j/500$  does not enable exact modeling of the geometry (radius) of the charge. The smallest cell size in last two intervals,  $20.0 \leq Z < 40.0$  m/kg<sup>1/3</sup>, is less than  $R_j/500$  because the distance  $R_j/500$  exceeds the charge radius and the charges must be modeled explicitly.

Simulations of normally reflected peak overpressure and impulse are performed in a two-dimensional (2D) domain using the Euler-FCT solver, which is preferred to the Euler-Godunov solver for reasons of accuracy (Borve et al. 2008). The results from 1D analysis are remapped into a one-quarter of the 2D air domain, as shown in Figure 3-7, to reduce the computational expense of the reflected peak overpressure and impulse calculations. For the reflected peak overpressure and impulse calculations reported here, the 1D results calculated using the smallest cell size in the interval considered are used as input to the 2D domain. The vertical dimension of the 2D plane is set equal to the horizontal dimension to avoid spurious reflections from the upper transmitting boundary as noted in Section 2.5. Normally reflected peak overpressure and impulse are calculated at monitoring location 1, as identified in Figure 3-7.

**Table 3-2 Cell sizes for incident peak overpressure and impulse; 960 kg charge with a radius of 520 mm**

$Z_i \leq Z < Z_j$ (m/kg <sup>1/3</sup> )	$R_j = Z_j \times W^{1/3}$ (mm)	$R_j/500$ (mm)	Cell size (mm)
$0.0553 \leq Z < 0.060$	592	1.18	1.18, 1, 0.5 and 0.25
$0.060 \leq Z < 0.070$	691	1.38	1.38, 1, 0.5 and 0.25
$0.070 \leq Z < 0.080$	789	1.58	1.58, 1, 0.5 and 0.25
$0.080 \leq Z < 0.090$	888	1.78	1.78, 1, 0.5 and 0.25
$0.090 \leq Z < 0.10$	986	1.97	1.98, 1, 0.5 and 0.25
$0.10 \leq Z < 0.15$	1480	2.96	2.97, 1, 0.5 and 0.25
$0.15 \leq Z < 0.20$	1973	3.95	3.97, 1, 0.5 and 0.25
$0.20 \leq Z < 0.25$	2466	4.93	4.95, 1, 0.5 and 0.25
$0.25 \leq Z < 0.30$	2959	5.92	5.98, 1, 0.5 and 0.25
$0.30 \leq Z < 0.40$	3946	7.89	8.00, 1, 0.5 and 0.25
$0.40 \leq Z < 0.50$	4932	9.86	10.00, 8, 4 and 2
$0.50 \leq Z < 0.60$	5919	11.8	12.1, 8, 4 and 2
$0.60 \leq Z < 0.70$	6905	13.8	14.1, 8, 4 and 2
$0.70 \leq Z < 0.80$	7892	15.8	16.3, 8, 4 and 2
$0.80 \leq Z < 0.90$	8878	17.8	17.9, 15.8, 8 and 4
$0.90 \leq Z < 1.0$	9865	19.7	20.0, 15.8, 8 and 4
$1.0 \leq Z < 1.2$	11838	23.7	24.8, 15.8, 8 and 4
$1.2 \leq Z < 1.5$	14797	29.6	30.6, 15.8, 8 and 4
$1.5 \leq Z < 2.0$	19730	39.5	40.0, 15.8, 8 and 4
$2.0 \leq Z < 3.0$	29595	59.2	65.0, 40, 20 and 10
$3.0 \leq Z < 4.0$	39459	78.9	86.7, 40, 20 and 10
$4.0 \leq Z < 5.0$	49324	98.6	104, 65, 32.5 and 16.25
$5.0 \leq Z < 6.0$	59189	118	130, 65, 32.5 and 16.25
$6.0 \leq Z < 7.0$	69054	138	173, 65, 32.5 and 16.25
$7.0 \leq Z < 8.0$	78919	158	173, 65, 32.5 and 16.25
$8.0 \leq Z < 9.0$	88784	178	260, 65, 32.5 and 16.25
$9.0 \leq Z < 10.0$	98648	197	260, 65, 32.5 and 16.25
$10.0 \leq Z < 20.0$	197297	395	520, 65, 32.5 and 16.25
$20.0 \leq Z < 30.0$	295945	592	520, 65, 32.5 and 16.25
$30.0 \leq Z < 40.0$	394594	789	520, 65, 32.5 and 16.25

**Table 3-3 Cell sizes for incident peak overpressure and impulse; 18735 kg charge with a radius of 1400 mm**

$Z_i \leq Z < Z_j$ ( $\text{m/kg}^{1/3}$ )	$R_j = Z_j \times W^{1/3}$ (mm)	$R_j/500$ (mm)	Cell size (mm)
$0.0553 \leq Z < 0.060$	1594	3.19	3.19, 2, 1 and 0.5
$0.060 \leq Z < 0.070$	1859	3.72	3.72, 2, 1 and 0.5
$0.070 \leq Z < 0.080$	2125	4.25	4.26, 2, 1 and 0.5
$0.080 \leq Z < 0.090$	2390	4.78	4.79, 2, 1 and 0.5
$0.090 \leq Z < 0.10$	2656	5.31	5.32, 2, 1 and 0.5
$0.10 \leq Z < 0.15$	3984	8.00	8.00, 2, 1 and 0.5
$0.15 \leq Z < 0.20$	5312	10.6	10.7, 2, 1 and 0.5
$0.20 \leq Z < 0.25$	6640	13.3	13.3, 2, 1 and 0.5
$0.25 \leq Z < 0.30$	7968	15.9	16.1, 2, 1 and 0.5
$0.30 \leq Z < 0.40$	10624	21.2	21.5, 2, 1 and 0.5
$0.40 \leq Z < 0.50$	13280	26.6	26.9, 20, 10 and 5
$1.0 \leq Z < 1.2$	31871	63.7	66.7, 50, 25 and 12.5
$1.2 \leq Z < 1.5$	39839	79.9	82.4, 50, 25 and 12.5
$1.5 \leq Z < 2.0$	53119	106	108, 50, 25 and 12.5
$5.0 \leq Z < 6.0$	159356	319	350, 200, 100 and 50
$6.0 \leq Z < 7.0$	185916	372	467, 200, 100 and 50
$7.0 \leq Z < 8.0$	212475	425	467, 200, 100 and 50
$8.0 \leq Z < 9.0$	239034	478	700, 200, 100 and 50
$9.0 \leq Z < 10.0$	265594	531	700, 200, 100 and 50
$10.0 \leq Z < 20.0$	531188	1062	1400, 200, 100 and 50
$20.0 \leq Z < 30.0$	796781	1594	1400, 200, 100 and 50
$30.0 \leq Z < 40.0$	1062375	2125	1400, 200, 100 and 50

**Table 3-4 Cell sizes for incident peak overpressure and impulse; 23 kg charge with a radius of 150 mm**

$Z_i \leq Z < Z_j$ (m/kg <sup>1/3</sup> )	$R_j = Z_j \times W^{1/3}$ (mm)	$R_j/500$ (mm)	Cell size (mm)
$0.0553 \leq Z < 0.060$	171	0.34	0.34, 0.3, 0.15 and 0.075
$0.060 \leq Z < 0.070$	199	0.40	0.40, 0.3, 0.15 and 0.075
$0.070 \leq Z < 0.080$	228	0.46	0.46, 0.3, 0.15 and 0.075
$0.080 \leq Z < 0.090$	256	0.51	0.51, 0.3, 0.15 and 0.075
$0.090 \leq Z < 0.10$	284	0.57	0.57, 0.3, 0.15 and 0.075
$0.10 \leq Z < 0.15$	427	0.85	0.86, 0.3, 0.15 and 0.075
$0.15 \leq Z < 0.20$	569	1.14	1.15, 0.3, 0.15 and 0.075
$0.20 \leq Z < 0.25$	711	1.42	1.43, 0.3, 0.15 and 0.075
$0.25 \leq Z < 0.30$	853	1.71	1.72, 0.3, 0.15 and 0.075
$0.30 \leq Z < 0.40$	1138	2.28	2.31, 0.3, 0.15 and 0.075
$0.40 \leq Z < 0.50$	1422	2.84	2.88, 2, 1 and 0.5
$1.0 \leq Z < 1.2$	3413	6.83	7.14, 5, 2.5 and 1.25
$1.2 \leq Z < 1.5$	4266	8.53	8.82, 5, 2.5 and 1.25
$1.5 \leq Z < 2.0$	5688	11.4	11.5, 5, 2.5 and 1.25
$5.0 \leq Z < 6.0$	17063	34.1	37.5, 25, 12.5 and 6.25
$6.0 \leq Z < 7.0$	19907	39.8	50, 25, 12.5 and 6.25
$7.0 \leq Z < 8.0$	22751	45.5	50, 25, 12.5 and 6.25
$8.0 \leq Z < 9.0$	25595	51.2	75, 25, 12.5 and 6.25
$9.0 \leq Z < 10.0$	28439	56.9	75, 25, 12.5 and 6.25
$10.0 \leq Z < 20.0$	56877	114	150, 25, 12.5 and 6.25
$20.0 \leq Z < 30.0$	85316	171	150, 25, 12.5 and 6.25
$30.0 \leq Z < 40.0$	113755	228	150, 25, 12.5 and 6.25

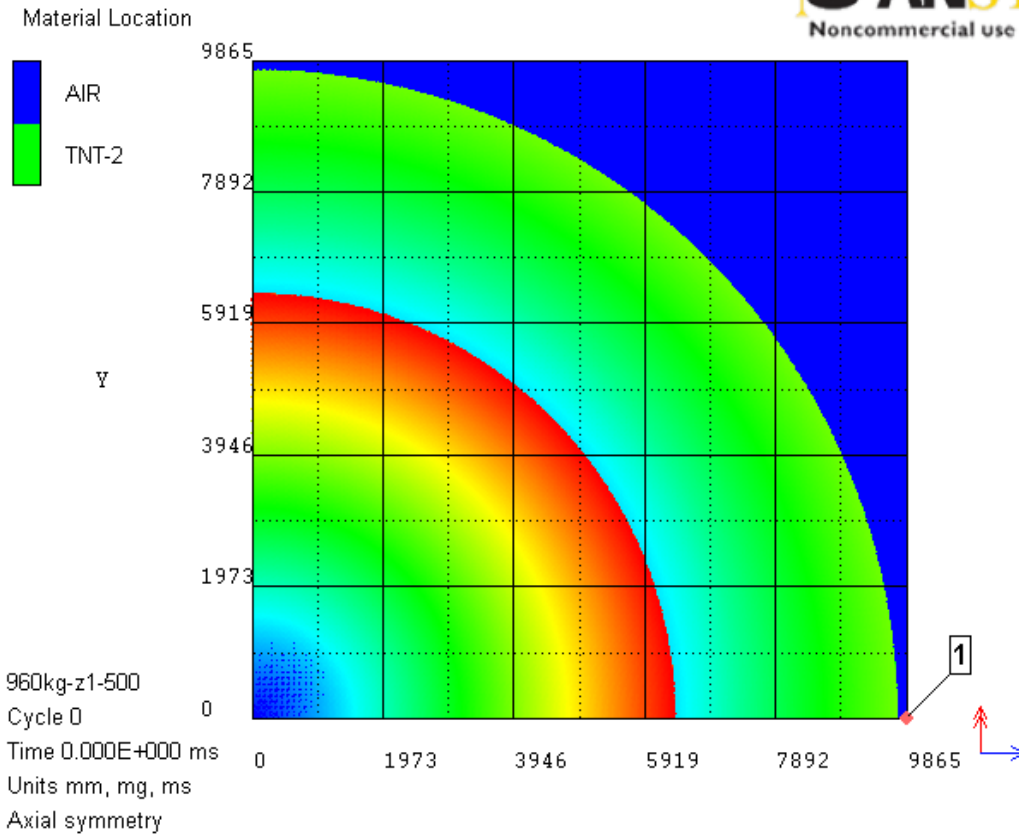


**Figure 3-7 AUTODYN 2D simulation using 1D remapped data for  $Z = 1.0 \text{ m/kg}^{1/3}$**

Fewer data are calculated for normally reflected peak overpressure and impulse, as shown in Table 3-5, because a) one 2D simulation is required to calculate reflected peak overpressure and reflected impulse at a monitoring location (e.g., point 1 in Figure 3-7) whereas a family of incident peak overpressures and impulses can be derived from a single 1D analysis, and b) evaluation of the results of the incident peak overpressure and impulse analysis indicated that fewer simulations are needed to develop robust conclusions. For  $Z < 0.4 \text{ m/kg}^{1/3}$ , calculations are performed at no less than five values of scaled distance in each interval. For  $Z \geq 0.4 \text{ m/kg}^{1/3}$ , simulations are performed at the boundaries of the intervals of scaled distance identified in Table 3-1.

Tables 3-6, 3-7 and 3-8 present the cell sizes used to calculate reflected data for the 960, 18735 and 23 kg charges, respectively. The results of the 1D analysis for the smallest cell size are used as input to the 2D analysis. (For example, the smallest cell size used for the 1D analysis of the

960 kg charge for  $0.0553 \leq Z < 0.060 \text{ m/kg}^{1/3}$  is 0.25 mm; see row 2 of Table 3-2.) Results of this 1D analysis are mapped into the 2D domain for analysis using the four cell sizes (4.36, 2.18, 1.09 and 0.546 mm) shown in row 2 of Table 3-6. Identical to the simulations of incident overpressure and impulse, most of the simulations are performed with the 960 kg charge. Square cells with side dimensions of  $R_j/125$ ,  $R_j/250$ ,  $R_j/500$  and  $R_j/1000$  are used for the 2D calculations.

For  $Z < 0.4 \text{ m/kg}^{1/3}$  and the 960 kg charge, four cell sizes are considered for analysis at boundaries of the intervals, and two cell sizes are considered at the monitoring locations within the interval. Of the four cell sizes at the boundaries of the intervals, the largest three are used to compute reflected impulse and reflected peak overpressure (e.g., 4.36, 2.18 and 1.09 mm for  $Z = 0.0553 \text{ m/kg}^{1/3}$ ) and the smallest (e.g., 0.546 mm) is used to compute reflected peak overpressure only. This choice of cell sizes is driven by the observation that the largest three cell sizes in each interval produce nearly identical values of reflected impulse, whereas only the smallest two cell sizes produced values of reflected peak overpressure within 10% of the other, with the smallest cell size assumed to produce the *true* (or correct) result. In the intervals for  $Z < 0.4 \text{ m/kg}^{1/3}$ , reflected impulse is calculated for the larger of the two cell sizes (taken from the converged solution at the lower limit of the interval) and reflected peak overpressure is calculated for the smaller of the two cell sizes (taken from the converged solution at the lower limit of the interval). Consider  $Z = 0.0553 \text{ m/kg}^{1/3}$  in Table 3-6. The reflected impulse converged for a cell size of larger than 2.18 mm and the reflected peak overpressure converged for a cell size greater than 1.09 mm. In the interval with  $Z = 0.0553 \text{ m/kg}^{1/3}$  as the lower limit, cell sizes of 1.09 and 0.546 mm are used for the impulse and overpressure calculations, respectively, thereby ensuring a converged solution.

The influence of charge size on the reflected peak overpressure and impulse is investigated at selected scaled distances using the 18735 and 23 kg charges, as shown in Tables 3-7 and 3-8, respectively. Identical to the analysis of the 960 kg charge, of the four cell sizes listed at each scaled distance in Tables 3-7 and 3-8, the largest three ( $R_j/125$ ,  $R_j/250$ ,  $R_j/500$ ) are used to compute reflected impulse and reflected peak overpressure and the smallest ( $R_j/1000$ ) is used to compute reflected peak overpressure only.

**Table 3-5 AUTODYN dataset for reflected calculations**

$Z_j < Z < Z_k$ or $Z = Z_j$ (m/kg <sup>1/3</sup> )	Number of monitoring locations
$0.0553 \leq Z < 0.060$	5
$0.060 \leq Z < 0.070$	5
$0.070 \leq Z < 0.080$	5
$0.080 \leq Z < 0.090$	5
$0.090 \leq Z < 0.10$	5
$0.10 \leq Z < 0.20$	5
$0.20 \leq Z < 0.30$	5
$0.30 \leq Z < 0.40$	5
$Z = 0.40$	1
$Z = 0.50$	1
$Z = 0.60$	1
$Z = 0.70$	1
$Z = 0.80$	1
$Z = 0.90$	1
$Z = 1.0$	1
$Z = 2.0$	1
$Z = 3.0$	1
$Z = 4.0$	1
$Z = 5.0$	1
$Z = 6.0$	1
$Z = 7.0$	1
$Z = 8.0$	1
$Z = 9.0$	1
$Z = 10.0$	1
$Z = 20.0$	1
$Z = 30.0$	1
$Z = 40.0$	1

**Table 3-6 Cell sizes for reflected peak overpressure and impulse; 960 kg charge with a radius of 520 mm**

$Z_j < Z < Z_k$ or $Z = Z_j$ (m/kg <sup>1/3</sup> )	$R_j = Z_j \times W^{1/3}$ (mm)	$R_j/500$ (mm)	Cell size (mm)
$Z = 0.0553$	546	1.09	4.36, 2.18, 1.09 and 0.546
$0.0553 < Z < 0.060$	546	1.09	1.09 and 0.546
$Z = 0.060$	592	1.18	4.74, 2.37, 1.18 and 0.592
$0.060 \leq Z < 0.070$	592	1.18	1.18 and 0.592
$Z = 0.070$	691	1.38	5.52, 2.76, 1.38 and 0.691
$0.070 \leq Z < 0.080$	691	1.38	1.38 and 0.691
$Z = 0.080$	789	1.58	6.31, 3.16, 1.58 and 0.789
$0.080 \leq Z < 0.090$	789	1.58	1.58 and 0.789
$Z = 0.090$	888	1.78	7.10, 3.55, 1.78 and 0.888
$0.090 \leq Z < 0.10$	888	1.78	1.78 and 0.888
$Z = 0.10$	986	1.97	7.89, 3.95, 1.97 and 0.986
$0.10 \leq Z < 0.20$	986	1.97	1.97 and 0.986
$Z = 0.20$	1973	3.95	15.8, 7.89, 3.95 and 1.98
$0.20 \leq Z < 0.30$	1973	3.95	3.95 and 1.98
$Z = 0.030$	2959	5.92	23.7, 11.8, 5.92 and 2.96
$0.30 \leq Z < 0.40$	2959	5.92	5.92 and 2.96
$Z = 0.40$	3946	7.89	31.6, 15.8, 7.89 and 3.95
$Z = 0.50$	4932	9.87	39.46, 19.7, 9.87 and 4.93
$Z = 0.60$	5919	11.8	47.4, 23.7, 11.8 and 5.92
$Z = 0.70$	6905	13.8	55.2, 27.6, 13.8 and 6.90
$Z = 0.80$	7892	15.8	63.1, 31.6, 15.8 and 7.89
$Z = 0.90$	8878	17.8	71.0, 35.5, 17.8 and 8.88
$Z = 1.0$	9865	19.7	78.9, 39.5, 19.7 and 9.87
$Z = 2.0$	19730	39.5	158, 78.9, 39.5 and 19.7
$Z = 3.0$	29595	59.2	237, 118, 59.2 and 29.6
$Z = 4.0$	39459	78.9	316, 158, 78.9 and 39.5
$Z = 5.0$	49324	98.6	395, 197, 98.6 and 49.3
$Z = 6.0$	59189	118	474, 237, 118 and 59.2
$Z = 7.0$	69054	138	552, 276, 138 and 69.0
$Z = 8.0$	78919	158	632, 316, 158 and 78.9
$Z = 9.0$	88784	178	710, 355, 178 and 88.8
$Z = 10.0$	98648	197	789, 395, 197 and 98.7
$Z = 20.0$	197297	395	1578, 789, 395 and 197
$Z = 30.0$	295945	592	2368, 1184, 592 and 296
$Z = 40.0$	394594	789	3157, 1578, 789 and 395

**Table 3-7 Cell sizes for reflected peak overpressure and impulse; 18735 kg charge with a radius of 1400 mm**

$Z = Z_j$ (m/kg <sup>1/3</sup> )	$R_j = Z_j \times W^{1/3}$ (mm)	$R_j / 500$ (mm)	Cell size (mm)
Z = 0.0553	1469	2.94	11.8, 5.88, 2.94 and 1.47
Z = 0.060	1594	3.19	12.7, 6.37, 3.19 and 1.59
Z = 0.080	2125	4.25	17.0, 8.50, 4.25 and 2.13
Z = 0.10	2656	5.31	21.2, 10.6, 5.31 and 2.66
Z = 0.20	5312	10.6	42.5, 21.2, 10.6 and 5.31
Z = 0.40	10624	21.2	85.0, 42.5, 21.2 and 10.6
Z = 1.0	26559	53.1	212, 106, 53.1 and 26.6
Z = 5.0	131797	266	1062, 531, 266 and 133
Z = 10.0	265594	531	2125, 1062, 531 and 266
Z = 40.0	1062375	2125	8500, 4250, 2125 and 1062

**Table 3-8 Cell sizes for reflected peak overpressure and impulse; 23 kg charge with a radius of 150 mm**

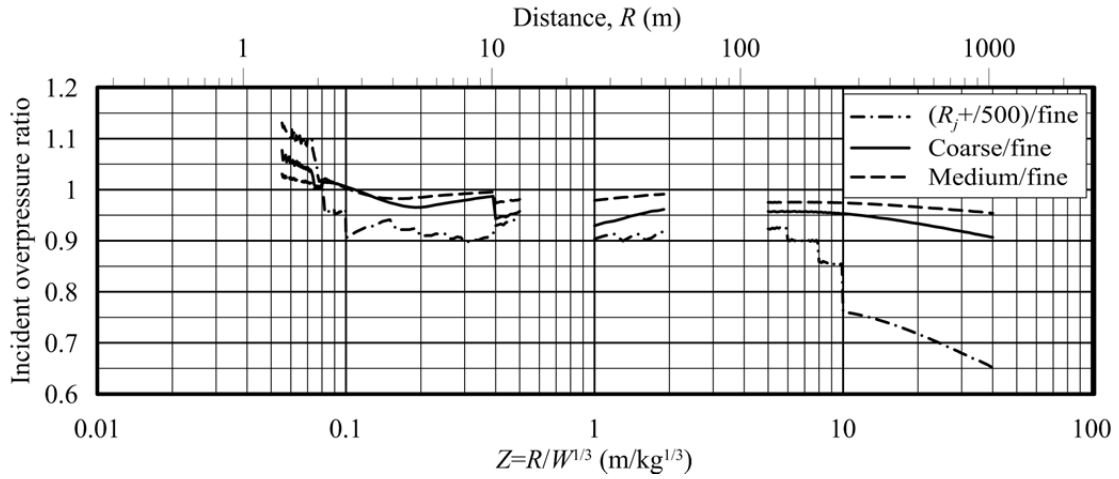
$Z = Z_j$ (m/kg <sup>1/3</sup> )	$R_j = Z_j \times W^{1/3}$ (mm)	$R_j / 500$ (mm)	Cell size (mm)
Z = 0.0553	157	0.315	1.26, 0.629, 0.315 and 0.157
Z = 0.060	171	0.341	1.37, 0.683, 0.341 and 0.171
Z = 0.080	228	0.455	1.82, 0.910, 0.455 and 0.228
Z = 0.10	284	0.569	2.28, 1.14, 0.569 and 0.284
Z = 0.20	569	1.14	4.55, 2.28, 1.14 and 0.569
Z = 0.40	1138	2.28	9.10, 4.55, 2.28 and 1.14
Z = 1.0	9865	5.69	22.8, 11.4, 5.69 and 2.84
Z = 5.0	14217	28.4	114, 56.9, 28.4 and 14.2
Z = 10.0	28439	56.9	228, 114, 56.9 and 28.4
Z = 40.0	113755	228	910, 455, 228 and 114

## 3.6 Incident Overpressure and Impulse

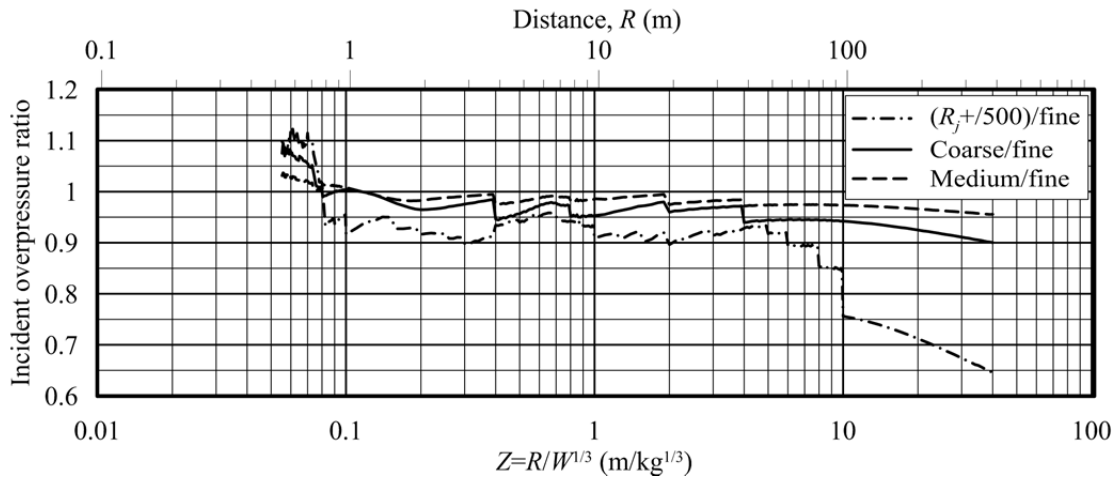
### 3.6.1 Results and Observations

Figures 3-8, 3-9, 3-10, 3-11 and 3-12 present results of calculations for incident peak overpressure and impulse. Figures 3-8 and 3-9 present the ratios of incident peak overpressure for the different cell sizes of Tables 3-2, 3-3 and 3-4. The legends in the panels identify three ratios that involve the  $R_j + 500$  (largest, greater than  $R_j/500$ ), coarse (second largest), medium (third largest) and fine (smallest) meshes. The coarse, medium and fine meshes involve cells smaller than  $R_j/500$ . The ratios of incident peak overpressure for the coarse-to-fine and medium-to-fine meshes are less than 10% at all scaled distances, namely,  $0.0553 \leq Z < 40 \text{ m/kg}^{1/3}$ , as seen in Figure 3-8. The ratios for the  $R_j/500$ -to-fine meshes are mostly less than 10% for  $Z < 8.0 \text{ m/kg}^{1/3}$ . For incident impulse, the three ratios are less than 10% at all scaled distances as seen in Figure 3-9. Figure 3-10 presents the ratios of incident peak overpressure and scaled incident impulse for the three charge weights (18735, 960 and 23 kg) and the smallest cells used for its analysis. The effect of charge weight is clearly insignificant.

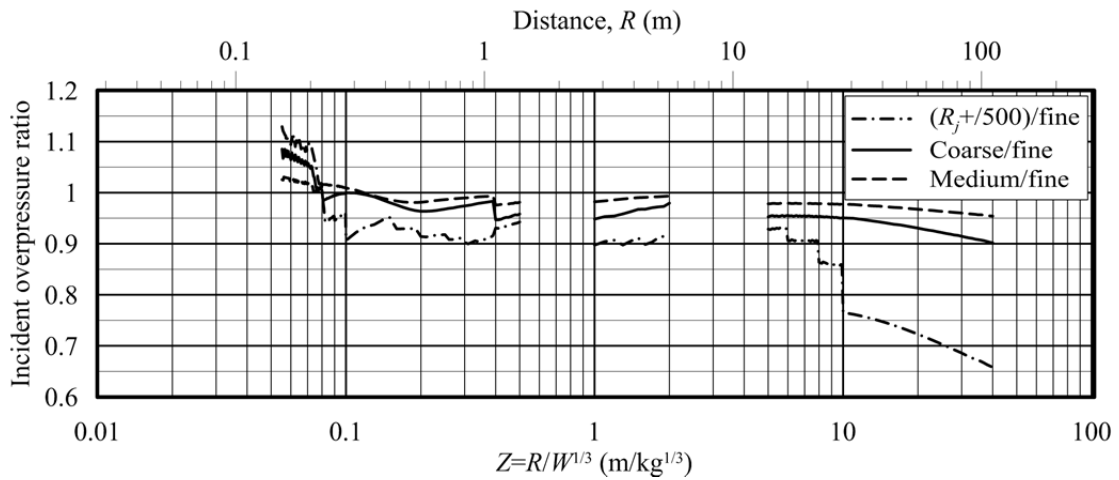
The incident peak overpressures calculated for the three charge weights, using the smallest cells in the intervals of Table 3-2, 3-3 and 3-4, are presented in Figure 3-11. The KB predictions and the data of Needham (2010) are included in the figures. Figure 3-11a presents data across the range  $0.0553 \leq Z \leq 40 \text{ m/kg}^{1/3}$ . Figures 3-11b through 3-11f present data across smaller ranges of scaled distance to aid interpretation. Figures 3-11g and 3-11h present the ratios of the AUTODYN-calculated to the KB-predicted values of incident peak overpressure for  $0.0553 \leq Z \leq 40 \text{ m/kg}^{1/3}$ , where the truncated y axis of Figure 3-11h allows the reader to judge the range over which the ratio is between 0.9 and 1.1. Figure 3-12 presents information for incident impulse, which are also calculated using the smallest cell size in the intervals of Tables 3-2, 3-3, and 3-4.



(a) 18735 kg charge

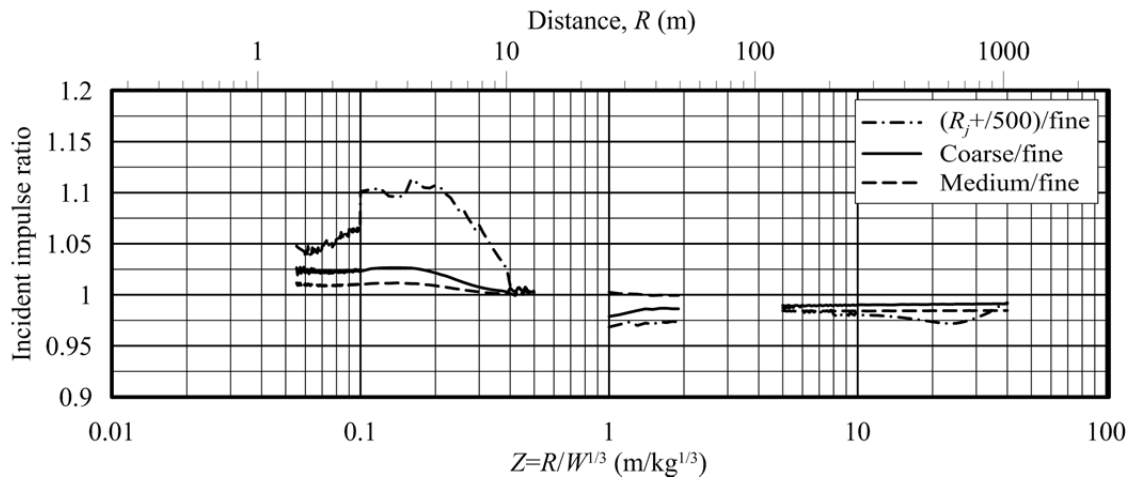


(b) 960 kg charge

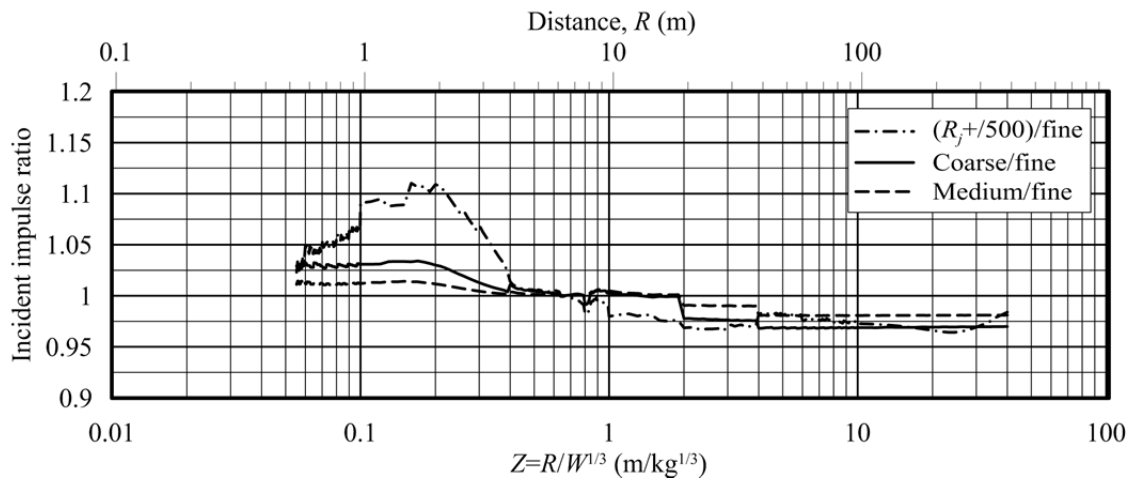


(c) 23 kg charge

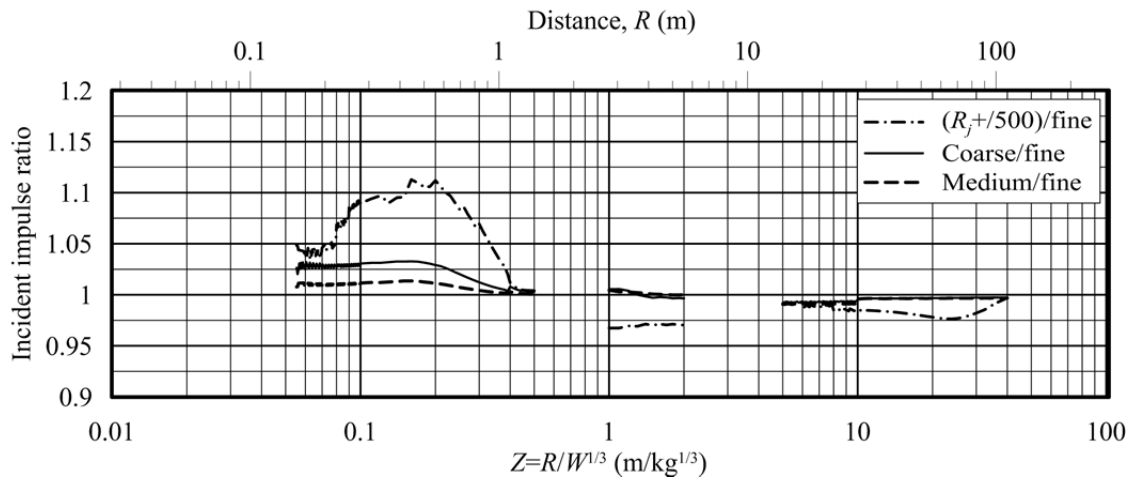
Figure 3-8 Ratios of incident peak overpressure for different cell sizes;  $0.0553 \leq Z < 40.0$  m/kg<sup>1/3</sup>



(a) 18735 kg charge

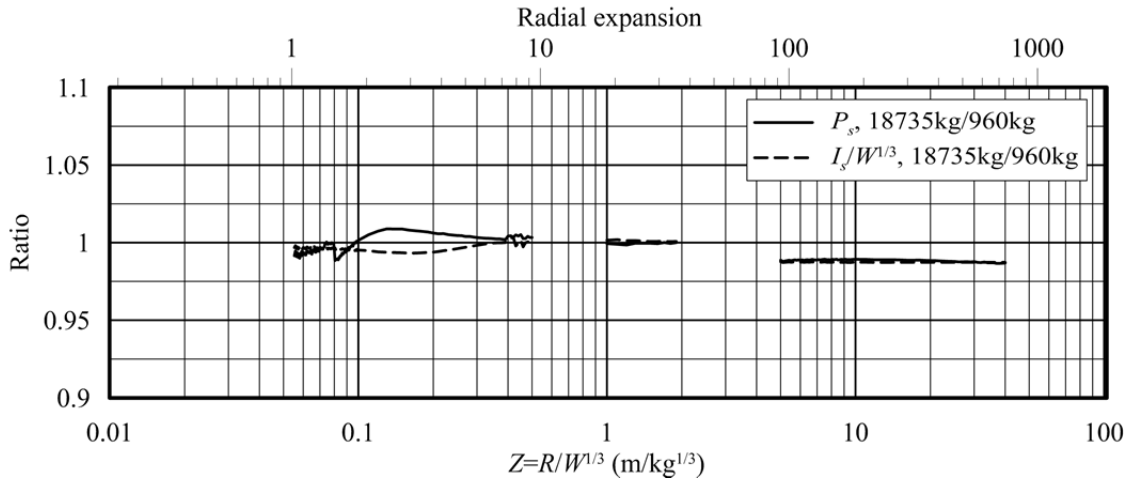


(b) 960 kg charge

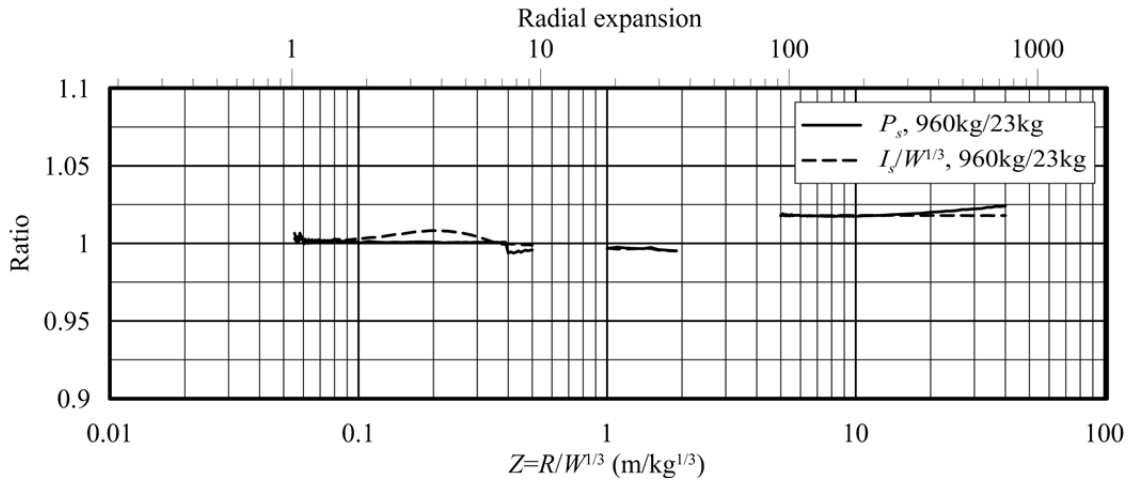


(c) 23 kg charge

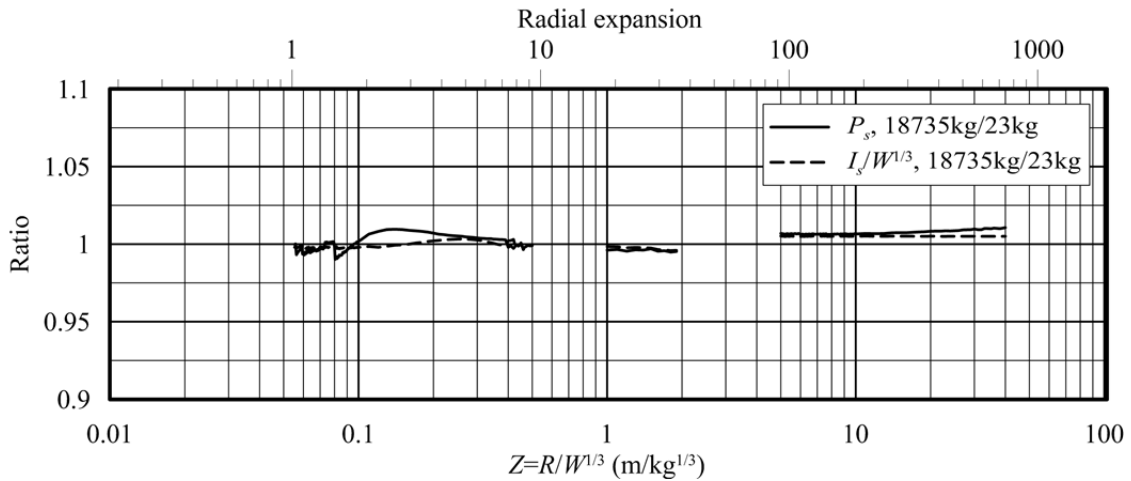
Figure 3-9 Ratios of incident impulse for different cell sizes;  $0.0553 \leq Z < 40.0 \text{ m/kg}^{1/3}$



(a) Charge weights of 18735 and 960 kg

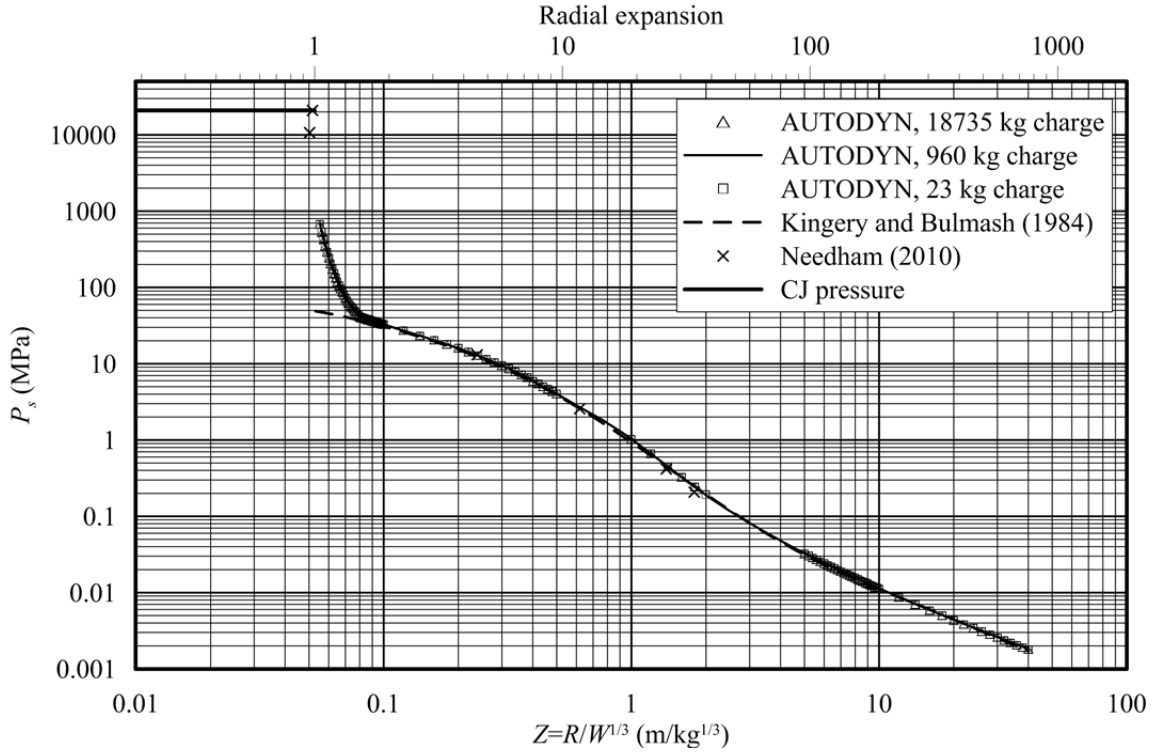


(b) Charge weights of 960 and 23 kg

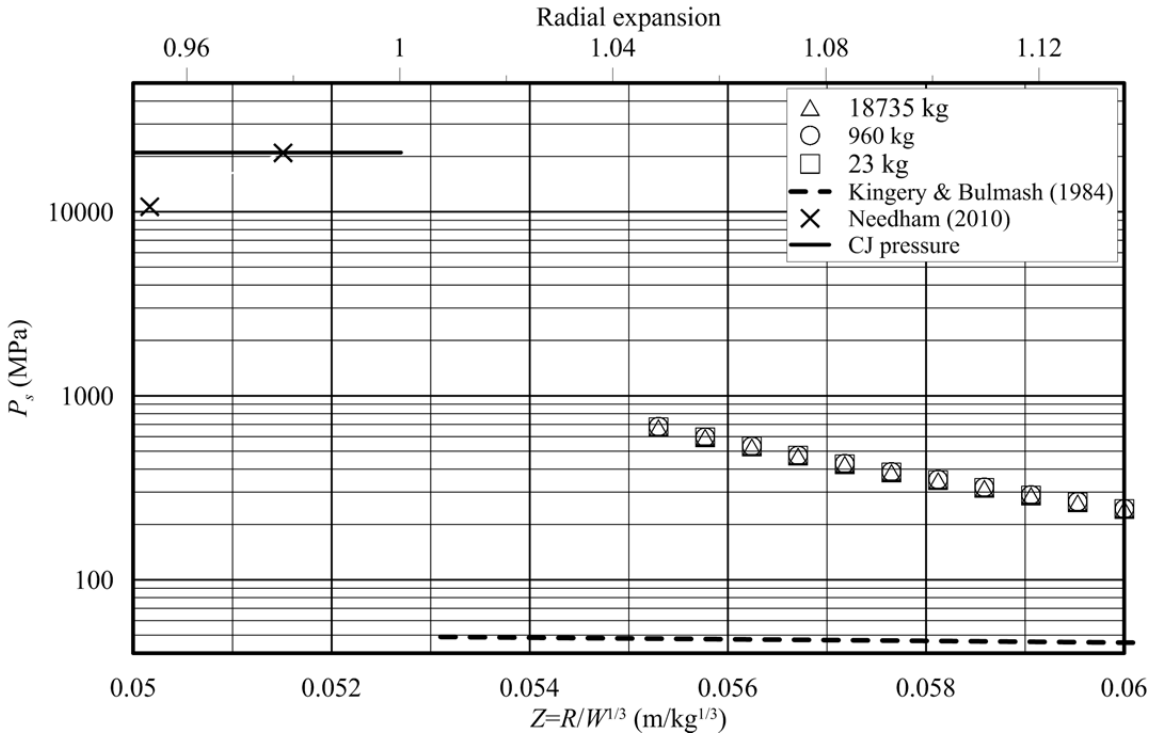


(c) Charge weights of 18735 and 23 kg

**Figure 3-10 Ratios of incident peak overpressure and impulse for the fine meshes; charge weights of 18735, 960 and 23 kg;  $0.0553 \leq Z < 40.0 \text{ m/kg}^{1/3}$**

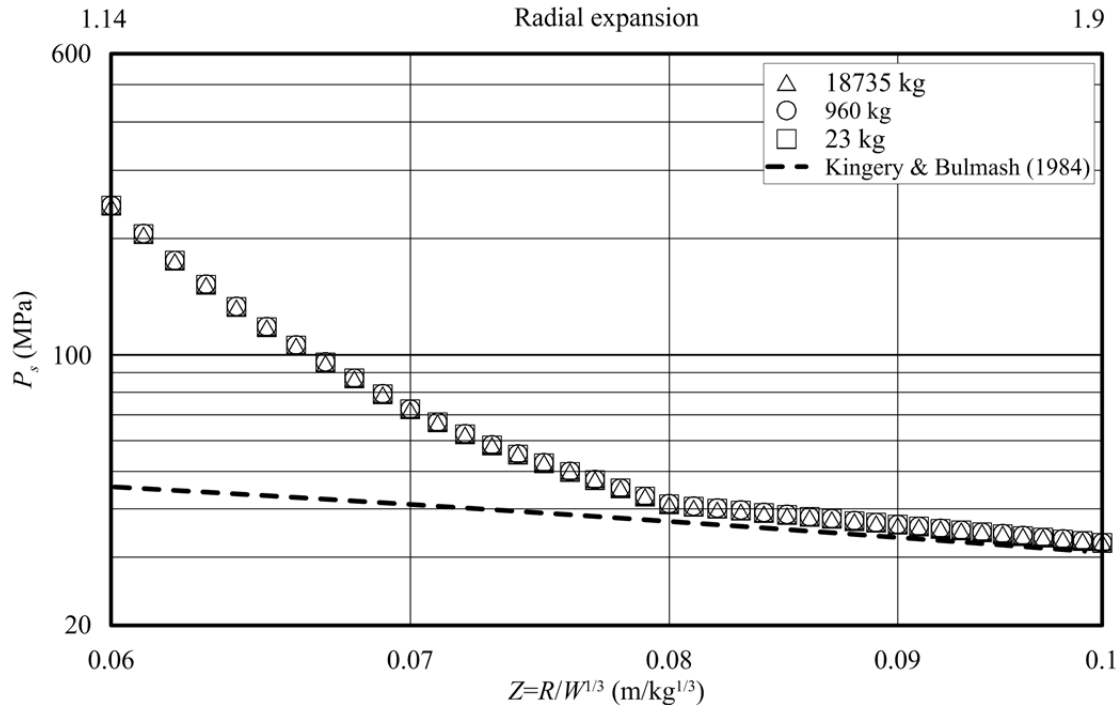


(a) Incident overpressure;  $0.0553 \leq Z \leq 40.0 \text{ m/kg}^{1/3}$

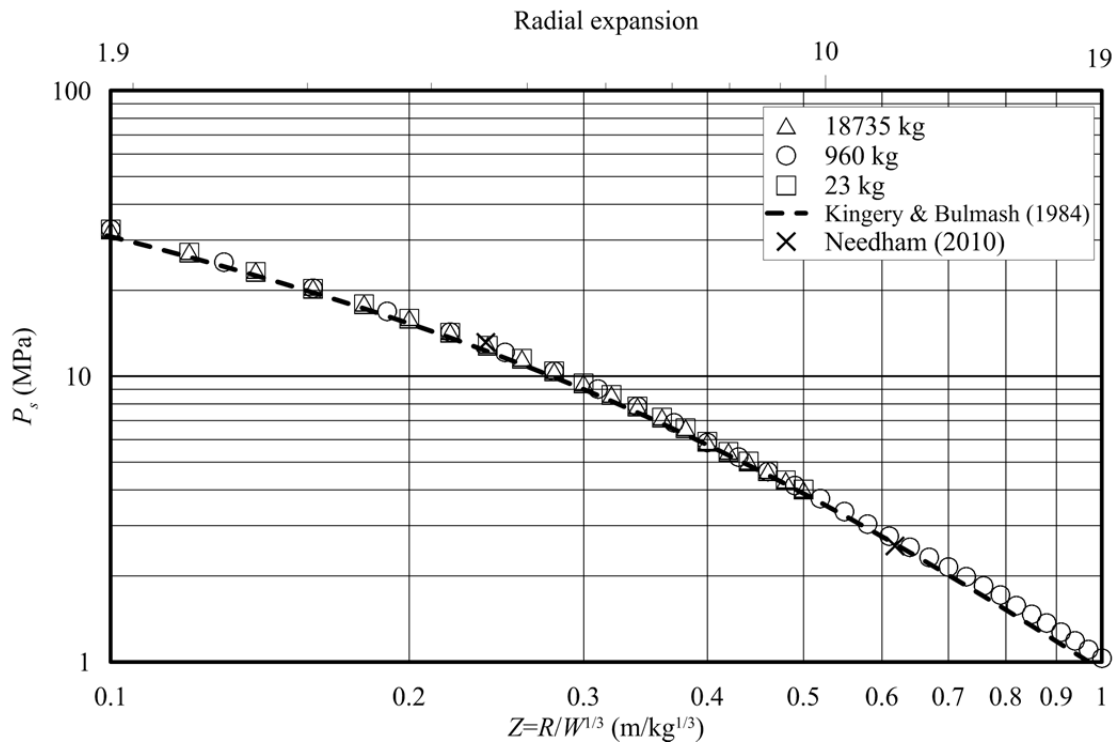


(b) Incident overpressure;  $0.0553 \leq Z \leq 0.06 \text{ m/kg}^{1/3}$

**Figure 3-11 Incident peak overpressure versus scaled distance**



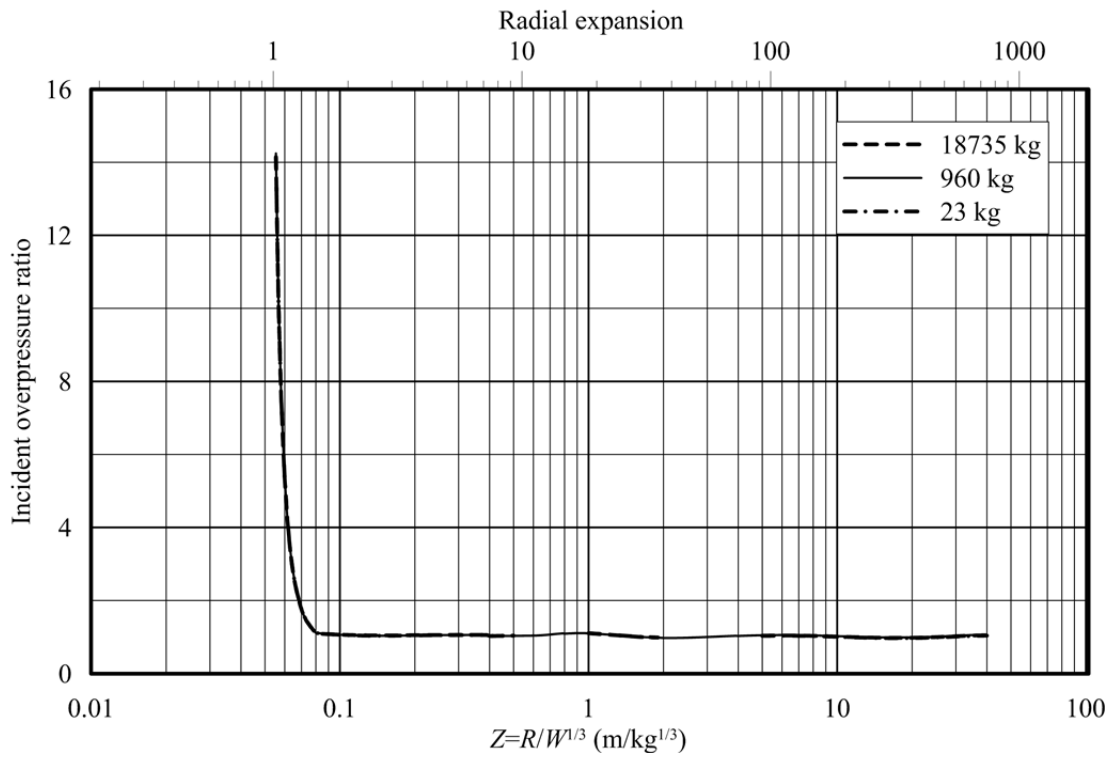
(c) Incident overpressure;  $0.06 \leq Z \leq 0.1$  m/kg<sup>1/3</sup>



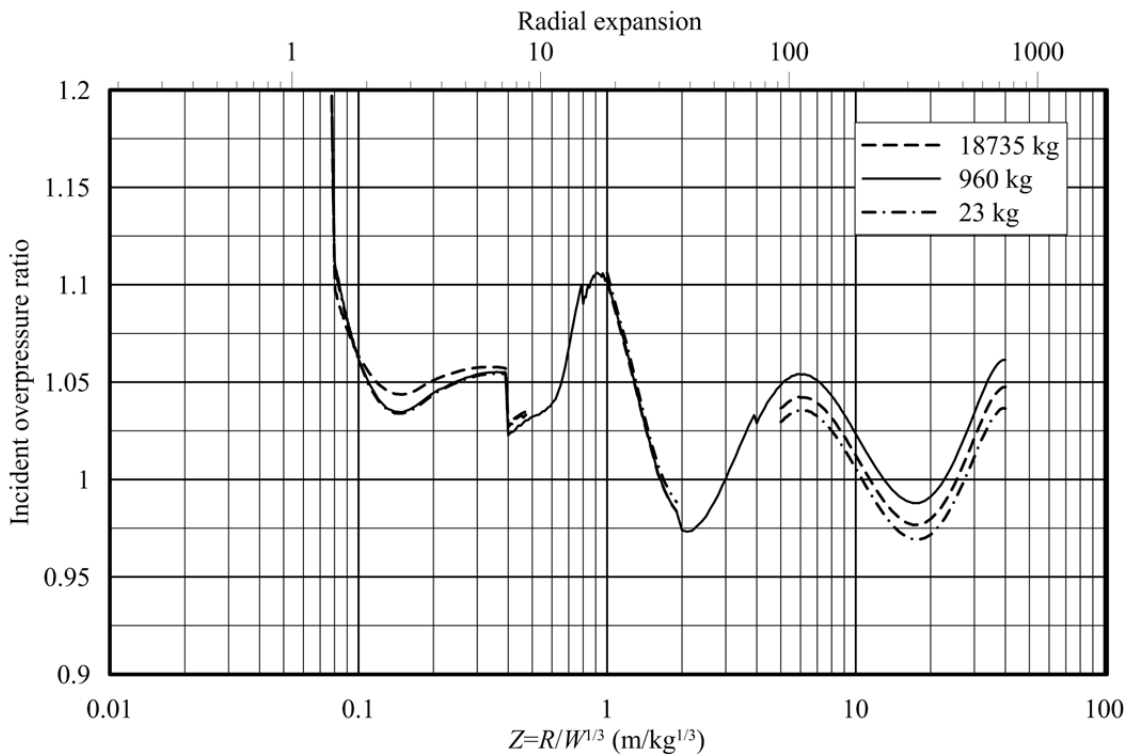
(d) Incident overpressure;  $0.1 \leq Z \leq 1$  m/kg<sup>1/3</sup>

**Figure 3-11 Incident peak overpressure versus scaled distance (cont.)**



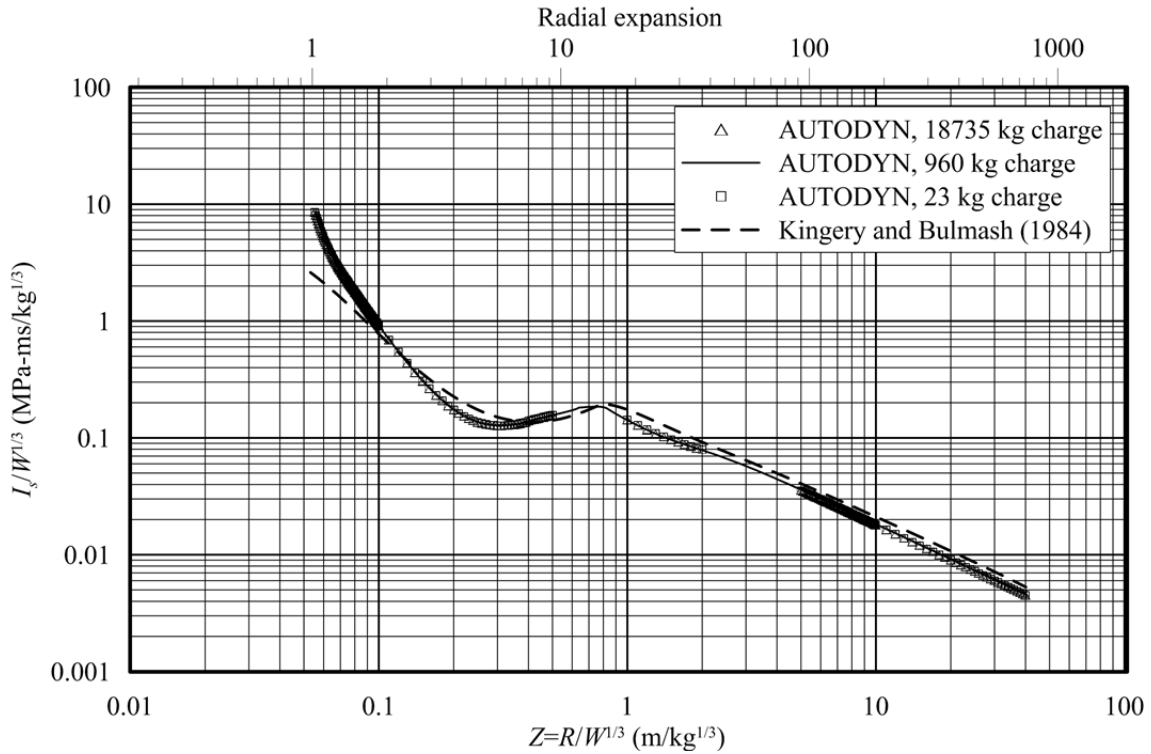


(g) Ratios of AUTODYN calculations to KB predictions

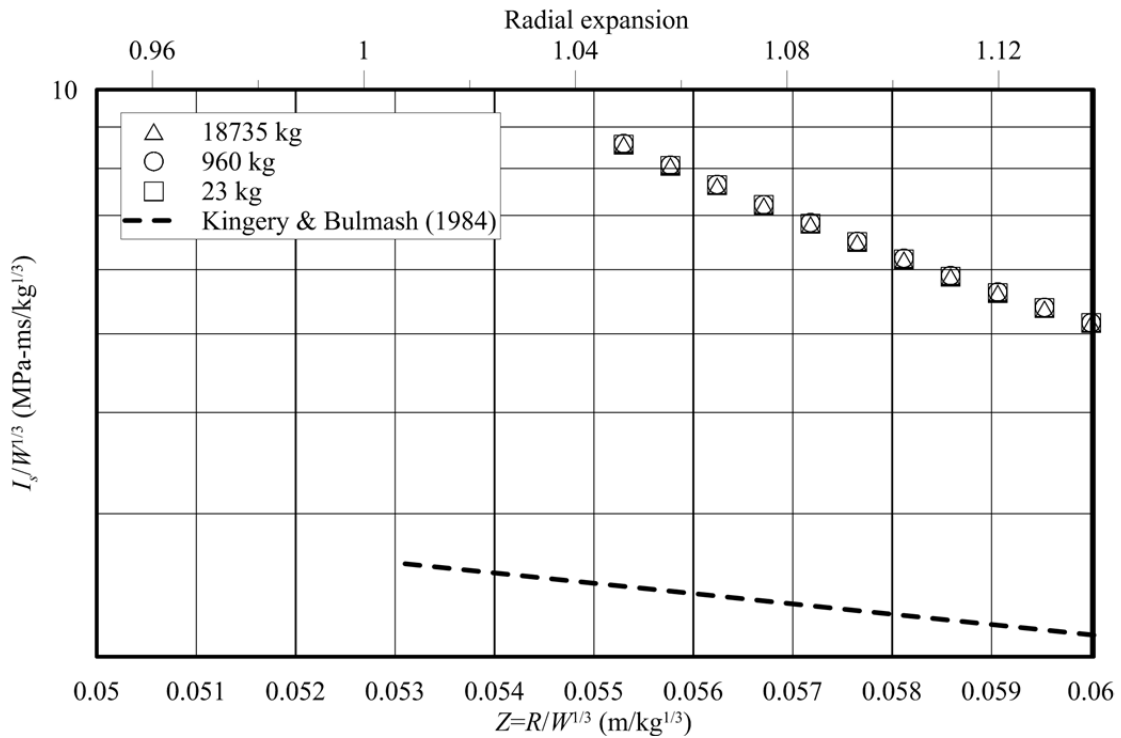


(h) Ratios of AUTODYN calculations to KB predictions; part range on ratio

**Figure 3-11 Incident peak overpressure versus scaled distance (cont.)**



(a) Incident impulse;  $0.0553 \leq Z \leq 40.0$  m/kg<sup>1/3</sup>



(b) Incident impulse;  $0.0553 \leq Z \leq 0.06$  m/kg<sup>1/3</sup>

**Figure 3-12 Incident impulse versus scaled distance**

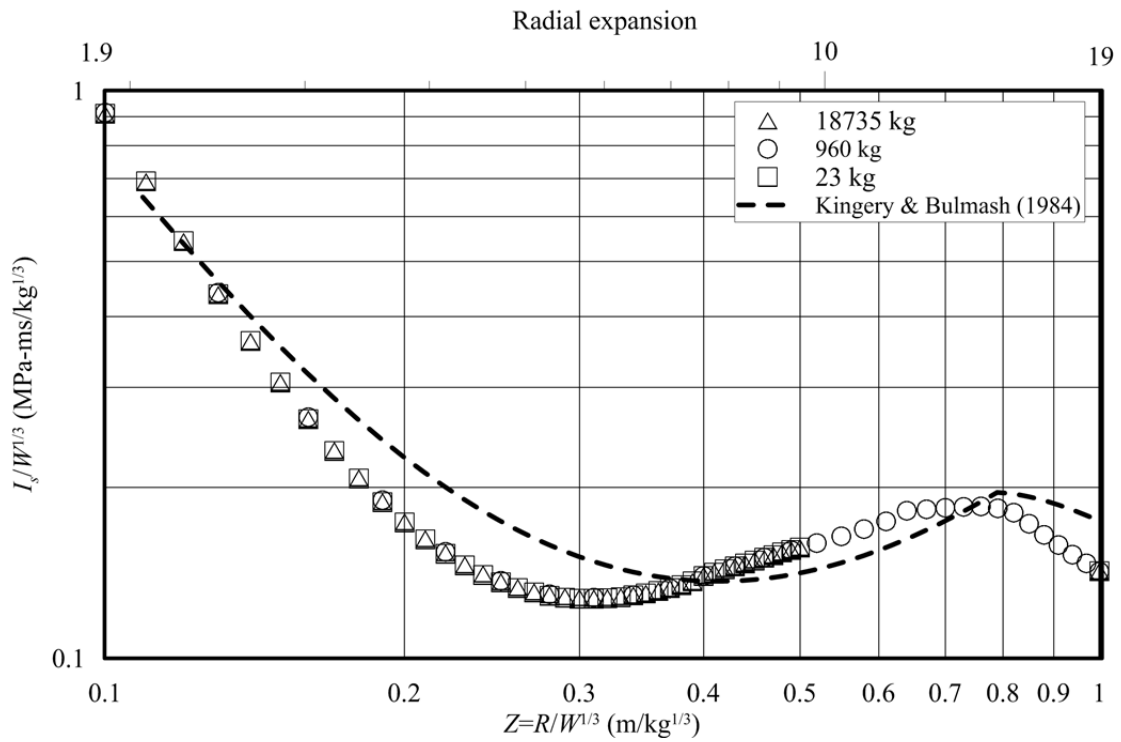
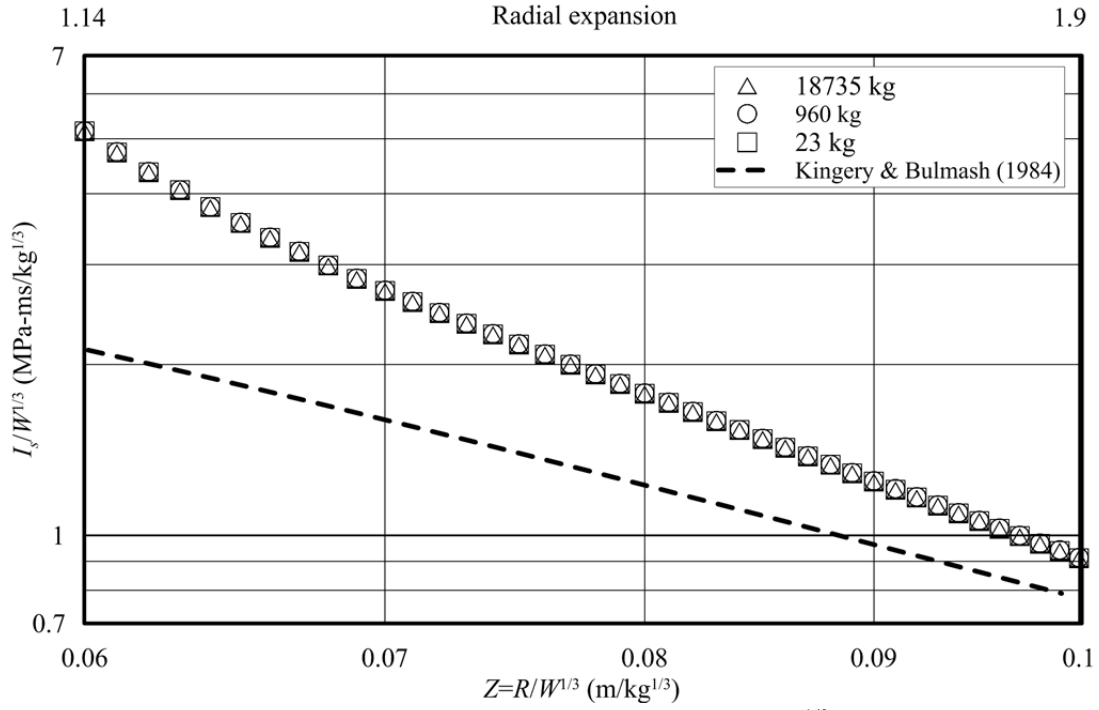


**Figure 3-12 Incident impulse versus scaled distance (cont.)**

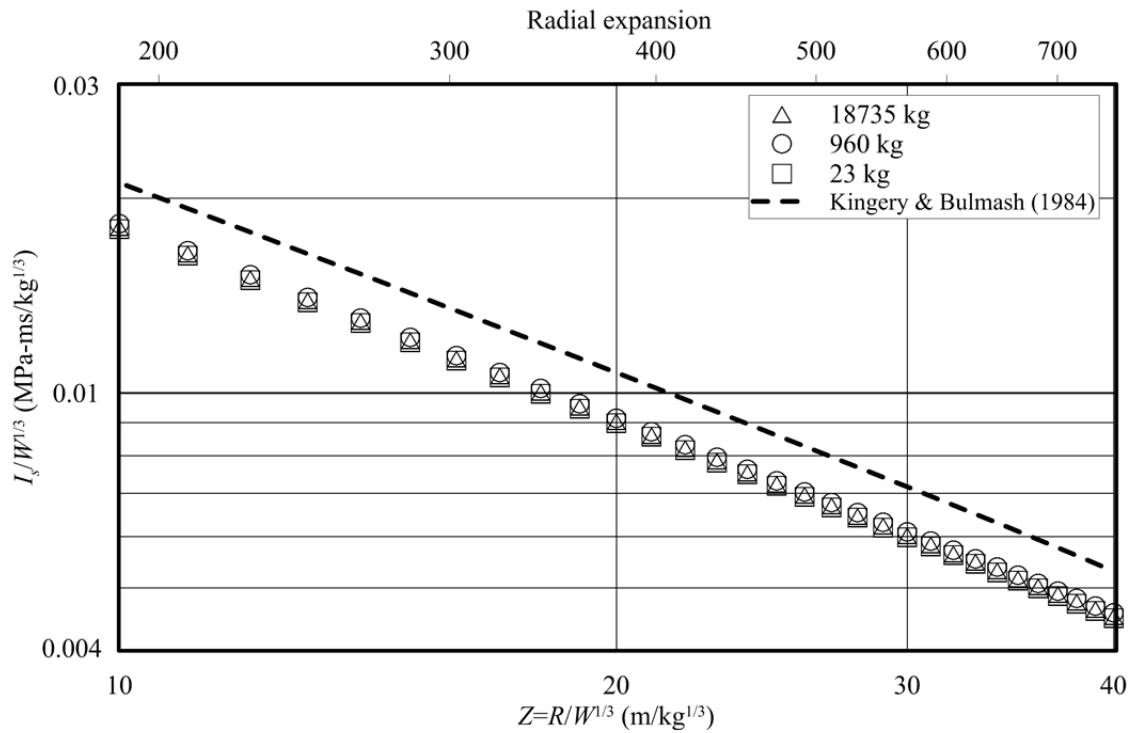
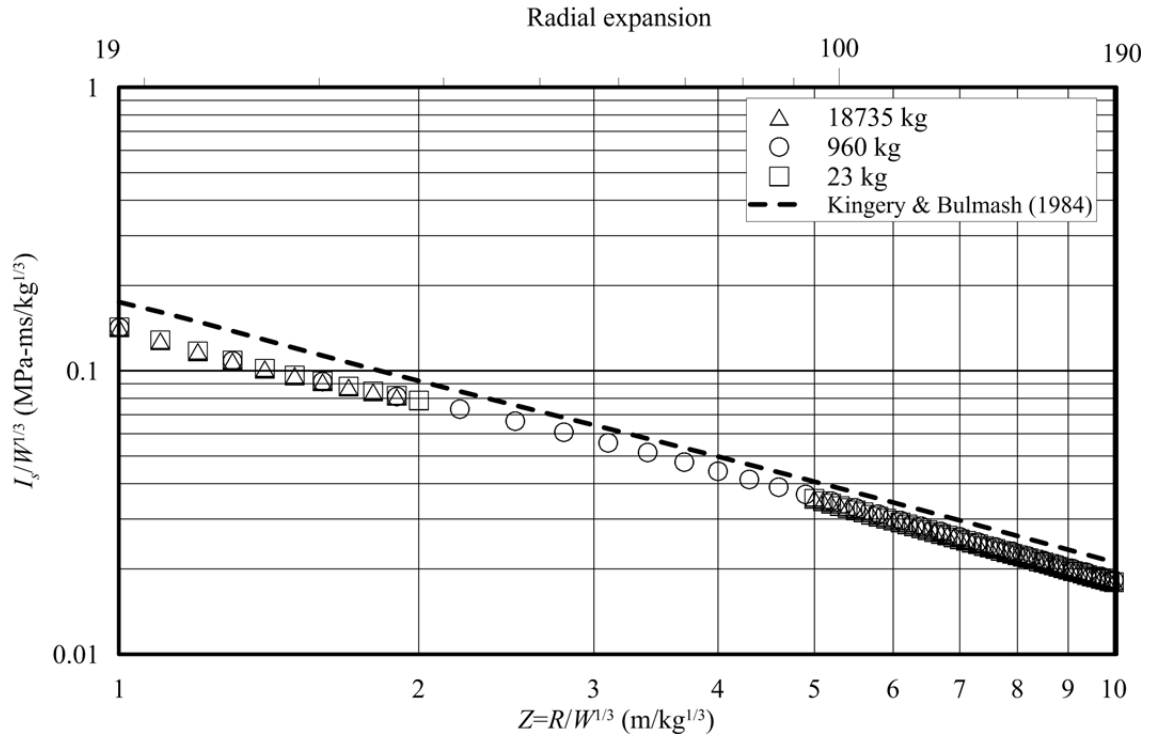
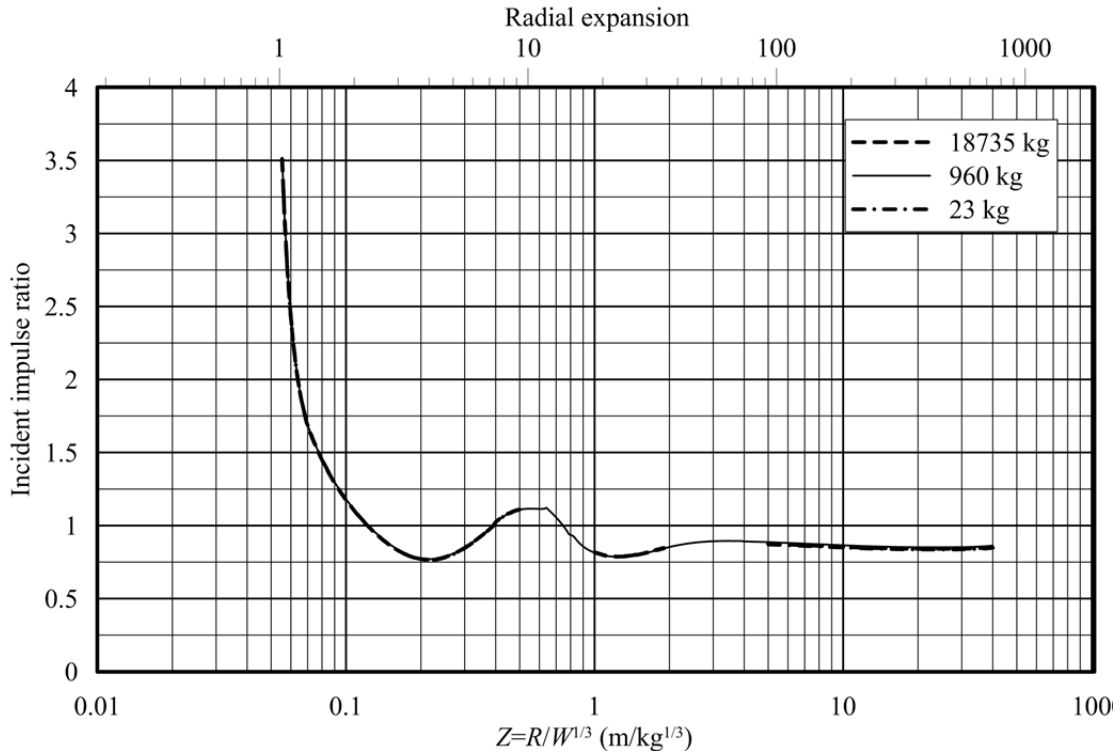
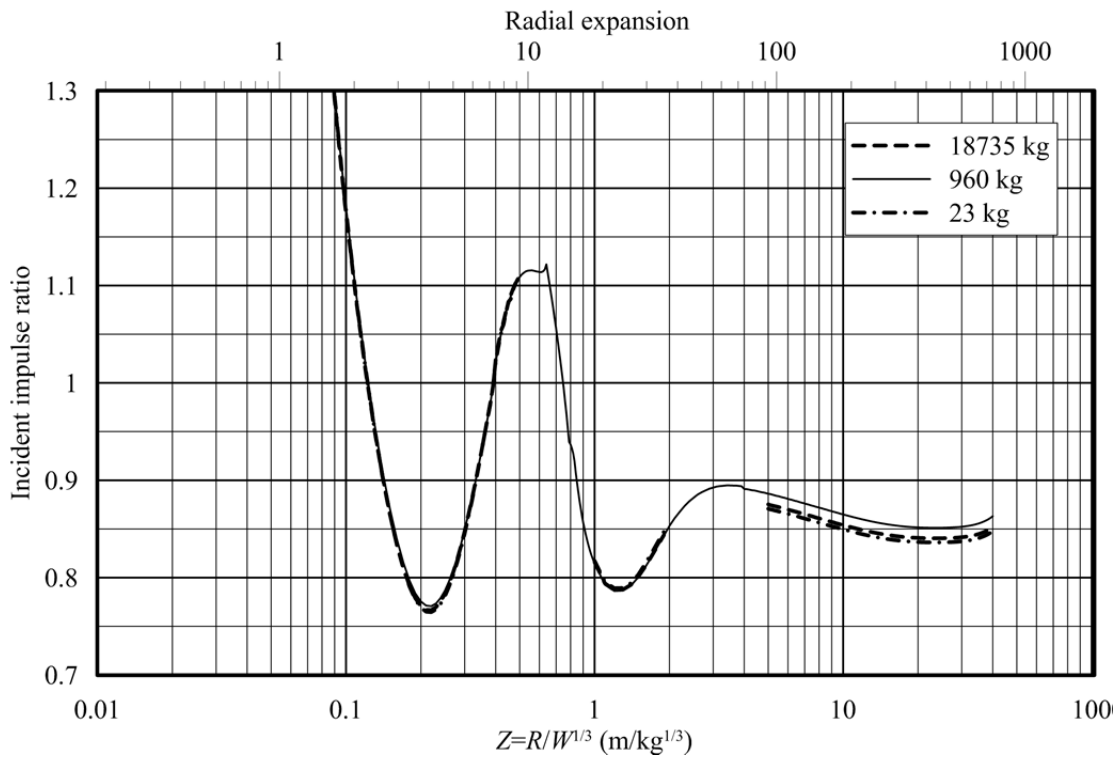


**Figure 3-12 Incident impulse versus scaled distance (cont.)**



(g) Ratio of AUTODYN calculations to KB predictions; full range



(h) Ratios of AUTODYN calculations to KB predictions; part range on ratio

**Figure 3-12 Incident impulse versus scaled distance (cont.)**

The AUTODYN calculations of incident peak overpressure are significantly greater than the KB predictions for  $Z < 0.08 \text{ m/kg}^{1/3}$  but are within 10% (generally) for  $Z > 0.08 \text{ m/kg}^{1/3}$ . The maximum difference is a factor of 14.2 at  $Z = 0.0553 \text{ m/kg}^{1/3}$ . For incident impulse, the ratio of the AUTODYN calculations to the KB predictions is generally either greater than 1.1 or less than 0.9. The maximum difference in incident impulse is a factor of 3.52 at  $Z = 0.0553 \text{ m/kg}^{1/3}$ . In the far field, say  $Z > 1.0 \text{ m/kg}^{1/3}$ , the KB predictions of incident impulse are 10% to 25% greater than the AUTODYN calculations, which is consistent with the observations of Bogosian et al. (2002), (see Section 3.3), and with the analysis of Browning et al. (2013) using the computer codes LS-DYNA (LSTC 2013) and CTH (McGlaun et al. 1990), as discussed in Section 2.3.

### **3.6.2 Cell Size for CFD Analysis**

One goal of this analysis was to provide recommendations on the choice of cell size for CFD analysis of detonation of high explosive.

For incident peak overpressure, a cell size equal to 0.002 times the distance to the monitoring location will provide results within 10% of the *converged* value for  $Z < 8.0 \text{ m/kg}^{1/3}$ , noting that the choice of cell size must allow the adequate meshing of the explosive. For  $Z > 8.0 \text{ m/kg}^{1/3}$ , a cell size smaller than 0.002 times the distance should be used to provide results within 10% of the *converged* value. (At  $Z = 8.0 \text{ m/kg}^{1/3}$ , the incident peak overpressure is approximately one-seventh of an atmosphere and the use of CFD tools to predict incident pressure and impulse is likely not warranted.) For incident impulse, a cell size equal to 0.002 times the distance to the monitoring location will provide results within 10% of the *converged* value across the range  $0.0553 \leq Z < 40 \text{ m/kg}^{1/3}$ .

In summary, a cell size of 0.002 times the distance from the point of detonation to the monitoring location is recommended for CFD analysis, noting that CFD analysis is likely not warranted for blast-resistant design at large values of scaled distance because the incident peak overpressure is small. The choice of cell size must accommodate the meshing of the charge and this may dictate the use of a smaller cell size than that required for the accurate calculation of values of peak overpressure and impulse.

## 3.7 Reflected Overpressure and Impulse

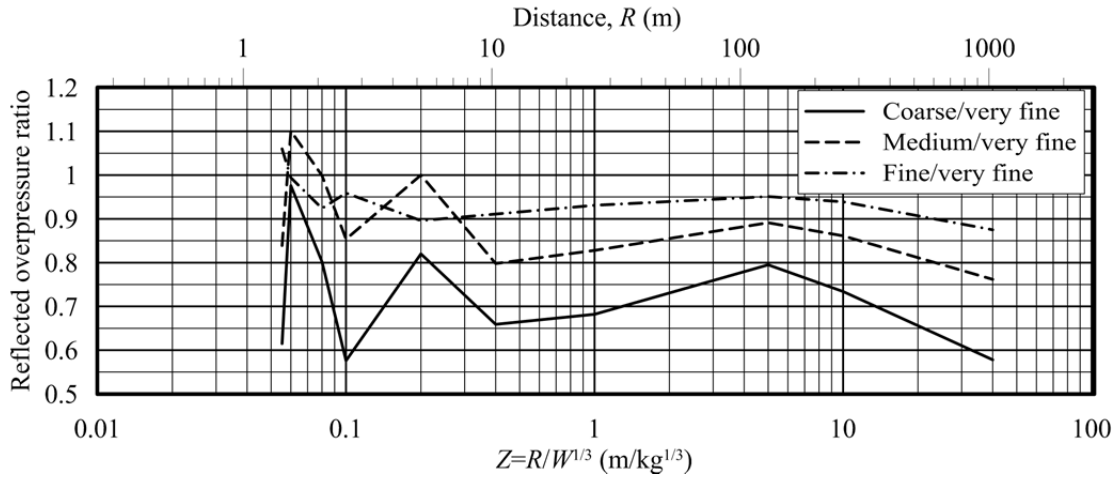
### 3.7.1 Results and Observations

Figures 3-13, 3-14, 3-15, 3-16 and 3-17 present results of calculations of normally reflected peak overpressure and impulse. Figure 3-13 presents the ratios of normally reflected peak overpressure for the coarse-to-very fine, medium-to-very fine, and fine-to-very fine cells. The ratios for  $R_j/500$  (fine) to  $R_j/1000$  (very fine) range between 0.9 and 1.1 and so a cell size of  $R/500$  is considered appropriate for simulating reflected peak overpressure in a 2D domain. Figure 3-14 presents the corresponding data for reflected impulse using coarse, medium and fine meshes. The ratios range between 0.95 and 1.05 for the three charge weights and all values of scaled distance, and so the cell size of  $R/500$  is also considered appropriate for simulating reflected impulse in a 2D domain.

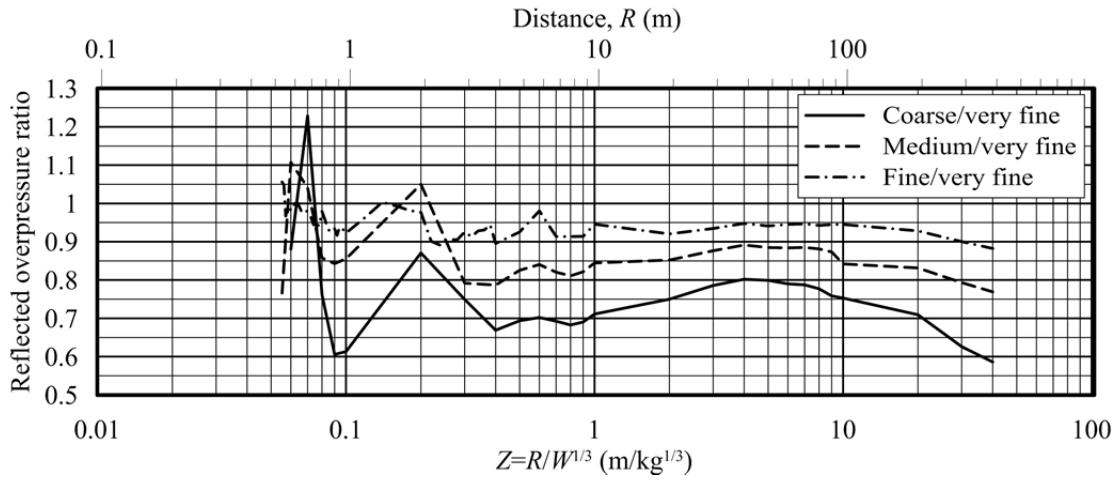
Figure 3-15 presents ratios of normally reflected peak overpressure and scaled reflected impulse for the three charge weights (18735, 960 and 23 kg) and the smallest cells used for analysis. The effect of charge weight is not significant.

The normally reflected peak overpressures for the three charge weights, using the  $R_j/1000$  cells, are presented in Figures 3-16a through 3-16d. The KB predictions are included in the figures. Figure 3-16a presents data across the range  $0.0553 \leq Z \leq 40 \text{ m/kg}^{1/3}$ . Figures 3-16b through 3-16d present data across smaller ranges of scaled distance to aid interpretation. Figure 3-16e and 3-16f present the ratios of the AUTODYN-calculated to the KB-predicted values of normally reflected peak overpressure for  $0.0553 \leq Z \leq 40 \text{ m/kg}^{1/3}$ , where the truncated y axis of Figure 3-16f allows the reader to judge the range over which the ratio is between 0.9 and 1.1. Figure 3-17 presents information for reflected impulse, which are also calculated using the  $R_j/500$  cell size in the intervals of Tables 3-6, 3-7, and 3-8.

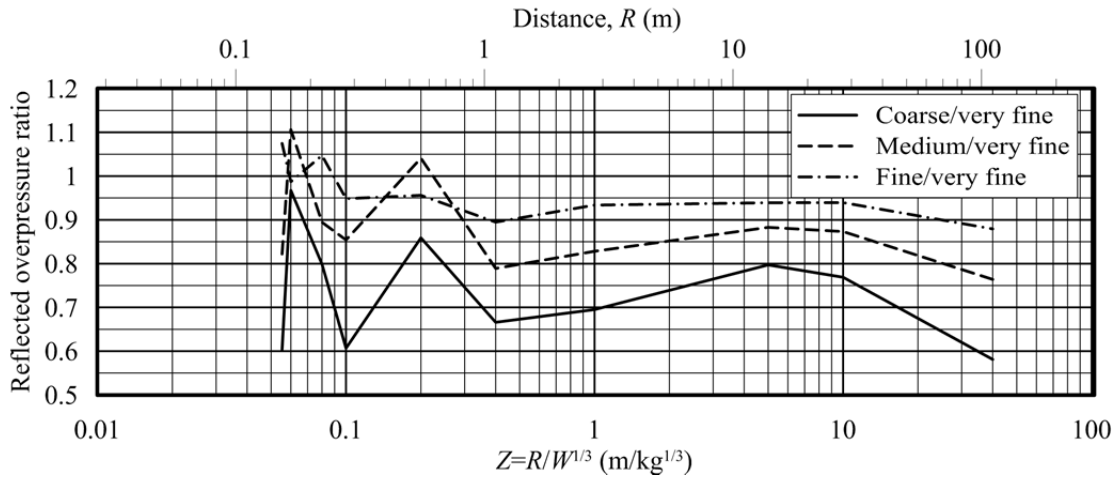
The AUTODYN calculations of normally reflected peak overpressure are significantly greater than the KB predictions for  $Z < 0.30 \text{ m/kg}^{1/3}$  but within 10% (generally) for  $Z > 0.30 \text{ m/kg}^{1/3}$ . The maximum difference is a factor of 20 at  $Z = 0.0553 \text{ m/kg}^{1/3}$ . The maximum difference in reflected impulse is approximately 10% across the entire range of scaled distance.



(a) 18735 kg charge

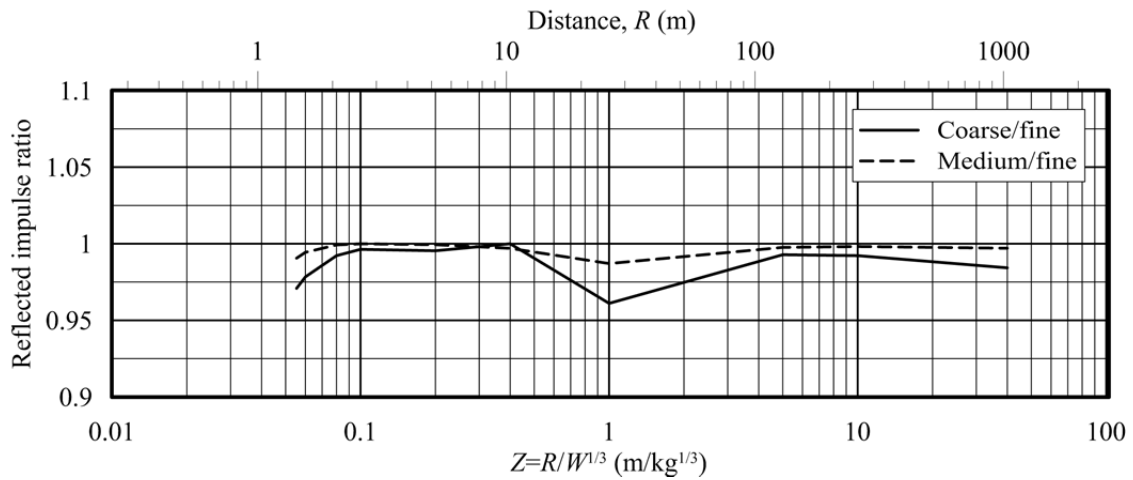


(b) 960 kg charge

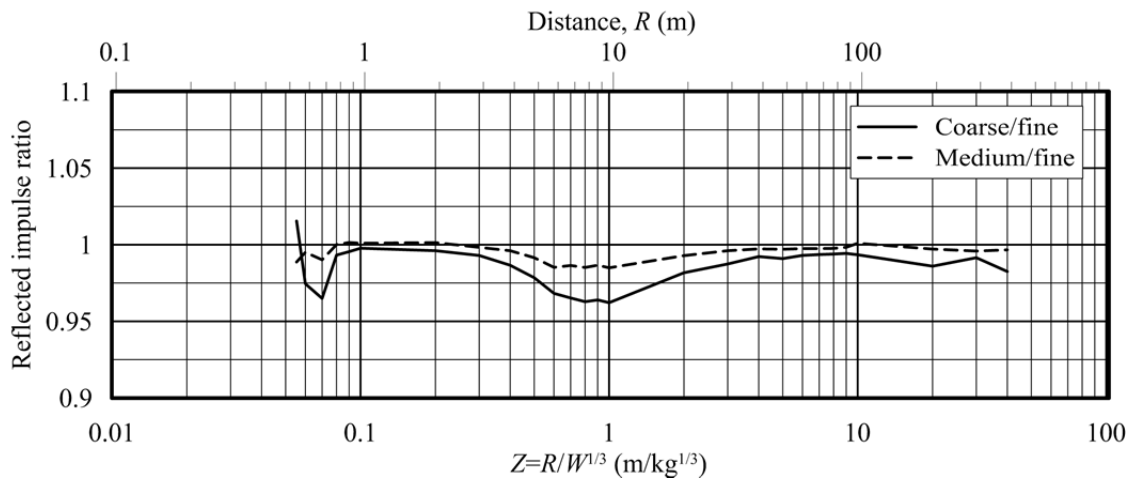


(c) 23 kg charge

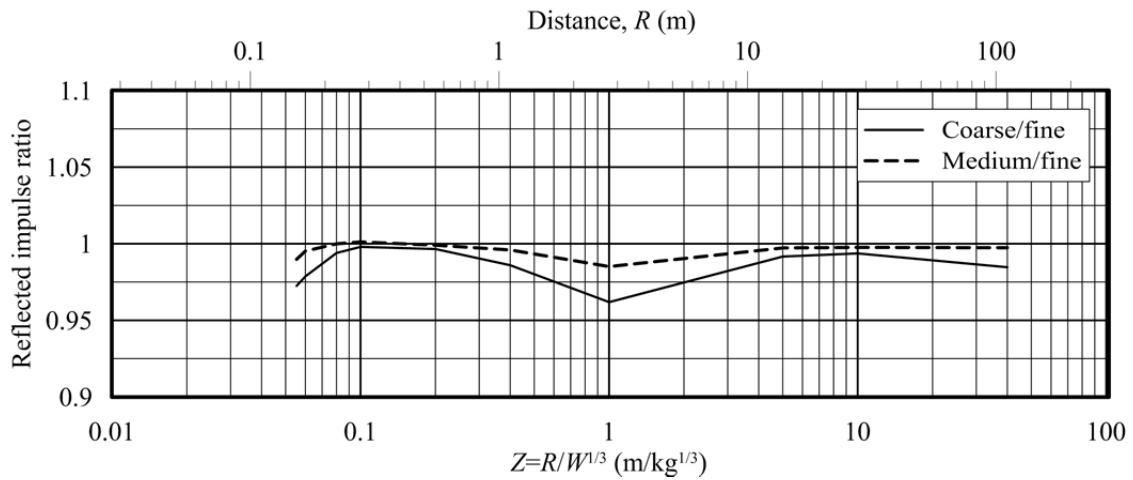
Figure 3-13 Ratios of reflected peak overpressure for different cell sizes;  $0.0553 \leq Z < 40.0$   $m/kg^{1/3}$



(a) 18735 kg charge

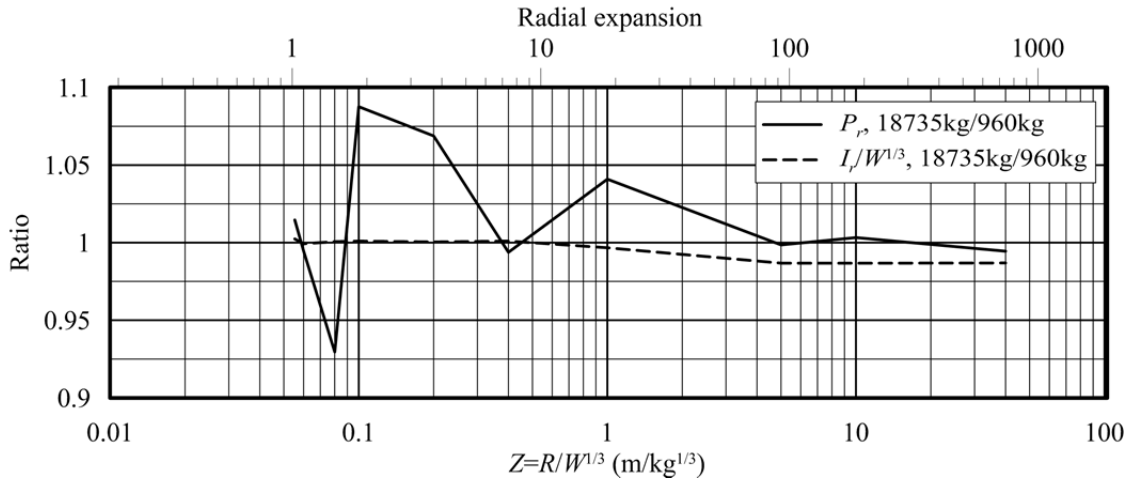


(b) 960 kg charge

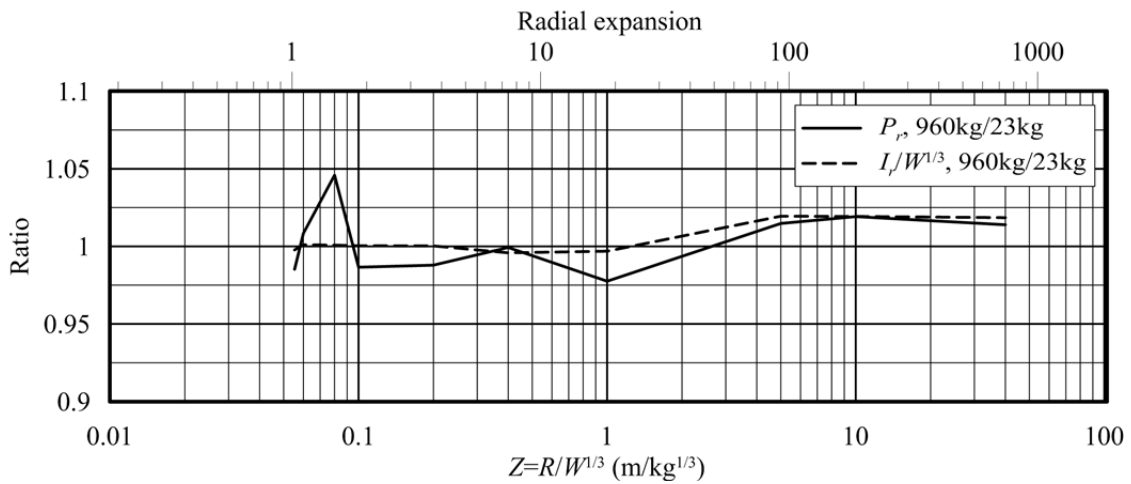


(c) 23 kg charge

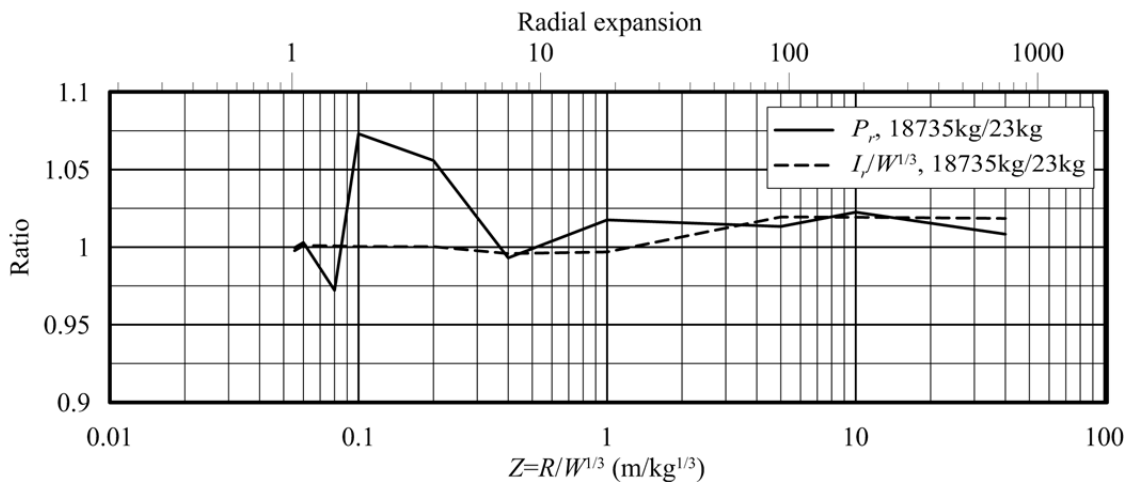
Figure 3-14 Ratios of reflected impulse for different cell sizes;  $0.0553 \leq Z < 40.0 \text{ m/kg}^{1/3}$



(a) Charge weights of 18735 and 960 kg

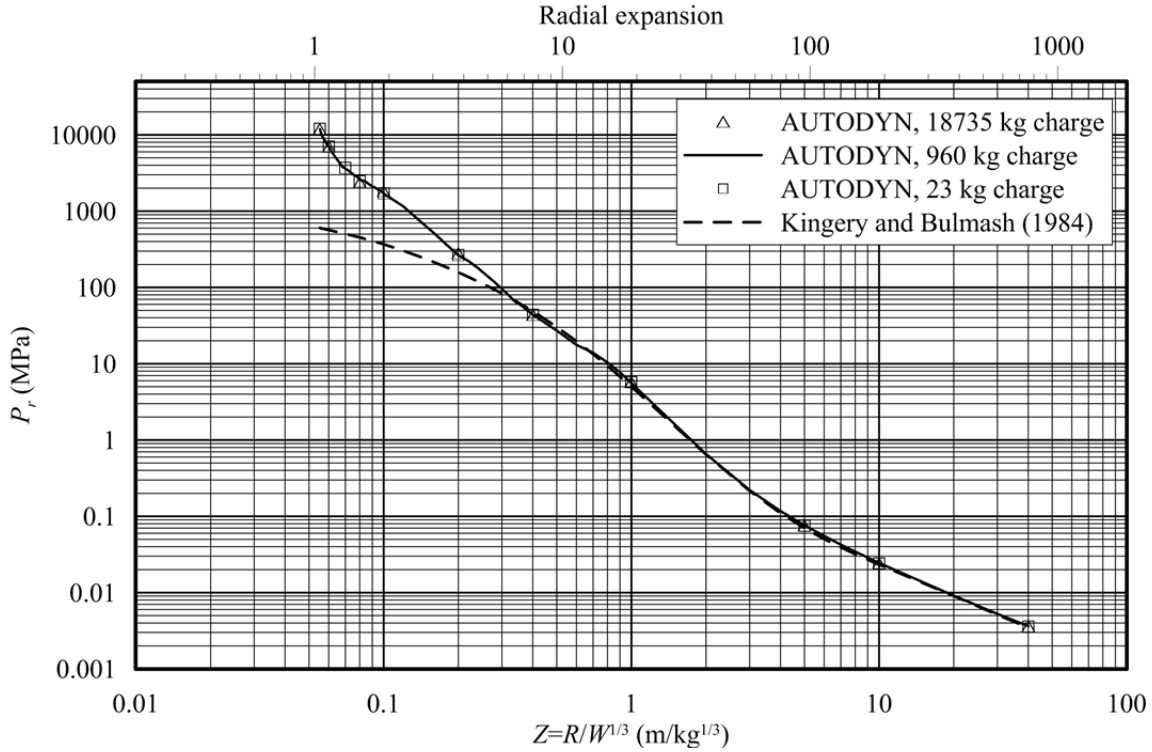


(b) Charge weights of 960 and 23 kg

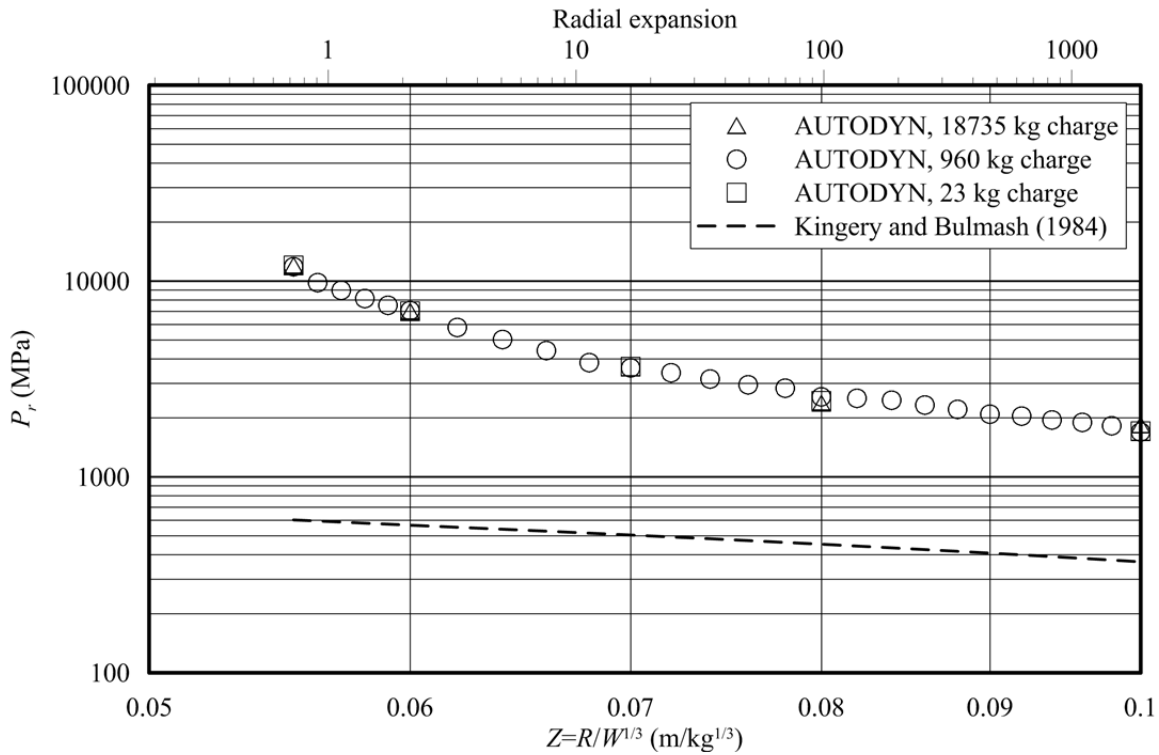


(c) Charge weights of 18735 and 23 kg

**Figure 3-15 Ratios of reflected peak overpressure and impulse for the smallest cell sizes; charge weights of 18735, 960 and 23 kg;  $0.0553 \leq Z < 40.0$  m/kg<sup>1/3</sup>**

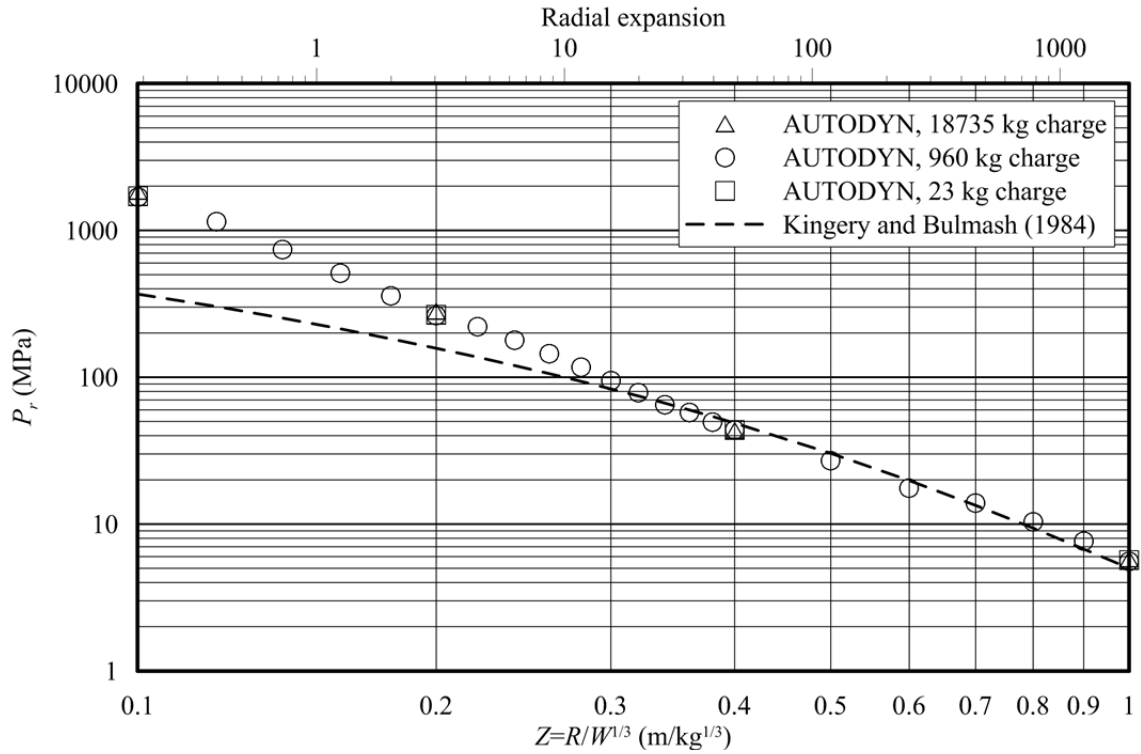


(a) Reflected overpressure;  $0.0553 \leq Z \leq 40.0$  m/kg<sup>1/3</sup>

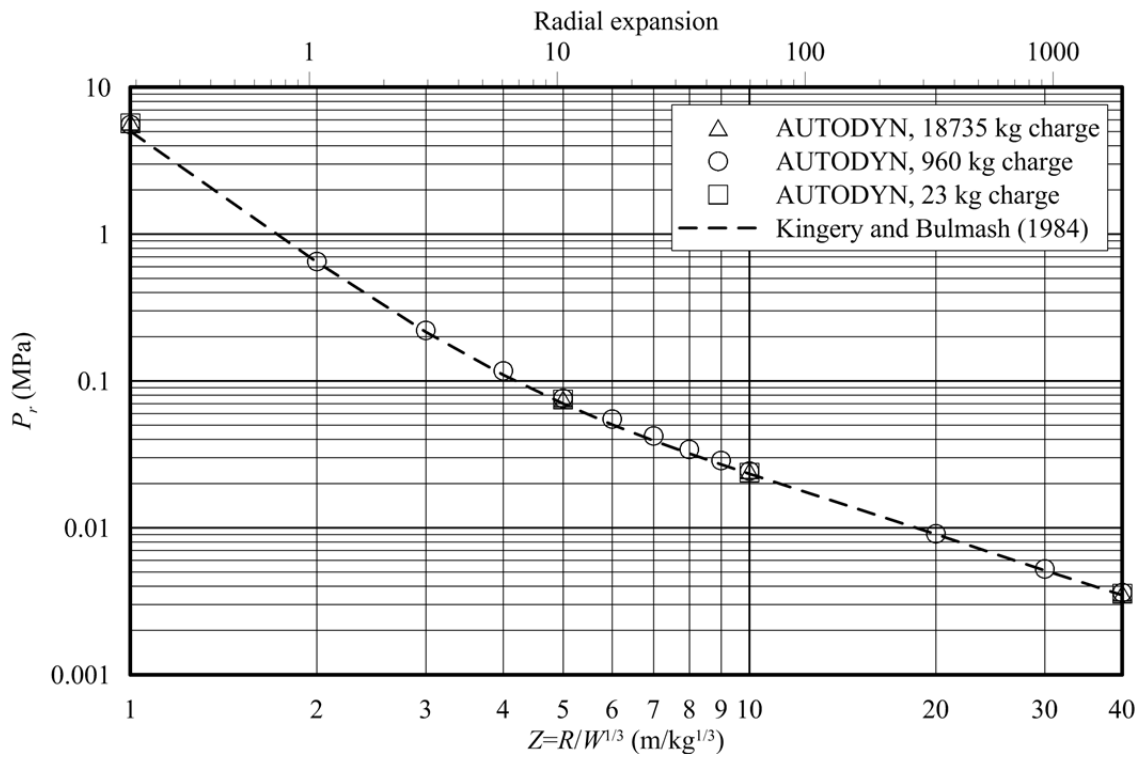


(b) Reflected overpressure;  $0.0553 \leq Z \leq 0.1$  m/kg<sup>1/3</sup>

**Figure 3-16 Normally reflected peak overpressure versus scaled distance**

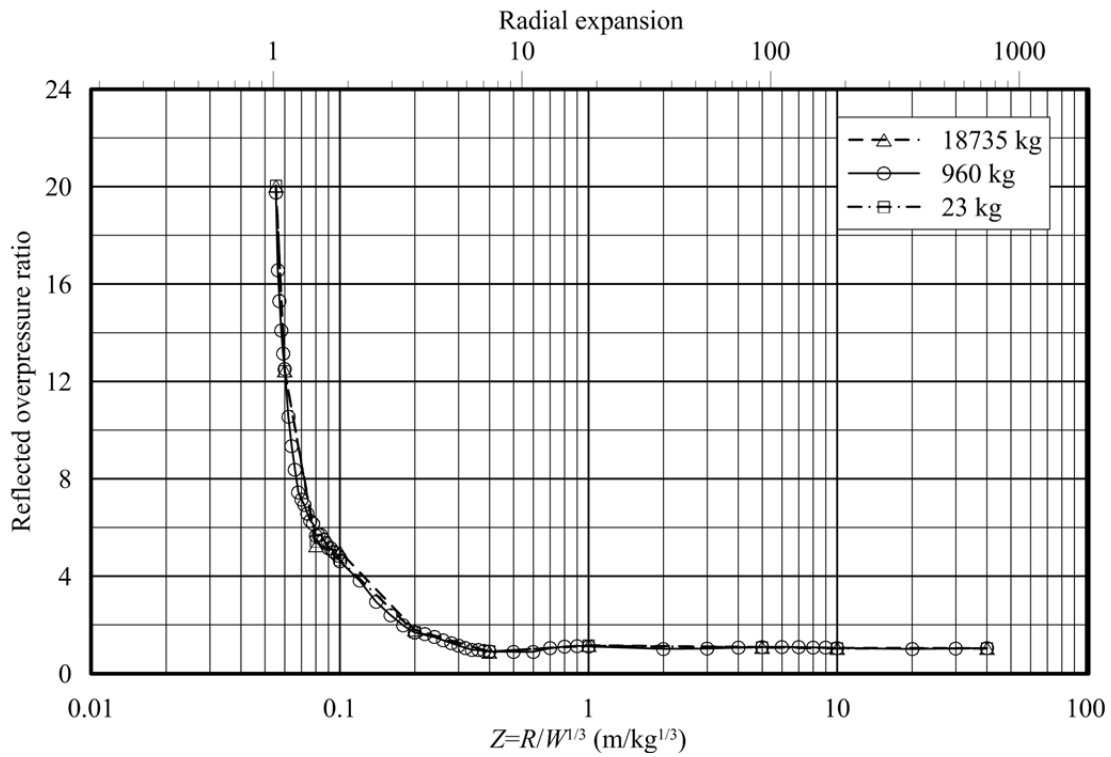


(c) Reflected overpressure;  $0.1 \leq Z \leq 1$  m/kg<sup>1/3</sup>

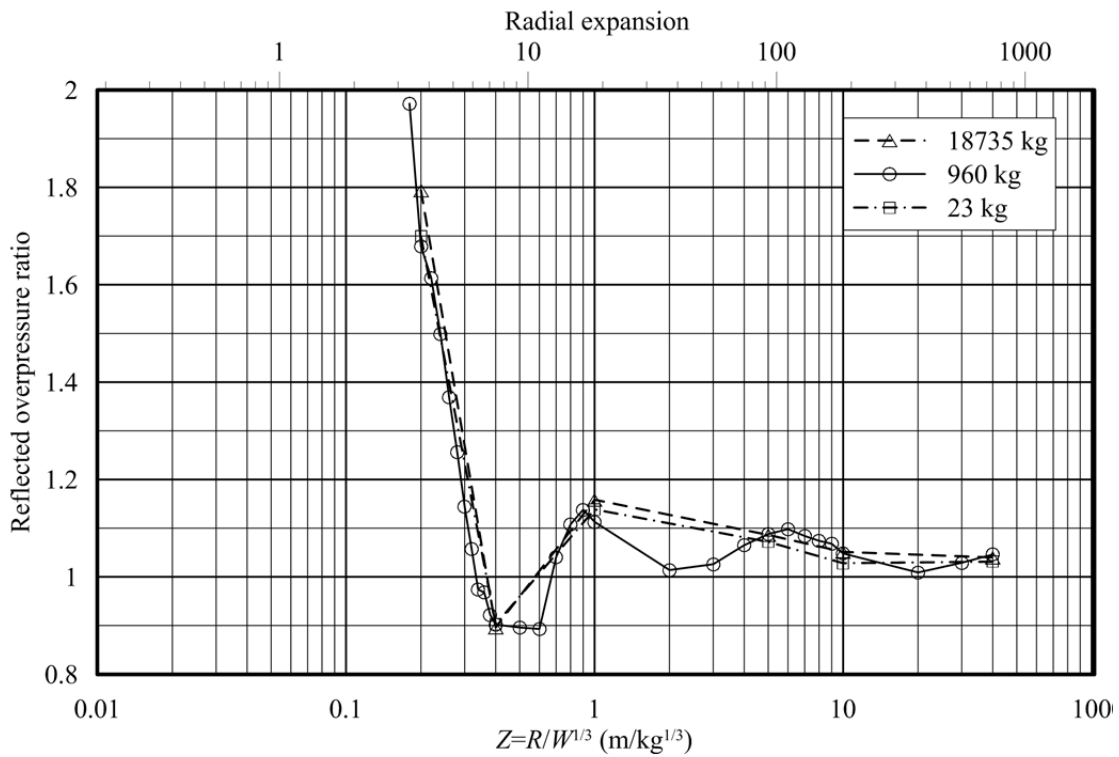


(d) Reflected overpressure;  $1 \leq Z \leq 40$  m/kg<sup>1/3</sup>

Figure 3-16 Normally reflected peak overpressure versus scaled distance (cont.)

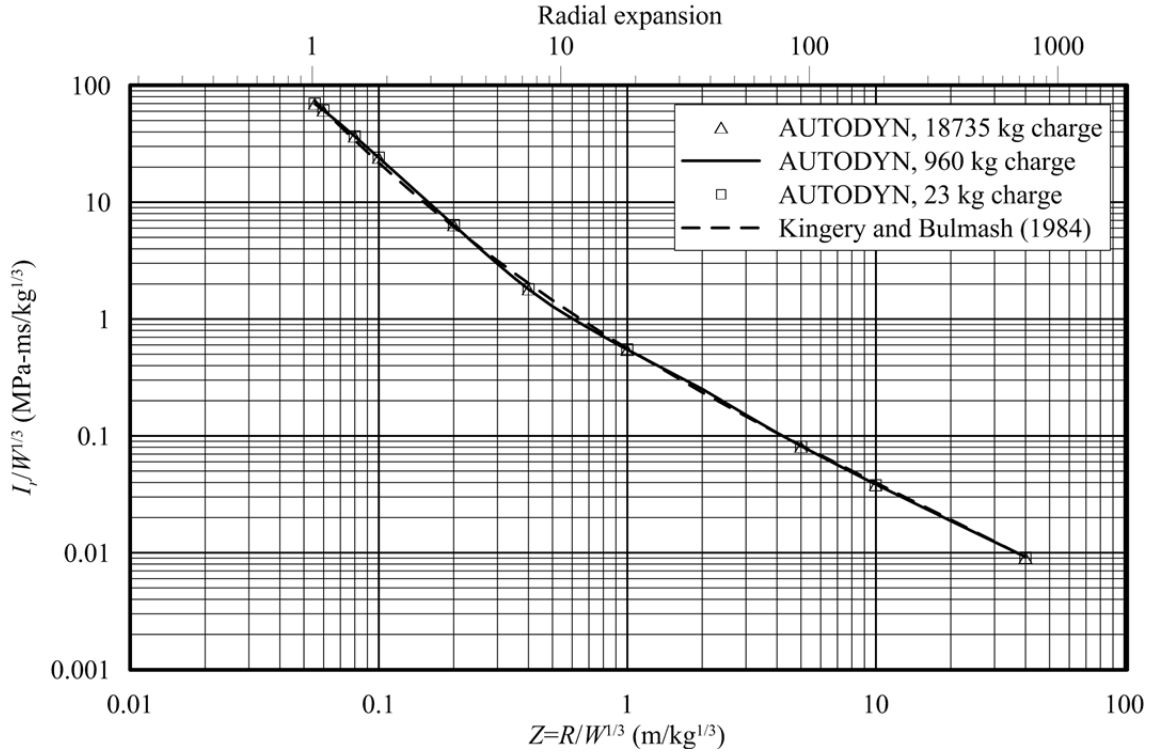


(e) Ratio of AUTODYN calculations to KB predictions; full range

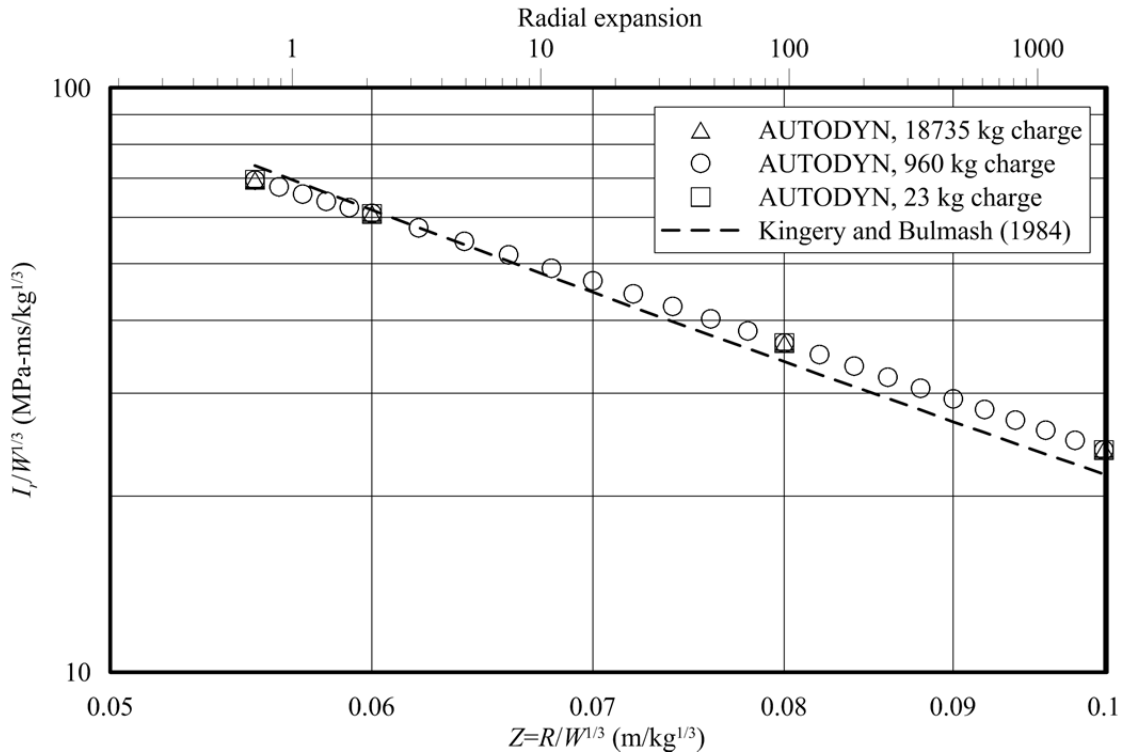


(f) Ratios of AUTODYN calculations to KB predictions; part range on ratio

**Figure 3-16 Normally reflected peak overpressure versus scaled distance (cont.)**

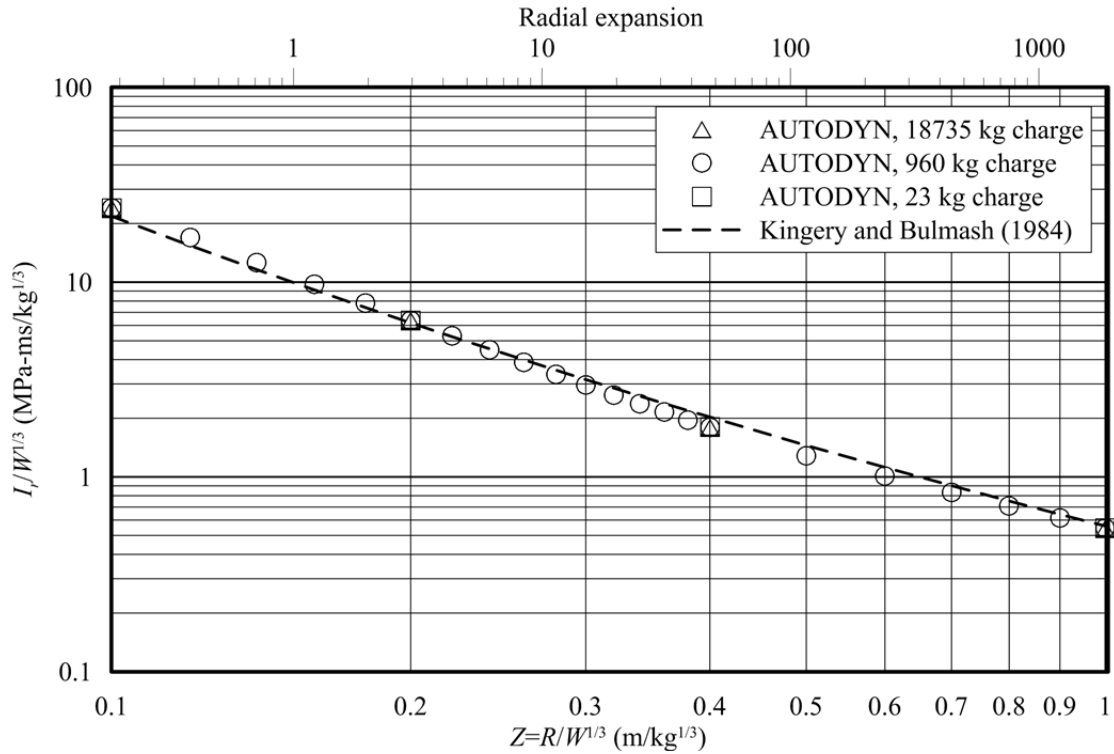


(a) Reflected impulse;  $0.0553 \leq Z \leq 40.0$  m/kg<sup>1/3</sup>

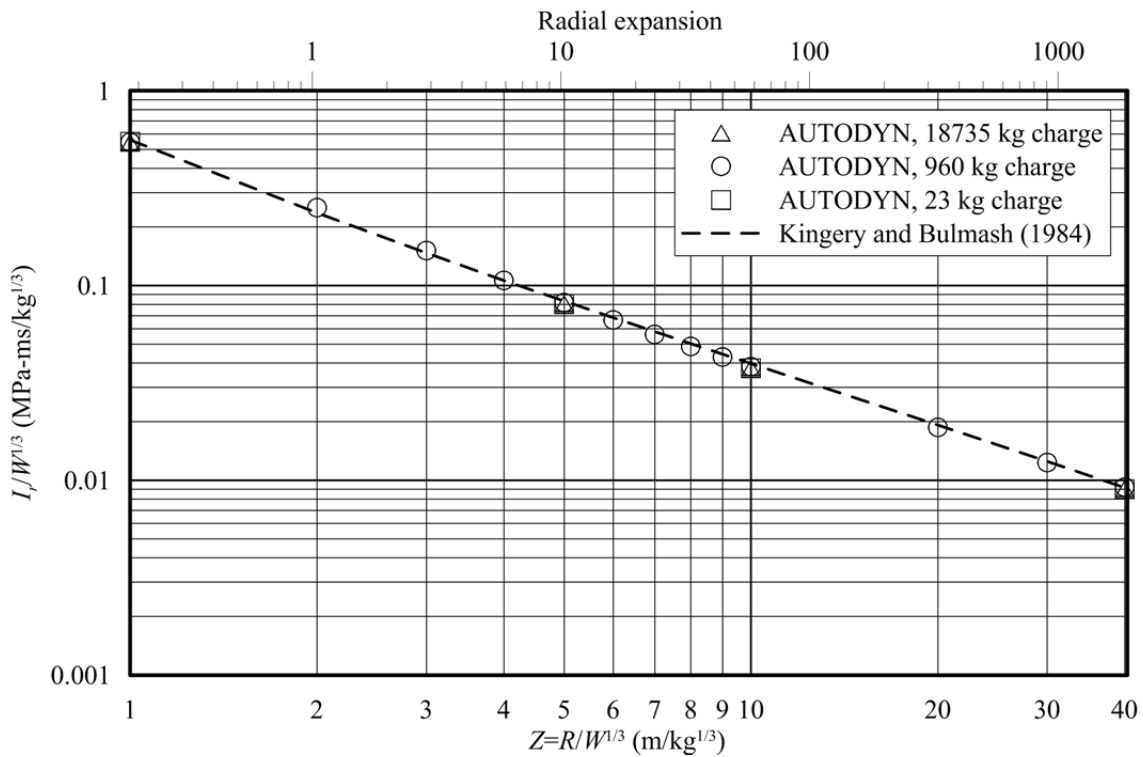


(b) Reflected impulse;  $0.0553 \leq Z \leq 0.1$  m/kg<sup>1/3</sup>

**Figure 3-17 Normally reflected impulse versus scaled distance**

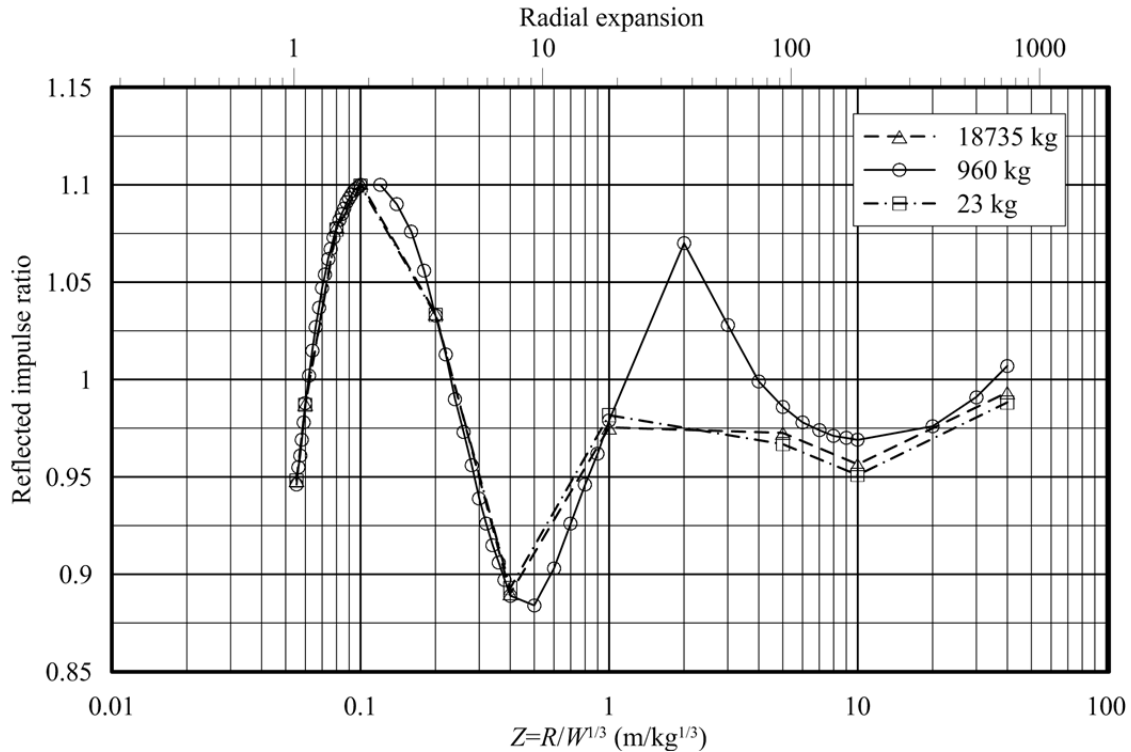


(c) Reflected impulse;  $0.1 \leq Z \leq 1$  m/kg<sup>1/3</sup>



(d) Reflected impulse;  $1 \leq Z \leq 40$  m/kg<sup>1/3</sup>

**Figure 3-17 Normally reflected impulse versus scaled distance (cont.)**



(e) Ratios of AUTODYN calculations to KB predictions

**Figure 3-17 Normally reflected impulse versus scaled distance (cont.)**

### 3.7.2 Cell Size for CFD Analysis

It is not straightforward to provide code-independent recommendations for 2D CFD analysis of the effects of detonations on rigid reflecting surfaces because a) codes employ different algorithms to map 1D results into a 2D domain, b) the cell size chosen for the 1D analysis will influence the initial conditions for the 2D analysis, regardless of the cell sizes chosen for the 2D analysis, c) the choice of perpendicular dimension will affect the accuracy of the results, and d) 3D analysis is generally required to characterize blast loading effects on components of structures. For 2D analysis using re-mapped 1D results as initial conditions, the computational time will generally be dominated by the 2D calculations and so as small a cell size as is practical should be used for the 1D analysis. For the calculations presented here, a 2D cell size equal to 0.002 times the distance to the monitoring location on the reflecting surface provided results within 10% of the *converged* value for  $0.0553 \leq Z < 40 \text{ m/kg}^{1/3}$ .

### 3.8 Shock Front Arrival Time

Arrival time is an important parameter for analysis and design when pressure histories are being computed across a reflecting surface such as a structural component or a structural system. The simulations in Section 3.6 for incident overpressure and impulse are mined here for arrival time data. Figure 3-18 presents the results of the AUTODYN simulations and the KB predictions for scaled arrival time. The numerical results and the KB predictions are virtually identical for all charge weights (18735, 960 and 23 kg) across the considered range of scaled distance,  $0.0553 \leq Z < 40.0 \text{ m/kg}^{1/3}$ . Figure 3-19 presents the ratio of the AUTODYN-calculated to KB-predicted arrival times. The effect of charge weight is insignificant as shown in Figures 3-19 and 3-20.

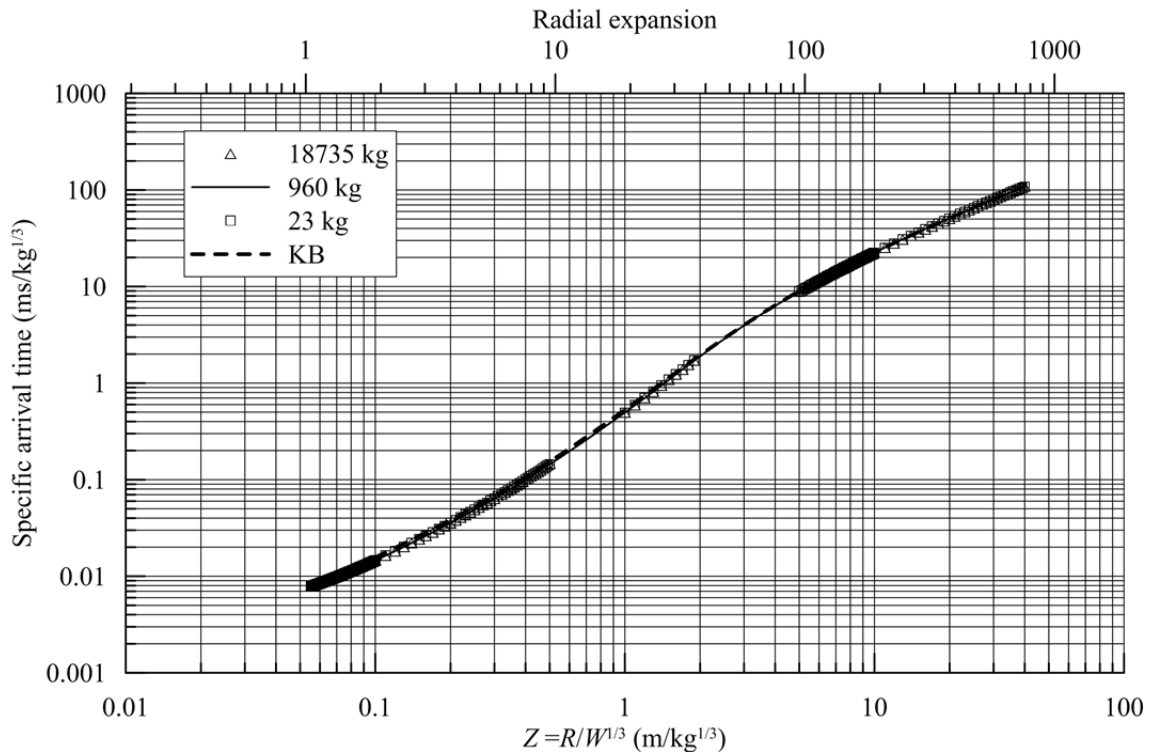
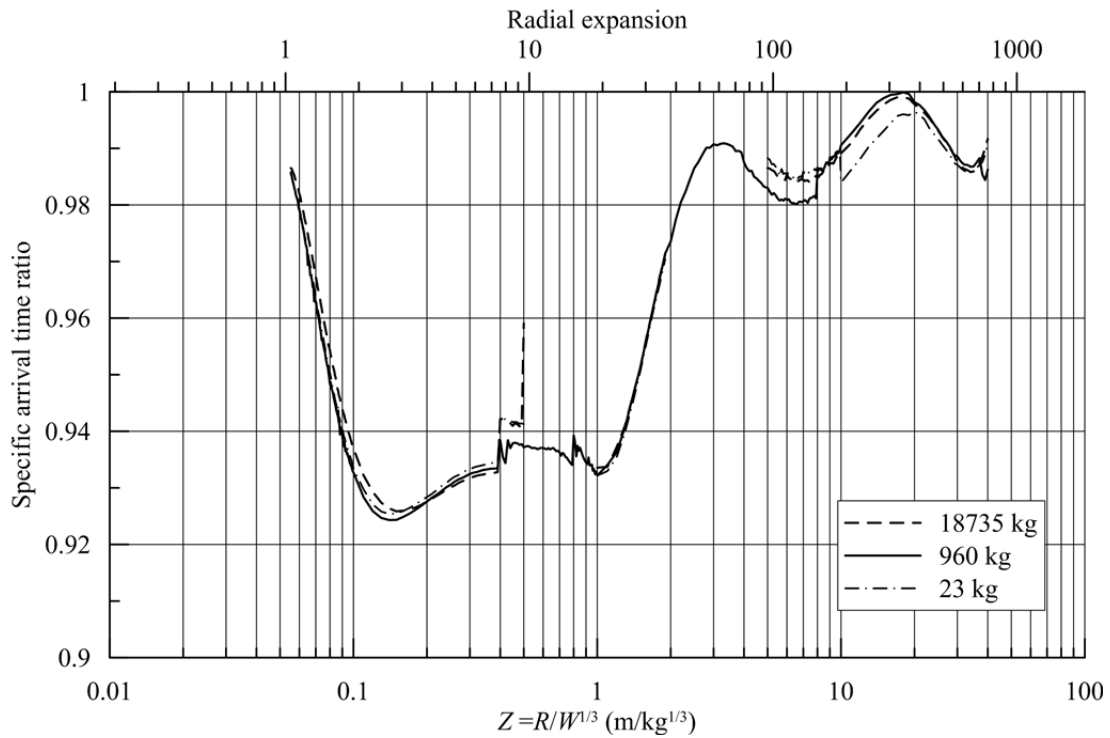
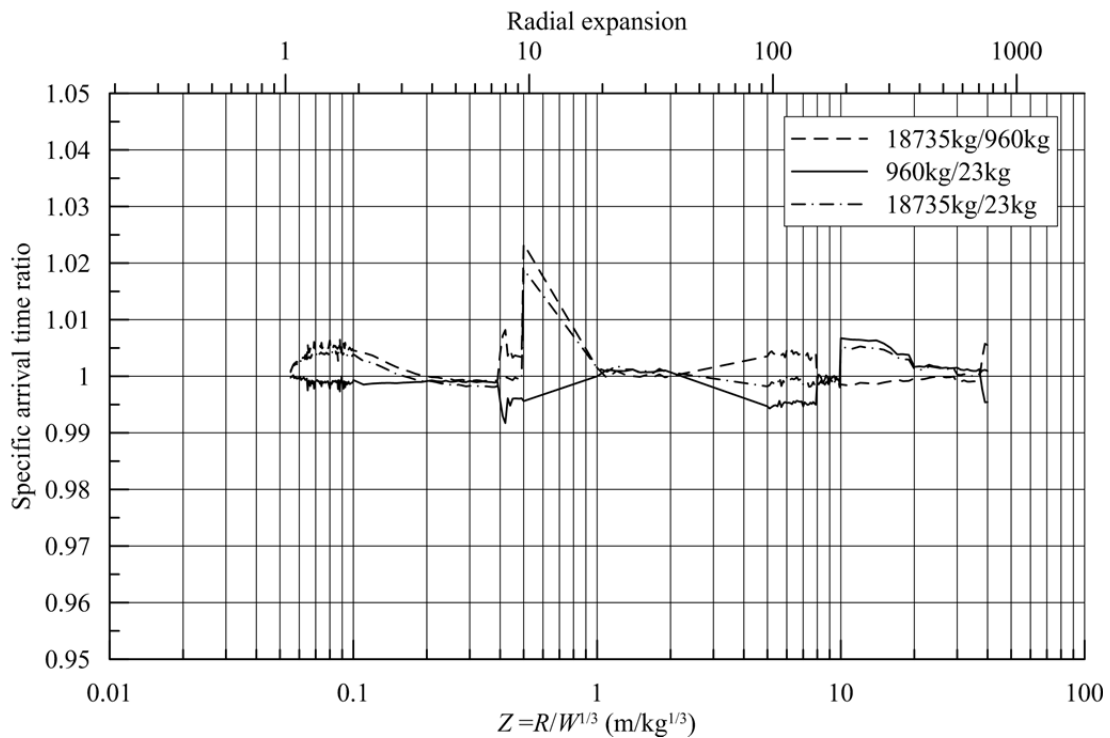


Figure 3-18 AUTODYN calculations and KB predictions for specific arrival time



**Figure 3-19 Ratios of AUTODYN calculations and KB predictions of specific arrival time**



**Figure 3-20 Effect of charge weight on specific arrival times calculations: 18735, 960 and 23 kg charges**



## SECTION 4

# DESIGN CHARTS AND POLYNOMIALS FOR AIR-BLAST PARAMETERS

### 4.1 Introduction

The empirical relationships developed by Kingery and Bulmash (1984) form the basis of design charts that are reproduced in textbooks and US government documents, including UFC 3-340-02 (DoD 2008). These relationships enable air-blast parameters such as incident peak overpressure and impulse, normally reflected peak overpressure and impulse, arrival time, and positive phase duration to be empirically derived for spherical free-air and hemispherical surface bursts of TNT. Pressure-time curves suitable for analysis and design of structural components and systems can be constructed using charted values of these air-blast parameters and the Friedlander overpressure history (see Section 1.1).

The accuracy of the Kingery and Bulmash (KB) charts was discussed in Chapter 3. The AUTODYN data reported in Chapter 3 are used here to generate a new family of polynomials and charts suitable for blast-resistant design.

### 4.2 Accuracy of KB and Numerical Predictions of Blast Parameters

#### *4.2.1 Incident Peak Overpressure and Impulse*

The KB (or UFC 3-340-02) predictions of incident overpressure for spherical free-air bursts were compared to AUTODYN CFD calculations in Chapter 3. The AUTODYN calculations of incident peak overpressure are more than 10% greater than the KB predictions for  $Z < 0.08 \text{ m/kg}^{1/3}$  (see Figure 3-11h) and are more than a factor of 10 greater than the KB predictions close to the face of the charge, at  $Z = 0.0567 \text{ m/kg}^{1/3}$ . There is no meaningful difference between the AUTODYN calculations and the KB predictions of incident peak overpressure in the range  $0.08 \leq Z < 40.0 \text{ m/kg}^{1/3}$ .

For incident impulse, the AUTODYN-calculated values in the range  $Z < 0.1 \text{ m/kg}^{1/3}$  are more than 20% greater than the KB predictions (see Figure 3-12g), with the difference being a factor of 3.5 at  $Z = 0.0553 \text{ m/kg}^{1/3}$ . For  $0.1 \leq Z < 40.0 \text{ m/kg}^{1/3}$ , the differences are between 10% and 25%, with the KB charts predicting greater values of impulse than AUTODYN. These CFD predictions in the far field are consistent with the observations of Bogosian et al. (2002), who noted that the KB charts overpredicted incident impulse for  $Z > 1.19 \text{ m/kg}^{1/3}$  ( $Z > 3.0 \text{ ft/lb}^{1/3}$ ) (see Section 3.3).

#### ***4.2.2 Normally Reflected Peak Overpressure and Impulse***

The normally reflected peak overpressures calculated by AUTODYN are more than 10% greater than the KB predictions for  $Z < 0.3 \text{ m/kg}^{1/3}$  (see Figure 3-16f). The differences in normally reflected peak overpressure are small for  $Z \geq 0.4 \text{ m/kg}^{1/3}$ . The AUTODYN calculations and KB predictions of reflected impulse differ by 10% or less across the range of scaled distance considered, namely,  $0.0553 \leq Z < 40 \text{ m/kg}^{1/3}$ .

#### ***4.2.3 Shock Front Arrival Time***

There are no meaningful differences in the shock front arrival time between the numerical calculations and the KB predictions across the range of scaled distance considered, namely,  $0.0553 \leq Z < 40.0 \text{ m/kg}^{1/3}$ .

### **4.3 Updated Polynomials and Charts for Overpressure, Impulse and Arrival Time**

#### ***4.3.1 Charts for Design***

Revisions to the spherical free-air burst charts in UFC 3-340-02 are proposed based on the discussions and AUTODYN simulations presented in Chapters 2 and 3, and in the preceding sections of this chapter. Polynomials and charts are generated for incident and normally reflected overpressure and impulse, and for arrival time, for  $0.0553 \leq Z \leq 40.0 \text{ m/kg}^{1/3}$ .

The lower limit on scaled distance of  $0.0553 \text{ m/kg}^{1/3}$  is used because the numerical simulations stabilize at this value of scaled distance,  $Z$ , as noted in Section 3.5.2. A value of  $Z = 0.0553 \text{ m/kg}^{1/3}$  corresponds to a radial expansion of the shock front,  $\bar{r} = 1.05$ . The *design* implications of not providing polynomials and charts for  $1.00 \leq \bar{r} \leq 1.05$  are insignificant. See Figure 4-1 that shows a spherical charge and rigid reflecting surface (hatched) to its right. The dashed, dash-dot, and dash-dot-dot lines represent radial expansions of 1.025, 1.050 and 1.100, respectively. For design against terrorist threats, a free-air detonation at a radial expansion of less than 1.05 should probably be treated as a contact detonation because the gap between the charge and reflecting surface is negligible.

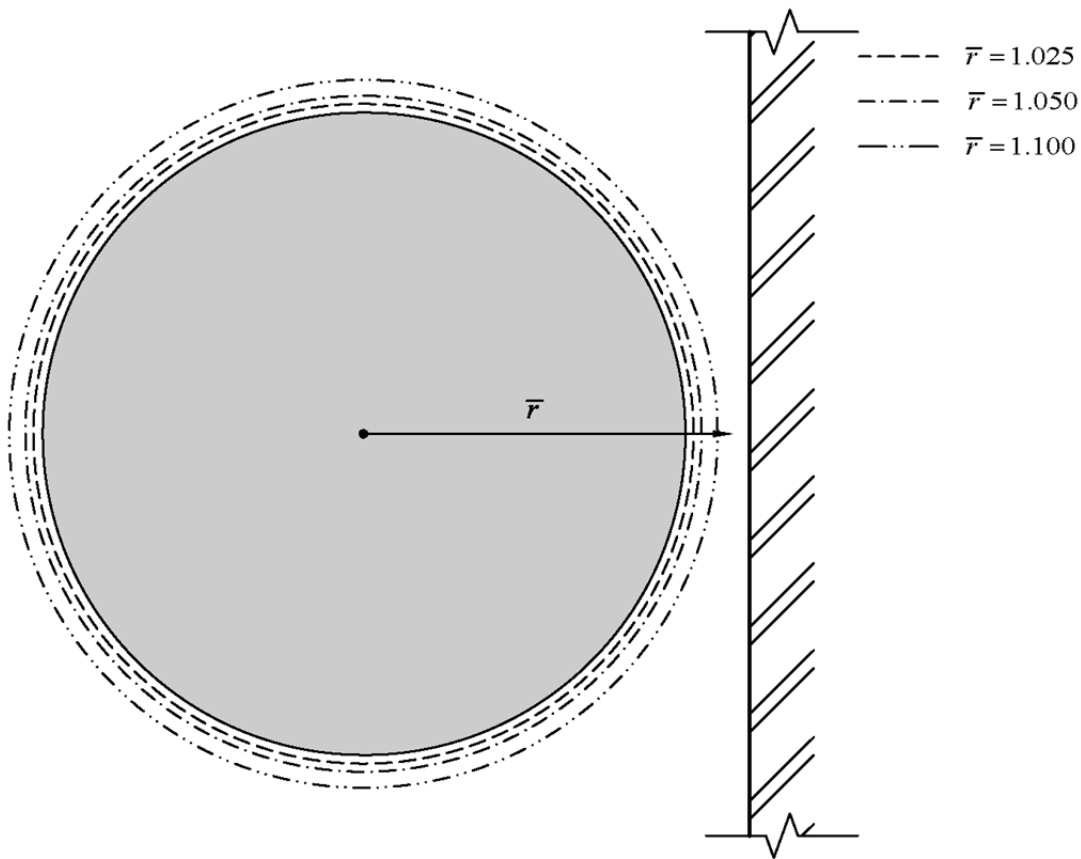


**Figure 4-1 Spherical charge and radial expansions,  $\bar{r}$ , of 1.025, 1.050 and 1.100**

## 4.3.2 Polynomials

### 4.3.2.1 Procedure

Polynomial functions of the form shown in Equation 4-1 are used to present air-blast parameters based on AUTODYN simulations. The functional form of the equations follows that adopted by Kingery and Bulmash (1984). Polynomials are derived for incident and normally reflected peak overpressures and impulses, and arrival time<sup>6</sup>. The constants are computed by least squares fitting:

$$Y = C_0 + C_1U + \dots + C_NU^N \quad (4-1)$$

where  $Y$  is the common (base 10) logarithm of the blast parameter,  $U = K_0 + K_1 \cdot \log(Z)$ ,  $C$  and  $K$  are constants, and  $N$  is the order of the polynomial.

The AUTODYN data are fitted using high-order polynomials. High-order polynomials are required to accommodate the rapid changes in pressure and impulse near the face of the charge. The order of each polynomial is selected such that the ratio of the polynomial calculation to the AUTODYN calculation lies close 1.0, which is deemed satisfactory for the purpose of design and better than the resolution enabled by the charts. Two families of polynomials are presented: 1)  $0.0553 \leq Z \leq 40.0 \text{ m/kg}^{1/3}$  describing the complete range of scaled distance considered by Kingery and Bulmash, and 2)  $0.0553 \leq Z < 0.5 \text{ m/kg}^{1/3}$  and  $0.5 \leq Z \leq 40 \text{ m/kg}^{1/3}$ , such that the KB polynomials may be substituted just in the range  $Z < 0.5 \text{ m/kg}^{1/3}$  if preferred.

### 4.3.2.2 Proposed Polynomials for Spherical Free Air Bursts

The first family of polynomials are established for the range of scaled distances  $0.0553 \leq Z \leq 40.0 \text{ m/kg}^{1/3}$  ( $1.05 \leq \bar{r} \leq 759$ ) for incident peak overpressure,  $P_s$ , incident specific impulse,  $I_s / W^{1/3}$ , reflected peak overpressure,  $P_r$ , reflected specific impulse,  $I_r / W^{1/3}$ , and specific arrival time,  $t_a / W^{1/3}$ . The ratios of the polynomial to AUTODYN calculations range between

---

<sup>6</sup> For near-field detonations and reflecting surfaces with the geometry of Figure 4-1, the reflected overpressures and impulses will decrease rapidly from the point of normal reflection due to increasing scaled distance and angle of incidence. Cormie et al. (2013) extend the utility of the design charts provided below to address pressures and impulses on reflecting surfaces in the near field.

0.90 and 1.10. The polynomial constants are presented in Table 4-1. A range on ratio of (0.95 to 1.05) can be achieved but at the expense of an order higher than 25.

The second set of polynomials are established for subsets of the total range on scaled distance, namely,  $0.0553 \leq Z \leq 0.5 \text{ m/kg}^{1/3}$  and  $0.5 \leq Z \leq 40.0 \text{ m/kg}^{1/3}$ . For these polynomials, the ratio of the polynomial to AUTODYN calculations range between 0.95 and 1.05. The polynomial constants are presented in Table 4-2. The two equations for each parameter share the same value to four significant figures, and very similar slopes at  $Z = 0.5 \text{ m/kg}^{1/3}$ , as presented in Table 4-3.

Figures 4-2 and 4-3 permit an evaluation of the accuracy of the proposed polynomials as calculated using the constants of Table 4-2. Data from Needham (2010) are included in Figure 4-2 for reference. These new polynomial functions are plotted in SI and US units in Figures 4-4 and 4-5, respectively.

**Table 4-1 Constants of polynomials for incident and normally reflected peak overpressure, impulse and arrival time for  $0.0553 \leq Z \leq 40 \text{ m/kg}^{1/3}$**

Parameter	$P_s$ (kPa)	$I_s/W^{1/3}$ (kPa-ms/kg <sup>1/3</sup> )	$P_r$ (kPa)	$I_r/W^{1/3}$ (kPa-ms/kg <sup>1/3</sup> )	$t_a/W^{1/3}$ (ms/kg <sup>1/3</sup> )
$K_0$	-0.1239	0.05671	0.1365	0.2044	-0.1674
$K_1$	0.8705	0.8363	0.9839	0.6997	0.4994
$C_0$	2.666	2.21	4.094	3.105	3.351
$C_1$	-2.769	-0.5499	-2.439	-2.032	3.627
$C_2$	-0.06247	-2.981	-1.212	1.36	-1.24
$C_3$	2.676	2.746	-1.301	-1.081	-3.226
$C_4$	0.06411	9.522	3.953	-2.305	3.144
$C_5$	-4.994	-13.01	1.69	3.143	6.048
$C_6$	0.181	-8.244	-4.843	1.151	-3.093
$C_7$	5.374	12.51	0.2562	-2.901	-5.209
$C_8$	-0.4159	-0.5068	2.207	1.003	
$C_9$	-2.715	2.939	-0.7651		
$C_{10}$	-0.05814	1.023	-0.1251		
$C_{11}$	0.6429	-4.748	0.0638		
$C_{12}$	0.208	1.028			
$C_{13}$	-0.1394	-3.996			
$C_{14}$		1.703			
$C_{15}$		0.5049			
$C_{16}$		0.8065			
$C_{17}$		2.006			
$C_{18}$		-1.44			
$C_{19}$		0.6624			
$C_{20}$		-2.118			
$C_{21}$		0.08177			
$C_{22}$		1.678			
$C_{23}$		-0.6299			
$C_{24}$		-0.1429			
$C_{25}$		0.07183			

**Table 4-2 Constants of polynomials for incident and normally reflected peak overpressure, impulse and arrival time for ranges of scaled distance  $0.0553 \leq Z < 0.5 \text{ m/kg}^{1/3}$  and  $0.5 \leq Z \leq 40 \text{ m/kg}^{1/3}$**

	$P_s$ (kPa)		$I_s/W^{1/3}$ (kPa-ms/kg <sup>1/3</sup> )		$P_r$ (kPa)		$I_r/W^{1/3}$ (kPa-ms/kg <sup>1/3</sup> )		$t_a/W^{1/3}$ (ms/kg <sup>1/3</sup> )	
	$Z < 0.5$	$Z \geq 0.5$	$Z < 0.5$	$Z \geq 0.5$	$Z < 0.5$	$Z \geq 0.5$	$Z < 0.5$	$Z \geq 0.5$	$Z < 0.5$	$Z \geq 0.5$
$K_0$	-1.888	0.165	1.206	-0.5596	1.613	-0.4784	0.2159	0.8609	0.8806	0.267
$K_1$	-2.603	1.339	1.62	1.175	1.98	0.9222	0.7506	1.265	0.4936	0.7019
$C_0$	4.225	3.266397	2.30772	1.76	5.74903	2.251	3.0934	3.839	0.36193	2.061
$C_1$	0.4076	-1.505	-1.136	-0.6897	-1.472	-2.444	-1.892	-2.128	1.932	2.148
$C_2$	-0.1996	-0.7112	1.322	-0.3701	0.1963	1.752	2.003	1.794	0.3132	1.98
$C_3$	0.2126	-0.02506	0.7022	-0.1443	1.416	-1.329	2.239	-1.256	0.6178	-2.805
$C_4$	0.826	1.842	-0.2583	1.512	-1.999	-1.514	0.6488	0.4165		1.121
$C_5$	-0.1719	-1.865	-0.5376	-0.7939	-2.735	4.729		-0.05467		-0.09299
$C_6$	-1.779	0.742	-1.223	-1.814	3.556	-3.051		0.0009718		
$C_7$	-0.587	-0.114	0.2194	1.639	1.131	-2.02				
$C_8$	1.192	0.002556	1.198	-0.2572	-0.8315	3.52				
$C_9$	1.346		-0.8426	0.4388	0.5336	-2.843				
$C_{10}$	0.2694		0.6599	0.1685	-1.676	3.272				
$C_{11}$	-1.024			-1.029	-0.2248	-1.233				
$C_{12}$	-0.503			0.5988	1.074	-0.6161				
$C_{13}$	0.3686			-0.08299	-0.2745	1.211				
$C_{14}$	0.1284					-3.61				
$C_{15}$	-0.05418					2.491				

**Table 4-3 Values and slopes at  $Z = 0.5 \text{ m/kg}^{1/3}$  on the polynomials curves plotted using the two ranges of scaled distance**

Parameter	Value		Slope	
	$Z < 0.5 \text{ m/kg}^{1/3}$	$Z \geq 0.5 \text{ m/kg}^{1/3}$	$Z < 0.5 \text{ m/kg}^{1/3}$	$Z \geq 0.5 \text{ m/kg}^{1/3}$
$P_s$	3.910 MPa		-13.43 MPa-kg <sup>1/3</sup> /m	-13.65 MPa-kg <sup>1/3</sup> /m
$I_s/W^{1/3}$	0.1522 MPa-ms/kg <sup>1/3</sup>		0.1496 MPa-ms/m	0.1803 MPa-ms/m
$P_r$	26.66 MPa		-108.1 MPa-kg <sup>1/3</sup> /m	-115.9 MPa-kg <sup>1/3</sup> /m
$I_r/W^{1/3}$	1.296 MPa-ms/kg <sup>1/3</sup>		-3.758 MPa-ms/m	-3.620 MPa-ms/m
$t_a/W^{1/3}$	0.1536 ms/kg <sup>1/3</sup>		0.5130 ms/m	0.5052 ms/m

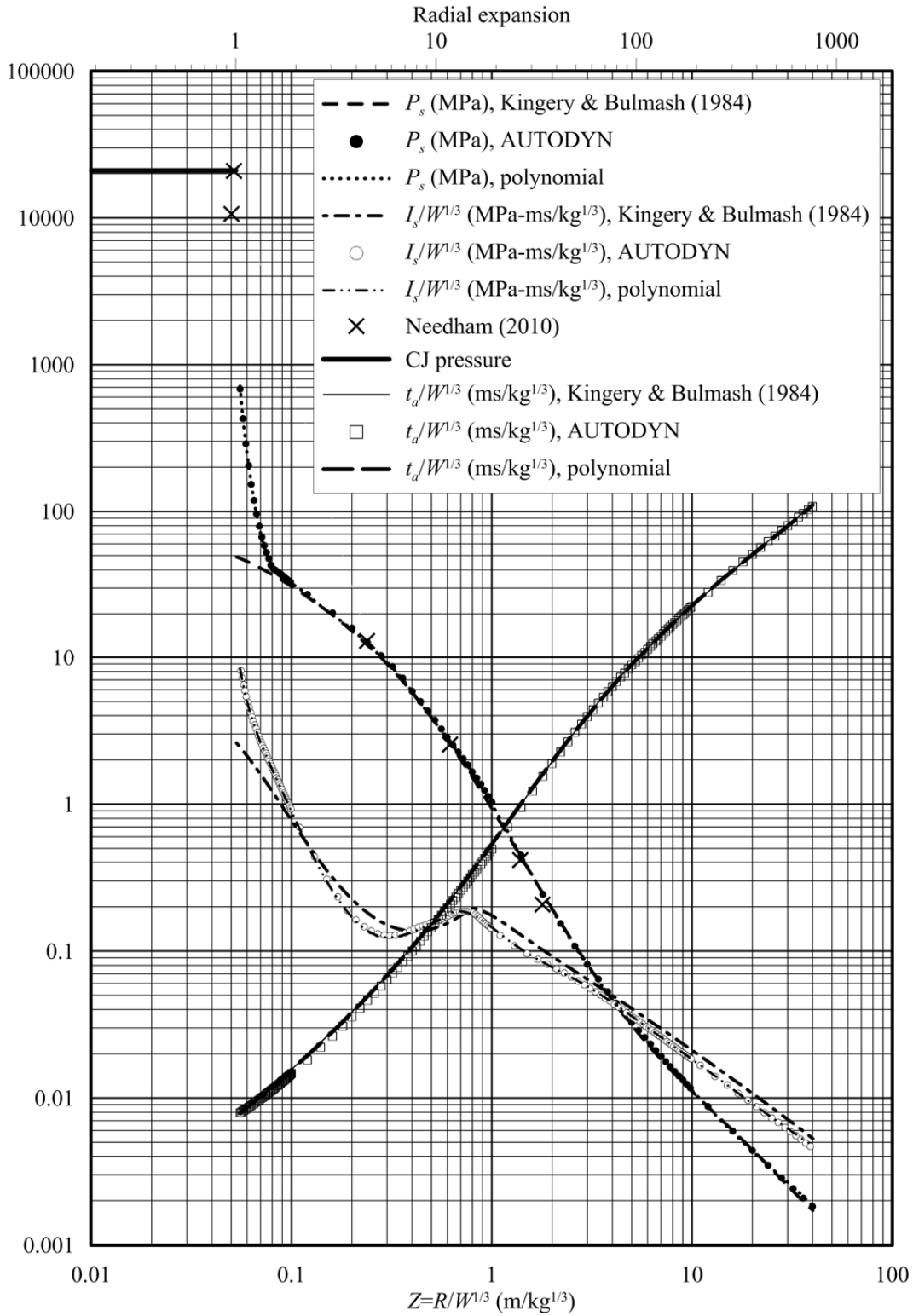


Figure 4-2 Incident peak overpressure impulse and arrival time, spherical free-air bursts

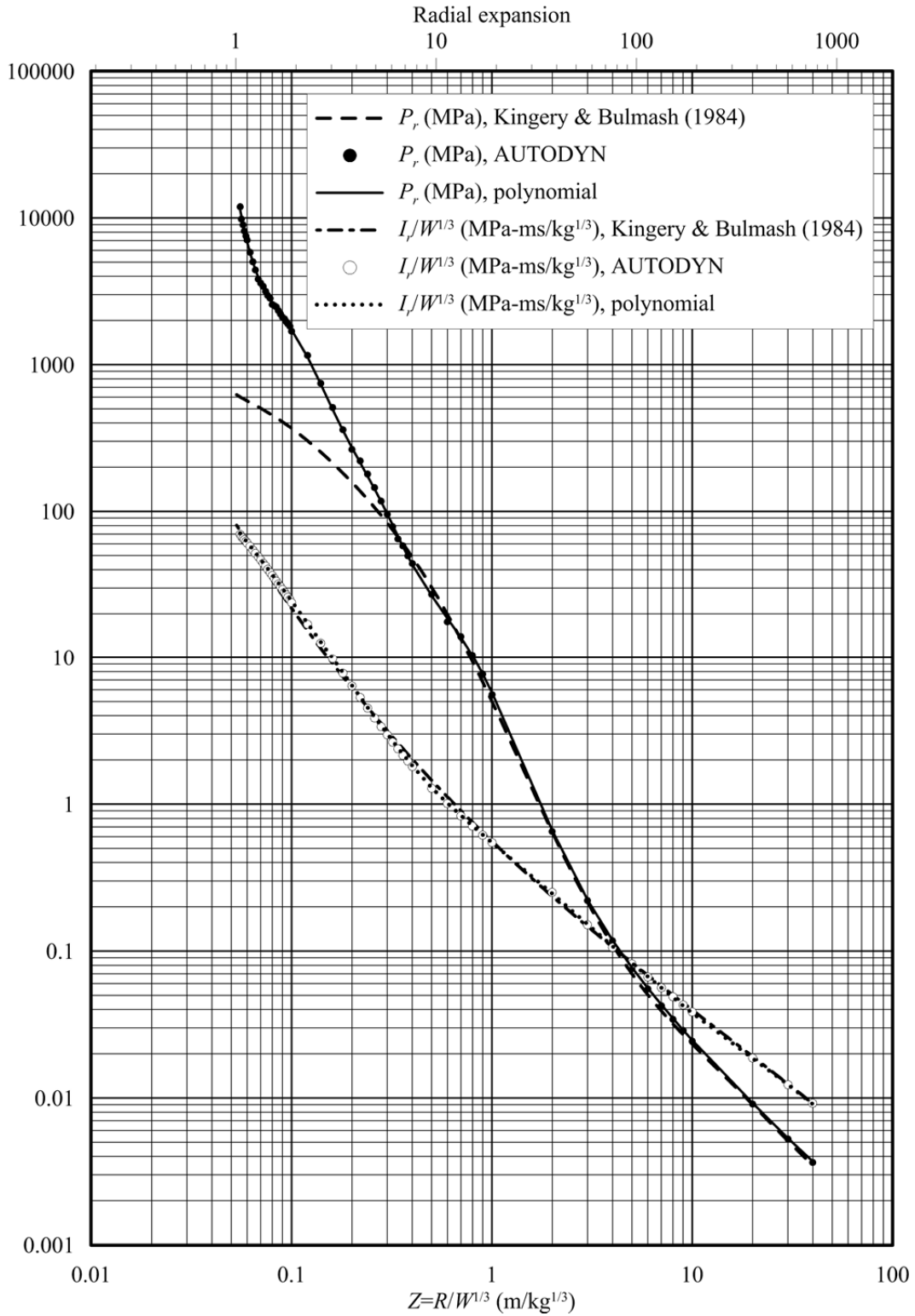


Figure 4-3 Reflected peak overpressure and impulse, spherical free-air bursts

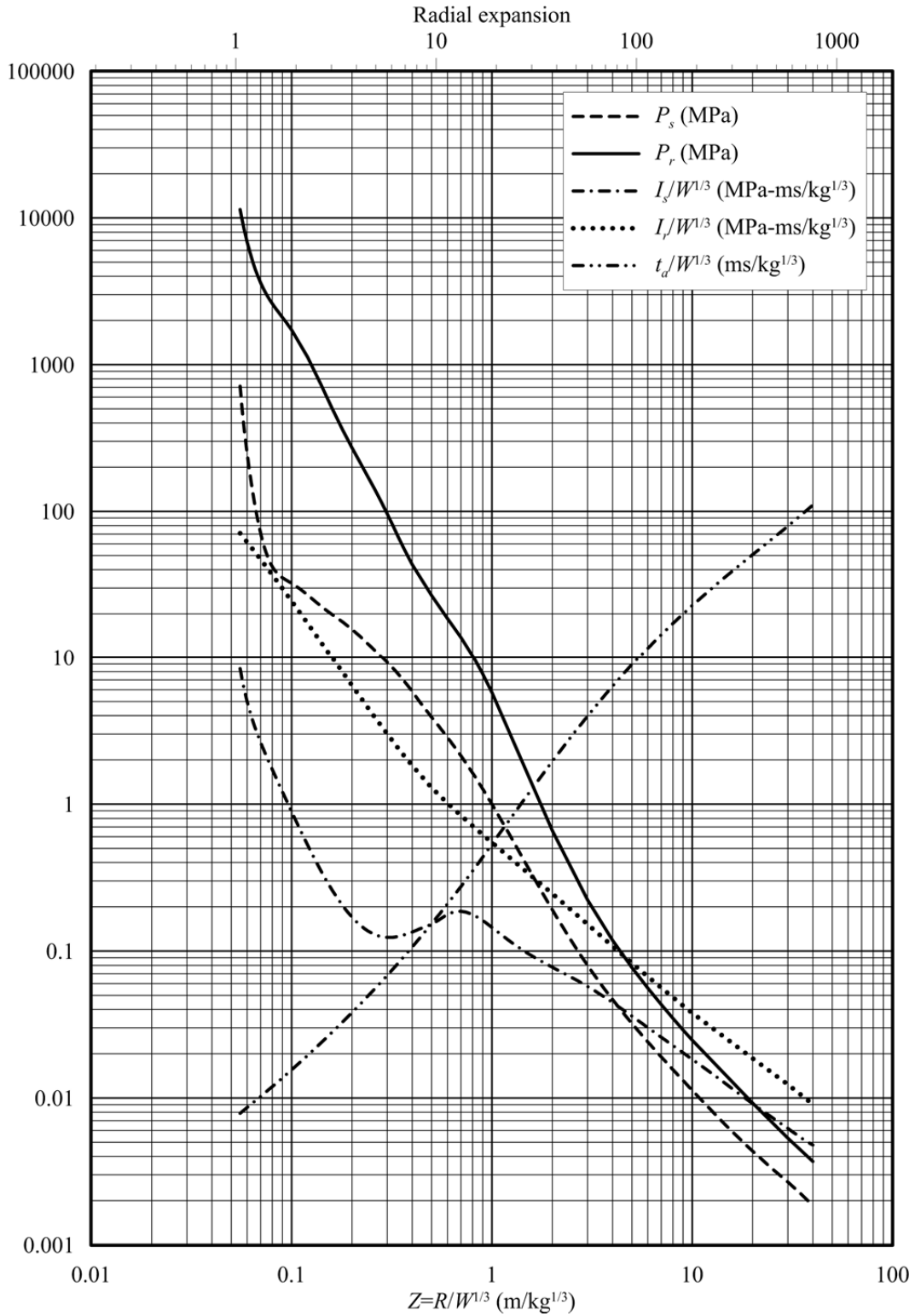
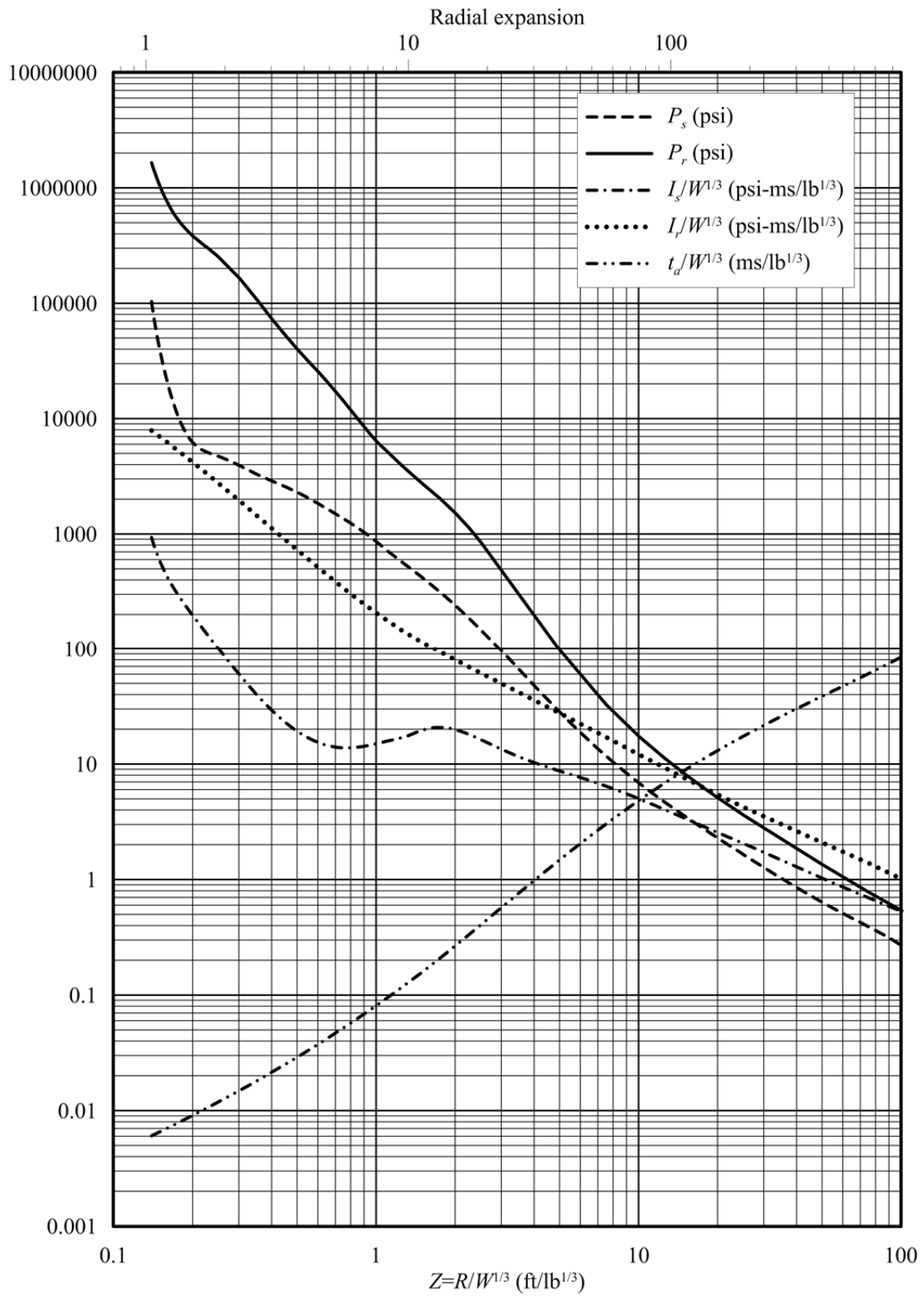


Figure 4-4 Proposed polynomial charts in SI units, spherical free-air bursts



**Figure 4-5 Proposed polynomial charts in US units, spherical free-air bursts**

#### *4.3.2.3 Proposed Polynomials for Hemispherical Free Air Bursts*

It is standard practice to increase the charge weight by a factor of 1.8 to transform a spherical free-air burst to a hemispherical surface burst. The factor is less than idealized value of 2.0 for a perfectly-reflecting plane, because part of the energy associated with a surface burst is associated with ground shock, and in forming the crater. To be consistent with current practice, and in the absence of information to the contrary, the charge weight should be increased by a factor of 1.8 if the charts provided herein are to be used to predict the effects of a hemispherical surface burst.

#### *4.3.3 Sample Results*

Table 4-4 presents results of sample calculations using the polynomials with constants per Table 4-2. Spherical 25 and 1000 kg charges (55 and 2200 lbs, respectively) are considered at scaled distances of 0.25 and 1.00 m/kg<sup>1/3</sup> (0.63 and 2.52 ft/lb<sup>1/3</sup>, respectively). All of the parameters in the table were defined previously. Results of the calculations are provided in Figure 4-6.

#### *4.3.4 Use of Design Charts and Considerations of Non-Ideal Explosives*

The polynomials and charts proposed in the prior subsection are intended to provide reasonable predictions for peak overpressure and impulse across a very wide range of scaled distance.

The numerical studies described in Chapters 2 and 3, and in the preceding sections of this chapter assumed a spherical charge of TNT with a packing density of 1630 kg/m<sup>3</sup>. Blast wave parameters for other ideal explosives such as RDX, PETN and Composition B and non-ideal explosives such as ammonium-nitrate-fuel-oil (ANFO) could be *estimated* by factoring the charge weight, with different factors often used for overpressure and impulse.

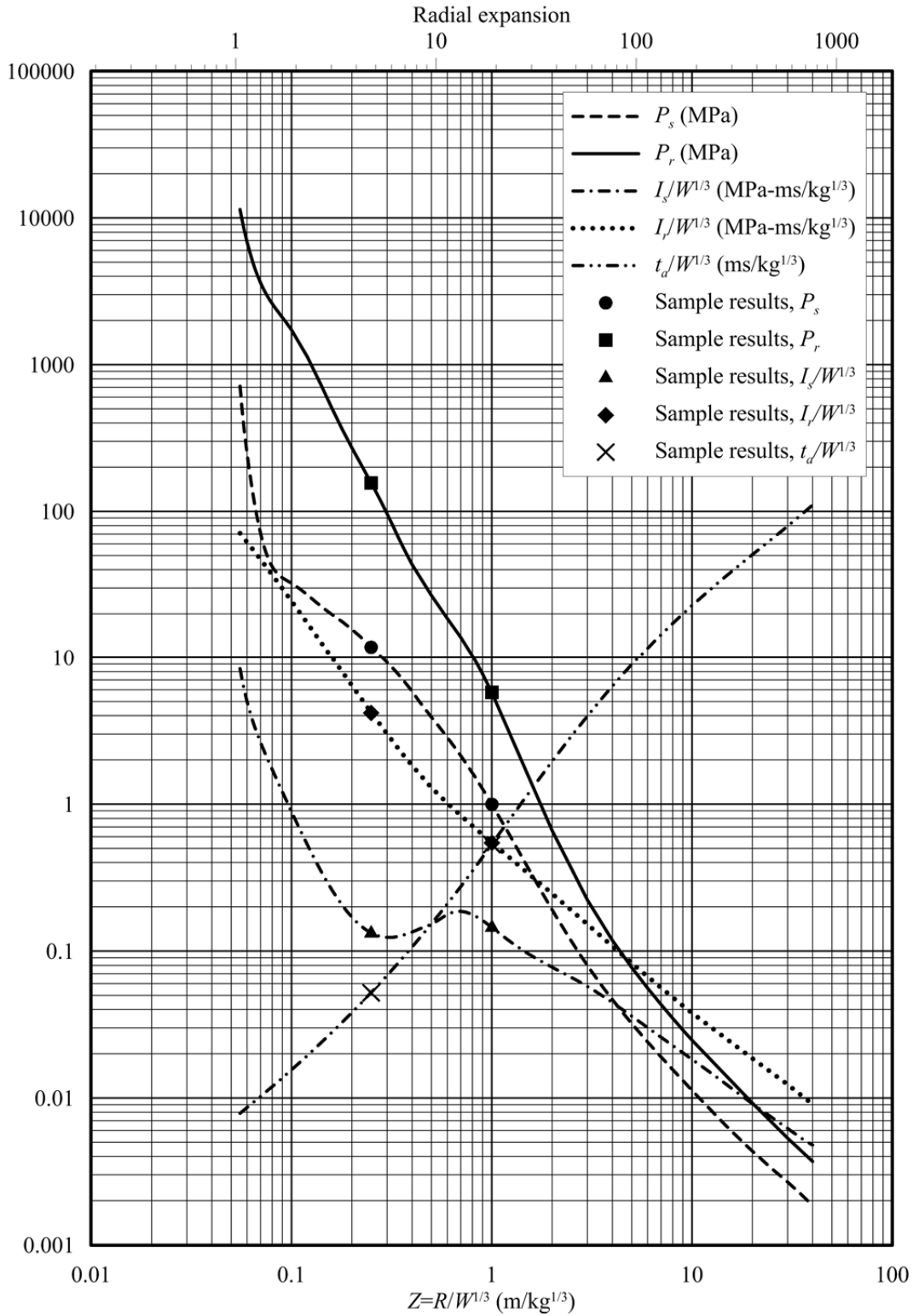
Two other assumptions were made for the numerical simulations, namely, 1) the explosive was a sphere, and 2) the explosive was detonated centrally. Physical experiments (e.g., Wu et al. 2009) and numerical simulations (e.g., Sherkar et al. 2010) have shown that charge shape, charge orientation and point of detonation within the charge can substantially affect overpressure and impulse, especially in the near field. Importantly, even the detonation of charges of an idealized

shape (e.g., sphere, vertical cylinder) will not necessarily produce a uniform wave field along all radial directions (e.g., Ngo et al. 2014).

The blast analyst must carefully consider the effect of these assumptions when calculating blast wave pressure histories. It is not practical to address these assumptions by adding variables to the polynomials presented previously.

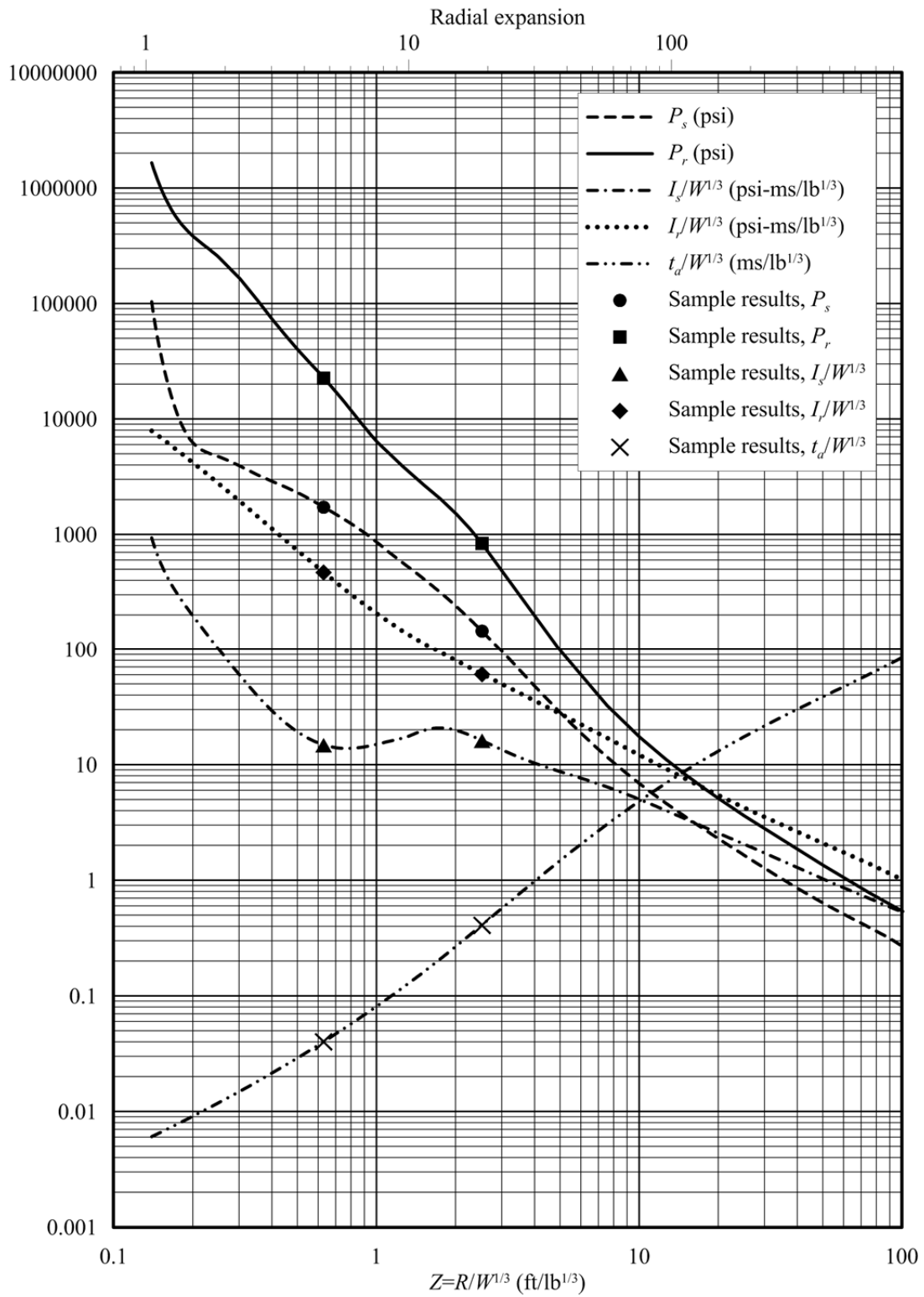
**Table 4-4 Sample calculations for spherical 25 kg and 1000 kg charges and scaled distances of 0.25 m/kg<sup>1/3</sup> and 1.00 m/kg<sup>1/3</sup>**

		W = 25 kg		W = 1000 kg	
		Z = 0.25 m/kg <sup>1/3</sup>	Z = 1.00 m/kg <sup>1/3</sup>	Z = 0.25 m/kg <sup>1/3</sup>	Z = 1.00 m/kg <sup>1/3</sup>
		R = 0.73 m	R = 2.92 m	R = 2.5 m	R = 10 m
Incident overpressure	<i>U</i>	-0.3208	0.1650	-0.3208	0.1650
	<i>Y</i>	4.074	3.000	4.074	3.000
	<i>P<sub>s</sub></i> (MPa)	11.87	0.9994	11.87	0.9994
Incident impulse	<i>U</i>	0.2307	-0.5596	0.2307	-0.5596
	<i>Y</i>	2.123	2.161	2.123	2.161
	<i>I<sub>s</sub></i> /W <sup>1/3</sup>	0.1329	0.1450	0.1329	0.1450
	<i>I<sub>s</sub></i> (MPa-ms)	0.3885	0.4239	1.328	1.450
Reflected overpressure	<i>U</i>	0.4209	-0.4784	0.4209	-0.4784
	<i>Y</i>	5.192	3.759	5.192	3.759
	<i>P<sub>r</sub></i> (MPa)	155.8	5.746	155.8	5.746
Reflected impulse	<i>U</i>	-0.2360	0.8609	-0.2360	0.8609
	<i>Y</i>	3.624	2.739	3.624	2.739
	<i>I<sub>r</sub></i> /W <sup>1/3</sup>	4.208	0.5477	4.208	0.5477
	<i>I<sub>r</sub></i> (MPa-ms)	12.304	1.602	42.08	5.477
Arrival time	<i>U</i>	0.5834	0.2670	0.5834	0.2670
	<i>Y</i>	1.718	2.728	1.718	2.728
	<i>t<sub>a</sub></i> /W <sup>1/3</sup>	0.05229	0.5344	0.05229	0.5344
	<i>t<sub>a</sub></i> (ms)	0.1529	1.563	0.5229	5.344



(a) Sample results in SI units

**Figure 4-6 Use of the proposed polynomials and charts**



(b) Sample results in US units

Figure 4-6 Use of the proposed polynomials and charts (cont.)



## SECTION 5

# REFLECTED OVERPRESSURE AND IMPULSE AS A FUNCTION OF ANGLE OF INCIDENCE

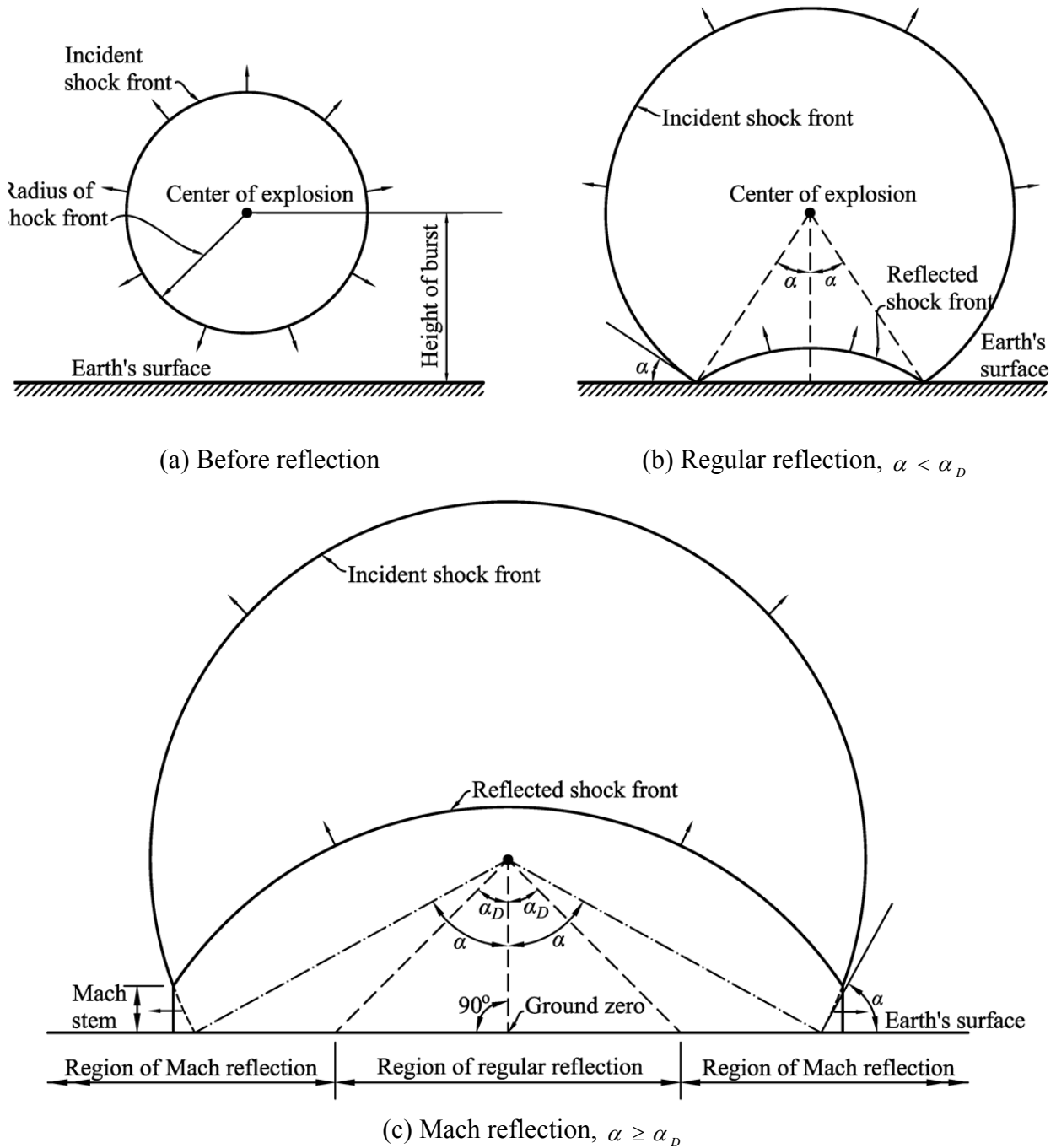
### 5.1 Introduction

Air-blast loading in the far field is typically characterized by a near-instantaneous increase in overpressure from zero to a peak value followed by an exponential decay to zero: the so-called positive loading phase. The pressure loading will then fall below ambient (i.e., underpressure), which is called the negative phase. The positive-phase impulse is the integral of the overpressure history over the duration of the positive phase. For design using single-degree-of-freedom procedures (e.g., Biggs 1964, DoD 2008, Cormie et al. 2009, Dusenberry 2010, ASCE 2011), the exponential decay of overpressure is often replaced by a linear decay to zero to enable the use of design charts based on triangular loading pulses. The duration of the positive phase for the linear-decay representation of the loading is chosen so as to preserve the reflected peak overpressure and reflected total impulse. The negative loading phase is often ignored for design.

Technical guidelines, manuals and textbooks, including TM 5-858-3 (DoA 1984), TM 5-1300 (Department of the Army, Navy and Air Force 1990), Smith and Hetherington (1994), UFC-3-340-02 (DoD 2008), Cormie et al. (2009) and Dusenberry (2010), present reflection coefficients for overpressure. This coefficient is the ratio of the reflected peak overpressure to the incident peak overpressure and it varies as a function of a) angle of incidence and b) the incident peak overpressure. Reflected scaled impulse is presented in UFC 3-340-02 as a function of the incident peak overpressure and the angle of incidence. Together, the reflected peak overpressure and the reflected impulse can describe a loading function for single-degree-of-freedom calculations.

Figure 5-1, which is adapted from Norris et al. (1959), illustrates stages in the propagation and reflection of a shock wave from a free-air burst, which include propagation in free air before reflection (Figure 5-1a), regular reflection (Figure 5-1b) and irregular or Mach reflection (Figure 5-1c). At an angle of incidence in the range of 40° and 50°, the incident and reflected waves

merge into a single, *reinforced* shock front, which is widely known as Mach reflection. The angle  $\alpha_D$  in Figure 5-1c is the angle of incidence,  $\alpha$ , associated with the initiation of Mach reflection.



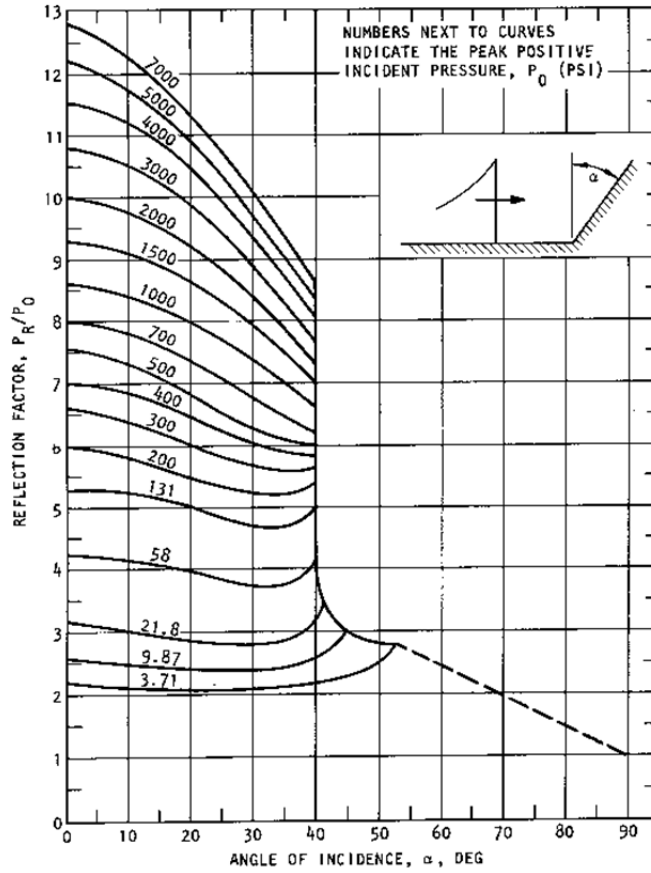
**Figure 5-1 Shock wave reflection phenomena from explosion in free air (adapted from Norris et al. 1959)**

Figure 5-2 presents reflection coefficients,  $C_r$ , for overpressure from TM 5-858-3 (reproduced in Smith and Hetherington) and UFC 3-340-02 (superseding TM 5-1300). For overpressure, the coefficient is two or greater for an angle of incidence of  $0^\circ$  (normal loading) and unity for an angle of incidence of  $90^\circ$  (side-on loading). The coefficients calculated using the two charts of Figure 5-2 vary significantly for angles of incidence between  $40^\circ$  and  $50^\circ$ , namely, the range associated with the formation of the Mach stem. Figure 5-3 presents reflected scaled impulse versus angle of incidence for different values of incident peak overpressure in UFC 3-340-2. The influence of the Mach stem is not observed in these curves.

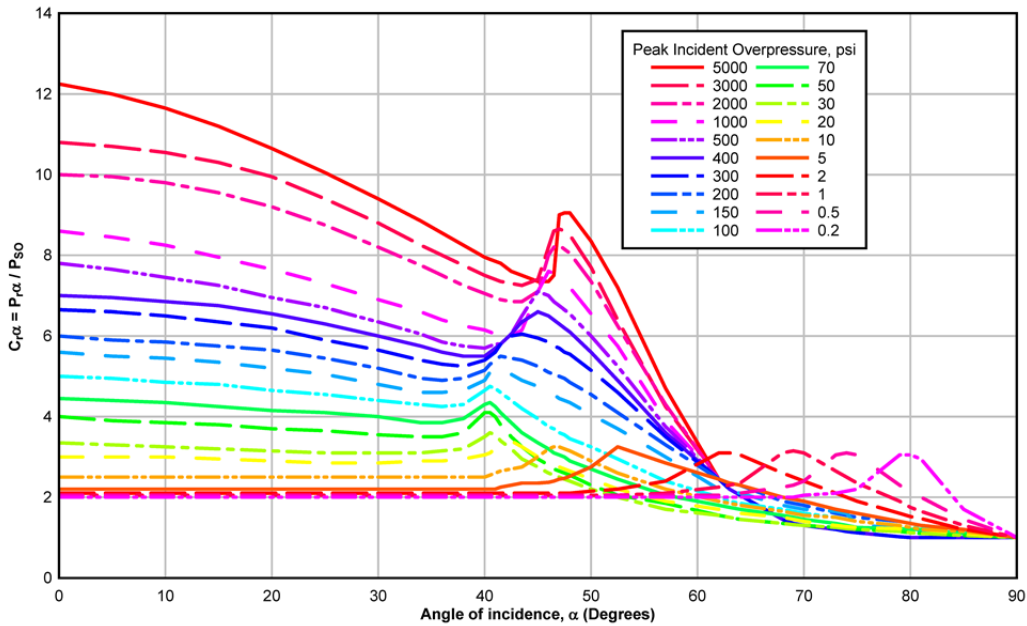
Kingery and Bulmash (KB, 1984) developed charts and polynomials for incident and *normally* reflected overpressures and impulses as a function of scaled distance,  $Z$ , as discussed in Chapter 3. The KB polynomials are implemented in government codes such as CONWEP (Hyde 1992) and form the basis of the charts in UFC 3-340-02 and TM 5-858-3. The reflection coefficients are used to compute reflected peak overpressure for non-normal reflection, namely,  $\alpha$  greater than  $0^\circ$ . The reflected impulse for a non-zero angle of incidence is calculated using the UFC 3-340-02 charts for reflected scaled impulse and the charge weight.

Chapter 3 demonstrated that the KB polynomials underestimate incident and normally reflected overpressures and incident impulse in the near field. Chapter 4 proposed new equations and charts for incident and normally reflected peak overpressure and impulse for  $0.0553 \leq Z \leq 40$   $\text{m/kg}^{1/3}$  ( $0.139 \leq Z \leq 100$   $\text{ft/lb}^{1/3}$ ), using numerical data reported in Chapter 3. Figures 5-4 and 5-5 present the charts proposed in Chapter 4 and these are used in the presentation that follows.

This chapter reconciles the differences between overpressure reflection coefficients in UFC 3-340-02 and TM 5-858-3 to enable accurate prediction of reflected peak overpressure for all angles of incidence and incident peak overpressure in the range from 0.016 MPa to 20 MPa. The CFD tool, AUTODYN (ANSYS 2013a), which is verified and validated in Chapter 2, is used for the analysis. Reflected scaled impulse is also studied to a) evaluate the charts in UFC 3-340-02 that are reproduced in Figure 5-3, and b) provide guidance on computational fluid dynamics (CFD) modeling of reflected impulse as a function of angle of incidence.

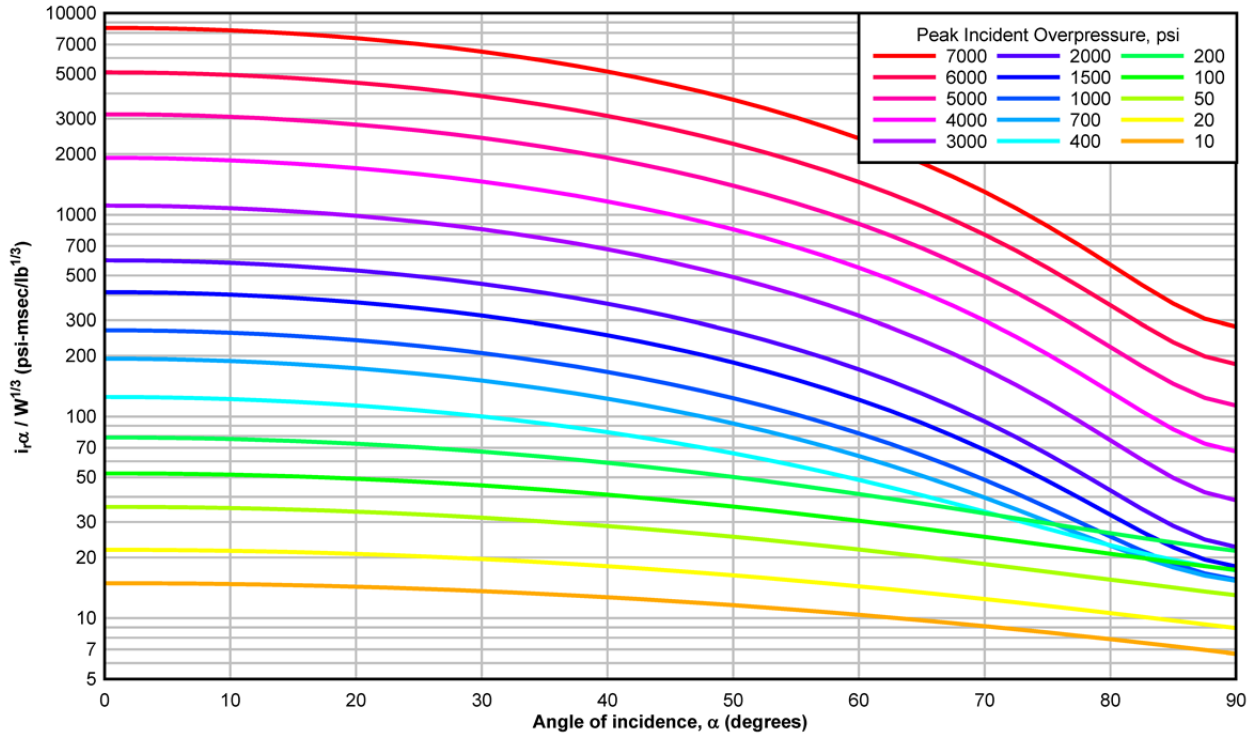


(a) TM 5-858-3 (DoA 1984)

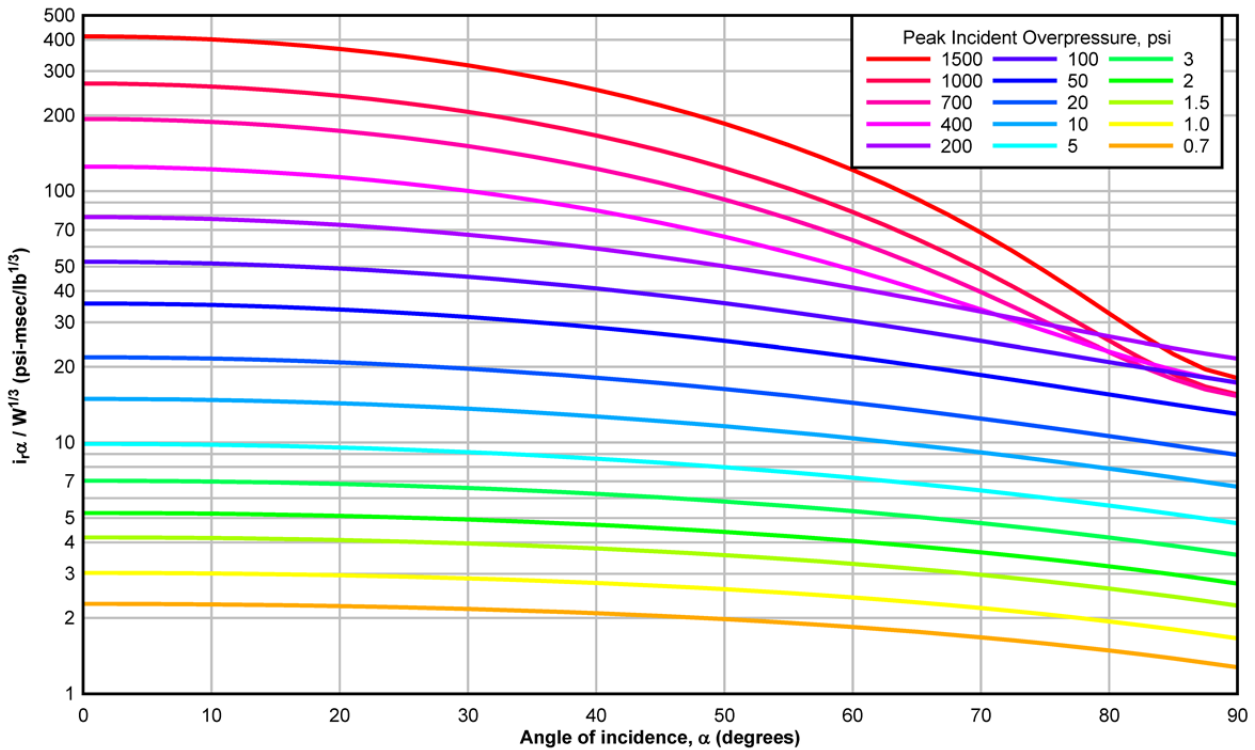


(b) UFC 3-340-02 (DoD 2008)

Figure 5-2 Reflection coefficient versus angle of incidence



(a)  $10 \leq P_s \leq 7000$  psi ( $0.069 \leq P_s \leq 48.3$  MPa)



(b)  $0.7 \leq P_s \leq 1500$  psi ( $0.0048 \leq P_s \leq 10.3$  MPa)

**Figure 5-3 Reflected scaled impulse versus angle of incidence (UFC 3-340-02 (DoD 2008))**

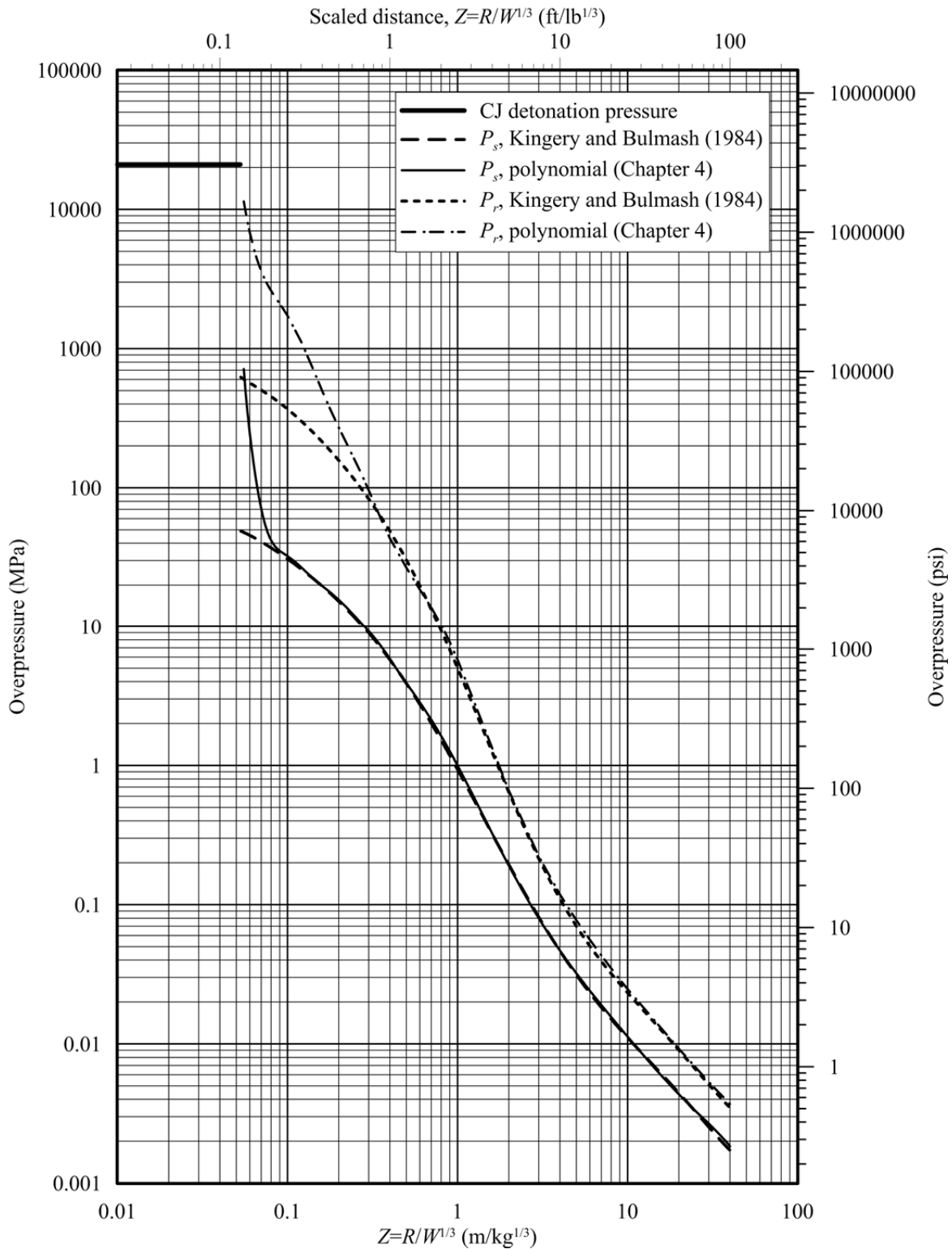


**Figure 5-4 Incident,  $P_s$ , and normally reflected,  $P_r$ , peak overpressures developed by Kingery and Bulmash (1984) and in Chapter 4**

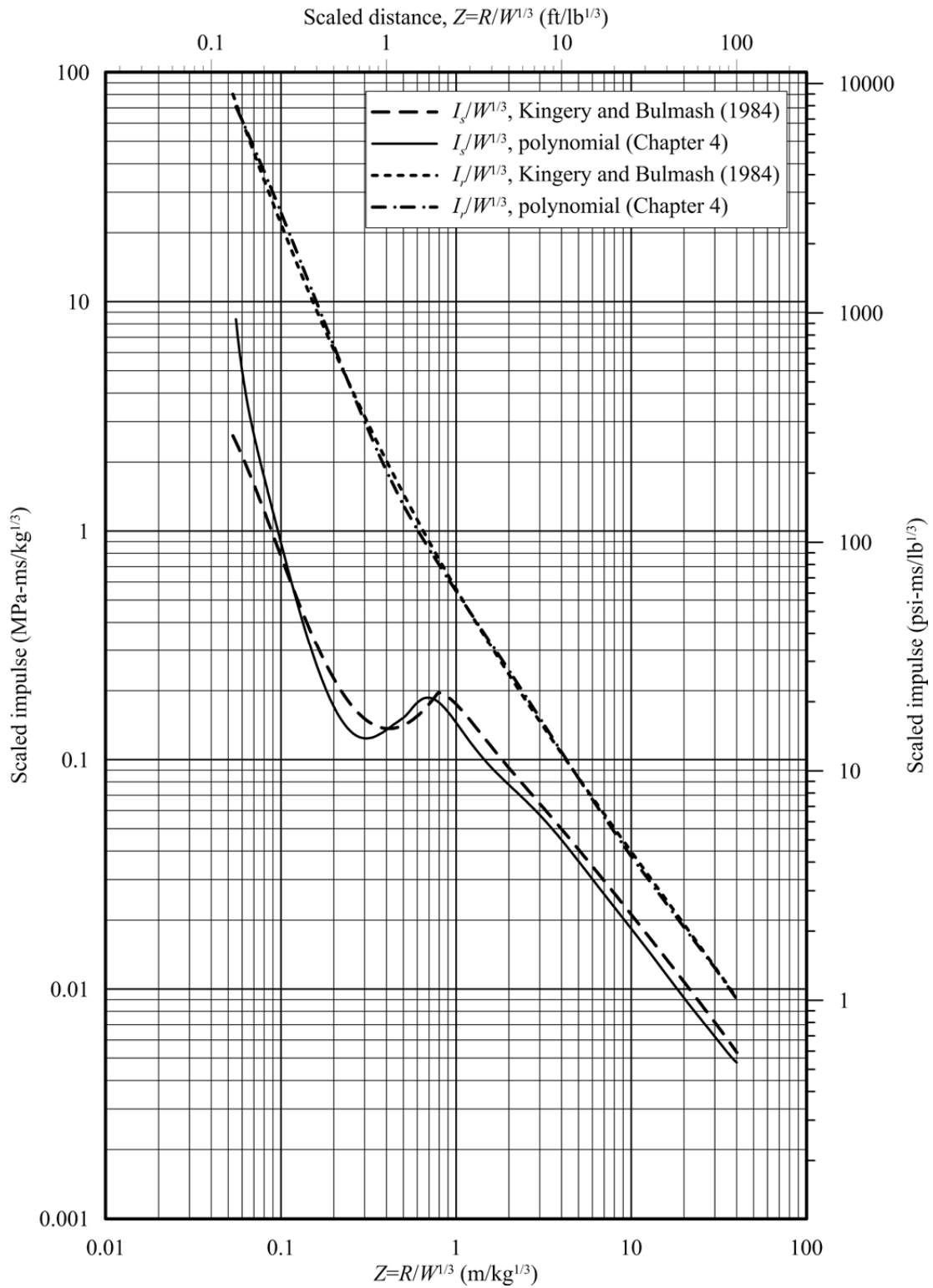


**Figure 5-5 Incident,  $I_s/W^{1/3}$ , and normally reflected,  $I_r/W^{1/3}$ , scaled impulses developed by Kingery and Bulmash (1984) and in Chapter 4**

## 5.2 Regular and Mach Reflections

Figures 5-2a and 5-2b show the value of the reflection coefficient,  $C_r$ , decreasing with increasing angle of incidence,  $\alpha$ , until the angle reaches approximately  $40^\circ$ , which is the region of regular reflection as illustrated in Figure 5-1b. At greater angles, the reflected wave, which is passing through heated and compressed air, and hence propagating faster than the incident wave, catches and merges with the incident wave at  $\alpha = \alpha_D$ , as shown in Figure 5-1c. The merging of the wave fronts gives rise to the Mach stem illustrated in the figure. For angles of incidence greater than that associated with the formation of a Mach stem, the reflection is termed a Mach, or irregular, reflection. The significant differences between Figures 5-2a and 5-2b are associated with Mach reflection. Figure 5-6, which is adapted from Smith and Hetherington (1994), provides a simple illustration of regular and Mach reflection. The angle of reflection,  $\beta$ , equals the angle of incidence,  $\alpha$ , for weak (acoustic) shocks. For strong shocks, Griffith and Bleakney (1954) reported that the ratio  $\alpha : \beta$  is greater than 1 and the ratio increases with the intensity of the shock.

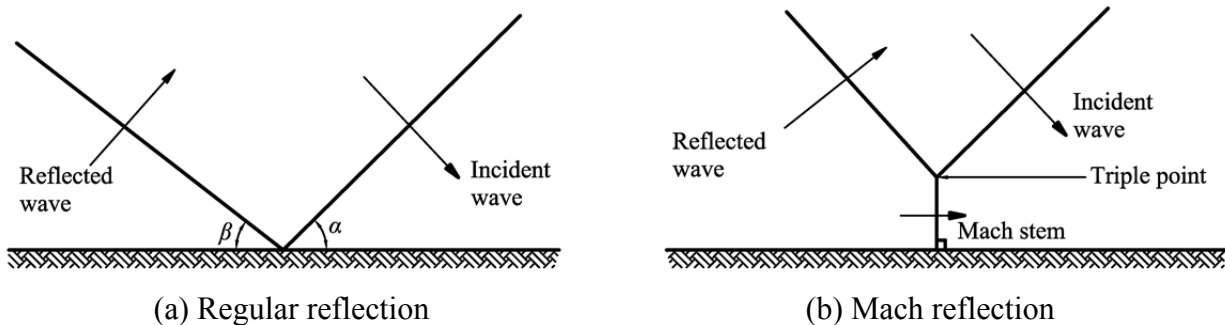


**Figure 5-6 Regular and Mach reflections (e.g., Smith and Hetherington 1994)**

The regions of regular and Mach reflections can be established as a function of the Mach number of the incident shock front (shock front velocity divided by sound speed in air) and the angle of incidence. Figure 5-7 (adapted from Ivanov et al. 2001) illustrates the relationships between these reflections, the Mach number,  $M$ , and the angle of incidence,  $\alpha$ , for an ideal gas. The angles,  $\alpha_N$  and  $\alpha_D$ , correspond to the von Neumann and detachment criteria, respectively. For  $\alpha < \alpha_N$ , only regular reflections are possible, and for  $\alpha > \alpha_D$ , only Mach reflections are possible. For  $M$  less than 2.2,  $\alpha_N$  and  $\alpha_D$  are identical. For  $M > 2.2$ , the difference between  $\alpha_N$  and  $\alpha_D$

increases with Mach number. Both regular and Mach reflections are possible in the domain  $\alpha_N < \alpha < \alpha_D$ . In this domain, which is described as the dual solution domain (DSD), reflections can transition between regular and Mach as a result of unsteadiness in the flow (Mouton 2007). For a steady flow, regular reflection is likely to occur in the DSD and this is assumed herein, namely,  $\alpha_D$ , is associated with Mach reflection.

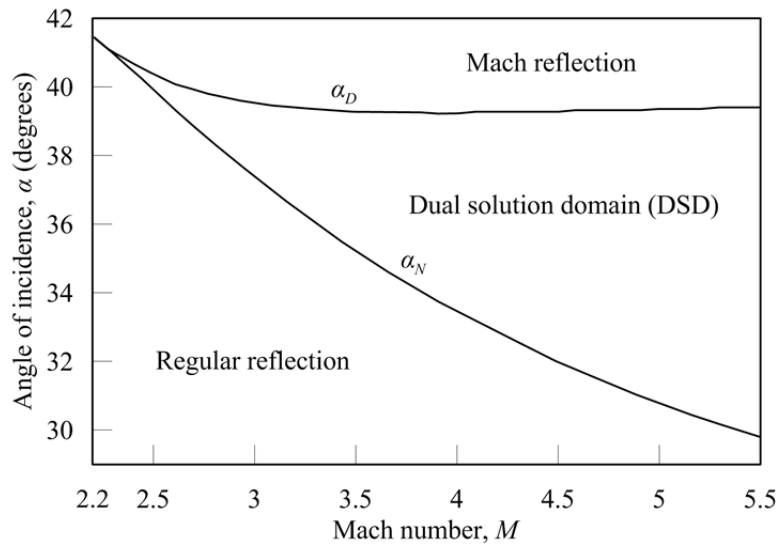


**Figure 5-7 Dual solution domain (Ivanov et al. 2001)**

For incident peak overpressures less than 0.34 MPa (50 psi), the Mach reflection angle increases as the incident overpressure decreases, as shown in Figure 5-8 and as reported by Courant and Friedrichs (1948) and Kinney and Graham (1985). This observation is consistent with the charts in TM 5-858-3 and UFC 3-340-02, which are reproduced in Figure 5-2.

TM 5-858-3 assumes the angle of incidence for Mach reflection to be approximately  $40^\circ$  for incident peak overpressures greater than approximately 0.34 MPa (50 psi). The assumption is appropriate for an ideal gas with a specific heat ratio of 1.4 (e.g., Courant and Friedrichs 1948, Kinney, 1962, Kinney and Graham 1985, Schwer 2008). Figure 5-8 (adapted from Kinney and Graham 1985) presents the relationship between the angle of incidence associated with the formation of a Mach stem (i.e., onset of Mach reflection) and the Mach number of the shock front. For Mach number greater than 2.0, the angle of incidence is approximately  $40^\circ$ ; which is seen in Figure 5-2a for incident overpressures greater than 50 psi (0.34 MPa). An incident peak

overpressure of 0.34 MPa corresponds to a shock front velocity of approximately Mach 2 (see Figure 5-9).

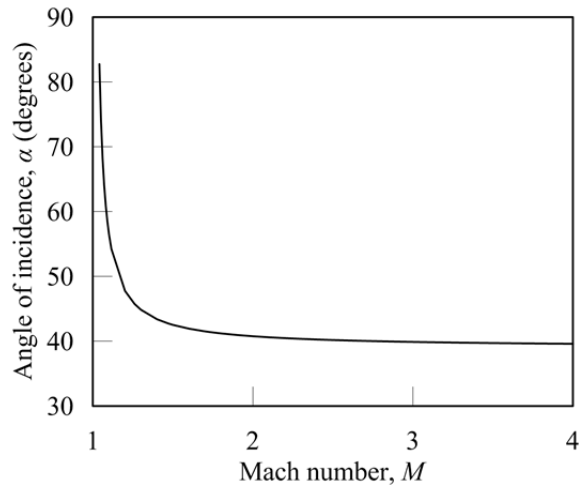


**Figure 5-8 Angle of incidence for Mach reflection as a function of Mach number for an ideal gas (Kinney and Graham 1985)**

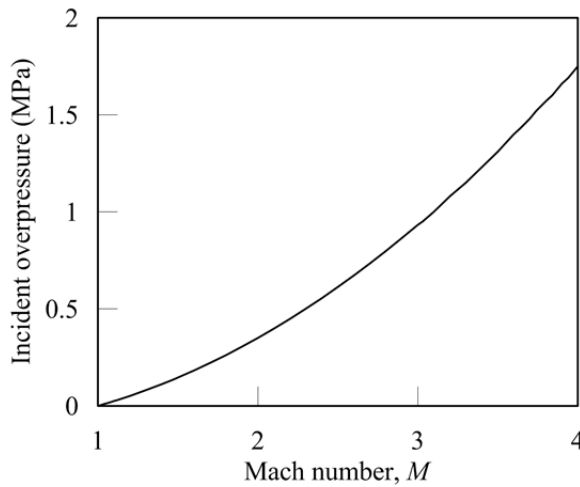


**Figure 5-9 Incident overpressure as a function of Mach number for an ideal gas (Kinney and Graham 1985)**

In UFC 3-340-02, the effect of Mach reflection is observed in the range  $45^\circ < \alpha < 50^\circ$  for incident peak overpressures of 2.8 MPa (400 psi) and greater, which corresponds approximately to  $C_r > 7$  at  $\alpha = 0^\circ$  (see Figure 5-2b). The angle of incidence associated with Mach reflection increases with a decrease in the specific heat ratio that accompanies higher incident overpressures (Schwer 2008). Schwer computed angles of incidence for Mach reflection, as a function of Mach number from 3 to 18, and reported that for an *ideal gas* with a specific heat

ratio a) of 1.4, the angle was constant at  $39.9^\circ$  between Mach 3 and Mach 18 (supporting the value of approximately  $40^\circ$  in TM 5-858-3), and b) of 1.2, the angle increased from  $42^\circ$  at Mach 3 to  $46^\circ$  at Mach 18 (supporting the increase in angle with increasing incident overpressure seen in the UFC).

The effect of Mach reflection is not observed in the UFC 3-340-02 charts of reflected scaled impulse that are reproduced in Figure 5-3, for the reason given below.

## **5.3 A Numerical Model for Calculating Reflection Coefficients**

### ***5.3.1 Modeling and Domains***

Reflection coefficients are calculated by simulating the detonation of a 960 kg spherical charge of TNT in free air, as described in Chapters 3 and 4. The expansion of the detonation products is modeled using the JWL Equation of State (EOS) in 1D multi-material Euler-Godunov grids (see Section 2.2.1). The 1D simulation proceeds until the shock wave reaches a reflecting boundary. The 1D results are then mapped into 2D Euler-FCT grids, as illustrated in Figure 3-7. After the detonation product has expanded to 10 times its original volume, standard practice replaces the JWL EOS with the ideal gas EOS to avoid possible numerical instability. The Dobratz and Crawford (1985) values of the parameters for the JWL EOS, presented in Table 2-1, are used for the simulations described below.

Calculations are performed for one charge weight only. The results of simulations of incident and reflected peak overpressure in Chapter 3 for three very different charge masses (18735, 960 and 23 kg) showed no influence of weight for a given scaled distance and so calculations are performed using only one charge mass.

In the model depicted in Figure 5-10, axial symmetry is used at the lower boundary and mirror symmetry is used at the left boundary; 1/4 of the explosive and air domains are analyzed. The mirrored-symmetric boundary is a perfectly reflecting surface. The monitoring location is varied by angle,  $\alpha$ , and distance,  $R$ , to calculate reflected peak overpressures as a function of the angle of incidence. The length and height of the air domain are  $R \cos \alpha$  and  $(R \cos \alpha + R/4)$ ,

respectively. The length of  $R/4$  is chosen to eliminate partial reflection<sup>7</sup> of overpressure from the horizontal transmitting (upstream) boundary on the reflected peak overpressure at the monitoring location. Numerical simulations are performed for fourteen scaled distances, 0.16, 0.2, 0.26, 0.3, 0.4, 0.6, 0.8, 1.2, 1.6, 2.4, 3.2, 4, 6 and 8  $\text{m/kg}^{1/3}$  (0.4, 0.5, 0.65, 0.75, 1, 1.5, 2, 3, 4, 6, 8, 10, 15 and 20  $\text{ft/lb}^{1/3}$ , respectively) and fifteen angles of incidence,  $0^\circ$ ,  $10^\circ$ ,  $20^\circ$ ,  $30^\circ$ ,  $40^\circ$ ,  $42.5^\circ$ ,  $45^\circ$ ,  $47.5^\circ$ ,  $50^\circ$ ,  $52.5^\circ$ ,  $55^\circ$ ,  $57.5^\circ$ ,  $60^\circ$ ,  $70^\circ$  and  $80^\circ$ , to establish the relationships between overpressure reflection coefficient, angle of incidence and incident peak overpressure. Smaller intervals are used in the range  $40^\circ \leq \alpha \leq 60^\circ$  to capture the effect of Mach reflection. For an angle of  $90^\circ$ , the reflected overpressure is identical to the incident overpressure. The scaled distances of 0.16, 0.2, 0.26 and 0.3  $\text{m/kg}^{1/3}$  are not simulated for  $\alpha = 80^\circ$  because the perpendicular distance from the reflecting surface to the center of the charge is less than the charge radius; see Figure 5-10. For  $Z = 0.3 \text{ m/kg}^{1/3}$  (or  $R = 2.96 \text{ m}$ ) and  $\alpha = 80^\circ$ , the length of the air domain,  $R \cos \alpha = 0.514 \text{ m}$  is smaller than the charge radius ( $= 0.520 \text{ m}$  for TNT weight of 960 kg and packing density of 1630  $\text{m/kg}^{1/3}$ ). The smallest scaled distance of 0.16  $\text{m/kg}^{1/3}$  enables calculation of reflection coefficients with angles of incidence up to  $70^\circ$ . (For  $R \cos \alpha = 0.520 \text{ m}$  and  $\alpha = 70^\circ$  in Figure 5-10,  $R = 1.52 \text{ m}$ , which corresponds to  $Z = 0.154 \text{ m/kg}^{1/3}$ .) The maximum scaled distance of 8  $\text{m/kg}^{1/3}$  used here produces an incident peak overpressure of 0.015 MPa, approximately 1/7 of ambient pressure at sea level ( $= 0.1 \text{ MPa}$ ), which is a practical lower limit for the blast-resistant design of structural components

---

<sup>7</sup> A transmitting boundary does not perfectly pass outgoing pressure. A small fraction of the outgoing wave is reflected due to numerical approximations. Although the amplitudes of the partially reflected waves are generally small, they can increase both the reflected peak overpressure and impulse if the distance of the transmitting boundary from the monitoring location is very small. A distance of  $R/4$  is sufficient to eliminate any significant effect of wave reflection; see Section 2.5 for details.

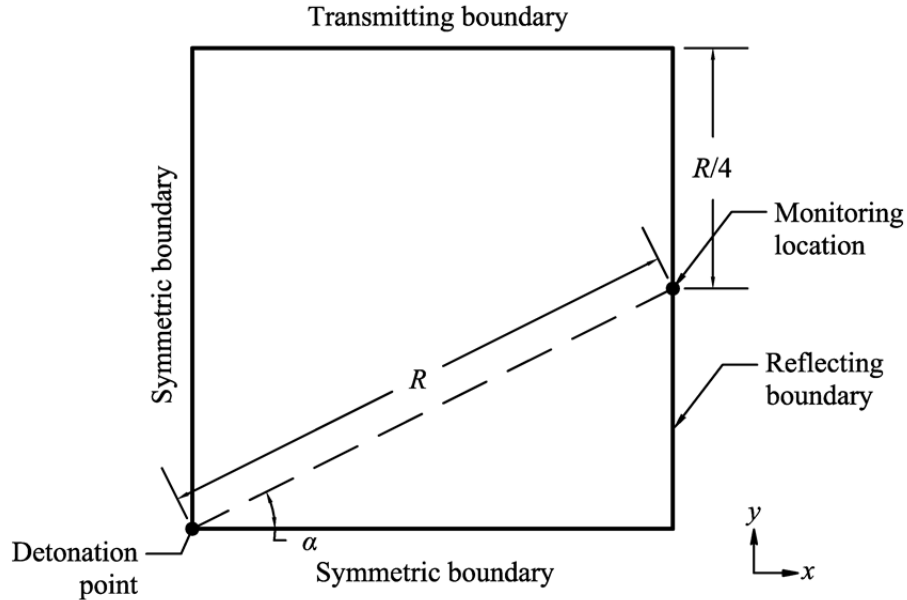


**Figure 5-10 2D numerical model of air for calculating reflection coefficients**

### 5.3.2 Cell Size

One advantage of the remapping procedure described previously is that fine meshes can be used for 1D simulations and coarser meshes used for 2D simulations. A cell size of  $R/1600$  is used for 1D radial analysis of incident peak overpressure, where  $R$  is the distance to the monitoring location from the center of the charge. Results are then mapped into a 2D domain, with a cell size of  $R/800$ . These cell sizes for 1D and 2D analysis are smaller than 0.002 times the distance to the monitoring location ( $R/500$ ) deemed appropriate in Chapter 3 for simulations of incident and reflected peak overpressures at  $Z \leq 8 \text{ m/kg}^{1/3}$ .

## 5.4 Numerical Models for Calculating Reflected Impulses

### 5.4.1 Modeling and Domains

Reflected impulse is calculated for the 960 kg spherical charge of TNT and scaled distances of 0.16 to  $8 \text{ m/kg}^{1/3}$ , used in the analysis of reflection coefficient in Section 5.3, but for fewer (nine) angles of incidence of  $0^\circ$ ,  $10^\circ$ ,  $20^\circ$ ,  $30^\circ$ ,  $40^\circ$ ,  $50^\circ$ ,  $60^\circ$ ,  $70^\circ$  and  $80^\circ$  because preliminary studies indicated that Mach reflection had no significant effect on reflected scaled impulse for angles of incidence in the range  $40^\circ \leq \alpha \leq 50^\circ$ . (This is confirmed in Section 5.8 using reflected

overpressure and scaled impulse histories for  $Z = 0.16, 0.40$  and  $1.2 \text{ m/kg}^{1/3}$  with  $\alpha = 30^\circ, 40^\circ, 45^\circ, 50^\circ$  and  $55^\circ$ .) For an angle of  $90^\circ$ , the reflected impulse for a given scaled distance is identical to the incident impulse. The modeling of the expansion of the detonation products (e.g., JWL EOS for TNT, 1D to 2D mapping) is similar to that described in the previous section.

Three AUTODYN 2D models of air are constructed to calculate reflected impulse as a function of angle of incidence; see Figure 5-11. A quarter of the charge is modeled with axial symmetry at the lower boundary. Model 1 is similar to that shown in Figure 5-10. The upper *transmitting* boundary in Figure 5-11a should prevent reflection of pressure waves that would affect the calculation of reflected impulse. However, as noted in Chapter 2, partial reflection is possible from a transmitting boundary, and the boundary must be located a sufficient distance from the monitoring locations. (In Chapter 2, the boundary was set 149 mm above the uppermost monitoring location: ④ in Figure 2-49a.) For these calculations, the height of the 2D domain is calculated by adding the shortest distance from the detonation point to the right reflecting boundary ( $= R \cos \alpha$ ) to the height of the monitoring location, which is sufficient to make accurate calculations of reflected impulse. The left *transmitting* boundary in Figure 5-11a should also prevent the reflection of pressure waves between the vertical boundaries. Energy will not be lost across this boundary in the initial phase of the expansion because the shock front propagates radially away from the source and thus away from this boundary. However, the wave that is reflected from the right boundary may be partially reflected from the left transmitting boundary, which would then increase the impulse if the partially reflected wave arrives at the monitoring location on the right boundary during the positive phase. This is more likely to occur for higher angles of incidence with a relatively small horizontal 2D domain. Models 2 and 3 increase the horizontal length of the 2D domain of Model 1 to evaluate the effect of location of the left transmitting boundary on reflected impulse for large angles of incidence. Models 1, 2 and 3 have horizontal dimensions of  $R \cos \alpha$ ,  $1.5 R \cos \alpha$  and  $2 R \cos \alpha$ , respectively, as shown in Figure 5-11. Figure 5-12 illustrates Models 1, 2 and 3 for an angle of incidence of  $80^\circ$ , where reflected scaled impulse is calculated at point 1. The use of the three models is discussed further in Section 5.4.3, noting that analysis of Model 3 is computationally more expensive than analysis of Model 1.

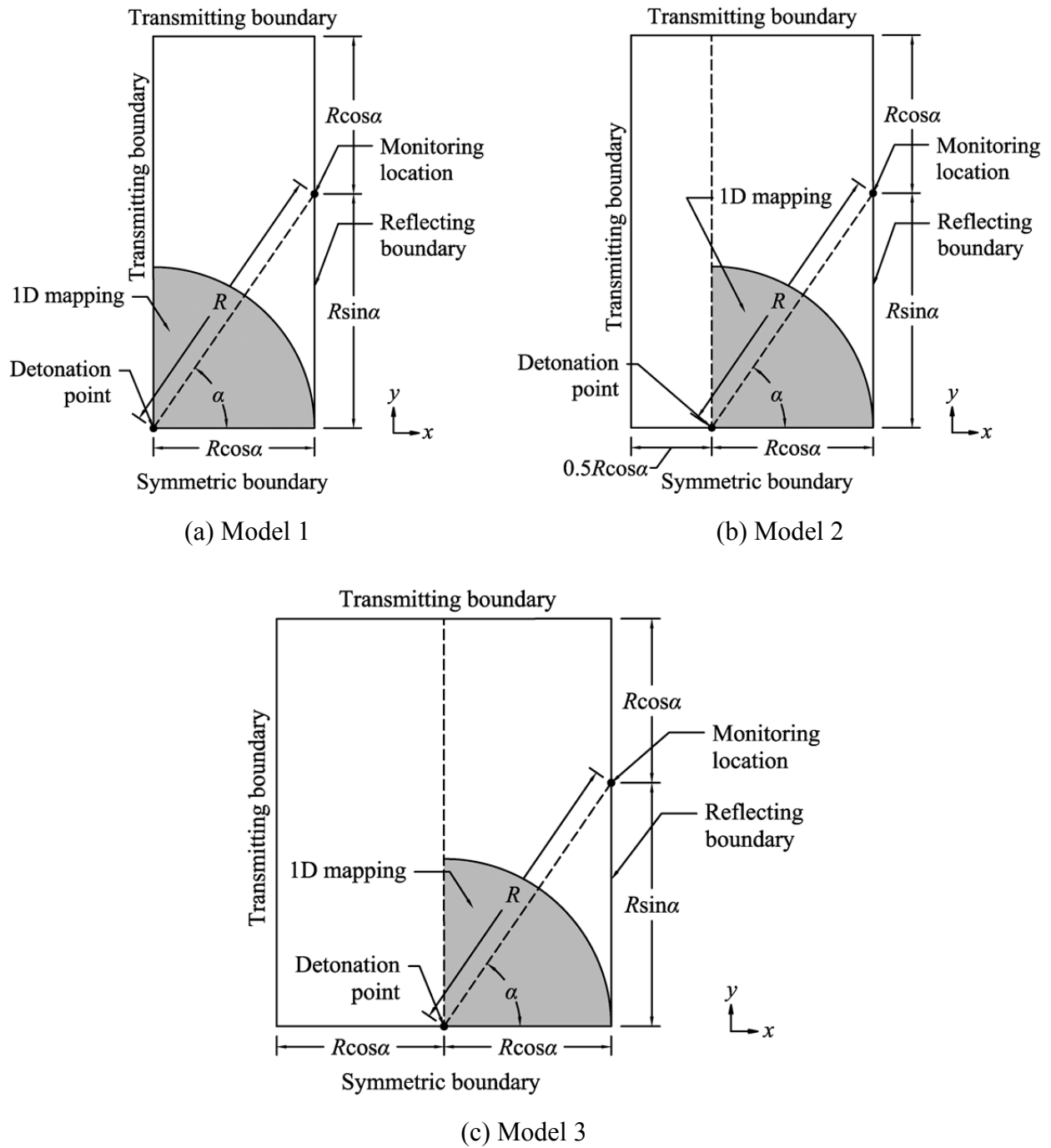
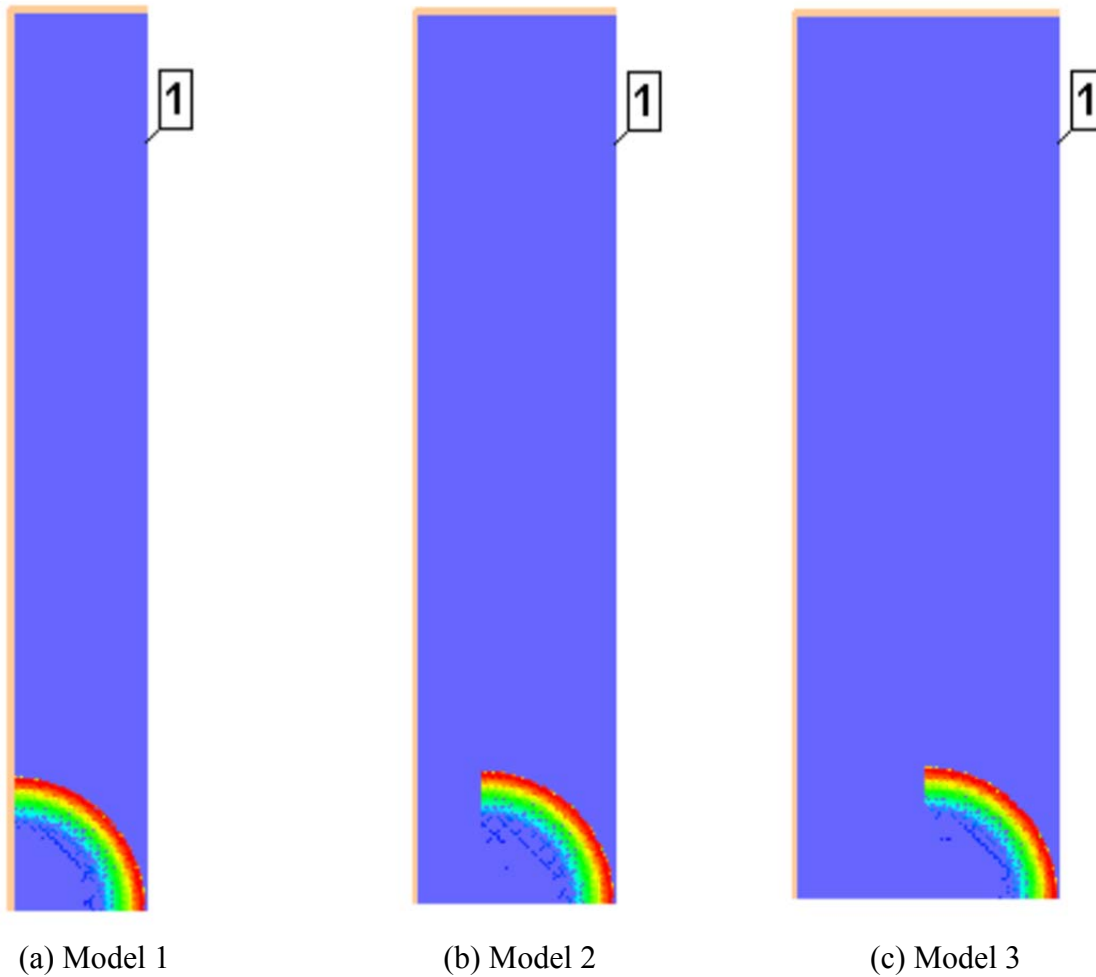


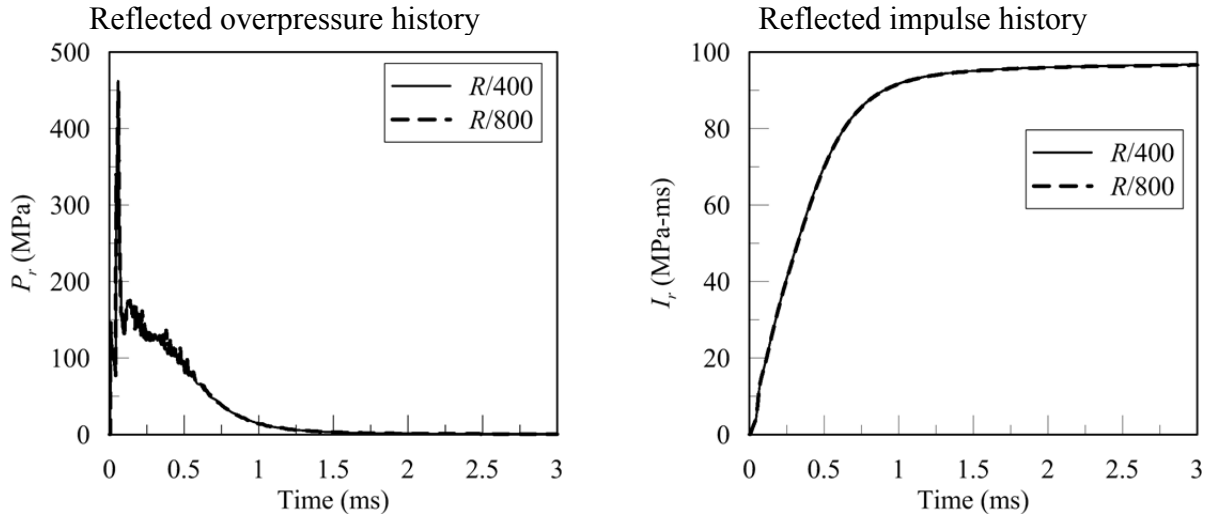
Figure 5-11 2D numerical models of air for calculating reflected impulses



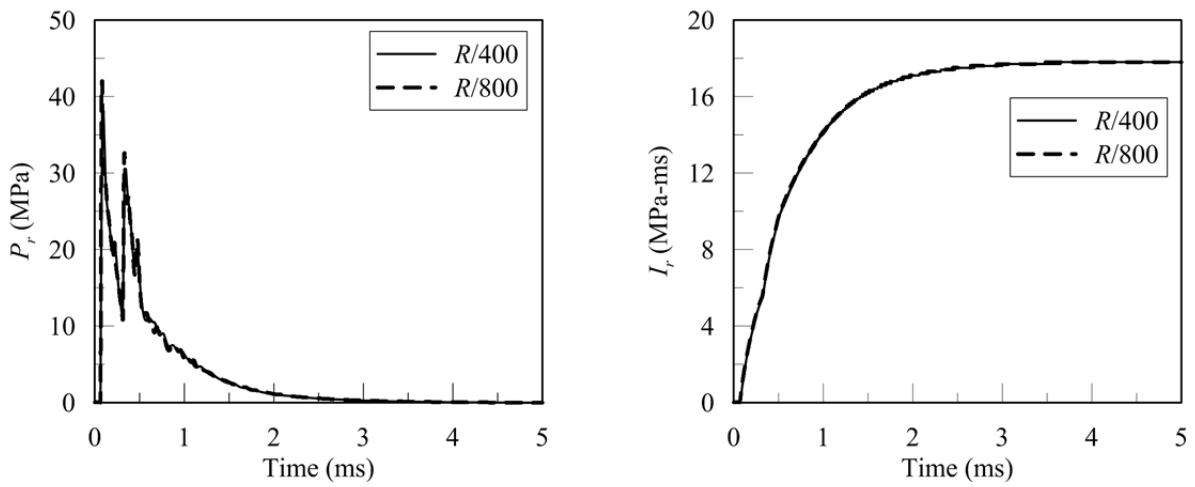
**Figure 5-12 Models 1, 2 and 3 in AUTODYN for angle of incidence of 80°**

#### **5.4.2 Cell Size**

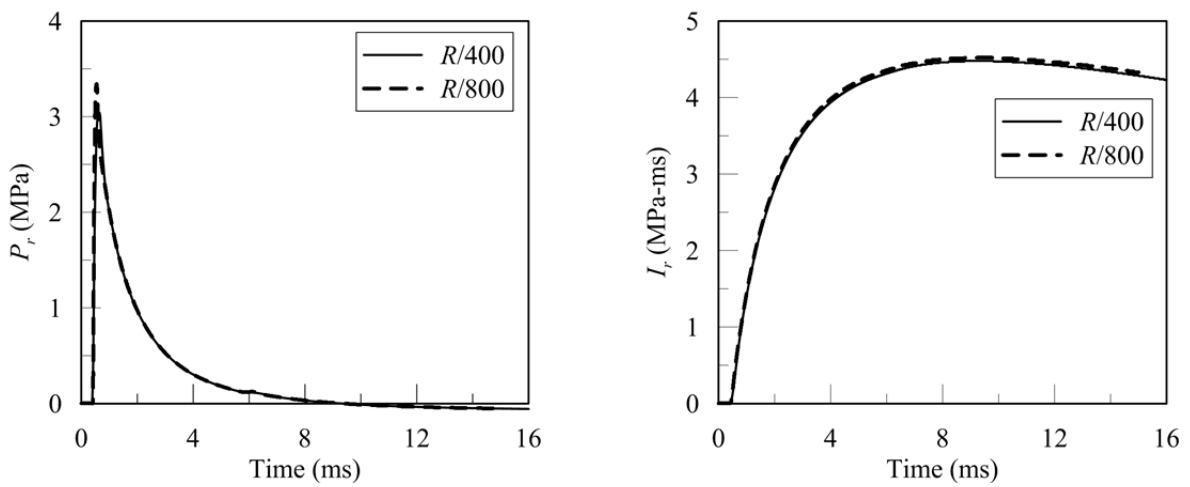
One-dimensional radial analysis is performed using a cell size of  $R/1600$  as discussed in Section 5.3. The 1D results are then mapped into a 2D domain. Two cell sizes,  $R/800$  and  $R/400$ , are considered for the 2D analysis because the calculation of reflected impulse converges for larger cell sizes than reflected peak overpressure, as reported in Section 3.7. Figure 5-13 presents normally reflected overpressure and impulse histories calculated using Model 1 for cell sizes of  $R/400$  and  $R/800$  and for  $Z = 0.16, 0.40$  and  $1.2 \text{ m/kg}^{1/3}$ . The results are essentially independent of cell size at each scaled distance. Since the use of the smaller cell size ( $R/800$ ) is computationally more expensive, the larger cell size ( $R/400$ ) is used to model the 2D domain for calculating reflected scaled impulse.



(a)  $Z = 0.16 \text{ m/kg}^{1/3}$



(b)  $Z = 0.40 \text{ m/kg}^{1/3}$



(c)  $Z = 1.2 \text{ m/kg}^{1/3}$

**Figure 5-13 Mesh sensitivity study for simulating reflected impulse; Model 1**

### 5.4.3 Effect of Transmitting Boundary

The effect of the location of the left transmitting boundary on the reflected impulse calculation is examined using Models 1, 2 and 3 for  $Z = 0.16, 0.40$  and  $1.2 \text{ m/kg}^{1/3}$ . Figure 5-14 presents results calculated using the cell size of  $R/400$  for  $Z = 0.16 \text{ m/kg}^{1/3}$  with  $\alpha = 30^\circ, 40^\circ, 50^\circ, 60^\circ$  and  $70^\circ$ . The reflected impulses for Models 1, 2 and 3 are very similar for  $\alpha = 30^\circ$  and  $40^\circ$ . For  $\alpha = 50^\circ, 60^\circ$  and  $70^\circ$ , the reflected impulses for Model 1 are significantly greater than those for Models 2 and 3 due to partial reflection of the shock waves from the left *transmitting* boundary. This outcome is similar for  $Z = 0.40$  and  $1.2 \text{ m/kg}^{1/3}$  with  $\alpha \geq 70^\circ$ , as shown in Figures 5-15 and 5-16, respectively. Results for Models 2 and 3 are essentially identical.

The influence of the location of the left transmitting boundary is greater for  $Z = 0.16 \text{ m/kg}^{1/3}$  than for  $Z = 0.40$  and  $1.2 \text{ m/kg}^{1/3}$  because a) the shock waves that are partially reflected from the left (transmitting) boundary propagate faster at smaller scaled distances, and b) the effect of the expanding detonation products can increase the positive phase duration for small values of scaled distance as demonstrated in Chapter 2 and discussed further in Section 5.6. Accordingly, for  $Z = 0.16, 0.20, 0.26$  and  $0.30 \text{ m/kg}^{1/3}$ , Model 1 is used for  $0^\circ \leq \alpha \leq 40^\circ$  and Model 2 is used for  $\alpha > 40^\circ$ . For  $Z \geq 0.40 \text{ m/kg}^{1/3}$ , Model 1 is used for  $0^\circ \leq \alpha \leq 60^\circ$  and Model 2 is used for  $\alpha > 60^\circ$ . Model 3 is not used for subsequent calculations.

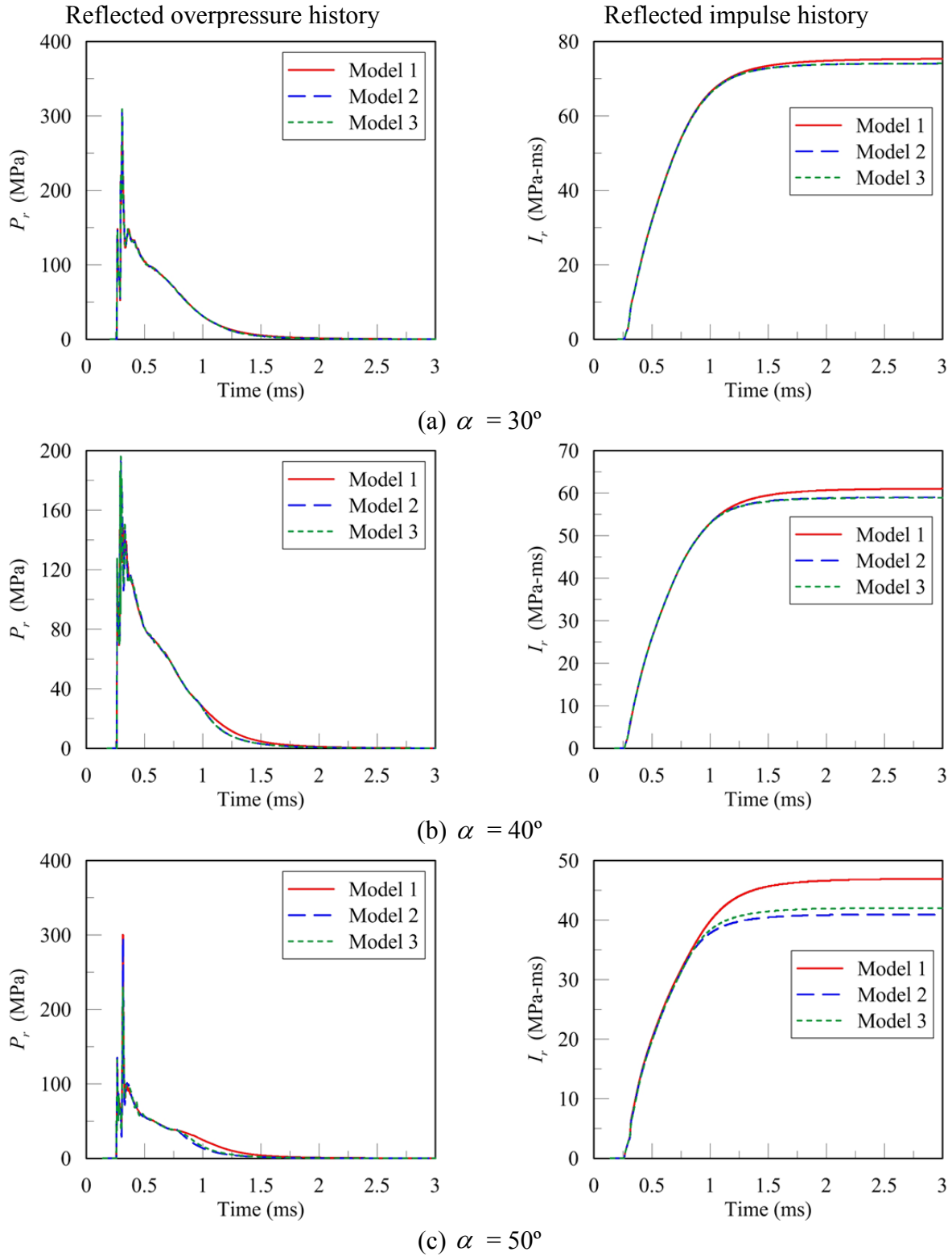
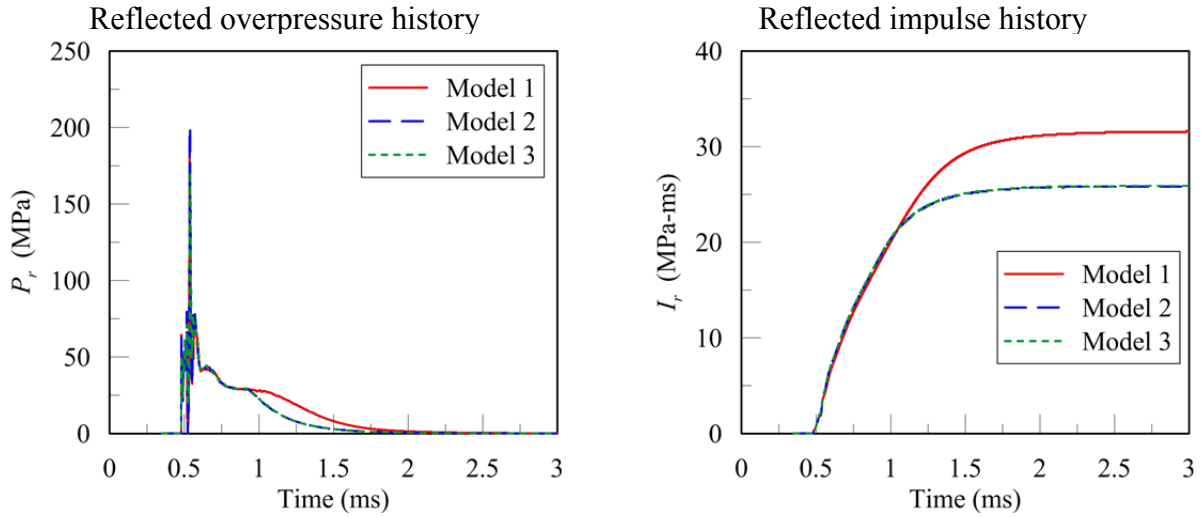
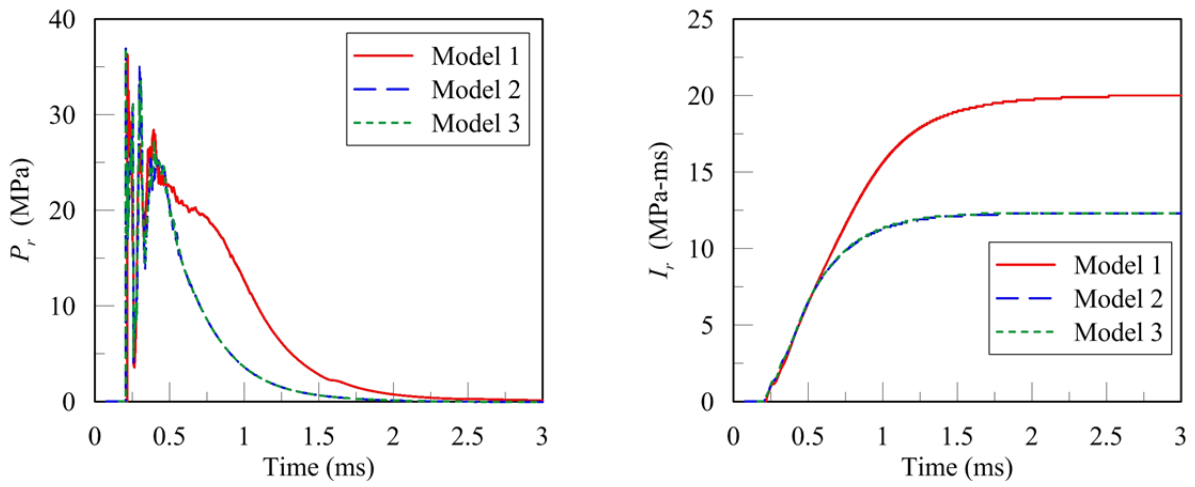


**Figure 5-14 Effect of transmitting boundary on calculation of reflected impulse for  $Z = 0.16 \text{ m/kg}^{1/3}$**



(d)  $\alpha = 60^\circ$



(e)  $\alpha = 70^\circ$

**Figure 5-14 Effect of transmitting boundary on calculation of reflected impulse for  $Z = 0.16$   $\text{m/kg}^{1/3}$  (cont.)**

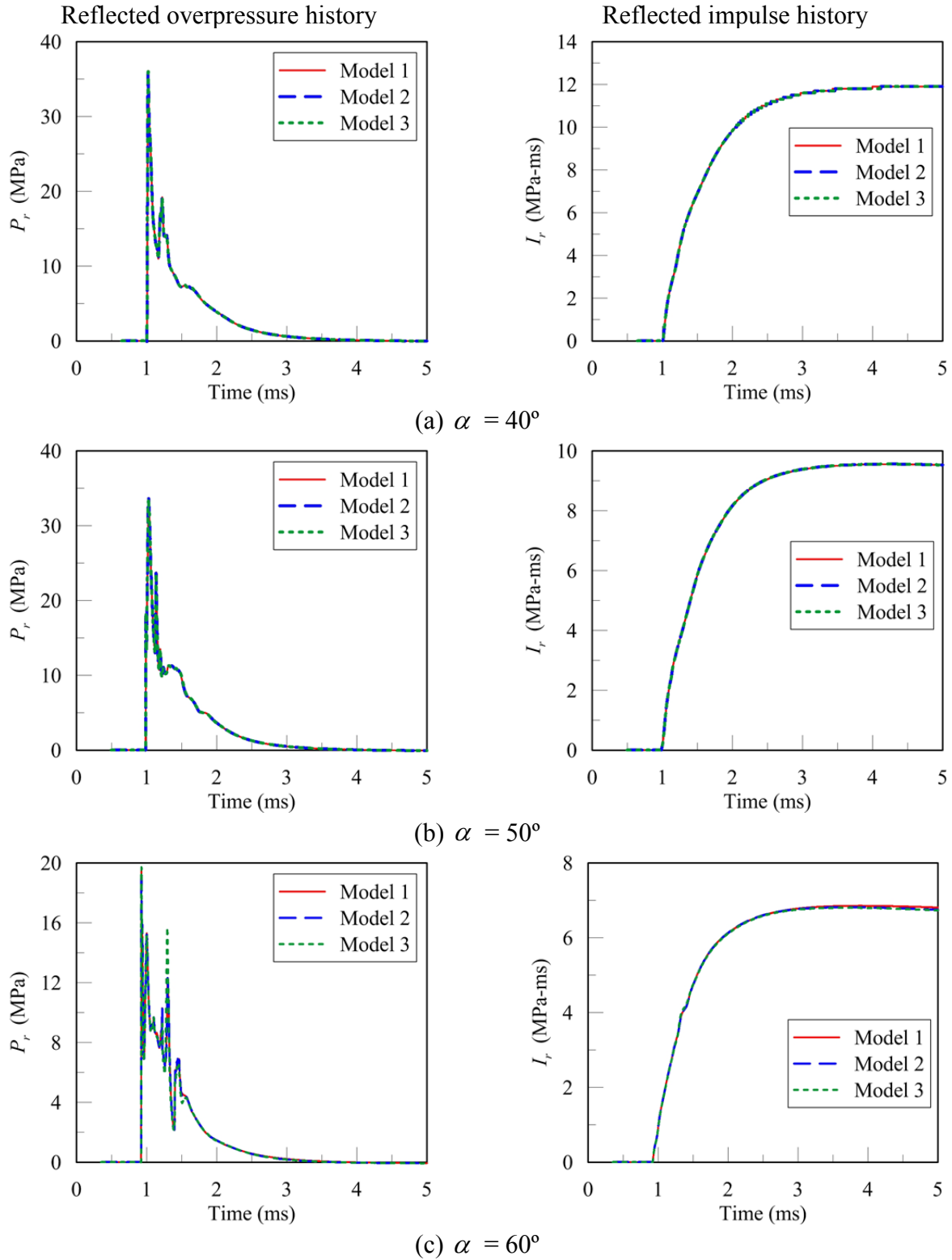
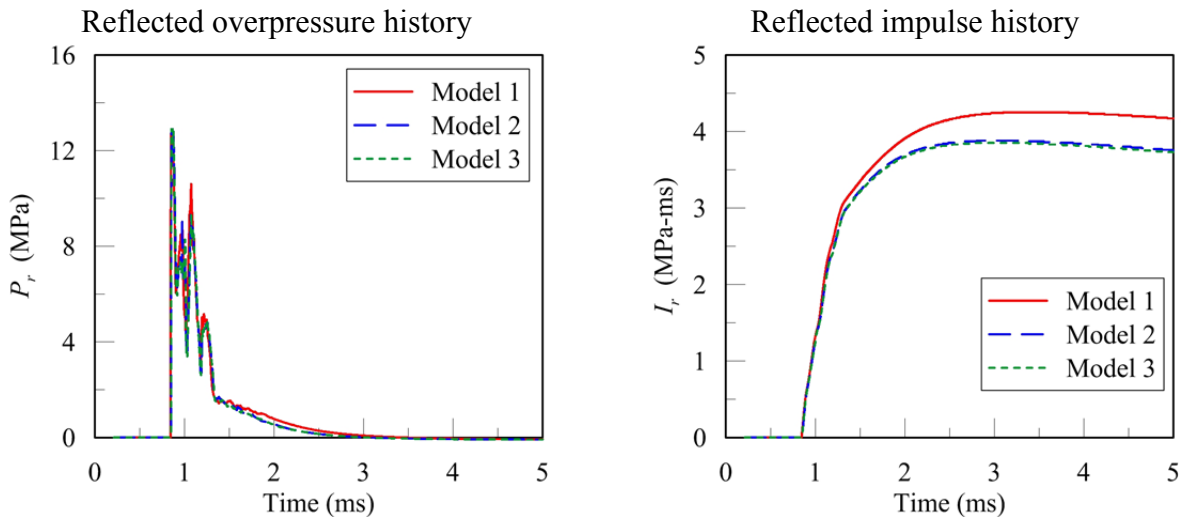
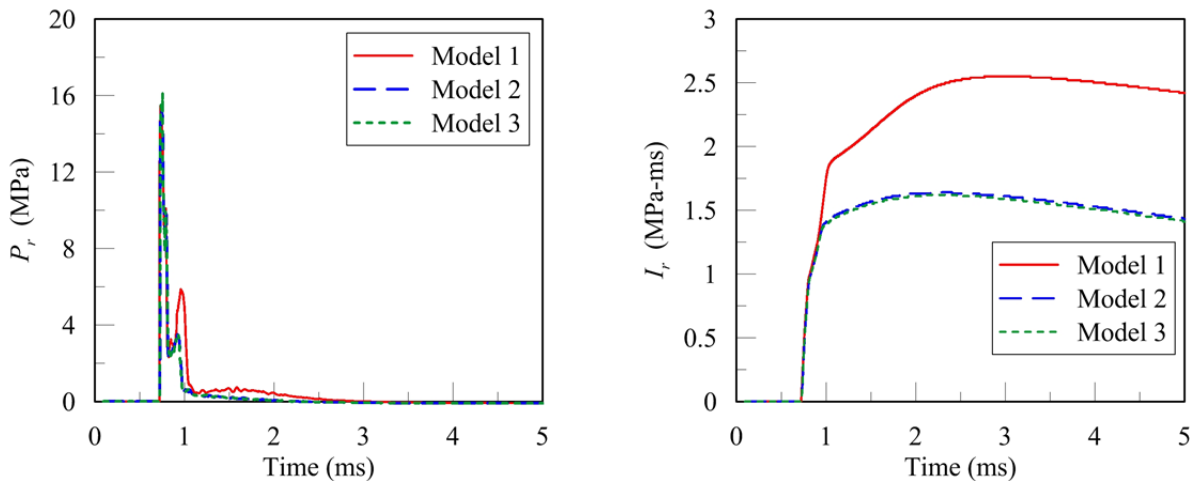


**Figure 5-15 Effect of transmitting boundary on calculation of reflected impulse for  $Z = 0.40$   $\text{m/kg}^{1/3}$**



(d)  $\alpha = 70^\circ$



(e)  $\alpha = 80^\circ$

**Figure 5-15 Effect of transmitting boundary on calculation of reflected impulse for  $Z = 0.40$   $\text{m/kg}^{1/3}$  (cont.)**

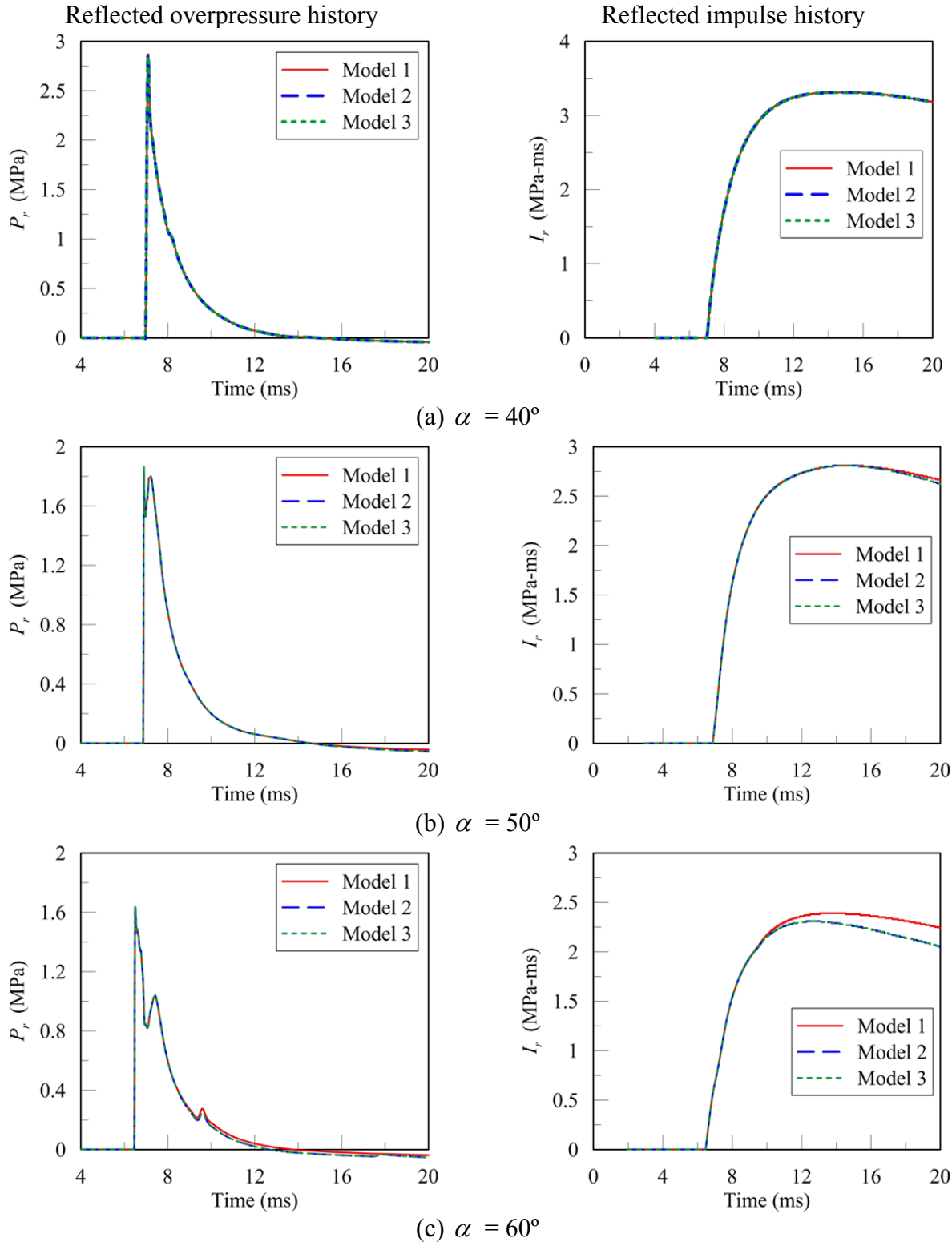
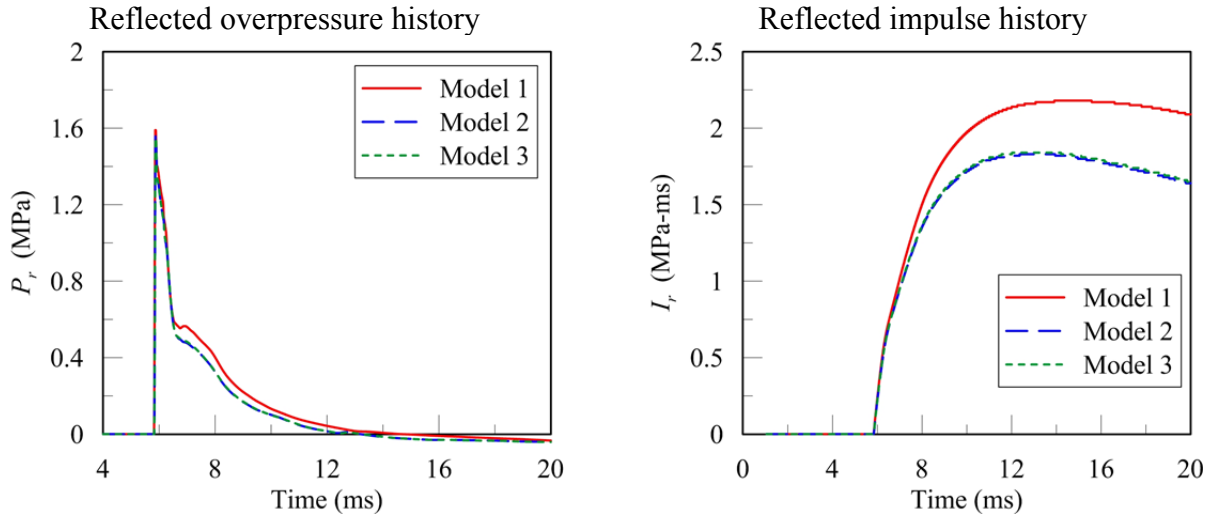
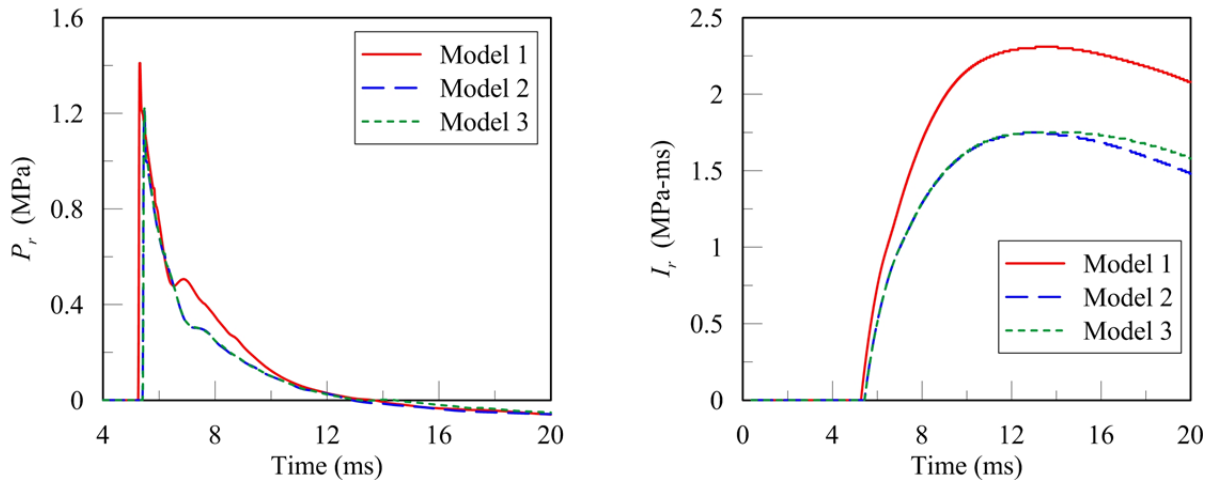


**Figure 5-16 Effect of transmitting boundary on calculation of reflected impulse for  $Z = 1.2$   $\text{m/kg}^{1/3}$**



(d)  $\alpha = 70^\circ$



(e)  $\alpha = 80^\circ$

**Figure 5-16 Effect of transmitting boundary on calculation of reflected impulse for  $Z = 1.2 \text{ m/kg}^{1/3}$  (cont.)**

## 5.5 Incident and Normally Reflected Overpressures

Incident,  $P_s$ , and reflected,  $P_r$ , peak overpressures for different values of scaled distance and normal incidence,  $\alpha = 0^\circ$ , are calculated using cell sizes of  $R/1600$  (1D) and  $R/800$  (2D). Results are presented in Figure 5-17, together with data from polynomials per Table 4-2 of Chapter 4 and from UFC 3-340-02. Values are reported in Table 5-1, noting that the polynomials were derived from AUTODYN analysis using finer meshes than those used in this chapter. Table 5-2 presents ratios of the AUTODYN calculations to a) the predictions of the polynomials of Chapter 4, and b) the UFC 3-340-02. (The ratio of AUTODYN-to-polynomials ranges between 0.9 and 1.1 because  $\pm 10\%$  was the limit set for a *converged* cell size, as noted in Sections 3.6 and 3.7.) For the scaled distances considered here ( $Z \geq 0.16 \text{ m/kg}^{1/3}$ ), the AUTODYN-calculated incident peak overpressures are very close to the values reported in UFC 3-340-02. The calculated normally reflected peak overpressures are also similar to those of UFC 3-340-02 for  $Z \geq 0.4 \text{ m/kg}^{1/3}$  (1 ft/lb<sup>1/3</sup>). For  $Z < 0.4 \text{ m/kg}^{1/3}$ , the AUTODYN-calculated normally reflected peak overpressure is much greater than that in UFC 3-340-02; see Figure 5-4, which is reproduced from Figures 4-5 and 4-6. Reflected peak overpressures for angles of incidence greater than  $0^\circ$  (normal reflection) are studied in the following section.

## 5.6 Reflected Overpressure as a Function of Angle of Incidence

Reflection coefficients,  $C_r$ , for different angles of incidence,  $\alpha$ , calculated using AUTODYN are presented in Figures 5-18a, 5-18b<sup>8</sup>, 5-18c<sup>8</sup> and Table 5-3. The effect of Mach reflection is identified by local increases in the plots for  $40^\circ < \alpha < 50^\circ$  in all these curves: similar to UFC 3-340-02 but dissimilar from TM 5-858-3 for incident peak overpressures greater than 2.8 MPa (400 psi).

---

<sup>8</sup> Figures 5-18b and 5-18c present the same data at Figure 5-18a but in a format that is simpler to interpret.

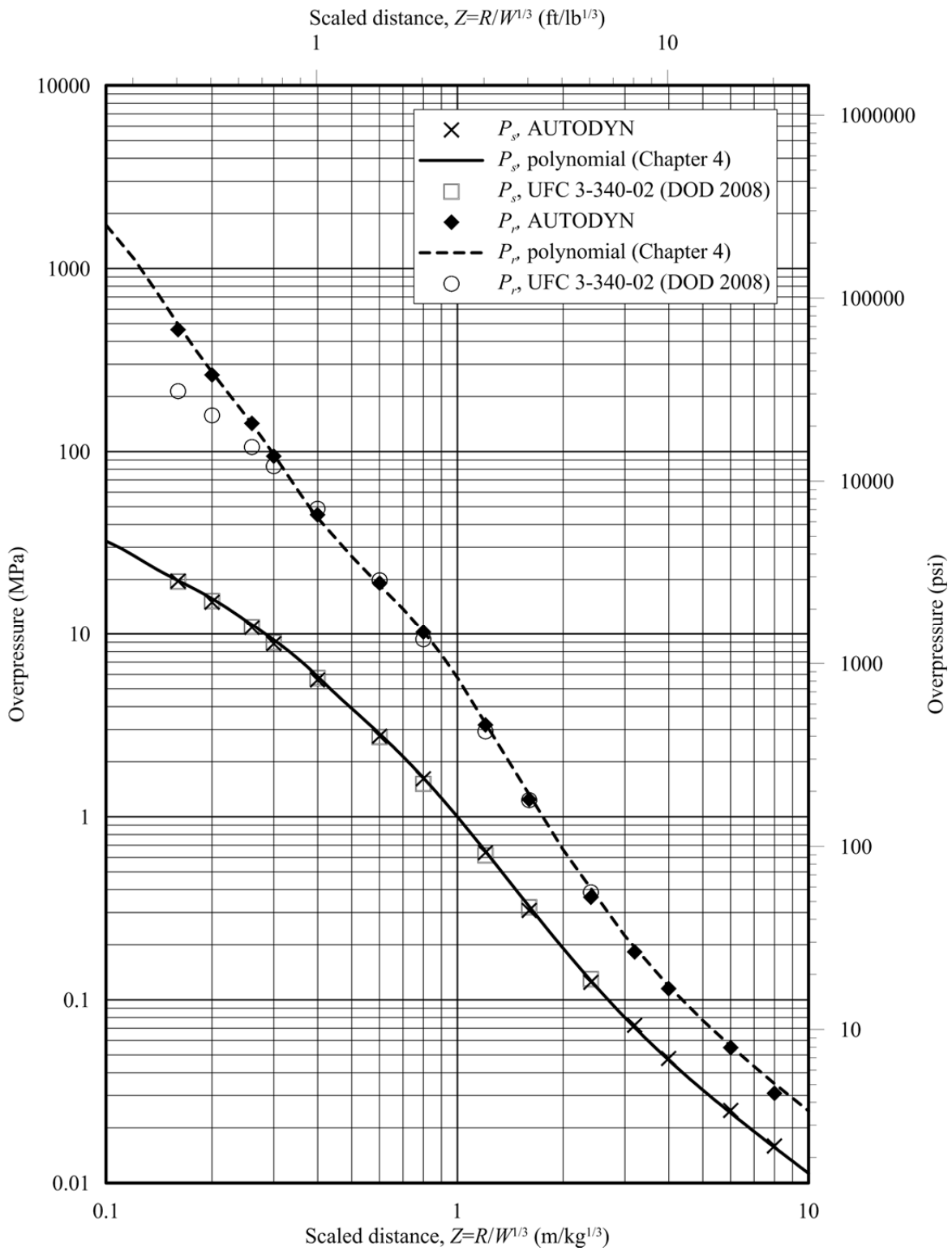


**Figure 5-17 Incident and normally reflected peak overpressures**

**Table 5-1 Incident and reflected overpressures for normal incidence**

<i>Z</i>		AUTODYN (ANSYS 2013a)				Proposed polynomials (Chapter 4)				UFC 3-340-02 (DoD 2008)			
		<i>P<sub>s</sub></i>		<i>P<sub>r</sub></i>		<i>P<sub>s</sub></i>		<i>P<sub>r</sub></i>		<i>P<sub>s</sub></i>		<i>P<sub>r</sub></i>	
m/kg <sup>1/3</sup>	ft/lb <sup>1/3</sup>	MPa	Psi	MPa	psi	MPa	psi	MPa	psi	MPa	psi	MPa	psi
0.16	0.40	19.7	2860	466	67570	19.7	2863	495	71810	19.6	2840	214	31000
0.20	0.50	15.1	2190	263	38100	15.7	2278	271	39260	15.3	2220	158	22900
0.26	0.65	10.9	1580	143	20700	11.3	1633	141	20450	11.0	1590	106	15400
0.30	0.75	8.86	1280	94.7	13700	9.26	1344	96.0	13920	9.00	1300	83.3	12100
0.40	1.0	5.62	815	45.3	6570	5.84	847	43.2	6269	5.75	833	48.8	7070
0.60	1.5	2.77	402	19.2	2790	2.84	412	18.5	2689	2.74	398	19.8	2870
0.80	2.0	1.62	235	10.3	1490	1.63	237	10.3	1493	1.52	221	9.38	1360
1.2	3.0	0.640	92.8	3.19	463	0.651	94.4	3.31	480	0.620	89.9	2.93	425
1.6	4.0	0.310	45.0	1.25	182	0.324	47.0	1.31	191	0.322	46.7	1.24	180
2.4	6.0	0.125	18.1	0.366	53.1	0.127	18.4	0.393	57.0	0.130	18.9	0.387	56.1
3.2	8.0	0.073	10.5	0.184	26.7	0.071	10.2	0.191	27.8	0.072	10.4	0.184	26.7
4.0	10	0.048	7.02	0.116	16.8	0.047	6.79	0.118	17.2	0.047	6.75	0.110	16.0
6.0	15	0.025	3.63	0.055	7.94	0.024	3.50	0.056	8.09	0.023	3.37	0.051	7.32
8.0	20	0.016	2.39	0.031	4.54	0.016	2.27	0.035	5.05	0.015	2.19	0.032	4.65

**Table 5-2 Ratios of AUTODYN calculations to proposed polynomial values and UFC 3-340-02 (DoD 2008) predictions**

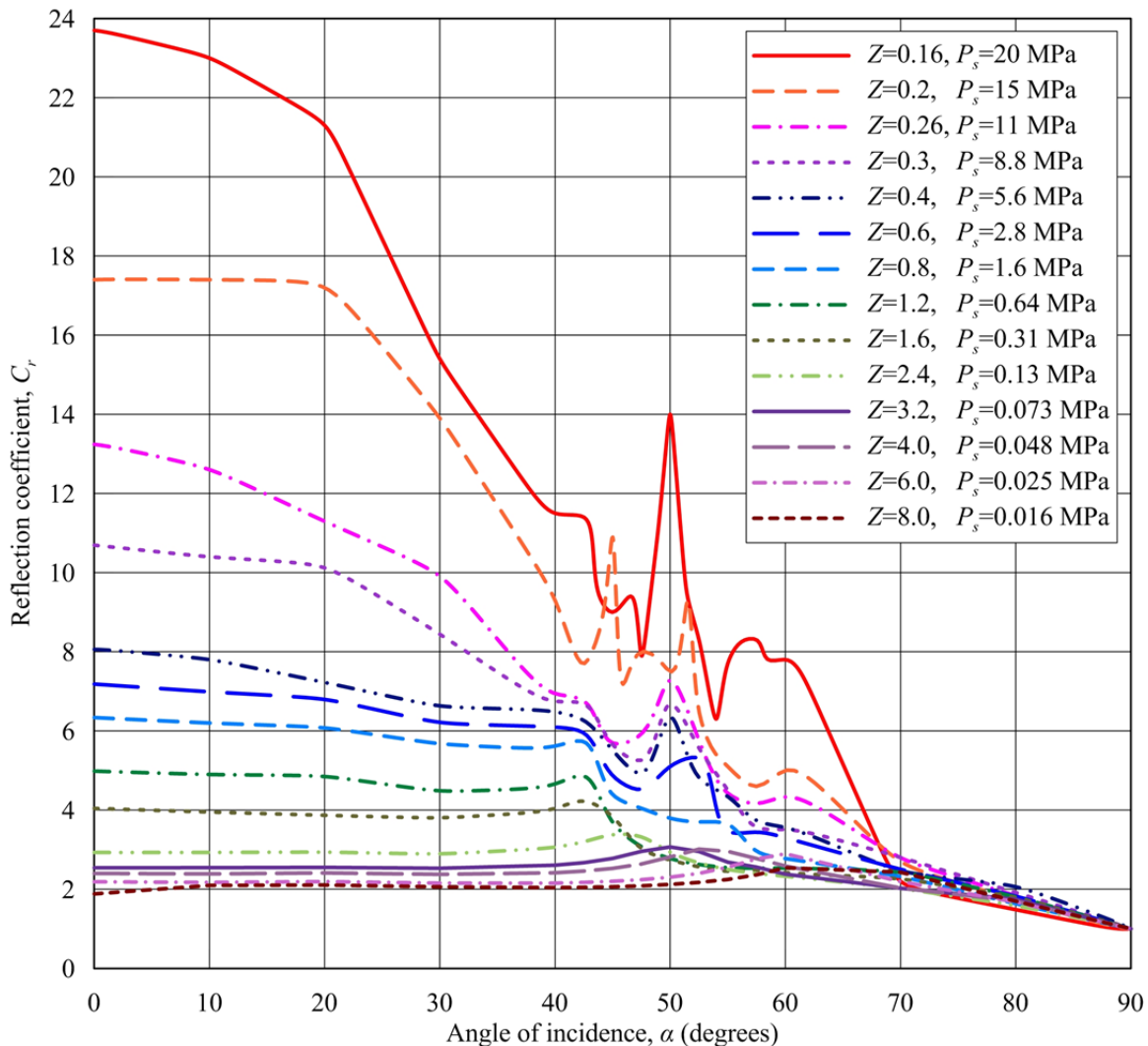
Z		AUTODYN/polynomials		AUTODYN/UFC 3-340-02	
m/kg <sup>1/3</sup>	ft/lb <sup>1/3</sup>	$P_s$	$P_r$	$P_s$	$P_r$
0.16	0.40	0.94	0.94	1.01	2.34
0.20	0.50	0.96	0.97	0.99	1.66
0.26	0.65	0.97	1.01	0.99	1.34
0.30	0.75	0.95	0.98	0.98	1.13
0.40	1.0	0.96	1.05	0.98	0.93
0.60	1.5	0.98	1.04	1.01	0.97
0.80	2.0	0.99	1.00	1.06	1.10
1.2	3.0	0.98	0.96	1.03	1.09
1.6	4.0	0.96	0.95	0.96	1.01
2.4	6.0	0.98	0.93	0.96	0.95
3.2	8.0	1.03	0.96	0.98	0.99
4.0	10	1.03	0.98	1.01	1.01
6.0	15	1.04	0.98	1.05	1.04
8.0	20	1.05	0.90	1.05	1.01

**Table 5-3 Reflection coefficients as a function of angle of incidence,  $\alpha$ , and scaled distance,  $Z$ , calculated using AUTODYN**

$Z$		Angle of incidence															
$m/kg^{1/3}$	$ft/lb^{1/3}$	0°	10°	20°	30°	40°	42.5°	45°	47.5°	50°	52.5°	55°	57.5°	60°	70°	80°	90°
0.16	0.40	23.7	23.0	21.3	15.4	11.5	11.4	9.0	7.9	14.5	8.3	7.7	8.3	7.8	2.2		1.0
0.20	0.50	17.4	17.4	17.2	13.9	9.3	7.7	7.9	10.9	7.5	6.5	5.1	4.6	5.0	2.7		1.0
0.26	0.65	13.2	12.6	11.3	9.9	6.9	6.8	5.7	5.9	7.3	5.8	4.4	4.2	4.3	2.8		1.0
0.30	0.75	10.7	10.4	10.1	8.4	6.7	6.7	5.7	5.3	6.7	5.6	4.5	3.6	3.5	2.8		1.0
0.40	1.0	8.1	7.8	7.2	6.6	6.5	6.3	5.5	4.9	6.3	4.8	4.3	3.7	3.6	2.5	2.1	1.0
0.60	1.5	6.9	6.7	6.5	6.0	5.9	5.7	4.7	4.4	4.9	5.1	3.3	3.3	3.2	2.4	1.8	1.0
0.80	2.0	6.3	6.2	6.1	5.7	5.6	5.7	4.4	4.0	3.8	3.7	3.6	3.0	2.8	2.3	1.6	1.0
1.2	3.0	5.0	4.9	4.8	4.5	4.7	4.9	3.7	3.1	2.8	2.6	2.5	2.5	2.5	2.4	1.8	1.0
1.6	4.0	4.0	4.0	3.9	3.8	4.0	4.2	3.8	3.0	2.7	2.6	2.5	2.5	2.4	2.3	1.8	1.0
2.4	6.0	2.9	2.9	2.9	2.9	3.1	3.2	3.4	3.3	2.9	2.7	2.5	2.4	2.3	2.0	1.6	1.0
3.2	8.0	2.5	2.5	2.6	2.5	2.6	2.7	2.8	3.0	3.1	3.0	2.7	2.6	2.4	2.0	1.7	1.0
4.0	10	2.4	2.4	2.4	2.4	2.4	2.5	2.5	2.6	2.8	3.0	3.0	2.8	2.6	2.0	1.7	1.0
6.0	15	2.2	2.2	2.2	2.2	2.2	2.2	2.2	2.2	2.3	2.4	2.6	2.8	2.9	2.2	1.7	1.0
8.0	20	1.9	2.1	2.1	2.1	2.0	2.0	2.1	2.1	2.1	2.2	2.2	2.4	2.5	2.4	1.7	1.0

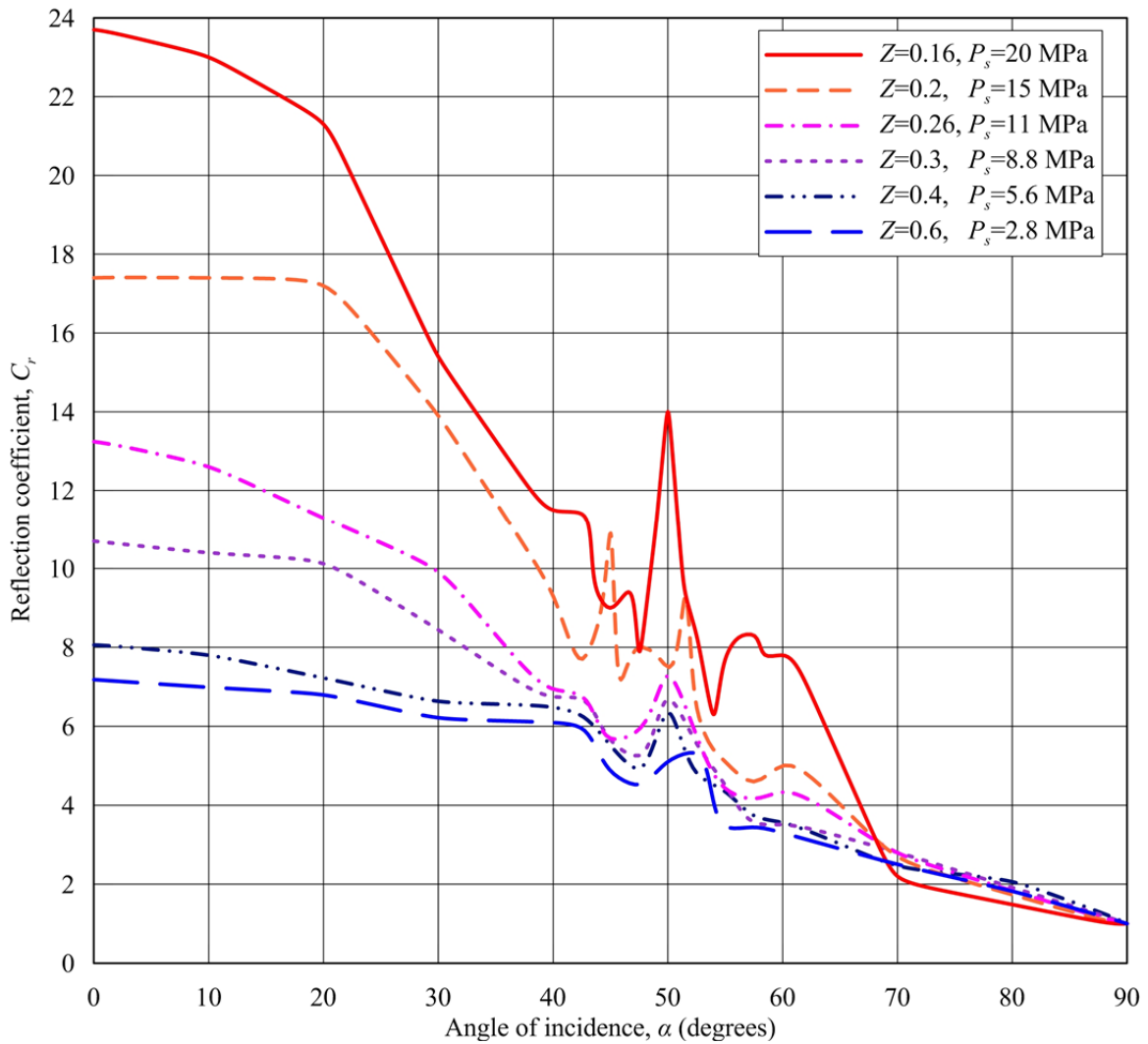
For incident peak overpressures of 0.016, 0.025, 0.048, 0.073 and 0.13 MPa ( $Z = 8.0, 6.0, 4.0, 3.2$  and  $2.4 \text{ m/kg}^{1/3}$ ; see Figure 5-18), the angle of incidence associated with Mach reflection is greater than  $40^\circ$  because the angle increases with decreasing incident peak overpressure below 0.31 MPa (or Mach number less than 2.0) per Figures 5-8 and 5-9.

The angles of incidence for Mach reflection for  $P_s = 0.31, 0.64$  and  $1.6 \text{ MPa}$  (associated with  $Z = 1.6, 1.2$  and  $0.8$ , respectively, and the curves with  $C_r = 4.0, 5.0$  and  $6.3$  for normal reflection, respectively, in Figure 5-18) are close to  $40^\circ$ : a result that is in good agreement with Figure 5-8.



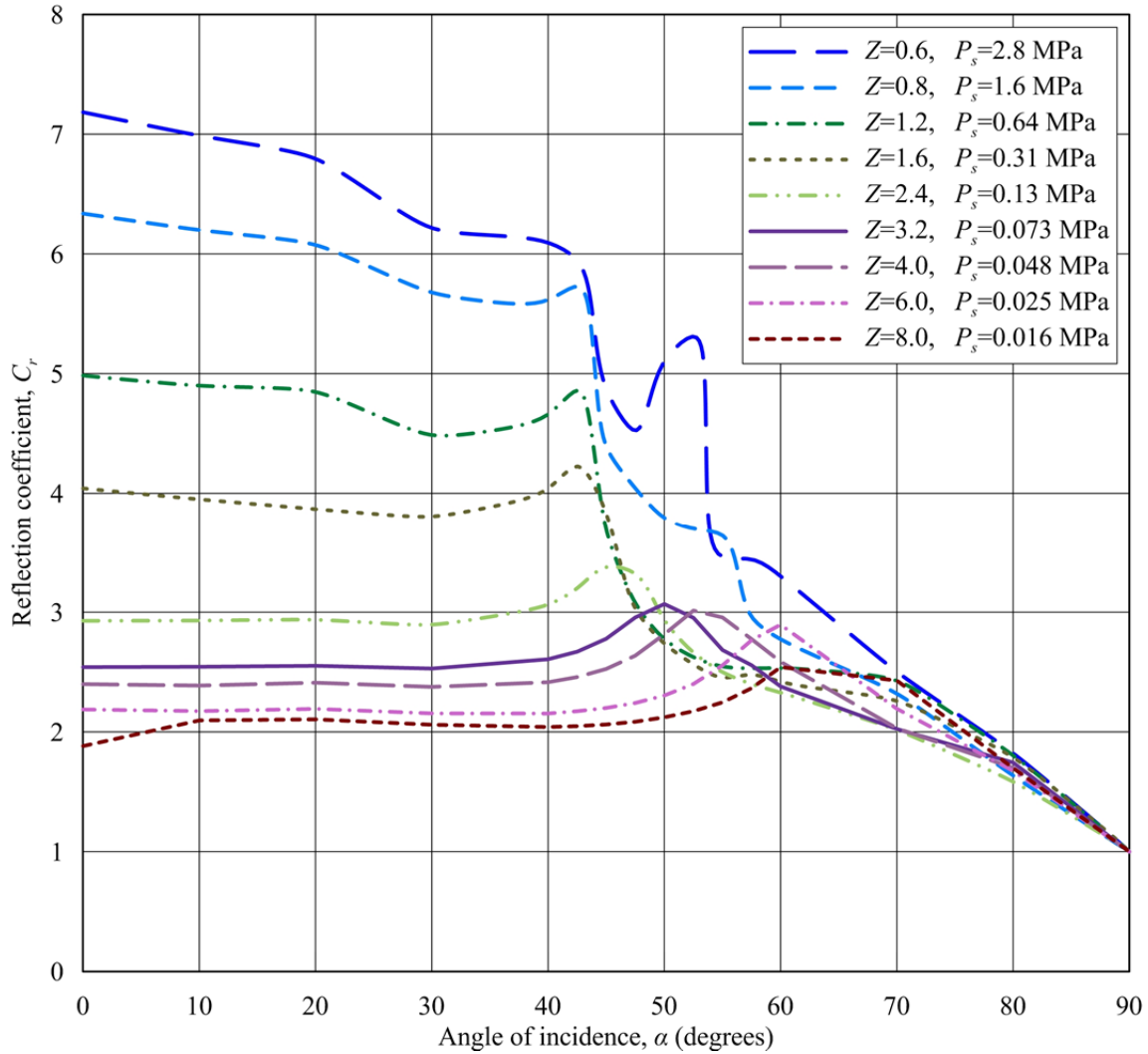
(a) Scaled distances,  $Z$ , between 0.16 and  $8.0 \text{ m/kg}^{1/3}$  ( $1 \text{ m/kg}^{1/3} = 2.52 \text{ ft/lb}^{1/3}$ ;  $1 \text{ MPa} = 145 \text{ psi}$ )

**Figure 5-18 Overpressure reflection coefficients as a function of angle of incidence**



(b) Scaled distances,  $Z$ , between 0.16 and 0.6  $\text{m}/\text{kg}^{1/3}$  ( $1 \text{ m}/\text{kg}^{1/3} = 2.52 \text{ ft}/\text{lb}^{1/3}$ ;  $1 \text{ MPa} = 145 \text{ psi}$ )

**Figure 5-18 Overpressure reflection coefficients as a function of angle of incidence (cont.)**



(c) Scaled distances,  $Z$ , between 0.6 and 8.0  $\text{m/kg}^{1/3}$  ( $1 \text{ m/kg}^{1/3} = 2.52 \text{ ft/lb}^{1/3}$ ;  $1 \text{ MPa} = 145 \text{ psi}$ )

**Figure 5-18 Overpressure reflection coefficients as a function of angle of incidence (cont.)**

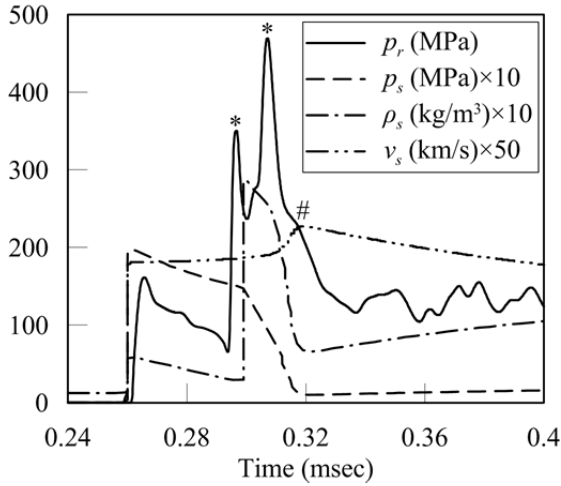
The angles of incidence associated with Mach reflection for  $P_s \geq 2.8 \text{ MPa}$  (associated with  $Z \leq 0.6 \text{ m/kg}^{1/3}$  and the curves with  $C_r \geq 7$  for normal reflection) are between  $45^\circ$  and  $50^\circ$ , and similar to the values in UFC 3-340-02 (see Figure 5-2b). For these higher incident overpressures, the specific heat ratio decreases and the Mach reflection angle increases, which is consistent with the observations of Schwer.

To understand the influence of the expanding detonation products on reflection coefficients for  $Z \leq 0.8 \text{ m/kg}^{1/3}$ , Figure 5-19 presents histories of reflected overpressure,  $p_r(t)$ , incident overpressure,  $p_s(t)$ , density,  $\rho_s(t)$ , and flow (particle) velocity,  $v_s(t)$ , for  $Z = 0.16, 0.4, 0.8$  and

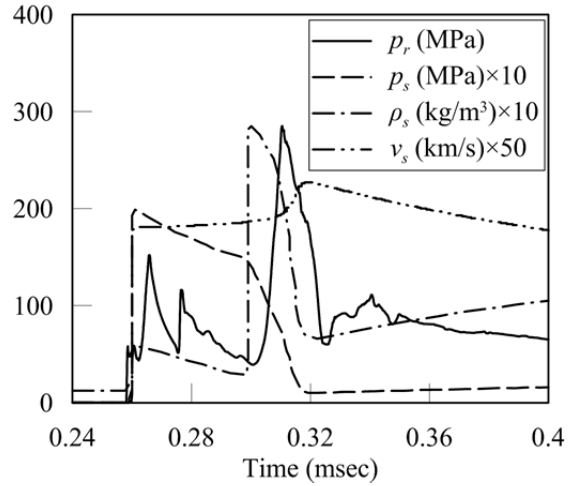
1.2 m/kg<sup>1/3</sup> for a) normal reflection, and b) the angle of incidence for which the peak overpressure is the greatest in the region of Mach reflection. The histories are amplitude scaled to facilitate presentation in one figure. For  $Z = 0.16 \text{ m/kg}^{1/3}$ , the arrival times of the shock front and detonation products are approximately  $t = 0.26$  and  $0.29$  msec, respectively, as shown in Figure 5-19a. The differences between the arrival times of the incident and reflected overpressures are caused by the use of different numerical procedures: 1D and Euler-Godunov grid for the incident overpressure, and 2D and Euler-FCT grid for the reflected overpressure. The reflected peak overpressures in Figure 5-19a are associated with the expanding detonation products and not the shock fronts. Two peaks are predicted in the normal reflection overpressure history and identified by (\*) in the Figure 5-19a. The first is associated with the arrival of the front of the detonation products. The second is associated with the peak particle velocity, identified by (#) in the figure, at the tail of the expanding detonation products (the second \* should align in time with # but is offset for the reason noted above). The reflected overpressure is a function of the static overpressure (twice the incident overpressure) and the dynamic overpressure (related to the air density and particle velocity): the greater density and higher velocity of the detonation products produces a larger reflected overpressure for this value of scaled distance than at the shock front. The reflected overpressures histories in Figure 5-19a fluctuate due to the influence of the expanding detonation products.

For  $Z = 0.4 \text{ m/kg}^{1/3}$ , the reflected peak overpressure is associated with the arrival of the shock front at  $t = 1.0$  msec, as seen in Figure 5-19c. The detonation products arrive at monitoring location at approximately  $t = 1.25$  msec. The arrival times of the incident and reflected shock fronts are again different for the reason given above. The expanding detonation products lead to fluctuations in the overpressure histories, similar to that observed for  $Z = 0.16 \text{ m/kg}^{1/3}$ .

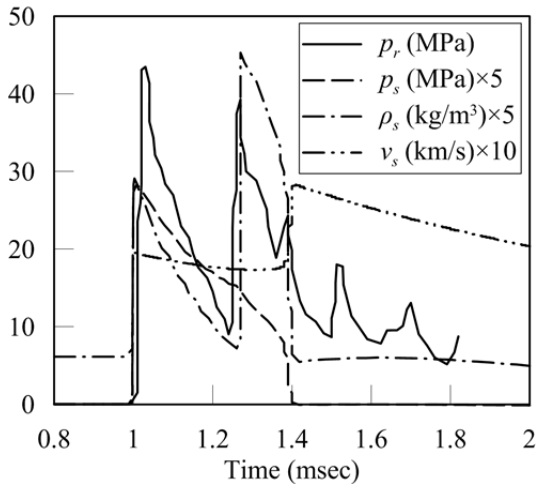
For  $Z = 0.8 \text{ m/kg}^{1/3}$ , the influence of the detonation products on the overpressure histories is negligible, as seen in Figure 5-19e: the shapes of the overpressure histories are similar to the Friedlander curve, namely, a smooth exponential decay from the peak overpressure to ambient (see Equation 1.1). The Friedlander overpressure history is achieved for incident and reflected peak overpressures of  $Z > 0.83 \text{ m/kg}^{1/3}$ , as seen in Figure 5-19g for  $Z = 1.2 \text{ m/kg}^{1/3}$ .



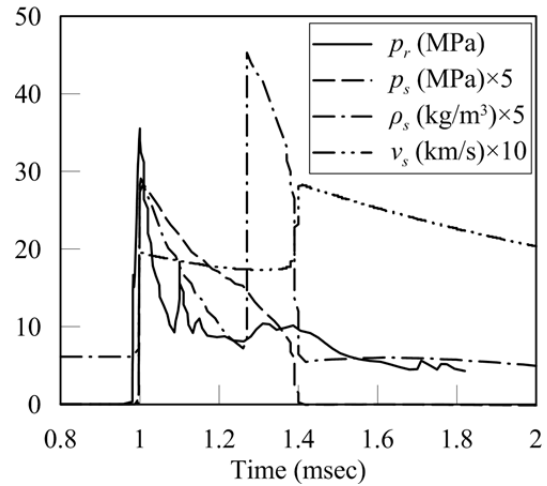
(a)  $Z = 0.16 \text{ m/kg}^{1/3}$ ,  $\alpha = 0^\circ$



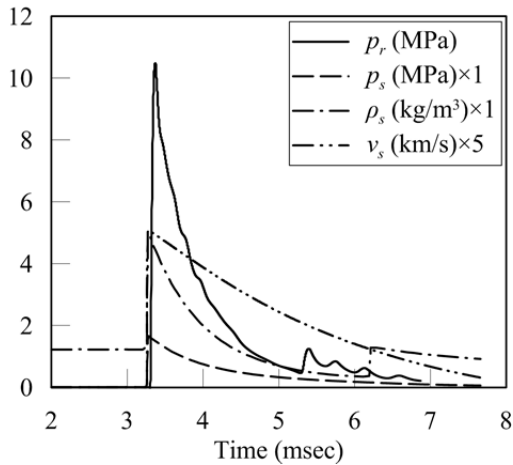
(b)  $Z = 0.16 \text{ m/kg}^{1/3}$ ,  $\alpha = 50^\circ$



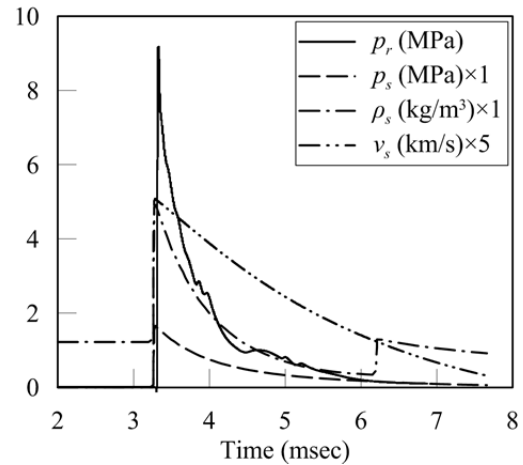
(c)  $Z = 0.40 \text{ m/kg}^{1/3}$ ,  $\alpha = 0^\circ$



(d)  $Z = 0.40 \text{ m/kg}^{1/3}$ ,  $\alpha = 50^\circ$



(e)  $Z = 0.80 \text{ m/kg}^{1/3}$ ,  $\alpha = 0^\circ$



(f)  $Z = 0.80 \text{ m/kg}^{1/3}$ ,  $\alpha = 42.5^\circ$

**Figure 5-19 Reflected overpressure histories;  $Z = 0.16, 0.40, 0.80$  and  $1.2 \text{ m/kg}^{1/3}$  ( $1 \text{ m/kg}^{1/3} = 2.52 \text{ ft/lb}^{1/3}$ ;  $1 \text{ MPa} = 145 \text{ psi}$ )**

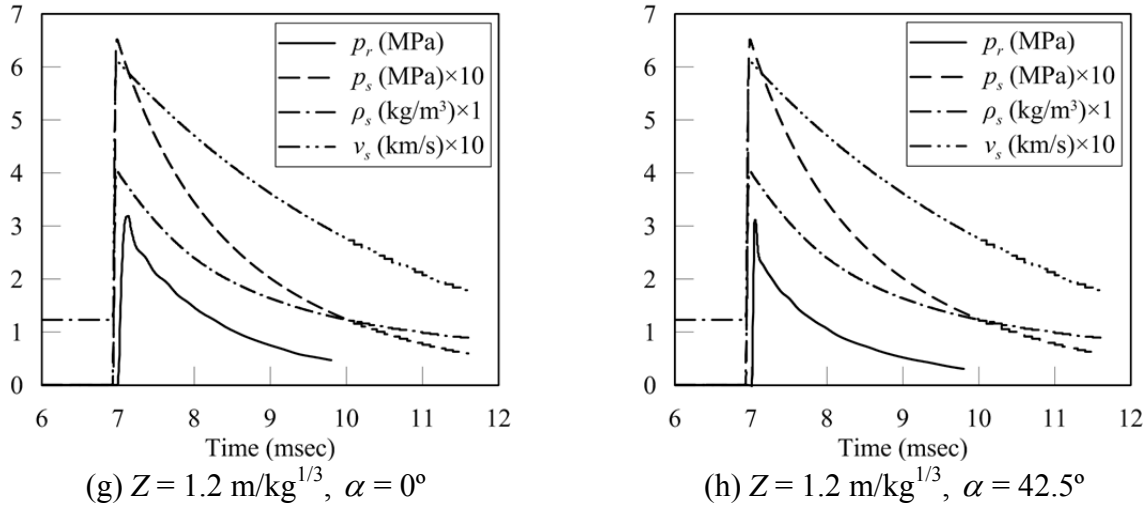
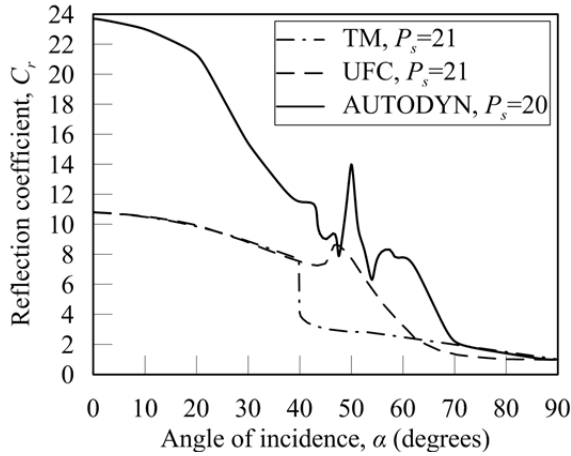
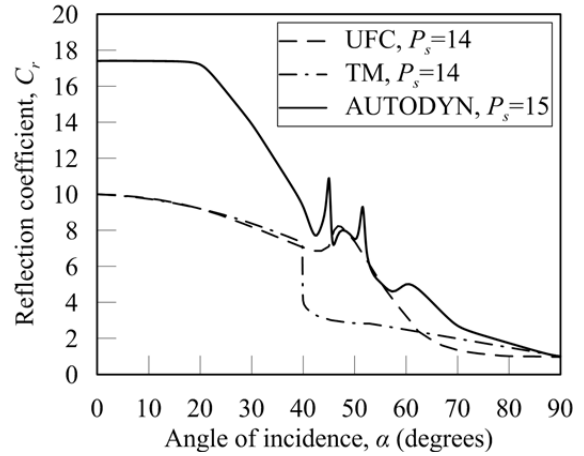


**Figure 5-19 Reflected overpressure histories;  $Z = 0.16, 0.40, 0.80$  and  $1.2 \text{ m/kg}^{1/3}$  ( $1 \text{ m/kg}^{1/3} = 2.52 \text{ ft/lb}^{1/3}$ ;  $1 \text{ MPa} = 145 \text{ psi}$ ) (cont.)**

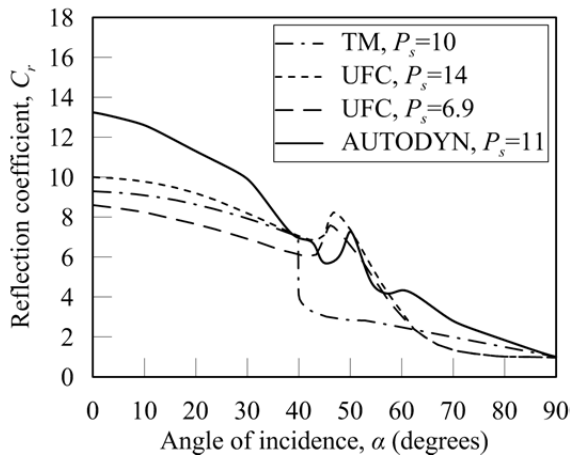
Figure 5-20 enables a comparison of data from the AUTODYN simulations and empirical results from TM 5-858-3 and UFC-3-340-02. The overpressure reflection coefficients obtained from the AUTODYN simulations for  $Z < 0.4 \text{ m/kg}^{1/3}$  ( $1 \text{ ft/lb}^{1/3}$ ) are greater than those reported in both UFC 3-340-02 and TM 5-858-3 for angles of incidence less than  $40^\circ$ , as shown in panels a, b, c and d of Figure 5-20 ( $Z = 0.16, 0.20, 0.26$  and  $0.30 \text{ m/kg}^{1/3}$ , respectively) due to the effects of the expanding detonation products on the reflected overpressure histories. For  $Z \geq 0.4 \text{ m/kg}^{1/3}$  and  $\alpha < 40^\circ$ , the overpressure reflection coefficients calculated with AUTODYN are in reasonable agreement with the values reported in both UFC 3-340-02 and TM 5-858-3, as shown in panels e, f, g, h, i, j, k, l, m and n of Figure 5-20. For  $Z \geq 0.4 \text{ m/kg}^{1/3}$  and  $\alpha > 40^\circ$ , the AUTODYN-based overpressure reflection coefficients are similar to the values reported in UFC 3-340-02 but are quite different from those of TM 5-858-3.



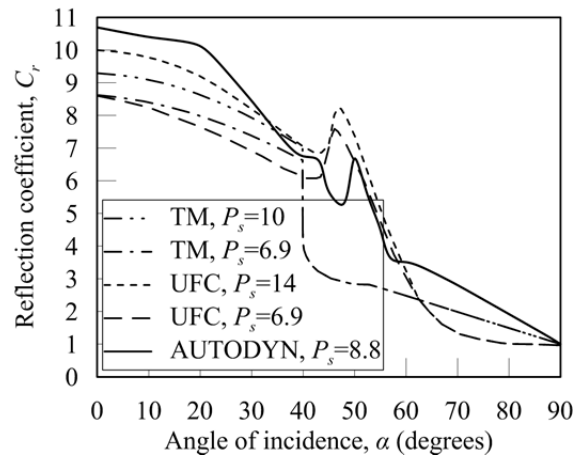
(a)  $Z = 0.16 \text{ m/kg}^{1/3}$  ( $0.4 \text{ ft/lb}^{1/3}$ )



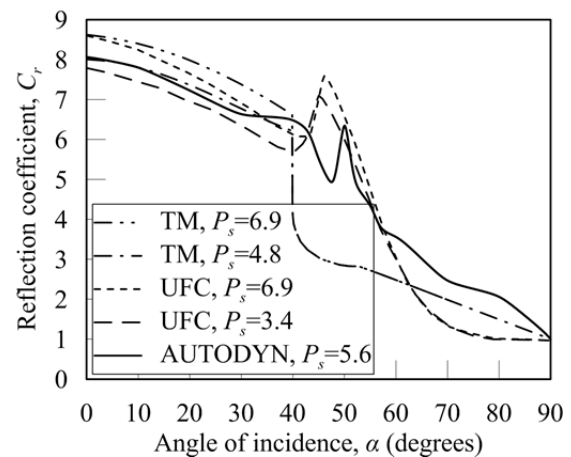
(b)  $Z = 0.2 \text{ m/kg}^{1/3}$  ( $0.5 \text{ ft/lb}^{1/3}$ )



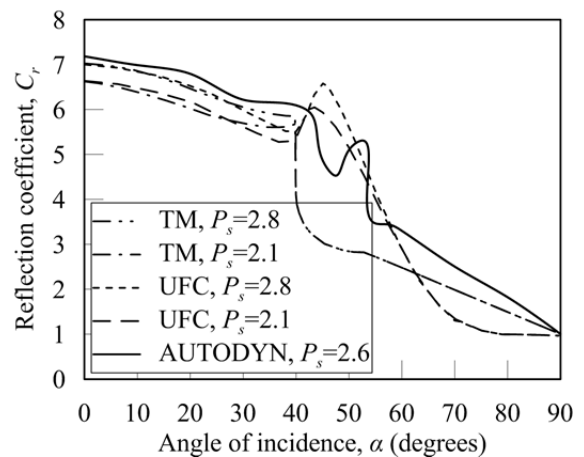
(c)  $Z = 0.26 \text{ m/kg}^{1/3}$  ( $0.66 \text{ ft/lb}^{1/3}$ )



(d)  $Z = 0.3 \text{ m/kg}^{1/3}$  ( $0.75 \text{ ft/lb}^{1/3}$ )

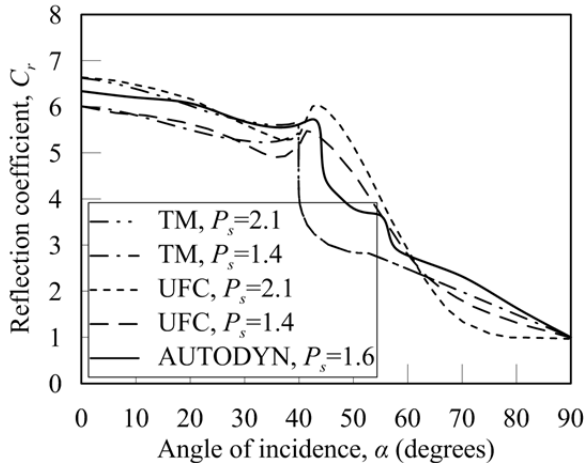


(e)  $Z = 0.4 \text{ m/kg}^{1/3}$  ( $1 \text{ ft/lb}^{1/3}$ )

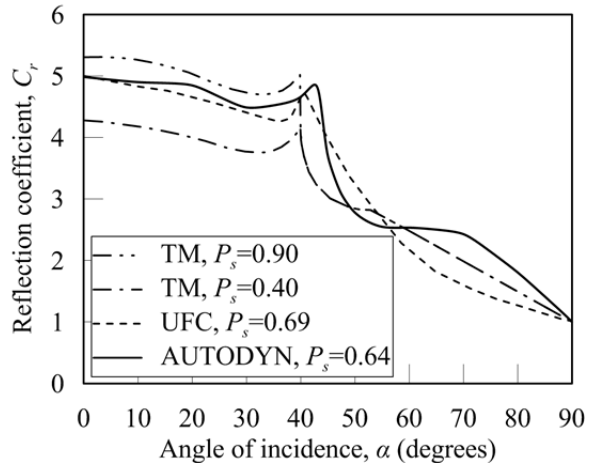


(f)  $Z = 0.6 \text{ m/kg}^{1/3}$  ( $1.5 \text{ ft/lb}^{1/3}$ )

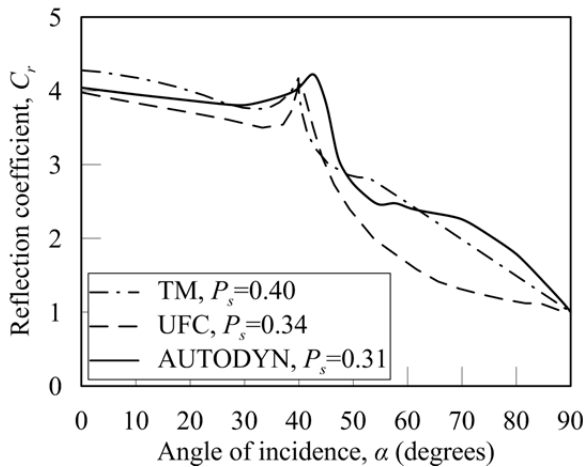
**Figure 5-20 Overpressure reflection coefficients with angle of incidence from TM 5-858-3 (DoA 1984), UFC 3-340-02 (DoD 2008), numerical analyses by AUTODYN;  $P_s$  in units of MPa**



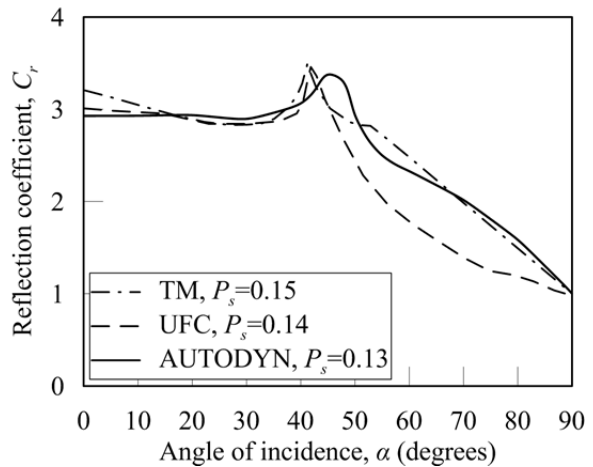
(g)  $Z = 0.8 \text{ m/kg}^{1/3}$  (2 ft/lb<sup>1/3</sup>)



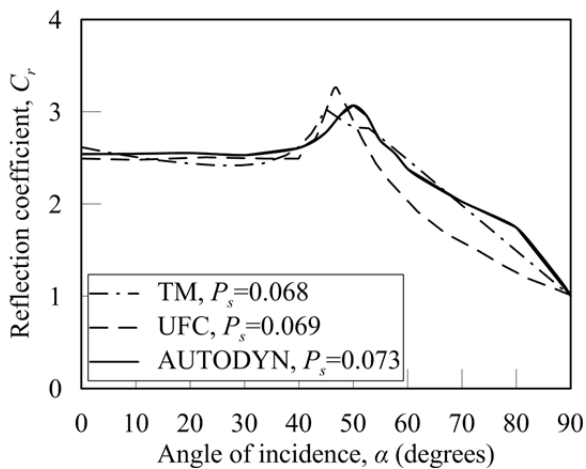
(h)  $Z = 1.2 \text{ m/kg}^{1/3}$  (3 ft/lb<sup>1/3</sup>)



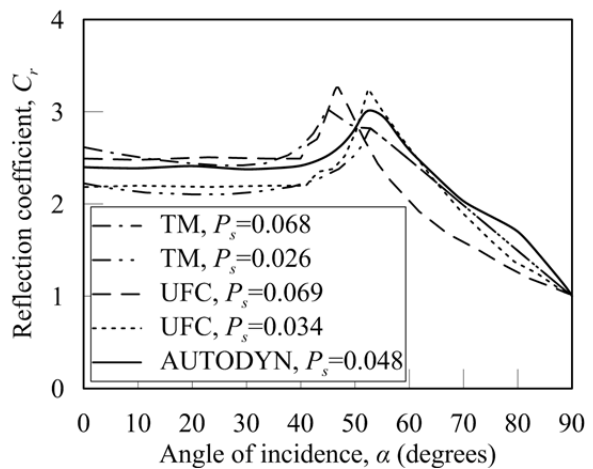
(i)  $Z = 1.6 \text{ m/kg}^{1/3}$  (4 ft/lb<sup>1/3</sup>)



(j)  $Z = 2.4 \text{ m/kg}^{1/3}$  (6 ft/lb<sup>1/3</sup>)



(k)  $Z = 3.2 \text{ m/kg}^{1/3}$  (8 ft/lb<sup>1/3</sup>)



(l)  $Z = 4 \text{ m/kg}^{1/3}$  (10 ft/lb<sup>1/3</sup>)

**Figure 5-20 Overpressure reflection coefficients with angle of incidence from TM 5-858-3 (DoA 1984), UFC 3-340-02 (DoD 2008), numerical analyses by AUTODYN;  $P_s$  in units of MPa (cont.)**

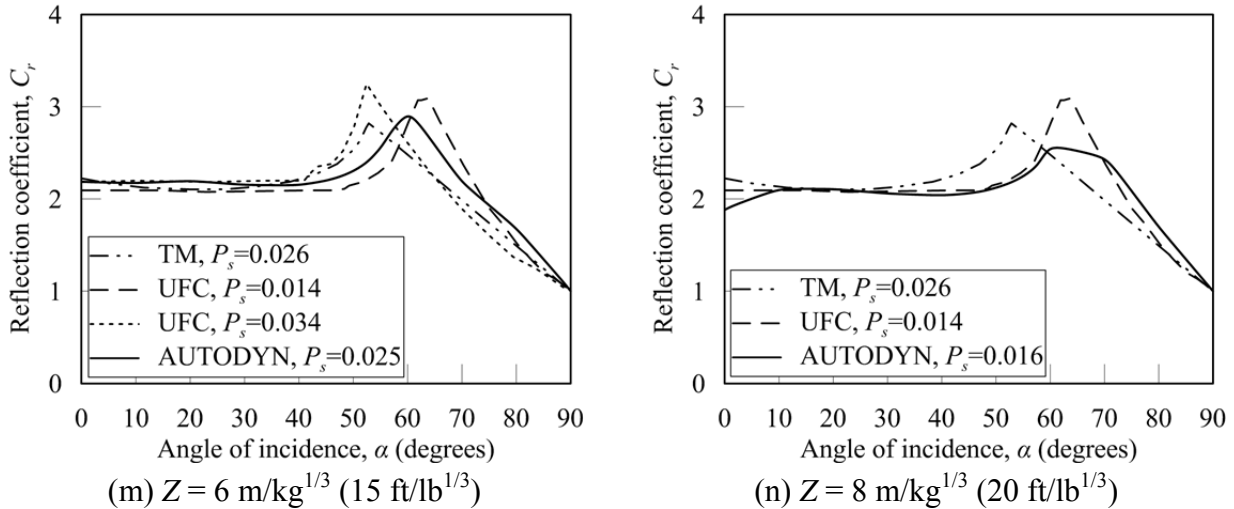


**Figure 5-20 Overpressure reflection coefficients with angle of incidence from TM 5-858-3 (DoA 1984), UFC 3-340-02 (DoD 2008), numerical analyses by AUTODYN;  $P_s$  in units of MPa (cont.)**

For reflection coefficients to be useful for design, the incident and reflected pressure histories should follow a standard shape, such as the Friedlander curve, with the same positive phase duration. TM 5-858-3 and UFC 3-340-02 present data (see Figure 5-2) for incident peak overpressures up to 7000 psi (48.3 MPa) and 5000 psi (34.5 MPa), respectively. Herein simulations were performed for incident peak overpressures up to 20 MPa (2900 psi). As seen in Figure 5-19, at  $Z = 0.4 \text{ m/kg}^{1/3}$  and  $P_s = 6 \text{ MPa}$  (870 psi), the incident and reflected overpressure histories are very different from the Friedlander curve, and values of reflected peak overpressure and scaled impulse alone are of no practical value for blast-resistant design: CFD analysis is needed to adequately characterize incident and reflected pressure histories. A practical lower limit on the use of reflection coefficients is  $Z = 0.8 \text{ m/kg}^{1/3}$ .

## 5.7 Incident and Normally Reflected Impulses

Incident,  $I_s/W^{1/3}$ , and normally reflected,  $I_r/W^{1/3}$ , scaled impulses are calculated using cell sizes of  $R/1600$  (1D) and  $R/400$  (2D). Results are presented in Figure 5-21, together with data from the polynomials per Table 4-2 of Chapter 4 and from UFC 3-340-02. Values are provided in Table 5-4. Table 5-5 presents ratios of the AUTODYN calculations to a) the polynomial predictions of Chapter 4, and b) the values calculated using UFC 3-340-02. (The ratio of AUTODYN-to-

polynomial ranges between 0.98 and 1.07.) The AUTODYN calculations and UFC 3-340-02-based predictions of incident scaled impulse differ by 10% to 20%, which is consistent with observations in Chapters 3 and 4. The AUTODYN-calculated normally reflected scaled impulses are very similar to those reported in UFC 3-340-02.

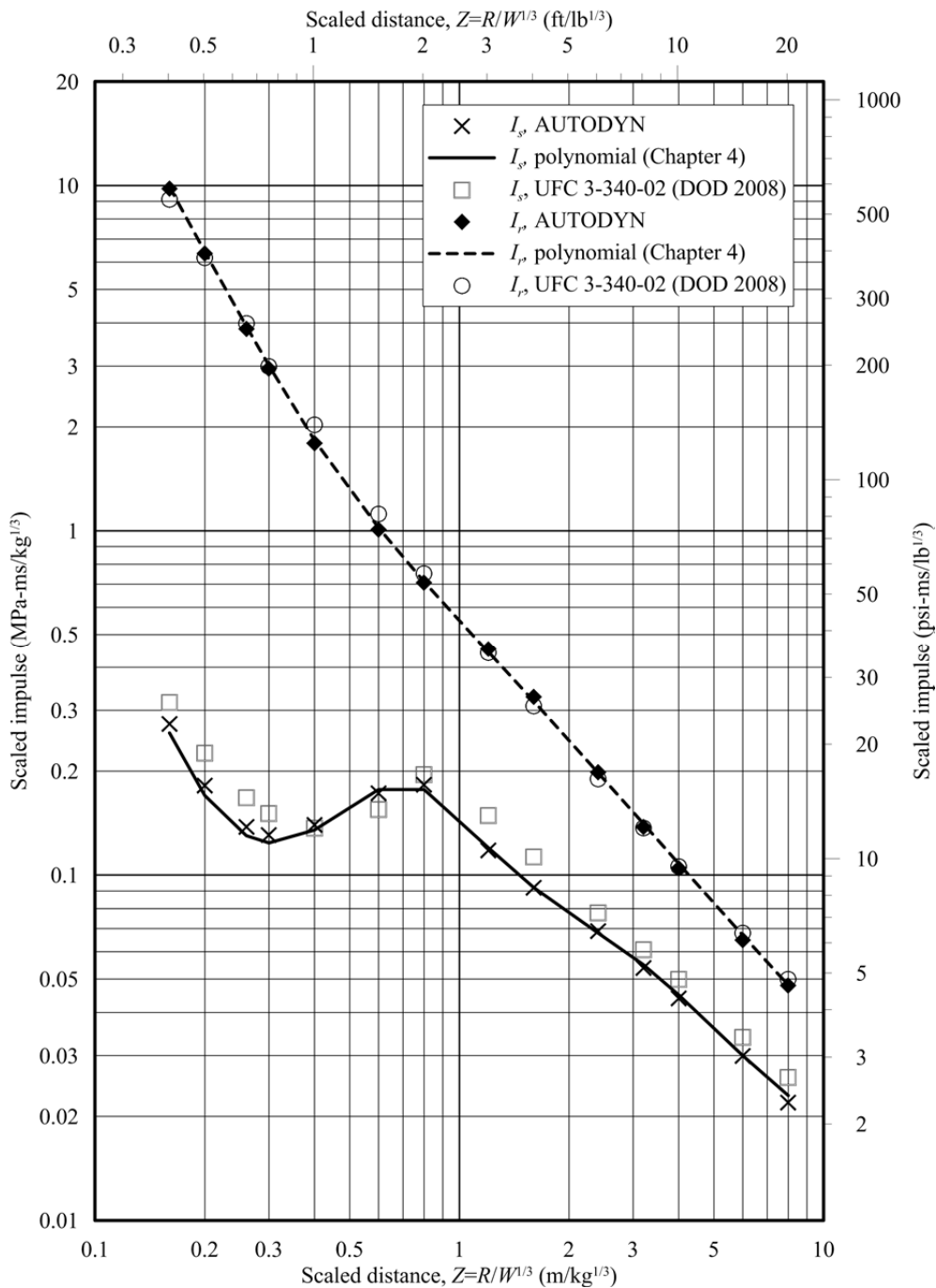


**Figure 5-21 Incident and normally reflected scaled impulses**

**Table 5-4 Incident and normally reflected scaled impulses in SI units of MPa-ms/kg<sup>1/3</sup> and US units of psi-ms/lb<sup>1/3</sup>**

Z		AUTODYN (ANSYS 2013a)				Proposed polynomials (Chapter 4)				UFC 3-340-02 (DoD 2008)			
		$I_s/W^{1/3}$		$I_r/W^{1/3}$		$I_s/W^{1/3}$		$I_r/W^{1/3}$		$I_s/W^{1/3}$		$I_r/W^{1/3}$	
m/kg <sup>1/3</sup>	ft/lb <sup>1/3</sup>	SI	US	SI	US	SI	US	SI	US	SI	US	SI	US
0.16	0.40	0.275	30.7	9.83	1096	0.258	28.7	9.91	1104	0.317	35.3	9.12	1016
0.20	0.50	0.182	20.3	6.37	710	0.170	19.0	6.43	717	0.226	25.2	6.18	688
0.26	0.65	0.138	15.4	3.86	430	0.130	14.4	3.91	436	0.168	18.7	3.99	444
0.30	0.75	0.131	14.6	2.96	330	0.124	13.8	3.01	335	0.151	16.8	3.00	335
0.40	1.0	0.140	15.6	1.80	201	0.135	15.0	1.83	204	0.137	15.2	2.03	226
0.60	1.5	0.173	19.3	1.01	112	0.177	19.8	1.02	113	0.155	17.2	1.12	125
0.80	2.0	0.183	20.4	0.709	79.1	0.177	19.7	0.712	79.3	0.196	21.8	0.752	83.8
1.2	3.0	0.118	13.1	0.454	50.6	0.120	13.3	0.444	49.5	0.149	16.6	0.442	49.3
1.6	4.0	0.092	10.3	0.329	36.7	0.092	10.2	0.319	35.5	0.113	12.6	0.309	34.4
2.4	6.0	0.069	7.64	0.199	22.2	0.068	7.60	0.198	22.1	0.078	8.73	0.190	21.2
3.2	8.0	0.054	6.01	0.138	15.4	0.055	6.07	0.141	15.7	0.061	6.77	0.137	15.2
4.0	10	0.044	4.88	0.105	11.7	0.045	4.98	0.108	12.0	0.050	5.55	0.106	11.9
6.0	15	0.030	3.29	0.065	7.27	0.030	3.36	0.067	7.48	0.034	3.82	0.068	7.62

**Table 5-5 Ratios of AUTODYN calculations to polynomial and UFC 3-340-02 predictions for reflected scaled impulse**

Z		AUTODYN/polynomials		AUTODYN/UFC 3-340-02	
m/kg <sup>1/3</sup>	ft/lb <sup>1/3</sup>	$I_s/W^{1/3}$	$I_r/W^{1/3}$	$I_s/W^{1/3}$	$I_r/W^{1/3}$
0.16	0.40	1.07	0.99	0.87	1.08
0.20	0.50	1.07	0.99	0.81	1.03
0.26	0.65	1.07	0.99	0.82	0.97
0.30	0.75	1.06	0.99	0.87	0.99
0.40	1.0	1.04	0.99	1.03	0.89
0.60	1.5	0.97	0.99	1.12	0.9
0.80	2.0	1.04	1.00	0.94	0.94
1.2	3.0	0.98	1.02	0.79	1.03
1.6	4.0	1.01	1.03	0.82	1.07
2.4	6.0	1.01	1.00	0.88	1.05
3.2	8.0	0.99	0.98	0.89	1.01
4.0	10	0.98	0.98	0.88	0.98
6.0	15	0.98	0.97	0.86	0.95
8.0	20	0.98	0.99	0.85	0.95

## 5.8 Reflected Impulse as a Function of Angle of Incidence

Figure 5-22 presents results of AUTODYN calculations of reflected scaled impulse. Values are provided in Table 5-6. The effect of Mach reflection on the calculated reflected scaled impulses is not seen in these results. To examine why, selected reflected overpressure and scaled impulse histories are presented in Figures 5-23, 5-24 and 5-25 for  $Z = 0.16, 0.40$  and  $1.2 \text{ m/kg}^{1/3}$ , respectively, and  $\alpha = 30^\circ, 40^\circ, 45^\circ, 50^\circ$  and  $55^\circ$ . Figures 5-23a and 5-23b present reflected overpressure histories calculated for  $Z = 0.16 \text{ m/kg}^{1/3}$  using cell sizes of  $R/800$  and  $R/400$ , respectively, for  $0.24 \leq t \leq 0.4$  msec to judge the effect of mesh size on the calculated reflected peak overpressure. These histories for all five angles are complex with multiple peaks due to the effects of Mach reflection and the expanding detonation products. The reflected peak overpressures for the two cell sizes are similar. The local increase observed in the reflection coefficient curve for  $Z = 0.16 \text{ m/kg}^{1/3}$  with  $\alpha = 50^\circ$ , as shown in Figure 5-18, is also identified in these history plots. The fluctuations in the reflected overpressure histories are more pronounced for the mesh with  $R/800$  cells. Figure 5-23c presents the reflected overpressure histories for the mesh with  $R/400$  cells for the duration of the positive phase. The contribution to the reflected peak impulse of the overpressure history in the time window of 0.24 to 0.40 msec, and around the time of reflected peak overpressure, is small. Further, given that the duration of the positive phase is greatest for  $\alpha = 30^\circ$  and smallest for  $\alpha = 55^\circ$ , and that the reflected overpressure at 0.40 msec is greatest for  $\alpha = 30^\circ$  and smallest for  $\alpha = 55^\circ$ , the effect of Mach reflection on reflected peak overpressure is not carried over to reflected peak impulse. The reflected peak impulse decreases gradually with an increasing angle of incidence, as seen in Figure 5-23d. Similar results are seen for  $Z = 0.40$  and  $1.2 \text{ m/kg}^{1/3}$  as presented in Figures 5-24 and 5-25, respectively, except that a) the reflected peak overpressures for both scaled distances are associated with the arrival of the incident or reflected shock front (depending on  $\alpha$ ), and b) there is no effect of the expanding detonation products on the reflected overpressure histories for  $Z = 1.2 \text{ m/kg}^{1/3}$ , as described in Section 5.6.

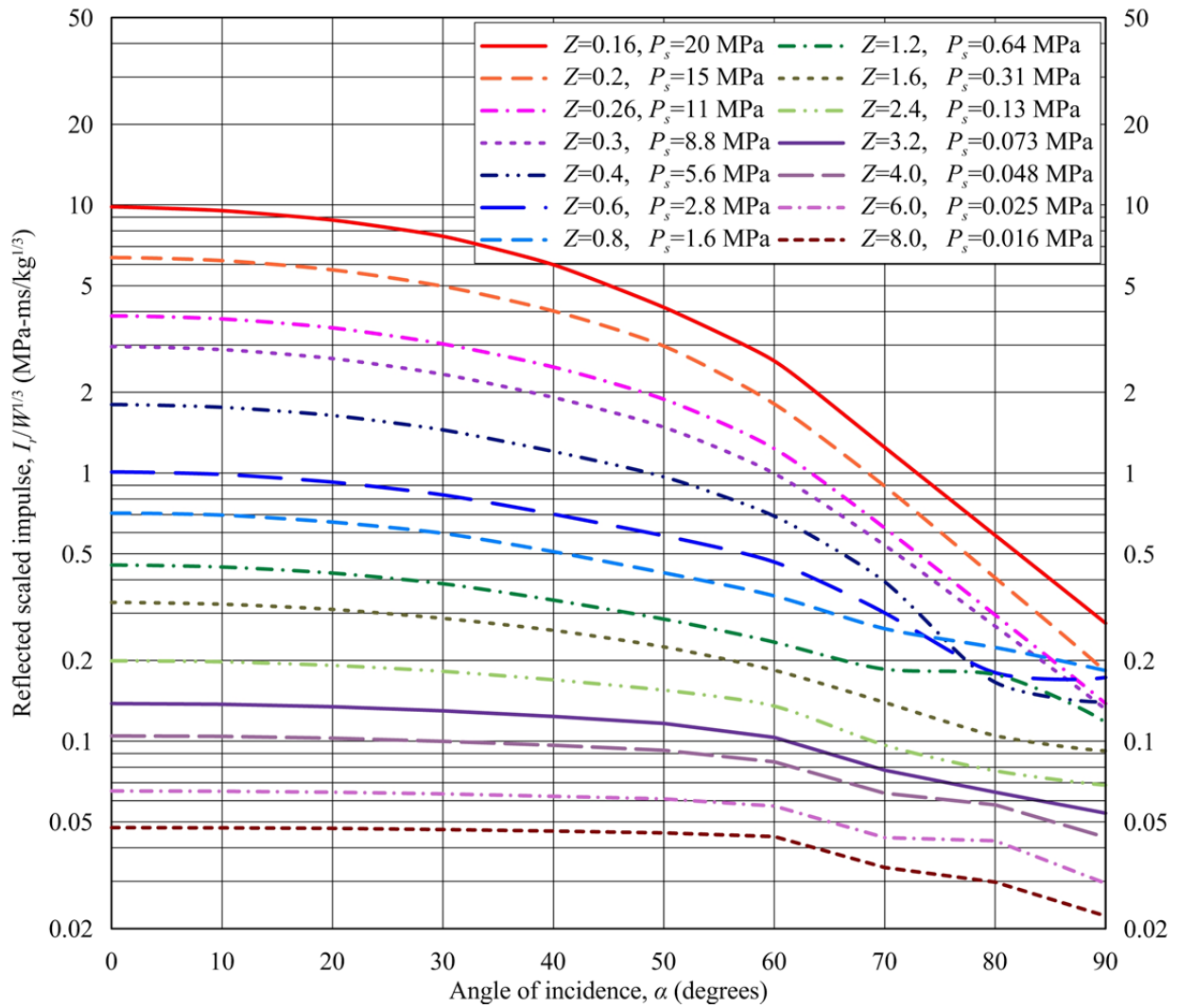
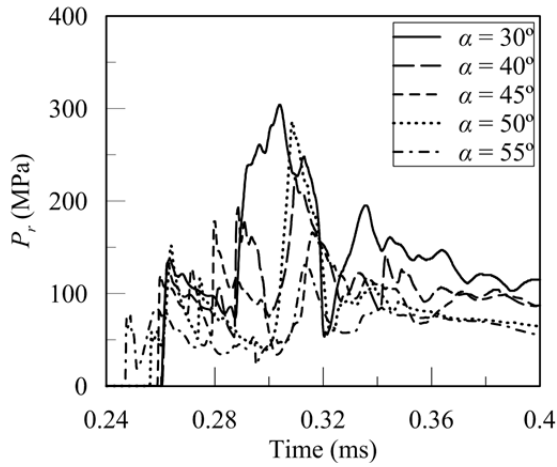


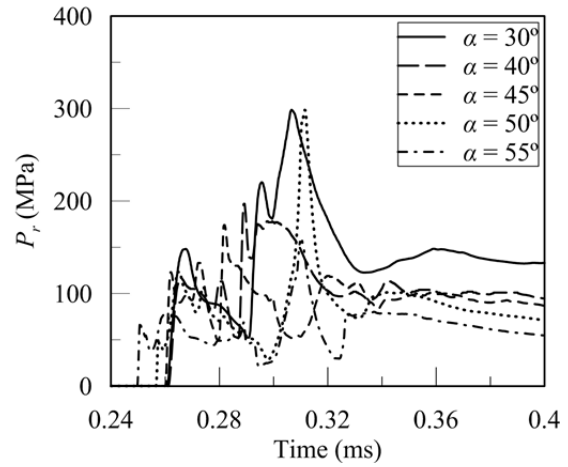
**Figure 5-22 Reflected scaled impulse as a function of angle of incidence ( $Z$  in units of  $m/kg^{1/3}$ )**

**Table 5-6 Reflected scaled impulses as a function of angle of incidence,  $\alpha$ , and scaled distance,  $Z$ , calculated using AUTODYN (units: MPa-ms/kg<sup>1/3</sup>; 1 MPa-ms/kg<sup>1/3</sup> = 111 psi-ms/lb<sup>1/3</sup>)**

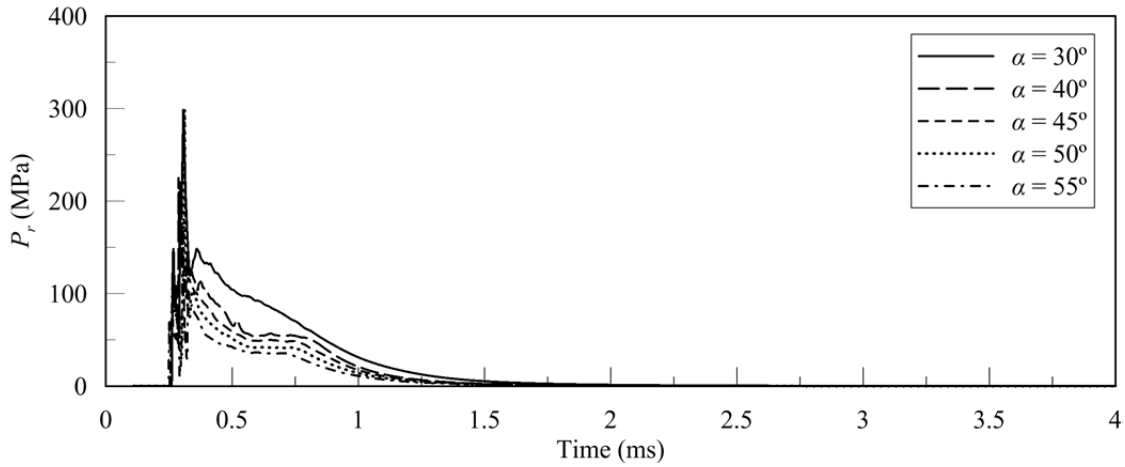
$Z$		Angle of incidence									
m/kg <sup>1/3</sup>	ft/lb <sup>1/3</sup>	0°	10°	20°	30°	40°	50°	60°	70°	80°	90°
0.16	0.40	9.83	9.52	8.78	7.63	5.98	4.15	2.62	1.25		0.275
0.20	0.50	6.37	6.20	5.72	4.970	4.02	2.97	1.81	0.892		0.182
0.26	0.65	3.86	3.76	3.48	3.031	2.49	1.89	1.23	0.624		0.138
0.30	0.75	2.96	2.89	2.67	2.34	1.91	1.48	0.996	0.538		0.131
0.40	1.0	1.80	1.76	1.64	1.45	1.20	0.968	0.690	0.393	0.166	0.140
0.60	1.5	1.01	0.989	0.924	0.829	0.702	0.584	0.466	0.301	0.180	0.173
0.80	2.0	0.709	0.697	0.656	0.596	0.509	0.424	0.348	0.263	0.224	0.183
1.2	3.0	0.454	0.446	0.424	0.386	0.336	0.285	0.234	0.186	0.177	0.118
1.6	4.0	0.329	0.324	0.310	0.287	0.259	0.225	0.184	0.139	0.105	0.092
2.4	6.0	0.199	0.198	0.192	0.182	0.169	0.155	0.135	0.097	0.078	0.069
3.2	8.0	0.138	0.137	0.134	0.130	0.124	0.116	0.103	0.078	0.065	0.054
4.0	10	0.105	0.104	0.103	0.100	0.097	0.092	0.084	0.064	0.058	0.044
6.0	15	0.065	0.065	0.065	0.064	0.062	0.061	0.057	0.044	0.043	0.030
8.0	20	0.048	0.048	0.047	0.047	0.046	0.046	0.044	0.034	0.030	0.022



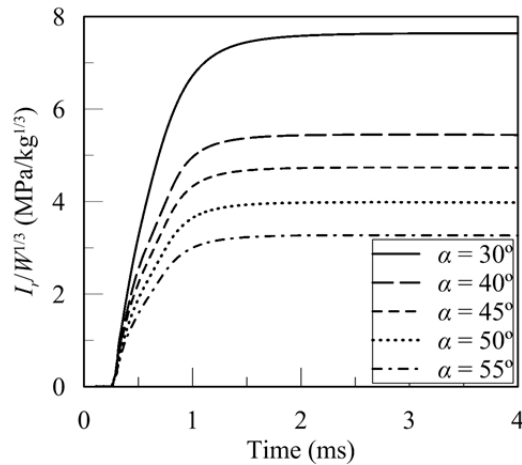
(a) Reflected overpressure history for the  $R/800$  cell size; part range on time



(b) Reflected overpressure history for the  $R/400$  cell size; part range on time

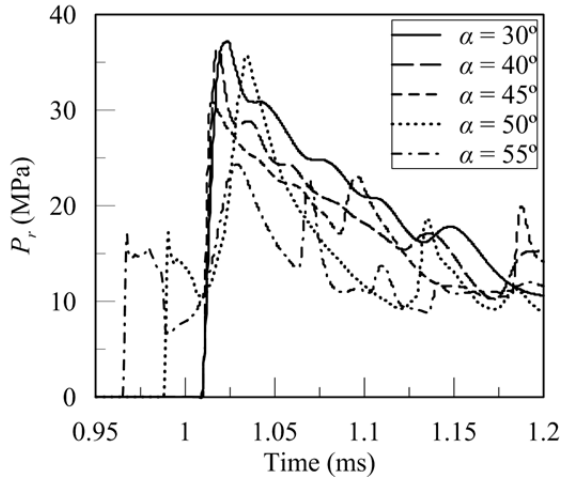


(c) Reflected overpressure history for the  $R/400$  cell size

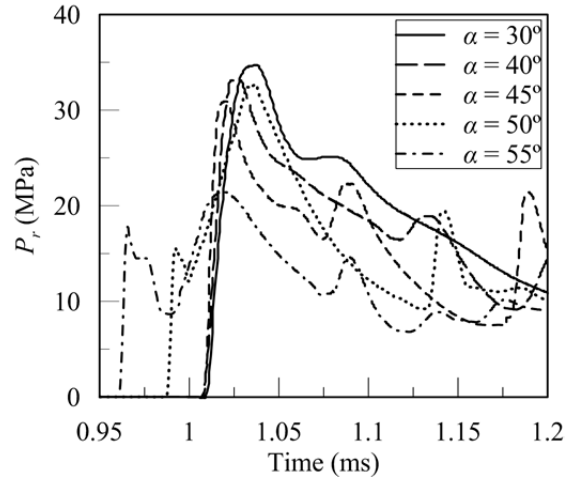


(d) Reflected impulse history from (c)

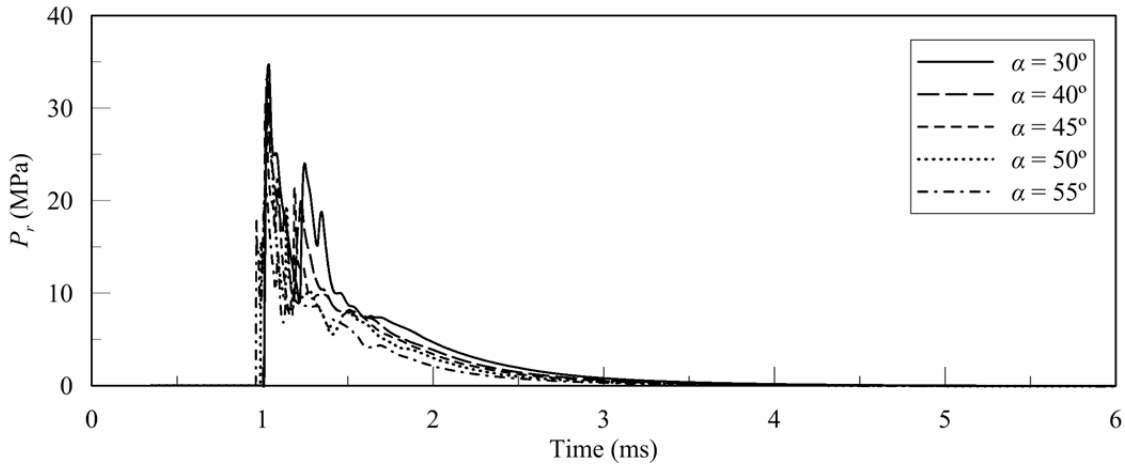
**Figure 5-23 Reflected overpressure and scaled impulse histories for cell sizes of  $R/400$  and  $R/800$ ;  $\alpha = 30^\circ, 40^\circ, 45^\circ, 50^\circ$  and  $55^\circ$ ;  $Z = 0.16 \text{ m/kg}^{1/3}$**



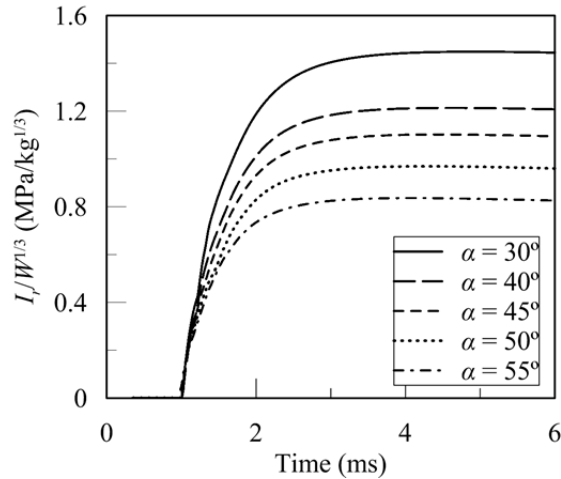
(a) Reflected overpressure history for the  $R/800$  cell size; part range on time



(b) Reflected overpressure history for the  $R/400$  cell size; part range on time

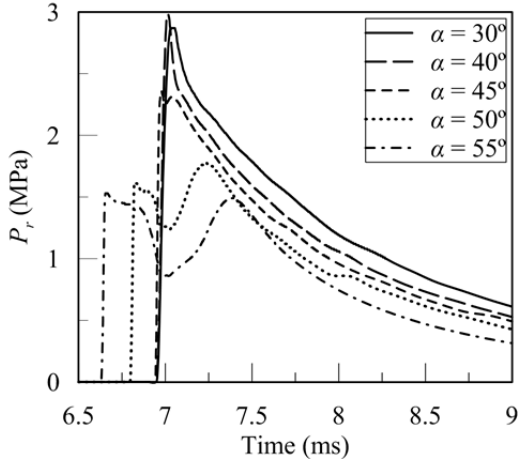


(c) Reflected overpressure history for the  $R/400$  cell size

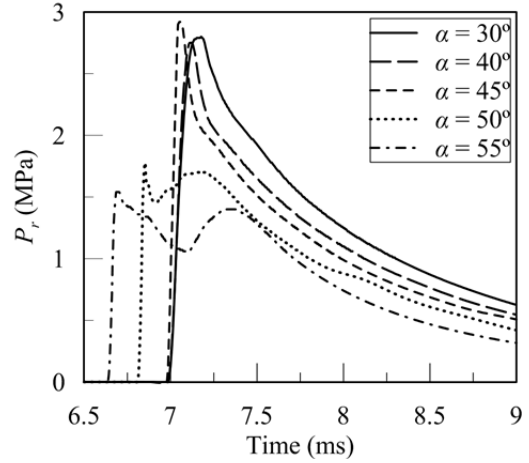


(d) Reflected impulse history from (c)

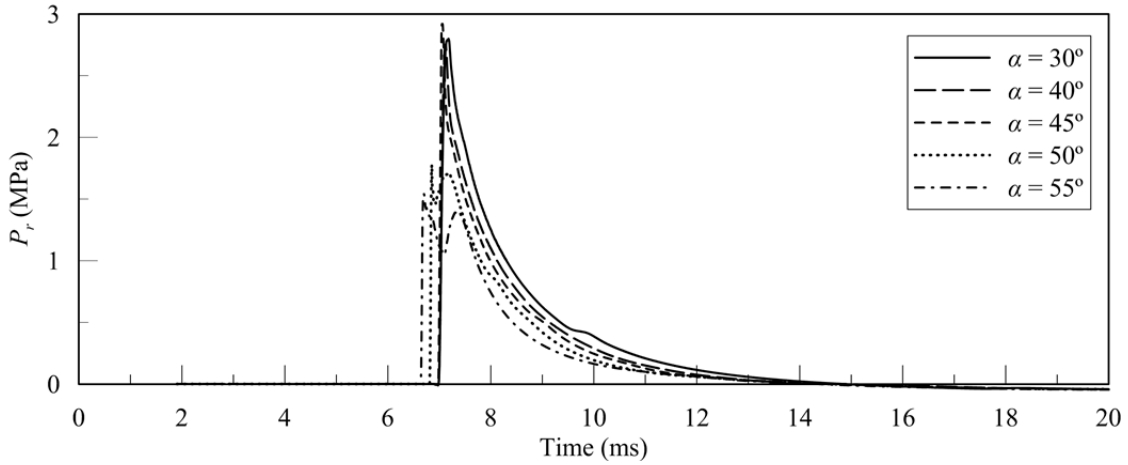
**Figure 5-24 Reflected overpressure and scaled impulse histories for cell sizes of  $R/400$  and  $R/800$ ;  $\alpha = 30^\circ, 40^\circ, 45^\circ, 50^\circ$  and  $55^\circ$ ;  $Z = 0.40 \text{ m/kg}^{1/3}$**



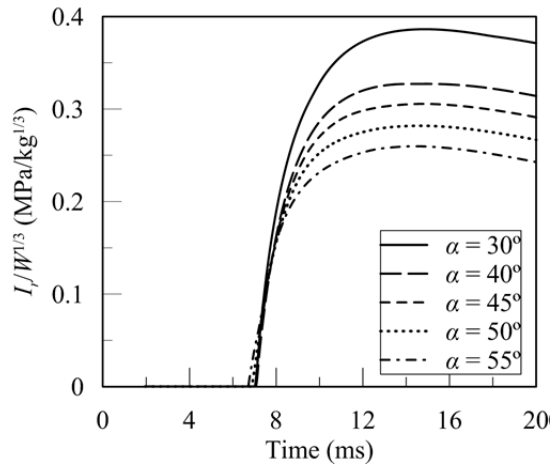
(a) Reflected overpressure history for the  $R/800$  cell size; part range on time



(b) Reflected overpressure history for the  $R/400$  cell size; part range on time



(c) Reflected overpressure history for the  $R/400$  cell size



(d) Reflected impulse history from (c)

**Figure 5-25 Reflected overpressure and scaled impulse histories for cell sizes of  $R/400$  and  $R/800$ ;  $\alpha = 30^\circ, 40^\circ, 45^\circ, 50^\circ$  and  $55^\circ$ ;  $Z = 1.2 \text{ m/kg}^{1/3}$**

Figures 5-23, 5-24 and 5-25 document the differences in arrival time of the shock front for the selected angles of incidence. The arrival times for the three scaled distances and  $\alpha = 30^\circ$ ,  $40^\circ$  and  $45^\circ$  are similar. However, the arrival times for  $\alpha = 50^\circ$  and  $55^\circ$  are smaller than those for other angles. Consider Figure 5-26 that presents pressure fringes at  $t = 1.0$  ms for  $Z = 0.4$  m/kg<sup>1/3</sup> with  $\alpha = 30^\circ$ ,  $40^\circ$ ,  $45^\circ$ ,  $50^\circ$  and  $55^\circ$ ; R/800 cells are used for analysis. The incident shock fronts have radiated to the same monitoring location (point 1) in all cases. For  $\alpha = 50^\circ$  and  $55^\circ$ , the Mach stems form and arrive at the monitoring locations before the incident waves because the Mach stem is a *reinforced* shock front that propagates faster than the incident wave. Similar differences in the arrival times are observed in the reflected overpressures histories for  $Z = 0.16$  and  $1.2$  m/kg<sup>1/3</sup>.

Figure 5-27 enables a comparison of the AUTODYN calculations and the empirical charts in UFC 3-340-02 for reflected scaled impulse as a function of angle of incidence. For each scaled distance,  $Z$ , considered in the AUTODYN analysis, three curves from UFC 3-340-02 are plotted for values of  $P_s$  close to the AUTODYN-calculated value of peak incident overpressure. The AUTODYN-calculated reflected scaled impulses for scaled distances between  $0.16$  and  $8$  m/kg<sup>1/3</sup> ( $P_s = 19.7$  and  $0.016$  MPa, respectively) are similar to the values reported in UFC 3-340-02. No changes are recommended to the UFC 3-340-02 charts for reflected scaled impulse.

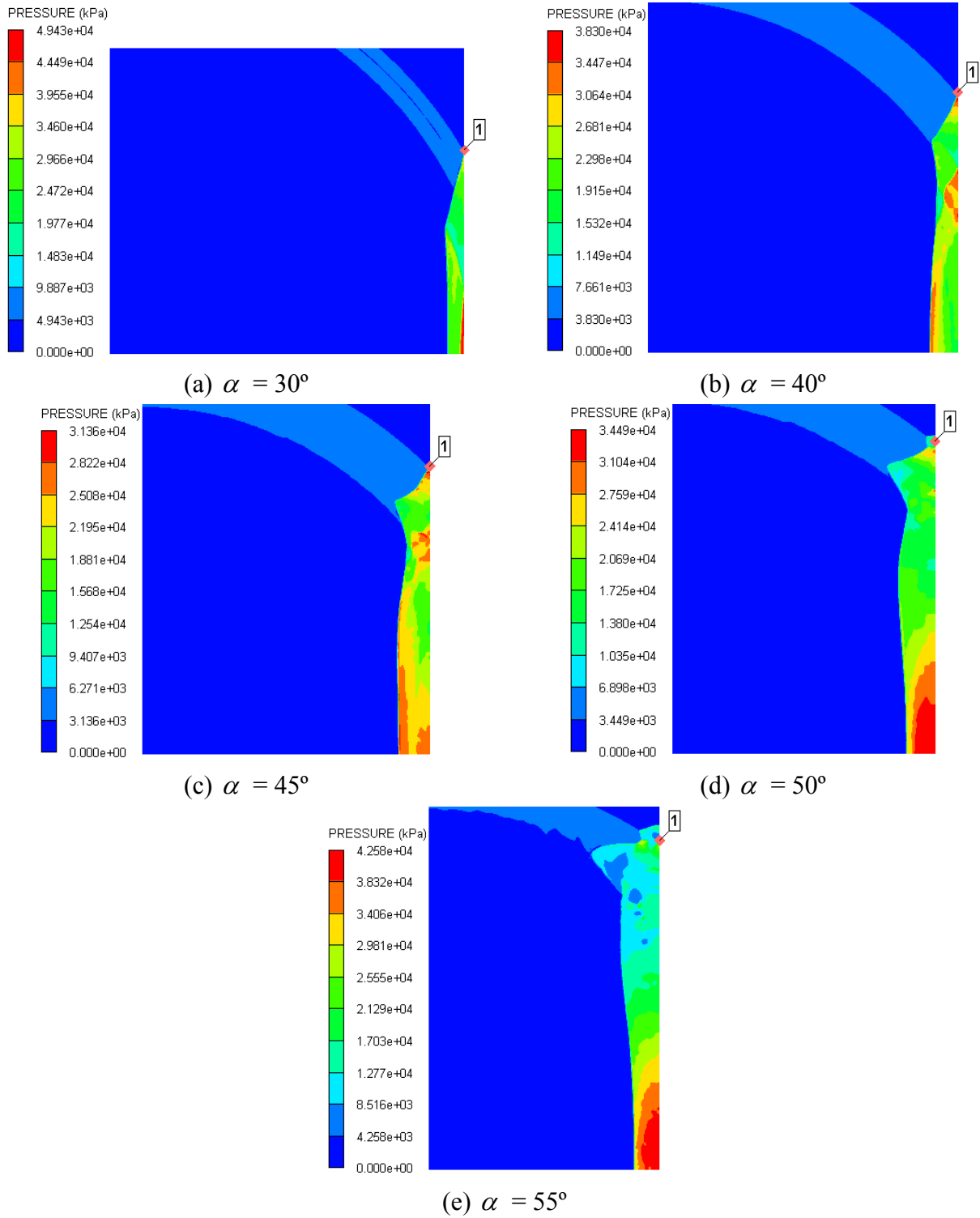
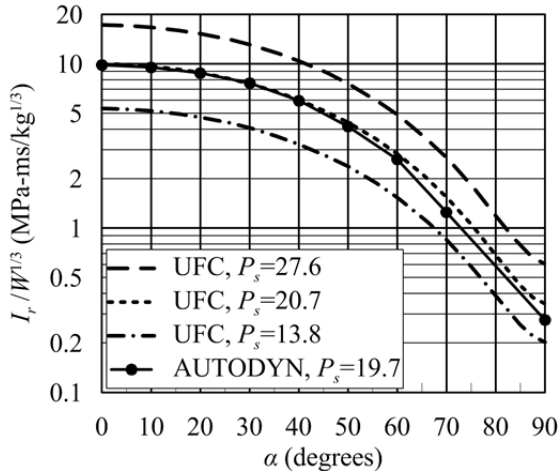
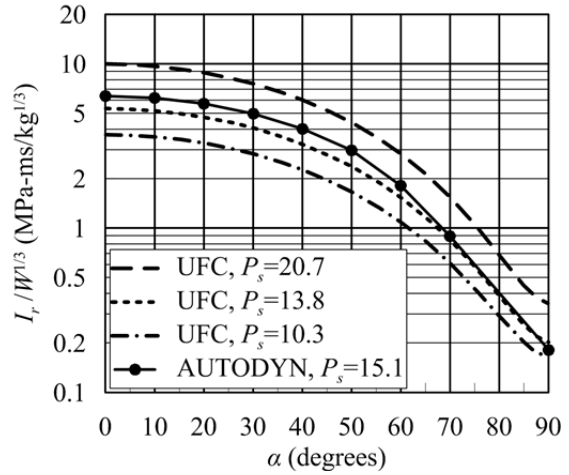


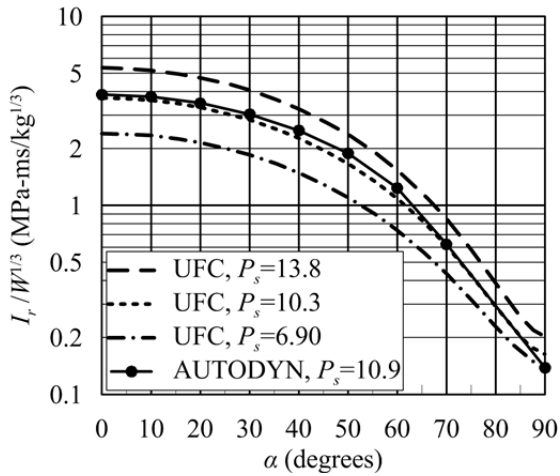
Figure 5-26 Pressure fringes at  $t = 1.0$  ms for  $Z = 0.4$  m/kg<sup>1/3</sup>;  $R/800$  cells



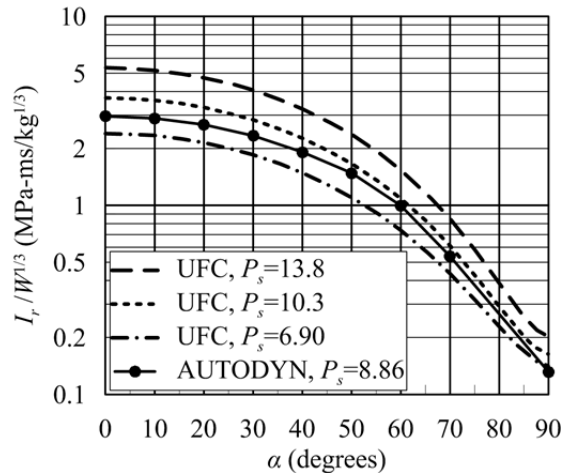
(a)  $Z = 0.16 \text{ m/kg}^{1/3}$  ( $0.4 \text{ ft/lb}^{1/3}$ )



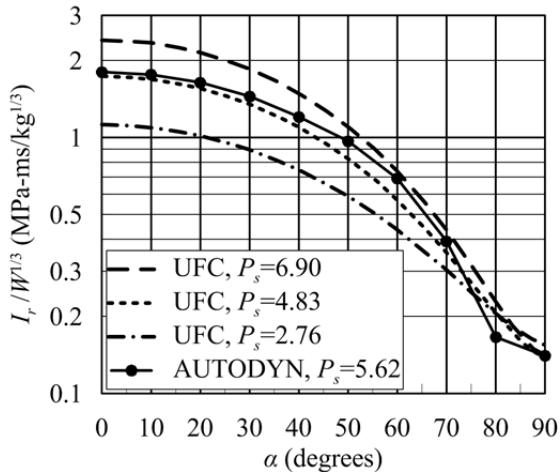
(b)  $Z = 0.20 \text{ m/kg}^{1/3}$  ( $0.5 \text{ ft/lb}^{1/3}$ )



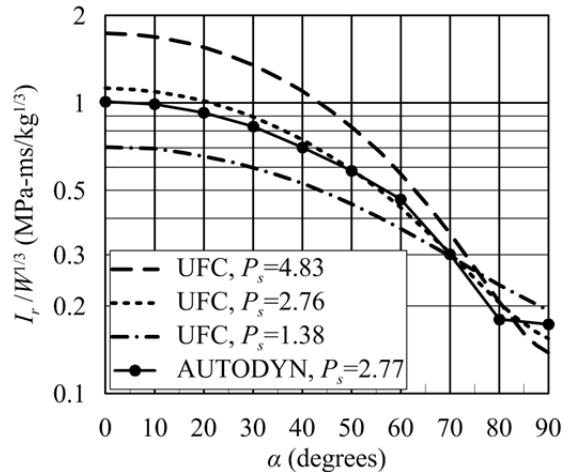
(c)  $Z = 0.26 \text{ m/kg}^{1/3}$  ( $0.65 \text{ ft/lb}^{1/3}$ )



(d)  $Z = 0.30 \text{ m/kg}^{1/3}$  ( $0.75 \text{ ft/lb}^{1/3}$ )

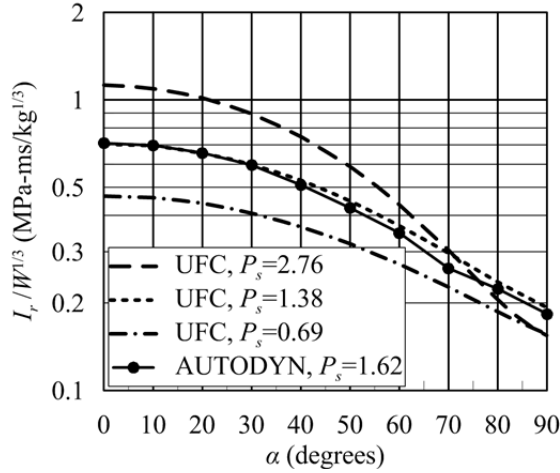


(e)  $Z = 0.40 \text{ m/kg}^{1/3}$  ( $1.0 \text{ ft/lb}^{1/3}$ )

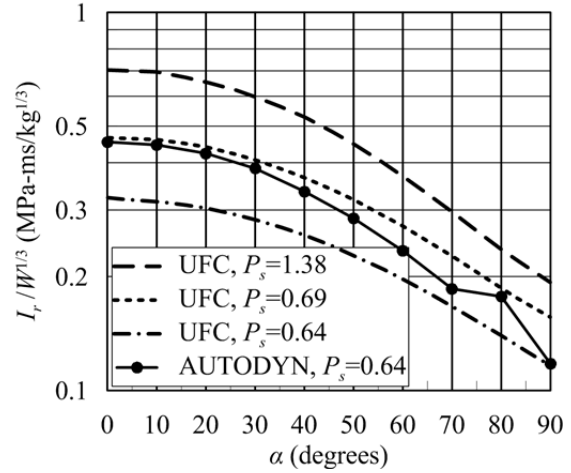


(f)  $Z = 0.60 \text{ m/kg}^{1/3}$  ( $1.5 \text{ ft/lb}^{1/3}$ )

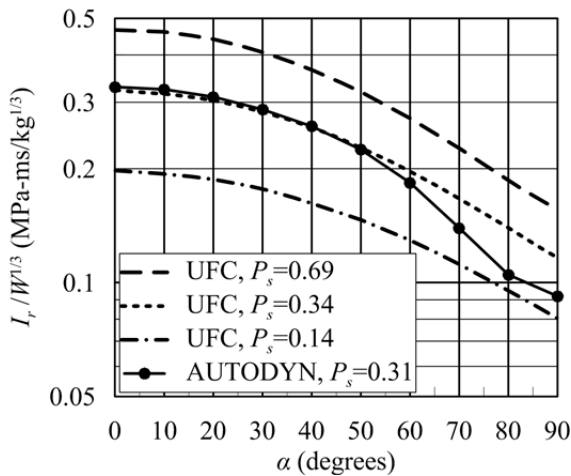
**Figure 5-27 Reflected scaled impulse as a function of angle of incidence;  $P_s$  in units of MPa**



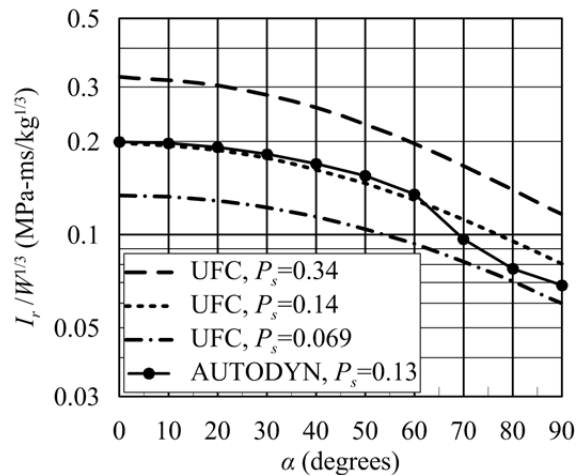
(g)  $Z = 0.80 \text{ m/kg}^{1/3}$  (2.0 ft/lb<sup>1/3</sup>)



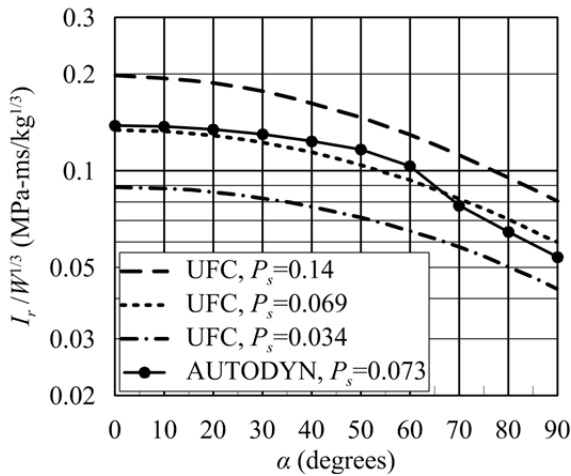
(h)  $Z = 1.2 \text{ m/kg}^{1/3}$  (3.0 ft/lb<sup>1/3</sup>)



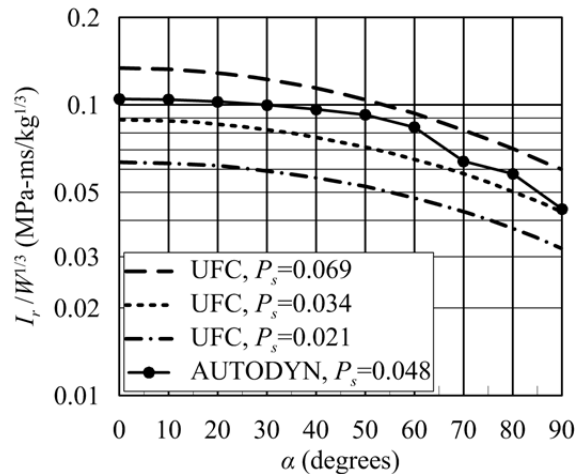
(i)  $Z = 1.6 \text{ m/kg}^{1/3}$  (4.0 ft/lb<sup>1/3</sup>)



(j)  $Z = 2.4 \text{ m/kg}^{1/3}$  (6.0 ft/lb<sup>1/3</sup>)

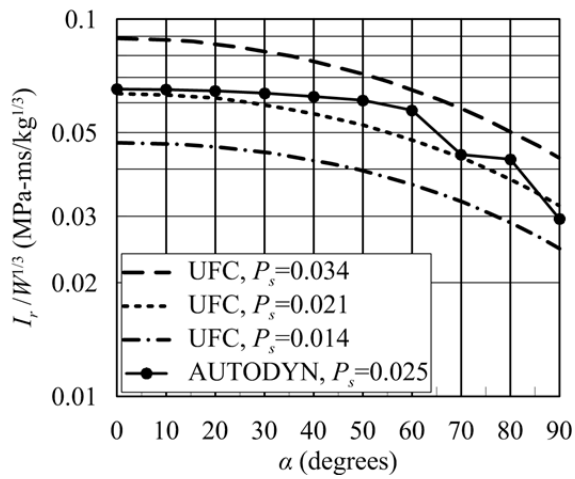


(k)  $Z = 3.2 \text{ m/kg}^{1/3}$  (8.0 ft/lb<sup>1/3</sup>)

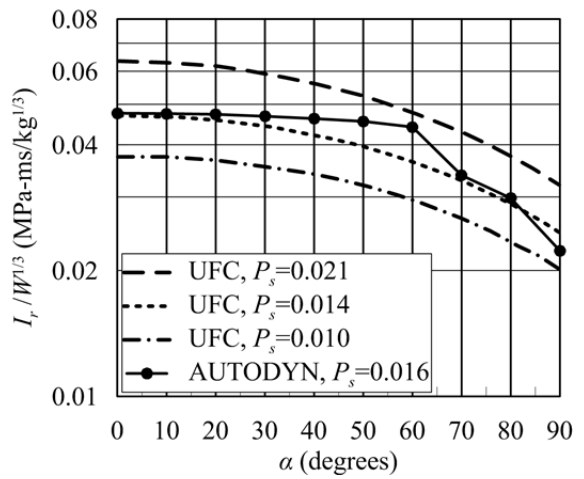


(l)  $Z = 4.0 \text{ m/kg}^{1/3}$  (10 ft/lb<sup>1/3</sup>)

**Figure 5-27 Reflected scaled impulse as a function of angle of incidence;  $P_s$  in units of MPa (cont.)**



(m)  $Z = 6.0 \text{ m/kg}^{1/3}$  (15 ft/lb<sup>1/3</sup>)



(n)  $Z = 8.0 \text{ m/kg}^{1/3}$  (20 ft/lb<sup>1/3</sup>)

**Figure 5-27 Reflected scaled impulse as a function of angle of incidence;  $P_s$  in units of MPa (cont.)**

## SECTION 6

# MODELING CONCRETE EROSION STRAIN FOR BLAST ANALYSIS OF STRUCTURAL COMPONENTS

### 6.1 Introduction

Structural components subjected to extreme loadings such as blast effects, missile impact and earthquakes often lose strength and stiffness due to damage and loss of material. Damage can be modeled coarsely at the component level using macro-models (e.g., Mehanny and Deierlein, 2000, Lignos et al. 2011) or more finely using finite elements (e.g., Malvar and Simons 1996, Murray 2007b). The latter approach is likely more accurate but computationally expensive.

Macro-models are best suited for earthquake analysis because all components in a structure directly experience the load effect. Macro-models are generally based on regression analysis of results of small-scale and large-scale tests and are not component specific. As such, macro models are not particularly suitable for analysis of components (and structures) subjected to more localized loadings such as detonations of 10s to low 1000s of kilograms of high explosives, tornado-borne missile impact, and ballistics including bullets and shoulder-launched missiles. For such loadings, detailed finite element (FE) models are preferred provided that robust constitutive models are available. Component modeling using finite elements is the subject of this study.

Blast and impact loadings can spall concrete from reinforced and pre-stressed concrete components. Blast and missile impact loadings may be considered for the design of mission-critical and defense-related structures and form part of the design basis for safety-related nuclear structures. High rates of straining are often generated in structural components due to the impulsive loadings due to blast or impact. Any constitutive model that is used to predict the response of structural components to blast and impact loadings should enable the analyst to address the effects of loading rate.

Fragmentation of concrete may accompany a near-field detonation of high explosives. For structural components such as columns that are susceptible to such loadings, the short duration of loading (msec) and short period of oscillation of the component (10s of msec) often result in a high rate of straining of the extreme fibers of components. Excessive strains will lead to material failure and strain rate will affect the threshold strain (termed here as the erosion strain) at which material is lost (or eroded) from the component. Erosion strain is usually tensile because strain capacity is smaller in tension than compression.

Erosion algorithms for concrete have been used in numerical simulations of blast and penetration events to eliminate material from a model (e.g., Schwer 2004, Luccioni et al. 2004, Teng et al. 2004, Xu and Lu 2006, Polanco-Loria et al. 2008, Islam et al. 2011). Although both the blast and ballistic (penetration) loadings can generate large local deformations, high straining, and damage or failure, they cannot be treated similarly because the loading conditions are quite different. This study focuses on blast loadings although some techniques used for penetration studies of concrete are described to aid in the determination of criteria for concrete erosion.

The effect of using alternate values of concrete erosion strain and alternate constitutive material models (concrete and reinforcement) is investigated in this study by simulating the response of a sample reinforced concrete (RC) column subjected to free-air TNT blast loadings using values of erosion adopted by Xu and Lu (2006) and Luccioni et al. (2004). The results of these simulations are compared with those performed using concrete erosion criterion established in this study. A model of the sample RC column is built in a finite element (FE) code, LS-DYNA (LSTC 2013) with pin-fixed boundary conditions to approximate a first story column founded in a raft foundation. The TNT detonation is modeled using two codes: Air3D (Rose 2006) and AUTODYN (ANSYS 2013a), to generate reflected pressure histories on the column. The reflected pressure histories are then directly applied to the sample RC column in LS-DYNA.

To enable the simulation of the response of the column to air-blast loading, trial analyses are performed to estimate the magnitude of the tensile stresses on the back face of the column resulting from reflection of the incident compressive shock front. The results of the trial analyses are described in Section 6.3. The effect of strain rate on material response and alternate material

models for concrete and steel reinforcement are described in Section 6.4, including the effects of strain rate. Single three-dimensional (3D) solid (finite) element simulations of concrete are described in Section 6.5 to evaluate the sensitivity of the values of concrete erosion strains to rate of loading, element dimension, loading condition and concrete compressive strength. Various dimensions of single elements are considered based on uniform  $h$ -refinement (Cook 2002). Each element is loaded in pure tension because erosion criteria for concrete are typically formulated using a maximum principal tensile strain (e.g., Teng et al. 2004, Xu and Lu 2006, Polanco-Loria et al. 2008, Islam et al. 2011), as noted above. LS-DYNA and its implementation of the CSCM model are used for the single element simulations. Force control and triangular loading functions are used to represent blast loadings.

## **6.2 Criteria for Eroding Elements**

Criteria for eroding concrete have been determined by judgment and use of empirical data, generally calibrated from but not measured directly in experiments. Luccioni et al. (2004) established an erosion strain as an incremental geometric strain of 0.075 for a concrete compressive strength of 25 MPa by calibration of AUTODYN simulations of uniformly supported concrete slabs subjected to blast loadings. However, incremental geometric strain is not an appropriate erosion parameter for brittle materials such as concrete, as discussed later, because it is a function of the effective strain rate, a scalar quantity, and the properties of concrete vary greatly in compression and tension.

Erosion strain for concrete should be determined by parameters such as principal stress and principal strain. Maximum principal tensile strain and minimum principal compressive strain have been used for this purpose (e.g., Schwer 2004, Teng et al. 2004, Islam et al. 2011). Xu and Lu (2006) numerically simulated spallation in reinforced concrete walls cast with 40 MPa concrete, fixed on four sides, and subjected to blast loadings. They proposed a maximum tensile principal strain of 0.010 as a concrete erosion strain on an empirical basis with consideration of typical concrete strain at peak tensile stress, strain softening, strain rate and confinement effects. Although both Luccioni et al. and Xu and Lu demonstrated good agreement between their

simulations and test data, neither provided a technical basis for determining concrete erosion strain.

Relationships among material parameters such as erosion strain, strain capacity and strain rate are discussed here first because an understanding of these relationships plays a pivotal role in establishing erosion strain for concrete. An erosion strain for concrete should be proportional to its tensile strain capacity, which in turn is a function of the stress state, concrete compressive and tensile strengths, loading history, and rate of strain. The compressive and tensile strengths of concrete increase with increasing strain rate (e.g., Dusenberry 2010). At low rates of strain, say  $\dot{\epsilon} \leq 10^{-5} \text{ sec}^{-1}$ , the tensile strain capacity of concrete tends to decrease with an increase in strength (Wight and MacGregor 2011). One might expect the tensile strain capacity to further decrease with increasing strain rate. Fracture energy is introduced below to clarify the relationship between the two.

Tensile strain capacity can be quantitatively measured by fracture energy, which is defined as the area under the stress-strain or stress-displacement curves after the peak stress (Xu et al. 2006). Fracture energy is used to model softening behavior of brittle materials and is proportional to tensile strain capacity. Lambert and Ross (2000), Lu and Xu (2004), Schuler et al. (2006), Brara and Klepaczko (2007), and Ruiz et al. (2009) have reported on the basis of test data that fracture energy increases with increasing strain rate, which takes into account the increase in the tensile strain capacity of concrete with strain rate. Grote et al. (2001), Ragueneau and Gatuingt (2003), and Ruiz et al. (2009) showed through compressive and tensile tests that maximum compressive and tensile stress, and maximum compressive and tensile strain increase with increasing strain rate.

Most simulations using erosion algorithms have been performed using LS-DYNA and AUTODYN. These programs provide multiple erosion parameters. Parameters based on von Mises theory (e.g., effective stress, effective strain, effective plastic strain) are well suited for isotropic materials like metals (e.g., steel, copper, iron) (e.g., Kurtaran et al. 2003, Fawaz et al. 2004). For anisotropic materials (e.g., concrete, orthotropic material), parameters such as

principal stress and principal strain have been employed (e.g., Schwer 2004, Teng et al. 2004, Islam et al. 2011). LS-DYNA supports the following parameters to erode material:

- Effective plastic strain,  $\varepsilon_{eff}^p$
- Effective strain,  $\varepsilon_{eff}$
- Effective stress,  $\sigma_{eff}$
- Failure time
- Maximum compressive pressure (positive in compression)
- Maximum principal tensile strain
- Maximum principal tensile stress
- Maximum shear strain  $(=\varepsilon_1 - \varepsilon_3) / 2$
- Minimum principal compressive strain
- Minimum tensile pressure (positive in compression)
- Stress impulse
- Threshold stress
- Volumetric strain  $(=\varepsilon_{jj})$

where  $\varepsilon_1$  and  $\varepsilon_3$  are the first and third principal strains, respectively, and  $\varepsilon_{jj}$  are the components of the strain tensor. The effective plastic strain,  $\varepsilon_{eff}^p$ , effective strain,  $\varepsilon_{eff}$ , and effective stress,  $\sigma_{eff}$ , are given by

$$\varepsilon_{eff}^p = \int_0^t \sqrt{\frac{2}{3} \dot{\varepsilon}_{ij}^p \dot{\varepsilon}_{ij}^p} dt \quad (6-1)$$

$$\varepsilon_{eff} = \sqrt{\frac{2}{3} \varepsilon_{ij}^{dev} \varepsilon_{ij}^{dev}} \quad (6-2)$$

$$\sigma_{eff} = \sqrt{\frac{2}{3} \sigma_{ij}^{dev} \sigma_{ij}^{dev}} \quad (6-3)$$

where  $\dot{\varepsilon}_{ij}^p$ ,  $\varepsilon_{ij}^{dev}$  and  $\sigma_{ij}^{dev}$  are the components of the plastic strain-rate tensor, deviatoric strain tensor, and deviatoric stress tensor, respectively. When the failure time is exceeded by a problem time, material is eroded. The threshold stress is specified with the Tuler-Butcher criterion (Tuler and Butcher 1968) as

$$\int_0^t [\max(0, \sigma_1 - \sigma_0)]^2 dt \geq K_f \quad (6-4)$$

where  $\sigma_1$  is the maximum principal stress,  $\sigma_0$  is a specified threshold stress ( $\sigma_1 \geq \sigma_0 \geq 0$ ), and  $K_f$  is the material constant for failure. The volumetric strain can be positive or negative depending upon whether failure is in tension or compression. LS-DYNA allows the use of one or more parameters to erode material in a given analysis (LSTC 2013).

AUTODYN enables material erosion using one of the following parameters:

- Effective plastic strain,  $\varepsilon_{eff}^p$
- Hydrostatic tensile pressure,  $p_t$
- Incremental geometric strain,  $\varepsilon_{incr}$
- Instantaneous geometric strain,  $\varepsilon_{inst}$
- Material strain: maximum tensile failure strains ( $\varepsilon_{11}^{ft}$ ,  $\varepsilon_{22}^{ft}$  and  $\varepsilon_{33}^{ft}$ ) and maximum shear strains ( $\varepsilon_{12}^{fs}$ ,  $\varepsilon_{23}^{fs}$  and  $\varepsilon_{31}^{fs}$ )
- Material stress: maximum tensile failure stresses ( $\sigma_{11}^{ft}$ ,  $\sigma_{22}^{ft}$  and  $\sigma_{33}^{ft}$ ) and maximum shear stresses ( $\sigma_{12}^{fs}$ ,  $\sigma_{23}^{fs}$  and  $\sigma_{31}^{fs}$ )
- Material stress/strain: coupling of the criteria of the material strain and material stress failures
- Principal strain: maximum principal tensile strain and  $(\varepsilon_1 - \varepsilon_3)/2$
- Principal stress: maximum principal tensile stress and  $(\sigma_1 - \sigma_3)/2$
- Principal stress/stress: coupling of the criteria of the principal strain and principal stress failures
- Time step: minimum element time step

where the effective plastic strain,  $\varepsilon_{eff}^p$ , is defined in the previous paragraph,  $\varepsilon_{ij}^{ft}$ ,  $\varepsilon_{ij}^{fs}$ ,  $\sigma_{ij}^{ft}$  and  $\sigma_{ij}^{fs}$  are the components of maximum tensile failure strain tensor, maximum shear strain tensor, maximum tensile failure stress tensor, and maximum shear stress tensor, respectively,  $\varepsilon_1$  and  $\varepsilon_3$  are defined previously, and  $\sigma_1$  and  $\sigma_3$  are the first and third principal stresses, respectively. The incremental geometric strain,  $\varepsilon_{incr}$ , is defined by

$$\varepsilon_{incr} = \int_0^t \sqrt{\frac{2}{3} \dot{\varepsilon}_{ij} \dot{\varepsilon}_{ij}} dt \quad (6-5)$$

where  $\dot{\varepsilon}_{ij}$  are the components of the strain rate tensor. The incremental geometric strain,  $\varepsilon_{incr}$ , is a non-decreasing cumulative function with time and increases continuously for both compressive and tensile stresses of elements, which can lead to erroneous material erosion in the elastic range,

especially for cyclic loading. ANSYS (2013a) introduces an instantaneous geometrical strain,  $\varepsilon_{\text{inst}}$ , in AUTODYN to overcome this shortcoming as

$$\varepsilon_{\text{inst}} = \frac{2}{3} \sqrt{(\varepsilon_{11}^2 + \varepsilon_{22}^2 + \varepsilon_{33}^2) + 5(\varepsilon_{11}\varepsilon_{22} + \varepsilon_{22}\varepsilon_{33} + \varepsilon_{33}\varepsilon_{11}) - 3(\varepsilon_{12}^2 + \varepsilon_{23}^2 + \varepsilon_{31}^2)} \quad (6-6)$$

where  $\varepsilon_{ij}$  are the components of the strain tensor. Unlike the incremental geometric strain,  $\varepsilon_{\text{incr}}$ , the instantaneous geometrical strain,  $\varepsilon_{\text{inst}}$ , can decrease for cyclic loading of elements and computes the equivalent strain in a similar manner to von Mises strain.

Material erosion can be also initiated by a limiting value of time step. A local time step is computed for each element in a model as a fraction of the time required for the passage of the dilatational wave across the minimum element dimension. The global time step for analysis of the mathematical model is taken as the minimum value of the local time steps. If elements are highly distorted, the minimum dimension of all distorted elements can be very small (indirectly suggesting failure), resulting in a very small local time step and a significant increase in computational effort. Elements can be eroded or deleted if the local time steps decrease to a user-specified minimum element time step to manage this effort.

### 6.3 Wave Passage Effects in Reinforced Concrete Columns

Wave passage effects through the cross section of reinforced concrete components are often idealized using one-dimensional propagation of impulsive loadings in rods (e.g., Timoshenko and Goodier 1970, Kolsky 1953). For a zero-damped rod, impulsively loaded at one end in compression, the wave is reflected at the free end as a tensile wave with the same amplitude as the incident compressive wave.

Impulsive loadings are imposed on the front face of a sample reinforced concrete column to provide insight into the propagation of stress waves through the column and their subsequent reflection from free surfaces: the back and front faces, respectively. The results of these numerical analyses are contrasted with one-dimensional wave propagation solutions to demonstrate that the classical one-dimensional solutions cannot predict stresses in three-dimensional structures such as columns.

Consider the reinforced concrete column of Figure 6-1 that is 600 mm by 600 mm in plan and 4 meters in height. For the purpose of this calculation, the material is assumed to be linearly elastic and the longitudinal and transverse reinforcement is ignored. (These assumptions are relaxed in following sections.) The column is meshed with solid cubic elements with a 40 mm side length. The Young's modulus and Poisson's ratio were assumed to be 28 GPa and 0.2, respectively.

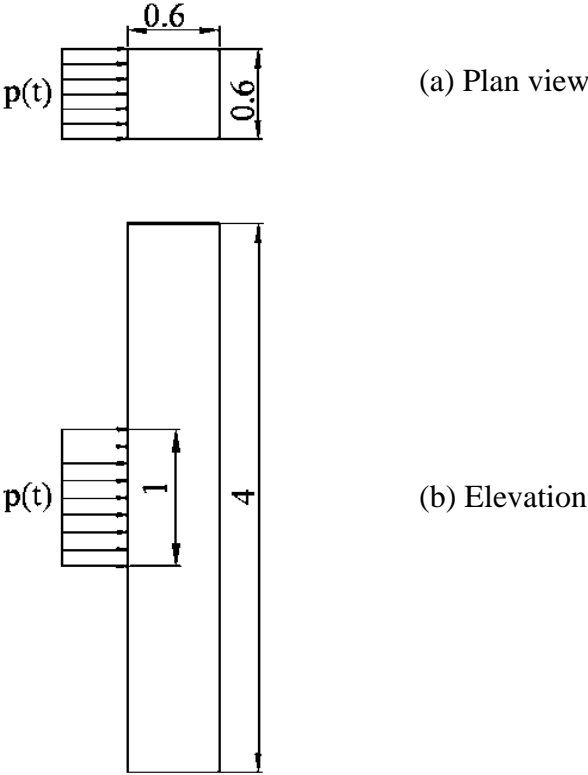


**Figure 6-1 Reinforced concrete column (units in meters)**

To study wave propagation in this column, an impulsive load is applied per Figure 6-2. The loaded area is at the midheight of the column and measured 1 meter by 600 mm (width). The reflected peak overpressure is 120 MPa, which is similar to that computed later in Section 6.6. The loading is imposed at  $t = 0.1$  msec. The duration of the impulse is 0.02 msec, which is the shortest possible based on the size of the element and the dilatational wave speed in concrete,  $c$ , which is

$$c = \sqrt{\frac{E(1-\nu)}{(1+\nu)(1-2\nu)\rho}} \approx 3600 \text{ m/sec} \tag{6-7}$$

where  $E$  is Young's modulus,  $\nu$  is Poisson's ratio and  $\rho$  is the mass density of concrete ( $= 2400 \text{ kg/m}^3$ ). For a mesh size of 40 mm, the duration of the pulse must be greater than 0.011 msec ( $= 40 \text{ mm}/3600 \text{ mm/msec}$ ) for the loading to be resolved.

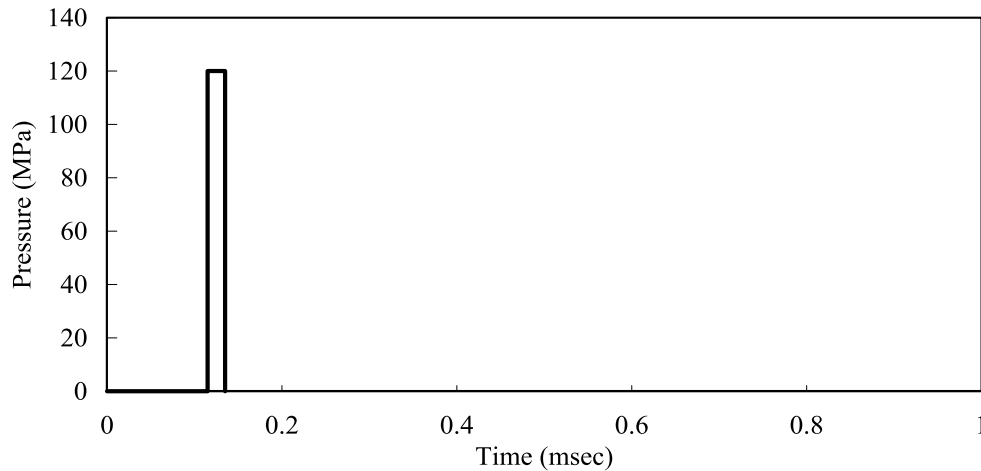


**Figure 6-2 Rectangular pulse used for the elastic simulation of the sample RC column**

Figure 6-3 is a cross section of the column at its midheight. The coordinate system is shown in the figure; loading is in the  $x$  direction. Stress histories are generated for seven elements through the depth, numbered 1 through 7 in the figure. Figure 6-4 presents histories in the  $x$  direction for elements 1, 3 and 7, where tensile stress is positive. The travel time for the compression wave through the column is 0.16 msec, with the wave arriving at the back face of the column at  $t = 0.26$  msec and arriving back at the front face at  $t = 0.42$  msec. Figure 6-5 presents stress histories for elements 4, 5, 6 and 7. The amplitude in compression diminishes with distance traveled due to wave scattering and the Poisson effect. The amplitude of the reflected wave (tensile) in element 7 is greater ( $= 50 \text{ MPa}$ ) than the amplitude of the incident compressive wave ( $= 20 \text{ MPa}$ ).

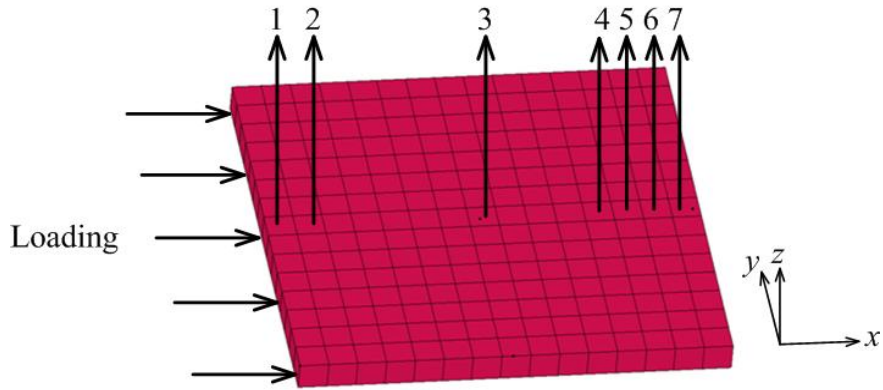


**Figure 6-3 Cross section at the mid-height of the sample RC column**

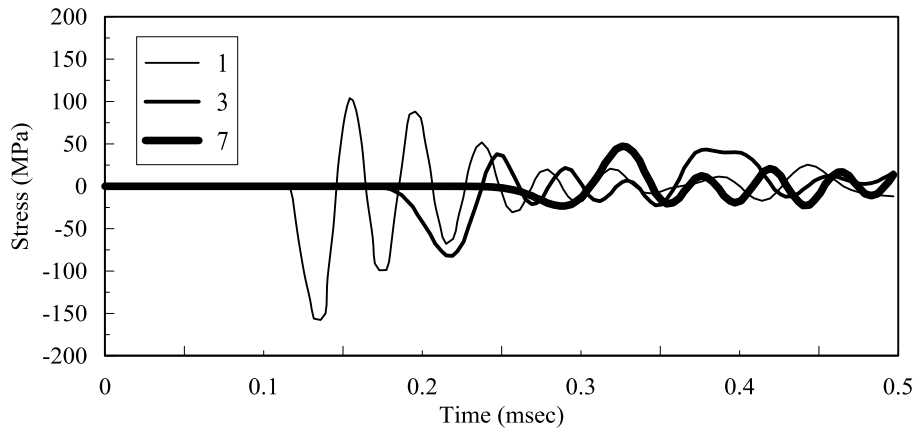


**Figure 6-4 Stress histories in the x-direction for elements No. 1, 3 and 7**

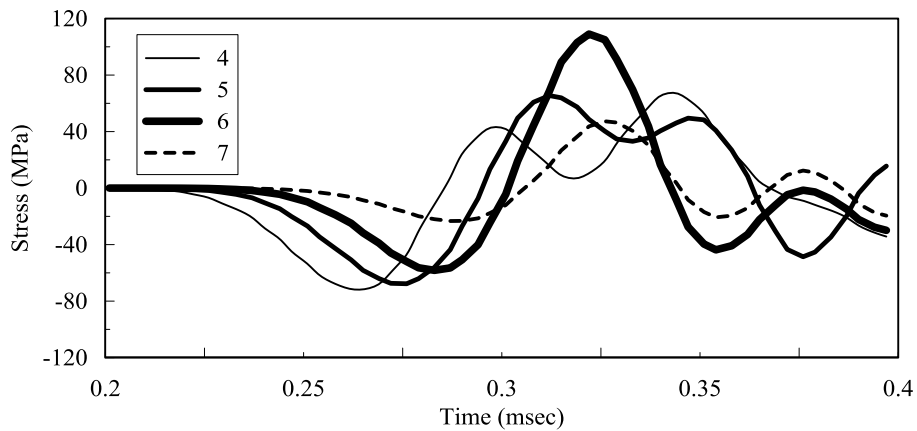


**Figure 6-5 Stress histories in the x-direction for elements No. 4, 5, 6 and 7**

To study the influence of wave reflection for this column, the depth of the column is doubled to 1.2 m as shown in Figure 6-6 and the loading of Figure 6-2 is applied. Figure 6-7 presents the stress histories in elements 1 through 7 in the  $x$  direction for both columns. The effects of reflection from the free surface are evident in the 600-mm-deep column at  $t = 0.42$  msec (element 1), 0.41 msec (element 2), 0.33 msec (element 3), 0.29 msec (element 4), 0.28 msec (element 5), 0.27 msec (element 6) and 0.26 msec (element 7). In panel (g), it can be seen that the reflected tensile stress wave reduces the amplitude of the incident compressive stress wave, which has an amplitude of approximately 60 MPa in panels (d) (element 4), (e) (element 5), and (f) (element 6). Figure 6-8 presents the differences in the stress histories for the two columns in elements 4, 5, 6 and 7; the differences (in tensile stress) are the result of wave reflection. The amplitude of the tensile reflected wave of approximately 60 MPa is approximately equal to the peak amplitude of the compressive wave in elements 5, 6 and 7 in the 1.2-m-deep column at  $t = 0.27$  to 0.30 msec. In this instance, the amplitude of the incident compressive wave in element 7 of the 1.2-m-deep column (the free or rear surface of the 600-mm-deep column) is approximately equal to the amplitude of the reflected tensile wave in the 600-mm-deep column.

This simple example has demonstrated that the extension of one-dimensional wave propagation results to simple two- and three-dimensional shapes leads to erroneous results. The amplitude of the compressive wave diminishes with distance traveled through the column; the reflection of the compressive wave from the back face of the column destroys the wave field. The calculation of stress histories is further complicated by a) the replacement of the simplified impulsive loading on part of the front face of the column with a temporal and spatially varying pressure history over the entire surface of the column, which is more representative of air-blast loading, b) the substitution of elastic material by a nonlinear concrete model, and c) the addition of longitudinal and transverse reinforcement to the column.

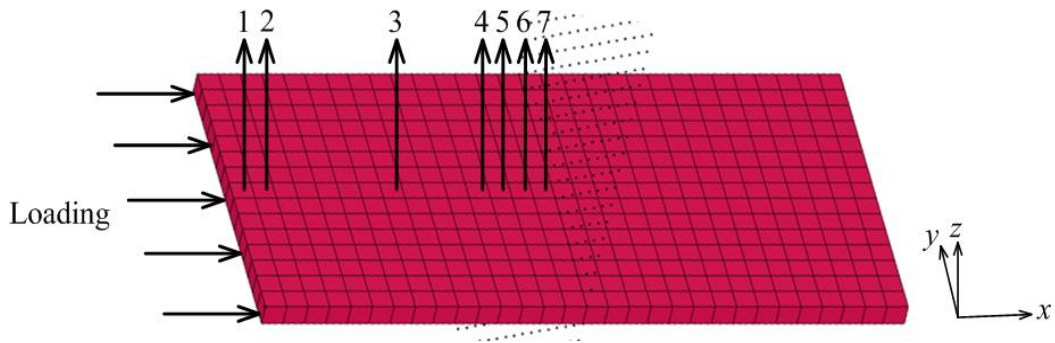
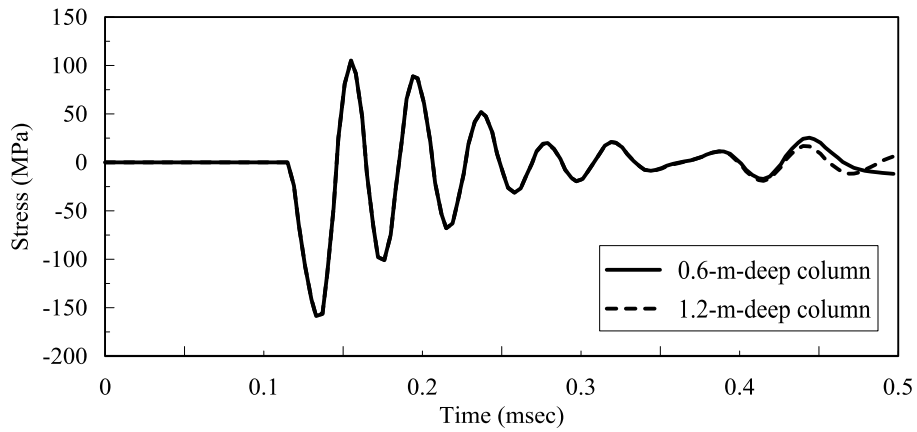
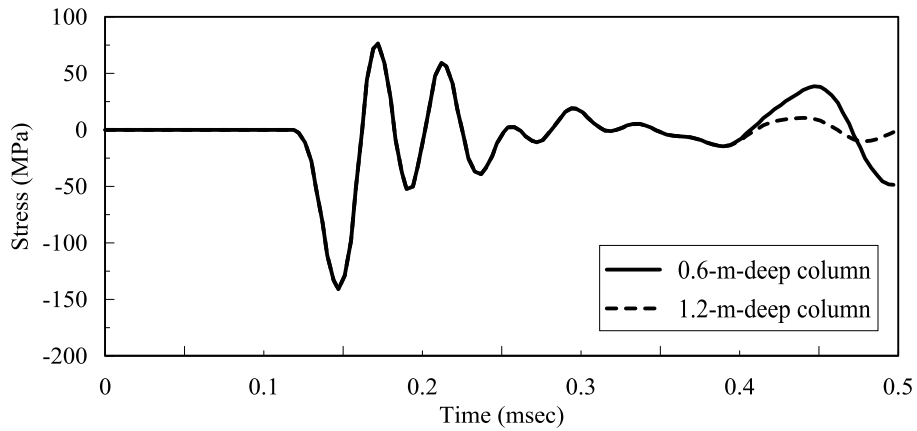


**Figure 6-6 Cross section at the mid-height of the 1.2-m-deep column**

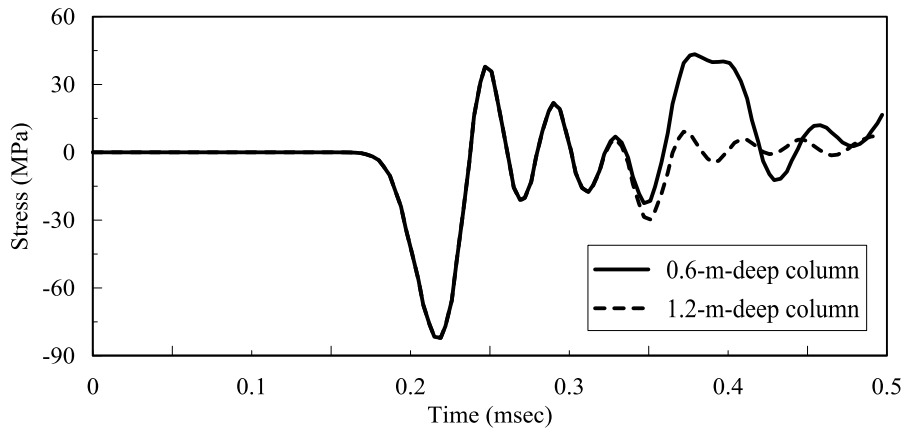


**(a) Element No. 1**

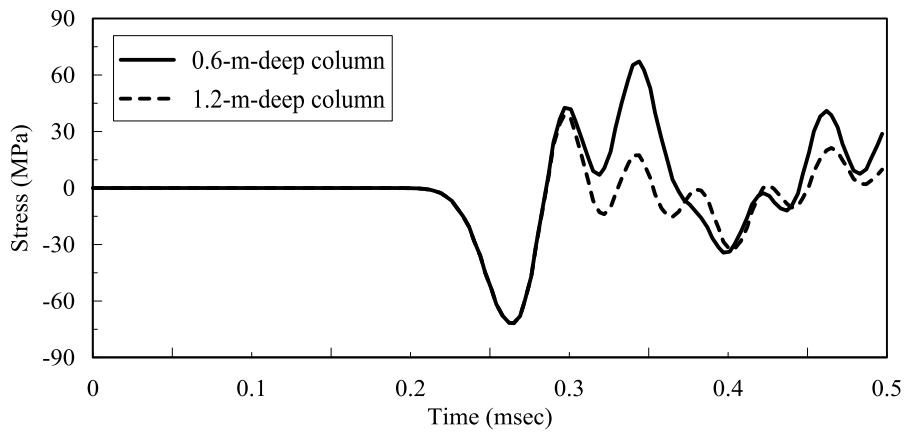


**(b) Element No. 2**

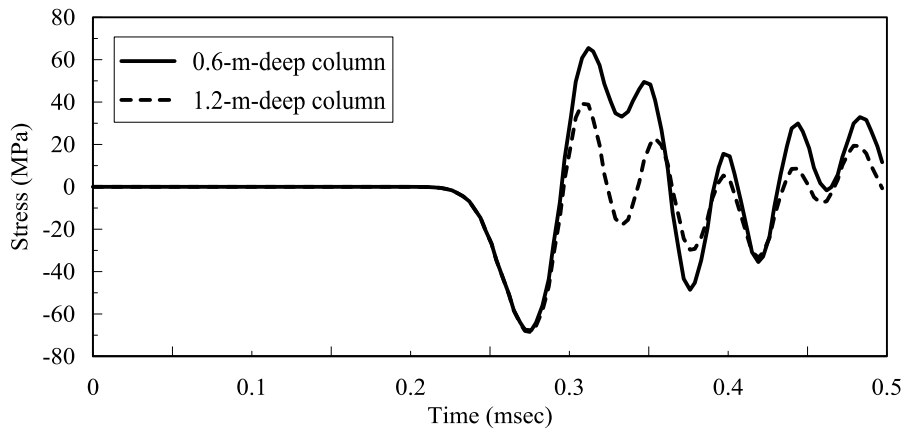
**Figure 6-7 Comparison of stress histories of elements No. 1 through 7 in the x-direction between 0.6-m- and 1.2-m-deep columns**



(c) Element No. 3

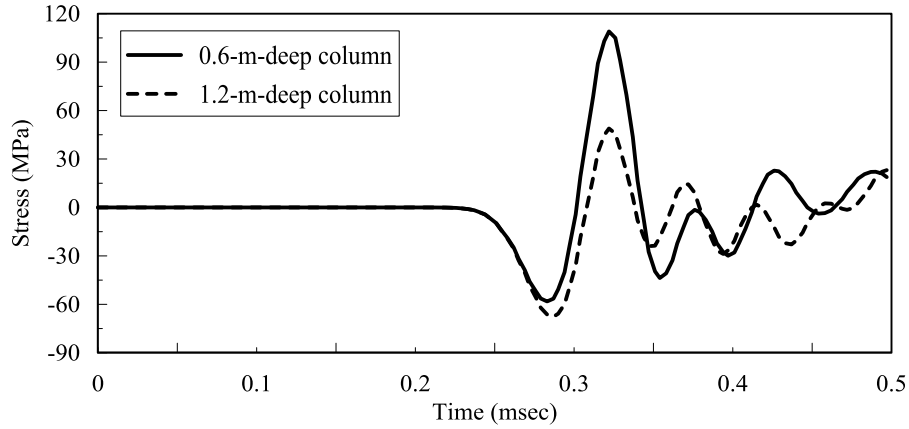


(d) Element No. 4

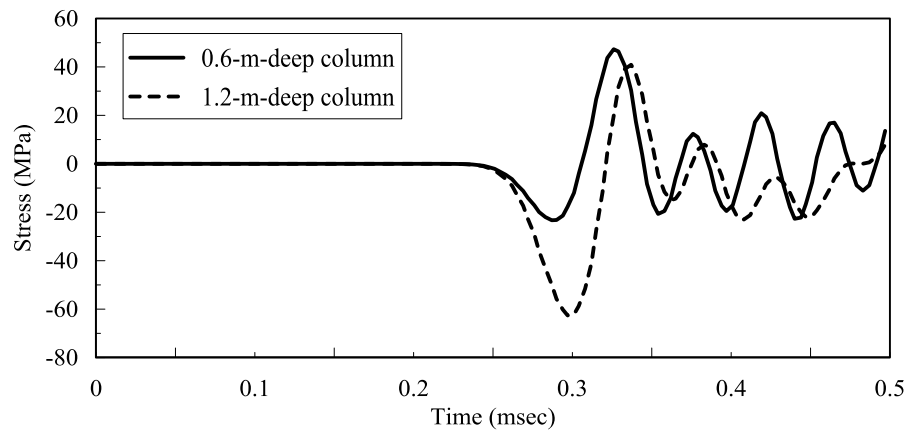


(e) Element No. 5

**Figure 6-7 Comparison of stress histories of elements No. 1 through 7 in the x-direction between 0.6-m- and 1.2-m-deep columns (cont.)**



(f) Element No. 6



(g) Element No. 7

**Figure 6-7 Comparison of stress histories of elements No. 1 through 7 in the x-direction between 0.6-m- and 1.2-m-deep columns (cont.)**

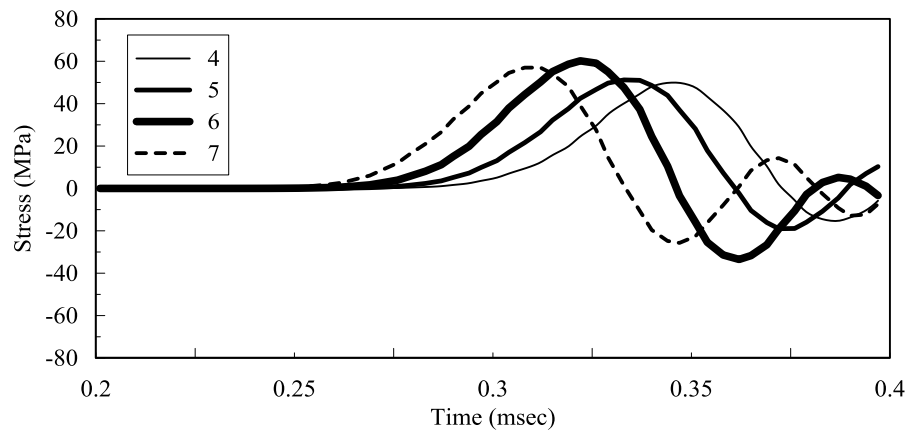


**Figure 6-8 Differences in the stress histories of elements No. 4, 5, 6 and 7 in the x-direction between the 0.6-m- and 1.2-m-deep columns**

## 6.4 Material Models

### 6.4.1 Concrete

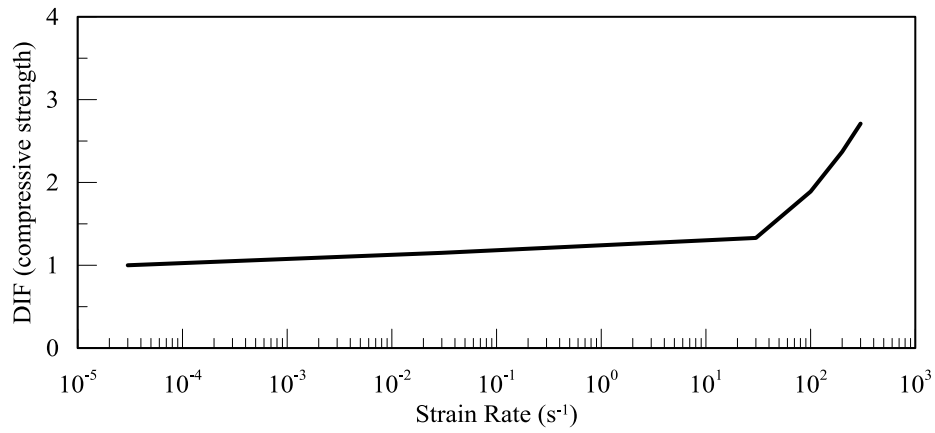
#### 6.4.1.1 Strain Rate Effects

Strain-rate effects for concrete are different for tensile and compressive loadings. A Dynamic Increase Factor (DIF) is often used to adjust the compressive and tensile strengths of concrete for high strain rates, and forms a basis for blast resistant design per UFC 3-340-02 (DoD 2008). Different values and equations for DIFs for concrete have been proposed (e.g., CEB 1993, Malvar and Ross 1998, Hao and Zhou 2007). For compressive strength, the CEB recommendation that is shown in Figure 6-9a is widely used (e.g., Dusenberry 2010, Hao and Zhou 2007, Murray 2007, Brannon and Leelavanichkul 2009, Coughlin et al. 2010) and is adopted for this study. For tensile strength, Hao and Zhou (2007) proposed DIFs based on extensive experimental data (e.g., Malvar and Ross 1998, Schuler et al. 2006). Their formulation for tensile strength is shown in Figure 6-9b together with the proposals of the CEB (1993) and Malvar and Ross (1998). Note the significant difference between the three curves in panel (b), which will inevitably impact the results of the simulations but cannot be addressed here.

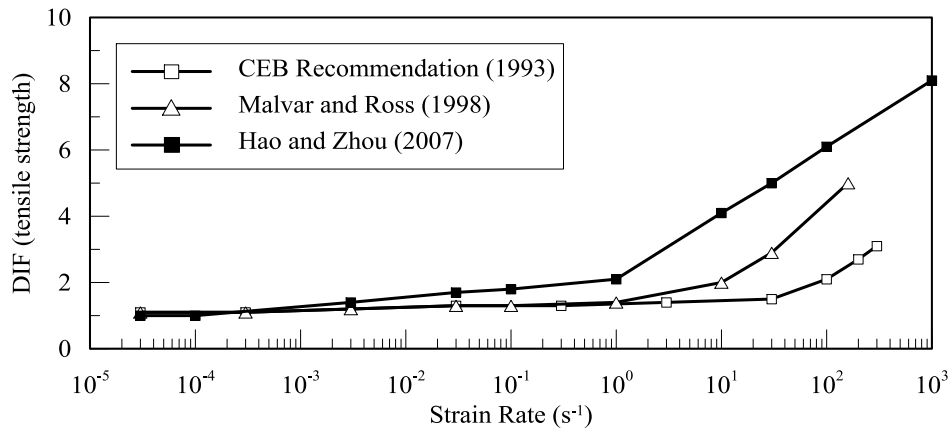
#### 6.4.1.2 Continuous Surface Cap Model (CSCM)

The Continuous Surface Cap Model (CSCM) (Murray 2007) is used to simulate the response of concrete. It was developed for the United States Federal Highway Administration to model the crashworthiness of concrete structures. The CSCM model includes a damage formulation, and can accommodate strain-rate effects and erosion due to damage accumulation. Strain-rate effects are modeled using a viscoplastic formulation. A general shape of the CSCM yield surface is shown in Figure 6-10. The yield surface is composed of the shear (failure) surface and hardening compaction surface (cap). The cap model smooths the intersection between the two surfaces to eliminate the likelihood of numerical instabilities. The yield surface is continuous and symmetric about the three principal stress axes and the hydrostatic axis (referred to as the pressure axis) serves as its center line. The CSCM model is formulated using equations for the yield surface,

strain-rate effects, damage formulation and strain softening, which are sequentially described below.



(a) DIF for compressive strength



(b) DIF for tensile strength

**Figure 6-9 Dynamic Increase Factor for compressive and tensile strength of concrete**

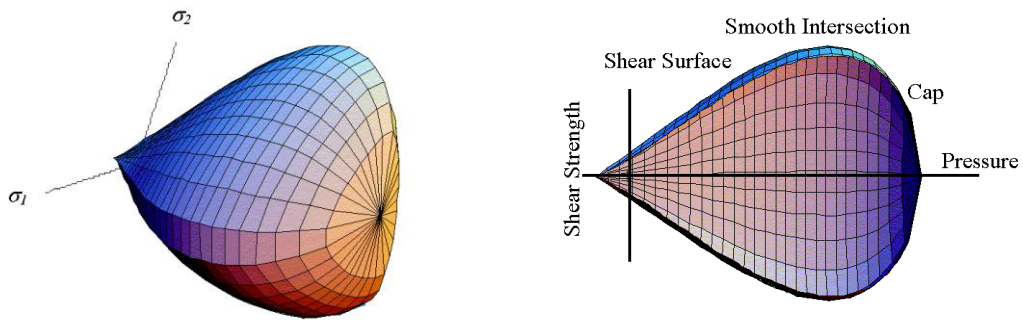


**Figure 6-10 General shape of the CSCM yield surface (Murray 2007)**

The yield surface of the CSCM model is formulated using three stress invariants (Chen 2007) as follows,

$$f(J_1, J_2, J_3, \kappa) = J_2 - \mathfrak{R}^2 F_f^2 F_c \quad (6-8)$$

where  $J_1$  is the first invariant of the stress tensor,  $J_2$  is the second invariant of the deviatoric stress tensor,  $S_{ij}$ ,  $J_3$  is the third invariant of the deviatoric stress tensor,  $\mathfrak{R}$  is the Rubin three-invariant reduction factor,  $F_f$  is a shear failure surface function,  $F_c$  is a hardening cap function, and  $\kappa$  is a cap hardening parameter. The three stress invariants are defined by using the deviatoric stress tensor,  $S_{ij}$ , and pressure,  $p$ , as

$$J_1 = 3p \quad (6-9)$$

$$J_2 = \frac{1}{2} S_{ij} S_{ij} \quad (6-10)$$

$$J_3 = \frac{1}{3} S_{ij} S_{jk} S_{ki} \quad (6-11)$$

The shear failure surface function,  $F_f$ , is defined as

$$F_f(J_1) = \alpha - \lambda e^{-\beta J_1} + \theta J_1 \quad (6-12)$$

where  $\alpha$ ,  $\beta$ ,  $\lambda$  and  $\theta$  are obtained by fitting the model surface to strength measurements from triaxial compression (TXC) tests. The Rubin reduction factor is a scaling function that determines the strength of concrete for any state of stress relative to the strength for the TXC tests (Rubin 1991). The hardening cap function,  $F_c$ , is used to model plastic volume change related to porosity. The function is expressed as

$$F_c(J_1, k) = 1 - \frac{[J_1 - L(k)][|J_1 - L(k)| + J_1 - L(k)]}{2[X(k) - L(k)]^2} \quad (6-13)$$

where  $L(k)$  is

$$L(k) \begin{cases} k & \text{if } k > k_0 \\ k_0 & \text{otherwise} \end{cases} \quad (6-14)$$

where  $k_0$  is the value of  $J_1$  at the initial intersection of the cap and shear surfaces before the cap moves. The function of  $L(k)$  prevent the cap from retracting into its initial location at  $k_0$ . The intersection of the cap with the  $J_1$  axis is at

$$X(k) = L(k) + RF_f(L(k)) \quad (6-15)$$

where  $R$  is the ellipticity ratio of the major to minor axes of the cap. The cap moves with change in plastic volume. The motion of expansion and contraction is based on the hardening rule

$$\varepsilon_v^p = W(1 - e^{-D_1(X-X_0) - D_2(X-X_0)^2}) \quad (6-16)$$

where  $\varepsilon_v^p$  is a plastic volume strain,  $W$  is a maximum plastic volume strain,  $D_1$  and  $D_2$  are shape parameters, and  $X_0$  is the initial location of the cap. The parameters of the plastic volume strain,  $\varepsilon_v^p$ , are obtained by fitting pressure-volumetric strain curves to data.

As noted previously (and by many others), the compressive and tensile strength of concrete increases with strain rate. The viscoplastic algorithm interpolates the elastic stress,  $\sigma_{ij}^T$ , and the elasto-plastic stress,  $\sigma_{ij}^p$ , as follows,

$$\sigma_{ij}^{vp} = (1 - \gamma)\sigma_{ij}^T + \gamma\sigma_{ij}^p \quad (6-17)$$

$$\gamma = \frac{\Delta t / \eta}{1 + \Delta t / \eta} \quad (6-18)$$

where  $\sigma_{ij}^{vp}$  is the viscoplastic stress, which addresses strain-rate effects using a parameter,  $\eta$ , as

$$\eta = \frac{\eta_0}{\dot{\varepsilon}^N} \quad (6-19)$$

where strain-rate effect parameters,  $\eta_0$  and  $N$ , are obtained by curve fitting (or calibration) to strain-rate data and are fitted to the CEB recommendation for concrete compressive strength and the Hao and Zhou recommendation for tensile strength.

Damage is addressed by considerations of strain softening and modulus reduction. The strain softening indicates a decrease in strength after peak strength is reached. Modulus reduction is a decrease in the unloading or loading slopes. The stress,  $\sigma_{ij}^d$ , is

$$\sigma_{ij}^d = (1-d)\sigma_{ij}^{vp} \quad (6-20)$$

where  $d$  is a damage parameter with a value between 0 and 1, and  $\sigma_{ij}^{vp}$  is the viscoplastic stress tensor without damage. Damage accumulation is either ductile or brittle. Ductile damage accumulates when the pressure is compressive and depends on the total strain components,  $\varepsilon_{ij}$ , as

$$\tau_c = \sqrt{\frac{1}{2}\sigma_{ij}\varepsilon_{ij}} \quad (6-21)$$

where  $\tau_c$  is an energy-type term, and  $\sigma_{ij}$  are the elasto-plastic stresses. Ductile damage initiates when  $\tau_c$  exceeds a ductile damage threshold,  $r_{0c}$ , which is associated with the onset of softening. Brittle damage accumulates when the pressure is tensile and depends on the maximum principal strain,  $\varepsilon_{\max}$ , as

$$\tau_t = \sqrt{E\varepsilon_{\max}^2} \quad (6-22)$$

where  $\tau_t$  is an energy-type term, and  $E$  is the initial elastic modulus of concrete. Brittle damage initiates when  $\tau_t$  exceeds the brittle damage threshold,  $r_{0b}$ , that shifts as a function of strain-rate as follows,

$$r_0 = \left(1 + \frac{E\dot{\varepsilon}\eta}{r_s\sqrt{E}}\right)r_s \quad (6-23)$$

where  $r_0$  is the shifted damage threshold,  $r_s$  is the damage threshold before applying viscoplasticity, and  $\eta$  is the strain-rate effect parameter introduced in Equation 6-19. The damage threshold grows with the increase in strain rate. As damage accumulates, the damage parameter,  $d$ , increases from a minimum value of zero toward a maximum value of 1.0. The damage parameters for compression and tension,  $d(\tau_b)$  and  $d(\tau_t)$ , respectively, are computed during the softening phase, namely,

$$d(\tau_c) = \frac{d_{\max}}{B} \left[ \frac{1+B}{1+Be^{-A(\tau_c-r_{0c})}} - 1 \right] \quad (6-24)$$

$$d(\tau_t) = \frac{0.999}{D} \left[ \frac{1+D}{1+De^{-C(\tau_t-r_{0t})}} - 1 \right] \quad (6-25)$$

where the parameters,  $A$ ,  $B$ ,  $C$  and  $D$ , are obtained by curve-fitting to stress-strain data,  $d_{\max}$  is a maximum damage level, defined as

$$d_{\max} = \begin{cases} \left( \frac{\sqrt{3J_2}}{J_1} \right)^{1.5} & \text{if } \frac{\sqrt{3J_2}}{J_1} < 1 \\ 1 & \text{if otherwise} \end{cases} \quad (6-26)$$

The maximum damage varies with strain-rate effects as (Murray 2007b)

$$d_{\max} = d_{\max} \times \max \left[ 1.0, \left( 1 + \frac{E\dot{\epsilon}\eta}{r_s\sqrt{E}} \right)^{1.5} \right] \quad (6-27)$$

Elements are eliminated when the damage parameter,  $d$ , exceeds 0.99.

Finite element analyses of models of materials with softening formulations such as concrete have been known not to converge due to strain localization (e.g., Bažant 1986, Belytschko et al. 1986, Bažant and Chang 1987, Bažant and Pijaudier-Cabot 1988). Consider a cube of concrete subjected to normal and shearing tractions, which is modeled with fine and coarse meshes. Damage accumulation will be greater in strain-localized elements of the finely meshed model, and the elements will then be eroded from this model first, which is a result of fracture energy being smaller in the smaller elements. Sandler and Wright (1984) asserted that the strain-softening models provide incorrect solutions because small differences in loading can lead to large changes in response. To remedy this situation, nonlocal formulations have been applied (e.g., Bažant and Chang 1987, Bažant and Pijaudier-Cabot 1988). The nonlocal formulation eliminates element-to-element variations in softening behavior by controlling fracture energy. Murray (2007) showed through simulations of tensile tests of concrete that converged solutions can be attained if the fracture energy is independent of mesh size. The fracture energy,  $G_f$ , is expressed as

$$G_f = \int_{x_0}^{\infty} (1-d)f' dx \quad (6-28)$$

where  $x_0$  is a displacement at peak strength,  $f'$ , and  $x$  is displacement. The fracture energy is computed using the damage parameter,  $d$ , as given in Equations 6-24 and 6-25, and element

dimensions. The CSCM model allows users to specify values of fracture energy for uniaxial tensile stress,  $G_{ft}$ , pure shear stress,  $G_{fs}$ , and uniaxial compressive stress,  $G_{fc}$ . The fracture energies for uniaxial tensile stress and pure shear stress correspond to the flexural and brittle failure modes, respectively. Strain-rate effects on the three fracture energies are formulated in the same way, namely,

$$G_f^{vp} = G_f \left( 1 + \frac{E \dot{\epsilon} \eta}{r^s \sqrt{E}} \right)^{repow} \quad (6-29)$$

where  $G_f^{vp}$  is the viscoplastic fracture energy,  $repow$  is a constant and other parameters were defined previously.

#### 6.4.2 Steel Reinforcement

Johnson and Cook (1983) proposed a constitutive model for metals subjected to high strain rates and high temperature. It is used in this study to model reinforcement in the sample RC column of Section 6.6. The basic form of the Johnson and Cook (JC) model is

$$\sigma_y = (A + B \epsilon_p^n) \left( 1 + C \ln \frac{\dot{\epsilon}_p}{\dot{\epsilon}_0} \right) (1 - [T^*]^m) \quad (6-30)$$

where  $\sigma_y$  is the yield stress,  $A$  is the yield stress per a reference strain rate,  $\dot{\epsilon}_0$ ,  $B$  and  $n$  are material constants that represent the effects of strain hardening,  $\dot{\epsilon}_p$  is the equivalent plastic strain rate,  $C$  and  $m$  are experimentally determined constants,  $\dot{\epsilon}_p$  is the equivalent plastic strain rate, and  $T^*$  is a normalized temperature, given by

$$T^* = \frac{T - T_r}{T_m - T_r} \quad (6-31)$$

where  $T$  is the temperature,  $T_r$  is the room temperature, and  $T_m$  is the melting point. The values of the constants for various metals in Equation 6-30 have been reported by Johnson and Cook (1983), Zukas (1990), and Meyers et al. (1992), among others. Thermal effects can generally be neglected for blast loadings on steel elements because the speed of heat conduction through the steel is much slower than the speed of the shock front (Ballantyne et al. 2009).

The Johnson-Cook (JC) constitutive model has been used widely for computing the response of metals deforming at high rates of strain. The model is available in LS-DYNA. Unfortunately, the values of the parameters of the JC model for typical grades of reinforcement (Grades 60 and 75, with yield stresses of 420 and 520 MPa, respectively) have not been published, requiring analysts and researchers to adopt published values determined for similar metals (e.g., Johnson and Cook 1983, Gray et al. 1994). Danielson et al. (2008) used the JC model for Grade 40 steel reinforcement (yield stress of 280 MPa, 40 ksi) but provided no information on the parameters of the model. Zhou et al. (2008) used the JC model for AISI 4340 steel to model steel reinforcement although the yield stress for AISI 4340 steel of 792 MPa is much higher than those of all grades of ASTM A615 reinforcement, which is routinely used for commercial reinforced concrete construction. Børvik et al. (2001) used values of the parameters for Weldox 460E, a high strength structural steel, to model Grade 60 rebar. Weldox 460E has minimum specified values for yield stress, ultimate stress and minimum elongation of 490 MPa, 580 MPa and 22%, respectively, which are reasonably close to the corresponding values of 420 MPa, 620 MPa and 7 to 9%, for ASTM A615 Grade 60 reinforcement. Accordingly, the JC parameters are used herein for Weldox 460E to model Grade 60 steel reinforcement but 420 MPa is substituted for the yield strength parameter,  $A$ . The values are tabulated in Table 6-1. The calculated stress-strain relationship for Grade 60 reinforcement at a reference strain rate equal to  $5 \times 10^{-4} \text{ s}^{-1}$  is shown in Figure 6-11.

**Table 6-1 Assumed model parameters for Grade 6d0 reinforcement (adopted from Børvik et al. 2001)**

Parameter	Value
Young's modulus, $E$ (GPa)	200
Poisson ratio, $\nu$	0.33
Density, $\rho$ ( $\text{kg/m}^3$ )	7850
Yield strength, $A$ (MPa)	420
Strain hardening parameter, $B$ (MPa)	383
Strain hardening parameter, $n$	0.45
Constant, $C$	0.0114
Constant, $m$	0.94
Reference strain rate, $\dot{\epsilon}_0$ ( $\text{s}^{-1}$ )	$5 \times 10^{-4}$

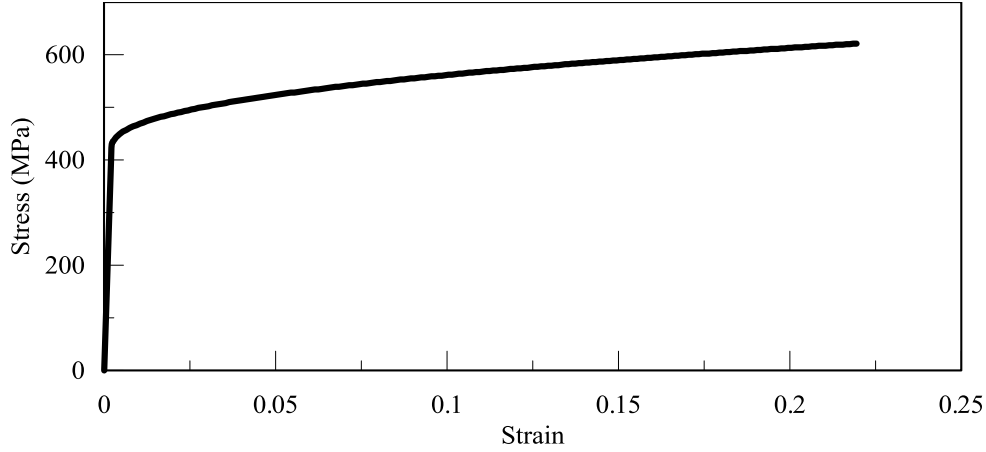


**Figure 6-11 Stress-strain relationship for Grade 60 rebar at a strain rate of  $5 \times 10^{-4} \text{ s}^{-1}$**

The JC model requires an Equation of State (EOS) as the hydrodynamic models compute only deviatoric stresses. The EOS provides a pressure-volume relationship for materials subjected to compression or tension.

The Gruneisen EOS is widely used in numerical simulations for metals to compute pressure (Meyers et al. 1992). The pressure,  $p$ , for materials in the compressed state is computed as

$$p = \frac{\rho_0 C^2 \mu \left[ 1 + \left(1 - \frac{\gamma_0}{2}\right) \mu - \frac{a}{2} \mu^2 \right]}{\left[ 1 - (S_1 - 1) \mu - S_2 \frac{\mu^2}{\mu + 1} - S_3 \frac{\mu^3}{(\mu + 1)^2} \right]^2} + (\gamma_0 + a\mu)E \quad (6-32)$$

and for expanded materials as

$$p = \rho_0 C^2 \mu + (\gamma_0 + a\mu)E \quad (6-33)$$

where  $\rho_0$  is the initial density,  $C$  is the sound speed in the material,  $S_1$ ,  $S_2$  and  $S_3$  are the coefficients of the slopes of a shock speed versus particle speed curve,  $\gamma_0$  is a Gruneisen coefficient,  $a$  is the first order volume correction to  $\gamma_0$ ,  $E$  is the internal energy per initial unit volume, and  $\mu$  is given by

$$\mu = \frac{\rho}{\rho_0} - 1 \quad (6-34)$$

where  $\rho$  is the current density. The parameters of the Gruneisen EOS in Equation 6-32 and 6-33 are obtained by Tan et al. (2009), as shown in Table 6-2.

**Table 6-2 Gruneisen EOS parameters for steel (Tan et al. 2009)**

$\rho_o$ (Kg/m <sup>3</sup> )	$c$ (m/s)	$S_1$	$S_2$	$S_3$	$\gamma_0$	$a$
7896	4569	1.49	0	0	2.17	0.5

Johnson and Cook expanded their constitutive strength model (1983) to a damage model (1985) as follows,

$$D = \sum \frac{\Delta \varepsilon_p}{\varepsilon_f} \quad (6-35)$$

where  $D$  is a damage index,  $\Delta \varepsilon_p$  is the increment of accumulated effective plastic strain, and  $\varepsilon_f$  is accumulated plastic strain to failure. The damage index  $D$  is zero for a virgin material and failure occurs when  $D$  reaches 1.0. The accumulated plastic strain at failure,  $\varepsilon_f$ , is

$$\varepsilon_f = \left( D_1 + D_2 \exp \left[ D_3 \frac{\sigma_m}{\sigma_{eff}} \right] \right) \left( 1 + D_4 \ln \dot{\varepsilon}_p^* \right) \left( 1 + D_5 T^* \right) \quad (6-36)$$

where  $D_1$  through  $D_5$  are material constants,  $\sigma_m$  is a hydrostatic stress,  $\sigma_{eff}$  is an effective stress,  $\dot{\varepsilon}_p^*$  is a dimensionless strain rate, given by  $\dot{\varepsilon}_p / \dot{\varepsilon}_0$ , and  $\dot{\varepsilon}_0$  is a reference strain rate. Equation 6-36 accounts for the effects of temperature, strain rate, and stress triaxiality. In FE simulations, elements are removed when the corresponding damage index equals 1.0. The parameters of the JC damage model for Weldox 460 E steel (Børvik et al. 2001) are presented in Table 6-3. These values are adopted for the Grade 60 steel reinforcement modeled in the sample RC column of Section 6.6.

**Table 6-3 Johnson and Cook damage model parameters for Weldox 460 E steel (Børvik et al. 2001)**

$D_1$	$D_2$	$D_3$	$D_4$	$D_5$
0.0705	1.732	-0.54	-0.015	0

## 6.5 Single Element Simulations

Single element simulations are performed in LS-DYNA using the CSCM model of Section 6.4.1.2 to evaluate concrete erosion strain with respect to strain rate, element size, compressive strength, and loading condition. The values of the parameters of the CSCM model for compressive strengths of 35.5 and 50 MPa<sup>9</sup> are listed in Appendix E. Values for strain-rate effects in compression and tension are obtained based on the CEB and Hao and Zhou recommendations, respectively.

The dimensions of the single elements are first considered to be 20×20×20, 40×40×40 and 80×80×80 mm based on uniform *h*-refinement (Cook 2002), noting that the size of the smallest element is on the order of a piece of aggregate. Elements sizes of 30×30×30 and 60×60×60 mm are also considered for completeness. Figure 6-12 enables a comparison of compressive stress-strain curves of the CSCM model for different element sizes and the concrete model reported by Popovics (1970), all for a compressive strength of 35.5 MPa. The Popovics curve lays between the CSCM curves for element dimensions of 20×20×20 and 40×40×40 mm, which is consistent with Murray’s description of a reasonable element size (19 to 38 mm).

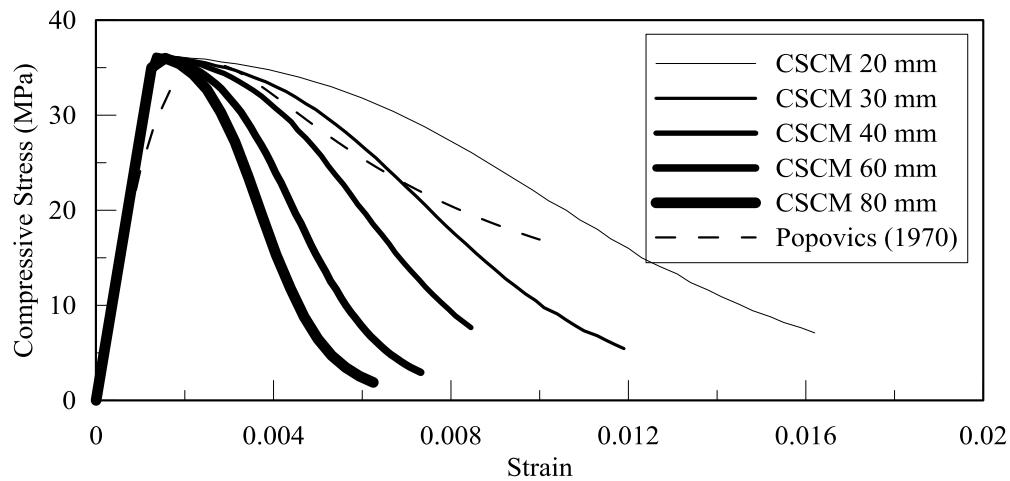


**Figure 6-12 Compressive stress–strain curves for concrete models of the CSCM and by Popovics (1970) for the compressive strength of 35.5 MPa**

<sup>9</sup> Normal and high strength concrete, respectively. Murray (2007) reported data for  $f'_c = 35$  MPa, and some of this data used below.

Strain capacity decreases with increasing element size in the CSCM model due to the use of constant fracture energy. Since the fracture energy is independent of element size, larger elements have less strain capacity per unit volume than smaller elements, as supported by Figure 6-12.

The forcing functions for the single element simulations are defined by traction rates between 50 and 400 MPa/msec, based on the results of simulations that are described in Section 6.6. The peak tensile tractions of the loadings are set equal to 10, 20 and 40 MPa based on the product of a) quasi-static tensile strength of about 10 percent of the compressive strength, and b) an increase associated with strain rate. Erosion did not occur for the peak tensile traction of 5 MPa. The duration of each loading is assumed to be 0.5 msec, which is appropriate for the weapon size and stand-off distance considered later. Figure 6-13 shows the loading conditions of tensile traction histories for a peak tensile traction of 10 MPa. The loadings for the peak tensile tractions of 20 and 40 MPa are generated in a similar manner.

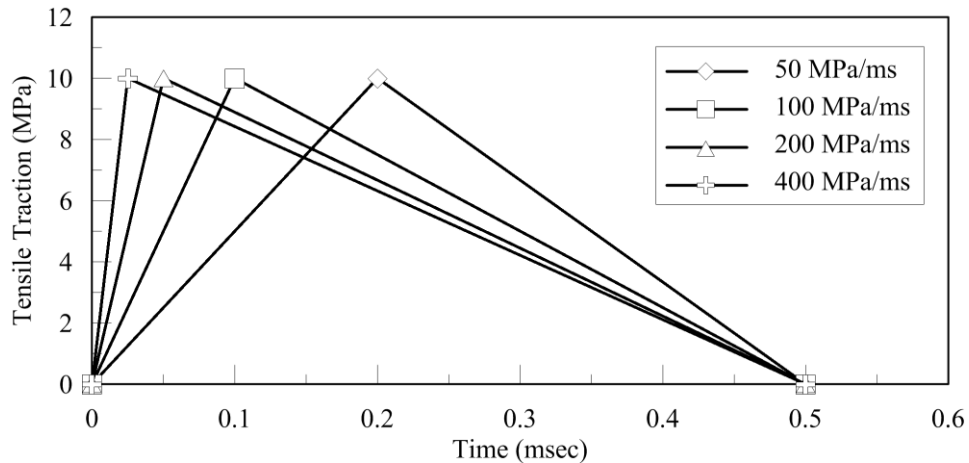


**Figure 6-13 Loading conditions used in single element simulations when the peak tensile load = 10 MPa**

Alternate restraint conditions (pinned or fixed) on one boundary are considered for the single element simulations to understand their impact on the calculated values of the erosion strain. The other end of the element is subjected to tensile loading. The values of erosion strain are not significantly affected by the choice of boundary condition. Results are presented in Table 6-4.

The remaining single element simulations are performed assuming one end of each element is fixed.

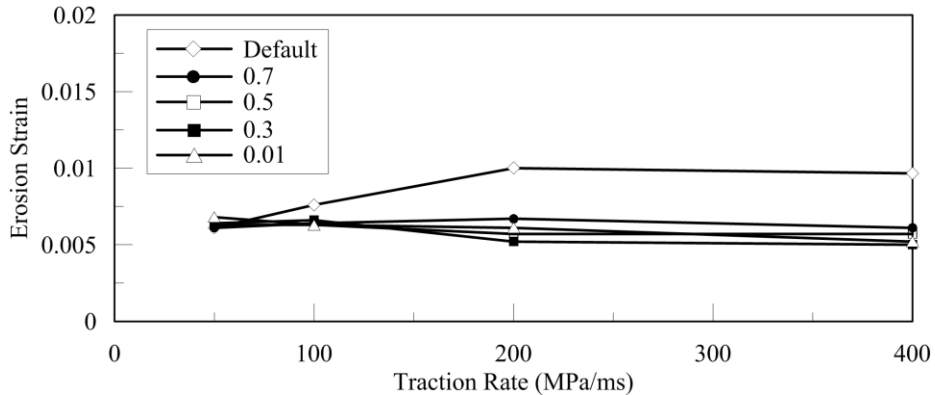
**Table 6-4 Influence of boundary conditions in the single element simulations for a compressive strength of 35.5 MPa at 200 MPa/msec**

Element size	Peak tensile traction	Erosion strain		Error (%)
		Simply supported	Fixed	
20×20×20 mm	10 MPa	0.0080	0.0074	7
	20 MPa	0.0095	0.0093	2
40×40×40 mm	10 MPa	0.0037	0.0034	8
	20 MPa	0.014	0.013	7
80×80×80 mm	10 MPa	0.0032	0.0030	6
	20 MPa	0.016	0.016	0

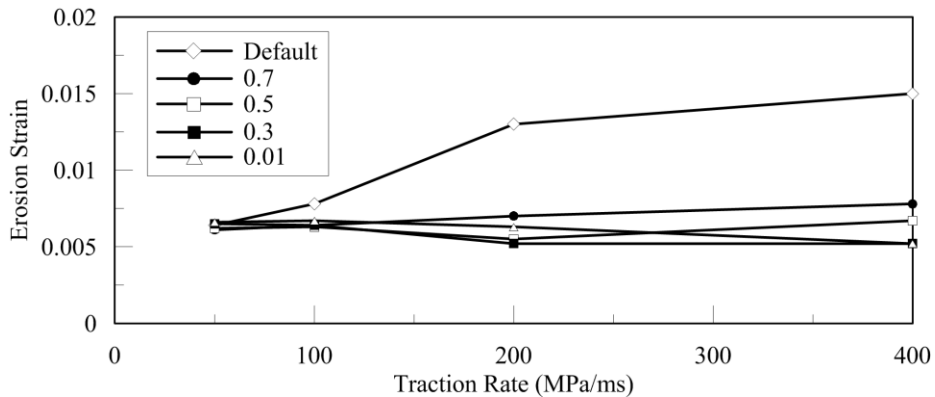
Erosion is assumed when the damage parameter for tension (Equation 6-25) equals or exceeds 0.99. Traction rate is used instead of strain rate to observe concrete erosion strains in this study for two reasons: 1) strain rate increases with traction rate and is proportional to velocity, which changes continuously with time for blast-type loadings (see Figure 6-13), and 2) strain rate increases rapidly during the softening phase of the concrete. Given that the purpose of the study is to evaluate concrete erosion strain for blast loadings rather than for a particular strain rate, parameters that best characterize the loading conditions such as traction rate and peak tensile traction are used to present the results of the single element simulations. Three single-degree-of-freedom (SDOF) calculations are performed to validate the LS-DYNA calculations of strain rate; results are presented in Appendix F.

The maximum time step for explicit analysis is established by the Courant condition: the length of the smallest element divided by the sound speed in the material (= 3600 m/sec for concrete). The effect of the time step on the results is investigated by performing analysis using time steps less than the maximum value: 0.7, 0.5, 0.3 and 0.01 times the maximum value. Analysis is performed for the 40×40×40 mm element subjected to the blast-type loadings of Figure 6-13 with peak tensile tractions of 10 and 20 MPa. Results are presented in Figure 6-14. “Default” in

the legend corresponds to the maximum time step. The five erosion strain versus traction rate relationships are similar except for the curve of the maximum time step. A factor of 0.5 on the default time step is used hereafter because the results are essentially unchanged for factors less than 0.5.



(a) Peak tensile traction = 10 MPa



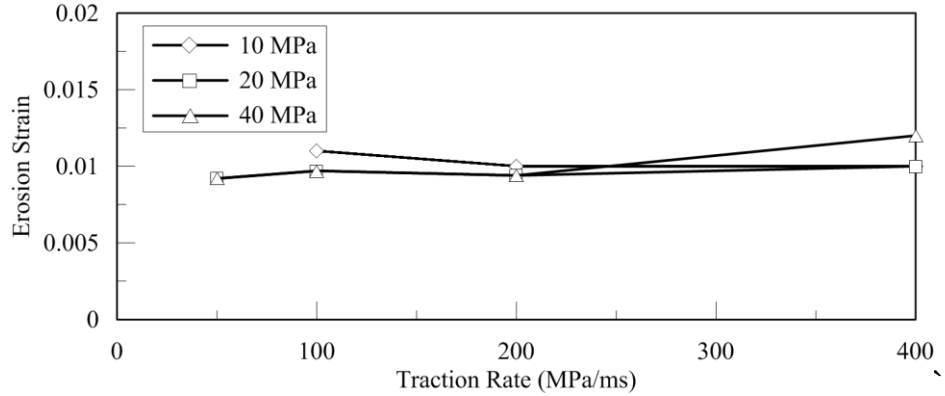
(b) Peak tensile traction = 20 MPa

**Figure 6-14 Time step convergence analysis for an element size of 40×40×40 mm**

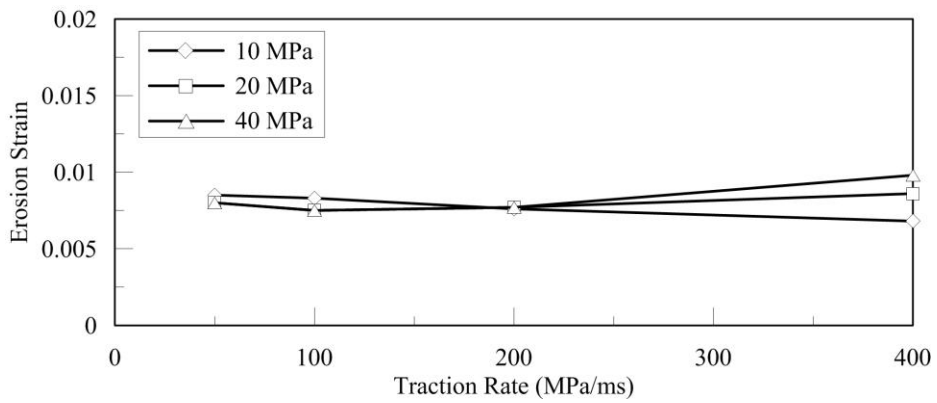
Figures 6-15 to 6-18 present erosion strain versus traction rate for different loading conditions and element sizes. Figure 6-15 illustrates the relationships between concrete erosion strain, traction rate and peak tensile tractions of 10, 20 and 40 MPa for each size of the single element: the assumed compressive strength is 35.5 MPa. Figure 6-16 presents similar data for a compressive strength of 50 MPa.

The erosion strains are similar for a given size of element across traction rates between 50 and 400 MPa/msec, both compressive strengths and all three peak tensile tractions. Figures 6-17 and

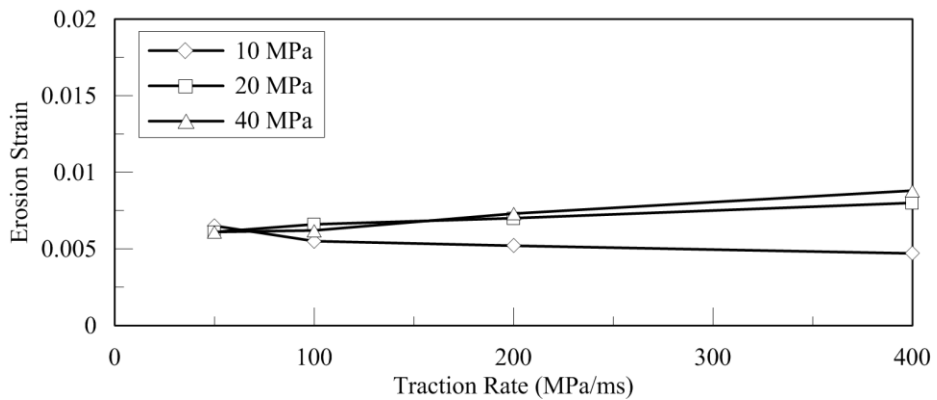
6-18 recast the data of Figures 6-15 and 6-16, respectively, to observe the effects of element size on erosion strain. The smaller the size of the element, the greater the erosion strain because the fracture energy is independent of element size.



(a) 20 mm element

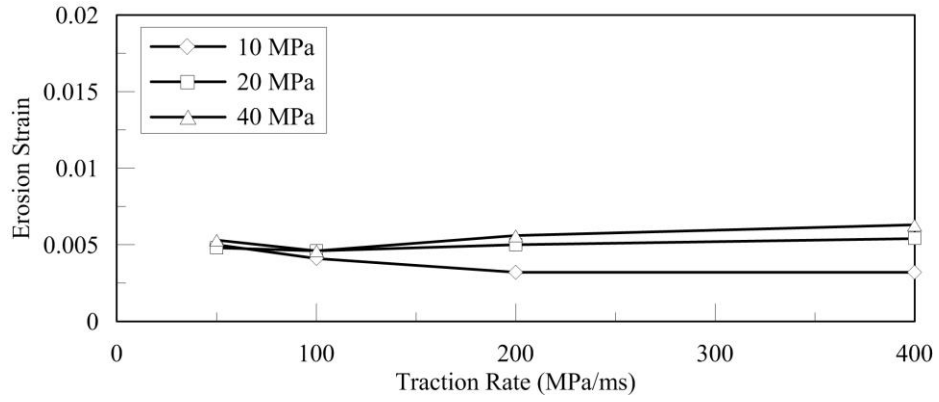


(b) 30 mm element

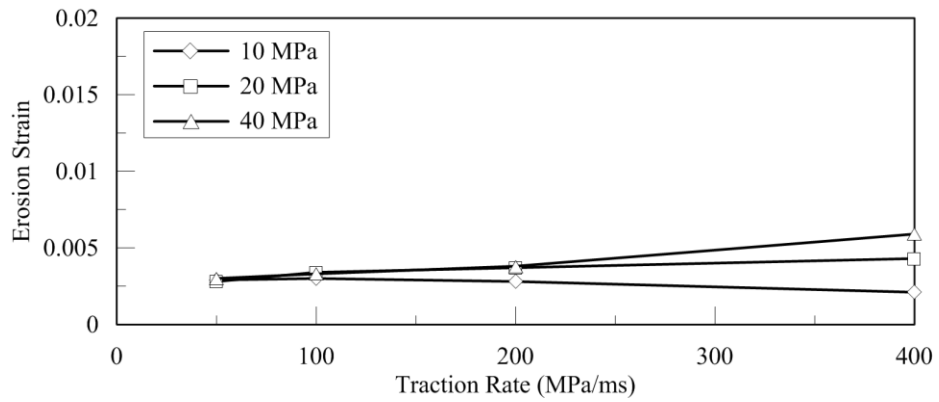


(c) 40 mm element

**Figure 6-15 Erosion strain versus traction rate in single element simulations for different peak tensile tractions,  $f'_c = 35.5$  MPa**

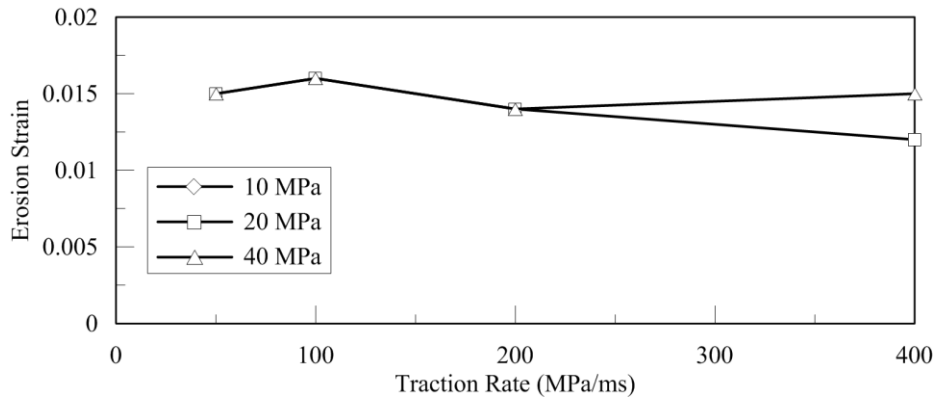


(d) 60 mm element

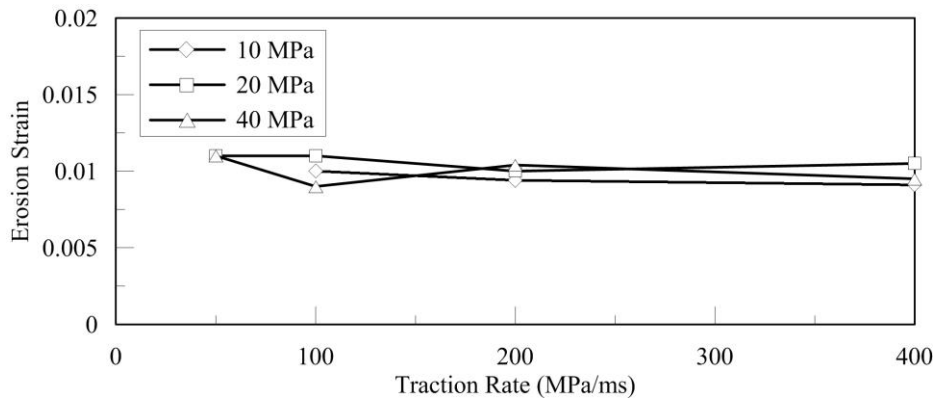


(e) 80 mm element

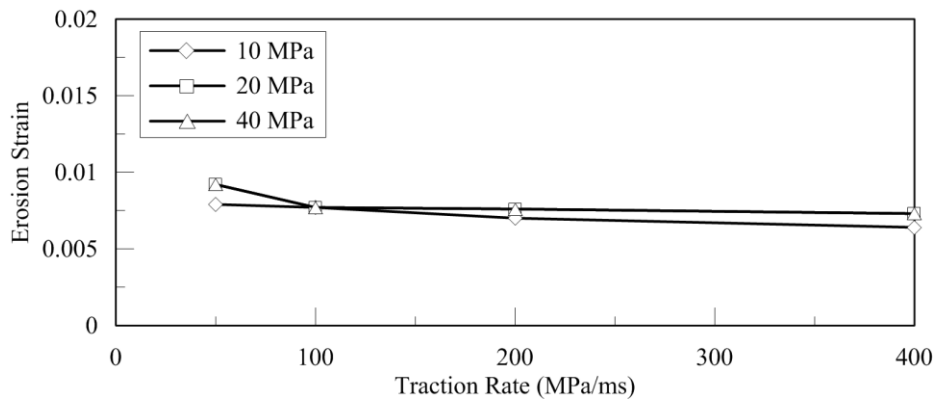
**Figure 6-15 Erosion strain versus traction rate in single element simulations for different peak tensile tractions,  $f'_c = 35.5$  MPa (cont.)**



(a) 20 mm element

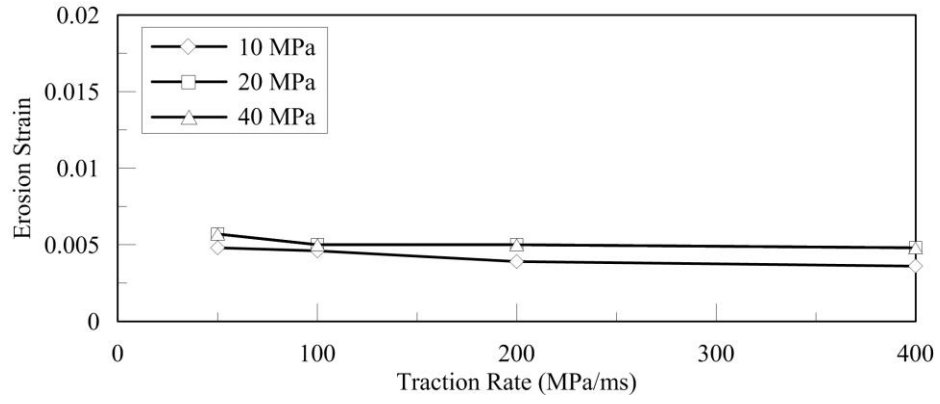


(b) 30 mm element

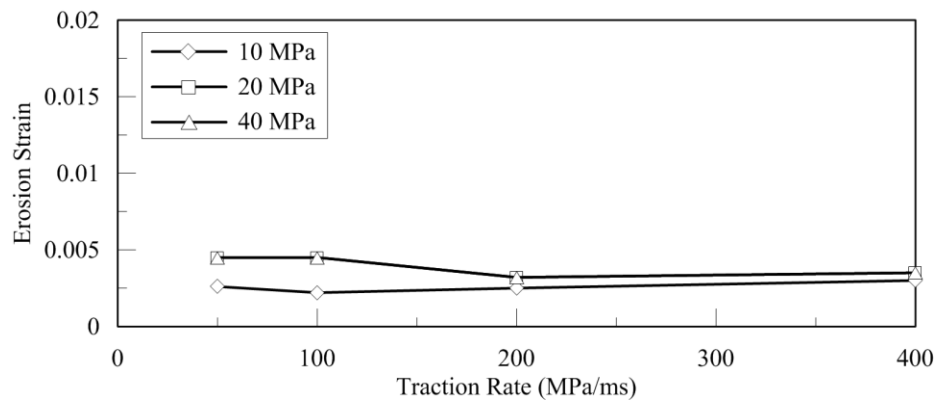


(c) 40 mm element

**Figure 6-16 Erosion strain versus traction rate in single element simulations for different peak tensile tractions,  $f'_c = 50$  MPa**

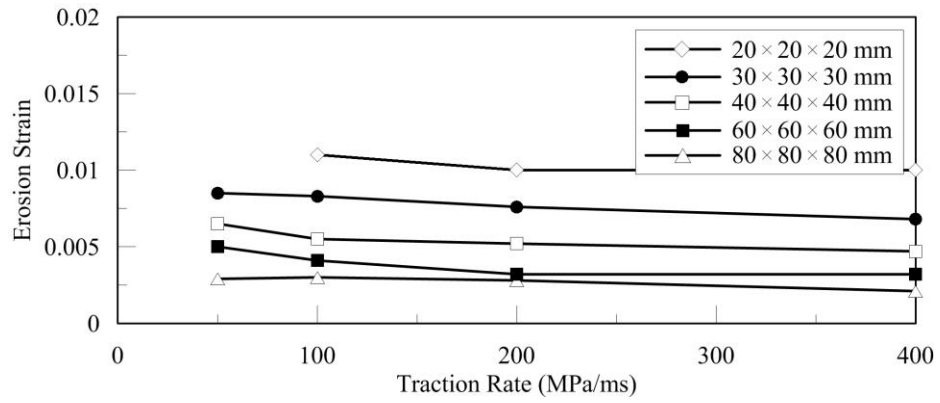


(d) 60 mm element

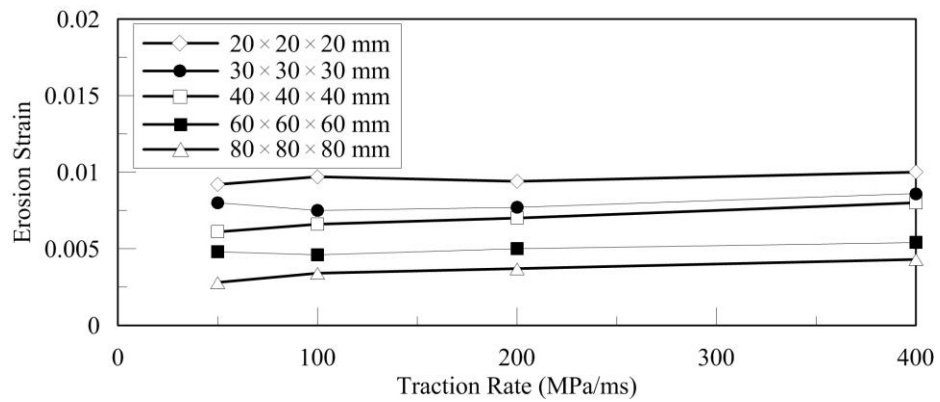


(e) 80 mm element

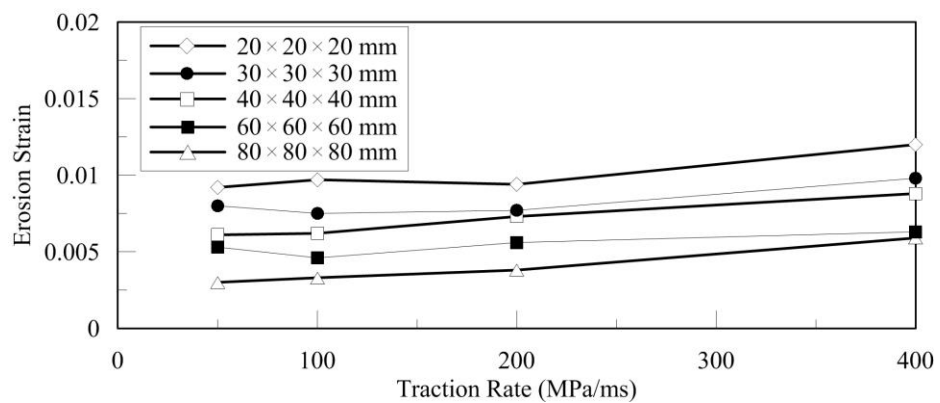
**Figure 6-16 Erosion strain versus traction rate in single element simulations for different peak tensile tractions,  $f'_c = 50$  MPa (cont.)**



(a) Peak tensile traction = 10 MPa

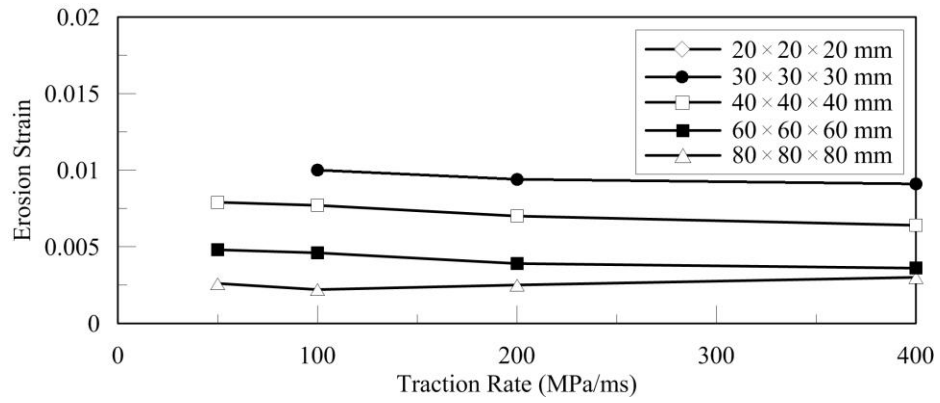


(b) Peak tensile traction = 20 MPa

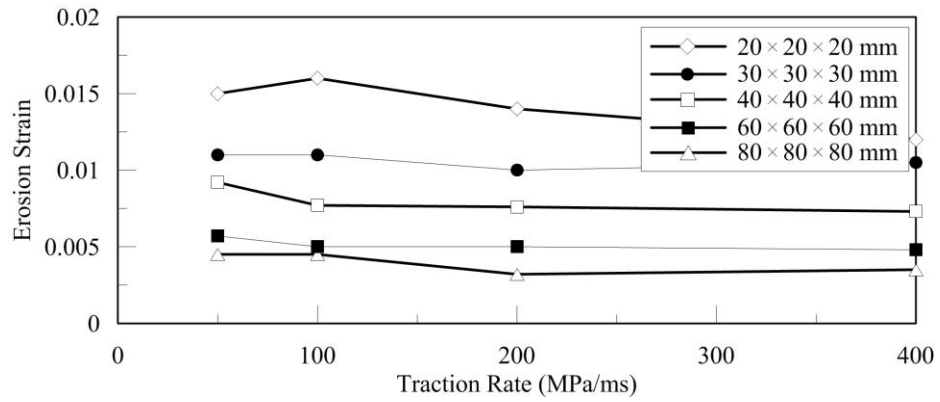


(c) Peak tensile traction = 40 MPa

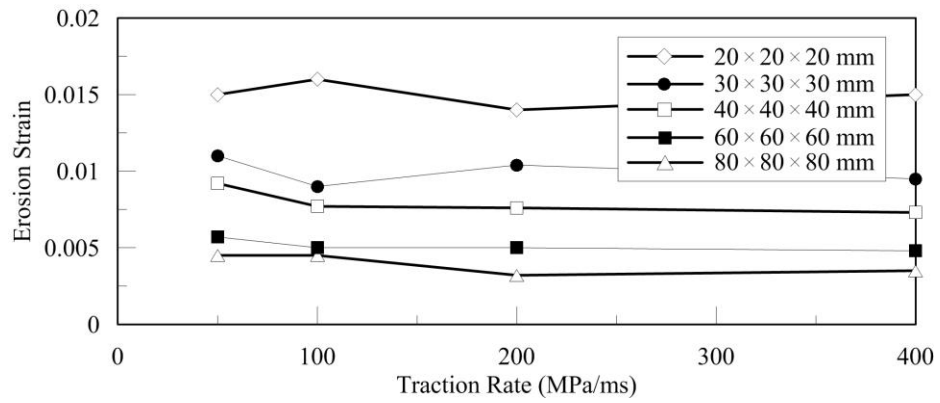
**Figure 6-17 Erosion strain versus traction rate in single element simulations for different element sizes,  $f'_c = 35.5$  MPa**



(a) Peak tensile traction = 10 MPa



(b) Peak tensile traction = 20 MPa



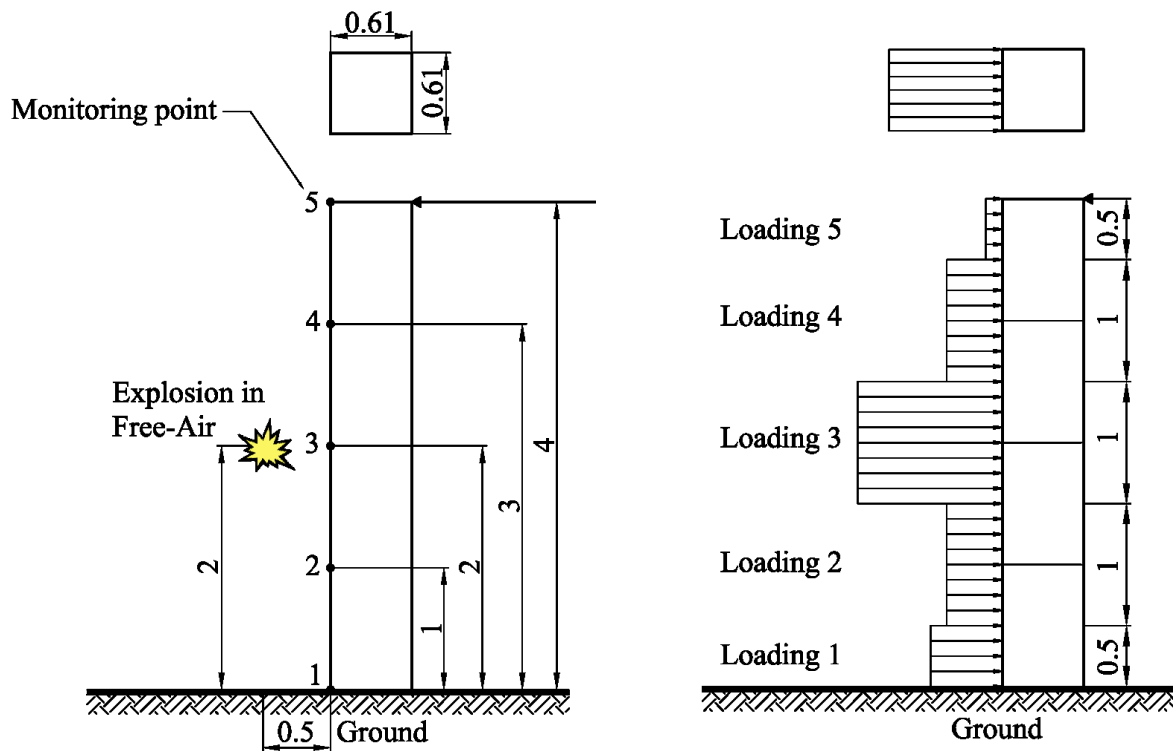
(c) Peak tensile traction = 40 MPa

**Figure 6-18 Erosion strain versus traction rate in single element simulations for different element sizes,  $f'_c = 50$  MPa**

## 6.6 Blast Analysis of a Sample Reinforced Concrete Column

### 6.6.1 Introduction

A sample RC column is subjected to air-blast loading to illustrate the differences in damage predictions that arise due to the use of alternate models for erosion strain. The column has a square cross section with plan dimensions of 0.61 m  $\times$  0.61 m (2 $\times$ 2 ft) and a height of 4 m (= 13 ft). The vertical reinforcement ratio is 2 percent (12 $\times$ #9 rebar of ASTM A615 Grade 60 uniformly distributed on all faces of the column; see ASTM 2003). The transverse reinforcement is #5 rebar perimeter seismic (or closed) hoops per ACI 318-11 (ACI 2011) with a vertical spacing of 10 cm (= 4 in). The 20 kg (= 44.1 lb) TNT explosive charge is spherical and located at the half height of the column at a stand-off distance of 0.5 m (= 20 in) as shown in Figure 6-19. The scaled distance,  $Z$ , is 0.19 m/kg<sup>1/3</sup>: a near-field detonation for which damage is expected.



(a) Monitoring locations of reflected pressures (b) Application of recorded reflected pressures

Figure 6-19 Blast loading calculations (units: m)

The analysis of the column is performed in LS-DYNA (LSTC 2013). Concrete and reinforcement are modeled in LS-DYNA using MAT\_CSCM and MAT\_JOHNSON\_COOK, respectively. Perfect bond between concrete and reinforcement is assumed. The air-blast pressure loadings on the front face of the column are computed using Air3D (Rose 2006), and AUTODYN (ANSYS 2013a) and then applied to the model of the sample RC column. A mesh convergence study is performed to identify reasonable element sizes for the simulations. Erosion strains of concrete are calculated for the element sizes established in the mesh convergence study using the single element simulations described in the previous section.

The blast analysis of the sample RC column is performed using the concrete erosion strains calculated in this study. Analysis is also performed using a) the erosion strains of 0.075 and 0.01 used by Luccioni et al. (2004) and Xu and Lu (2006), respectively, and b) the damage functions of the CSCM model that do not require the user to specify an erosion strain. Simulations are performed to ensure transportability to other concrete models of the erosion strains computed using the CSCM model. The influence of concrete compressive strength, confinement using transverse reinforcement, and axial pressure loading on damage to the column are also addressed through simulation.

### ***6.6.2 Blast Loading***

The histories of the reflected overpressures are computed along the height of the sample RC column using Air3D and AUTODYN. One-dimensional analysis is performed for the explosion in free air before the shock front reaches a reflecting surface (the target or the ground in this instance) and the results of the one-dimensional analysis are then mapped into a three-dimensional domain.

For the purpose of the simulations, pressure histories or time series are monitored in Air3D and AUTODYN on the centerline of the sample RC column at the five locations shown in Figure 6-19(a). The pressure histories calculated at the monitoring locations 1, 2, 3, 4 and 5 are applied to the column modeled in LS-DYNA as loadings 1, 2, 3, 4 and 5, respectively, as shown in Figure 6-19(b). The reflected peak pressure at monitoring location 3 is approximately 10 times greater than at monitoring locations 2 and 4. The reflected pressure histories obtained from Air3D and

AUTODYN are similar as presented in Figure 6-20. The reflected peak pressures at monitoring location 1 are greater than at monitoring location 5 due to the reflection of the shock front at the ground surface. The AUTODYN results are used for the simulations because of concerns regarding the accuracy of Air3D for near-field detonations (Anderson 2003) although the differences between the AUTODYN and Air3D results are small.

The use of these pressure histories for analyses will overestimate the loading on the column because clearing will reduce the reflected pressure at the edges of the column and pressure loading on the back face of the column will reduce the net loading. Axial load will accumulate in the column due to pressure loading on the underside of the floor system that the column is supporting but this is not considered here.

### ***6.6.3 Mesh Convergence Study***

A mesh convergence study is performed to determine a reasonable balance between solution accuracy and computation expense. Five finite element meshes ( $20 \times 20 \times 20$ ,  $30 \times 30 \times 30$ ,  $40 \times 40 \times 40$ ,  $60 \times 60 \times 60$  and  $80 \times 80 \times 80$  mm) of the sample RC column are prepared and analyzed using the AUTODYN pressure histories. Erosion is not implemented for these calculations.

The points of reference for the mesh convergence study are the horizontal displacement history at the mid-height of the column and the horizontal reaction history at the bottom of the column. Results are presented in Figure 6-21. Although the horizontal reaction histories are similar for all mesh sizes, the displacement history for the  $80 \times 80 \times 80$  mm mesh is somewhat different from those for the  $20 \times 20 \times 20$ ,  $30 \times 30 \times 30$ ,  $40 \times 40 \times 40$  and  $60 \times 60 \times 60$  mm meshes. Accordingly, the four smaller mesh sizes are used for the simulations that included erosion.

The mesh convergence study provides an initial estimate of the response of the sample column. The maximum displacement of the column at its mid-height is on the order of 20 mm, or span/200, which is unlikely to produce significant flexural damage. The maximum reaction is 3000 kN, which greatly exceeds the ACI limit of  $V_n = 0.83\sqrt{f'_c}b_wd = 1840$  kN ( $10\sqrt{f'_c}b_wd$  in US

units). Although strain rate effects may substantially increase shear resistance above this ACI limit, the magnitude of the peak shearing force indicates that damage near the support is likely.

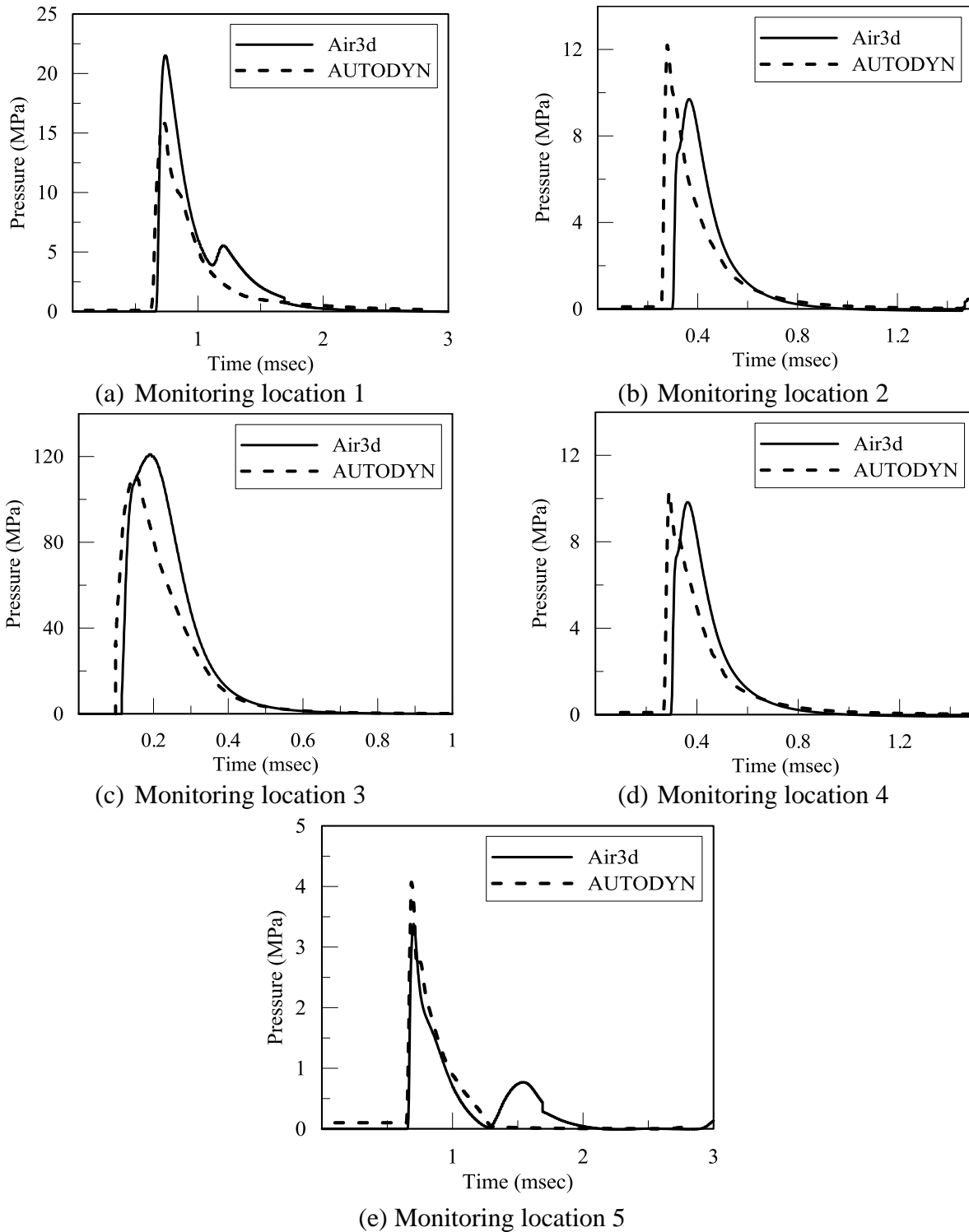
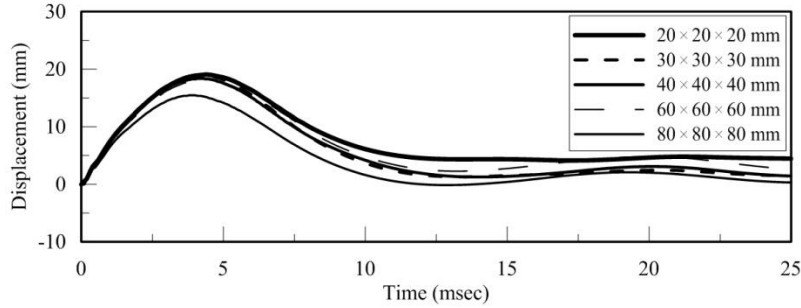
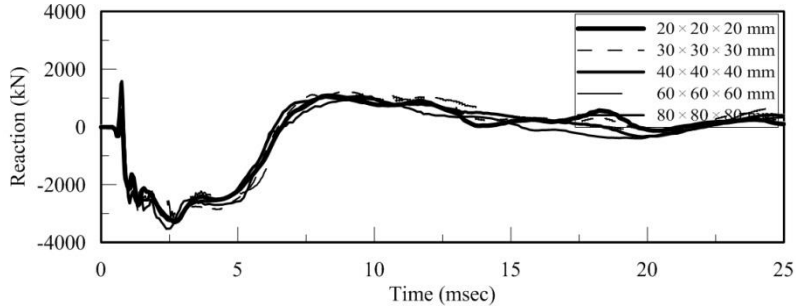


**Figure 6-20 Reflected pressure histories on the sample reinforced concrete column**



(a) Horizontal displacement histories at mid-height



(b) Horizontal reaction histories at bottom

**Figure 6-21 Mesh convergence study of the sample RC column**

#### **6.6.4 Values of Concrete Erosion Strain**

If discrete values of erosion strain are to be used to predict damage in a reinforced concrete column, the expected tensile pressures (tractions) and traction rates in the regions of the expected damage must be established. For the sample column, the greatest damage in terms of eroded material is expected on the rear face of the column, near its mid-height. To guide the calculation of these tractions and traction rates, two analyses of the column are performed using different material models and assuming a concrete compressive strength of 35.5 MPa: 1) elastic finite elements with the small-strain values of modulus and Poisson’s ratio, and 2) a composite of CSCM and elastic elements. Figure 6-22 shows the second model for the 20×20×20 and 40×40×40 mm meshes, where the 30 solid filled elements are elastic and the remainder are CSCM. The small number of embedded elastic elements will not affect the global response of the column. Erosion is not considered. Figure 6-23 presents the maximum principal stress histories of an elastic element near the rear face and mid-height of the column for the two analyses. Model 1 is denoted “Elastic”; model 2, “CSCM” embeds 30 elastic elements in the mesh. The results of

the analysis of the “Elastic” models grossly overestimate the expected peak tensile traction and traction rates and so the computationally more expensive CSCM model must be used.

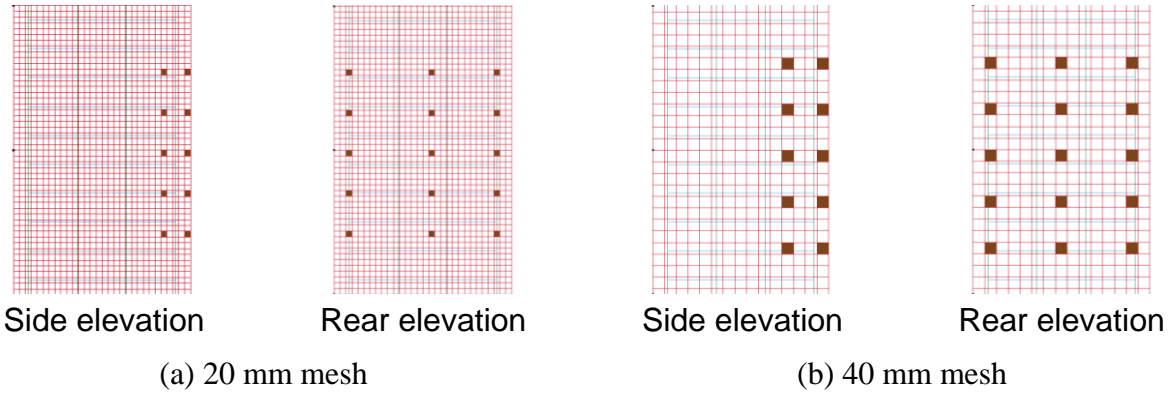


**Figure 6-22 FE models of the sample RC column to estimate traction rates and peak tensile stresses (tractions) for 30 elements near or on the rear face of the column at its mid-height**

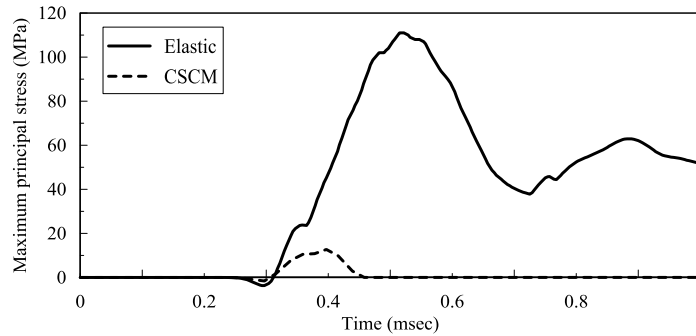


**Figure 6-23 Maximum principal tensile stress history of an elastic element in models 1 and 2, 40 mm mesh**

The maximum (tensile) principal stress histories for the 30 elastic elements in model 2 are presented in Figure 6-24. The peak tensile stresses (tractions) range between 15 and 20 MPa and the tensile stress (traction) rates are between 150 and 200 MPa/msec. A number of loading pulses are evident in these stress histories, which are associated with the arrival of the first incident and subsequent reflected shock waves.

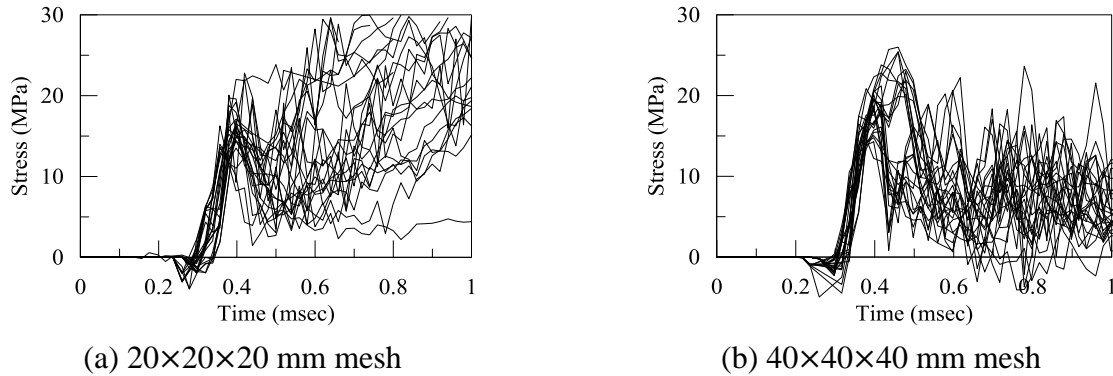


**Figure 6-24 Maximum principal tensile stress histories for 30 elements near or on the rear face of the column at its mid-height; model 2**

Values of erosion strain can be estimated for concrete compressive strengths of 35.5 and 50 MPa from Figures 6-15, 6-16, 6-17 and 6-18. From Figure 6-15, for element sizes of  $20 \times 20 \times 20$ ,  $30 \times 30 \times 30$ ,  $40 \times 40 \times 40$  and  $60 \times 60 \times 60$  mm, 35.5 MPa concrete, peak tensile tractions between 15 and 20 MPa, and loading rates between 150 and 200 MPa/msec, the erosion strains are approximately 0.01, 0.008, 0.006 and 0.005, respectively. These four values of erosion strains are used in the simulations presented in the following section.

### **6.6.5 Simulation Results**

Simulations of the blast response of the sample RC column are performed using  $20 \times 20 \times 20$ ,  $30 \times 30 \times 30$ ,  $40 \times 40 \times 40$ , and  $60 \times 60 \times 60$  mm meshes of the column. Calculations are made for the four mesh-dependent values of erosion strain identified above, the damage-based erosion algorithm of Section 6.4.1.2, and the mesh-independent values of 0.01 (Xu and Lu, 2006) and 0.075 (Luccioni et al. 2004).

Figures 6-25 through 6-28 present displacement histories at the mid-height of the column on the loading face for the  $20 \times 20 \times 20$ ,  $30 \times 30 \times 30$ ,  $40 \times 40 \times 40$ , and  $60 \times 60 \times 60$  mm meshes, respectively. Horizontal reaction histories at the bottom of the column are presented in Figures 6-29 through 6-32. The displacement and reaction are positive in the direction of the loading. The displacement histories are essentially independent of mesh size for a given value of erosion strain or if the damage-based algorithm is used. The peak displacement and time to peak displacement calculated with considerations of erosion are similar to those of Figure 6-21. The

implementation of erosion results in substantially greater calculated values of residual displacements, and, as expected, the smaller the value of the erosion strain, the greater the residual displacement. The displacement history computed using an erosion strain of 0.075 is most similar to that of Figure 6-21, where erosion was not considered.

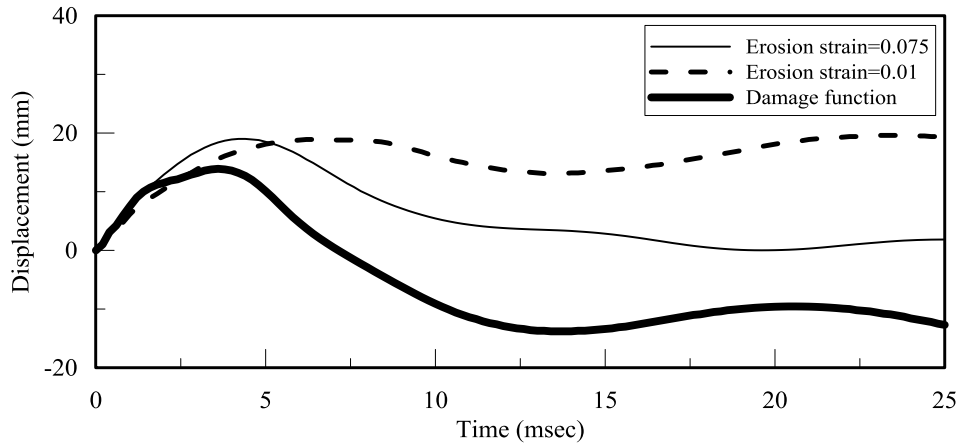


**Figure 6-25 Displacement histories at the mid-height of the column for the 20×20×20 mm mesh**

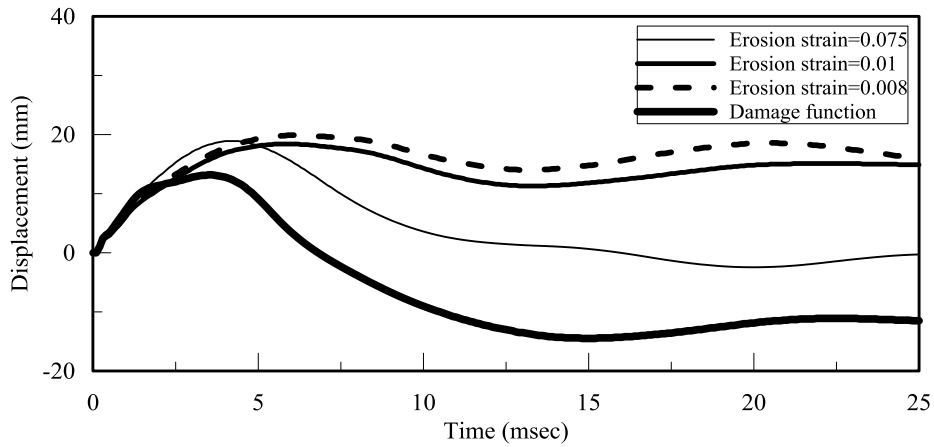


**Figure 6-26 Displacement histories at the mid-height of the column for the 30×30×30 mm mesh**

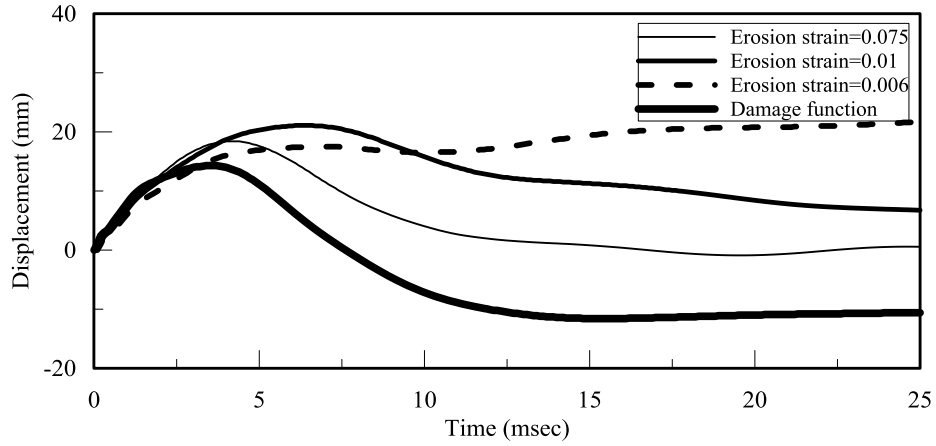


**Figure 6-27 Displacement histories at the mid-height of the column for the 40×40×40 mm mesh**

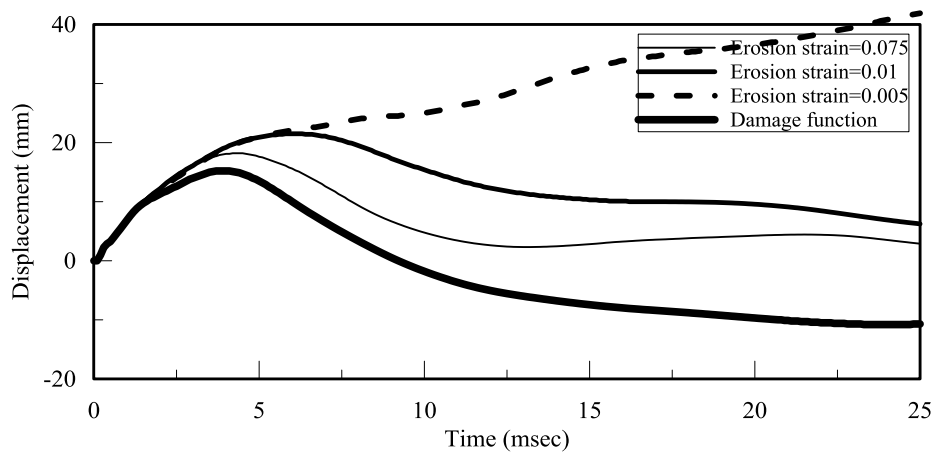


**Figure 6-28 Displacement histories at the mid-height of the column for the 60×60×60 mm mesh**

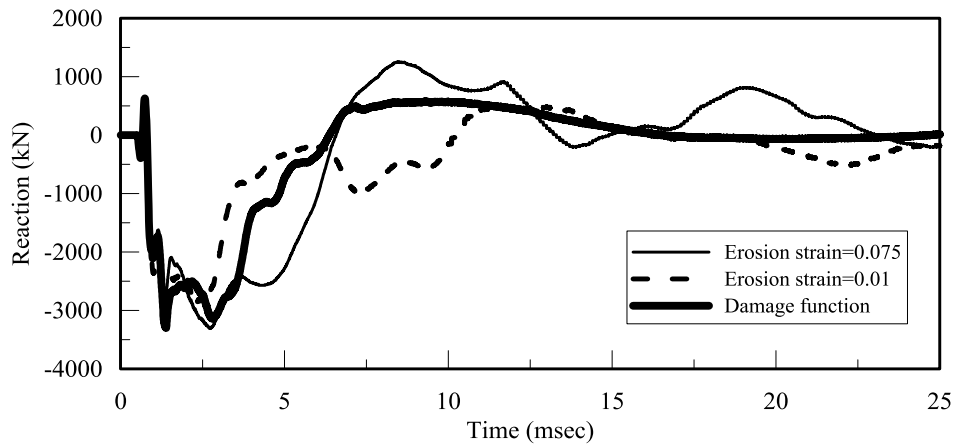


**Figure 6-29 Reaction histories at the bottom of the column for the 20×20×20 mm mesh**

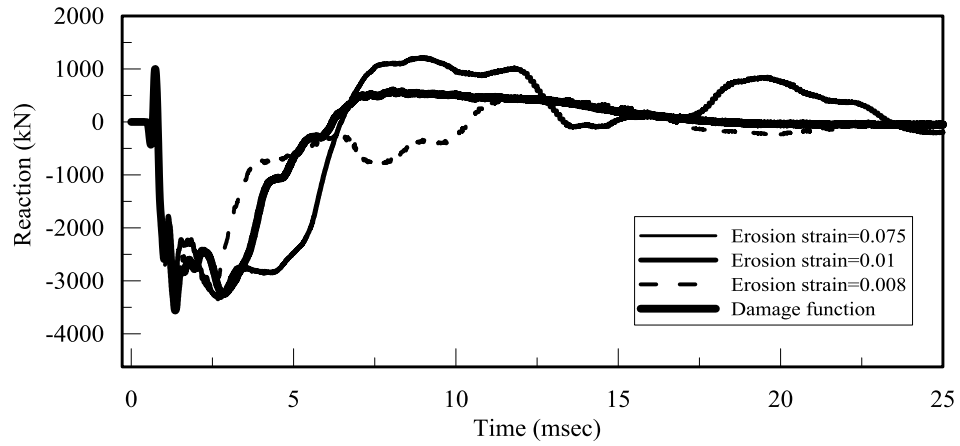


**Figure 6-30 Reaction histories at the bottom of the column for the 30×30×30 mm mesh**

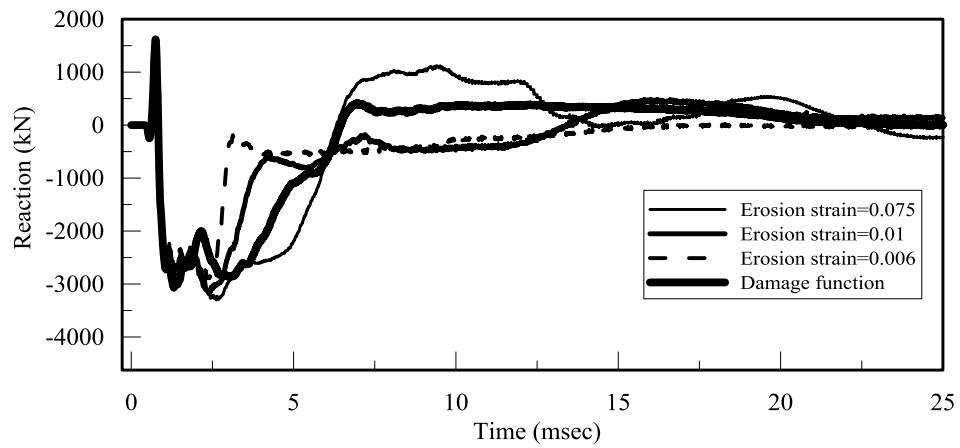


**Figure 6-31 Reaction histories at the bottom of the column for the 40×40×40 mm mesh**

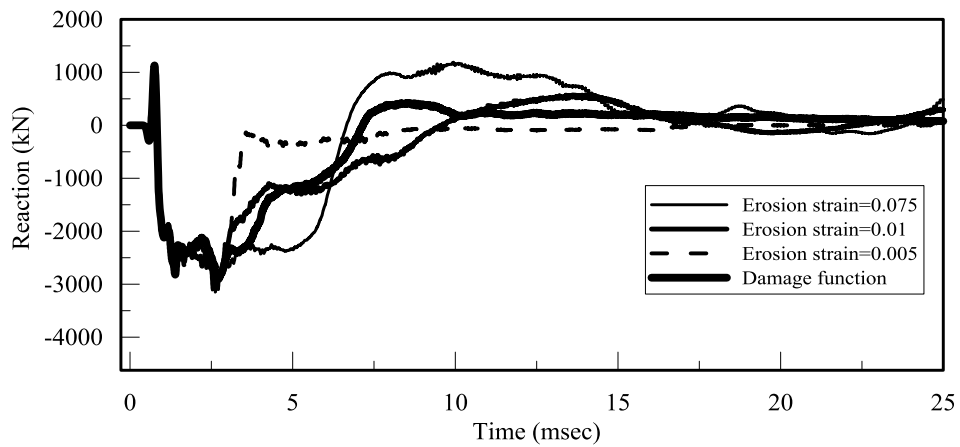


**Figure 6-32 Reaction histories at the bottom of the column for the 60×60×60 mm mesh**

The peak reactions are similar for all meshes and all simulations of erosion. The times to peak reactions are smaller than the corresponding times to peak displacement. The reaction is negative at approximately 0.75 msec, which is counter-intuitive. The negative reaction at this time instant is due to wave propagation, up and down the column, where the wave fields are complex due to reflection of compressive and tensile waves from the four free surfaces of the column. Figures 6-33 through 6-36 present internal energy histories for the 20×20×20, 30×30×30, 40×40×40, and 60×60×60 mm meshes, respectively. The internal energy (or deformation energy) is the sum of energies computed incrementally based on six components of stress and strain for all elements in the mesh. Internal energy is not recorded for eroded elements.

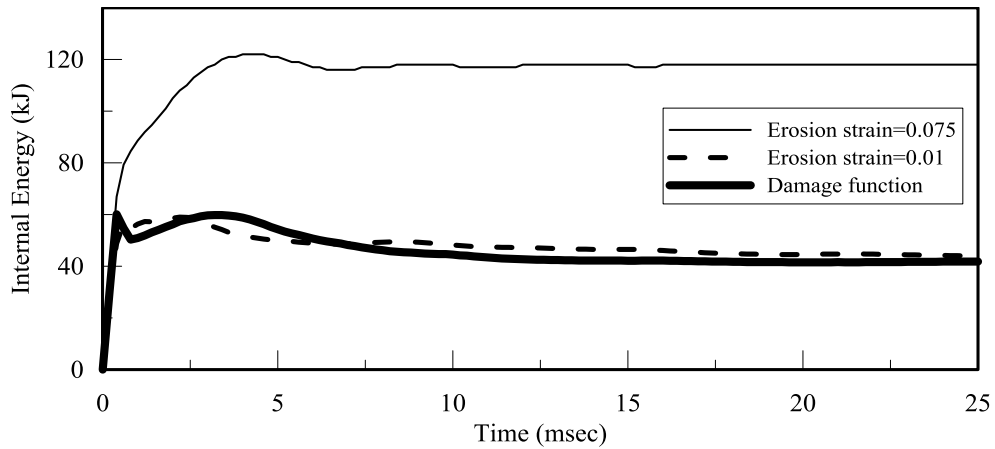


**Figure 6-33 Internal energy histories for the 20×20×20 mm mesh**

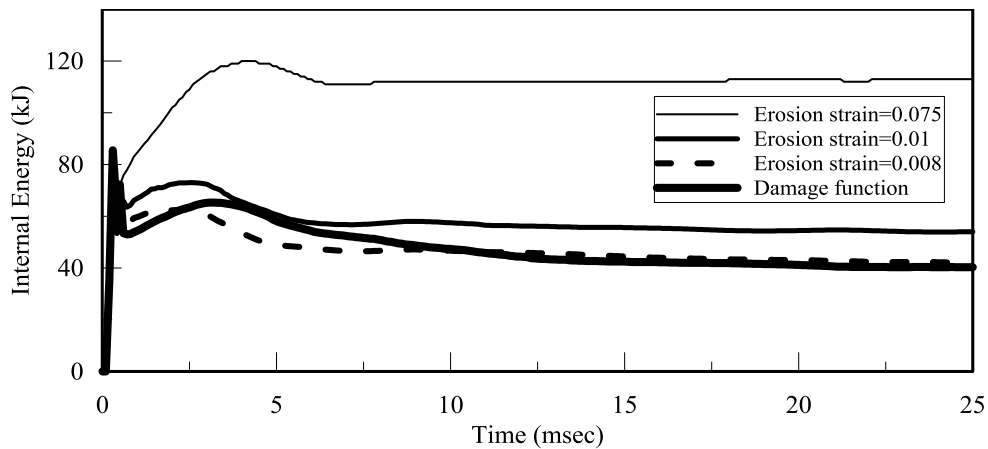


**Figure 6-34 Internal energy histories for the 30×30×30 mm mesh**

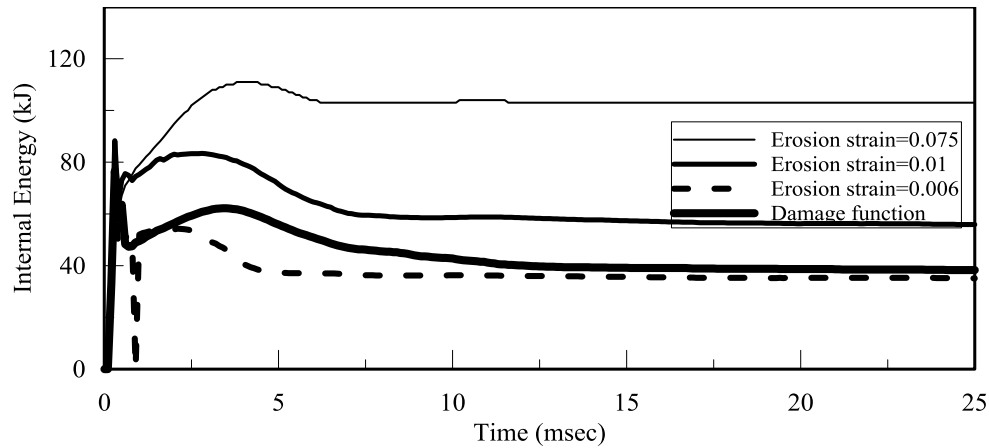


**Figure 6-35 Internal energy histories for the 40×40×40 mm mesh**

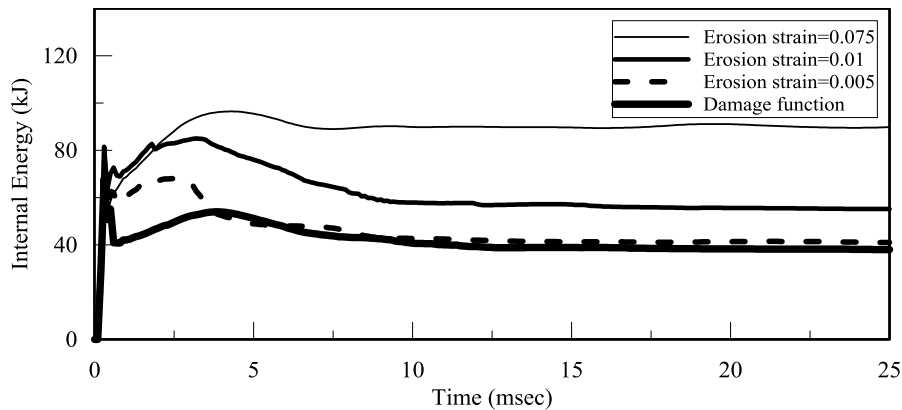


**Figure 6-36 Internal energy histories for the 60×60×60 mm mesh**

The internal energies for the two simulations using an erosion strain of 0.075 are considerably greater than for the other simulations because very few elements are eroded from the model as seen in Figures 6-37(a), 6-38(a), 6-39(a) and 6-40(a). For the 20×20×20 mm mesh, the internal energy histories associated with the mesh-dependent erosion strain of 0.01 and the damage-based erosion algorithm are very similar, with peak values of approximately 60 kJ. Similar trends are seen for other meshes. The internal energies do not return to zero after loading because of the permanent (residual) deformation of the column, as shown in Figures 6-25 through 6-28.

Figures 6-37 through 6-40 describe the damage to the sample column using side elevations and cross sections at the mid-height of the column for the simulations using the 20×20×20, 30×30×30, 40×40×40, and 60×60×60 mm meshes, respectively. Information is presented at a

time equal to 25 msec. Damage is acute for all meshes and simulations except those using an erosion strain of 0.075. Consistent with the internal energy histories of Figures 6-33 through 6-36, the extent of the damage to the column is similar for the simulations using the mesh-independent erosion strains and the damage-based erosion algorithm: panels (b) and (c) of Figure 6-37 and panels (c) and (d) of Figures 6-38, 6-39 and 6-40. Table 6-5 summarizes the percentage of the cross section lost at the mid-height of the column for each of the simulations. Axial load was not applied to the sample column but would have exacerbated the calculated damage. The effect of axial load on the predicted damage is presented in the following section.

**Table 6-5 Percentage erosion of the cross section at the mid-height of the column**

		20×20×20 mm	30×30×30 mm	40×40×40 mm	60×60×60 mm
Erosion strain	0.075	7 %	5 %	7%	0 %
	0.01	77 %	55 %	46 %	44 %
	0.008	Not calculated <sup>10</sup>	69	Not calculated	Not calculated
	0.006	Not calculated	Not calculated	64 %	Not calculated
	0.005	Not calculated	Not calculated	Not calculated	65
Damage function		73 %	75 %	70 %	69

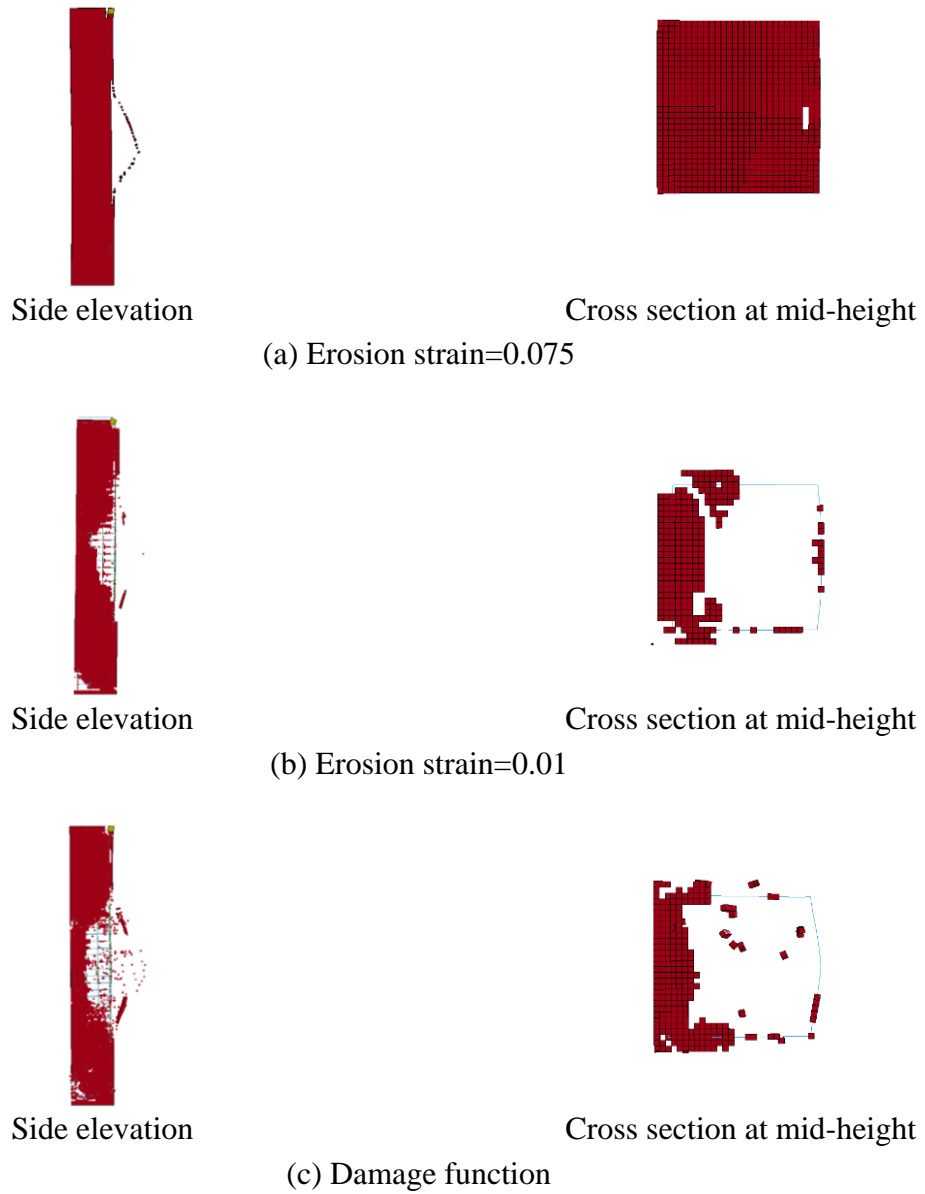


**Figure 6-37 Simulation results for the 20×20×20 mm mesh at time = 25 msec**

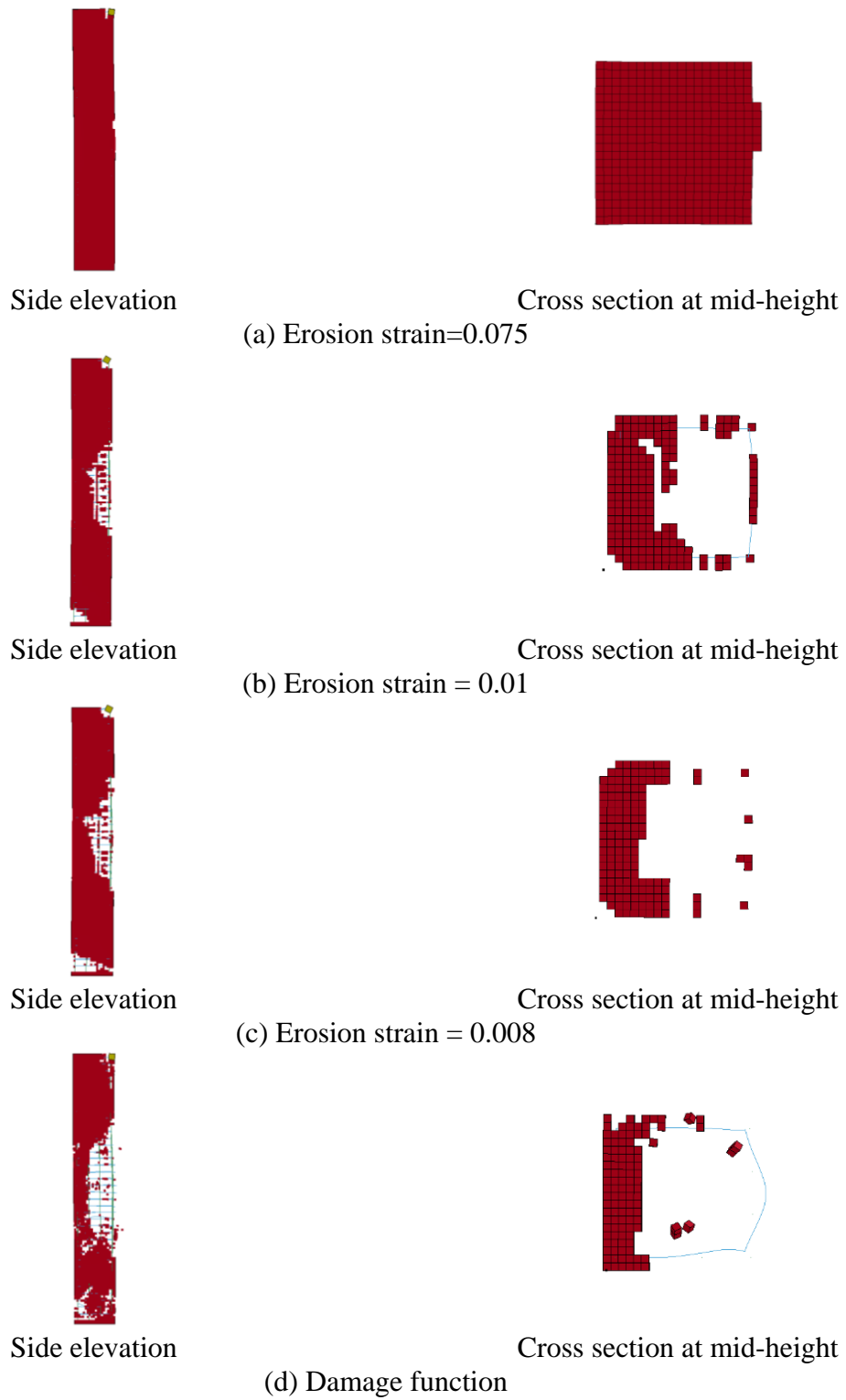


**Figure 6-38 Simulation results for the 30×30×30 mm mesh at time = 25 msec**

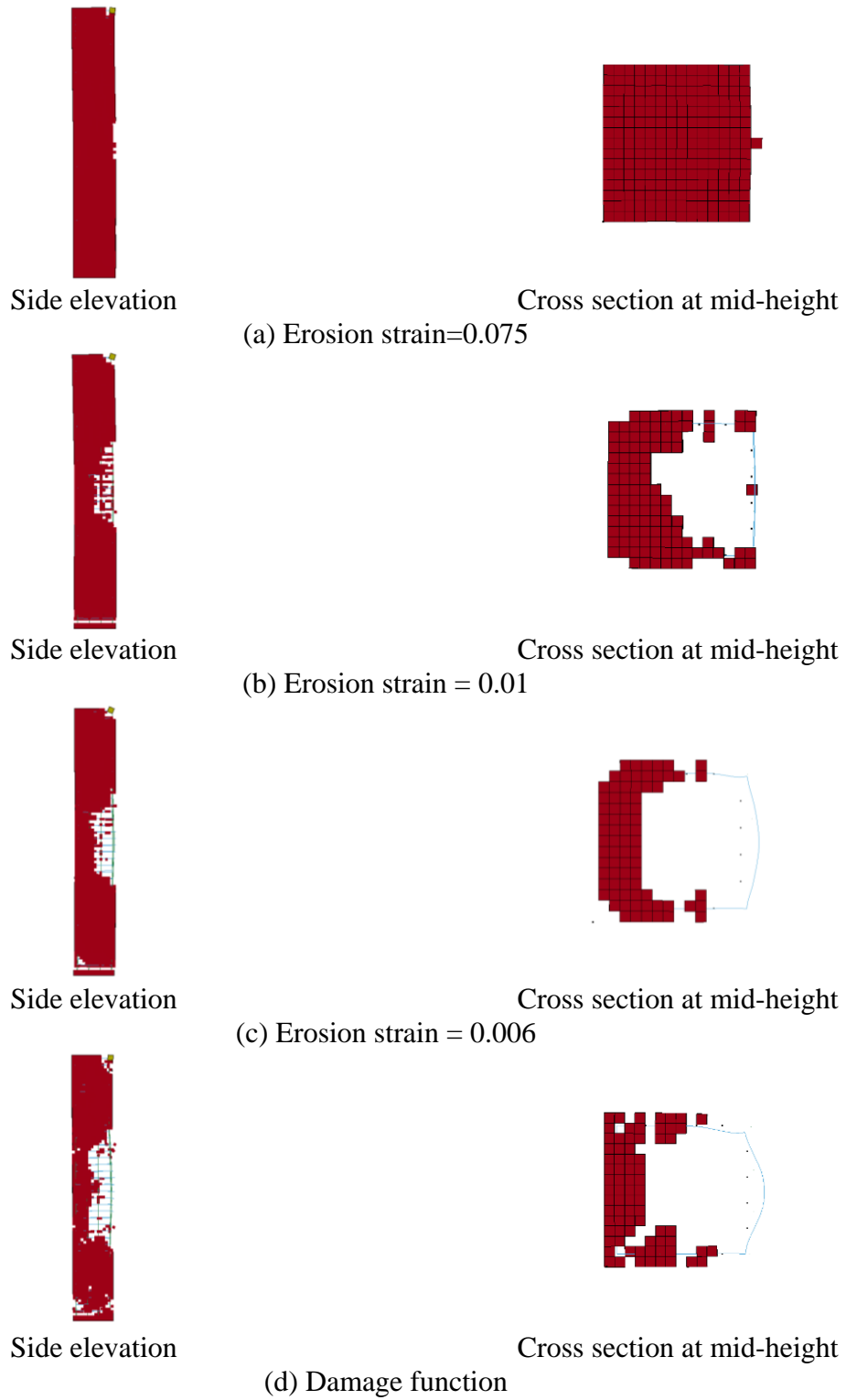


**Figure 6-39 Simulation results for the 40×40×40 mm mesh at time = 25 msec**

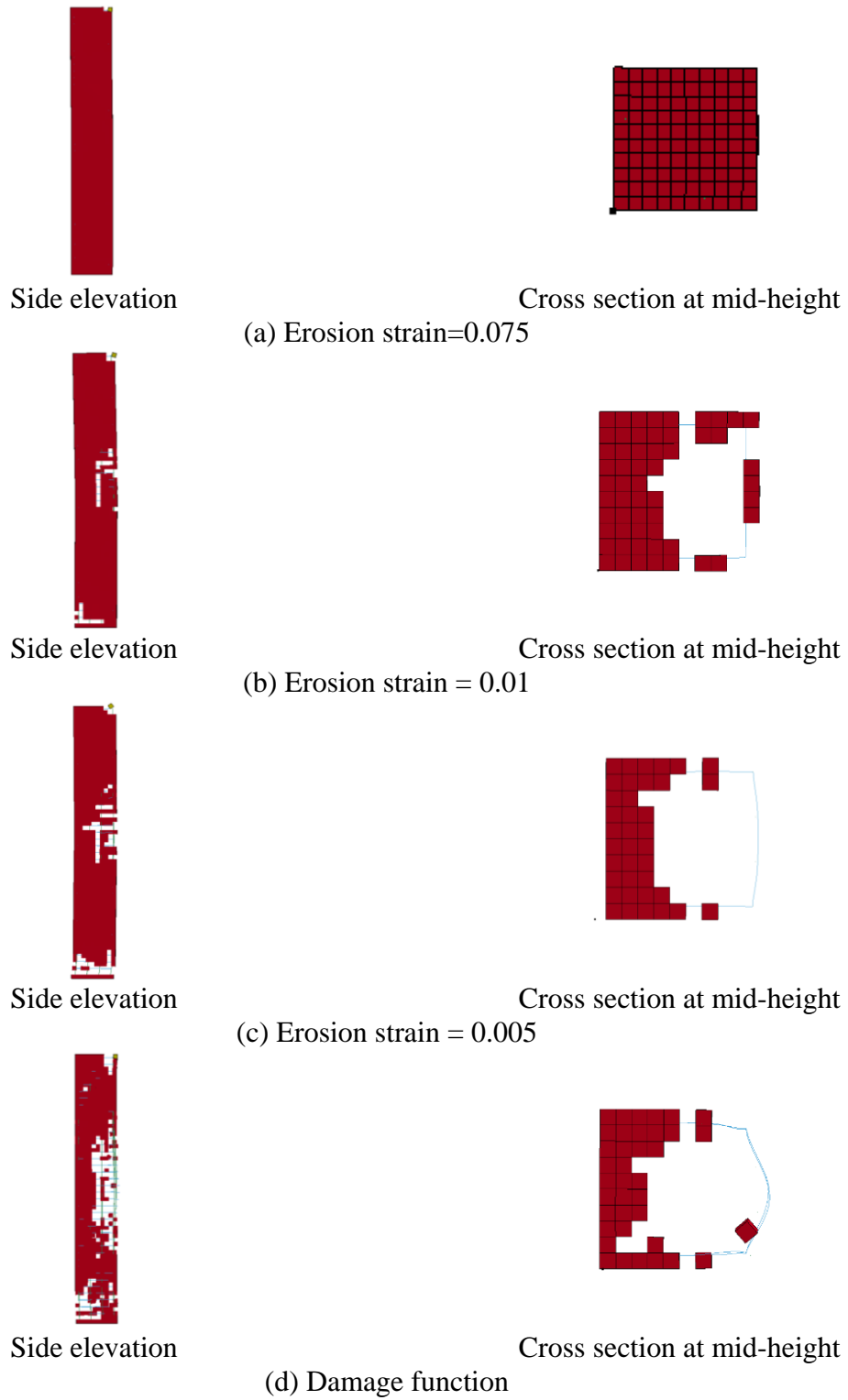


**Figure 6-40 Simulation results for the 60×60×60 mm mesh at time = 25 msec**

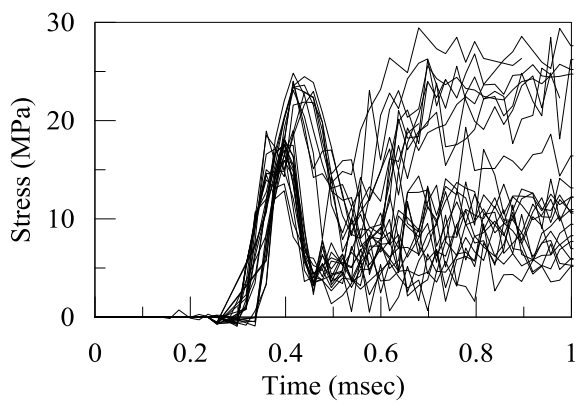
## ***6.6.6 Alternate Concrete Material Models, Influence of Concrete Compressive Strength, Confinement, and Axial Pressure Loading***

### *6.6.6.1 Introduction*

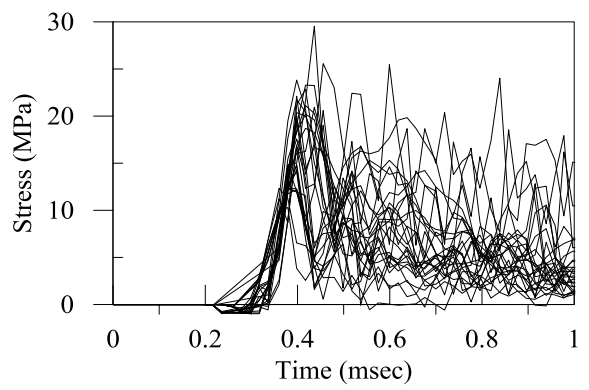
The sample RC column is further analyzed to understand 1) the utility of the discrete values of erosion strain when used with alternate concrete material models, 2) the influence of concrete compressive strength on the volume of eroded material, 3) the effect of confinement in the form of transverse reinforcement on the volume of eroded material, and 4) the effect of axial loading on the column on residual lateral displacements and damage. Mesh sizes of 20×20×20 mm, 30×30×30 mm and 40×40×40 mm are used for these analyses. The mesh-independent values of 0.01 (Xu and Lu, 2006) and 0.075 (Luccioni et al. 2004) are not considered.

### *6.6.6.2 Alternate Concrete Material Models*

The CONCRETE\_DAMAGE\_REL3 model (Malvar and Simons 1996) is used to judge the utility of the erosion strains proposed previously to predict damage using material models other than the CSCM. A concrete compressive strength of 35.5 MPa is used for the analysis. Figure 6-41 shows the maximum principal stress histories for the 30 elastic elements near or on the rear face of the column, near its mid-height, which are estimated for the alternate material model. The peak tensile stresses and stress rates shown in this figure are very similar to those calculated for the CSCM model and shown in Figure 6-24. Accordingly, the values of erosion strain used for the analysis of the CSCM model are adopted for analysis of the CONCRETE\_DAMAGE\_REL3 model. Figure 6-42 enables a comparison of the internal energy histories for the CSCM model using calculated erosion strains and the damage-based erosion algorithm, and the CONCRETE\_DAMAGE\_REL3 model using calculated erosion strains, for the 20×20×20 mm, 30×30×30 mm and 40×40×40 mm meshes. The results are virtually identical for all three meshes and the two concrete models. Descriptions of damage are presented in Figure 6-43. The eroded zones in the side elevation and cross section at mid-height for all three meshes are qualitatively similar to those for the CSCM model; see Figure 6-37b, Figure 6-38c and Figure 6-39c. The values of erosion strain computed using the CSCM model appear to be transportable across concrete material models.

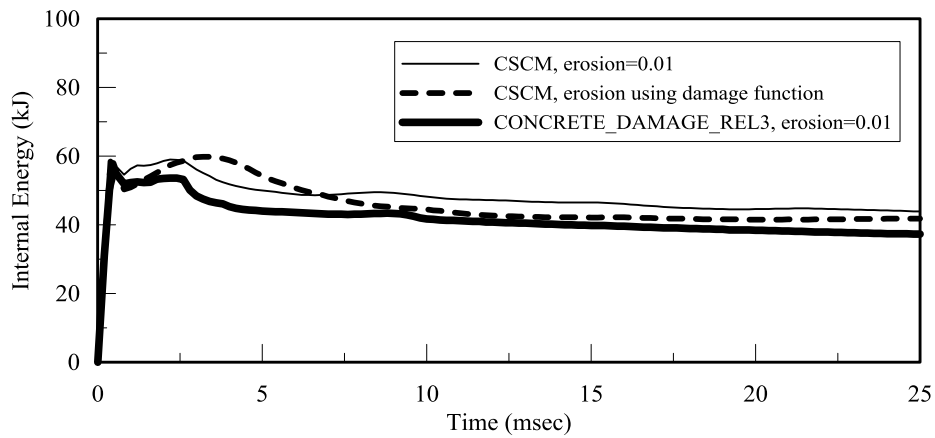


(a) 20×20×20 mm mesh

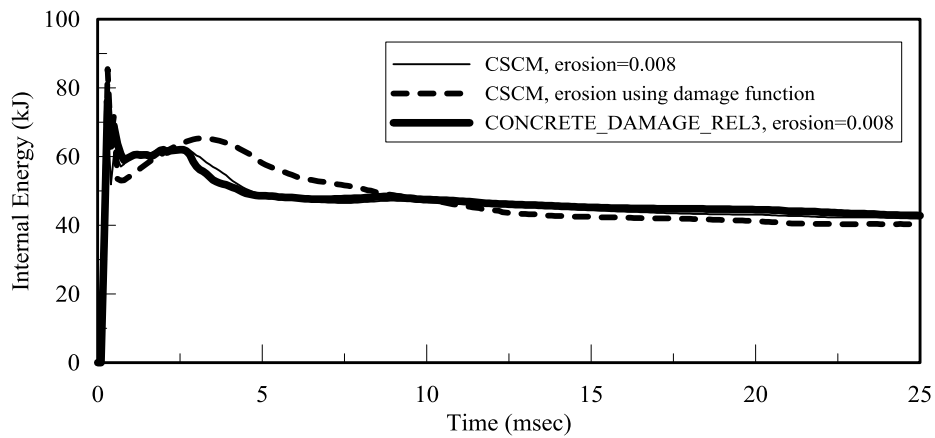


(b) 40×40×40 mm mesh

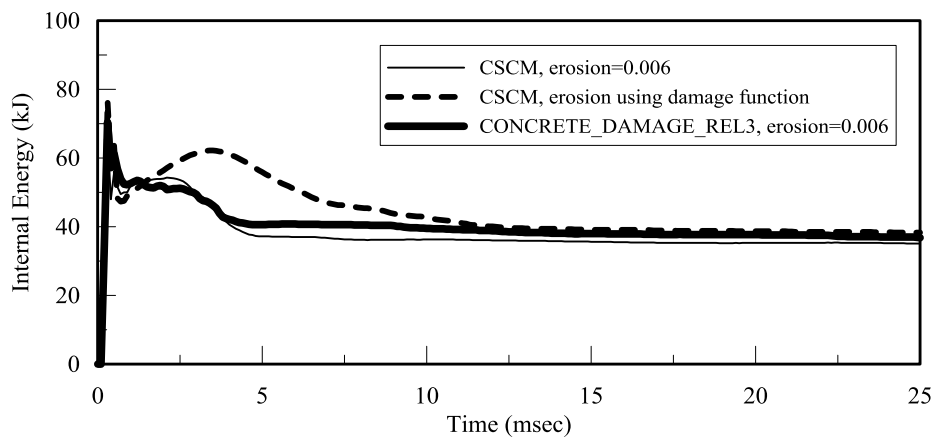
**Figure 6-41 Maximum principal stress histories for 30 elements near or on the rear face of the column, near its mid-height, CONCRETE\_DAMAGE\_REL3**



(a) 20×20×20 mm mesh



(b) 30×30×30 mm mesh

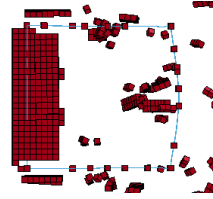


(c) 40×40×40 mm mesh

**Figure 6-42 Internal energy histories for the concrete material models of the CSCM using calculated erosion strains and an erosion algorithm of damage function, and the CONCRETE\_DAMAGE\_REL3 model using calculated erosion strains**



Side elevation

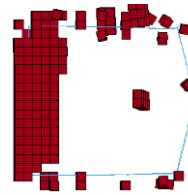


Cross section at mid-height

(a) 20×20×20 mm mesh



Side elevation

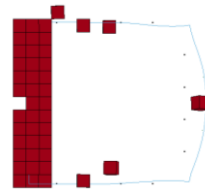


Cross section at mid-height

(b) 30×30×30 mm mesh



Side elevation



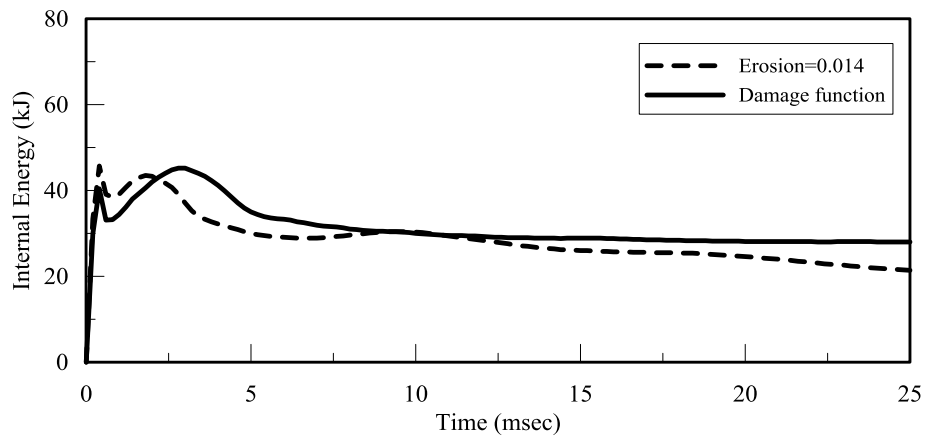
Cross section at mid-height

(c) 40×40×40 mm mesh

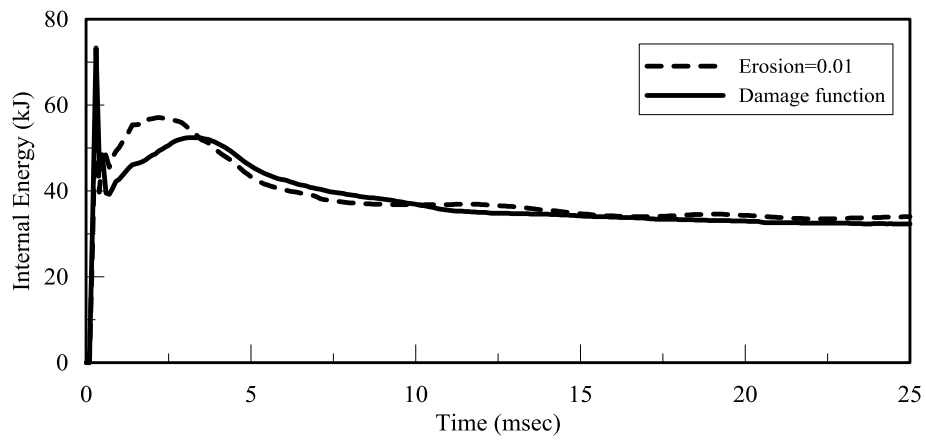
**Figure 6-43 Simulation results for the CONCRETE\_DAMAGE\_REL3 model**

### 6.6.6.3 Concrete Compressive Strength

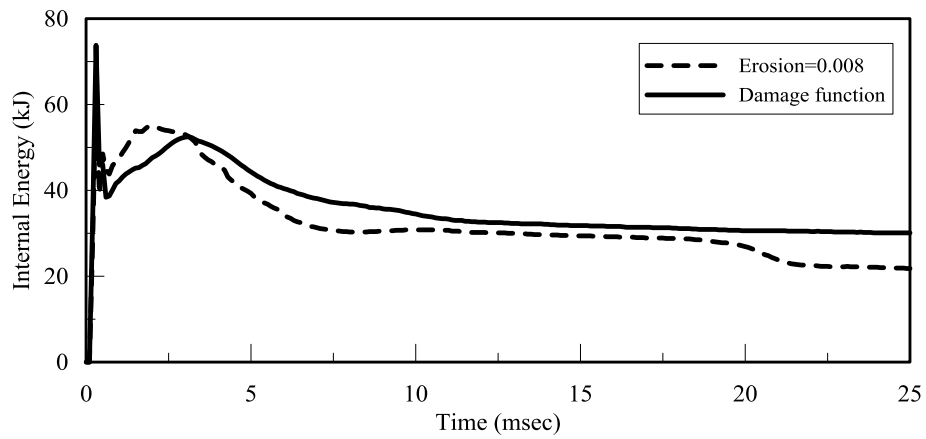
The influence of concrete compressive strength on damage, measured here using volume of eroded material, is characterized by repeating some of the analysis described in prior sections using 50 MPa concrete. The average peak tensile stress (traction) and traction rate for elements near the rear face and mid-height of the column are approximately 20 MPa and 200 MPa/msec, respectively. Per Figure 6-16, the corresponding erosion strains for the  $20 \times 20 \times 20$  mm,  $30 \times 30 \times 30$  mm and  $40 \times 40 \times 40$  mm meshes are 0.14, 0.010 and 0.008, respectively. Figure 6-44 shows internal energy histories for the 50 MPa concrete. For all three meshes, the internal energy histories for the calculated erosion strains are similar to those for the damage-based erosion algorithm. The damage, as described by eroded material and calculated using the damage-based erosion algorithm (see Figures 6-45, 6-46 and 6-47), discrete values of erosion strain are similar for the 30 and 40 mm meshes. The degree of damage is not substantially reduced by the use of higher strength concrete; although the influence of concrete strength is likely masked somewhat by the presence of transverse reinforcement.



(a) 20x20x20 mm mesh



(b) 30x30x30 mm mesh



(c) 40x40x40 mm mesh

Figure 6-44 Internal energy histories for  $f'_c = 50$  MPa

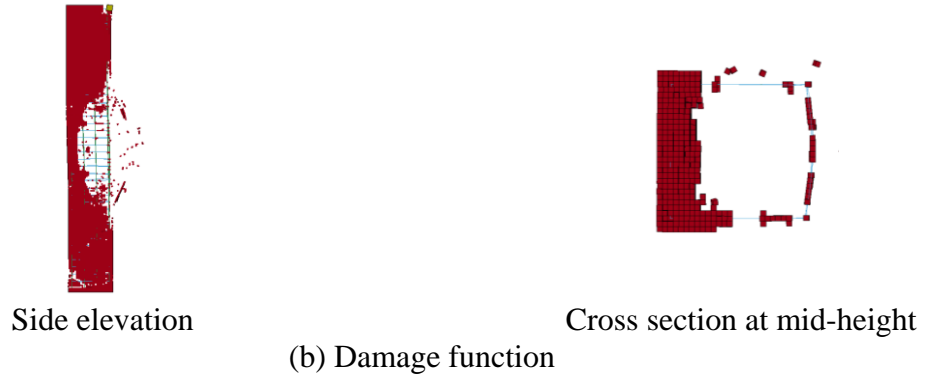
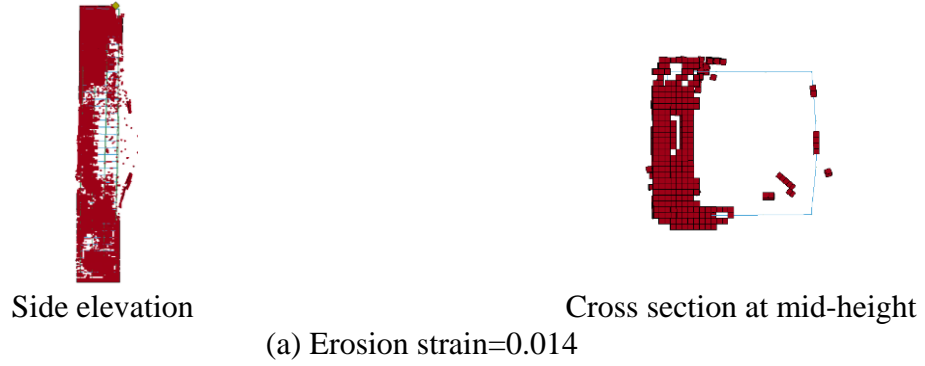


**Figure 6-45 Simulation results for the 20 mm mesh at time = 25 msec,  $f'_c = 50$  MPa**

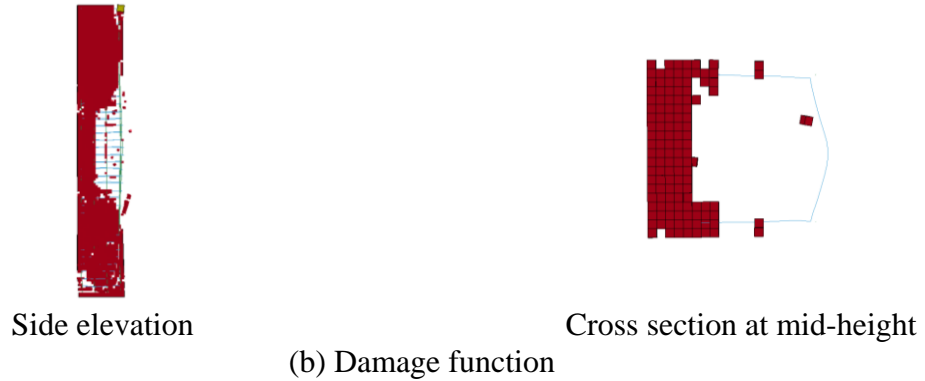
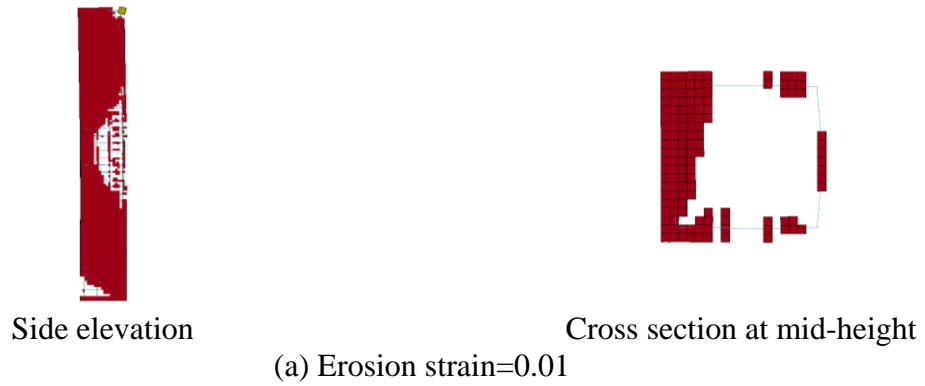


**Figure 6-46 Simulation results for the 30 mm mesh at time = 25 msec,  $f'_c = 50$  MPa**

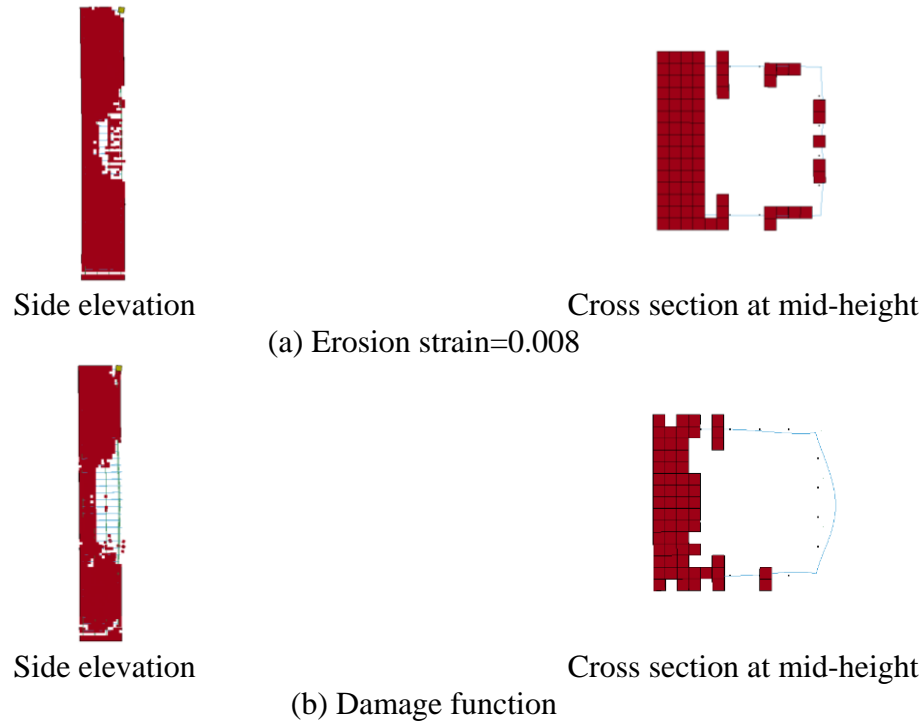


**Figure 6-47 Simulation results for the 40 mm mesh at time = 25 msec,  $f'_c = 50$  MPa**

#### 6.6.6.4 Confinement

Confinement of concrete is realized by transverse reinforcement, which is also used in reinforced concrete columns to provide shear resistance. The vertical spacing of shear reinforcement in a column often ranges between 25% and 50% of its effective depth. The spacing of the transverse reinforcement for seismic applications may be as small as 100 mm. Closely spaced transverse reinforcement is often specified for blast-resistant columns to better basket the core concrete and increase the column's global and local deformation capacity.

Analyses are performed on a single cubical element and a model of a concrete cylinder to demonstrate that the CSCM model for plain concrete adequately captures the influence of passive confinement. An unconfined uniaxial compressive strength of 35.5 MPa is assumed. The single element has dimensions of 20×20×20 mm. Figure 6-48 shows the loading and boundary conditions; the base of the element is free to expand. Lateral confining pressures,  $p$ , of 4, 8 and 16 MPa are applied to all four sides of the single element. The top of the single element is subjected to a compressive, displacement-controlled loading, as shown in Figure 6-49. The

bottom of the element is uniformly supported. Figure 6-50 shows that the peak compressive stress and ultimate strain increase with increasing confining pressure.

A standard 6-inch (152.4 mm) diameter by 12-inch (304.8 mm) tall concrete cylinder is analyzed using the CSCM model and results are compared with those generated by the widely used Mander model (Mander et al. 1988). Figure 6-51 shows the model used for analysis, which invoked symmetry, allowing one quarter of the cylinder to be modeled;  $u_x$ ,  $u_y$  and  $u_z$  denote translational displacement, and  $r_x$ ,  $r_y$  and  $r_z$  denote rotational displacements, in the  $x$ ,  $y$  and  $z$  directions, respectively. Uniform support is provided at the base of the model, with the base of the model free to expand. An unconfined uniaxial compressive strength of 35.5 MPa is assumed. Passive confining pressures of 4 and 8 MPa are imposed on the perimeter of the cylinder; results are presented in Figure 6-52. Results of analysis using the Mander model are also presented in the figures, where the uniaxial confined stress-strain relationships are calculated by substituting 4 and 8 MPa for the effective confining pressure,  $f'_l$ . Although there are differences between the CSCM and Mander models, the results are quantitatively similar, and enable the use of the CSCM model for considerations of the effect of passive confinement provided by transverse reinforcement.

To understand the effect of transverse reinforcement (passive confinement) on damage, the spacing of the transverse reinforcement assumed in prior sections (= 100 mm) is doubled to 200 mm or approximately 35% of the effective depth of the column. Simulation results for the 20×20×20 mm, 30×30×30 mm and 40×40×40 mm meshes are presented in Figure 6-53, 6-54 and 6-55, respectively. As expected, the damage (or volume of eroded elements) increases with the significant increase in the spacing of transverse reinforcement, as seen by comparing the results in Figure 6-53 with those in panels (b) and (c) of Figure 6-37, the results in Figure 6-54 with those in panels (c) and (d) of Figure 6-38, and the results in Figure 6-55 with those in panels (c) and (d) of Figure 6-39.

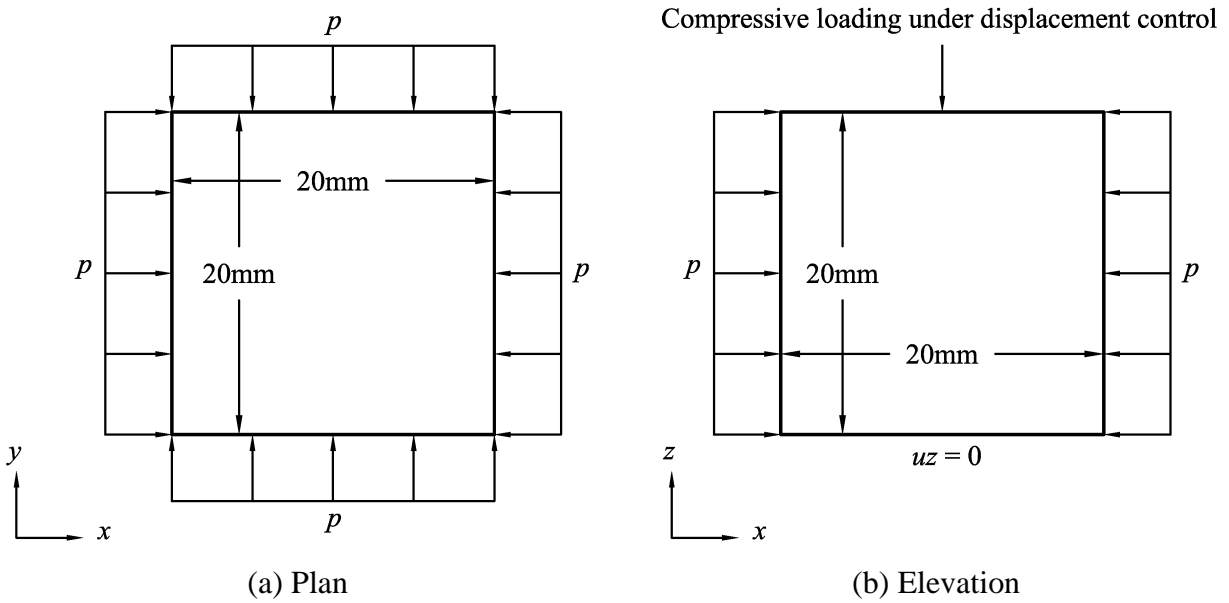


**Figure 6-48 Loading and boundary conditions of the single element for studying the effects of confinement**

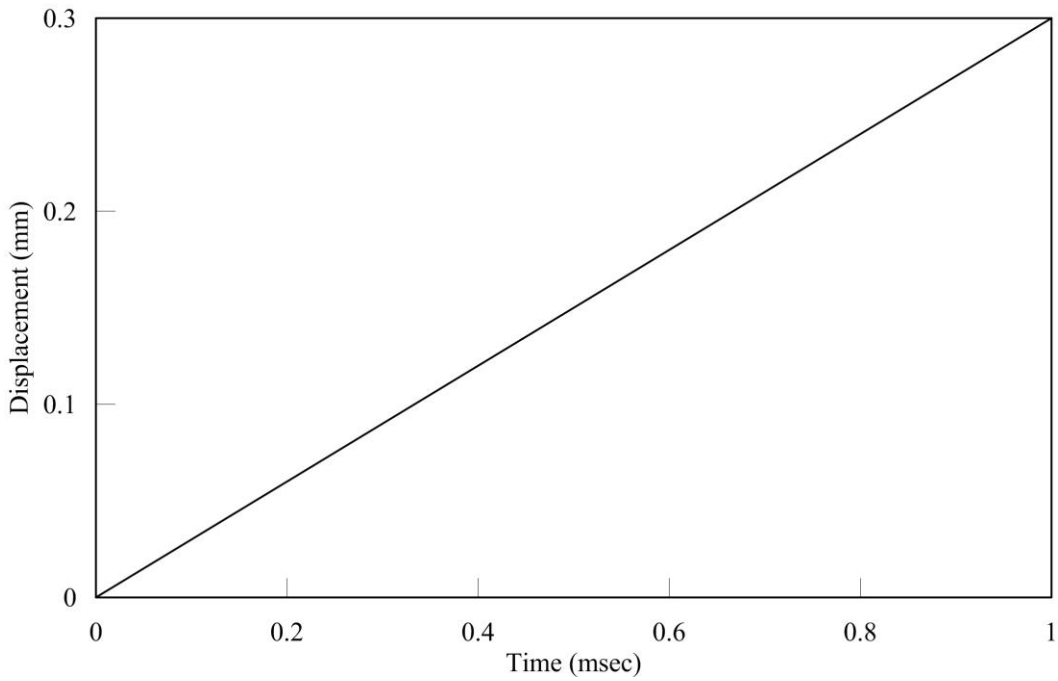


**Figure 6-49 Displacement-controlled loading at the top of the single element**

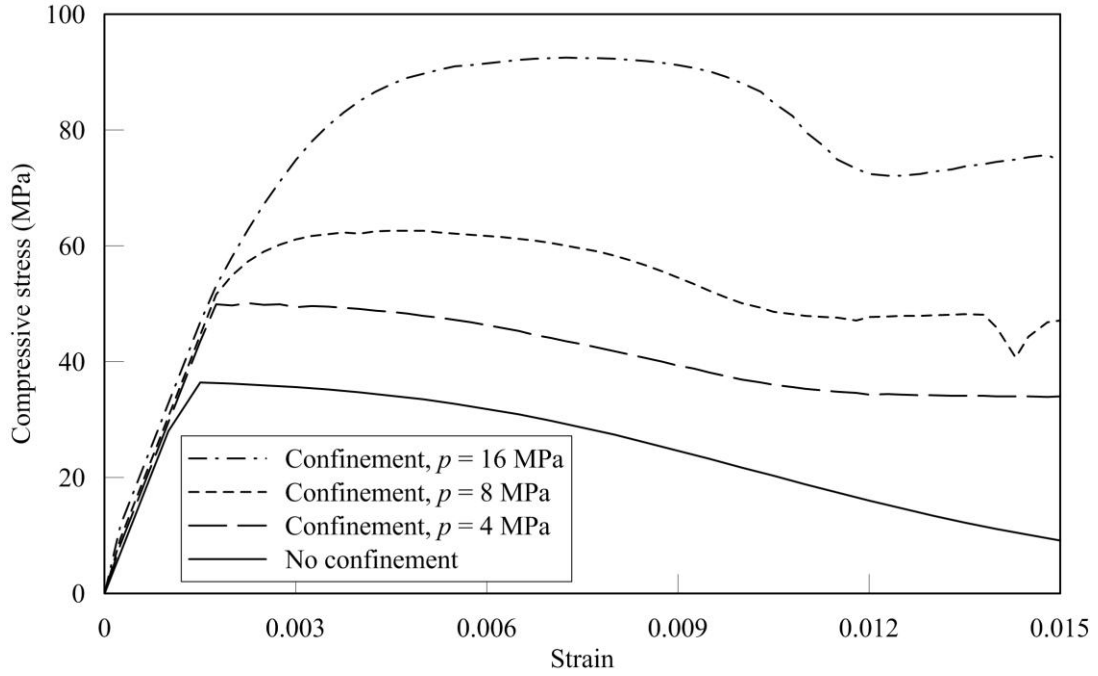


Figure 6-50 Confinement effects on stress-strain relationships, 20×20×20 mm element

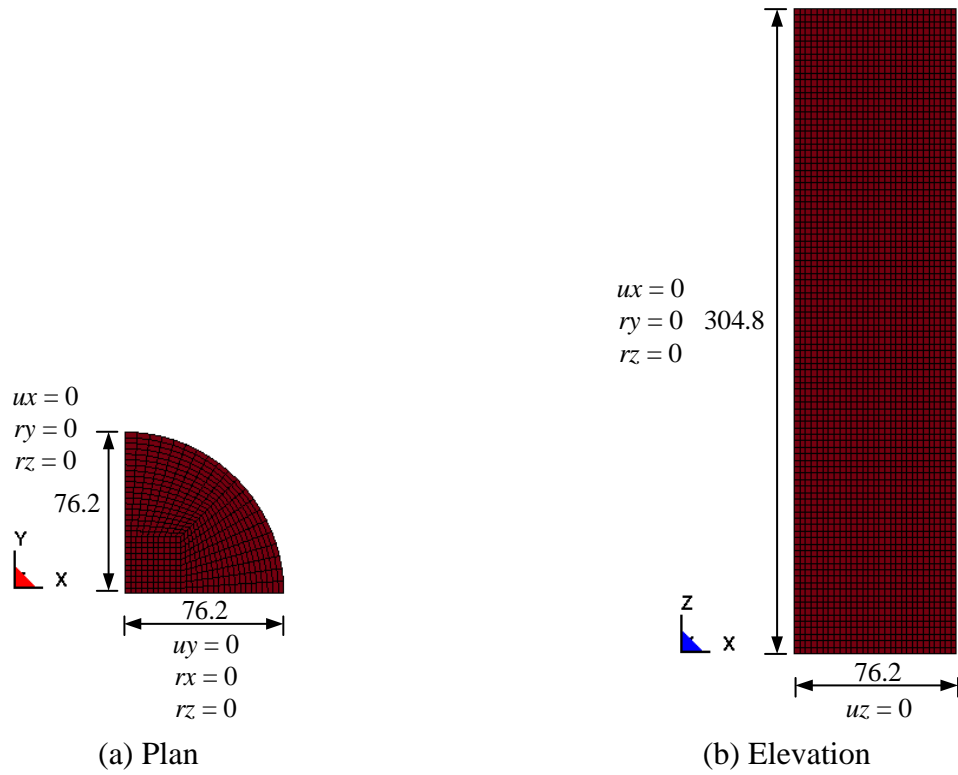
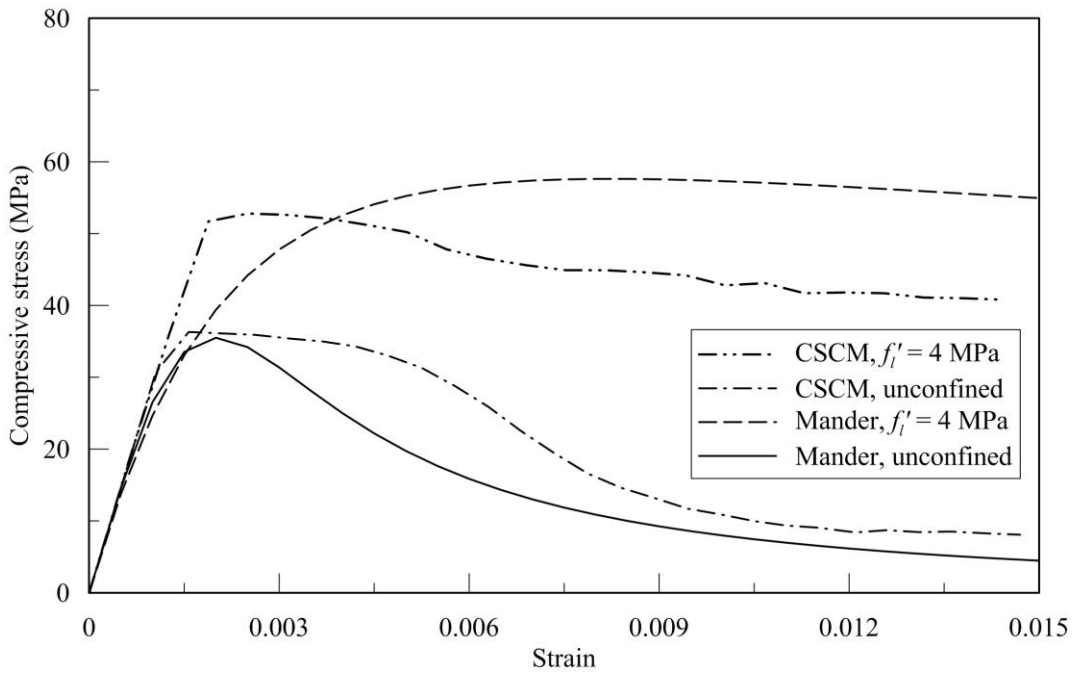
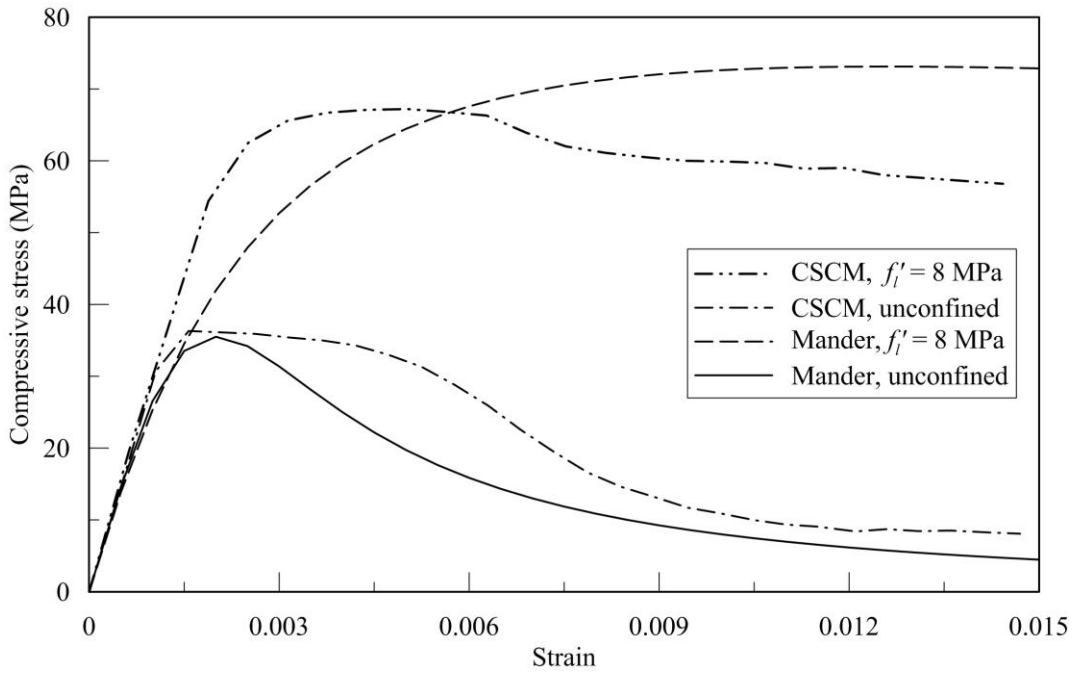


Figure 6-51 3D symmetry model of concrete cylinder (units: mm)



(a) Confining pressure,  $f'_i = 4$  MPa



(b) Confining pressure,  $f'_i = 8$  MPa

**Figure 6-52 Compressive stress versus strain relationships**

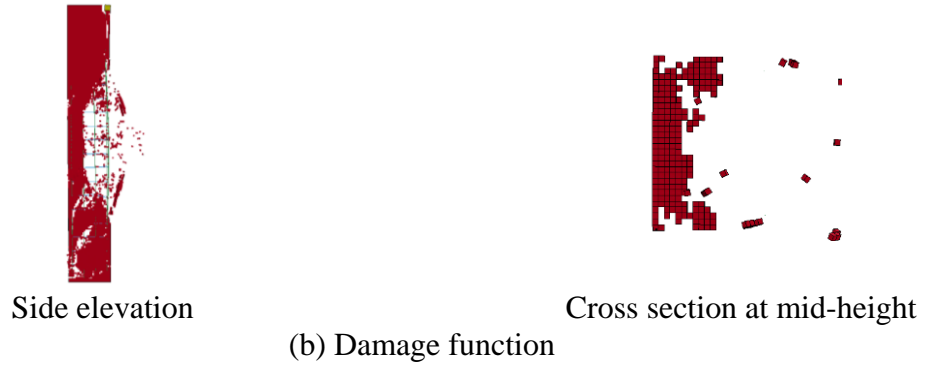
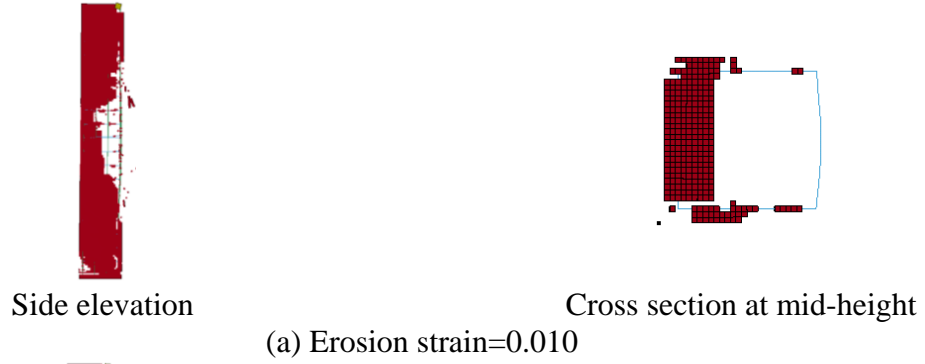


**Figure 6-53 Simulation results for the 20 mm mesh with the spacing of transverse reinforcement of 20 cm at time = 25 msec,  $f'_c = 35.5$  MPa**

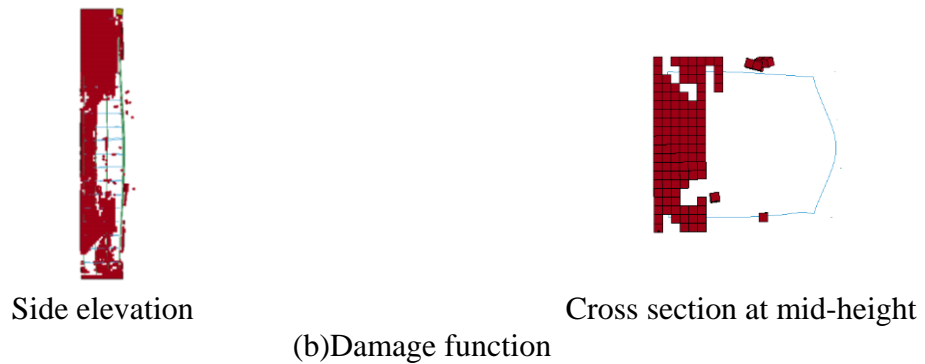
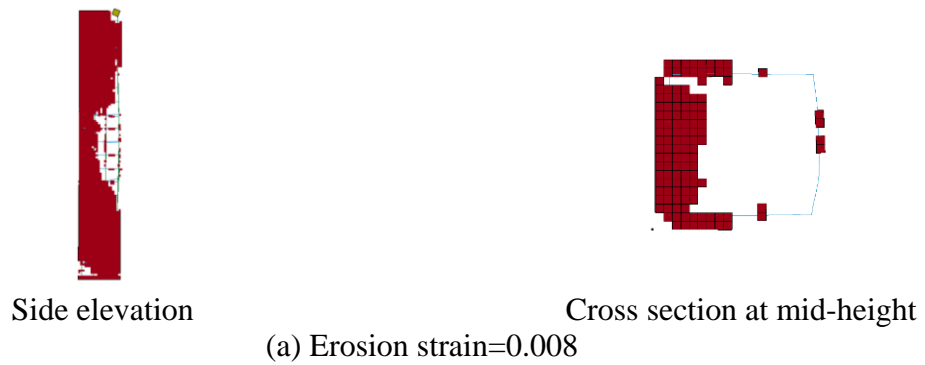


**Figure 6-54 Simulation results for the 30 mm mesh with the spacing of transverse reinforcement of 20 cm at time = 25 msec,  $f'_c = 35.5$  MPa**

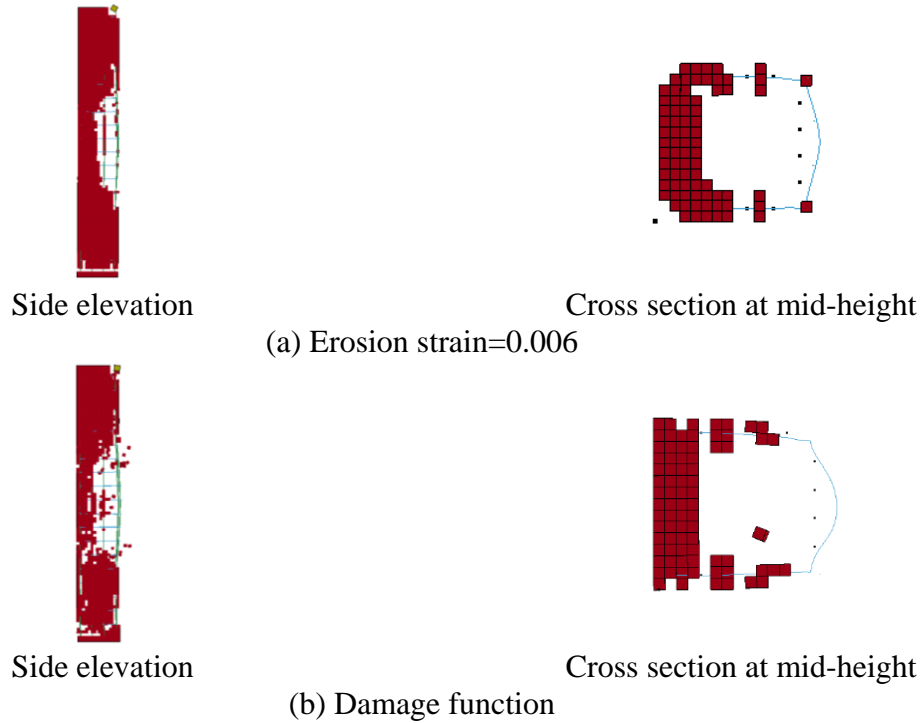


**Figure 6-55 Simulation results for the 40 mm mesh with the spacing of transverse reinforcement of 20 cm at time = 25 msec,  $f'_c = 35.5$  MPa**

#### 6.6.6.5 Axial Load

The effect of axial loading due to gravity-load effects on the predicted damage to the column is examined by applying axial static pressures of 0.1, 0.2 and 0.4  $f'_c$  to the top of the column prior to imposing the air-blast loading. A concrete strength of 35.5 MPa is assumed. The transverse reinforcement is spaced at 100 mm over the height of the column. Two erosion strategies are employed: calculated erosion strain and damage-based erosion algorithm. Results are presented in Figures 6-56, 6-57 and 6-58 for the different mesh sizes; the case of zero axial load is included for completeness. The column collapsed for all axial loadings and all mesh sizes due to extreme damage in the cross section, principally at the mid-height of the column. The time to collapse decreases with increasing axial load. It is important to note that if erosion is ignored, failure of the column is not predicted, even for the axial pressure of 0.4  $f'_c$ , which emphasizes the importance of considering erosion when predicting damage to reinforced concrete columns.

Time = 25 msec

60 msec

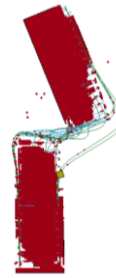
90 msec



(a) Zero axial pressure, erosion strain=0.01



(b) Zero axial pressure, damage function



(c) Axial pressure:  $0.1 f'_c$ , erosion strain=0.01



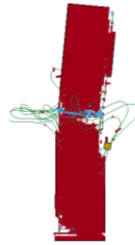
(d) Axial pressure:  $0.1 f'_c$ , damage function

**Figure 6-56 Simulation results for the 20 mm mesh with axial pressure loading,  $f'_c = 35.5$  MPa**

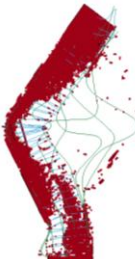
Time = 25 msec

60 msec

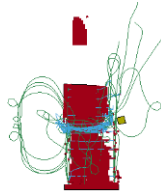
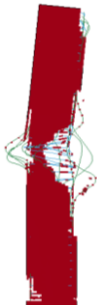
90 msec



(e) Axial pressure:  $0.2 f'_c$ , erosion strain=0.01



(f) Axial pressure:  $0.2 f'_c$ , damage function

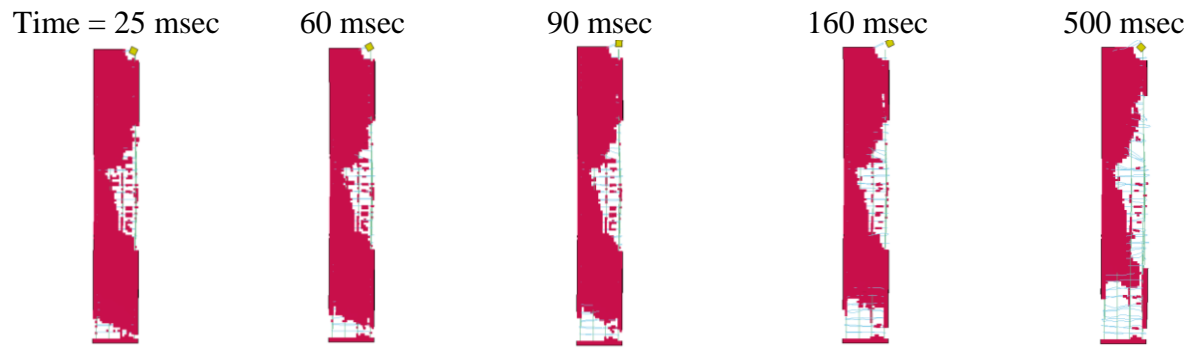


(g) Axial pressure:  $0.4 f'_c$ , erosion strain=0.01



(h) Axial pressure:  $0.4 f'_c$ , damage function

**Figure 6-56 Simulation results for the 20 mm mesh with axial pressure loading,  $f'_c = 35.5$  MPa (cont.)**



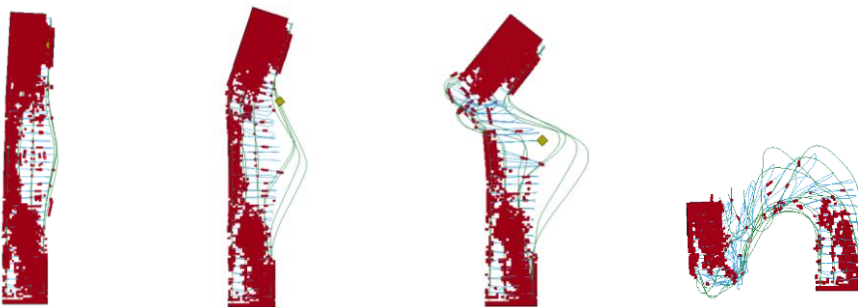
(a) Zero axial pressure, erosion strain=0.008



(b) Zero axial pressure, damage function



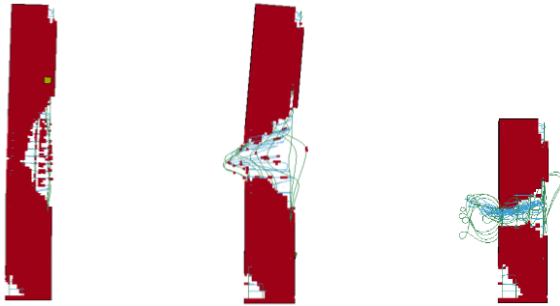
(c) Axial pressure:  $0.1 f'_c$ , erosion strain=0.008



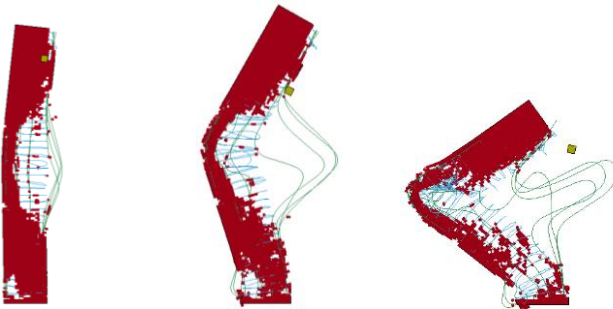
(d) Axial pressure:  $0.1 f'_c$ , damage function

**Figure 6-57 Simulation results for the 30 mm mesh with axial pressure loading,  $f'_c = 35.5$  MPa**

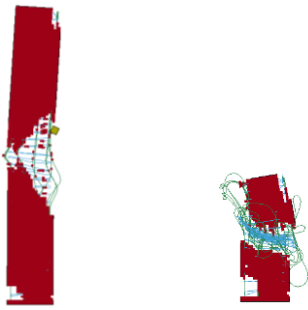
Time = 25 msec      60 msec      90 msec      160 msec      500 msec



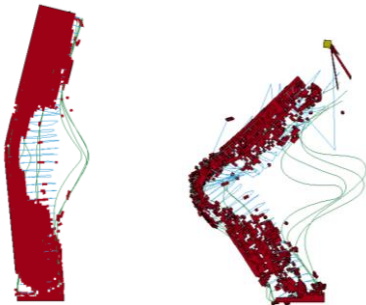
(e) Axial pressure:  $0.2 f'_c$ , erosion strain=0.008



(f) Axial pressure:  $0.2 f'_c$ , damage function



(g) Axial pressure:  $0.4 f'_c$ , erosion strain=0.008



(h) Axial pressure:  $0.4 f'_c$ , damage function

**Figure 6-57 Simulation results for the 30 mm mesh with axial pressure loading,  $f'_c = 35.5$  MPa (cont.)**

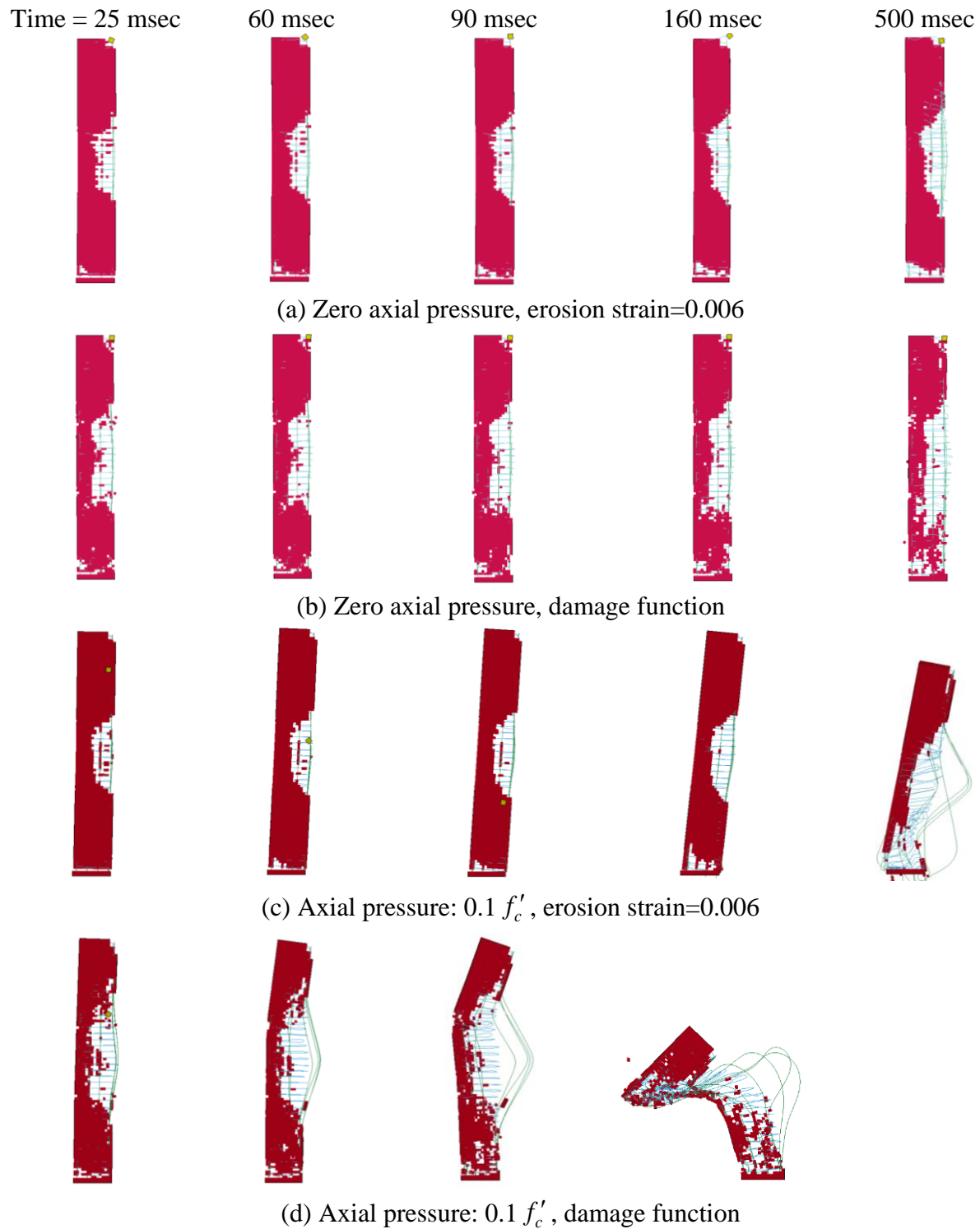
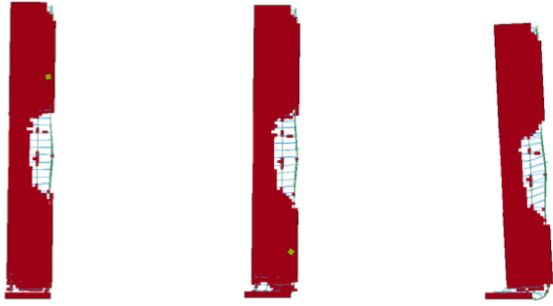
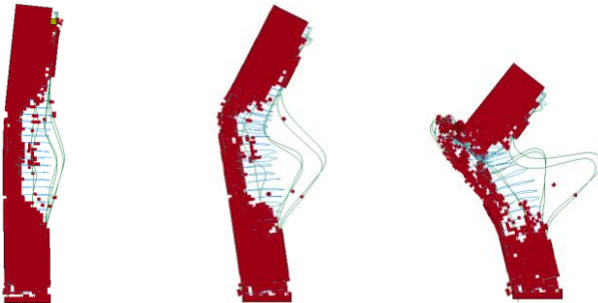


**Figure 6-58 Simulation results for the 40 mm mesh with axial pressure loading,  $f'_c = 35.5$  MPa**

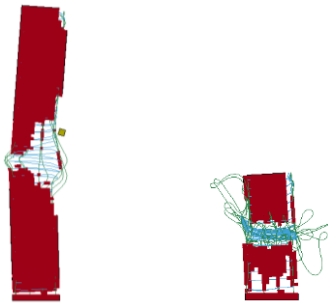
Time = 25 msec      60 msec      90 msec      160 msec      500 msec



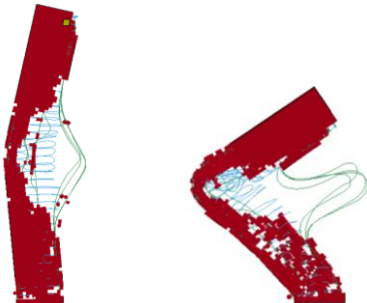
(e) Axial pressure:  $0.2 f'_c$ , erosion strain=0.006



(f) Axial pressure:  $0.2 f'_c$ , damage function



(g) Axial pressure:  $0.4 f'_c$ , erosion strain=0.006



(h) Axial pressure:  $0.4 f'_c$ , damage function

**Figure 6-58 Simulation results for the 40 mm mesh with axial pressure loading,  $f'_c = 35.5$  MPa (cont.)**

## **6.7 Values of Erosion Strain for Near-Field Blast Analysis**

Step-by-step instructions are provided below to implement a unique value of erosion strain for the near-field blast analysis of reinforced concrete components. The instructions are based on the results of analysis presented in prior sections.

1. Prepare a numerical model of the component that explicitly models the vertical and transverse reinforcement and the concrete. An element size of 40 mm is reasonable for the concrete.
2. Assign an appropriate constitutive model to the concrete (e.g., CSCM (Murray 2007), CONCRETE\_DAMAGE\_REL3 (Malvar and Simons 1996) and CDP (Lee and Fenves, 1998)) and embed a limited number of linear elastic elements on and near the back face of the component (expected to experience tensile stress upon wave reflection) to compute the traction loading rate and maximum applied tensile stress.
3. Perform a simulation ignoring erosion to compute representative values of the traction loading rate and maximum applied tensile stress on the elastic elements of step 2.
4. Using the representative values from step 3, select a value of erosion strain based on concrete strength (proximity to either 35 MPa or 50 MPa). Set the peak principal tensile strain to the erosion strain and perform the blast simulation.

## SECTION 7

### SUMMARY AND CONCLUSIONS

#### 7.1 Summary

Air-blast loadings for security design of geometrically simple, components and structures are typically calculated using empirical charts available in textbooks and US government-published documents such as TM 5-1300 (Department of the Army, Navy and Air Force 1969 and 1990), TM 5-858-3 (DoA 1984), UFC 3-340-02 (DoD 2008), Smith and Hetherington (1994), Cormie et al. (2009), Dusenberry (2010) and ASCE (2011). These charts are based on studies performed by Kingery and his co-workers (e.g., Kingery and Bulmash, 1984). Computational fluid dynamics (CFD) codes such as CTH (McGlaun et al. 1990), Air3d (Rose 2006), AUTODYN (ANSYS 2013a) and LS-DYNA (LSTC 2013) can also be used to calculate air-blast loadings on geometrically simple shapes but are preferred for complex shapes and geometries such as urban environments and streetscapes.

The empirical charts of Kingery and Bulmash, and their underlying polynomials, were constructed around measured and inferred data. These charts have not been validated in the near field because pressures and temperatures are very high. Although commercially available pressure transducers are now capable of measuring pressures expected in the near field, they cannot sustain the co-existing temperatures of thousands Kelvin. The only practical strategy to confirm pressures and impulses in the near field, both incident and reflected, is to use verified and validated CFD codes.

The goal of this report was to characterize the effects of detonations of ideal high explosives and their influence on geometrically simple structures and components, for the purpose of informing blast-resistant design. The near-field region was emphasized because there are virtually no measured data available for validation. This report has provided 1) validated methodologies and guidance for modeling detonations of high explosives, 2) an assessment of the accuracy of the widely used empirical charts for air-blast loading through CFD analysis, 3) new polynomials and design charts for air-blast loadings suitable for inclusion in design standards, 4) an assessment of

the reflection coefficients presented in government manuals and textbooks for peak overpressure, and 5) a detailed discussion of the blast analysis of a sample reinforced concrete column and the development of a technical basis for selecting values of erosion strain.

AUTODYN was verified and validated in Chapter 2 for 1D and 2D air-blast calculations through 1) 1D simulations and comparisons of results with those presented by Needham (2010), who performed numerical and first-principles calculations for near- and intermediate-field detonations, 2) cross-code comparisons in 1D and 2D using CTH and LS-DYNA for far-field detonations, 3) 2D simulations and comparisons of results to measurements reported by Goodman (1960) and Huffington and Ewing (1985) for near-field detonations, and 4) 2D simulations and comparisons of results to measurements reported by Frost et al. (2008) for far-field detonations. Incident and reflected overpressure histories were simulated to examine the influences of mesh size, expansion of detonation products and afterburning, temperatures near the charge face, and the efficacy of reflecting and transmitting boundaries.

Chapter 3 presented the results of AUTODYN studies of air-blast parameters over a wide range of scaled distance. Incident and normally reflected peak overpressures and impulses, and shock front arrival times, were compared with predictions from the Kingery and Bulmash (or UFC 3-340-02) charts.

Chapter 4 proposed new polynomials and design charts, based on the CFD calculations of Chapter 3, for air-blast parameters over a wide range of scaled distance, namely,  $0.0553 \leq Z \leq 40 \text{ m/kg}^{1/3}$  ( $0.139 \leq Z \leq 100 \text{ ft/lb}^{1/3}$ ).

Overpressure reflection coefficients and reflected scaled impulses as a function of the angle of incidence for airblast calculations were studied in Chapter 5, using a verified CFD code, AUTODYN, and using data reported in TM 5-858-3 (DoA 1984) and UFC 3-340-02 (DoD 2008). The study was motivated by the significant differences in the coefficients in the Mach reflection region between TM 5-858-03 and UFC 3-340-02. Incident and reflected peak overpressures and impulses were simulated using AUTODYN for  $0.16 \leq Z \leq 8 \text{ m/kg}^{1/3}$  and angles of incidence between zero and ninety degrees. The effects of Mach reflection and

expanding detonation product on the reflection coefficient and reflected scaled impulse were examined.

Chapter 6 presented analytical studies performed to characterize erosion strain in concrete for the purpose of damage analysis. Single element simulations were undertaken to characterize erosion strain as a function of variables such as concrete strength, rate of traction loading, maximum traction loading, and size of finite element. Finite element analysis of a sample reinforced concrete column was performed using alternate representations of erosion strain and the damage-based erosion algorithm developed by Murray (2007). Other factors that affect the response of a reinforced concrete column, including concrete compressive strength, volume of transverse reinforcement, and co-existing axial (gravity) load, were studied.

## 7.2 Conclusions

The key findings and recommendations in this report are:

1. AUTODYN produces similar predictions of 1) hydrodynamic parameters to those of Needham (2010) for near-field detonations, 2) incident overpressure and impulse histories to those obtained using CTH and LS-DYNA for far-field detonations, 3) reflected scaled impulses to measurements reported by Goodman (1960) and Huffington and Ewing (1985) for near-field detonations, and 4) normally reflected peak overpressures and impulses to measurements of Frost et al. (2008) for far-field detonations. AUTODYN is verified and validated for near- and far-field air-blast calculations in 1D and 2D.
2. For CFD calculations of incident and reflected overpressure histories, a trial cell size of  $R/500$  is sufficient for  $Z \leq 8 \text{ m/kg}^{1/3}$ , where  $R$  is the distance from the center of the charge to the monitoring location and  $Z$  is scaled distance. The choice of cell size must also allow the accurate meshing of the charge.
3. The widely used Friedlander equation does not capture the shape of the overpressure history in the near field due to the expansion of detonation products, afterburning, and Mach stem formation. CFD tools must be used to characterize overpressure histories in the near field.

The Friedlander equation can be used to characterize incident and normally reflected overpressure histories for  $Z \geq 0.83 \text{ m/kg}^{1/3}$ .

4. Afterburning has no effect on peak overpressure but can increase impulse if sufficient oxygen is present, the available oxygen mixes well with the fuels, and the temperature is greater than 1800 K (for TNT). The effect of afterburning is likely small in the near field.
5. Transmitting boundaries may partially reflect incident pressures in 3D models. The location of a perpendicular transmitting boundary in a 3D problem should be established using a process similar to that reported in Section 2.6. A minimum perpendicular dimension equal to the charge radius is recommended.
6. AUTODYN simulations predict values of incident peak overpressure, incident impulse, and normally reflected peak overpressure that are much greater than those presented in UFC 3-340-02 for  $Z < 0.08, 0.1, \text{ and } 0.4 \text{ m/kg}^{1/3}$ , respectively. UFC 3-340-02 overpredicts the AUTODYN calculations of incident impulse for  $0.1 < Z < 40 \text{ m/kg}^{1/3}$  by 10% to 25%, which is consistent with the observations of Bogosian et al. (2002).
7. The design polynomials and charts of Chapter 4 enable good predictions of incident and normally reflected peak overpressure and impulse across a wide range of scaled distance, namely,  $0.0553 \leq Z < 40 \text{ m/kg}^{1/3}$ .
8. For  $Z < 0.4 \text{ m/kg}^{1/3}$ , the AUTODYN-calculated reflection coefficients are much greater than the values presented in UFC 3-340-02, although this may be of little practical importance because CFD tools should be used in the near field to estimate the overpressure histories for design.
9. For  $Z \geq 0.4 \text{ m/kg}^{1/3}$  (1 ft/lb<sup>1/3</sup>) (or  $P_s \geq$  approximately 5.6 MPa [815 psi]) and  $\alpha \leq 40^\circ$ , the overpressure reflection coefficients calculated using AUTODYN are similar to those reported in both UFC 3-340-02 and TM 5-858-3. For  $Z \geq 0.4 \text{ m/kg}^{1/3}$  and  $\alpha > 40^\circ$ , AUTODYN calculates similar values of overpressure reflection coefficients to those in UFC 3-340-02; the corresponding chart in TM 5-858-3 does not capture the effect of Mach reflection.

10. The use of an erosion strain that is independent of concrete strength, rate of traction loading, maximum tensile traction and element size is inappropriate for damage and/or failure calculations. For 35.5 MPa and 50 MPa concrete, and a 40 mm element size or smaller, the erosion strain varies between 0.005 and 0.015 for maximum applied tensile tractions ranging between 10 MPa and 40 MPa and loading traction rates of between 50 MPa/msec and 250 MPa/msec. The use of an unreasonably high value of erosion strain will underestimate the volume of eroded material and underpredict the likelihood of gravity-load collapse.
11. Given that the maximum aggregate size in a reinforced concrete column will typically exceed 20 mm, an element size of 40 mm appears reasonable for the finite element analysis of a reinforced concrete column.
12. The use of the damage-based erosion algorithm in LS-DYNA resulted in similar predictions of damage, including volume of eroded material, to that predicted by analysis using the step-by-step procedure and a robust value for the erosion strain. There is no benefit to using erosion strain for analysis if a robust damage-based erosion algorithm is available.



## SECTION 8

### REFERENCES

- ACI. 2011. *Building Code Requirements for Structural Concrete (ACI 318-11) and Commentary*. American Concrete Institute, Farmington Hills, MI.
- ASCE. 2011. *Blast Protection of Buildings (ASCE/Structural Engineering Institute (SEI) 59-11)*. American Society of Civil Engineers, Reston, VA.
- ASME. 2006. *Guide for Verification and Validation in Computational Solid Mechanics*. ASME V & V 10-2006, American Society of Mechanical Engineers, New York, NY.
- ASTM. 2003. *Standard Specification for Deformed and Plain Billet-Steel Bars for Concrete Reinforcement (ASTM A 615/A 615M-03a)*. American Society of Testing and Materials, Philadelphia, PA.
- Anderson, J. D. 2003. *Modern Compressible Flow: with Historical Perspective, 3rd edition*. McGraw-Hill, Boston, MA.
- ANSYS. 2005. *Remapping Tutorial, Revision 4.3*. ANSYS, Inc., Canonsburg, PA.
- ANSYS. 2013a. *AUTODYN User's Manual Version 15.0*. ANSYS, Inc., Canonsburg, PA.
- ANSYS. 2013b. *Personal Communication*. ANSYS, Inc., Canonsburg, PA.
- Baker, W. E. 1973. *Explosions in Air*. University of Texas Press, Austin, TX.
- Baker, W. E., Cox, P. A., Westine, P. S., Kulesz, J. J. and Strehlow, R. A. 1983. *Explosion Hazards and Evaluation*. Elsevier Scientific Publishing Company, Amsterdam; Oxford; New York.
- Ballantyne, G. J., Whittaker, A. S., Aref, A. J. and Dargush, G. F. 2009. "Air-blast effects on structural shapes." *Technical Report MCEER-09-0002*, The State University of New York at Buffalo, Buffalo, NY.

- Bažant, Z. P. 1986. Mechanics of distributed cracking. *Journal of Applied Mechanics* 39 (5): 675-705.
- Bažant, Z. P. and Chang, T. P. 1987. Nonlocal finite-element analysis of strain-softening solids. *Journal of Engineering Mechanics* 113 (1): 89-105.
- Bažant, Z. P. and Pijaudier-Cabot, G. 1988. Nonlocal continuum damage, localization instability and convergence. *Journal of Applied Mechanics* 55 (2): 287-293.
- Belytschko, T., Bažant, Z. P., Hyun, Y. W. and Chang, T. P. 1986. Strain-softening materials and finite-element solutions. *Computers & Structures* 23 (2): 163-180.
- Biggs, J. M. 1964. *Introduction to Structural Dynamics*. McGraw-Hill, NY.
- Bogosian, D., Ferritto, J., and Shi, Y. 2002. Measuring uncertainty and conservatism in simplified blast models. *Proceedings, 30th Explosives Safety Seminar, Atlanta, Georgia*.
- Boris, J. P and Book, D. L. 1971. Flux-correct-transport: I. SHASTA, a fluid transport algorithm that works. *Journal of Computational Physics* 11: 38-69.
- Borve, S., Bjerke, A., Omang, M. and Truslen, J. 2008. A comparative study of ANSYS AUTODYN and RSPH simulations of blast waves. *Proceedings, 3rd ERCOFTAC SPHERIC Workshop on SPH applications, Lausanne, Switzerland*.
- Børvik, T., Hopperstad, O., Berstad, T. and Langseth, M. 2001. A computational model of viscoplasticity and ductile damage for impact and penetration. *European Journal of Mechanics-A/Solids* 20 (5): 685-712.
- Brannon, R. M. and Leelavanichkul, S. 2009. Survey of four damage models for concrete. *Sandia Report No. SAND2009-5544*. Sandia National Laboratories, University of Utah, Albuquerque, NM ; Livermore, CA.
- Brara, A. and Klepaczko, J. R. 2007. Fracture energy of concrete at high loading rates in tension. *International Journal of Impact Engineering* 34 (3): 424-435.

- Brode, H. L. 1955. Numerical solution of spherical blast waves. *Journal of Applied Physics* 26 (6): 766-776.
- Browning, R. S., Sherburn, J. A. and Schwer, L. E. 2013. Predicting blast loads using LS-DYNA and CTH. *Proceedings*, ASCE Structures Congress, Pittsburgh, PA.
- Chen, W.-F. 2007. *Plasticity in Reinforced Concrete*. J. Ross Publishing Inc., Fort Lauderdale, FL.
- Chopra, A. K. 2012. *Dynamics of Structures: Theory and Applications to Earthquake Engineering, 4th edition*. Prentice Hall, Upper Saddle River, NJ.
- Comité euro-international du béton (CEB). 1993. *CEB-FIP Model Code 1990: Design Code*. T. Telford, London.
- Cook, R. D. 2002. *Concepts and Applications of Finite Element Analysis, 4th edition*. Wiley, New York, NY.
- Cormie, D., Mays, G. and Smith, P. 2009. *Blast Effects on Buildings, 2nd edition*. London: Thomas Telford.
- Cormie, D., Wilkinson, W., Shin, J. and Whittaker, A. S. 2013. Scaled-distance relationships for close-in detonations. *Proceedings*, 15th International Symposium on Interaction of the Effects of Munitions with Structures, Potsdam, Germany.
- Coughlin, A. M., Musselman, E. S., Schokker, A. J. and Linzell, D. G. 2010. Behavior of portable fiber reinforced concrete vehicle barriers subject to blasts from contact charges. *International Journal of Impact Engineering* 37 (5): 521-529.
- Courant, R. and Friedrichs, K. O. 1948. *Supersonic Flow and Shock Waves*. Interscience Publishers, New York, NY.
- Cullis, I. G. and Huntington-Thresher, W. 2007. Blast structure interaction and the role of secondary combustion. *Proceedings*, 23rd International Symposium on Ballistics, Tarragona, Spain.

Danielson, K. T., O'Daniel, J. L., Akers, S. A. and Adley, M. D. 2008. Numerical aspects and procedures for modeling reinforced concrete structures under extreme impulsive loadings. *Materials under Extreme Loadings - Application to Penetration and Impact. Proceedings*, 2nd US-France Conference Organized by the International Center for Applied Computational Mechanics. Rocamadour, France.

Davison, L. 2008. *Fundamentals of Shock Wave Propagation in Solids*. Springer, NY.

DoA. 1984. *Designing Facilities to Resist Nuclear Weapons Effects: Structures (TM 5-858-3)*. Department of the Army, Headquarters, United States. Washington, DC.

DoA. 1986. *Fundamentals of Protective Design for Conventional Weapons (TM 5-855-1)*. Department of the Army, Headquarters, United States. Washington, DC.

Department of the Army, Navy and Air Force. 1969. *Structures to Resist the Effects of Accidental Explosions (with Addenda)*. Army Technical Manual (TM 5-1300), Navy Publication (NAVFAC P-397), Air Force Manual (AFM 88-22). Washington, DC.

Department of the Army, Navy and Air Force. 1990. *Structures to Resist the Effects of Accidental Explosions (with Addenda)*. Army Technical Manual (TM 5-1300), Navy Publication (NAVFAC P-397), Air Force Manual (AFM 88-22), Revision 1. Washington, DC.

DoD. 2008. *Unified Facilities Criteria (UFC): Structures to Resist the Effects of Accidental Explosions (UFC 3-340-02)*. Departments of Defense, Washington, DC.

Doan, L. R. and Nickel, G. H. 1963. A subroutine for the equation of state of air. *RTD (WLR) TN63-2*. Air Force Weapons Laboratory.

Dobratz, B. M. and Crawford, P. C. 1985. LLNL Explosive Handbook, Properties of chemical explosives and explosive simulants. *Report UCRL-52997*, Lawrence Livermore National Laboratory, Livermore, CA.

Donahue, L. K. 2008. Afterburning of TNT detonation in air. *M.A.Sc. Thesis*. Dalhousie University, Halifax, Nova Scotia.

Dusenberry, D. O. 2010. ed. *Handbook for Blast-Resistant Design of Buildings*. Wiley, Hoboken, NJ.

Fawaz, Z., Zheng, W. and Behdian, K. 2004. Numerical simulation of normal and oblique ballistic impact on ceramic composite armours. *Composite Structures* 63 (3-4): 387–395.

Federal Emergency Management Agency (FEMA). 2003. *Reference Manual to Mitigate Potential Terrorist Attacks against Buildings*. FEMA-426, Washing DC.

Fickett, W. and Davis W. C. 1979. *Detonation: Theory and Experiment*. Dover Publications Inc., Mineola, NY.

Frost, D.L., Cairns, M., Goroshin, S., Leadbetter, J., Ripley, R., and Zhang, F. 2008. Reflected heterogeneous blast. *Proceedings*, 20th International Symposium on Military Aspects of Blast and Shock, Oslo, Norway.

Godunov, S. K. 1959. A difference scheme for numerical solution of discontinuous solution of hydrodynamic equations. *Math. Sbornik*, 47, 271-306, translated US Joint Publ. Res. Service, JPRS 7226, 1969.

Goodman, H. J. 1960. Compiled free-air blast data on bare spherical Pentolite. *BRL Report No. 1092*, US Army Ballistic Research Laboratory, Aberdeen Proving Ground, MD.

Gray, G. T., Chen, S. R., Wright, W. and Lopez, M. F. 1994. Constitutive equations for annealed metals under compression at high strain rates and high temperatures. *LA-12669-MS*. Los Alamos National Laboratory, Los Alamos, NM.

Griffith, W. C. and Bleakney, W. 1954. Shock waves in gases. *American Journal of Physics* 22 (9): 597-612.

Grote, D. L., Park, S. W. and Zhou, M. 2001. Dynamic behavior of concrete at high strain rates and pressures: I. experimental characterization. *International Journal of Impact Engineering* 25 (9): 869-886.

Hao, H. and Zhou, X. Q. 2007. Concrete material model for high rate dynamic analysis. *Proceedings, 7th International Conference on Shock and Impact Loads on Structures*. Beijing, China. p. 753-768.

Henrych, J. 1979. *The Dynamics of Explosion and Its Use*. Elsevier Scientific Pub. Co., Amsterdam ; New York.

Huffington, Jr., N. J. and Ewing, W. O. 1985. Reflected impulse near spherical charges. *Technical Report BRL-TR-2678*, US Army Ballistic Research Laboratory, Aberdeen Proving Ground, MD.

Hyde, D. W. 1992. *ConWep: Conventional Weapons Effects (Application of TM 5-855-1)*. US Army Corps of Engineers, Waterways Experiment Station, Vicksburg, MS.

Islam, M. J., Liu, Z. and Swaddiwudhipong, S. 2011. Numerical study on concrete penetration/perforation under high velocity impact by ogive-nose steel projectile. *Computers and Concrete* 8 (1): 111-123.

Ivanov, M. S., Vandromme, D., Fomin, V. M., Kudryavtsev, A. N., Hadjadj, A., and Khotyanovsky, D. V. 2011. Transition between regular and Mach reflection of shock waves: new numerical and experimental results. *Shock Waves* 11: 199–207

Johnson, G. R. and Cook, W. H. 1983. A constitutive model and data for metals subjected to large strains, high strain rates and high temperatures. *Proceedings, 7th International Symposium on Ballistics*. International Ballistics Committee, The Hague, Netherlands. p. 541-547.

Johnson, O. T., Patterson, II, J. D. and Olson, W. C. 1957. A simple mechanical method for measuring the reflected impulse of air blast waves. *BRL Memorandum Report No. 1088*, US Army Ballistic Research Laboratory, Aberdeen Proving Ground, MD.

Kingery, C. N. 1966. Air blast parameters versus distance for hemispherical TNT surface bursts. *Report No. 1344*, Ballistic Research Laboratories, Aberdeen Proving Ground, MD.

- Kingery, C. N. and Bulmash, G. 1984. Airblast parameters from TNT spherical air burst and hemispherical surface burst. *Report ARBRL-TR-02555*, US Army Ballistic Research Laboratory, Aberdeen Proving Ground, MD.
- Kingery, C. N. and Pannill, B. F. 1964. Peak overpressure vs scaled distance for TNT surface bursts (hemispherical charges). *BRL Memorandum Report 1518*, Ballistic Research Laboratories, Aberdeen Proving Ground, MD.
- Kinney, G. F. 1962. *Explosive Shocks in Air*. The Macmillan Company, New York, NY.
- Kinney, G. F. and Graham, K. J. 1985. *Explosive Shocks in Air. 2nd edition*. Springer-Verlag, New York, NY.
- Kolsky, H. 1953. *Stress Waves in Solids*. Clarendon Press Oxford.
- Krauthammer, T. 2008. *Modern Protective Structures*. CRC Press, Boca Raton, FL.
- Kurtaran, H., Buyuk, M. and Eskandarian, A. 2003. Ballistic impact simulation of GT model vehicle door using finite element method. *Theoretical and Applied Fracture Mechanics* 40 (2): 113-121.
- Lambert, D. E. and Ross, C. A. 2000. Strain rate effects on dynamic fracture and strength. *International Journal of Impact Engineering* 24 (10): 985-998.
- Lee, J and Fenves, G. 1998. Plastic-damage model for cyclic loading of concrete structures. *Journal of Engineering Mechanics*, 124 (8): 892-900.
- Lignos, D. G., Chung, Y., Nagae, T. and Nakashima, M. 2011. Numerical and experimental evaluation of seismic capacity of high-rise steel buildings subjected to long duration earthquakes. *Computers & Structures* 89 (11-12): 959-967.
- LSTC. 2013. *LS-DYNA Keyword User's Manual Ver. R7.0*. Livermore Software Technology Corporation, Livermore, CA.

- Lu, Y. and Xu, K. 2004. Modelling of dynamic behaviour of concrete materials under blast loading. *International Journal of Solids and Structures* 41 (1): 131-143.
- Luccioni, B. M., Ambrosini, R. D. and Danesi, R. F. 2004. Analysis of building collapse under blast loads. *Engineering Structures* 26 (1): 63-71.
- Malvar, L. J. and Ross, C. A. 1998. Review of strain rate effects for concrete in tension. *ACI Materials Journal* 95 (6): 735-739.
- Malvar, L. J. and Simons, D. 1996. Concrete material modeling in explicit computations. *Proceedings, Workshop on Recent Advances in Computational Structural Dynamics and High Performance Computing*, USAE Waterways Experiment Station, Vicksburg, MS, p. 165-194
- Mander, J. B., Priestley, M. J. N. and Park, R. 1988. Theoretical stress-strain model of confined concrete. *Journal of Structural Engineering* 114 (8): 1804-1826.
- McGlaun, J. M., Thompson, S. L. and Elrick, M. G. 1990. CTH: a three-dimensional shock wave physics code. *International Journal of Impact Engineering* 10 (1-4): 351-360.
- McNesby, K. L., Homan, B. E., Ritter, J. J., Quine, Z., Ehlers, R. Z. and McAndrew, B. A. 2010. Afterburn ignition delay and shock augmentation in fuel rich solid explosives. *Propellants, Explosives, Pyrotechnics* 35 (1): 57-65.
- Mehanny, S. S. and Deierlein, G. G. 2000. Modeling and assessment of seismic performance of composite frames with reinforced concrete columns and steel beams. *Report No. 135*. John A. Blume Earthquake Engineering Research Center, Stanford, CA.
- Meyers, M. A., Murr, L. E. and Staudhammer, K. P. 1992. *Shock-Wave and High-Strain-Rate Phenomena in Materials*. CRC Press, NY.
- Mouton, C. A. 2007. Transition between regular and Mach reflection in the dual-solution domain. *PhD. Dissertation*, California Institute of Technology, Pasadena, CA.

- Murray, Y. D. 2007a. Evaluation of LS-DYNA Concrete Material Model 159. *Report No. FHWA-HRT-05-063*. Federal Highway Administration, DC.
- Murray, Y. D. 2007b. User's Manual for LS-DYNA Concrete Material Model 159. *Report No. FHWA-HRT-05-063*. Federal Highway Administration, DC.
- Needham, C. E. 2010. *Blast Waves*. Springer, NY.
- Ngo, T., Lumantarna, R., Whittaker, A. S. and Mendis, P. 2014. Arena testing using a large high explosive, submitted to *Journal of Structural Engineering*.
- Norris, C. H., Hansen, R. J., Holley, JR. M. J., Biggs, J. M., Namyet, S. and Minami, J. K. 1959. *Structural Design for Dynamic Loads*. McGraw-Hill, New York; Toronto; London.
- Oberkampf, W. L. and Trucano, T. G. 2002. Verification and validation in computational fluid dynamics. SAND2002-0529, Sandia National Laboratories, Albuquerque, NM.
- Polanco-Loria, M., Hopperstad, O. S., Børvik, T. and Berstad, T. 2008. Numerical predictions of ballistic limits for concrete slabs using a modified version of the HJC concrete model. *International Journal of Impact Engineering* 35 (5): 290-303.
- Popovics, S. 1970. A review of stress-strain relationships for concrete. *ACI Journal* 67 (3): 243-248.
- Ragueneau, F. and Gatuingt, F. 2003. Inelastic behavior modelling of concrete in low and high strain rate dynamics. *Computers & Structures* 81 (12): 1287-1299.
- Ritzel, D. V. and Matthews, K. 1997. An adjustable explosion-source model for CFD blast calculations. *Proceedings, 21st International Symposium on Shock Waves*, Great Keppel Island, Australia, 1: 97-102.
- Rose, T. A. 2006. *A Computational Tool for Airblast Calculations - Air3D version 9 users' guide*. Engineering Systems Department, Cranfield University, United Kingdom.

- Rubin, M. B. 1991. Simple, convenient isotropic failure surface. *Journal of Engineering Mechanics* 117 (2): 348-369.
- Ruiz, G., Zhang, X. X., Tarifa, M., Yu, R. C. and Camara, M. 2009. Fracture energy of high-strength concrete under different loading rates. *Anales de Mecánica de la Fractura* 26 2: 513-518.
- Sandler, I. S. and Wright, J. P. 1984. Summary of strain-softening. *Proceedings, DARPA-NSF Workshop on the Theoretical Foundations for Large-Scale Computations for Nonlinear Material Behavior*. Edited by Nemat-Nasser, S. Northwestern University, Evanston, IL. p. 285-315.
- Schuler, H., Mayrhofer, C. and Thoma, K. 2006. Spall experiments for the measurement of the tensile strength and fracture energy of concrete at high strain rates. *International Journal of Impact Engineering* 32 (10): 1635-1650.
- Schwer, D. 2008. Regular and Mach reflections to Mach 18 with air and TNT detonation products. *NRL/MR/6410—08-9132*, Naval Research Laboratory, Washington, DC.
- Schwer, L. E. 2004. Preliminary assessment of non-Lagrangian methods for penetration simulation. *Proceedings, 8th International LS-DYNA Users Conference*. Dearborn, MI. p. 8.1-8.12.
- Sherkar, P., Whittaker A. S. and Aref, A. J. 2010. “Modeling the effects of detonations of high explosives to inform blast-resistant design.” *Technical Report MCEER-10-0009*, The State University of New York at Buffalo, Buffalo, NY.
- Smith, P. D. and Hetherington, J. G. 1994. *Blast and Ballistic Loading of Structures*. Butterworth-Heinemann, Oxford; Boston.
- Souers, P. C., Forbes, J. W., Fried, L. E., Howard, W. M., Anderson, S., Dawson, S., Vitello, P. and Garza, R. 2001. Detonation energies from the cylinder test and CHEETAH V3.0. *Propellants, Explosives, Pyrotechnics* 26 (4): 180-190.

- Swisdak, M. M., Jr. 1994. Simplified Kingery airblast calculations. Naval Surface Warfare Center, Indian Head Division, Silver Spring, MD.
- Tan, P., Lee, B. and Tsangalis, C. 2009. FEA modelling prediction of the transmitted overpressure and particle acceleration within a frame subjected to shock tube blast loadings. *Proceedings*, 18th World IMACS / MODSIM Congress. Cairns, Australia. p. 1657-1663.
- Teng, T. L., Chu, Y. A., Chang, F. A. and Chin, H. S. 2004. Simulation model of impact on reinforced concrete. *Cement and Concrete Research* 34 (11): 2067-2077.
- Timoshenko, S. P. and Goodier, J. N. 1970. *Theory of Elasticity, 3rd edition*. McGraw-Hill, NY.
- Tuler, F. R. and Butcher, B. M. 1984. A criterion for the time-dependence of dynamic fracture. *International Journal of Fracture* 26 (4): 322-328.
- Wight, J. K. and MacGregor, J. G. 2011. *Reinforced Concrete: Mechanics and Design, 6th edition*. Prentice Hall, Upper Saddle River, NJ.
- Wu, C., Oehlers, D. J., Rebentrost, M., Leach, J., Whittaker, A. S. 2009. Blast testing of ultra-high performance fibre and FRP-retrofitted concrete. *Engineering Structures* 31 (9): 2060-2069.
- Xu, K. and Lu, Y. 2006. Numerical simulation study of spallation in reinforced concrete plates subjected to blast loading. *Computers & Structures* 84 (5-6): 431-438.
- Xu, S., Zhao, Y. and Wu, Z. 2006. Study on the average fracture energy for crack propagation in concrete. *Journal of Materials in Civil Engineering* 18 (6): 817-824.
- Zhou, X. Q., Kuznetsov, V. A., Hao, H. and Waschl, J. 2008. Numerical prediction of concrete slab response to blast loading. *International Journal of Impact Engineering* 35 (10): 1186-1200.
- Zukas, J. A. 1990. *High Velocity Impact Dynamics*. Wiley, New York, NY.



## APPENDIX A

### SPEED OF SOUND

#### A.1 Introduction

The speed of sound is a pressure disturbance that propagates through a medium. In a solid, stress or pressure waves propagate at the speed of sound because particles oscillate around their original positions due to strong intermolecular forces (attractions) that hold adjacent particles together. In a fluid, materials move with time because intermolecular forces are weak. Pressure waves in a fluid propagate at the sum of the speed of sound in the medium (e.g., air) and the particle velocity.

#### A.2 Determination of Speed of Sound in Solids and Fluids

For an elastic solid with a constant bulk modulus, the speed of sound,  $c_{solid}$ , in the longitudinal direction is (Kolsky 1953)

$$c_{solid} = \sqrt{\frac{E}{\rho}} \quad (\text{A-1})$$

where  $E$  is the Young's modulus and  $\rho$  is density. In a fluid, the speed of sound,  $c_{fluid}$ , is given by (Kinney and Graham 1985)

$$c_{fluid} = \sqrt{\frac{dp}{d\rho}} \text{ or } \sqrt{\frac{K}{\rho}} \quad (\text{A-2})$$

where  $p$  is pressure and  $K$  is the bulk modulus, which is volumetric elasticity and an extension of the Young's modulus,  $E$ , to three dimensions. The bulk modulus is calculated as

$$K = -v \frac{dp}{dv} \text{ or } \rho \frac{dp}{d\rho} \quad (\text{A-3})$$

For an ideal gas, the formula of the speed of sound in a fluid in Equation A-2 is further simplified using entropy, which is defined as a measure of disorder or dissipated energy in a system. For an idea gas, the entropy,  $s$ , remains constant, namely,

$$ds = 0 = c_v \frac{dT}{T} + pd\left(\frac{1}{\rho}\right) = c_p \frac{dT}{T} - \frac{1}{\rho} dp \quad (\text{A-4})$$

where  $c_v$  is the specific heat at constant volume,  $c_p$  is the specific heat at constant pressure,  $T$  is temperature. Equation A-4 can be rewritten for  $dT/T$  as a function of other variables:

$$\frac{dT}{T} = \frac{c_p p d\rho}{\rho^2} = \frac{c_v dp}{\rho} \text{ or } \frac{dp}{d\rho} = \frac{\gamma p}{\rho} \quad (\gamma = \frac{c_p}{c_v}) \quad (\text{A-5})$$

Using Equation A-5, the speed of sound in a fluid for an ideal gas can be simplified:

$$c_{fluid} = \sqrt{\frac{dp}{d\rho}} = \sqrt{\frac{\gamma p}{\rho}} = \sqrt{\rho RT} \quad (p = \rho RT) \quad (\text{A-6})$$

where  $R$  is the gas constant.

## APPENDIX B

### DETONATION WAVE AND PRESSURE

#### B.1 Introduction

The pressure after detonation in a high explosive is well described by the Chapman-Jouguet (CJ) conditions (e.g., Fickett and David 1979, Smith and Hetherington 1994), which are a restatement of the Rankine-Hugoniot relationships for one-dimensional (1D) steady<sup>11</sup> and inviscid<sup>12</sup> flow. A detonation (shock) wave propagates at constant velocity through an unreacted high explosive. The velocity at the detonation front is equal to the sum of the speed of sound and the local particle velocity immediately behind the detonation front. A thin chemical reaction zone follows the front of the detonation wave, which is explained by the Zeldovich-von Neumann-Döring (ZND) theory (e.g., Davison 2008). The detonation wave compresses the charge to a high pressure termed the von Neumann spike, at which the charge is still unreacted. The spike indicates the onset of chemical reactions. The chemical reactions terminate with chemical equilibrium<sup>13</sup> immediately behind the reaction zone, which is defined as the CJ plane. The pressure measured at the CJ plane is termed the CJ pressure or the detonation pressure. Figure B-1 shows pressures and other states across the shock front. The ZND theory assumes that the reaction zone is steady; thermodynamic states (e.g., pressure, density, internal energy) in the reaction zone are maintained constant by the chemical reactions. The region behind the CJ plane is unsteady, where the states vary continuously with time. The unsteady flow is described by a Taylor wave (e.g., Davison 2008), which is a rarefaction wave centered at the origin of the explosive. The centered rarefaction wave expands at the velocity equal to the sum of the sound speed and the local flow (particle) velocity and the wave expansion decreases pressures and

---

<sup>11</sup> In steady flow, all conditions at any point are constant with respect to time, whereas in unsteady flow, all conditions at any point are not constant with respect to time.

<sup>12</sup> Inviscid flow assumes no viscosity in the flow. The viscous effects can be neglected for a gas in a supersonic flow resulted from detonation.

<sup>13</sup> Chemical equilibrium is the state in which the forward and backward reactions proceed at the same rate, or reactions halt. There are thus no net changes in the concentrations of reactants and products (Anderson 2003).

temperatures in the region behind the CJ plane. When the detonation wave exits the surface of the charge, another rarefaction wave is created and propagates toward the origin of the charge at the speed of sound minus the local particle velocity. The relationships of the CJ detonation pressure and states across the detonation front are formulated using the Rankine-Hugoniot equations in the following section.

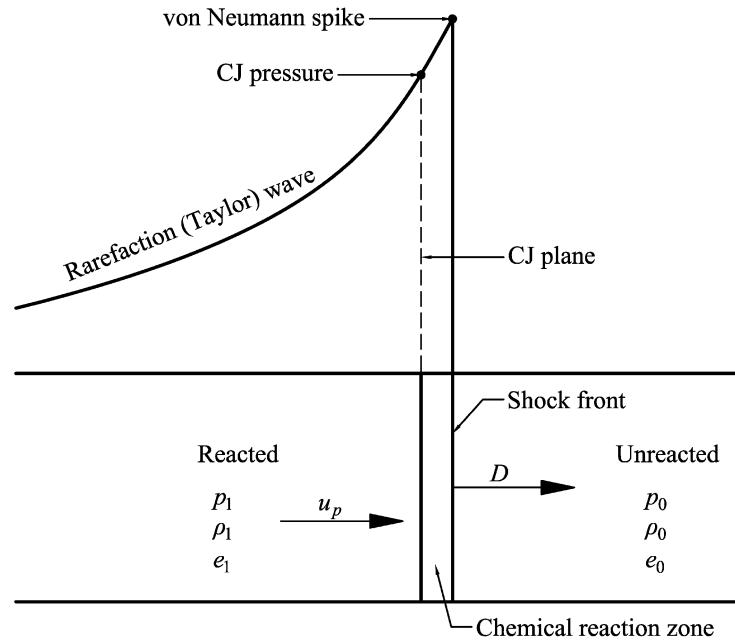


**Figure B-1 States across a detonation (shock) wave in unsteady flow (adapted from Fickett and Davis 1979)**

## B.2 Hugoniot Curves and Rayleigh Line for the Detonation Front

The Rankine-Hugoniot equations in a steady and inviscid flow, conserving mass, momentum and energy, are

$$\rho_1 u_1 = \rho_0 u_0 \quad (\text{B-1})$$

$$p_1 + \rho_1 u_1^2 = p_0 + \rho_0 u_0^2 \quad (\text{B-2})$$

$$h_1 + \frac{1}{2} u_1^2 = h_0 + \frac{1}{2} u_0^2 \quad (\text{B-3})$$

where  $\rho$  is density,  $u$  is particle velocity,  $p$  is pressure,  $h$  is enthalpy, and subscripts 1 and 0 denote the compressed and undisturbed media, respectively, immediately behind and ahead of

the detonation front, respectively. Figure B-1 shows the states across the detonation front in unsteady flow, which is transformed to steady flow in Figure B-2. Equations are derived across the detonation front using the Rankin-Hugoniot equations, CJ conditions, and steady-state variables of Figure B-2. Equation B-1 can be rewritten by replacing  $u_1$  and  $u_0$  by  $D - u_p$  and  $D$ , respectively,

$$\rho_1(D - u_p) = \rho_0 D \quad (\text{B-4})$$

where  $D$  is the detonation velocity,  $u_p$  is particle velocity, in the unsteady flow, immediately behind the detonation front. Similar to Equation B-4, Equation B-2 is expressed as

$$p_1 - p_0 = \rho_0 D u_p \quad (\text{B-5})$$

The enthalpy,  $h$ , is a measure of energy effects for systems and also called *total energy*. The enthalpy is calculated as the sum of the internal energy and the pressure-volume product:

$$h = pv + e = p / \rho + e \quad (\text{B-6})$$

where  $v$  is the specific volume and  $e$  is the specific internal energy. Substituting Equation B-6 into Equation C-3 yields

$$\frac{p_1}{\rho_1} + \frac{(u_p - D)^2}{2} + e_1 = \frac{p_0}{\rho_0} + \frac{D^2}{2} + e_0 \quad (\text{B-7})$$

Equations B-4 and B-5 can be rewritten for  $u_p$  as

$$u_p = \frac{D(\rho_1 - \rho_0)}{\rho_1} \quad (\text{B-8})$$

$$u_p = \frac{p_1 - p_0}{\rho_0 D} \quad (\text{B-9})$$

From Equations B-5, B-7 and B-8,

$$u_p^2 = \frac{(\rho_1 - \rho_0)(p_1 - p_0)}{\rho_1 \rho_0} \quad (\text{B-10})$$

$$D u_p = \frac{p_1 - p_0}{\rho_0} \quad (\text{B-11})$$

Substituting Equations B-10 and B-11 into Equation B-7 to eliminate the parameters,  $u_p$  and  $D$ , yields

$$e_1 - e_0 = \frac{1}{2}(p_1 + p_0)\left(\frac{1}{\rho_0} - \frac{1}{\rho_1}\right) \text{ or } \frac{1}{2}(p_1 + p_0)(v_0 - v_1) \quad (\text{B-12})$$

The  $p$ - $v$  diagram using this equation is called the Hugoniot curve for unreacted explosives. To produce the Hugoniot curve for the reacted explosives, the energy of chemical reactions,  $Q$ , should be added to the equation, such that  $e_1$  is replaced by  $e_1 - Q$ .

The equations of conservations of mass and momentum in Equations B-4 and B-5, respectively, are reorganized to give

$$p_1 - p_0 = \rho_0^2 D^2 \left( \frac{1}{\rho_0} - \frac{1}{\rho_1} \right) \text{ or } \rho_0^2 D^2 (v_0 - v_1) \quad (\text{B-13})$$

This is the equation of the Rayleigh line, which is a straight line with slope of  $-\rho_0^2 D^2$ . The Hugoniot curve and the Rayleigh line are illustrated in Figure B-3, where  $p = p_1$  and  $v = v_1$ . The point  $(p_0, v_0)$  is the origin, which is the initial state of an unreacted explosive. The Rayleigh line passes through the origin and always has a negative slope of  $-\rho_0^2 D^2$  as shown in Equation B-13, such that the regions, in which straight lines passing the origin has positive slopes, in the  $p$ - $v$  diagram are theoretically impossible, as shown in the figure. The location at which the Rayleigh line is tangent to the reacted Hugoniot curve is the CJ plane, which was introduced previously. The Rayleigh line intersects the unreacted Hugoniot curve at the von Neumann spike. The pressure at the CJ plane,  $p_{CJ}$ , can be derived from Equation B-5 by replacing  $p_1$  by  $p_{CJ}$ :

$$p_{CJ} = \rho_0 D u_p + p_0 \approx \rho_0 D u_p \quad (\text{B-14})$$

where  $p_0$  is approximately 0.1 MPa and can be thus ignored (the CJ pressure is approximately 21 GPa). On the reacted Hugoniot curve, the region above the CJ plane represents strong (overdriven) detonations and that between the CJ plane and the location at  $v = v_0$  weak detonations. The overdriven detonation phenomena can occur in some special conditions such as high velocity impacts of a flyer plate and strong detonations with properties higher than the CJ values, thereby leading to higher detonation pressures or velocities than the CJ values. The weak

detonations are seldom observed but can be caused by multiple chemical reactions such as a single reaction with positive heat release but negative volume change, two reactions of one exothermic<sup>14</sup> and the other endothermic<sup>14</sup>, and transport effects, thereby attenuating energy release or pressure (Fickett and Davis 1979), but are seldom observed. Materials that detonate at supersonic speed are called high explosives (e.g., PETN, Nitroglycerine, RDX, TNT). The speed of detonation is controlled by the shock wave, which causes a rapid increase in pressure and temperature. The region below the location at  $p = p_0$  on the reacted Hugoniot curve represents deflagration, which is propagated at subsonic speed, on the order of 1-100 m/s, and the speed is governed by heat conduction and diffusion. Deflagration is the characteristic of low explosives (e.g., Lead azide, Mercury fulminate).

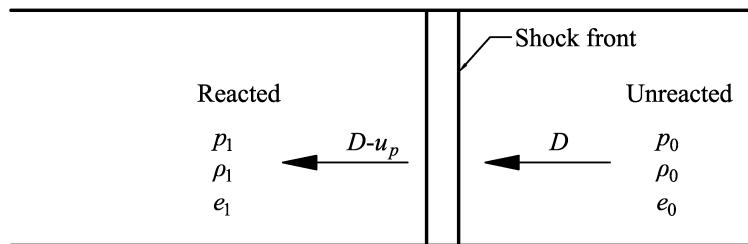


**Figure B-2 States across a detonation (shock) wave in steady flow flow (adapted from Fickett and Davis 1979)**

<sup>14</sup> In thermodynamics, the term *exothermic* describes a process or reaction in which the system releases energy from its surroundings in the form of heat. On the contrary, while the term *endothermic* indicates a process in which the system absorbs energy.

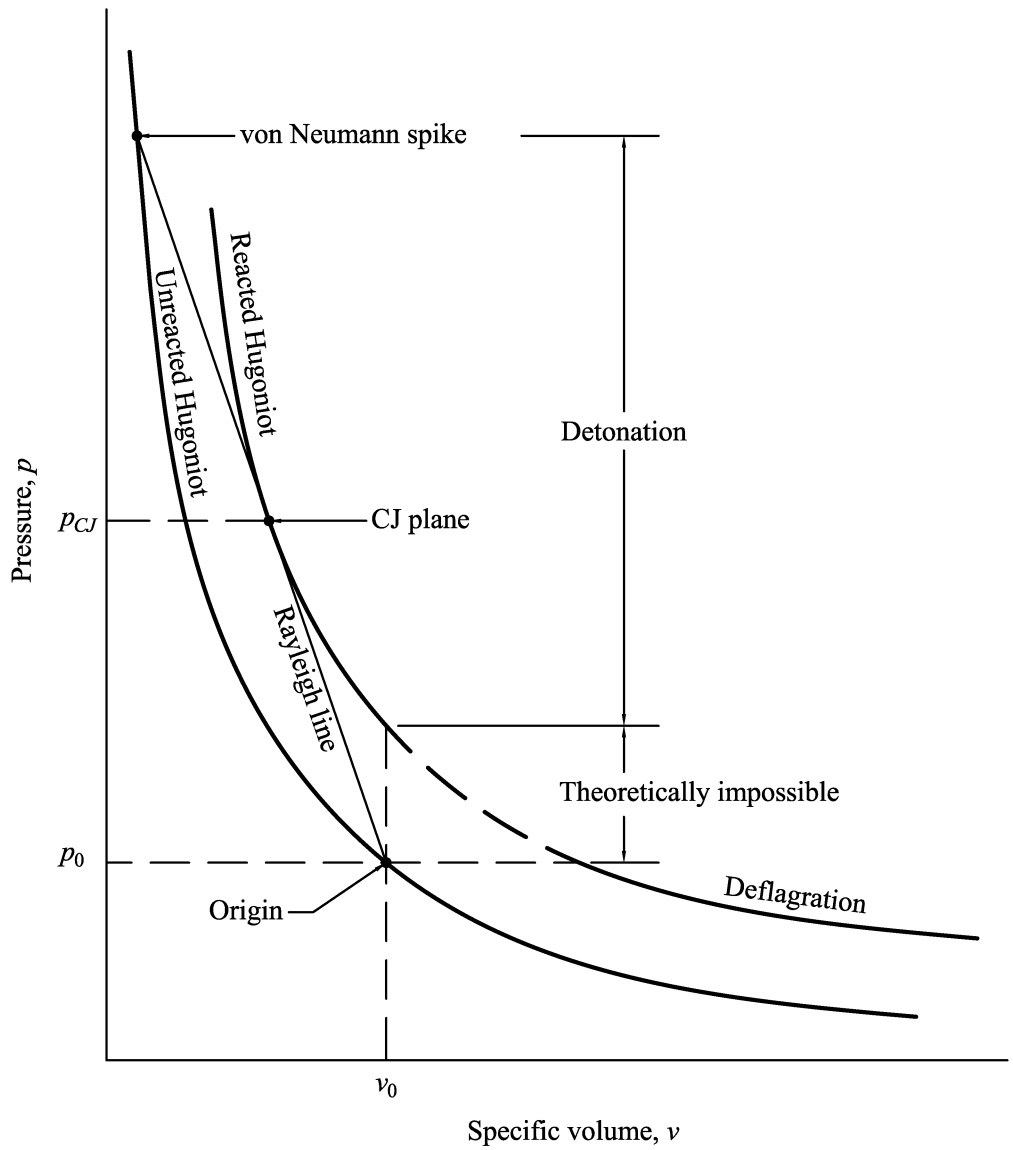


Figure B-3 Hugoniot curves and Rayleigh line (adapted from Smith and Hetherington 1994)

## **APPENDIX C**

### **INCIDENT AND REFLECTED OVERPRESSURES VERY CLOSE TO THE CHARGE FACE**

#### **C.1 Introduction**

Numerical studies are performed using AUTODYN (ANSYS 2013a) for incident and reflected peak overpressure very close to the face of a TNT charge with a radius of 150 mm. Two cells sizes are selected for analysis (0.1 mm and 0.05 mm) based on the studies in Section 3.5.2. Data are monitored at 0.33 mm intervals for distances between 149 mm and 151 mm, and at 1 mm intervals between 147 mm and 149 mm, and between 151 mm and 155 mm.

#### **C.2 AUTODYN Results**

Results for CFD analysis are presented over a distance from 3 mm inside (147 mm,  $Z = 0.0517 \text{ m/kg}^{1/3}$ ) to 5 mm beyond (155 mm,  $Z = 0.0545 \text{ m/kg}^{1/3}$ ) the face of the charge. Results for the two cell sizes are similar, as seen in Figure C-1. Inside the charge, the incident overpressures are close to the CJ pressure (21 GPa) but increase within 1 mm of the charge face and then decrease rapidly immediately beyond the charge face. This rapid change is attributed to the many orders of magnitude differences in pressure, density and internal energy across the charge face. The drop in overpressure at the charge surface is better resolved with the finer cell size of 0.05 mm. The reflected peak overpressure at 0.33 mm from the charge surface for the 0.1 mm cells are greater than for the 0.05 mm cells because the mesh with the 0.1 mm cells is somewhat coarse for the distance of 0.33 mm.

The reflected overpressures at the charge face are also simulated using five small cell sizes: 1, 0.5, 0.25, 0.1, 0.05 mm. For each cell size, the reflected peak overpressure is nearly twice the incident peak overpressure, as shown in Figure C-2, which indicates that in this case, the influence of particle velocity is insignificant for the reflected peak overpressures. The reflected overpressure is a combination of static pressures and dynamic (wind) pressures, where the latter is a function of particle velocity. For the charge of TNT in direct contact with a reflecting surface,

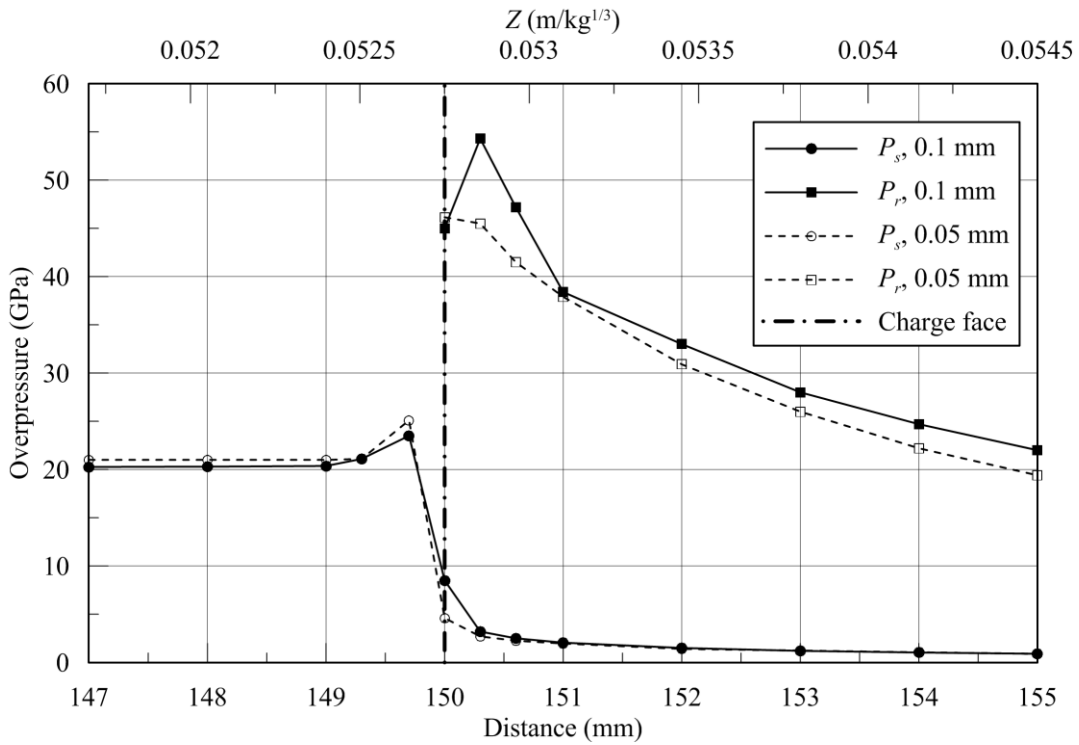


**Figure C-1 Incident and reflected peak overpressures near the charge face for cell sizes of 0.1 mm and 0.05 mm**

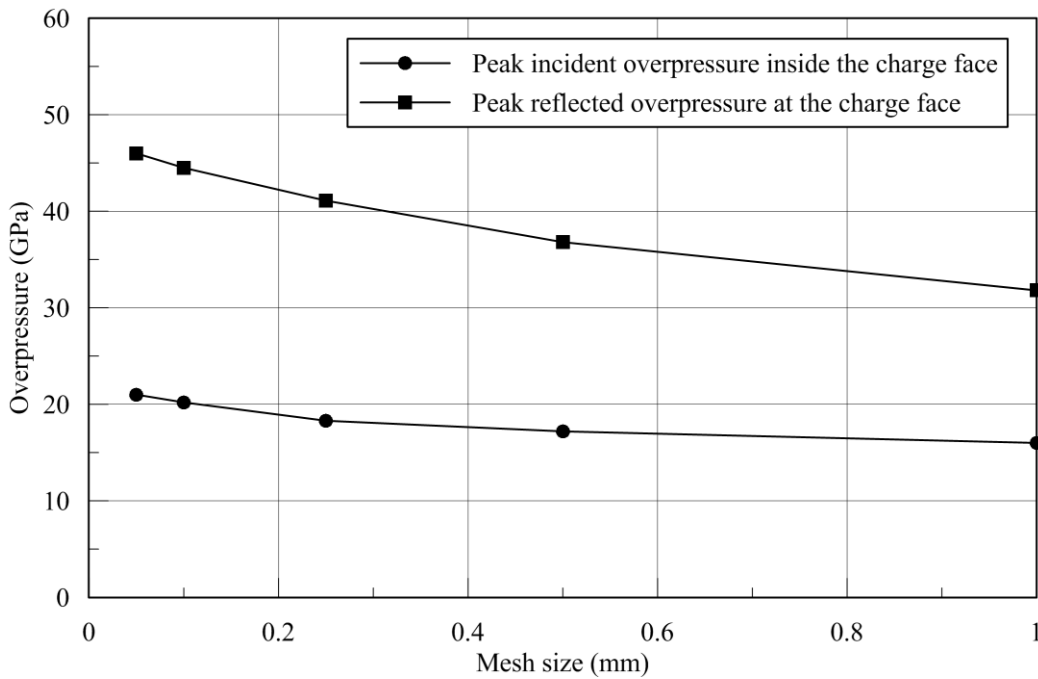


**Figure C-2 Incident peak overpressures inside and reflected peak overpressures at the charge face as a function of cell size**

shock wave reflections at the contact location occur within a solid area, before exiting the face of the charge into the surrounding air. As particles in a solid are held at their original positions by their intermolecular forces, as described in Appendix A, the effect of particle velocity is insignificant in the calculation of the reflected pressure. When waves are reflected from a perfect boundary, their amplitudes are momentarily doubled (e.g., Kolsky 1953), which is associated with the static pressure<sup>15</sup>. For normal reflection, the reflected peak overpressure,  $p_r$ , is calculated by

$$p_r = 2p_s + (\gamma + 1)q_s \quad (C-1)$$

where  $p_s$  is an incident overpressure,  $\gamma$  is the specific heat ratio, and  $q_s$  is dynamic pressure. The first and second terms correspond to the static and dynamic responses, respectively. The particle velocity becomes very important as the shock front exits the face of the charge into the surrounding air. Reflection coefficients for distances between 151 and 155 mm are plotted in Figure C-3, where the reflection coefficient is the ratio of the reflected to incident overpressures. The reflection coefficients vary between 20 and 25 at these distances, which indicates that the reflection coefficient is related principally to particle velocity. Immediately after the shock front exits the face of the charge, the particle acceleration is on the order of 1.0E10g. The peak particle velocities across the charge surface for distances between 147 and 155 mm are presented in Figure C-4. The peak particle velocity is approximately 2 km/s inside the charge face and increases to 6 to 7 km/s at approximately 1 mm beyond the face of the charge.

---

<sup>15</sup> To explain this, consider a rectangular wave having only a positive compression phase and moving through a medium with wavelength,  $\lambda$ , velocity,  $v$ , and amplitude,  $A$ . When the wave reaches a reflecting surface, a particle at the front of the wave exerts a force upon a particle of the reflecting surface, which also pushes the particle at the wave front with the same force at the same time, based on the Newton's third law. This is *reflection*. The reflected wave has same wavelength,  $\lambda$ , velocity,  $v$ , amplitude,  $A$ , as the incident wave but acts in the opposite direction. The incident and reflected waves consequently merge at the boundary during the period of  $\lambda / v$  and the amplitude of the merged waves becomes  $2A$  before the waves separate completely into single waves.

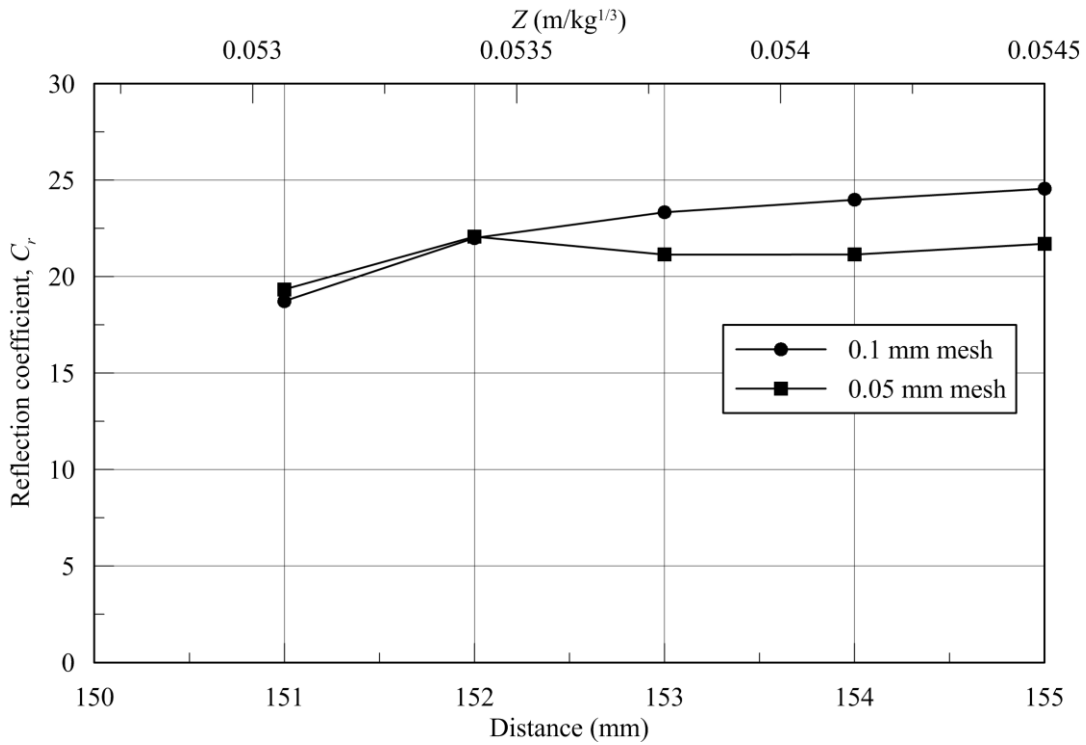


**Figure C-3 Reflection coefficients for distances between 151 and 155 mm**

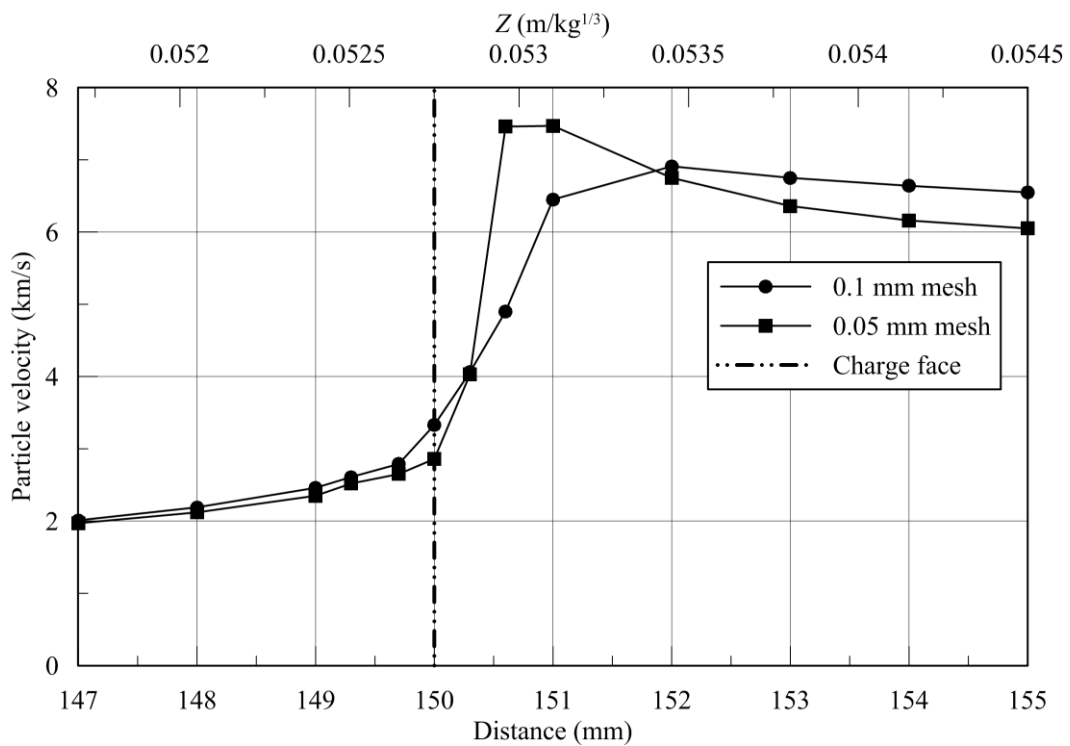


**Figure C-4 Peak particle velocities for distances between 151 and 155 mm**

## APPENDIX D

### KINGERY AND BULMASH CHARTS

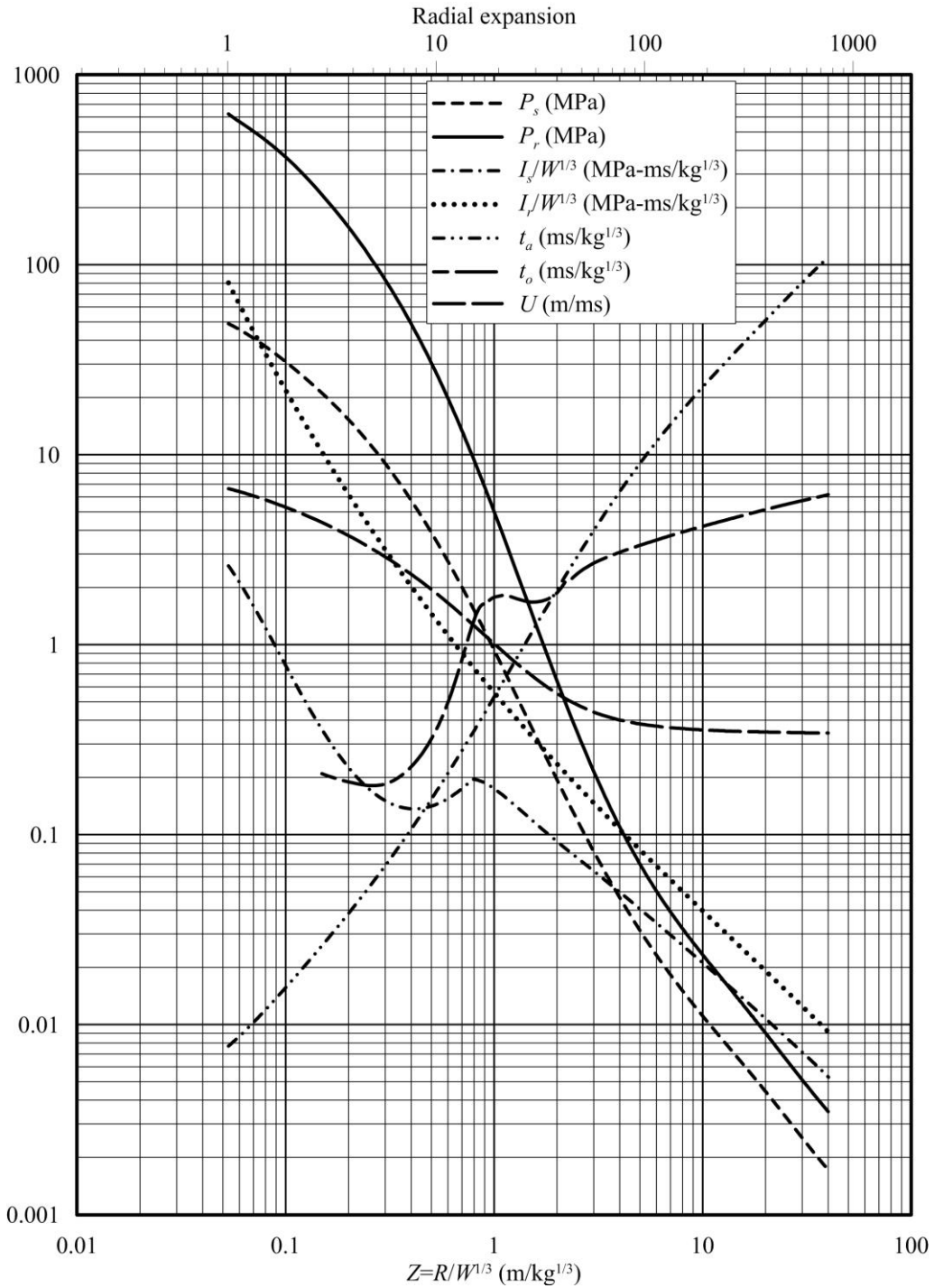


**Figure D-1 Air-blast parameters as a function of scaled distance in SI units; spherical free-air burst of TNT**

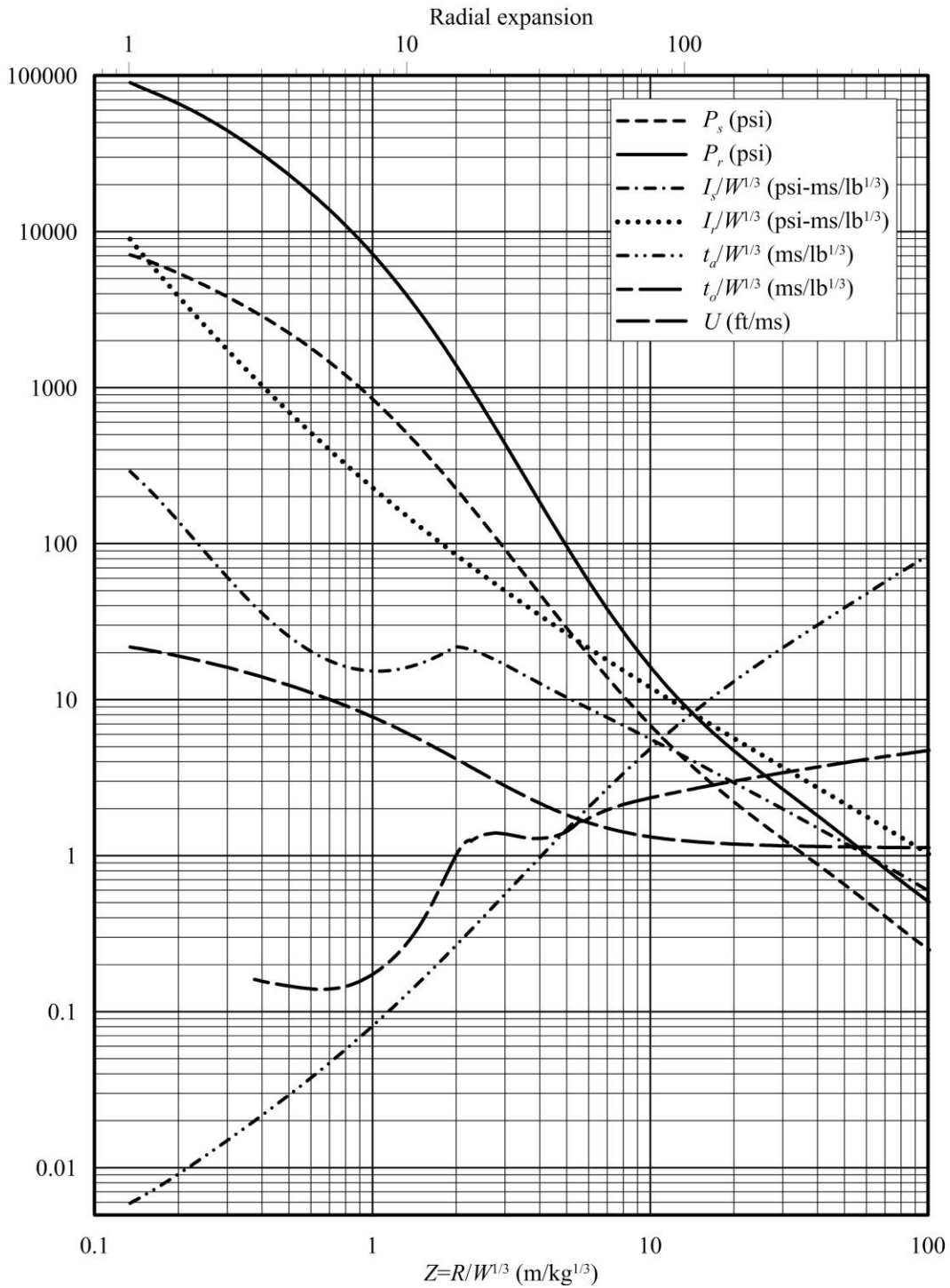


**Figure D-2 Air-blast parameters as a function of scaled distance in US units; spherical free-air burst of TNT**

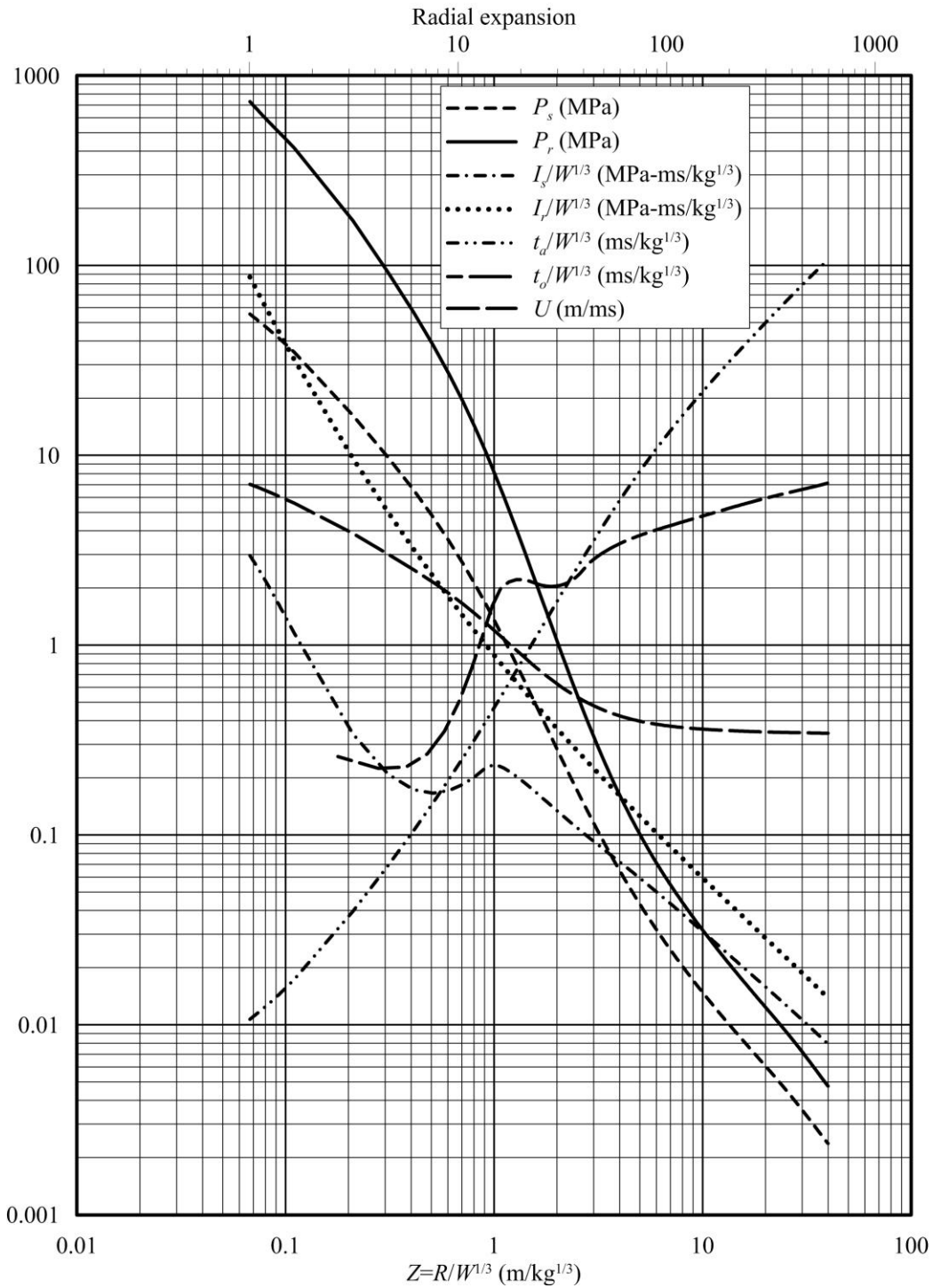


**Figure D-3 Air-blast parameters as a function of scaled distance in SI units; hemispherical surface burst of TNT**

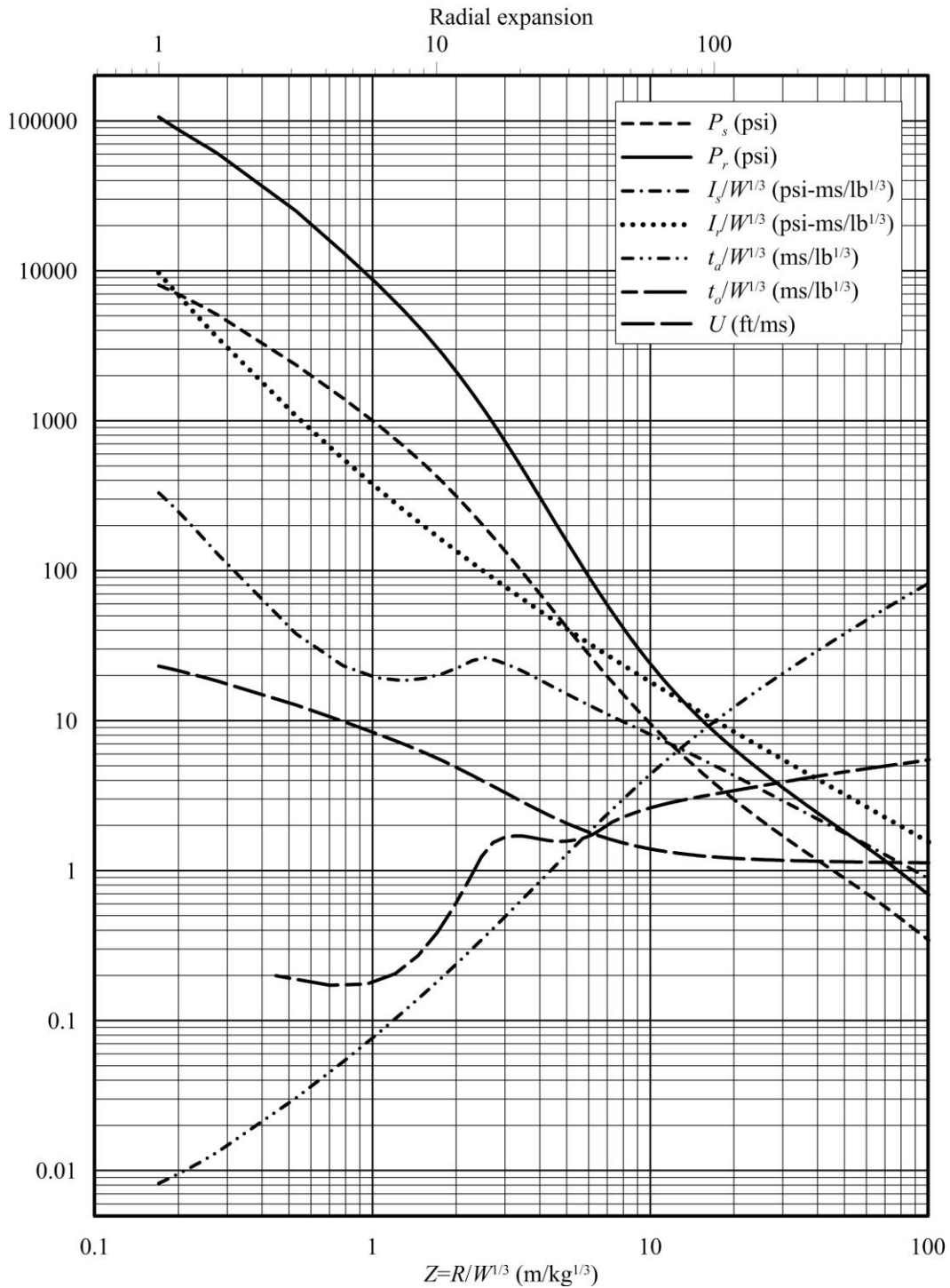


**Figure D-4 Air-blast parameters as a function of scaled distance in US units; hemispherical surface burst of TNT**

**APPENDIX E**  
**CSCM MODEL PARAMETERS IN LS-DYNA**

Values of parameters of the CSCM model for concrete compressive strengths of 35.5 and 50 MPa used in LS-DYNA are presented in Table E-1. The values were chosen based on experimental data reported by Murray (2007).

**Table E-1 CSCM model parameters in LS-DYNA**

Parameter	Value	
Compressive strength (MPa)	35.5	50
Mass density (kg/m <sup>3</sup> )	2400	2400
Pre-existing damage	0	0
Shear modulus, $G$ (GPa)	12.2	13.6
Bulk modulus, $K$ (GPa)	13.3	14.9
Tri-axial compression surface constant term, $\alpha$ (MPa)	15.2	15.9
Tri-axial compression surface linear term, $\theta$	0.3143	0.3651
Tri-axial compression surface nonlinear term, $\lambda$ (MPa)	10.5	10.5
Tri-axial compression surface exponent, $\beta$ (MPa <sup>-1</sup> )	0.01929	0.01929
Torsion surface constant term, $\alpha_1$	0.7473	0.7473
Torsion compression surface linear term, $\theta_1$ (MPa <sup>-1</sup> )	$9.95 \times 10^{-4}$	$4.64 \times 10^{-4}$
Torsion compression surface nonlinear term, $\lambda_1$	0.17	0.17
Torsion compression surface exponent, $\beta_1$ (MPa <sup>-1</sup> )	0.0646	0.04255
Tri-axial extension surface constant term, $\alpha_2$	0.66	0.66
Tri-axial extension surface linear term, $\theta_2$ (MPa <sup>-1</sup> )	$1.20 \times 10^{-3}$	$556 \times 10^{-4}$
Tri-axial extension surface nonlinear term, $\lambda_2$	0.16	0.16
Tri-axial extension surface exponent, $\beta_2$ (MPa <sup>-1</sup> )	0.0646	0.04255
Cap aspect ratio, $R$	5	5

**Table E-1 CSCM model parameters in LS-DYNA (cont.)**

Parameter	Value	
Cap initial location, $X_0$ (MPa)	93.3	104
Maximum plastic volume compaction, $W$	0.05	0.05
Linear shape parameter, $D_1$ (MPa <sup>-1</sup> )	$2.50 \times 10^{-4}$	$2.50 \times 10^{-4}$
Quadratic shape parameter, $D_2$ (MPa <sup>-2</sup> )	$3.49 \times 10^{-7}$	$3.49 \times 10^{-7}$
Ductile shape softening parameter, $B$	100	100
Fracture energy in uniaxial stress, $G_{fc}$ (N/mm)	7.65	9.72
Brittle shape softening parameter, $D$	0.1	0.1
Fracture energy in uniaxial tension, $G_{ft}$ (N/mm)	0.0765	0.0972
Fracture energy in uniaxial tension, $G_{fs}$ (N/mm)	0.0765	0.0972
Shear-to-compression transition parameter, $PWRC$	5	5
Shear-to-tension transition parameter, $PWRT$	1	1
Modify moderate pressure softening parameter, $PMOD$	0	0
Rate-effect parameter for uniaxial compression, $\eta_{0c}$	$1.90 \times 10^{-4}$	$1.64 \times 10^{-4}$
Rate-effect power for uniaxial compression, $N_c$	0.57	0.54
Rate-effect parameter for uniaxial tension, $\eta_{0t}$	$2.1 \times 10^{-4}$	$2.1 \times 10^{-4}$
Rate-effect power for uniaxial tension, $N_t$	0.71	0.71
Maximum stress in compression (MPa)	59.5	85
Maximum stress in tension (MPa)	59.5	85

**APPENDIX F**  
**SINGLE-DEGREE-OF-FREEDOM (SDOF) CALCULATIONS FOR**  
**STRAIN RATE**

**F.1 Introduction**

Single-degree-of-freedom (SDOF) calculations of strain rate are performed to validate results from LS-DYNA for selected single element simulations presented in Section 6.5. Strain-rate histories are generated for three linearly increasing force histories, adapted from the blast-type loadings presented in Figure 6-13. The force histories are applied to one end of the 20 mm, 40 mm and 80 mm cubic elements. The properties of the elements are presented in Table F-1.

**Table F-1 Properties of single elements**

Parameter	20×20×20 mm	40×40×40 mm	80×80×80 mm
Young's modulus (MPa)	$2.8 \times 10^4$		
Density (tonne/mm <sup>3</sup> )	$2.4 \times 10^{-9}$		
Area (mm <sup>2</sup> )	400	1600	6400
Length, $L$ (mm)	20	40	80
Volume (mm <sup>3</sup> )	$8.0 \times 10^3$	$6.4 \times 10^4$	$5.1 \times 10^5$
Stiffness, $k$ (N/mm)	$5.6 \times 10^5$	$1.1 \times 10^6$	$2.2 \times 10^6$
Mass, $m$ (tonne)	$9.6 \times 10^{-6}$	$7.7 \times 10^{-5}$	$6.1 \times 10^{-4}$
Circular frequency, $w_n$ (rad/sec)	$2.4 \times 10^5$	$1.2 \times 10^5$	$6.0 \times 10^4$
Cyclic frequency, $f_n$ (Hz)	$3.8 \times 10^4$	$1.9 \times 10^4$	$9.6 \times 10^3$
Period, $T_n$ (sec)	$2.6 \times 10^{-5}$	$5.2 \times 10^{-5}$	$1.0 \times 10^{-4}$
$t_d / T_n$	19	14	4.8

## F.2 SDOF Calculations

The equation of motion for linearly increasing force acting on a single-degree-of-freedom system is

$$m\ddot{u} + ku = p_o \frac{t}{t_d} \quad (\text{F-1})$$

where  $m$ ,  $u$ ,  $k$ ,  $p_o$ ,  $t$  and  $t_d$  are the mass, displacement, stiffness, peak force, time, and time corresponding to the peak force, respectively. The solution of Equation F-1 for  $0 < t \leq t_d$  is (Chopra 2012)

$$u(t) = \frac{p_o}{k} \left( \frac{t}{t_d} - \frac{\sin w_n t}{w_n t_d} \right) \quad (\text{F-2})$$

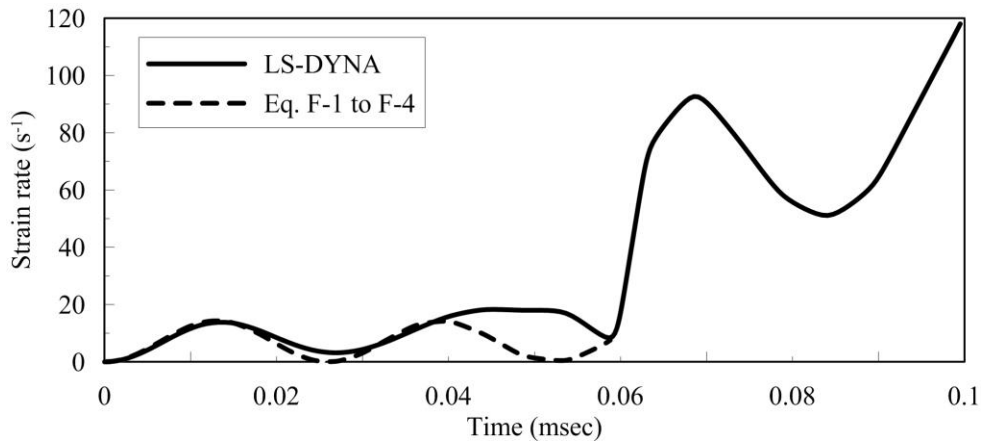
$$\dot{u}(t) = \frac{p_o}{k} \left( \frac{1}{t_d} - \frac{\cos w_n t}{t_d} \right) \quad (\text{F-3})$$

where  $w_n$  is natural circular frequency.

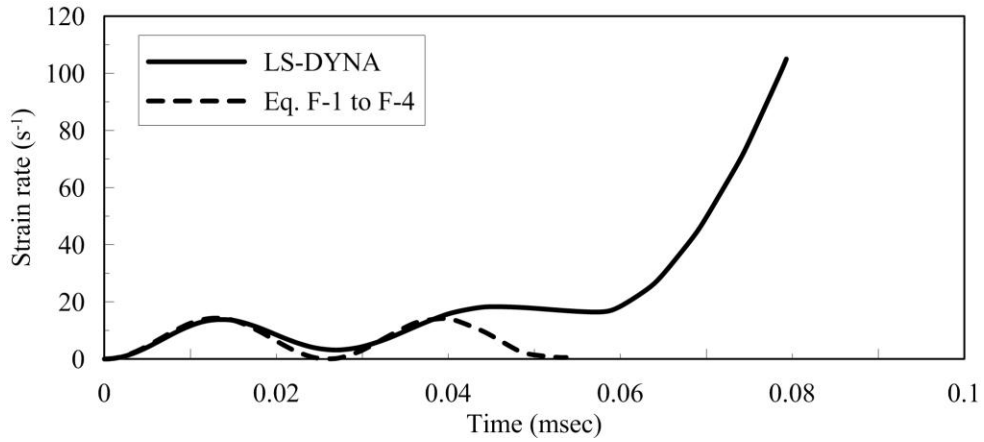
Strain-rate histories are plotted using Equation F-3 because strain rate is proportional to velocity. The relationship between strain rate,  $\dot{\epsilon}$ , and velocity,  $V$ , is

$$V = L\dot{\epsilon} \quad (\text{F-4})$$

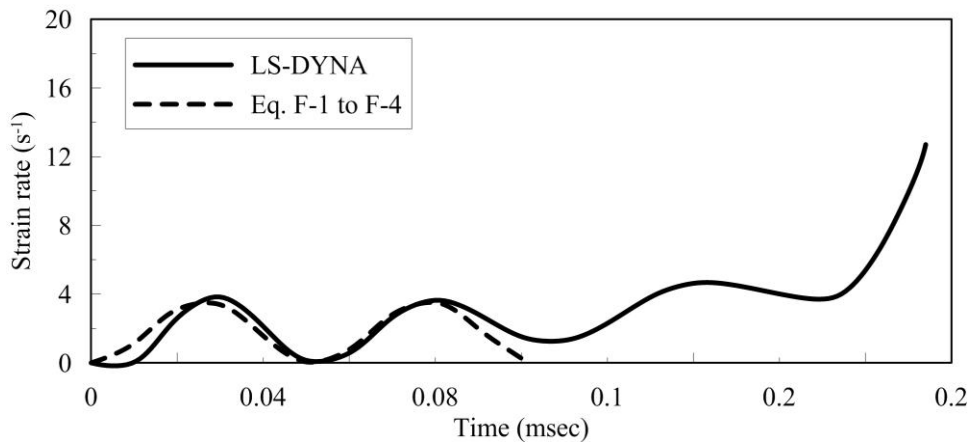
where  $L$  is the length of an element. Figure F-1 shows that the results of the LS-DYNA analysis and the SDOF analysis are in good agreement before the compressive strength of the concrete is reached. The CSCM model assumes linear elastic response up to peak compressive strength, and the strain-rate histories have similar peak amplitudes and natural periods in this range. The strain rates computed by numerical simulations increase rapidly due to strain softening. The SDOF analysis results validate the LS-DYNA analysis, albeit over only part of the loading phase.



(a) 20×20×20 mm element, peak tensile pressure of 10 MPa, 200 MPa/msec



(b) 20×20×20 mm element, peak tensile pressure of 20 MPa, 200 MPa/msec



(c) 40×40×40 mm element , peak tensile pressure of 20 MPa, 50 MPa/msec

**Figure F-1 Strain-rate histories for three single element simulations**



## MCEER Technical Reports

MCEER publishes technical reports on a variety of subjects written by authors funded through MCEER. These reports are available from both MCEER Publications and the National Technical Information Service (NTIS). Requests for reports should be directed to MCEER Publications, MCEER, University at Buffalo, State University of New York, 133A Ketter Hall, Buffalo, New York 14260. Reports can also be requested through NTIS, P.O. Box 1425, Springfield, Virginia 22151. NTIS accession numbers are shown in parenthesis, if available.

- NCEER-87-0001 "First-Year Program in Research, Education and Technology Transfer," 3/5/87, (PB88-134275, A04, MF-A01).
- NCEER-87-0002 "Experimental Evaluation of Instantaneous Optimal Algorithms for Structural Control," by R.C. Lin, T.T. Soong and A.M. Reinhorn, 4/20/87, (PB88-134341, A04, MF-A01).
- NCEER-87-0003 "Experimentation Using the Earthquake Simulation Facilities at University at Buffalo," by A.M. Reinhorn and R.L. Ketter, not available.
- NCEER-87-0004 "The System Characteristics and Performance of a Shaking Table," by J.S. Hwang, K.C. Chang and G.C. Lee, 6/1/87, (PB88-134259, A03, MF-A01). This report is available only through NTIS (see address given above).
- NCEER-87-0005 "A Finite Element Formulation for Nonlinear Viscoplastic Material Using a Q Model," by O. Gyebe and G. Dasgupta, 11/2/87, (PB88-213764, A08, MF-A01).
- NCEER-87-0006 "Symbolic Manipulation Program (SMP) - Algebraic Codes for Two and Three Dimensional Finite Element Formulations," by X. Lee and G. Dasgupta, 11/9/87, (PB88-218522, A05, MF-A01).
- NCEER-87-0007 "Instantaneous Optimal Control Laws for Tall Buildings Under Seismic Excitations," by J.N. Yang, A. Akbarpour and P. Ghaemmaghami, 6/10/87, (PB88-134333, A06, MF-A01). This report is only available through NTIS (see address given above).
- NCEER-87-0008 "IDARC: Inelastic Damage Analysis of Reinforced Concrete Frame - Shear-Wall Structures," by Y.J. Park, A.M. Reinhorn and S.K. Kunnath, 7/20/87, (PB88-134325, A09, MF-A01). This report is only available through NTIS (see address given above).
- NCEER-87-0009 "Liquefaction Potential for New York State: A Preliminary Report on Sites in Manhattan and Buffalo," by M. Budhu, V. Vijayakumar, R.F. Giese and L. Baumgras, 8/31/87, (PB88-163704, A03, MF-A01). This report is available only through NTIS (see address given above).
- NCEER-87-0010 "Vertical and Torsional Vibration of Foundations in Inhomogeneous Media," by A.S. Veletsos and K.W. Dotson, 6/1/87, (PB88-134291, A03, MF-A01). This report is only available through NTIS (see address given above).
- NCEER-87-0011 "Seismic Probabilistic Risk Assessment and Seismic Margins Studies for Nuclear Power Plants," by Howard H.M. Hwang, 6/15/87, (PB88-134267, A03, MF-A01). This report is only available through NTIS (see address given above).
- NCEER-87-0012 "Parametric Studies of Frequency Response of Secondary Systems Under Ground-Acceleration Excitations," by Y. Yong and Y.K. Lin, 6/10/87, (PB88-134309, A03, MF-A01). This report is only available through NTIS (see address given above).
- NCEER-87-0013 "Frequency Response of Secondary Systems Under Seismic Excitation," by J.A. HoLung, J. Cai and Y.K. Lin, 7/31/87, (PB88-134317, A05, MF-A01). This report is only available through NTIS (see address given above).
- NCEER-87-0014 "Modelling Earthquake Ground Motions in Seismically Active Regions Using Parametric Time Series Methods," by G.W. Ellis and A.S. Cakmak, 8/25/87, (PB88-134283, A08, MF-A01). This report is only available through NTIS (see address given above).
- NCEER-87-0015 "Detection and Assessment of Seismic Structural Damage," by E. DiPasquale and A.S. Cakmak, 8/25/87, (PB88-163712, A05, MF-A01). This report is only available through NTIS (see address given above).

- NCEER-87-0016 "Pipeline Experiment at Parkfield, California," by J. Isenberg and E. Richardson, 9/15/87, (PB88-163720, A03, MF-A01). This report is available only through NTIS (see address given above).
- NCEER-87-0017 "Digital Simulation of Seismic Ground Motion," by M. Shinozuka, G. Deodatis and T. Harada, 8/31/87, (PB88-155197, A04, MF-A01). This report is available only through NTIS (see address given above).
- NCEER-87-0018 "Practical Considerations for Structural Control: System Uncertainty, System Time Delay and Truncation of Small Control Forces," J.N. Yang and A. Akbarpour, 8/10/87, (PB88-163738, A08, MF-A01). This report is only available through NTIS (see address given above).
- NCEER-87-0019 "Modal Analysis of Nonclassically Damped Structural Systems Using Canonical Transformation," by J.N. Yang, S. Sarkani and F.X. Long, 9/27/87, (PB88-187851, A04, MF-A01).
- NCEER-87-0020 "A Nonstationary Solution in Random Vibration Theory," by J.R. Red-Horse and P.D. Spanos, 11/3/87, (PB88-163746, A03, MF-A01).
- NCEER-87-0021 "Horizontal Impedances for Radially Inhomogeneous Viscoelastic Soil Layers," by A.S. Veletsos and K.W. Dotson, 10/15/87, (PB88-150859, A04, MF-A01).
- NCEER-87-0022 "Seismic Damage Assessment of Reinforced Concrete Members," by Y.S. Chung, C. Meyer and M. Shinozuka, 10/9/87, (PB88-150867, A05, MF-A01). This report is available only through NTIS (see address given above).
- NCEER-87-0023 "Active Structural Control in Civil Engineering," by T.T. Soong, 11/11/87, (PB88-187778, A03, MF-A01).
- NCEER-87-0024 "Vertical and Torsional Impedances for Radially Inhomogeneous Viscoelastic Soil Layers," by K.W. Dotson and A.S. Veletsos, 12/87, (PB88-187786, A03, MF-A01).
- NCEER-87-0025 "Proceedings from the Symposium on Seismic Hazards, Ground Motions, Soil-Liquefaction and Engineering Practice in Eastern North America," October 20-22, 1987, edited by K.H. Jacob, 12/87, (PB88-188115, A23, MF-A01). This report is available only through NTIS (see address given above).
- NCEER-87-0026 "Report on the Whittier-Narrows, California, Earthquake of October 1, 1987," by J. Pantelic and A. Reinhorn, 11/87, (PB88-187752, A03, MF-A01). This report is available only through NTIS (see address given above).
- NCEER-87-0027 "Design of a Modular Program for Transient Nonlinear Analysis of Large 3-D Building Structures," by S. Srivastav and J.F. Abel, 12/30/87, (PB88-187950, A05, MF-A01). This report is only available through NTIS (see address given above).
- NCEER-87-0028 "Second-Year Program in Research, Education and Technology Transfer," 3/8/88, (PB88-219480, A04, MF-A01).
- NCEER-88-0001 "Workshop on Seismic Computer Analysis and Design of Buildings With Interactive Graphics," by W. McGuire, J.F. Abel and C.H. Conley, 1/18/88, (PB88-187760, A03, MF-A01). This report is only available through NTIS (see address given above).
- NCEER-88-0002 "Optimal Control of Nonlinear Flexible Structures," by J.N. Yang, F.X. Long and D. Wong, 1/22/88, (PB88-213772, A06, MF-A01).
- NCEER-88-0003 "Substructuring Techniques in the Time Domain for Primary-Secondary Structural Systems," by G.D. Manolis and G. Juhn, 2/10/88, (PB88-213780, A04, MF-A01).
- NCEER-88-0004 "Iterative Seismic Analysis of Primary-Secondary Systems," by A. Singhal, L.D. Lutes and P.D. Spanos, 2/23/88, (PB88-213798, A04, MF-A01).
- NCEER-88-0005 "Stochastic Finite Element Expansion for Random Media," by P.D. Spanos and R. Ghanem, 3/14/88, (PB88-213806, A03, MF-A01).

- NCEER-88-0006 "Combining Structural Optimization and Structural Control," by F.Y. Cheng and C.P. Pantelides, 1/10/88, (PB88-213814, A05, MF-A01).
- NCEER-88-0007 "Seismic Performance Assessment of Code-Designed Structures," by H.H-M. Hwang, J-W. Jaw and H-J. Shau, 3/20/88, (PB88-219423, A04, MF-A01). This report is only available through NTIS (see address given above).
- NCEER-88-0008 "Reliability Analysis of Code-Designed Structures Under Natural Hazards," by H.H-M. Hwang, H. Ushiba and M. Shinozuka, 2/29/88, (PB88-229471, A07, MF-A01). This report is only available through NTIS (see address given above).
- NCEER-88-0009 "Seismic Fragility Analysis of Shear Wall Structures," by J-W Jaw and H.H-M. Hwang, 4/30/88, (PB89-102867, A04, MF-A01).
- NCEER-88-0010 "Base Isolation of a Multi-Story Building Under a Harmonic Ground Motion - A Comparison of Performances of Various Systems," by F-G Fan, G. Ahmadi and I.G. Tadjbakhsh, 5/18/88, (PB89-122238, A06, MF-A01). This report is only available through NTIS (see address given above).
- NCEER-88-0011 "Seismic Floor Response Spectra for a Combined System by Green's Functions," by F.M. Lavelle, L.A. Bergman and P.D. Spanos, 5/1/88, (PB89-102875, A03, MF-A01).
- NCEER-88-0012 "A New Solution Technique for Randomly Excited Hysteretic Structures," by G.Q. Cai and Y.K. Lin, 5/16/88, (PB89-102883, A03, MF-A01).
- NCEER-88-0013 "A Study of Radiation Damping and Soil-Structure Interaction Effects in the Centrifuge," by K. Weissman, supervised by J.H. Prevost, 5/24/88, (PB89-144703, A06, MF-A01).
- NCEER-88-0014 "Parameter Identification and Implementation of a Kinematic Plasticity Model for Frictional Soils," by J.H. Prevost and D.V. Griffiths, not available.
- NCEER-88-0015 "Two- and Three- Dimensional Dynamic Finite Element Analyses of the Long Valley Dam," by D.V. Griffiths and J.H. Prevost, 6/17/88, (PB89-144711, A04, MF-A01).
- NCEER-88-0016 "Damage Assessment of Reinforced Concrete Structures in Eastern United States," by A.M. Reinhorn, M.J. Seidel, S.K. Kunnath and Y.J. Park, 6/15/88, (PB89-122220, A04, MF-A01). This report is only available through NTIS (see address given above).
- NCEER-88-0017 "Dynamic Compliance of Vertically Loaded Strip Foundations in Multilayered Viscoelastic Soils," by S. Ahmad and A.S.M. Israil, 6/17/88, (PB89-102891, A04, MF-A01).
- NCEER-88-0018 "An Experimental Study of Seismic Structural Response With Added Viscoelastic Dampers," by R.C. Lin, Z. Liang, T.T. Soong and R.H. Zhang, 6/30/88, (PB89-122212, A05, MF-A01). This report is available only through NTIS (see address given above).
- NCEER-88-0019 "Experimental Investigation of Primary - Secondary System Interaction," by G.D. Manolis, G. Juhn and A.M. Reinhorn, 5/27/88, (PB89-122204, A04, MF-A01).
- NCEER-88-0020 "A Response Spectrum Approach For Analysis of Nonclassically Damped Structures," by J.N. Yang, S. Sarkani and F.X. Long, 4/22/88, (PB89-102909, A04, MF-A01).
- NCEER-88-0021 "Seismic Interaction of Structures and Soils: Stochastic Approach," by A.S. Veletsos and A.M. Prasad, 7/21/88, (PB89-122196, A04, MF-A01). This report is only available through NTIS (see address given above).
- NCEER-88-0022 "Identification of the Serviceability Limit State and Detection of Seismic Structural Damage," by E. DiPasquale and A.S. Cakmak, 6/15/88, (PB89-122188, A05, MF-A01). This report is available only through NTIS (see address given above).
- NCEER-88-0023 "Multi-Hazard Risk Analysis: Case of a Simple Offshore Structure," by B.K. Bhartia and E.H. Vanmarcke, 7/21/88, (PB89-145213, A05, MF-A01).

- NCEER-88-0024 "Automated Seismic Design of Reinforced Concrete Buildings," by Y.S. Chung, C. Meyer and M. Shinozuka, 7/5/88, (PB89-122170, A06, MF-A01). This report is available only through NTIS (see address given above).
- NCEER-88-0025 "Experimental Study of Active Control of MDOF Structures Under Seismic Excitations," by L.L. Chung, R.C. Lin, T.T. Soong and A.M. Reinhorn, 7/10/88, (PB89-122600, A04, MF-A01).
- NCEER-88-0026 "Earthquake Simulation Tests of a Low-Rise Metal Structure," by J.S. Hwang, K.C. Chang, G.C. Lee and R.L. Ketter, 8/1/88, (PB89-102917, A04, MF-A01).
- NCEER-88-0027 "Systems Study of Urban Response and Reconstruction Due to Catastrophic Earthquakes," by F. Kozin and H.K. Zhou, 9/22/88, (PB90-162348, A04, MF-A01).
- NCEER-88-0028 "Seismic Fragility Analysis of Plane Frame Structures," by H.H-M. Hwang and Y.K. Low, 7/31/88, (PB89-131445, A06, MF-A01).
- NCEER-88-0029 "Response Analysis of Stochastic Structures," by A. Kardara, C. Bucher and M. Shinozuka, 9/22/88, (PB89-174429, A04, MF-A01).
- NCEER-88-0030 "Nonnormal Accelerations Due to Yielding in a Primary Structure," by D.C.K. Chen and L.D. Lutes, 9/19/88, (PB89-131437, A04, MF-A01).
- NCEER-88-0031 "Design Approaches for Soil-Structure Interaction," by A.S. Veletsos, A.M. Prasad and Y. Tang, 12/30/88, (PB89-174437, A03, MF-A01). This report is available only through NTIS (see address given above).
- NCEER-88-0032 "A Re-evaluation of Design Spectra for Seismic Damage Control," by C.J. Turkstra and A.G. Tallin, 11/7/88, (PB89-145221, A05, MF-A01).
- NCEER-88-0033 "The Behavior and Design of Noncontact Lap Splices Subjected to Repeated Inelastic Tensile Loading," by V.E. Sagan, P. Gergely and R.N. White, 12/8/88, (PB89-163737, A08, MF-A01).
- NCEER-88-0034 "Seismic Response of Pile Foundations," by S.M. Mamoon, P.K. Banerjee and S. Ahmad, 11/1/88, (PB89-145239, A04, MF-A01).
- NCEER-88-0035 "Modeling of R/C Building Structures With Flexible Floor Diaphragms (IDARC2)," by A.M. Reinhorn, S.K. Kunnath and N. Panahshahi, 9/7/88, (PB89-207153, A07, MF-A01).
- NCEER-88-0036 "Solution of the Dam-Reservoir Interaction Problem Using a Combination of FEM, BEM with Particular Integrals, Modal Analysis, and Substructuring," by C-S. Tsai, G.C. Lee and R.L. Ketter, 12/31/88, (PB89-207146, A04, MF-A01).
- NCEER-88-0037 "Optimal Placement of Actuators for Structural Control," by F.Y. Cheng and C.P. Pantelides, 8/15/88, (PB89-162846, A05, MF-A01).
- NCEER-88-0038 "Teflon Bearings in Aseismic Base Isolation: Experimental Studies and Mathematical Modeling," by A. Mokha, M.C. Constantinou and A.M. Reinhorn, 12/5/88, (PB89-218457, A10, MF-A01). This report is available only through NTIS (see address given above).
- NCEER-88-0039 "Seismic Behavior of Flat Slab High-Rise Buildings in the New York City Area," by P. Weidlinger and M. Ettouney, 10/15/88, (PB90-145681, A04, MF-A01).
- NCEER-88-0040 "Evaluation of the Earthquake Resistance of Existing Buildings in New York City," by P. Weidlinger and M. Ettouney, 10/15/88, not available.
- NCEER-88-0041 "Small-Scale Modeling Techniques for Reinforced Concrete Structures Subjected to Seismic Loads," by W. Kim, A. El-Attar and R.N. White, 11/22/88, (PB89-189625, A05, MF-A01).
- NCEER-88-0042 "Modeling Strong Ground Motion from Multiple Event Earthquakes," by G.W. Ellis and A.S. Cakmak, 10/15/88, (PB89-174445, A03, MF-A01).

- NCEER-88-0043 "Nonstationary Models of Seismic Ground Acceleration," by M. Grigoriu, S.E. Ruiz and E. Rosenblueth, 7/15/88, (PB89-189617, A04, MF-A01).
- NCEER-88-0044 "SARCF User's Guide: Seismic Analysis of Reinforced Concrete Frames," by Y.S. Chung, C. Meyer and M. Shinozuka, 11/9/88, (PB89-174452, A08, MF-A01).
- NCEER-88-0045 "First Expert Panel Meeting on Disaster Research and Planning," edited by J. Pantelic and J. Stoyke, 9/15/88, (PB89-174460, A05, MF-A01).
- NCEER-88-0046 "Preliminary Studies of the Effect of Degrading Infill Walls on the Nonlinear Seismic Response of Steel Frames," by C.Z. Chrysostomou, P. Gergely and J.F. Abel, 12/19/88, (PB89-208383, A05, MF-A01).
- NCEER-88-0047 "Reinforced Concrete Frame Component Testing Facility - Design, Construction, Instrumentation and Operation," by S.P. Pessiki, C. Conley, T. Bond, P. Gergely and R.N. White, 12/16/88, (PB89-174478, A04, MF-A01).
- NCEER-89-0001 "Effects of Protective Cushion and Soil Compliancy on the Response of Equipment Within a Seismically Excited Building," by J.A. HoLung, 2/16/89, (PB89-207179, A04, MF-A01).
- NCEER-89-0002 "Statistical Evaluation of Response Modification Factors for Reinforced Concrete Structures," by H.H-M. Hwang and J-W. Jaw, 2/17/89, (PB89-207187, A05, MF-A01).
- NCEER-89-0003 "Hysteretic Columns Under Random Excitation," by G-Q. Cai and Y.K. Lin, 1/9/89, (PB89-196513, A03, MF-A01).
- NCEER-89-0004 "Experimental Study of 'Elephant Foot Bulge' Instability of Thin-Walled Metal Tanks," by Z-H. Jia and R.L. Ketter, 2/22/89, (PB89-207195, A03, MF-A01).
- NCEER-89-0005 "Experiment on Performance of Buried Pipelines Across San Andreas Fault," by J. Isenberg, E. Richardson and T.D. O'Rourke, 3/10/89, (PB89-218440, A04, MF-A01). This report is available only through NTIS (see address given above).
- NCEER-89-0006 "A Knowledge-Based Approach to Structural Design of Earthquake-Resistant Buildings," by M. Subramani, P. Gergely, C.H. Conley, J.F. Abel and A.H. Zaghaw, 1/15/89, (PB89-218465, A06, MF-A01).
- NCEER-89-0007 "Liquefaction Hazards and Their Effects on Buried Pipelines," by T.D. O'Rourke and P.A. Lane, 2/1/89, (PB89-218481, A09, MF-A01).
- NCEER-89-0008 "Fundamentals of System Identification in Structural Dynamics," by H. Imai, C-B. Yun, O. Maruyama and M. Shinozuka, 1/26/89, (PB89-207211, A04, MF-A01).
- NCEER-89-0009 "Effects of the 1985 Michoacan Earthquake on Water Systems and Other Buried Lifelines in Mexico," by A.G. Ayala and M.J. O'Rourke, 3/8/89, (PB89-207229, A06, MF-A01).
- NCEER-89-R010 "NCEER Bibliography of Earthquake Education Materials," by K.E.K. Ross, Second Revision, 9/1/89, (PB90-125352, A05, MF-A01). This report is replaced by NCEER-92-0018.
- NCEER-89-0011 "Inelastic Three-Dimensional Response Analysis of Reinforced Concrete Building Structures (IDARC-3D), Part I - Modeling," by S.K. Kunnath and A.M. Reinhorn, 4/17/89, (PB90-114612, A07, MF-A01). This report is available only through NTIS (see address given above).
- NCEER-89-0012 "Recommended Modifications to ATC-14," by C.D. Poland and J.O. Malley, 4/12/89, (PB90-108648, A15, MF-A01).
- NCEER-89-0013 "Repair and Strengthening of Beam-to-Column Connections Subjected to Earthquake Loading," by M. Corazao and A.J. Durrani, 2/28/89, (PB90-109885, A06, MF-A01).
- NCEER-89-0014 "Program EXKAL2 for Identification of Structural Dynamic Systems," by O. Maruyama, C-B. Yun, M. Hoshiya and M. Shinozuka, 5/19/89, (PB90-109877, A09, MF-A01).

- NCEER-89-0015 "Response of Frames With Bolted Semi-Rigid Connections, Part I - Experimental Study and Analytical Predictions," by P.J. DiCorso, A.M. Reinhorn, J.R. Dickerson, J.B. Radzimirski and W.L. Harper, 6/1/89, not available.
- NCEER-89-0016 "ARMA Monte Carlo Simulation in Probabilistic Structural Analysis," by P.D. Spanos and M.P. Mignolet, 7/10/89, (PB90-109893, A03, MF-A01).
- NCEER-89-P017 "Preliminary Proceedings from the Conference on Disaster Preparedness - The Place of Earthquake Education in Our Schools," Edited by K.E.K. Ross, 6/23/89, (PB90-108606, A03, MF-A01).
- NCEER-89-0017 "Proceedings from the Conference on Disaster Preparedness - The Place of Earthquake Education in Our Schools," Edited by K.E.K. Ross, 12/31/89, (PB90-207895, A012, MF-A02). This report is available only through NTIS (see address given above).
- NCEER-89-0018 "Multidimensional Models of Hysteretic Material Behavior for Vibration Analysis of Shape Memory Energy Absorbing Devices, by E.J. Graesser and F.A. Cozzarelli, 6/7/89, (PB90-164146, A04, MF-A01).
- NCEER-89-0019 "Nonlinear Dynamic Analysis of Three-Dimensional Base Isolated Structures (3D-BASIS)," by S. Nagarajaiah, A.M. Reinhorn and M.C. Constantinou, 8/3/89, (PB90-161936, A06, MF-A01). This report has been replaced by NCEER-93-0011.
- NCEER-89-0020 "Structural Control Considering Time-Rate of Control Forces and Control Rate Constraints," by F.Y. Cheng and C.P. Pantelides, 8/3/89, (PB90-120445, A04, MF-A01).
- NCEER-89-0021 "Subsurface Conditions of Memphis and Shelby County," by K.W. Ng, T-S. Chang and H-H.M. Hwang, 7/26/89, (PB90-120437, A03, MF-A01).
- NCEER-89-0022 "Seismic Wave Propagation Effects on Straight Jointed Buried Pipelines," by K. Elhmadi and M.J. O'Rourke, 8/24/89, (PB90-162322, A10, MF-A02).
- NCEER-89-0023 "Workshop on Serviceability Analysis of Water Delivery Systems," edited by M. Grigoriu, 3/6/89, (PB90-127424, A03, MF-A01).
- NCEER-89-0024 "Shaking Table Study of a 1/5 Scale Steel Frame Composed of Tapered Members," by K.C. Chang, J.S. Hwang and G.C. Lee, 9/18/89, (PB90-160169, A04, MF-A01).
- NCEER-89-0025 "DYNA1D: A Computer Program for Nonlinear Seismic Site Response Analysis - Technical Documentation," by Jean H. Prevost, 9/14/89, (PB90-161944, A07, MF-A01). This report is available only through NTIS (see address given above).
- NCEER-89-0026 "1:4 Scale Model Studies of Active Tendon Systems and Active Mass Dampers for Aseismic Protection," by A.M. Reinhorn, T.T. Soong, R.C. Lin, Y.P. Yang, Y. Fukao, H. Abe and M. Nakai, 9/15/89, (PB90-173246, A10, MF-A02). This report is available only through NTIS (see address given above).
- NCEER-89-0027 "Scattering of Waves by Inclusions in a Nonhomogeneous Elastic Half Space Solved by Boundary Element Methods," by P.K. Hadley, A. Askar and A.S. Cakmak, 6/15/89, (PB90-145699, A07, MF-A01).
- NCEER-89-0028 "Statistical Evaluation of Deflection Amplification Factors for Reinforced Concrete Structures," by H.H.M. Hwang, J-W. Jaw and A.L. Ch'ng, 8/31/89, (PB90-164633, A05, MF-A01).
- NCEER-89-0029 "Bedrock Accelerations in Memphis Area Due to Large New Madrid Earthquakes," by H.H.M. Hwang, C.H.S. Chen and G. Yu, 11/7/89, (PB90-162330, A04, MF-A01).
- NCEER-89-0030 "Seismic Behavior and Response Sensitivity of Secondary Structural Systems," by Y.Q. Chen and T.T. Soong, 10/23/89, (PB90-164658, A08, MF-A01).
- NCEER-89-0031 "Random Vibration and Reliability Analysis of Primary-Secondary Structural Systems," by Y. Ibrahim, M. Grigoriu and T.T. Soong, 11/10/89, (PB90-161951, A04, MF-A01).

- NCEER-89-0032 "Proceedings from the Second U.S. - Japan Workshop on Liquefaction, Large Ground Deformation and Their Effects on Lifelines, September 26-29, 1989," Edited by T.D. O'Rourke and M. Hamada, 12/1/89, (PB90-209388, A22, MF-A03).
- NCEER-89-0033 "Deterministic Model for Seismic Damage Evaluation of Reinforced Concrete Structures," by J.M. Bracci, A.M. Reinhorn, J.B. Mander and S.K. Kunnath, 9/27/89, (PB91-108803, A06, MF-A01).
- NCEER-89-0034 "On the Relation Between Local and Global Damage Indices," by E. DiPasquale and A.S. Cakmak, 8/15/89, (PB90-173865, A05, MF-A01).
- NCEER-89-0035 "Cyclic Undrained Behavior of Nonplastic and Low Plasticity Silts," by A.J. Walker and H.E. Stewart, 7/26/89, (PB90-183518, A10, MF-A01).
- NCEER-89-0036 "Liquefaction Potential of Surficial Deposits in the City of Buffalo, New York," by M. Budhu, R. Giese and L. Baumgrass, 1/17/89, (PB90-208455, A04, MF-A01).
- NCEER-89-0037 "A Deterministic Assessment of Effects of Ground Motion Incoherence," by A.S. Veletsos and Y. Tang, 7/15/89, (PB90-164294, A03, MF-A01).
- NCEER-89-0038 "Workshop on Ground Motion Parameters for Seismic Hazard Mapping," July 17-18, 1989, edited by R.V. Whitman, 12/1/89, (PB90-173923, A04, MF-A01).
- NCEER-89-0039 "Seismic Effects on Elevated Transit Lines of the New York City Transit Authority," by C.J. Costantino, C.A. Miller and E. Heymsfield, 12/26/89, (PB90-207887, A06, MF-A01).
- NCEER-89-0040 "Centrifugal Modeling of Dynamic Soil-Structure Interaction," by K. Weissman, Supervised by J.H. Prevost, 5/10/89, (PB90-207879, A07, MF-A01).
- NCEER-89-0041 "Linearized Identification of Buildings With Cores for Seismic Vulnerability Assessment," by I-K. Ho and A.E. Aktan, 11/1/89, (PB90-251943, A07, MF-A01).
- NCEER-90-0001 "Geotechnical and Lifeline Aspects of the October 17, 1989 Loma Prieta Earthquake in San Francisco," by T.D. O'Rourke, H.E. Stewart, F.T. Blackburn and T.S. Dickerman, 1/90, (PB90-208596, A05, MF-A01).
- NCEER-90-0002 "Nonnormal Secondary Response Due to Yielding in a Primary Structure," by D.C.K. Chen and L.D. Lutes, 2/28/90, (PB90-251976, A07, MF-A01).
- NCEER-90-0003 "Earthquake Education Materials for Grades K-12," by K.E.K. Ross, 4/16/90, (PB91-251984, A05, MF-A05). This report has been replaced by NCEER-92-0018.
- NCEER-90-0004 "Catalog of Strong Motion Stations in Eastern North America," by R.W. Busby, 4/3/90, (PB90-251984, A05, MF-A01).
- NCEER-90-0005 "NCEER Strong-Motion Data Base: A User Manual for the GeoBase Release (Version 1.0 for the Sun3)," by P. Friberg and K. Jacob, 3/31/90 (PB90-258062, A04, MF-A01).
- NCEER-90-0006 "Seismic Hazard Along a Crude Oil Pipeline in the Event of an 1811-1812 Type New Madrid Earthquake," by H.H.M. Hwang and C-H.S. Chen, 4/16/90, (PB90-258054, A04, MF-A01).
- NCEER-90-0007 "Site-Specific Response Spectra for Memphis Sheahan Pumping Station," by H.H.M. Hwang and C.S. Lee, 5/15/90, (PB91-108811, A05, MF-A01).
- NCEER-90-0008 "Pilot Study on Seismic Vulnerability of Crude Oil Transmission Systems," by T. Ariman, R. Dobry, M. Grigoriu, F. Kozin, M. O'Rourke, T. O'Rourke and M. Shinozuka, 5/25/90, (PB91-108837, A06, MF-A01).
- NCEER-90-0009 "A Program to Generate Site Dependent Time Histories: EQGEN," by G.W. Ellis, M. Srinivasan and A.S. Cakmak, 1/30/90, (PB91-108829, A04, MF-A01).
- NCEER-90-0010 "Active Isolation for Seismic Protection of Operating Rooms," by M.E. Talbott, Supervised by M. Shinozuka, 6/8/9, (PB91-110205, A05, MF-A01).

- NCEER-90-0011 "Program LINEARID for Identification of Linear Structural Dynamic Systems," by C-B. Yun and M. Shinozuka, 6/25/90, (PB91-110312, A08, MF-A01).
- NCEER-90-0012 "Two-Dimensional Two-Phase Elasto-Plastic Seismic Response of Earth Dams," by A.N. Yiagos, Supervised by J.H. Prevost, 6/20/90, (PB91-110197, A13, MF-A02).
- NCEER-90-0013 "Secondary Systems in Base-Isolated Structures: Experimental Investigation, Stochastic Response and Stochastic Sensitivity," by G.D. Manolis, G. Juhn, M.C. Constantinou and A.M. Reinhorn, 7/1/90, (PB91-110320, A08, MF-A01).
- NCEER-90-0014 "Seismic Behavior of Lightly-Reinforced Concrete Column and Beam-Column Joint Details," by S.P. Pessiki, C.H. Conley, P. Gergely and R.N. White, 8/22/90, (PB91-108795, A11, MF-A02).
- NCEER-90-0015 "Two Hybrid Control Systems for Building Structures Under Strong Earthquakes," by J.N. Yang and A. Daniellians, 6/29/90, (PB91-125393, A04, MF-A01).
- NCEER-90-0016 "Instantaneous Optimal Control with Acceleration and Velocity Feedback," by J.N. Yang and Z. Li, 6/29/90, (PB91-125401, A03, MF-A01).
- NCEER-90-0017 "Reconnaissance Report on the Northern Iran Earthquake of June 21, 1990," by M. Mehrain, 10/4/90, (PB91-125377, A03, MF-A01).
- NCEER-90-0018 "Evaluation of Liquefaction Potential in Memphis and Shelby County," by T.S. Chang, P.S. Tang, C.S. Lee and H. Hwang, 8/10/90, (PB91-125427, A09, MF-A01).
- NCEER-90-0019 "Experimental and Analytical Study of a Combined Sliding Disc Bearing and Helical Steel Spring Isolation System," by M.C. Constantinou, A.S. Mokha and A.M. Reinhorn, 10/4/90, (PB91-125385, A06, MF-A01). This report is available only through NTIS (see address given above).
- NCEER-90-0020 "Experimental Study and Analytical Prediction of Earthquake Response of a Sliding Isolation System with a Spherical Surface," by A.S. Mokha, M.C. Constantinou and A.M. Reinhorn, 10/11/90, (PB91-125419, A05, MF-A01).
- NCEER-90-0021 "Dynamic Interaction Factors for Floating Pile Groups," by G. Gazetas, K. Fan, A. Kaynia and E. Kausel, 9/10/90, (PB91-170381, A05, MF-A01).
- NCEER-90-0022 "Evaluation of Seismic Damage Indices for Reinforced Concrete Structures," by S. Rodriguez-Gomez and A.S. Cakmak, 9/30/90, PB91-171322, A06, MF-A01).
- NCEER-90-0023 "Study of Site Response at a Selected Memphis Site," by H. Desai, S. Ahmad, E.S. Gazetas and M.R. Oh, 10/11/90, (PB91-196857, A03, MF-A01).
- NCEER-90-0024 "A User's Guide to Strongmo: Version 1.0 of NCEER's Strong-Motion Data Access Tool for PCs and Terminals," by P.A. Friberg and C.A.T. Susch, 11/15/90, (PB91-171272, A03, MF-A01).
- NCEER-90-0025 "A Three-Dimensional Analytical Study of Spatial Variability of Seismic Ground Motions," by L-L. Hong and A.H.-S. Ang, 10/30/90, (PB91-170399, A09, MF-A01).
- NCEER-90-0026 "MUMOID User's Guide - A Program for the Identification of Modal Parameters," by S. Rodriguez-Gomez and E. DiPasquale, 9/30/90, (PB91-171298, A04, MF-A01).
- NCEER-90-0027 "SARCF-II User's Guide - Seismic Analysis of Reinforced Concrete Frames," by S. Rodriguez-Gomez, Y.S. Chung and C. Meyer, 9/30/90, (PB91-171280, A05, MF-A01).
- NCEER-90-0028 "Viscous Dampers: Testing, Modeling and Application in Vibration and Seismic Isolation," by N. Makris and M.C. Constantinou, 12/20/90 (PB91-190561, A06, MF-A01).
- NCEER-90-0029 "Soil Effects on Earthquake Ground Motions in the Memphis Area," by H. Hwang, C.S. Lee, K.W. Ng and T.S. Chang, 8/2/90, (PB91-190751, A05, MF-A01).

- NCEER-91-0001 "Proceedings from the Third Japan-U.S. Workshop on Earthquake Resistant Design of Lifeline Facilities and Countermeasures for Soil Liquefaction, December 17-19, 1990," edited by T.D. O'Rourke and M. Hamada, 2/1/91, (PB91-179259, A99, MF-A04).
- NCEER-91-0002 "Physical Space Solutions of Non-Proportionally Damped Systems," by M. Tong, Z. Liang and G.C. Lee, 1/15/91, (PB91-179242, A04, MF-A01).
- NCEER-91-0003 "Seismic Response of Single Piles and Pile Groups," by K. Fan and G. Gazetas, 1/10/91, (PB92-174994, A04, MF-A01).
- NCEER-91-0004 "Damping of Structures: Part 1 - Theory of Complex Damping," by Z. Liang and G. Lee, 10/10/91, (PB92-197235, A12, MF-A03).
- NCEER-91-0005 "3D-BASIS - Nonlinear Dynamic Analysis of Three Dimensional Base Isolated Structures: Part II," by S. Nagarajaiah, A.M. Reinhorn and M.C. Constantinou, 2/28/91, (PB91-190553, A07, MF-A01). This report has been replaced by NCEER-93-0011.
- NCEER-91-0006 "A Multidimensional Hysteretic Model for Plasticity Deforming Metals in Energy Absorbing Devices," by E.J. Graesser and F.A. Cozzarelli, 4/9/91, (PB92-108364, A04, MF-A01).
- NCEER-91-0007 "A Framework for Customizable Knowledge-Based Expert Systems with an Application to a KBES for Evaluating the Seismic Resistance of Existing Buildings," by E.G. Ibarra-Anaya and S.J. Fennes, 4/9/91, (PB91-210930, A08, MF-A01).
- NCEER-91-0008 "Nonlinear Analysis of Steel Frames with Semi-Rigid Connections Using the Capacity Spectrum Method," by G.G. Deierlein, S-H. Hsieh, Y-J. Shen and J.F. Abel, 7/2/91, (PB92-113828, A05, MF-A01).
- NCEER-91-0009 "Earthquake Education Materials for Grades K-12," by K.E.K. Ross, 4/30/91, (PB91-212142, A06, MF-A01). This report has been replaced by NCEER-92-0018.
- NCEER-91-0010 "Phase Wave Velocities and Displacement Phase Differences in a Harmonically Oscillating Pile," by N. Makris and G. Gazetas, 7/8/91, (PB92-108356, A04, MF-A01).
- NCEER-91-0011 "Dynamic Characteristics of a Full-Size Five-Story Steel Structure and a 2/5 Scale Model," by K.C. Chang, G.C. Yao, G.C. Lee, D.S. Hao and Y.C. Yeh," 7/2/91, (PB93-116648, A06, MF-A02).
- NCEER-91-0012 "Seismic Response of a 2/5 Scale Steel Structure with Added Viscoelastic Dampers," by K.C. Chang, T.T. Soong, S-T. Oh and M.L. Lai, 5/17/91, (PB92-110816, A05, MF-A01).
- NCEER-91-0013 "Earthquake Response of Retaining Walls; Full-Scale Testing and Computational Modeling," by S. Alampalli and A-W.M. Elgamal, 6/20/91, not available.
- NCEER-91-0014 "3D-BASIS-M: Nonlinear Dynamic Analysis of Multiple Building Base Isolated Structures," by P.C. Tsopelas, S. Nagarajaiah, M.C. Constantinou and A.M. Reinhorn, 5/28/91, (PB92-113885, A09, MF-A02).
- NCEER-91-0015 "Evaluation of SEAOC Design Requirements for Sliding Isolated Structures," by D. Theodossiou and M.C. Constantinou, 6/10/91, (PB92-114602, A11, MF-A03).
- NCEER-91-0016 "Closed-Loop Modal Testing of a 27-Story Reinforced Concrete Flat Plate-Core Building," by H.R. Somaprasad, T. Toksoy, H. Yoshiyuki and A.E. Aktan, 7/15/91, (PB92-129980, A07, MF-A02).
- NCEER-91-0017 "Shake Table Test of a 1/6 Scale Two-Story Lightly Reinforced Concrete Building," by A.G. El-Attar, R.N. White and P. Gergely, 2/28/91, (PB92-222447, A06, MF-A02).
- NCEER-91-0018 "Shake Table Test of a 1/8 Scale Three-Story Lightly Reinforced Concrete Building," by A.G. El-Attar, R.N. White and P. Gergely, 2/28/91, (PB93-116630, A08, MF-A02).
- NCEER-91-0019 "Transfer Functions for Rigid Rectangular Foundations," by A.S. Veletsos, A.M. Prasad and W.H. Wu, 7/31/91, not available.

- NCEER-91-0020 "Hybrid Control of Seismic-Excited Nonlinear and Inelastic Structural Systems," by J.N. Yang, Z. Li and A. Daniellians, 8/1/91, (PB92-143171, A06, MF-A02).
- NCEER-91-0021 "The NCEER-91 Earthquake Catalog: Improved Intensity-Based Magnitudes and Recurrence Relations for U.S. Earthquakes East of New Madrid," by L. Seeber and J.G. Armbruster, 8/28/91, (PB92-176742, A06, MF-A02).
- NCEER-91-0022 "Proceedings from the Implementation of Earthquake Planning and Education in Schools: The Need for Change - The Roles of the Changemakers," by K.E.K. Ross and F. Winslow, 7/23/91, (PB92-129998, A12, MF-A03).
- NCEER-91-0023 "A Study of Reliability-Based Criteria for Seismic Design of Reinforced Concrete Frame Buildings," by H.H.M. Hwang and H-M. Hsu, 8/10/91, (PB92-140235, A09, MF-A02).
- NCEER-91-0024 "Experimental Verification of a Number of Structural System Identification Algorithms," by R.G. Ghanem, H. Gavin and M. Shinozuka, 9/18/91, (PB92-176577, A18, MF-A04).
- NCEER-91-0025 "Probabilistic Evaluation of Liquefaction Potential," by H.H.M. Hwang and C.S. Lee, 11/25/91, (PB92-143429, A05, MF-A01).
- NCEER-91-0026 "Instantaneous Optimal Control for Linear, Nonlinear and Hysteretic Structures - Stable Controllers," by J.N. Yang and Z. Li, 11/15/91, (PB92-163807, A04, MF-A01).
- NCEER-91-0027 "Experimental and Theoretical Study of a Sliding Isolation System for Bridges," by M.C. Constantinou, A. Kartoum, A.M. Reinhorn and P. Bradford, 11/15/91, (PB92-176973, A10, MF-A03).
- NCEER-92-0001 "Case Studies of Liquefaction and Lifeline Performance During Past Earthquakes, Volume 1: Japanese Case Studies," Edited by M. Hamada and T. O'Rourke, 2/17/92, (PB92-197243, A18, MF-A04).
- NCEER-92-0002 "Case Studies of Liquefaction and Lifeline Performance During Past Earthquakes, Volume 2: United States Case Studies," Edited by T. O'Rourke and M. Hamada, 2/17/92, (PB92-197250, A20, MF-A04).
- NCEER-92-0003 "Issues in Earthquake Education," Edited by K. Ross, 2/3/92, (PB92-222389, A07, MF-A02).
- NCEER-92-0004 "Proceedings from the First U.S. - Japan Workshop on Earthquake Protective Systems for Bridges," Edited by I.G. Buckle, 2/4/92, (PB94-142239, A99, MF-A06).
- NCEER-92-0005 "Seismic Ground Motion from a Haskell-Type Source in a Multiple-Layered Half-Space," A.P. Theoharis, G. Deodatis and M. Shinozuka, 1/2/92, not available.
- NCEER-92-0006 "Proceedings from the Site Effects Workshop," Edited by R. Whitman, 2/29/92, (PB92-197201, A04, MF-A01).
- NCEER-92-0007 "Engineering Evaluation of Permanent Ground Deformations Due to Seismically-Induced Liquefaction," by M.H. Baziar, R. Dobry and A-W.M. Elgamel, 3/24/92, (PB92-222421, A13, MF-A03).
- NCEER-92-0008 "A Procedure for the Seismic Evaluation of Buildings in the Central and Eastern United States," by C.D. Poland and J.O. Malley, 4/2/92, (PB92-222439, A20, MF-A04).
- NCEER-92-0009 "Experimental and Analytical Study of a Hybrid Isolation System Using Friction Controllable Sliding Bearings," by M.Q. Feng, S. Fujii and M. Shinozuka, 5/15/92, (PB93-150282, A06, MF-A02).
- NCEER-92-0010 "Seismic Resistance of Slab-Column Connections in Existing Non-Ductile Flat-Plate Buildings," by A.J. Durrani and Y. Du, 5/18/92, (PB93-116812, A06, MF-A02).
- NCEER-92-0011 "The Hysteretic and Dynamic Behavior of Brick Masonry Walls Upgraded by Ferrocement Coatings Under Cyclic Loading and Strong Simulated Ground Motion," by H. Lee and S.P. Pravel, 5/11/92, not available.
- NCEER-92-0012 "Study of Wire Rope Systems for Seismic Protection of Equipment in Buildings," by G.F. Demetriades, M.C. Constantinou and A.M. Reinhorn, 5/20/92, (PB93-116655, A08, MF-A02).

- NCEER-92-0013 "Shape Memory Structural Dampers: Material Properties, Design and Seismic Testing," by P.R. Witting and F.A. Cozzarelli, 5/26/92, (PB93-116663, A05, MF-A01).
- NCEER-92-0014 "Longitudinal Permanent Ground Deformation Effects on Buried Continuous Pipelines," by M.J. O'Rourke, and C. Nordberg, 6/15/92, (PB93-116671, A08, MF-A02).
- NCEER-92-0015 "A Simulation Method for Stationary Gaussian Random Functions Based on the Sampling Theorem," by M. Grigoriu and S. Balopoulou, 6/11/92, (PB93-127496, A05, MF-A01).
- NCEER-92-0016 "Gravity-Load-Designed Reinforced Concrete Buildings: Seismic Evaluation of Existing Construction and Detailing Strategies for Improved Seismic Resistance," by G.W. Hoffmann, S.K. Kunnath, A.M. Reinhorn and J.B. Mander, 7/15/92, (PB94-142007, A08, MF-A02).
- NCEER-92-0017 "Observations on Water System and Pipeline Performance in the Limón Area of Costa Rica Due to the April 22, 1991 Earthquake," by M. O'Rourke and D. Ballantyne, 6/30/92, (PB93-126811, A06, MF-A02).
- NCEER-92-0018 "Fourth Edition of Earthquake Education Materials for Grades K-12," Edited by K.E.K. Ross, 8/10/92, (PB93-114023, A07, MF-A02).
- NCEER-92-0019 "Proceedings from the Fourth Japan-U.S. Workshop on Earthquake Resistant Design of Lifeline Facilities and Countermeasures for Soil Liquefaction," Edited by M. Hamada and T.D. O'Rourke, 8/12/92, (PB93-163939, A99, MF-E11).
- NCEER-92-0020 "Active Bracing System: A Full Scale Implementation of Active Control," by A.M. Reinhorn, T.T. Soong, R.C. Lin, M.A. Riley, Y.P. Wang, S. Aizawa and M. Higashino, 8/14/92, (PB93-127512, A06, MF-A02).
- NCEER-92-0021 "Empirical Analysis of Horizontal Ground Displacement Generated by Liquefaction-Induced Lateral Spreads," by S.F. Bartlett and T.L. Youd, 8/17/92, (PB93-188241, A06, MF-A02).
- NCEER-92-0022 "IDARC Version 3.0: Inelastic Damage Analysis of Reinforced Concrete Structures," by S.K. Kunnath, A.M. Reinhorn and R.F. Lobo, 8/31/92, (PB93-227502, A07, MF-A02).
- NCEER-92-0023 "A Semi-Empirical Analysis of Strong-Motion Peaks in Terms of Seismic Source, Propagation Path and Local Site Conditions, by M. Kamiyama, M.J. O'Rourke and R. Flores-Berrones, 9/9/92, (PB93-150266, A08, MF-A02).
- NCEER-92-0024 "Seismic Behavior of Reinforced Concrete Frame Structures with Nonductile Details, Part I: Summary of Experimental Findings of Full Scale Beam-Column Joint Tests," by A. Beres, R.N. White and P. Gergely, 9/30/92, (PB93-227783, A05, MF-A01).
- NCEER-92-0025 "Experimental Results of Repaired and Retrofitted Beam-Column Joint Tests in Lightly Reinforced Concrete Frame Buildings," by A. Beres, S. El-Borgi, R.N. White and P. Gergely, 10/29/92, (PB93-227791, A05, MF-A01).
- NCEER-92-0026 "A Generalization of Optimal Control Theory: Linear and Nonlinear Structures," by J.N. Yang, Z. Li and S. Vongchavalitkul, 11/2/92, (PB93-188621, A05, MF-A01).
- NCEER-92-0027 "Seismic Resistance of Reinforced Concrete Frame Structures Designed Only for Gravity Loads: Part I - Design and Properties of a One-Third Scale Model Structure," by J.M. Bracci, A.M. Reinhorn and J.B. Mander, 12/1/92, (PB94-104502, A08, MF-A02).
- NCEER-92-0028 "Seismic Resistance of Reinforced Concrete Frame Structures Designed Only for Gravity Loads: Part II - Experimental Performance of Subassemblages," by L.E. Aycaardi, J.B. Mander and A.M. Reinhorn, 12/1/92, (PB94-104510, A08, MF-A02).
- NCEER-92-0029 "Seismic Resistance of Reinforced Concrete Frame Structures Designed Only for Gravity Loads: Part III - Experimental Performance and Analytical Study of a Structural Model," by J.M. Bracci, A.M. Reinhorn and J.B. Mander, 12/1/92, (PB93-227528, A09, MF-A01).

- NCEER-92-0030 "Evaluation of Seismic Retrofit of Reinforced Concrete Frame Structures: Part I - Experimental Performance of Retrofitted Subassemblages," by D. Choudhuri, J.B. Mander and A.M. Reinhorn, 12/8/92, (PB93-198307, A07, MF-A02).
- NCEER-92-0031 "Evaluation of Seismic Retrofit of Reinforced Concrete Frame Structures: Part II - Experimental Performance and Analytical Study of a Retrofitted Structural Model," by J.M. Bracci, A.M. Reinhorn and J.B. Mander, 12/8/92, (PB93-198315, A09, MF-A03).
- NCEER-92-0032 "Experimental and Analytical Investigation of Seismic Response of Structures with Supplemental Fluid Viscous Dampers," by M.C. Constantinou and M.D. Symans, 12/21/92, (PB93-191435, A10, MF-A03). This report is available only through NTIS (see address given above).
- NCEER-92-0033 "Reconnaissance Report on the Cairo, Egypt Earthquake of October 12, 1992," by M. Khater, 12/23/92, (PB93-188621, A03, MF-A01).
- NCEER-92-0034 "Low-Level Dynamic Characteristics of Four Tall Flat-Plate Buildings in New York City," by H. Gavin, S. Yuan, J. Grossman, E. Pekelis and K. Jacob, 12/28/92, (PB93-188217, A07, MF-A02).
- NCEER-93-0001 "An Experimental Study on the Seismic Performance of Brick-Infilled Steel Frames With and Without Retrofit," by J.B. Mander, B. Nair, K. Wojtkowski and J. Ma, 1/29/93, (PB93-227510, A07, MF-A02).
- NCEER-93-0002 "Social Accounting for Disaster Preparedness and Recovery Planning," by S. Cole, E. Pantoja and V. Razak, 2/22/93, (PB94-142114, A12, MF-A03).
- NCEER-93-0003 "Assessment of 1991 NEHRP Provisions for Nonstructural Components and Recommended Revisions," by T.T. Soong, G. Chen, Z. Wu, R-H. Zhang and M. Grigoriu, 3/1/93, (PB93-188639, A06, MF-A02).
- NCEER-93-0004 "Evaluation of Static and Response Spectrum Analysis Procedures of SEAOC/UBC for Seismic Isolated Structures," by C.W. Winters and M.C. Constantinou, 3/23/93, (PB93-198299, A10, MF-A03).
- NCEER-93-0005 "Earthquakes in the Northeast - Are We Ignoring the Hazard? A Workshop on Earthquake Science and Safety for Educators," edited by K.E.K. Ross, 4/2/93, (PB94-103066, A09, MF-A02).
- NCEER-93-0006 "Inelastic Response of Reinforced Concrete Structures with Viscoelastic Braces," by R.F. Lobo, J.M. Bracci, K.L. Shen, A.M. Reinhorn and T.T. Soong, 4/5/93, (PB93-227486, A05, MF-A02).
- NCEER-93-0007 "Seismic Testing of Installation Methods for Computers and Data Processing Equipment," by K. Kosar, T.T. Soong, K.L. Shen, J.A. HoLung and Y.K. Lin, 4/12/93, (PB93-198299, A07, MF-A02).
- NCEER-93-0008 "Retrofit of Reinforced Concrete Frames Using Added Dampers," by A. Reinhorn, M. Constantinou and C. Li, not available.
- NCEER-93-0009 "Seismic Behavior and Design Guidelines for Steel Frame Structures with Added Viscoelastic Dampers," by K.C. Chang, M.L. Lai, T.T. Soong, D.S. Hao and Y.C. Yeh, 5/1/93, (PB94-141959, A07, MF-A02).
- NCEER-93-0010 "Seismic Performance of Shear-Critical Reinforced Concrete Bridge Piers," by J.B. Mander, S.M. Waheed, M.T.A. Chaudhary and S.S. Chen, 5/12/93, (PB93-227494, A08, MF-A02).
- NCEER-93-0011 "3D-BASIS-TABS: Computer Program for Nonlinear Dynamic Analysis of Three Dimensional Base Isolated Structures," by S. Nagarajaiah, C. Li, A.M. Reinhorn and M.C. Constantinou, 8/2/93, (PB94-141819, A09, MF-A02).
- NCEER-93-0012 "Effects of Hydrocarbon Spills from an Oil Pipeline Break on Ground Water," by O.J. Helweg and H.H.M. Hwang, 8/3/93, (PB94-141942, A06, MF-A02).
- NCEER-93-0013 "Simplified Procedures for Seismic Design of Nonstructural Components and Assessment of Current Code Provisions," by M.P. Singh, L.E. Suarez, E.E. Matheu and G.O. Maldonado, 8/4/93, (PB94-141827, A09, MF-A02).
- NCEER-93-0014 "An Energy Approach to Seismic Analysis and Design of Secondary Systems," by G. Chen and T.T. Soong, 8/6/93, (PB94-142767, A11, MF-A03).

- NCEER-93-0015 "Proceedings from School Sites: Becoming Prepared for Earthquakes - Commemorating the Third Anniversary of the Loma Prieta Earthquake," Edited by F.E. Winslow and K.E.K. Ross, 8/16/93, (PB94-154275, A16, MF-A02).
- NCEER-93-0016 "Reconnaissance Report of Damage to Historic Monuments in Cairo, Egypt Following the October 12, 1992 Dahshur Earthquake," by D. Sykora, D. Look, G. Croci, E. Karaesmen and E. Karaesmen, 8/19/93, (PB94-142221, A08, MF-A02).
- NCEER-93-0017 "The Island of Guam Earthquake of August 8, 1993," by S.W. Swan and S.K. Harris, 9/30/93, (PB94-141843, A04, MF-A01).
- NCEER-93-0018 "Engineering Aspects of the October 12, 1992 Egyptian Earthquake," by A.W. Elgamal, M. Amer, K. Adalier and A. Abul-Fadl, 10/7/93, (PB94-141983, A05, MF-A01).
- NCEER-93-0019 "Development of an Earthquake Motion Simulator and its Application in Dynamic Centrifuge Testing," by I. Krstelj, Supervised by J.H. Prevost, 10/23/93, (PB94-181773, A-10, MF-A03).
- NCEER-93-0020 "NCEER-Taisei Corporation Research Program on Sliding Seismic Isolation Systems for Bridges: Experimental and Analytical Study of a Friction Pendulum System (FPS)," by M.C. Constantinou, P. Tsopelas, Y-S. Kim and S. Okamoto, 11/1/93, (PB94-142775, A08, MF-A02).
- NCEER-93-0021 "Finite Element Modeling of Elastomeric Seismic Isolation Bearings," by L.J. Billings, Supervised by R. Shepherd, 11/8/93, not available.
- NCEER-93-0022 "Seismic Vulnerability of Equipment in Critical Facilities: Life-Safety and Operational Consequences," by K. Porter, G.S. Johnson, M.M. Zadeh, C. Scawthorn and S. Eder, 11/24/93, (PB94-181765, A16, MF-A03).
- NCEER-93-0023 "Hokkaido Nansei-oki, Japan Earthquake of July 12, 1993, by P.I. Yanev and C.R. Scawthorn, 12/23/93, (PB94-181500, A07, MF-A01).
- NCEER-94-0001 "An Evaluation of Seismic Serviceability of Water Supply Networks with Application to the San Francisco Auxiliary Water Supply System," by I. Markov, Supervised by M. Grigoriu and T. O'Rourke, 1/21/94, (PB94-204013, A07, MF-A02).
- NCEER-94-0002 "NCEER-Taisei Corporation Research Program on Sliding Seismic Isolation Systems for Bridges: Experimental and Analytical Study of Systems Consisting of Sliding Bearings, Rubber Restoring Force Devices and Fluid Dampers," Volumes I and II, by P. Tsopelas, S. Okamoto, M.C. Constantinou, D. Ozaki and S. Fujii, 2/4/94, (PB94-181740, A09, MF-A02 and PB94-181757, A12, MF-A03).
- NCEER-94-0003 "A Markov Model for Local and Global Damage Indices in Seismic Analysis," by S. Rahman and M. Grigoriu, 2/18/94, (PB94-206000, A12, MF-A03).
- NCEER-94-0004 "Proceedings from the NCEER Workshop on Seismic Response of Masonry Infills," edited by D.P. Abrams, 3/1/94, (PB94-180783, A07, MF-A02).
- NCEER-94-0005 "The Northridge, California Earthquake of January 17, 1994: General Reconnaissance Report," edited by J.D. Goltz, 3/11/94, (PB94-193943, A10, MF-A03).
- NCEER-94-0006 "Seismic Energy Based Fatigue Damage Analysis of Bridge Columns: Part I - Evaluation of Seismic Capacity," by G.A. Chang and J.B. Mander, 3/14/94, (PB94-219185, A11, MF-A03).
- NCEER-94-0007 "Seismic Isolation of Multi-Story Frame Structures Using Spherical Sliding Isolation Systems," by T.M. Al-Hussaini, V.A. Zayas and M.C. Constantinou, 3/17/94, (PB94-193745, A09, MF-A02).
- NCEER-94-0008 "The Northridge, California Earthquake of January 17, 1994: Performance of Highway Bridges," edited by I.G. Buckle, 3/24/94, (PB94-193851, A06, MF-A02).
- NCEER-94-0009 "Proceedings of the Third U.S.-Japan Workshop on Earthquake Protective Systems for Bridges," edited by I.G. Buckle and I. Friedland, 3/31/94, (PB94-195815, A99, MF-A06).

- NCEER-94-0010 "3D-BASIS-ME: Computer Program for Nonlinear Dynamic Analysis of Seismically Isolated Single and Multiple Structures and Liquid Storage Tanks," by P.C. Tsopelas, M.C. Constantinou and A.M. Reinhorn, 4/12/94, (PB94-204922, A09, MF-A02).
- NCEER-94-0011 "The Northridge, California Earthquake of January 17, 1994: Performance of Gas Transmission Pipelines," by T.D. O'Rourke and M.C. Palmer, 5/16/94, (PB94-204989, A05, MF-A01).
- NCEER-94-0012 "Feasibility Study of Replacement Procedures and Earthquake Performance Related to Gas Transmission Pipelines," by T.D. O'Rourke and M.C. Palmer, 5/25/94, (PB94-206638, A09, MF-A02).
- NCEER-94-0013 "Seismic Energy Based Fatigue Damage Analysis of Bridge Columns: Part II - Evaluation of Seismic Demand," by G.A. Chang and J.B. Mander, 6/1/94, (PB95-18106, A08, MF-A02).
- NCEER-94-0014 "NCEER-Taisei Corporation Research Program on Sliding Seismic Isolation Systems for Bridges: Experimental and Analytical Study of a System Consisting of Sliding Bearings and Fluid Restoring Force/Damping Devices," by P. Tsopelas and M.C. Constantinou, 6/13/94, (PB94-219144, A10, MF-A03).
- NCEER-94-0015 "Generation of Hazard-Consistent Fragility Curves for Seismic Loss Estimation Studies," by H. Hwang and J-R. Huo, 6/14/94, (PB95-181996, A09, MF-A02).
- NCEER-94-0016 "Seismic Study of Building Frames with Added Energy-Absorbing Devices," by W.S. Pong, C.S. Tsai and G.C. Lee, 6/20/94, (PB94-219136, A10, A03).
- NCEER-94-0017 "Sliding Mode Control for Seismic-Excited Linear and Nonlinear Civil Engineering Structures," by J. Yang, J. Wu, A. Agrawal and Z. Li, 6/21/94, (PB95-138483, A06, MF-A02).
- NCEER-94-0018 "3D-BASIS-TABS Version 2.0: Computer Program for Nonlinear Dynamic Analysis of Three Dimensional Base Isolated Structures," by A.M. Reinhorn, S. Nagarajaiah, M.C. Constantinou, P. Tsopelas and R. Li, 6/22/94, (PB95-182176, A08, MF-A02).
- NCEER-94-0019 "Proceedings of the International Workshop on Civil Infrastructure Systems: Application of Intelligent Systems and Advanced Materials on Bridge Systems," Edited by G.C. Lee and K.C. Chang, 7/18/94, (PB95-252474, A20, MF-A04).
- NCEER-94-0020 "Study of Seismic Isolation Systems for Computer Floors," by V. Lambrou and M.C. Constantinou, 7/19/94, (PB95-138533, A10, MF-A03).
- NCEER-94-0021 "Proceedings of the U.S.-Italian Workshop on Guidelines for Seismic Evaluation and Rehabilitation of Unreinforced Masonry Buildings," Edited by D.P. Abrams and G.M. Calvi, 7/20/94, (PB95-138749, A13, MF-A03).
- NCEER-94-0022 "NCEER-Taisei Corporation Research Program on Sliding Seismic Isolation Systems for Bridges: Experimental and Analytical Study of a System Consisting of Lubricated PTFE Sliding Bearings and Mild Steel Dampers," by P. Tsopelas and M.C. Constantinou, 7/22/94, (PB95-182184, A08, MF-A02).
- NCEER-94-0023 "Development of Reliability-Based Design Criteria for Buildings Under Seismic Load," by Y.K. Wen, H. Hwang and M. Shinozuka, 8/1/94, (PB95-211934, A08, MF-A02).
- NCEER-94-0024 "Experimental Verification of Acceleration Feedback Control Strategies for an Active Tendon System," by S.J. Dyke, B.F. Spencer, Jr., P. Quast, M.K. Sain, D.C. Kaspari, Jr. and T.T. Soong, 8/29/94, (PB95-212320, A05, MF-A01).
- NCEER-94-0025 "Seismic Retrofitting Manual for Highway Bridges," Edited by I.G. Buckle and I.F. Friedland, published by the Federal Highway Administration (PB95-212676, A15, MF-A03).
- NCEER-94-0026 "Proceedings from the Fifth U.S.-Japan Workshop on Earthquake Resistant Design of Lifeline Facilities and Countermeasures Against Soil Liquefaction," Edited by T.D. O'Rourke and M. Hamada, 11/7/94, (PB95-220802, A99, MF-E08).

- NCEER-95-0001 “Experimental and Analytical Investigation of Seismic Retrofit of Structures with Supplemental Damping: Part 1 - Fluid Viscous Damping Devices,” by A.M. Reinhorn, C. Li and M.C. Constantinou, 1/3/95, (PB95-266599, A09, MF-A02).
- NCEER-95-0002 “Experimental and Analytical Study of Low-Cycle Fatigue Behavior of Semi-Rigid Top-And-Seat Angle Connections,” by G. Pekcan, J.B. Mander and S.S. Chen, 1/5/95, (PB95-220042, A07, MF-A02).
- NCEER-95-0003 “NCEER-ATC Joint Study on Fragility of Buildings,” by T. Anagnos, C. Rojahn and A.S. Kiremidjian, 1/20/95, (PB95-220026, A06, MF-A02).
- NCEER-95-0004 “Nonlinear Control Algorithms for Peak Response Reduction,” by Z. Wu, T.T. Soong, V. Gattulli and R.C. Lin, 2/16/95, (PB95-220349, A05, MF-A01).
- NCEER-95-0005 “Pipeline Replacement Feasibility Study: A Methodology for Minimizing Seismic and Corrosion Risks to Underground Natural Gas Pipelines,” by R.T. Eguchi, H.A. Seligson and D.G. Honegger, 3/2/95, (PB95-252326, A06, MF-A02).
- NCEER-95-0006 “Evaluation of Seismic Performance of an 11-Story Frame Building During the 1994 Northridge Earthquake,” by F. Naeim, R. DiSulio, K. Benuska, A. Reinhorn and C. Li, not available.
- NCEER-95-0007 “Prioritization of Bridges for Seismic Retrofitting,” by N. Basöz and A.S. Kiremidjian, 4/24/95, (PB95-252300, A08, MF-A02).
- NCEER-95-0008 “Method for Developing Motion Damage Relationships for Reinforced Concrete Frames,” by A. Singhal and A.S. Kiremidjian, 5/11/95, (PB95-266607, A06, MF-A02).
- NCEER-95-0009 “Experimental and Analytical Investigation of Seismic Retrofit of Structures with Supplemental Damping: Part II - Friction Devices,” by C. Li and A.M. Reinhorn, 7/6/95, (PB96-128087, A11, MF-A03).
- NCEER-95-0010 “Experimental Performance and Analytical Study of a Non-Ductile Reinforced Concrete Frame Structure Retrofitted with Elastomeric Spring Dampers,” by G. Pekcan, J.B. Mander and S.S. Chen, 7/14/95, (PB96-137161, A08, MF-A02).
- NCEER-95-0011 “Development and Experimental Study of Semi-Active Fluid Damping Devices for Seismic Protection of Structures,” by M.D. Symans and M.C. Constantinou, 8/3/95, (PB96-136940, A23, MF-A04).
- NCEER-95-0012 “Real-Time Structural Parameter Modification (RSPM): Development of Innervated Structures,” by Z. Liang, M. Tong and G.C. Lee, 4/11/95, (PB96-137153, A06, MF-A01).
- NCEER-95-0013 “Experimental and Analytical Investigation of Seismic Retrofit of Structures with Supplemental Damping: Part III - Viscous Damping Walls,” by A.M. Reinhorn and C. Li, 10/1/95, (PB96-176409, A11, MF-A03).
- NCEER-95-0014 “Seismic Fragility Analysis of Equipment and Structures in a Memphis Electric Substation,” by J-R. Huo and H.H.M. Hwang, 8/10/95, (PB96-128087, A09, MF-A02).
- NCEER-95-0015 “The Hanshin-Awaji Earthquake of January 17, 1995: Performance of Lifelines,” Edited by M. Shinozuka, 11/3/95, (PB96-176383, A15, MF-A03).
- NCEER-95-0016 “Highway Culvert Performance During Earthquakes,” by T.L. Youd and C.J. Beckman, available as NCEER-96-0015.
- NCEER-95-0017 “The Hanshin-Awaji Earthquake of January 17, 1995: Performance of Highway Bridges,” Edited by I.G. Buckle, 12/1/95, not available.
- NCEER-95-0018 “Modeling of Masonry Infill Panels for Structural Analysis,” by A.M. Reinhorn, A. Madan, R.E. Valles, Y. Reichmann and J.B. Mander, 12/8/95, (PB97-110886, MF-A01, A06).
- NCEER-95-0019 “Optimal Polynomial Control for Linear and Nonlinear Structures,” by A.K. Agrawal and J.N. Yang, 12/11/95, (PB96-168737, A07, MF-A02).

- NCEER-95-0020 “Retrofit of Non-Ductile Reinforced Concrete Frames Using Friction Dampers,” by R.S. Rao, P. Gergely and R.N. White, 12/22/95, (PB97-133508, A10, MF-A02).
- NCEER-95-0021 “Parametric Results for Seismic Response of Pile-Supported Bridge Bents,” by G. Mylonakis, A. Nikolaou and G. Gazetas, 12/22/95, (PB97-100242, A12, MF-A03).
- NCEER-95-0022 “Kinematic Bending Moments in Seismically Stressed Piles,” by A. Nikolaou, G. Mylonakis and G. Gazetas, 12/23/95, (PB97-113914, MF-A03, A13).
- NCEER-96-0001 “Dynamic Response of Unreinforced Masonry Buildings with Flexible Diaphragms,” by A.C. Costley and D.P. Abrams, 10/10/96, (PB97-133573, MF-A03, A15).
- NCEER-96-0002 “State of the Art Review: Foundations and Retaining Structures,” by I. Po Lam, not available.
- NCEER-96-0003 “Ductility of Rectangular Reinforced Concrete Bridge Columns with Moderate Confinement,” by N. Wehbe, M. Saiidi, D. Sanders and B. Douglas, 11/7/96, (PB97-133557, A06, MF-A02).
- NCEER-96-0004 “Proceedings of the Long-Span Bridge Seismic Research Workshop,” edited by I.G. Buckle and I.M. Friedland, not available.
- NCEER-96-0005 “Establish Representative Pier Types for Comprehensive Study: Eastern United States,” by J. Kulicki and Z. Prucz, 5/28/96, (PB98-119217, A07, MF-A02).
- NCEER-96-0006 “Establish Representative Pier Types for Comprehensive Study: Western United States,” by R. Imbsen, R.A. Schamber and T.A. Osterkamp, 5/28/96, (PB98-118607, A07, MF-A02).
- NCEER-96-0007 “Nonlinear Control Techniques for Dynamical Systems with Uncertain Parameters,” by R.G. Ghanem and M.I. Bujakov, 5/27/96, (PB97-100259, A17, MF-A03).
- NCEER-96-0008 “Seismic Evaluation of a 30-Year Old Non-Ductile Highway Bridge Pier and Its Retrofit,” by J.B. Mander, B. Mahmoodzadegan, S. Bhadra and S.S. Chen, 5/31/96, (PB97-110902, MF-A03, A10).
- NCEER-96-0009 “Seismic Performance of a Model Reinforced Concrete Bridge Pier Before and After Retrofit,” by J.B. Mander, J.H. Kim and C.A. Ligozio, 5/31/96, (PB97-110910, MF-A02, A10).
- NCEER-96-0010 “IDARC2D Version 4.0: A Computer Program for the Inelastic Damage Analysis of Buildings,” by R.E. Valles, A.M. Reinhorn, S.K. Kunnath, C. Li and A. Madan, 6/3/96, (PB97-100234, A17, MF-A03).
- NCEER-96-0011 “Estimation of the Economic Impact of Multiple Lifeline Disruption: Memphis Light, Gas and Water Division Case Study,” by S.E. Chang, H.A. Seligson and R.T. Eguchi, 8/16/96, (PB97-133490, A11, MF-A03).
- NCEER-96-0012 “Proceedings from the Sixth Japan-U.S. Workshop on Earthquake Resistant Design of Lifeline Facilities and Countermeasures Against Soil Liquefaction, Edited by M. Hamada and T. O’Rourke, 9/11/96, (PB97-133581, A99, MF-A06).
- NCEER-96-0013 “Chemical Hazards, Mitigation and Preparedness in Areas of High Seismic Risk: A Methodology for Estimating the Risk of Post-Earthquake Hazardous Materials Release,” by H.A. Seligson, R.T. Eguchi, K.J. Tierney and K. Richmond, 11/7/96, (PB97-133565, MF-A02, A08).
- NCEER-96-0014 “Response of Steel Bridge Bearings to Reversed Cyclic Loading,” by J.B. Mander, D-K. Kim, S.S. Chen and G.J. Premus, 11/13/96, (PB97-140735, A12, MF-A03).
- NCEER-96-0015 “Highway Culvert Performance During Past Earthquakes,” by T.L. Youd and C.J. Beckman, 11/25/96, (PB97-133532, A06, MF-A01).
- NCEER-97-0001 “Evaluation, Prevention and Mitigation of Pounding Effects in Building Structures,” by R.E. Valles and A.M. Reinhorn, 2/20/97, (PB97-159552, A14, MF-A03).
- NCEER-97-0002 “Seismic Design Criteria for Bridges and Other Highway Structures,” by C. Rojahn, R. Mayes, D.G. Anderson, J. Clark, J.H. Hom, R.V. Nutt and M.J. O’Rourke, 4/30/97, (PB97-194658, A06, MF-A03).

- NCEER-97-0003 "Proceedings of the U.S.-Italian Workshop on Seismic Evaluation and Retrofit," Edited by D.P. Abrams and G.M. Calvi, 3/19/97, (PB97-194666, A13, MF-A03).
- NCEER-97-0004 "Investigation of Seismic Response of Buildings with Linear and Nonlinear Fluid Viscous Dampers," by A.A. Seleemah and M.C. Constantinou, 5/21/97, (PB98-109002, A15, MF-A03).
- NCEER-97-0005 "Proceedings of the Workshop on Earthquake Engineering Frontiers in Transportation Facilities," edited by G.C. Lee and I.M. Friedland, 8/29/97, (PB98-128911, A25, MR-A04).
- NCEER-97-0006 "Cumulative Seismic Damage of Reinforced Concrete Bridge Piers," by S.K. Kunnath, A. El-Bahy, A. Taylor and W. Stone, 9/2/97, (PB98-108814, A11, MF-A03).
- NCEER-97-0007 "Structural Details to Accommodate Seismic Movements of Highway Bridges and Retaining Walls," by R.A. Imbsen, R.A. Schamber, E. Thorkildsen, A. Kartoum, B.T. Martin, T.N. Rosser and J.M. Kulicki, 9/3/97, (PB98-108996, A09, MF-A02).
- NCEER-97-0008 "A Method for Earthquake Motion-Damage Relationships with Application to Reinforced Concrete Frames," by A. Singhal and A.S. Kiremidjian, 9/10/97, (PB98-108988, A13, MF-A03).
- NCEER-97-0009 "Seismic Analysis and Design of Bridge Abutments Considering Sliding and Rotation," by K. Fishman and R. Richards, Jr., 9/15/97, (PB98-108897, A06, MF-A02).
- NCEER-97-0010 "Proceedings of the FHWA/NCEER Workshop on the National Representation of Seismic Ground Motion for New and Existing Highway Facilities," edited by I.M. Friedland, M.S. Power and R.L. Mayes, 9/22/97, (PB98-128903, A21, MF-A04).
- NCEER-97-0011 "Seismic Analysis for Design or Retrofit of Gravity Bridge Abutments," by K.L. Fishman, R. Richards, Jr. and R.C. Divito, 10/2/97, (PB98-128937, A08, MF-A02).
- NCEER-97-0012 "Evaluation of Simplified Methods of Analysis for Yielding Structures," by P. Tsopelas, M.C. Constantinou, C.A. Kircher and A.S. Whittaker, 10/31/97, (PB98-128929, A10, MF-A03).
- NCEER-97-0013 "Seismic Design of Bridge Columns Based on Control and Repairability of Damage," by C-T. Cheng and J.B. Mander, 12/8/97, (PB98-144249, A11, MF-A03).
- NCEER-97-0014 "Seismic Resistance of Bridge Piers Based on Damage Avoidance Design," by J.B. Mander and C-T. Cheng, 12/10/97, (PB98-144223, A09, MF-A02).
- NCEER-97-0015 "Seismic Response of Nominally Symmetric Systems with Strength Uncertainty," by S. Balopoulou and M. Grigoriu, 12/23/97, (PB98-153422, A11, MF-A03).
- NCEER-97-0016 "Evaluation of Seismic Retrofit Methods for Reinforced Concrete Bridge Columns," by T.J. Wipf, F.W. Klaiber and F.M. Russo, 12/28/97, (PB98-144215, A12, MF-A03).
- NCEER-97-0017 "Seismic Fragility of Existing Conventional Reinforced Concrete Highway Bridges," by C.L. Mullen and A.S. Cakmak, 12/30/97, (PB98-153406, A08, MF-A02).
- NCEER-97-0018 "Loss Assessment of Memphis Buildings," edited by D.P. Abrams and M. Shinozuka, 12/31/97, (PB98-144231, A13, MF-A03).
- NCEER-97-0019 "Seismic Evaluation of Frames with Infill Walls Using Quasi-static Experiments," by K.M. Mosalam, R.N. White and P. Gergely, 12/31/97, (PB98-153455, A07, MF-A02).
- NCEER-97-0020 "Seismic Evaluation of Frames with Infill Walls Using Pseudo-dynamic Experiments," by K.M. Mosalam, R.N. White and P. Gergely, 12/31/97, (PB98-153430, A07, MF-A02).
- NCEER-97-0021 "Computational Strategies for Frames with Infill Walls: Discrete and Smeared Crack Analyses and Seismic Fragility," by K.M. Mosalam, R.N. White and P. Gergely, 12/31/97, (PB98-153414, A10, MF-A02).

- NCEER-97-0022 "Proceedings of the NCEER Workshop on Evaluation of Liquefaction Resistance of Soils," edited by T.L. Youd and I.M. Idriss, 12/31/97, (PB98-155617, A15, MF-A03).
- MCEER-98-0001 "Extraction of Nonlinear Hysteretic Properties of Seismically Isolated Bridges from Quick-Release Field Tests," by Q. Chen, B.M. Douglas, E.M. Maragakis and I.G. Buckle, 5/26/98, (PB99-118838, A06, MF-A01).
- MCEER-98-0002 "Methodologies for Evaluating the Importance of Highway Bridges," by A. Thomas, S. Eshenaur and J. Kulicki, 5/29/98, (PB99-118846, A10, MF-A02).
- MCEER-98-0003 "Capacity Design of Bridge Piers and the Analysis of Overstrength," by J.B. Mander, A. Dutta and P. Goel, 6/1/98, (PB99-118853, A09, MF-A02).
- MCEER-98-0004 "Evaluation of Bridge Damage Data from the Loma Prieta and Northridge, California Earthquakes," by N. Basoz and A. Kiremidjian, 6/2/98, (PB99-118861, A15, MF-A03).
- MCEER-98-0005 "Screening Guide for Rapid Assessment of Liquefaction Hazard at Highway Bridge Sites," by T. L. Youd, 6/16/98, (PB99-118879, A06, not available on microfiche).
- MCEER-98-0006 "Structural Steel and Steel/Concrete Interface Details for Bridges," by P. Ritchie, N. Kauh and J. Kulicki, 7/13/98, (PB99-118945, A06, MF-A01).
- MCEER-98-0007 "Capacity Design and Fatigue Analysis of Confined Concrete Columns," by A. Dutta and J.B. Mander, 7/14/98, (PB99-118960, A14, MF-A03).
- MCEER-98-0008 "Proceedings of the Workshop on Performance Criteria for Telecommunication Services Under Earthquake Conditions," edited by A.J. Schiff, 7/15/98, (PB99-118952, A08, MF-A02).
- MCEER-98-0009 "Fatigue Analysis of Unconfined Concrete Columns," by J.B. Mander, A. Dutta and J.H. Kim, 9/12/98, (PB99-123655, A10, MF-A02).
- MCEER-98-0010 "Centrifuge Modeling of Cyclic Lateral Response of Pile-Cap Systems and Seat-Type Abutments in Dry Sands," by A.D. Gadre and R. Dobry, 10/2/98, (PB99-123606, A13, MF-A03).
- MCEER-98-0011 "IDARC-BRIDGE: A Computational Platform for Seismic Damage Assessment of Bridge Structures," by A.M. Reinhorn, V. Simeonov, G. Mylonakis and Y. Reichman, 10/2/98, (PB99-162919, A15, MF-A03).
- MCEER-98-0012 "Experimental Investigation of the Dynamic Response of Two Bridges Before and After Retrofitting with Elastomeric Bearings," by D.A. Wendichansky, S.S. Chen and J.B. Mander, 10/2/98, (PB99-162927, A15, MF-A03).
- MCEER-98-0013 "Design Procedures for Hinge Restrainers and Hinge Sear Width for Multiple-Frame Bridges," by R. Des Roches and G.L. Fenves, 11/3/98, (PB99-140477, A13, MF-A03).
- MCEER-98-0014 "Response Modification Factors for Seismically Isolated Bridges," by M.C. Constantinou and J.K. Quarshie, 11/3/98, (PB99-140485, A14, MF-A03).
- MCEER-98-0015 "Proceedings of the U.S.-Italy Workshop on Seismic Protective Systems for Bridges," edited by I.M. Friedland and M.C. Constantinou, 11/3/98, (PB2000-101711, A22, MF-A04).
- MCEER-98-0016 "Appropriate Seismic Reliability for Critical Equipment Systems: Recommendations Based on Regional Analysis of Financial and Life Loss," by K. Porter, C. Scawthorn, C. Taylor and N. Blais, 11/10/98, (PB99-157265, A08, MF-A02).
- MCEER-98-0017 "Proceedings of the U.S. Japan Joint Seminar on Civil Infrastructure Systems Research," edited by M. Shinozuka and A. Rose, 11/12/98, (PB99-156713, A16, MF-A03).
- MCEER-98-0018 "Modeling of Pile Footings and Drilled Shafts for Seismic Design," by I. PoLam, M. Kapuskar and D. Chaudhuri, 12/21/98, (PB99-157257, A09, MF-A02).

- MCEER-99-0001 "Seismic Evaluation of a Masonry Infilled Reinforced Concrete Frame by Pseudodynamic Testing," by S.G. Buonopane and R.N. White, 2/16/99, (PB99-162851, A09, MF-A02).
- MCEER-99-0002 "Response History Analysis of Structures with Seismic Isolation and Energy Dissipation Systems: Verification Examples for Program SAP2000," by J. Scheller and M.C. Constantinou, 2/22/99, (PB99-162869, A08, MF-A02).
- MCEER-99-0003 "Experimental Study on the Seismic Design and Retrofit of Bridge Columns Including Axial Load Effects," by A. Dutta, T. Kokorina and J.B. Mander, 2/22/99, (PB99-162877, A09, MF-A02).
- MCEER-99-0004 "Experimental Study of Bridge Elastomeric and Other Isolation and Energy Dissipation Systems with Emphasis on Uplift Prevention and High Velocity Near-source Seismic Excitation," by A. Kasalanati and M. C. Constantinou, 2/26/99, (PB99-162885, A12, MF-A03).
- MCEER-99-0005 "Truss Modeling of Reinforced Concrete Shear-flexure Behavior," by J.H. Kim and J.B. Mander, 3/8/99, (PB99-163693, A12, MF-A03).
- MCEER-99-0006 "Experimental Investigation and Computational Modeling of Seismic Response of a 1:4 Scale Model Steel Structure with a Load Balancing Supplemental Damping System," by G. Pekcan, J.B. Mander and S.S. Chen, 4/2/99, (PB99-162893, A11, MF-A03).
- MCEER-99-0007 "Effect of Vertical Ground Motions on the Structural Response of Highway Bridges," by M.R. Button, C.J. Cronin and R.L. Mayes, 4/10/99, (PB2000-101411, A10, MF-A03).
- MCEER-99-0008 "Seismic Reliability Assessment of Critical Facilities: A Handbook, Supporting Documentation, and Model Code Provisions," by G.S. Johnson, R.E. Sheppard, M.D. Quilici, S.J. Eder and C.R. Scawthorn, 4/12/99, (PB2000-101701, A18, MF-A04).
- MCEER-99-0009 "Impact Assessment of Selected MCEER Highway Project Research on the Seismic Design of Highway Structures," by C. Rojahn, R. Mayes, D.G. Anderson, J.H. Clark, D'Appolonia Engineering, S. Gloyd and R.V. Nutt, 4/14/99, (PB99-162901, A10, MF-A02).
- MCEER-99-0010 "Site Factors and Site Categories in Seismic Codes," by R. Dobry, R. Ramos and M.S. Power, 7/19/99, (PB2000-101705, A08, MF-A02).
- MCEER-99-0011 "Restrainer Design Procedures for Multi-Span Simply-Supported Bridges," by M.J. Randall, M. Saiidi, E. Maragakis and T. Isakovic, 7/20/99, (PB2000-101702, A10, MF-A02).
- MCEER-99-0012 "Property Modification Factors for Seismic Isolation Bearings," by M.C. Constantinou, P. Tsopelas, A. Kasalanati and E. Wolff, 7/20/99, (PB2000-103387, A11, MF-A03).
- MCEER-99-0013 "Critical Seismic Issues for Existing Steel Bridges," by P. Ritchie, N. Kauh and J. Kulicki, 7/20/99, (PB2000-101697, A09, MF-A02).
- MCEER-99-0014 "Nonstructural Damage Database," by A. Kao, T.T. Soong and A. Vender, 7/24/99, (PB2000-101407, A06, MF-A01).
- MCEER-99-0015 "Guide to Remedial Measures for Liquefaction Mitigation at Existing Highway Bridge Sites," by H.G. Cooke and J. K. Mitchell, 7/26/99, (PB2000-101703, A11, MF-A03).
- MCEER-99-0016 "Proceedings of the MCEER Workshop on Ground Motion Methodologies for the Eastern United States," edited by N. Abrahamson and A. Becker, 8/11/99, (PB2000-103385, A07, MF-A02).
- MCEER-99-0017 "Quindío, Colombia Earthquake of January 25, 1999: Reconnaissance Report," by A.P. Asfura and P.J. Flores, 10/4/99, (PB2000-106893, A06, MF-A01).
- MCEER-99-0018 "Hysteretic Models for Cyclic Behavior of Deteriorating Inelastic Structures," by M.V. Sivaselvan and A.M. Reinhorn, 11/5/99, (PB2000-103386, A08, MF-A02).

- MCEER-99-0019 "Proceedings of the 7<sup>th</sup> U.S.- Japan Workshop on Earthquake Resistant Design of Lifeline Facilities and Countermeasures Against Soil Liquefaction," edited by T.D. O'Rourke, J.P. Bardet and M. Hamada, 11/19/99, (PB2000-103354, A99, MF-A06).
- MCEER-99-0020 "Development of Measurement Capability for Micro-Vibration Evaluations with Application to Chip Fabrication Facilities," by G.C. Lee, Z. Liang, J.W. Song, J.D. Shen and W.C. Liu, 12/1/99, (PB2000-105993, A08, MF-A02).
- MCEER-99-0021 "Design and Retrofit Methodology for Building Structures with Supplemental Energy Dissipating Systems," by G. Pekcan, J.B. Mander and S.S. Chen, 12/31/99, (PB2000-105994, A11, MF-A03).
- MCEER-00-0001 "The Marmara, Turkey Earthquake of August 17, 1999: Reconnaissance Report," edited by C. Scawthorn; with major contributions by M. Bruneau, R. Eguchi, T. Holzer, G. Johnson, J. Mander, J. Mitchell, W. Mitchell, A. Papageorgiou, C. Scaethorn, and G. Webb, 3/23/00, (PB2000-106200, A11, MF-A03).
- MCEER-00-0002 "Proceedings of the MCEER Workshop for Seismic Hazard Mitigation of Health Care Facilities," edited by G.C. Lee, M. Ettouney, M. Grigoriu, J. Hauer and J. Nigg, 3/29/00, (PB2000-106892, A08, MF-A02).
- MCEER-00-0003 "The Chi-Chi, Taiwan Earthquake of September 21, 1999: Reconnaissance Report," edited by G.C. Lee and C.H. Loh, with major contributions by G.C. Lee, M. Bruneau, I.G. Buckle, S.E. Chang, P.J. Flores, T.D. O'Rourke, M. Shinozuka, T.T. Soong, C-H. Loh, K-C. Chang, Z-J. Chen, J-S. Hwang, M-L. Lin, G-Y. Liu, K-C. Tsai, G.C. Yao and C-L. Yen, 4/30/00, (PB2001-100980, A10, MF-A02).
- MCEER-00-0004 "Seismic Retrofit of End-Sway Frames of Steel Deck-Truss Bridges with a Supplemental Tendon System: Experimental and Analytical Investigation," by G. Pekcan, J.B. Mander and S.S. Chen, 7/1/00, (PB2001-100982, A10, MF-A02).
- MCEER-00-0005 "Sliding Fragility of Unrestrained Equipment in Critical Facilities," by W.H. Chong and T.T. Soong, 7/5/00, (PB2001-100983, A08, MF-A02).
- MCEER-00-0006 "Seismic Response of Reinforced Concrete Bridge Pier Walls in the Weak Direction," by N. Abo-Shadi, M. Saiidi and D. Sanders, 7/17/00, (PB2001-100981, A17, MF-A03).
- MCEER-00-0007 "Low-Cycle Fatigue Behavior of Longitudinal Reinforcement in Reinforced Concrete Bridge Columns," by J. Brown and S.K. Kunnath, 7/23/00, (PB2001-104392, A08, MF-A02).
- MCEER-00-0008 "Soil Structure Interaction of Bridges for Seismic Analysis," I. PoLam and H. Law, 9/25/00, (PB2001-105397, A08, MF-A02).
- MCEER-00-0009 "Proceedings of the First MCEER Workshop on Mitigation of Earthquake Disaster by Advanced Technologies (MEDAT-1), edited by M. Shinozuka, D.J. Inman and T.D. O'Rourke, 11/10/00, (PB2001-105399, A14, MF-A03).
- MCEER-00-0010 "Development and Evaluation of Simplified Procedures for Analysis and Design of Buildings with Passive Energy Dissipation Systems, Revision 01," by O.M. Ramirez, M.C. Constantinou, C.A. Kircher, A.S. Whittaker, M.W. Johnson, J.D. Gomez and C. Chrysostomou, 11/16/01, (PB2001-105523, A23, MF-A04).
- MCEER-00-0011 "Dynamic Soil-Foundation-Structure Interaction Analyses of Large Caissons," by C-Y. Chang, C-M. Mok, Z-L. Wang, R. Settgast, F. Waggoner, M.A. Ketchum, H.M. Gonnermann and C-C. Chin, 12/30/00, (PB2001-104373, A07, MF-A02).
- MCEER-00-0012 "Experimental Evaluation of Seismic Performance of Bridge Restrainers," by A.G. Vlassis, E.M. Maragakis and M. Saiid Saiidi, 12/30/00, (PB2001-104354, A09, MF-A02).
- MCEER-00-0013 "Effect of Spatial Variation of Ground Motion on Highway Structures," by M. Shinozuka, V. Saxena and G. Deodatis, 12/31/00, (PB2001-108755, A13, MF-A03).
- MCEER-00-0014 "A Risk-Based Methodology for Assessing the Seismic Performance of Highway Systems," by S.D. Werner, C.E. Taylor, J.E. Moore, II, J.S. Walton and S. Cho, 12/31/00, (PB2001-108756, A14, MF-A03).

- MCEER-01-0001 "Experimental Investigation of P-Delta Effects to Collapse During Earthquakes," by D. Vian and M. Bruneau, 6/25/01, (PB2002-100534, A17, MF-A03).
- MCEER-01-0002 "Proceedings of the Second MCEER Workshop on Mitigation of Earthquake Disaster by Advanced Technologies (MEDAT-2)," edited by M. Bruneau and D.J. Inman, 7/23/01, (PB2002-100434, A16, MF-A03).
- MCEER-01-0003 "Sensitivity Analysis of Dynamic Systems Subjected to Seismic Loads," by C. Roth and M. Grigoriu, 9/18/01, (PB2003-100884, A12, MF-A03).
- MCEER-01-0004 "Overcoming Obstacles to Implementing Earthquake Hazard Mitigation Policies: Stage 1 Report," by D.J. Alesch and W.J. Petak, 12/17/01, (PB2002-107949, A07, MF-A02).
- MCEER-01-0005 "Updating Real-Time Earthquake Loss Estimates: Methods, Problems and Insights," by C.E. Taylor, S.E. Chang and R.T. Eguchi, 12/17/01, (PB2002-107948, A05, MF-A01).
- MCEER-01-0006 "Experimental Investigation and Retrofit of Steel Pile Foundations and Pile Bents Under Cyclic Lateral Loadings," by A. Shama, J. Mander, B. Blabac and S. Chen, 12/31/01, (PB2002-107950, A13, MF-A03).
- MCEER-02-0001 "Assessment of Performance of Bolu Viaduct in the 1999 Duzce Earthquake in Turkey" by P.C. Roussis, M.C. Constantinou, M. Erdik, E. Durukal and M. Dicleli, 5/8/02, (PB2003-100883, A08, MF-A02).
- MCEER-02-0002 "Seismic Behavior of Rail Counterweight Systems of Elevators in Buildings," by M.P. Singh, Rildova and L.E. Suarez, 5/27/02. (PB2003-100882, A11, MF-A03).
- MCEER-02-0003 "Development of Analysis and Design Procedures for Spread Footings," by G. Mylonakis, G. Gazetas, S. Nikolaou and A. Chauncey, 10/02/02, (PB2004-101636, A13, MF-A03, CD-A13).
- MCEER-02-0004 "Bare-Earth Algorithms for Use with SAR and LIDAR Digital Elevation Models," by C.K. Huyck, R.T. Eguchi and B. Houshmand, 10/16/02, (PB2004-101637, A07, CD-A07).
- MCEER-02-0005 "Review of Energy Dissipation of Compression Members in Concentrically Braced Frames," by K.Lee and M. Bruneau, 10/18/02, (PB2004-101638, A10, CD-A10).
- MCEER-03-0001 "Experimental Investigation of Light-Gauge Steel Plate Shear Walls for the Seismic Retrofit of Buildings" by J. Berman and M. Bruneau, 5/2/03, (PB2004-101622, A10, MF-A03, CD-A10).
- MCEER-03-0002 "Statistical Analysis of Fragility Curves," by M. Shinozuka, M.Q. Feng, H. Kim, T. Uzawa and T. Ueda, 6/16/03, (PB2004-101849, A09, CD-A09).
- MCEER-03-0003 "Proceedings of the Eighth U.S.-Japan Workshop on Earthquake Resistant Design of Lifeline Facilities and Countermeasures Against Liquefaction," edited by M. Hamada, J.P. Bardet and T.D. O'Rourke, 6/30/03, (PB2004-104386, A99, CD-A99).
- MCEER-03-0004 "Proceedings of the PRC-US Workshop on Seismic Analysis and Design of Special Bridges," edited by L.C. Fan and G.C. Lee, 7/15/03, (PB2004-104387, A14, CD-A14).
- MCEER-03-0005 "Urban Disaster Recovery: A Framework and Simulation Model," by S.B. Miles and S.E. Chang, 7/25/03, (PB2004-104388, A07, CD-A07).
- MCEER-03-0006 "Behavior of Underground Piping Joints Due to Static and Dynamic Loading," by R.D. Meis, M. Maragakis and R. Siddharthan, 11/17/03, (PB2005-102194, A13, MF-A03, CD-A00).
- MCEER-04-0001 "Experimental Study of Seismic Isolation Systems with Emphasis on Secondary System Response and Verification of Accuracy of Dynamic Response History Analysis Methods," by E. Wolff and M. Constantinou, 1/16/04 (PB2005-102195, A99, MF-E08, CD-A00).
- MCEER-04-0002 "Tension, Compression and Cyclic Testing of Engineered Cementitious Composite Materials," by K. Kesner and S.L. Billington, 3/1/04, (PB2005-102196, A08, CD-A08).

- MCEER-04-0003 "Cyclic Testing of Braces Laterally Restrained by Steel Studs to Enhance Performance During Earthquakes," by O.C. Celik, J.W. Berman and M. Bruneau, 3/16/04, (PB2005-102197, A13, MF-A03, CD-A00).
- MCEER-04-0004 "Methodologies for Post Earthquake Building Damage Detection Using SAR and Optical Remote Sensing: Application to the August 17, 1999 Marmara, Turkey Earthquake," by C.K. Huyck, B.J. Adams, S. Cho, R.T. Eguchi, B. Mansouri and B. Houshmand, 6/15/04, (PB2005-104888, A10, CD-A00).
- MCEER-04-0005 "Nonlinear Structural Analysis Towards Collapse Simulation: A Dynamical Systems Approach," by M.V. Sivaselvan and A.M. Reinhorn, 6/16/04, (PB2005-104889, A11, MF-A03, CD-A00).
- MCEER-04-0006 "Proceedings of the Second PRC-US Workshop on Seismic Analysis and Design of Special Bridges," edited by G.C. Lee and L.C. Fan, 6/25/04, (PB2005-104890, A16, CD-A00).
- MCEER-04-0007 "Seismic Vulnerability Evaluation of Axially Loaded Steel Built-up Laced Members," by K. Lee and M. Bruneau, 6/30/04, (PB2005-104891, A16, CD-A00).
- MCEER-04-0008 "Evaluation of Accuracy of Simplified Methods of Analysis and Design of Buildings with Damping Systems for Near-Fault and for Soft-Soil Seismic Motions," by E.A. Pavlou and M.C. Constantinou, 8/16/04, (PB2005-104892, A08, MF-A02, CD-A00).
- MCEER-04-0009 "Assessment of Geotechnical Issues in Acute Care Facilities in California," by M. Lew, T.D. O'Rourke, R. Dobry and M. Koch, 9/15/04, (PB2005-104893, A08, CD-A00).
- MCEER-04-0010 "Scissor-Jack-Damper Energy Dissipation System," by A.N. Sigaher-Boyle and M.C. Constantinou, 12/1/04 (PB2005-108221).
- MCEER-04-0011 "Seismic Retrofit of Bridge Steel Truss Piers Using a Controlled Rocking Approach," by M. Pollino and M. Bruneau, 12/20/04 (PB2006-105795).
- MCEER-05-0001 "Experimental and Analytical Studies of Structures Seismically Isolated with an Uplift-Restraint Isolation System," by P.C. Roussis and M.C. Constantinou, 1/10/05 (PB2005-108222).
- MCEER-05-0002 "A Versatile Experimentation Model for Study of Structures Near Collapse Applied to Seismic Evaluation of Irregular Structures," by D. Kusumastuti, A.M. Reinhorn and A. Rutenberg, 3/31/05 (PB2006-101523).
- MCEER-05-0003 "Proceedings of the Third PRC-US Workshop on Seismic Analysis and Design of Special Bridges," edited by L.C. Fan and G.C. Lee, 4/20/05, (PB2006-105796).
- MCEER-05-0004 "Approaches for the Seismic Retrofit of Braced Steel Bridge Piers and Proof-of-Concept Testing of an Eccentrically Braced Frame with Tubular Link," by J.W. Berman and M. Bruneau, 4/21/05 (PB2006-101524).
- MCEER-05-0005 "Simulation of Strong Ground Motions for Seismic Fragility Evaluation of Nonstructural Components in Hospitals," by A. Wanitkorkul and A. Filiatrault, 5/26/05 (PB2006-500027).
- MCEER-05-0006 "Seismic Safety in California Hospitals: Assessing an Attempt to Accelerate the Replacement or Seismic Retrofit of Older Hospital Facilities," by D.J. Alesch, L.A. Arendt and W.J. Petak, 6/6/05 (PB2006-105794).
- MCEER-05-0007 "Development of Seismic Strengthening and Retrofit Strategies for Critical Facilities Using Engineered Cementitious Composite Materials," by K. Kesner and S.L. Billington, 8/29/05 (PB2006-111701).
- MCEER-05-0008 "Experimental and Analytical Studies of Base Isolation Systems for Seismic Protection of Power Transformers," by N. Murota, M.Q. Feng and G-Y. Liu, 9/30/05 (PB2006-111702).
- MCEER-05-0009 "3D-BASIS-ME-MB: Computer Program for Nonlinear Dynamic Analysis of Seismically Isolated Structures," by P.C. Tsopelas, P.C. Roussis, M.C. Constantinou, R. Buchanan and A.M. Reinhorn, 10/3/05 (PB2006-111703).
- MCEER-05-0010 "Steel Plate Shear Walls for Seismic Design and Retrofit of Building Structures," by D. Vian and M. Bruneau, 12/15/05 (PB2006-111704).

- MCEER-05-0011 "The Performance-Based Design Paradigm," by M.J. Astrella and A. Whittaker, 12/15/05 (PB2006-111705).
- MCEER-06-0001 "Seismic Fragility of Suspended Ceiling Systems," H. Badillo-Almaraz, A.S. Whittaker, A.M. Reinhorn and G.P. Cimellaro, 2/4/06 (PB2006-111706).
- MCEER-06-0002 "Multi-Dimensional Fragility of Structures," by G.P. Cimellaro, A.M. Reinhorn and M. Bruneau, 3/1/06 (PB2007-106974, A09, MF-A02, CD A00).
- MCEER-06-0003 "Built-Up Shear Links as Energy Dissipators for Seismic Protection of Bridges," by P. Dusicka, A.M. Itani and I.G. Buckle, 3/15/06 (PB2006-111708).
- MCEER-06-0004 "Analytical Investigation of the Structural Fuse Concept," by R.E. Vargas and M. Bruneau, 3/16/06 (PB2006-111709).
- MCEER-06-0005 "Experimental Investigation of the Structural Fuse Concept," by R.E. Vargas and M. Bruneau, 3/17/06 (PB2006-111710).
- MCEER-06-0006 "Further Development of Tubular Eccentrically Braced Frame Links for the Seismic Retrofit of Braced Steel Truss Bridge Piers," by J.W. Berman and M. Bruneau, 3/27/06 (PB2007-105147).
- MCEER-06-0007 "REDARS Validation Report," by S. Cho, C.K. Huyck, S. Ghosh and R.T. Eguchi, 8/8/06 (PB2007-106983).
- MCEER-06-0008 "Review of Current NDE Technologies for Post-Earthquake Assessment of Retrofitted Bridge Columns," by J.W. Song, Z. Liang and G.C. Lee, 8/21/06 (PB2007-106984).
- MCEER-06-0009 "Liquefaction Remediation in Silty Soils Using Dynamic Compaction and Stone Columns," by S. Thevanayagam, G.R. Martin, R. Nashed, T. Shenthan, T. Kanagalingam and N. Ecemis, 8/28/06 (PB2007-106985).
- MCEER-06-0010 "Conceptual Design and Experimental Investigation of Polymer Matrix Composite Infill Panels for Seismic Retrofitting," by W. Jung, M. Chiewanichakorn and A.J. Aref, 9/21/06 (PB2007-106986).
- MCEER-06-0011 "A Study of the Coupled Horizontal-Vertical Behavior of Elastomeric and Lead-Rubber Seismic Isolation Bearings," by G.P. Warn and A.S. Whittaker, 9/22/06 (PB2007-108679).
- MCEER-06-0012 "Proceedings of the Fourth PRC-US Workshop on Seismic Analysis and Design of Special Bridges: Advancing Bridge Technologies in Research, Design, Construction and Preservation," Edited by L.C. Fan, G.C. Lee and L. Ziang, 10/12/06 (PB2007-109042).
- MCEER-06-0013 "Cyclic Response and Low Cycle Fatigue Characteristics of Plate Steels," by P. Dusicka, A.M. Itani and I.G. Buckle, 11/1/06 06 (PB2007-106987).
- MCEER-06-0014 "Proceedings of the Second US-Taiwan Bridge Engineering Workshop," edited by W.P. Yen, J. Shen, J-Y. Chen and M. Wang, 11/15/06 (PB2008-500041).
- MCEER-06-0015 "User Manual and Technical Documentation for the REDARS<sup>TM</sup> Import Wizard," by S. Cho, S. Ghosh, C.K. Huyck and S.D. Werner, 11/30/06 (PB2007-114766).
- MCEER-06-0016 "Hazard Mitigation Strategy and Monitoring Technologies for Urban and Infrastructure Public Buildings: Proceedings of the China-US Workshops," edited by X.Y. Zhou, A.L. Zhang, G.C. Lee and M. Tong, 12/12/06 (PB2008-500018).
- MCEER-07-0001 "Static and Kinetic Coefficients of Friction for Rigid Blocks," by C. Kafali, S. Fathali, M. Grigoriu and A.S. Whittaker, 3/20/07 (PB2007-114767).
- MCEER-07-0002 "Hazard Mitigation Investment Decision Making: Organizational Response to Legislative Mandate," by L.A. Arendt, D.J. Alesch and W.J. Petak, 4/9/07 (PB2007-114768).
- MCEER-07-0003 "Seismic Behavior of Bidirectional-Resistant Ductile End Diaphragms with Unbonded Braces in Straight or Skewed Steel Bridges," by O. Celik and M. Bruneau, 4/11/07 (PB2008-105141).

- MCEER-07-0004 “Modeling Pile Behavior in Large Pile Groups Under Lateral Loading,” by A.M. Dodds and G.R. Martin, 4/16/07(PB2008-105142).
- MCEER-07-0005 “Experimental Investigation of Blast Performance of Seismically Resistant Concrete-Filled Steel Tube Bridge Piers,” by S. Fujikura, M. Bruneau and D. Lopez-Garcia, 4/20/07 (PB2008-105143).
- MCEER-07-0006 “Seismic Analysis of Conventional and Isolated Liquefied Natural Gas Tanks Using Mechanical Analogs,” by I.P. Christovasilis and A.S. Whittaker, 5/1/07, not available.
- MCEER-07-0007 “Experimental Seismic Performance Evaluation of Isolation/Restraint Systems for Mechanical Equipment – Part 1: Heavy Equipment Study,” by S. Fathali and A. Filiatrault, 6/6/07 (PB2008-105144).
- MCEER-07-0008 “Seismic Vulnerability of Timber Bridges and Timber Substructures,” by A.A. Sharma, J.B. Mander, I.M. Friedland and D.R. Allicock, 6/7/07 (PB2008-105145).
- MCEER-07-0009 “Experimental and Analytical Study of the XY-Friction Pendulum (XY-FP) Bearing for Bridge Applications,” by C.C. Marin-Artieda, A.S. Whittaker and M.C. Constantinou, 6/7/07 (PB2008-105191).
- MCEER-07-0010 “Proceedings of the PRC-US Earthquake Engineering Forum for Young Researchers,” Edited by G.C. Lee and X.Z. Qi, 6/8/07 (PB2008-500058).
- MCEER-07-0011 “Design Recommendations for Perforated Steel Plate Shear Walls,” by R. Purba and M. Bruneau, 6/18/07, (PB2008-105192).
- MCEER-07-0012 “Performance of Seismic Isolation Hardware Under Service and Seismic Loading,” by M.C. Constantinou, A.S. Whittaker, Y. Kalpakidis, D.M. Fenz and G.P. Warn, 8/27/07, (PB2008-105193).
- MCEER-07-0013 “Experimental Evaluation of the Seismic Performance of Hospital Piping Subassemblies,” by E.R. Goodwin, E. Maragakis and A.M. Itani, 9/4/07, (PB2008-105194).
- MCEER-07-0014 “A Simulation Model of Urban Disaster Recovery and Resilience: Implementation for the 1994 Northridge Earthquake,” by S. Miles and S.E. Chang, 9/7/07, (PB2008-106426).
- MCEER-07-0015 “Statistical and Mechanistic Fragility Analysis of Concrete Bridges,” by M. Shinozuka, S. Banerjee and S-H. Kim, 9/10/07, (PB2008-106427).
- MCEER-07-0016 “Three-Dimensional Modeling of Inelastic Buckling in Frame Structures,” by M. Schachter and AM. Reinhorn, 9/13/07, (PB2008-108125).
- MCEER-07-0017 “Modeling of Seismic Wave Scattering on Pile Groups and Caissons,” by I. Po Lam, H. Law and C.T. Yang, 9/17/07 (PB2008-108150).
- MCEER-07-0018 “Bridge Foundations: Modeling Large Pile Groups and Caissons for Seismic Design,” by I. Po Lam, H. Law and G.R. Martin (Coordinating Author), 12/1/07 (PB2008-111190).
- MCEER-07-0019 “Principles and Performance of Roller Seismic Isolation Bearings for Highway Bridges,” by G.C. Lee, Y.C. Ou, Z. Liang, T.C. Niu and J. Song, 12/10/07 (PB2009-110466).
- MCEER-07-0020 “Centrifuge Modeling of Permeability and Pinning Reinforcement Effects on Pile Response to Lateral Spreading,” by L.L. Gonzalez-Lagos, T. Abdoun and R. Dobry, 12/10/07 (PB2008-111191).
- MCEER-07-0021 “Damage to the Highway System from the Pisco, Perú Earthquake of August 15, 2007,” by J.S. O’Connor, L. Mesa and M. Nykamp, 12/10/07, (PB2008-108126).
- MCEER-07-0022 “Experimental Seismic Performance Evaluation of Isolation/Restraint Systems for Mechanical Equipment – Part 2: Light Equipment Study,” by S. Fathali and A. Filiatrault, 12/13/07 (PB2008-111192).
- MCEER-07-0023 “Fragility Considerations in Highway Bridge Design,” by M. Shinozuka, S. Banerjee and S.H. Kim, 12/14/07 (PB2008-111193).

- MCEER-07-0024 “Performance Estimates for Seismically Isolated Bridges,” by G.P. Warn and A.S. Whittaker, 12/30/07 (PB2008-112230).
- MCEER-08-0001 “Seismic Performance of Steel Girder Bridge Superstructures with Conventional Cross Frames,” by L.P. Carden, A.M. Itani and I.G. Buckle, 1/7/08, (PB2008-112231).
- MCEER-08-0002 “Seismic Performance of Steel Girder Bridge Superstructures with Ductile End Cross Frames with Seismic Isolators,” by L.P. Carden, A.M. Itani and I.G. Buckle, 1/7/08 (PB2008-112232).
- MCEER-08-0003 “Analytical and Experimental Investigation of a Controlled Rocking Approach for Seismic Protection of Bridge Steel Truss Piers,” by M. Pollino and M. Bruneau, 1/21/08 (PB2008-112233).
- MCEER-08-0004 “Linking Lifeline Infrastructure Performance and Community Disaster Resilience: Models and Multi-Stakeholder Processes,” by S.E. Chang, C. Pasion, K. Tatebe and R. Ahmad, 3/3/08 (PB2008-112234).
- MCEER-08-0005 “Modal Analysis of Generally Damped Linear Structures Subjected to Seismic Excitations,” by J. Song, Y-L. Chu, Z. Liang and G.C. Lee, 3/4/08 (PB2009-102311).
- MCEER-08-0006 “System Performance Under Multi-Hazard Environments,” by C. Kafali and M. Grigoriu, 3/4/08 (PB2008-112235).
- MCEER-08-0007 “Mechanical Behavior of Multi-Spherical Sliding Bearings,” by D.M. Fenz and M.C. Constantinou, 3/6/08 (PB2008-112236).
- MCEER-08-0008 “Post-Earthquake Restoration of the Los Angeles Water Supply System,” by T.H.P. Tabucchi and R.A. Davidson, 3/7/08 (PB2008-112237).
- MCEER-08-0009 “Fragility Analysis of Water Supply Systems,” by A. Jacobson and M. Grigoriu, 3/10/08 (PB2009-105545).
- MCEER-08-0010 “Experimental Investigation of Full-Scale Two-Story Steel Plate Shear Walls with Reduced Beam Section Connections,” by B. Qu, M. Bruneau, C-H. Lin and K-C. Tsai, 3/17/08 (PB2009-106368).
- MCEER-08-0011 “Seismic Evaluation and Rehabilitation of Critical Components of Electrical Power Systems,” S. Ersoy, B. Feizi, A. Ashrafi and M. Ala Saadeghvaziri, 3/17/08 (PB2009-105546).
- MCEER-08-0012 “Seismic Behavior and Design of Boundary Frame Members of Steel Plate Shear Walls,” by B. Qu and M. Bruneau, 4/26/08 . (PB2009-106744).
- MCEER-08-0013 “Development and Appraisal of a Numerical Cyclic Loading Protocol for Quantifying Building System Performance,” by A. Filiatrault, A. Wanitkorkul and M. Constantinou, 4/27/08 (PB2009-107906).
- MCEER-08-0014 “Structural and Nonstructural Earthquake Design: The Challenge of Integrating Specialty Areas in Designing Complex, Critical Facilities,” by W.J. Petak and D.J. Alesch, 4/30/08 (PB2009-107907).
- MCEER-08-0015 “Seismic Performance Evaluation of Water Systems,” by Y. Wang and T.D. O’Rourke, 5/5/08 (PB2009-107908).
- MCEER-08-0016 “Seismic Response Modeling of Water Supply Systems,” by P. Shi and T.D. O’Rourke, 5/5/08 (PB2009-107910).
- MCEER-08-0017 “Numerical and Experimental Studies of Self-Centering Post-Tensioned Steel Frames,” by D. Wang and A. Filiatrault, 5/12/08 (PB2009-110479).
- MCEER-08-0018 “Development, Implementation and Verification of Dynamic Analysis Models for Multi-Spherical Sliding Bearings,” by D.M. Fenz and M.C. Constantinou, 8/15/08 (PB2009-107911).
- MCEER-08-0019 “Performance Assessment of Conventional and Base Isolated Nuclear Power Plants for Earthquake Blast Loadings,” by Y.N. Huang, A.S. Whittaker and N. Luco, 10/28/08 (PB2009-107912).

- MCEER-08-0020 “Remote Sensing for Resilient Multi-Hazard Disaster Response – Volume I: Introduction to Damage Assessment Methodologies,” by B.J. Adams and R.T. Eguchi, 11/17/08 (PB2010-102695).
- MCEER-08-0021 “Remote Sensing for Resilient Multi-Hazard Disaster Response – Volume II: Counting the Number of Collapsed Buildings Using an Object-Oriented Analysis: Case Study of the 2003 Bam Earthquake,” by L. Gusella, C.K. Huyck and B.J. Adams, 11/17/08 (PB2010-100925).
- MCEER-08-0022 “Remote Sensing for Resilient Multi-Hazard Disaster Response – Volume III: Multi-Sensor Image Fusion Techniques for Robust Neighborhood-Scale Urban Damage Assessment,” by B.J. Adams and A. McMillan, 11/17/08 (PB2010-100926).
- MCEER-08-0023 “Remote Sensing for Resilient Multi-Hazard Disaster Response – Volume IV: A Study of Multi-Temporal and Multi-Resolution SAR Imagery for Post-Katrina Flood Monitoring in New Orleans,” by A. McMillan, J.G. Morley, B.J. Adams and S. Chesworth, 11/17/08 (PB2010-100927).
- MCEER-08-0024 “Remote Sensing for Resilient Multi-Hazard Disaster Response – Volume V: Integration of Remote Sensing Imagery and VIEWS™ Field Data for Post-Hurricane Charley Building Damage Assessment,” by J.A. Womble, K. Mehta and B.J. Adams, 11/17/08 (PB2009-115532).
- MCEER-08-0025 “Building Inventory Compilation for Disaster Management: Application of Remote Sensing and Statistical Modeling,” by P. Sarabandi, A.S. Kiremidjian, R.T. Eguchi and B. J. Adams, 11/20/08 (PB2009-110484).
- MCEER-08-0026 “New Experimental Capabilities and Loading Protocols for Seismic Qualification and Fragility Assessment of Nonstructural Systems,” by R. Retamales, G. Mosqueda, A. Filiatrault and A. Reinhorn, 11/24/08 (PB2009-110485).
- MCEER-08-0027 “Effects of Heating and Load History on the Behavior of Lead-Rubber Bearings,” by I.V. Kalpakidis and M.C. Constantinou, 12/1/08 (PB2009-115533).
- MCEER-08-0028 “Experimental and Analytical Investigation of Blast Performance of Seismically Resistant Bridge Piers,” by S.Fujikura and M. Bruneau, 12/8/08 (PB2009-115534).
- MCEER-08-0029 “Evolutionary Methodology for Aseismic Decision Support,” by Y. Hu and G. Dargush, 12/15/08.
- MCEER-08-0030 “Development of a Steel Plate Shear Wall Bridge Pier System Conceived from a Multi-Hazard Perspective,” by D. Keller and M. Bruneau, 12/19/08 (PB2010-102696).
- MCEER-09-0001 “Modal Analysis of Arbitrarily Damped Three-Dimensional Linear Structures Subjected to Seismic Excitations,” by Y.L. Chu, J. Song and G.C. Lee, 1/31/09 (PB2010-100922).
- MCEER-09-0002 “Air-Blast Effects on Structural Shapes,” by G. Ballantyne, A.S. Whittaker, A.J. Aref and G.F. Dargush, 2/2/09 (PB2010-102697).
- MCEER-09-0003 “Water Supply Performance During Earthquakes and Extreme Events,” by A.L. Bonneau and T.D. O’Rourke, 2/16/09 (PB2010-100923).
- MCEER-09-0004 “Generalized Linear (Mixed) Models of Post-Earthquake Ignitions,” by R.A. Davidson, 7/20/09 (PB2010-102698).
- MCEER-09-0005 “Seismic Testing of a Full-Scale Two-Story Light-Frame Wood Building: NEESWood Benchmark Test,” by I.P. Christovasilis, A. Filiatrault and A. Wanitkorkul, 7/22/09 (PB2012-102401).
- MCEER-09-0006 “IDARC2D Version 7.0: A Program for the Inelastic Damage Analysis of Structures,” by A.M. Reinhorn, H. Roh, M. Sivaselvan, S.K. Kunnath, R.E. Valles, A. Madan, C. Li, R. Lobo and Y.J. Park, 7/28/09 (PB2010-103199).
- MCEER-09-0007 “Enhancements to Hospital Resiliency: Improving Emergency Planning for and Response to Hurricanes,” by D.B. Hess and L.A. Arendt, 7/30/09 (PB2010-100924).

- MCEER-09-0008 "Assessment of Base-Isolated Nuclear Structures for Design and Beyond-Design Basis Earthquake Shaking," by Y.N. Huang, A.S. Whittaker, R.P. Kennedy and R.L. Mayes, 8/20/09 (PB2010-102699).
- MCEER-09-0009 "Quantification of Disaster Resilience of Health Care Facilities," by G.P. Cimellaro, C. Fumo, A.M. Reinhorn and M. Bruneau, 9/14/09 (PB2010-105384).
- MCEER-09-0010 "Performance-Based Assessment and Design of Squat Reinforced Concrete Shear Walls," by C.K. Gulec and A.S. Whittaker, 9/15/09 (PB2010-102700).
- MCEER-09-0011 "Proceedings of the Fourth US-Taiwan Bridge Engineering Workshop," edited by W.P. Yen, J.J. Shen, T.M. Lee and R.B. Zheng, 10/27/09 (PB2010-500009).
- MCEER-09-0012 "Proceedings of the Special International Workshop on Seismic Connection Details for Segmental Bridge Construction," edited by W. Phillip Yen and George C. Lee, 12/21/09 (PB2012-102402).
- MCEER-10-0001 "Direct Displacement Procedure for Performance-Based Seismic Design of Multistory Woodframe Structures," by W. Pang and D. Rosowsky, 4/26/10 (PB2012-102403).
- MCEER-10-0002 "Simplified Direct Displacement Design of Six-Story NEESWood Capstone Building and Pre-Test Seismic Performance Assessment," by W. Pang, D. Rosowsky, J. van de Lindt and S. Pei, 5/28/10 (PB2012-102404).
- MCEER-10-0003 "Integration of Seismic Protection Systems in Performance-Based Seismic Design of Woodframed Structures," by J.K. Shinde and M.D. Symans, 6/18/10 (PB2012-102405).
- MCEER-10-0004 "Modeling and Seismic Evaluation of Nonstructural Components: Testing Frame for Experimental Evaluation of Suspended Ceiling Systems," by A.M. Reinhorn, K.P. Ryu and G. Maddaloni, 6/30/10 (PB2012-102406).
- MCEER-10-0005 "Analytical Development and Experimental Validation of a Structural-Fuse Bridge Pier Concept," by S. El-Bahey and M. Bruneau, 10/1/10 (PB2012-102407).
- MCEER-10-0006 "A Framework for Defining and Measuring Resilience at the Community Scale: The PEOPLES Resilience Framework," by C.S. Renschler, A.E. Frazier, L.A. Arendt, G.P. Cimellaro, A.M. Reinhorn and M. Bruneau, 10/8/10 (PB2012-102408).
- MCEER-10-0007 "Impact of Horizontal Boundary Elements Design on Seismic Behavior of Steel Plate Shear Walls," by R. Purba and M. Bruneau, 11/14/10 (PB2012-102409).
- MCEER-10-0008 "Seismic Testing of a Full-Scale Mid-Rise Building: The NEESWood Capstone Test," by S. Pei, J.W. van de Lindt, S.E. Pryor, H. Shimizu, H. Isoda and D.R. Rammer, 12/1/10 (PB2012-102410).
- MCEER-10-0009 "Modeling the Effects of Detonations of High Explosives to Inform Blast-Resistant Design," by P. Sherkar, A.S. Whittaker and A.J. Aref, 12/1/10 (PB2012-102411).
- MCEER-10-0010 "L'Aquila Earthquake of April 6, 2009 in Italy: Rebuilding a Resilient City to Withstand Multiple Hazards," by G.P. Cimellaro, I.P. Christovasilis, A.M. Reinhorn, A. De Stefano and T. Kirova, 12/29/10.
- MCEER-11-0001 "Numerical and Experimental Investigation of the Seismic Response of Light-Frame Wood Structures," by I.P. Christovasilis and A. Filiatrault, 8/8/11 (PB2012-102412).
- MCEER-11-0002 "Seismic Design and Analysis of a Precast Segmental Concrete Bridge Model," by M. Anagnostopoulou, A. Filiatrault and A. Aref, 9/15/11.
- MCEER-11-0003 "Proceedings of the Workshop on Improving Earthquake Response of Substation Equipment," Edited by A.M. Reinhorn, 9/19/11 (PB2012-102413).
- MCEER-11-0004 "LRFD-Based Analysis and Design Procedures for Bridge Bearings and Seismic Isolators," by M.C. Constantinou, I. Kalpakidis, A. Filiatrault and R.A. Ecker Lay, 9/26/11.

- MCEER-11-0005 “Experimental Seismic Evaluation, Model Parameterization, and Effects of Cold-Formed Steel-Framed Gypsum Partition Walls on the Seismic Performance of an Essential Facility,” by R. Davies, R. Retamales, G. Mosqueda and A. Filiatrault, 10/12/11.
- MCEER-11-0006 “Modeling and Seismic Performance Evaluation of High Voltage Transformers and Bushings,” by A.M. Reinhorn, K. Oikonomou, H. Roh, A. Schiff and L. Kempner, Jr., 10/3/11.
- MCEER-11-0007 “Extreme Load Combinations: A Survey of State Bridge Engineers,” by G.C. Lee, Z. Liang, J.J. Shen and J.S. O’Connor, 10/14/11.
- MCEER-12-0001 “Simplified Analysis Procedures in Support of Performance Based Seismic Design,” by Y.N. Huang and A.S. Whittaker.
- MCEER-12-0002 “Seismic Protection of Electrical Transformer Bushing Systems by Stiffening Techniques,” by M. Koliou, A. Filiatrault, A.M. Reinhorn and N. Oliveto, 6/1/12.
- MCEER-12-0003 “Post-Earthquake Bridge Inspection Guidelines,” by J.S. O’Connor and S. Alampalli, 6/8/12.
- MCEER-12-0004 “Integrated Design Methodology for Isolated Floor Systems in Single-Degree-of-Freedom Structural Fuse Systems,” by S. Cui, M. Bruneau and M.C. Constantinou, 6/13/12.
- MCEER-12-0005 “Characterizing the Rotational Components of Earthquake Ground Motion,” by D. Basu, A.S. Whittaker and M.C. Constantinou, 6/15/12.
- MCEER-12-0006 “Bayesian Fragility for Nonstructural Systems,” by C.H. Lee and M.D. Grigoriu, 9/12/12.
- MCEER-12-0007 “A Numerical Model for Capturing the In-Plane Seismic Response of Interior Metal Stud Partition Walls,” by R.L. Wood and T.C. Hutchinson, 9/12/12.
- MCEER-12-0008 “Assessment of Floor Accelerations in Yielding Buildings,” by J.D. Wieser, G. Pekcan, A.E. Zaghi, A.M. Itani and E. Maragakis, 10/5/12.
- MCEER-13-0001 “Experimental Seismic Study of Pressurized Fire Sprinkler Piping Systems,” by Y. Tian, A. Filiatrault and G. Mosqueda, 4/8/13.
- MCEER-13-0002 “Enhancing Resource Coordination for Multi-Modal Evacuation Planning,” by D.B. Hess, B.W. Conley and C.M. Farrell, 2/8/13.
- MCEER-13-0003 “Seismic Response of Base Isolated Buildings Considering Pounding to Moat Walls,” by A. Masroor and G. Mosqueda, 2/26/13.
- MCEER-13-0004 “Seismic Response Control of Structures Using a Novel Adaptive Passive Negative Stiffness Device,” by D.T.R. Pasala, A.A. Sarlis, S. Nagarajaiah, A.M. Reinhorn, M.C. Constantinou and D.P. Taylor, 6/10/13.
- MCEER-13-0005 “Negative Stiffness Device for Seismic Protection of Structures,” by A.A. Sarlis, D.T.R. Pasala, M.C. Constantinou, A.M. Reinhorn, S. Nagarajaiah and D.P. Taylor, 6/12/13.
- MCEER-13-0006 “Emilia Earthquake of May 20, 2012 in Northern Italy: Rebuilding a Resilient Community to Withstand Multiple Hazards,” by G.P. Cimellaro, M. Chiriatti, A.M. Reinhorn and L. Tirca, June 30, 2013.
- MCEER-13-0007 “Precast Concrete Segmental Components and Systems for Accelerated Bridge Construction in Seismic Regions,” by A.J. Aref, G.C. Lee, Y.C. Ou and P. Sideris, with contributions from K.C. Chang, S. Chen, A. Filiatrault and Y. Zhou, June 13, 2013.
- MCEER-13-0008 “A Study of U.S. Bridge Failures (1980-2012),” by G.C. Lee, S.B. Mohan, C. Huang and B.N. Fard, June 15, 2013.
- MCEER-13-0009 “Development of a Database Framework for Modeling Damaged Bridges,” by G.C. Lee, J.C. Qi and C. Huang, June 16, 2013.

- MCEER-13-0010 “Model of Triple Friction Pendulum Bearing for General Geometric and Frictional Parameters and for Uplift Conditions,” by A.A. Sarlis and M.C. Constantinou, July 1, 2013.
- MCEER-13-0011 “Shake Table Testing of Triple Friction Pendulum Isolators under Extreme Conditions,” by A.A. Sarlis, M.C. Constantinou and A.M. Reinhorn, July 2, 2013.
- MCEER-13-0012 “Theoretical Framework for the Development of MH-LRFD,” by G.C. Lee (coordinating author), H.A. Capers, Jr., C. Huang, J.M. Kulicki, Z. Liang, T. Murphy, J.J.D. Shen, M. Shinozuka and P.W.H. Yen, July 31, 2013.
- MCEER-13-0013 “Seismic Protection of Highway Bridges with Negative Stiffness Devices,” by N.K.A. Attary, M.D. Symans, S. Nagarajaiah, A.M. Reinhorn, M.C. Constantinou, A.A. Sarlis, D.T.R. Pasala, and D.P. Taylor, September 3, 2014.
- MCEER-14-0001 “Simplified Seismic Collapse Capacity-Based Evaluation and Design of Frame Buildings with and without Supplemental Damping Systems,” by M. Hamidia, A. Filiatrault, and A. Aref, May 19, 2014.
- MCEER-14-0002 “Comprehensive Analytical Seismic Fragility of Fire Sprinkler Piping Systems,” by Siavash Soroushian, Emmanuel “Manos” Maragakis, Arash E. Zaghi, Alicia Echevarria, Yuan Tian and Andre Filiatrault, August 26, 2014.
- MCEER-14-0003 “Hybrid Simulation of the Seismic Response of a Steel Moment Frame Building Structure through Collapse,” by M. Del Carpio Ramos, G. Mosqueda and D.G. Lignos, October 20, 2014.
- MCEER-14-0005 “Seismic Performance of Steel Plate Shear Walls Considering Various Design Approaches,” by R. Purba and M. Bruneau, October 31, 2014.
- MCEER-14-0006 “Air-Blast Effects on Civil Structures,” by Jinwon Shin, Andrew S. Whittaker, Amjad J. Aref and David Cormie, October 30, 2014.



**EARTHQUAKE ENGINEERING TO EXTREME EVENTS**

University at Buffalo, The State University of New York

133A Ketter Hall ■ Buffalo, New York 14260-4300

Phone: (716) 645-3391 ■ Fax: (716) 645-3399

Email: [mceer@buffalo.edu](mailto:mceer@buffalo.edu) ■ Web: <http://mceer.buffalo.edu>



**University at Buffalo** *The State University of New York*

ISSN 1520-295X